

CHARACTERIZATION OF FLORIDA LIGHTNING WITH EMPHASIS ON THE
PRELIMINARY BREAKDOWN PROCESS, BIPOLAR LIGHTNING, AND LIGHTNING
INTERACTION WITH A 257-M TOWER

By

YANAN ZHU

A DISSERTATION PRESENTED TO THE GRADUATE SCHOOL
OF THE UNIVERSITY OF FLORIDA IN PARTIAL FULFILLMENT
OF THE REQUIREMENTS FOR THE DEGREE OF
DOCTOR OF PHILOSOPHY

UNIVERSITY OF FLORIDA

2017

© 2017 Yanan Zhu

To my mother, Ping Liu, and my father, Ruiming Zhu

ACKNOWLEDGMENTS

I would like to thank Dr. Vladimir Rakov for giving me the opportunity to do lightning research in the Lightning Lab at the University of Florida. I appreciate his inspiration and patient guidance in my research work.

I would like to thank Dr. Martin Uman, Dr. Robert Moore, Dr. Douglas Jordan, and Dr. William Hager for serving on my supervisory committee.

I would like to thank Shreeharsh Mallick for making great contributions to upgrade the Lightning Observatory in Gainesville (LOG) and the Golf Course site (GC). I would like to thank Manh Tran for operating the LOG and providing the LOG data for my research work. I would like to thank Vijaya Somu, Keith Rambo, and Sam Brake for helping with maintaining the GC site. I would like to thank Dr. Weitao Lu for providing optical data and useful comments for my research. I would like to thank Shuji Fujimaru and Daniel Kotovsky who are always willing to help and give suggestions. I would like to thank John Pilkey for providing LMA data for the fast-stepped leader events. I also thank Terry Ngin, John Pilkey, William Gamarota, Jamie Caicedo, Daniel Kotovksy, Felipe Carvalho, Robert Wilkes, Brian Hare, Dr. Jordan, and Dr. Uman for acquiring and providing the rocket-triggered lightning data for the ENTLN performance evaluation study. I would like to thank Amitabh Nag and William Brooks of Vaisala Inc. for providing NLDN data. I would also like to thank Christopher Sloop, Stan Heckman, Charlie Liu, and Michael Stock of Earth Networks for providing ENTLN data and other support needed to complete the ENTLN performance evaluation study.

I would also extend my deepest thanks to my beautiful fiancée and my wonderful parents for their forever supports and encouragement.

TABLE OF CONTENTS

	<u>page</u>
ACKNOWLEDGMENTS	4
LIST OF TABLES	8
LIST OF FIGURES	10
ABSTRACT.....	24
CHAPTER	
1 INTRODUCTION	26
1.1 Cloud-to-Ground Lightning	26
1.2 Rocket-Triggered Lightning	28
1.3 Preliminary Breakdown	30
2 RESEARCH FACILITIES	33
2.1 Lightning Observatory in Gainesville (LOG)	33
2.2 Golf Course Site in Starke (GC)	36
2.3 Camp Blanding Facility (CB)	37
3 CHARACTERIZATION OF FLORIDA NEGATIVE CLOUD-TO-GROUND LIGHTNING	40
3.1 Literature Review.....	40
3.2 Data	41
3.3 Results	42
3.3.1 Multiplicity and Percentage of Single-Stroke Flashes	42
3.3.2 Interstroke Interval and Flash Duration	43
3.3.3 First to Subsequent Return Stroke Field Peak Ratio.....	46
3.3.4 Variation of Lightning Parameters from One Storm to Another	48
3.4 Summary	49
4 ELECTRIC FIELD SIGNATURES OF PRELIMINARY BREAKDOWN AND AUTOMATED ANALYSIS FOR HIGH-INTENSITY EVENTS	51
4.1 Literature Review	51
4.2 Factors Affecting Detectability of PB Pulse Trains	54
4.2.1 Signal/Noise Ratio of Recording System.....	54
4.2.2 Type of Storm	55
4.2.3 Prospective Return-Stroke Peak Current	56
4.2.4 Distance from the Strike-Point Location to the Observation Point	59

4.3	Automated Analysis of Preliminary Breakdown and Return Stroke Processes in High-Intensity Negative Lightning Discharges	59
4.3.1	Data	59
4.3.2	Methodology	60
4.3.3	Characteristics of PB Pulse Trains in High-Intensity Negative Flashes	66
4.3.4	Correlation between Parameters of Preliminary Breakdown and Return Stroke Processes.....	69
4.4	Summary	77
5	A SUBSEQUENT POSITIVE STROKE DEVELOPING IN THE CHANNEL OF PRECEEDING NEGATIVE STROKE AND CONTAINING BIPOLAR CONTINUING CURRENT.....	79
5.1	Literature Review.....	79
5.2	Instrumentation	80
5.3	Observations and Analysis	81
5.3.1	General Description	81
5.3.2	Characteristics of the Negative and Positive Leaders	87
5.4	Discussion	89
5.5	Summary	92
6	OPTICAL AND ELECTRIC FIELD SIGNATURES OF LIGHTNING INTERACTION WITH THE 257-M TOWER IN FLORIDA.....	94
6.1	Literature Review.....	94
6.2	Observations and Analysis.....	99
6.2.1	General Description of two Flashes Terminated on the 257-m and 60-m Towers in Florida	101
6.2.2	NLDN Responses to the 257-m and 60-m Tower Strokes.....	103
6.2.3	High-Speed Camera and Electric Field Data for Eight Negative Strokes of Flashes 1593 and 1594	104
6.3	Summary	108
7	MODELING OF LIGHTNING INTERACTION WITH THE TOWER.....	111
7.1	Literature Review.....	111
7.2	Model Description.....	114
7.3	Sensitivity Analysis.....	117
7.4	Modeling of Lightning Events Terminated on the 257-m Tower	124
7.4	Summary	130
8	NATIONAL LIGHTNING DETECTION NETWORK RESPONSES TO NATURAL LIGHTNING BASED ON GROUND-TRUTH DATA ACQUIRED AT LOG	132
8.1	Literature Review.....	132
8.2	Data and Methodology	134
8.3	Analysis and Discussion	143
8.3.1	Detection Efficiency and Classification Accuracy of IC Events	143

8.3.2 Detection Efficiency and Classification Accuracy of CG Strokes.....	145
8.4 Summary	146
9 EVALUATION OF ENTLN PERFORMANCE CHARACTERISTICS BASED ON THE NATURAL AND ROCKET-TRIGGERED LIGHTNING DATA ACQUIRED IN FLORIDA	149
9.1 Literature Review.....	149
9.2 Data and Methodology.....	151
9.3 Analysis and Discussion	155
9.3.1 Natural Lightning	155
9.3.2 Rocket-Triggered Lightning	157
9.4 Summary	162
10 SUMMARY OF RESULTS AND RECOMMENDATIONS FOR FUTURE RESEARCH	164
10.1 Summary of Results	164
10.2 Recommendations for Future Research	167
APPENDIX	
A TWO-STATION MEASUREMENTS OF ROCKET-TRIGGERED LIGHTNING ELECTRIC FIELD WAVEFORMS (2013-2016)	169
B TWO-STATION MEASUREMENTS OF ELECTRIC FIELD WAVEFORMS OF NATURAL NEGATIVE CLOUD-TO-GROUND LIGHTNING	351
C TWO-STATION MEASUREMENTS OF ELECTRIC FIELD WAVEFORMS OF NATURAL POSITIVE CLOUD-TO-GROUND LIGHTNING.....	395
D HIGH-SPEED VIDEO RECORDS OF THE TWO FLASHES TERMINATED ON THE 257-M TOWER	417
LIST OF REFERENCES	429
BIOGRAPHICAL SKETCH	439

LIST OF TABLES

Table

	<u>page</u>
3-1 Summary of multiplicity of negative flashes and percentage of single-stroke flashes in different regions	44
3-2 Summary of geometric mean interstroke intervals and flash durations.....	46
3-3 Summary of statistics on the ratio of the first to subsequent return stroke field peaks	47
3-4 Variation of lightning parameters from one storm to another	50
4-1 Percentages of flashes with detectable PB pulses before and after filtering for 17 storms	55
4-2 Characterization of PB pulses in 3077 negative flashes each containing a single PB pulse train.....	65
4-3 Summary of short PB-RS interval events	70
5-1 Comparison of bipolar flashes with a positive stroke following the negative-stroke channel	92
6-1 NLDN data on 8 negative strokes in flashes 1593 and 1594 terminated on the 257-m tower.	102
6-2 NLDN data on the first, positive stroke of bipolar flash 1594, which terminated on the 60-m tower, located 3.6 km from the 257-m tower.	102
6-3 Electric field waveform parameters for the seven negative strokes terminated on the 257-m tower.	107
6-4 Characteristics of narrow bipolar electric field waveforms observed in different studies	110
7-1 Current equations for transmission-line-type return stroke models.....	112
7-2 Model input parameters used for computing electric field waveforms shown in Figure 7-11	126
7-3 Model input parameters used for computing electric field waveforms shown in Figure 7-13 and NLDN-reported peak current for the 7 strokes	128
8-1 Summary of the Ground-Truth Dataset for IC Events.....	137
8-2 Summary of the Ground-Truth Dataset for CG Strokes	141

8-3	Summary of the NLDN Detection Efficiency (DE) and Classification Accuracy (CA) for IC Events	144
8-4	Summary of the NLDN Detection Efficiency (DE) and Classification Accuracy (CA) for CG Strokes	145
8-5	NLDN DE and CA for CG strokes obtained in different studies	148
9-1	Summary of ground-truth datasets for natural and rocket-triggered lightning acquired in Florida and used in this study	152
9-2	Summary of the ENTLN performance characteristics evaluated using natural lightning data	156
9-3	Summary of the estimated values of ENTLN stroke DE and CA for different types of strokes in natural lightning.....	156
9-4	Summary of the ENTLN performance characteristics evaluated using rocket-triggered lightning data	158
9-5	Comparison of ENTLN performance characteristics evaluated for four different processors using rocket-triggered lightning data	162
A-1	Inventory of two-station (LOG-GC) waveforms of rocket-triggered flashes from 2013 to 2016	169
B-1	Inventory of two-station (LOG-GC) field measurements for 10 natural negative cloud-to-ground lightning	351
C-1	Inventory of two-station (LOG-GC) field measurements for 10 natural positive cloud-to-ground lightning	395

LIST OF FIGURES

<u>Figure</u>		<u>page</u>
1-1	Four types of cloud-to-ground lightning.....	26
1-2	A nearly complete sequence of processes of a typical downward negative flash.	28
1-3	Sequence of events in classical triggered lightning.	29
2-1	Overview of Lightning Observatory in Gainesville (LOG), Florida.	33
2-2	Photographs of Lightning Observatory in Gainesville.	34
2-3	Three-station and two-station trigger schemes.	36
2-4	Overview of the Golf Course (GC) site.	37
2-5	Overview of the ICLRT. Buildings and measurement stations are labeled.....	38
3-1	Histogram of the number of strokes per flash (multiplicity).	43
3-2	Histogram of the interstroke interval.	45
3-3	Histogram of the flash duration.	45
3-4	Histogram of the ratio of the first to subsequent return stroke field peaks.....	47
3-5	Normalized electric field peaks for strokes of different order.	48
4-1	Schematic representation of four types of lightning (left) and the expected electric field waveforms (right).	51
4-2	Locations of 478 flashes (first strokes only) recorded at LOG and reported by the NLDN.	53
4-3	Comparison of the electric field waveforms before and after filtering.....	54
4-4	Percentage of flashes with detectable PB pulse trains versus peak current.	57
4-5	Percentage of flashes with detectable PB pulse trains versus distance.....	58
4-6	Flowchart of the automated data processing algorithm.	61
4-7	An example of the output figure produced by the automated data processing algorithm	64
4-8	NLDN-reported locations of the 5498 negative first strokes within 50 to 500 km of LOG.	65

4-9	Histogram of NLDN-reported peak currents for the 3496 negative first strokes in flashes with detectable PB pulse trains.....	66
4-10	Histogram of PB/RS pulse peak ratio for the 3077 flashes.	67
4-11	Histogram of PB-RS interval for the 3077 flashes.	68
4-12	Histogram of PB pulse train duration for the 3077 flashes.....	68
4-13	Histogram of bipolar pulse width in the 3077 flashes.	69
4-14	PB-RS interval versus NLDN-reported RS peak current for 3077 negative first strokes.	71
4-15	PB-RS interval versus NLDN-reported RS peak current for 3363 negative first strokes.	72
4-16	Peak of the largest PB pulse normalized to 100 km versus NLDN-reported RS peak current for the 3077 negative first strokes.	73
4-17	Peak of the largest PB pulse normalized to 100 km versus NLDN-reported RS peak current for the 3363 negative first strokes.	74
4-18	Peak of the largest PB pulse normalized to 100 km versus PB-RS interval for the 3077 negative first strokes.	75
4-19	Peak of the largest PB pulse normalized to 100 km versus PB-RS interval for the 3363 negative first strokes.	76
5-1	Composite Phantom images of the negative first stroke (left panel labeled -CG) and the positive second stroke (right panel labeled +CG).....	83
5-2	Electric field and dE/dt records of the bipolar flash.	84
5-3	The frame-to-frame 2D speeds of the negative stepped leader (L1) and the following positive leader (L2) versus height of the leader tip above ground.....	88
5-4	Sequence of events that lead to a bipolar flash with the negative second stroke initiated in a decayed branch of positive leader.....	89
6-1	Current derivative, current, electric field, and magnetic field records of the 2 nd stroke of the flash striking the 553-m CN tower on August 19 th , 2015.....	96
6-2	The observed and simulated “ground-to-cloud” (GC) discharge.	97
6-3	Current and electric field records of a negative lightning stroke terminated on the 100-m Gaisberg tower.....	98

6-4	Electric field waveforms of a typical LBE recorded by nine stations at distances ranging from 37.5 to 236.1 km in winter in Japan.....	98
6-5	A subsequent return stroke terminated on the Tokoyo Skytree showing the narrow bipolar signature in electric field records.....	99
6-6	Simulated electric field waveforms of LBEs at 100 km.....	100
6-7	Locations of strike points reported by the NLDN for 8 negative strokes terminated on the 257-m tower.	103
6-8	First video frames showing the channel of each of the eight negative strokes terminated on the 257-m tower.	105
6-9	Electric field waveforms of 8 negative strokes terminated on the 257-m tower.	106
6-10	Measurements (definitions) of electric field waveform parameters.	107
7-1	Measured current waveform (black line) associated with the first return stroke in a downward flash recorded at the Santis tower.	114
7-2	Transmission line representation of lightning strike to a tall object.	116
7-3	Typical current waveform of subsequent stroke (left panel) and the computed electric field (right panel) at a distance of 10 km from the tower.	119
7-4	Similar to Figure 7-3, but for symmetric Gaussian waveform.	119
7-5	The asymmetric Gaussian waveforms with different rise times and fall times and their corresponding simulated electric field waveforms.	121
7-6	Electric field waveforms computed for different reflection coefficients at the tower top (ρ_t) and tower bottom (ρ_g).	121
7-7	Electric field waveforms computed for different heights of the strike object.	123
7-8	Electric field waveforms computed for different return-stroke speeds.	123
7-9	Electric field waveforms computed for different return-stroke models.	124
7-10	The current waveforms used for computing the electric field waveforms shown in Figure 7-11.	125
7-11	The measured and computed electric field waveforms. The corresponding I_{sc} for each event is shown in Figure 7-10.	126
7-12	The current waveforms (with continuing current components) used for computing the electric field waveforms shown in Figure 7-13.	127

7-13	The measured and computed electric field waveforms. The corresponding I_{sc} for each event is shown in Figure 7-12.....	129
8-1	Example of an isolated IC event.....	136
8-2	Examples of PB pulse trains in negative (left panels) and positive (right panels) CG flashes.....	137
8-3	An example of regular pulse burst (RPB) that occurred in the later stage of a K-change.....	138
8-4	Histogram of durations of 153 IC events.....	139
8-5	Flow chart used to determine the detection efficiency and classification accuracy for IC events.....	140
8-6	An example of ground-truth data for a two-stroke CG flash.....	142
9-1	Locations of LOG (gray square), CB (yellow square) and ENTLN sensors (red circles) in the Florida region.....	150
9-2	Histogram of peak currents for 171 return strokes in 18 flashes triggered using the rocket-and-wire technique at Camp Blanding, Florida.....	153
9-3	Flowchart showing the methodology to determine the detection efficiency and classification accuracy for natural cloud-to-ground lightning.....	155
9-4	Histograms of absolute (upper panels) and signed (lower panels) peak current estimation errors for old (left panels) and new (right panels) processors.....	159
9-5	Scatterplots of peak current estimated by the ENTLN vs. ground-truth peak current measured at CB for old (left panel) and new (right panel) processors.....	160
9-6	Histograms of location error for the old (left panel) and new (right panel) processors.....	160
9-7	Plots of ENTLN-reported locations for old (left panels) and new (right panels) processors.....	161
A-1	Two-station electric field waveforms of flash UF 13-31.....	171
A-2	Two-station electric field waveforms of the RS1 of flash UF 13-31.....	172
A-3	Two-station electric field waveforms of the RS2 of flash UF 13-31.....	173
A-4	Two-station electric field waveforms of the RS3 of flash UF 13-31.....	174
A-5	Two-station electric field waveforms of the RS4 of flash UF 13-31.....	175
A-6	Two-station electric field waveforms of the RS5 of flash UF 13-31.....	176

A-7	Two-station electric field waveforms of the RS6 of flash UF 13-31.....	177
A-8	Two-station electric field waveforms of the RS7 of flash UF 13-31.....	178
A-9	Two-station electric field waveforms of the RS8 of flash UF 13-31.....	179
A-10	Two-station electric field waveforms of the RS9 of flash UF 13-31.....	180
A-11	Two-station electric field waveforms of the RS10 of flash UF 13-31.....	181
A-12	Two-station electric field waveforms of the RS11 of flash UF 13-31.....	182
A-13	Two-station electric field waveforms of flash UF 13-33.....	183
A-14	Two-station electric field waveforms of the RS1 of flash UF 13-33.....	184
A-15	Two-station electric field waveforms of the RS2 of flash UF 13-33.....	185
A-16	Two-station electric field waveforms of the RS3 of flash UF 13-33.....	186
A-17	Two-station electric field waveforms of the RS4 of flash UF 13-33.....	187
A-18	Two-station electric field waveforms of the RS5 of flash UF 13-33.....	188
A-19	Two-station electric field waveforms of the RS6 of flash UF 13-33.....	189
A-20	Two-station electric field waveforms of flash UF 13-34.....	190
A-21	Two-station electric field waveforms of the RS1 of flash UF 13-34.....	191
A-22	Two-station electric field waveforms of the RS2 of flash UF 13-34.....	192
A-23	Two-station electric field waveforms of the RS3 of flash UF 13-34.....	193
A-24	Two-station electric field waveforms of the RS4 of flash UF 13-34.....	194
A-25	Two-station electric field waveforms of flash UF 14-01.....	195
A-26	Two-station electric field waveforms of the RS1 of flash UF 14-01.....	196
A-27	Two-station electric field waveforms of flash UF 14-05.....	197
A-28	Two-station electric field waveforms of the RS1 of flash UF 14-05.....	198
A-30	Two-station electric field waveforms of the RS3 of flash UF 14-05.....	200
A-31	Two-station electric field waveforms of the RS4 of flash UF 14-05.....	201
A-32	Two-station electric field waveforms of the RS5 of flash UF 14-05.....	202

A-33	Two-station electric field waveforms of flash UF 14-06.....	203
A-34	Two-station electric field waveforms of the RS1 of flash UF 14-06.....	204
A-35	Two-station electric field waveforms of the RS2 of flash UF 14-06.....	205
A-36	Two-station electric field waveforms of flash UF 14-07.....	206
A-37	Two-station electric field waveforms of the RS1 of flash UF 14-07.....	207
A-38	Two-station electric field waveforms of the RS2 of flash UF 14-07.....	208
A-39	Two-station electric field waveforms of the RS3 of flash UF 14-07.....	209
A-40	Two-station electric field waveforms of flash UF 14-08.....	210
A-41	Two-station electric field waveforms of the RS1 of flash UF 14-08.....	211
A-42	Two-station electric field waveforms of the RS2 of flash UF 14-08.....	212
A-43	Two-station electric field waveforms of the RS3 of flash UF 14-08.....	213
A-44	Two-station electric field waveforms of the RS4 of flash UF 14-08.....	214
A-45	Two-station electric field waveforms of flash UF 14-11.....	215
A-46	Two-station electric field waveforms of the RS1 of flash UF 14-11.....	216
A-47	Two-station electric field waveforms of the RS2 of flash UF 14-11.....	217
A-48	Two-station electric field waveforms of the RS3 of flash UF 14-11.....	218
A-49	Two-station electric field waveforms of the RS4 of flash UF 14-11.....	219
A-50	Two-station electric field waveforms of the RS5 of flash UF 14-11.....	220
A-51	Two-station electric field waveforms of the RS6 of flash UF 14-11.....	221
A-52	Two-station electric field waveforms of the RS7 of flash UF 14-11.....	222
A-53	Two-station electric field waveforms of the RS8 of flash UF 14-11.....	223
A-54	Two-station electric field waveforms of flash UF 14-12.....	224
A-55	Two-station electric field waveforms of the RS1 of flash UF 14-12.....	225
A-56	Two-station electric field waveforms of the RS2 of flash UF 14-12.....	226
A-57	Two-station electric field waveforms of the RS3 of flash UF 14-12.....	227

A-58	Two-station electric field waveforms of the RS4 of flash UF 14-12.....	228
A-59	Two-station electric field waveforms of the RS5 of flash UF 14-12.....	229
A-60	Two-station electric field waveforms of the RS6 of flash UF 14-12.....	230
A-61	Two-station electric field waveforms of the RS7 of flash UF 14-12.....	231
A-62	Two-station electric field waveforms of flash UF 14-35.....	232
A-63	Two-station electric field waveforms of the RS1 of flash UF 14-35.....	233
A-64	Two-station electric field waveforms of the RS2 of flash UF 14-35.....	234
A-65	Two-station electric field waveforms of the RS3 of flash UF 14-35.....	235
A-66	Two-station electric field waveforms of the RS4 of flash UF 14-35.....	236
A-67	Two-station electric field waveforms of flash UF 14-36.....	237
A-68	Two-station electric field waveforms of the RS1 of flash UF 14-36.....	238
A-69	Two-station electric field waveforms of the RS2 of flash UF 14-36.....	239
A-70	Two-station electric field waveforms of flash UF 14-43.....	240
A-71	Two-station electric field waveforms of the RS1 of flash UF 14-43.....	241
A-72	Two-station electric field waveforms of the RS2 of flash UF 14-43.....	242
A-73	Two-station electric field waveforms of the RS3 of flash UF 14-43.....	243
A-74	Two-station electric field waveforms of the RS4 of flash UF 14-43.....	244
A-75	Two-station electric field waveforms of the RS5 of flash UF 14-43.....	245
A-76	Two-station electric field waveforms of the RS6 of flash UF 14-43.....	246
A-77	Two-station electric field waveforms of the RS7 of flash UF 14-43.....	247
A-78	Two-station electric field waveforms of flash UF 14-51.....	248
A-79	Two-station electric field waveforms of the RS1 of flash UF 14-51.....	249
A-80	Two-station electric field waveforms of the RS2 of flash UF 14-51.....	250
A-81	Two-station electric field waveforms of the RS3 of flash UF 14-51.....	251
A-82	Two-station electric field waveforms of the RS4 of flash UF 14-51.....	252

A-83	Two-station electric field waveforms of the RS5 of flash UF 14-51.....	253
A-84	Two-station electric field waveforms of the RS6 of flash UF 14-51.....	254
A-85	Two-station electric field waveforms of the RS7 of flash UF 14-51.....	255
A-86	Two-station electric field waveforms of the RS8 of flash UF 14-51.....	256
A-87	Two-station electric field waveforms of flash UF 14-52.....	257
A-88	Two-station electric field waveforms of the RS1 of flash UF 14-52.....	258
A-89	Two-station electric field waveforms of the RS2 of flash UF 14-52.....	259
A-90	Two-station electric field waveforms of the RS3 of flash UF 14-52.....	260
A-91	Two-station electric field waveforms of the RS4 of flash UF 14-52.....	261
A-92	Two-station electric field waveforms of the RS5 of flash UF 14-52.....	262
A-93	Two-station electric field waveforms of flash UF 14-53.....	263
A-94	Two-station electric field waveforms of the RS1 of flash UF 14-53.....	264
A-95	Two-station electric field waveforms of the RS2 of flash UF 14-53.....	265
A-96	Two-station electric field waveforms of the RS3 of flash UF 14-53.....	266
A-97	Two-station electric field waveforms of the RS4 of flash UF 14-53.....	267
A-98	Two-station electric field waveforms of the RS5 of flash UF 14-53.....	268
A-99	Two-station electric field waveforms of flash UF 15-11.....	269
A-100	Two-station electric field waveforms of the RS1 of flash UF 15-11.....	270
A-101	Two-station electric field waveforms of the RS2 of flash UF 15-11.....	271
A-102	Two-station electric field waveforms of flash UF 15-12.....	272
A-103	Two-station electric field waveforms of the RS1 of flash UF 15-12.....	273
A-104	Two-station electric field waveforms of the RS2 of flash UF 15-12.....	274
A-105	Two-station electric field waveforms of the RS3 of flash UF 15-12.....	275
A-106	Two-station electric field waveforms of the RS4 of flash UF 15-12.....	276
A-107	Two-station electric field waveforms of the RS5 of flash UF 15-12.....	277

A-108	Two-station electric field waveforms of flash UF 15-15.....	278
A-109	Two-station electric field waveforms of the RS1 of flash UF 15-15.....	279
A-110	Two-station electric field waveforms of the RS2 of flash UF 15-15.....	280
A-111	Two-station electric field waveforms of the RS3 of flash UF 15-15.....	281
A-112	Two-station electric field waveforms of the RS4 of flash UF 15-15.....	282
A-113	Two-station electric field waveforms of the RS5 of flash UF 15-15.....	283
A-114	Two-station electric field waveforms of the RS6 of flash UF 15-15.....	284
A-115	Two-station electric field waveforms of the RS7 of flash UF 15-15.....	285
A-116	Two-station electric field waveforms of the RS8 of flash UF 15-15.....	286
A-117	Two-station electric field waveforms of flash UF 15-16.....	287
A-118	Two-station electric field waveforms of the RS1 of flash UF 15-16.....	288
A-119	Two-station electric field waveforms of the RS2 of flash UF 15-16.....	289
A-120	Two-station electric field waveforms of the RS3 of flash UF 15-16.....	290
A-121	Two-station electric field waveforms of the RS4 of flash UF 15-16.....	291
A-122	Two-station electric field waveforms of the RS5 of flash UF 15-16.....	292
A-123	Two-station electric field waveforms of the RS6 of flash UF 15-16.....	293
A-124	Two-station electric field waveforms of the RS7 of flash UF 15-16.....	294
A-125	Two-station electric field waveforms of the RS8 of flash UF 15-16.....	295
A-126	Two-station electric field waveforms of the RS9 of flash UF 15-16.....	296
A-127	Two-station electric field waveforms of the RS10 of flash UF 15-16.....	297
A-128	Two-station electric field waveforms of the RS11 of flash UF 15-16.....	298
A-129	Two-station electric field waveforms of the RS12 of flash UF 15-16.....	299
A-130	Two-station electric field waveforms of the RS13 of flash UF 15-16.....	300
A-131	Two-station electric field waveforms of the RS14 of flash UF 15-16.....	301
A-132	Two-station electric field waveforms of flash UF 15-20.....	302

A-133	Two-station electric field waveforms of the RS1 of flash UF 15-20.....	303
A-134	Two-station electric field waveforms of the RS2 of flash UF 15-20.....	304
A-135	Two-station electric field waveforms of flash UF 15-25.....	305
A-136	Two-station electric field waveforms of the RS1 of flash UF 15-25.....	306
A-137	Two-station electric field waveforms of the RS2 of flash UF 15-25.....	307
A-138	Two-station electric field waveforms of the RS3 of flash UF 15-25.....	308
A-139	Two-station electric field waveforms of the RS4 of flash UF 15-25.....	309
A-140	Two-station electric field waveforms of flash UF 15-26.....	310
A-141	Two-station electric field waveforms of the RS1 of flash UF 15-26.....	311
A-142	Two-station electric field waveforms of the RS2 of flash UF 15-26.....	312
A-143	Two-station electric field waveforms of the RS3 of flash UF 15-26.....	313
A-144	Two-station electric field waveforms of the RS4 of flash UF 15-26.....	314
A-145	Two-station electric field waveforms of the RS5 of flash UF 15-26.....	315
A-146	Two-station electric field waveforms of the RS6 of flash UF 15-26.....	316
A-147	Two-station electric field waveforms of the RS7 of flash UF 15-26.....	317
A-148	Two-station electric field waveforms of the RS8 of flash UF 15-26.....	318
A-149	Two-station electric field waveforms of flash UF 15-38.....	319
A-150	Two-station electric field waveforms of the RS1 of flash UF 15-38.....	320
A-151	Two-station electric field waveforms of the RS2 of flash UF 15-38.....	321
A-152	Two-station electric field waveforms of the RS3 of flash UF 15-38.....	322
A-153	Two-station electric field waveforms of the RS4 of flash UF 15-38.....	323
A-154	Two-station electric field waveforms of the RS5 of flash UF 15-38.....	324
A-155	Two-station electric field waveforms of flash UF 15-39.....	325
A-156	Two-station electric field waveforms of the RS1 of flash UF 15-39.....	326
A-157	Two-station electric field waveforms of the RS2 of flash UF 15-39.....	327

A-158	Two-station electric field waveforms of the RS3 of flash UF 15-39.....	328
A-159	Two-station electric field waveforms of the RS4 of flash UF 15-39.....	329
A-160	Two-station electric field waveforms of the RS5 of flash UF 15-39.....	330
A-161	Two-station electric field waveforms of the RS6 of flash UF 15-39.....	331
A-162	Two-station electric field waveforms of flash UF 15-41.....	332
A-163	Two-station electric field waveforms of the RS1 of flash UF 15-41.....	333
A-164	Two-station electric field waveforms of the RS2 of flash UF 15-41.....	334
A-165	Two-station electric field waveforms of the RS3 of flash UF 15-41.....	335
A-166	Two-station electric field waveforms of the RS4 of flash UF 15-41.....	336
A-167	Two-station electric field waveforms of the RS5 of flash UF 15-41.....	337
A-168	Two-station electric field waveforms of flash UF 15-42.....	338
A-169	Two-station electric field waveforms of the RS1 of flash UF 15-42.....	339
A-170	Two-station electric field waveforms of the RS2 of flash UF 15-42.....	340
A-171	Two-station electric field waveforms of the RS3 of flash UF 15-42.....	341
A-172	Two-station electric field waveforms of the RS4 of flash UF 15-42.....	342
A-173	Two-station electric field waveforms of the RS5 of flash UF 15-42.....	343
A-174	Two-station electric field waveforms of the RS6 of flash UF 15-42.....	344
A-175	Two-station electric field waveforms of flash UF 15-43.....	345
A-176	Two-station electric field waveforms of the RS1 of flash UF 15-43.....	346
A-177	Two-station electric field waveforms of the RS2 of flash UF 15-43.....	347
A-178	Two-station electric field waveforms of the RS3 of flash UF 15-43.....	348
A-179	Two-station electric field waveforms of flash UF 16-04.....	349
A-180	Two-station electric field waveforms of the RS1 of flash UF 16-0.....	350
B-1	Two-station electric field waveforms of flash 00389.	352
B-2	Two-station electric field waveforms of RS1 of flash 00389.	353

B-3	Two-station electric field waveforms of RS2 of flash 00389	354
B-4	Two-station electric field waveforms of RS3 of flash 00389	355
B-5	Two-station electric field waveforms of flash 00390	356
B-6	Two-station electric field waveforms of RS1 of flash 00390	357
B-7	Two-station electric field waveforms of RS2 of flash 00390	358
B-8	Two-station electric field waveforms of RS3 of flash 00390	359
B-9	Two-station electric field waveforms of flash 00467	360
B-10	Two-station electric field waveforms of the RS1 of flash 00467	361
B-12	Two-station electric field waveforms of the RS3 of flash 00467	363
B-13	Two-station electric field waveforms of flash 00468	364
B-14	Two-station electric field waveforms of the RS1 of flash 00468	365
B-15	Two-station electric field waveforms of the RS2 of flash 00468	366
B-16	Two-station electric field waveforms of the RS3 of flash 00468	367
B-17	Two-station electric field waveforms of the RS4 of flash 00468	368
B-18	Two-station electric field waveforms of flash 00491	369
B-19	Two-station electric field waveforms of the RS1 of flash 00491	370
B-20	Two-station electric field waveforms of the RS2 of flash 00491	371
B-21	Two-station electric field waveforms of the RS3 of flash 00491	372
B-22	Two-station electric field waveforms of the RS4 of flash 00491	373
B-23	Two-station electric field waveforms of flash 00532	374
B-24	Two-station electric field waveforms of the RS1 of flash 00532	375
B-25	Two-station electric field waveforms of the RS2 of flash 00532	376
B-26	Two-station electric field waveforms of the RS3 of flash 00532	377
B-27	Two-station electric field waveforms of the RS4 of flash 00532	378
B-28	Two-station electric field waveforms of flash 00537	379

B-29	Two-station electric field waveforms of the RS1 of flash 00537.....	380
B-30	Two-station electric field waveforms of the RS2 of flash 00537.....	381
B-31	Two-station electric field waveforms of flash 00564.	382
B-32	Two-station electric field waveforms of the RS1 of flash 00564.	383
B-33	Two-station electric field waveforms of the RS2 of flash 00564.	384
B-34	Two-station electric field waveforms of the RS3 of flash 00564.	385
B-35	Two-station electric field waveforms of the RS4 of flash 00564.	386
B-36	Two-station electric field waveforms of the RS5 of flash 00564.	387
B-37	Two-station electric field waveforms of flash 00569.	388
B-38	Two-station electric field waveforms of the RS1 of flash 00569.	389
B-39	Two-station electric field waveforms of the RS2 of flash 00569.	390
B-40	Two-station electric field waveforms of the RS3 of flash 00569.	391
B-41	Two-station electric field waveforms of the RS4 of flash 00569.	392
B-42	Two-station electric field waveforms of flash 00620.	393
B-43	Two-station electric field waveforms of the RS1 of flash 00620	394
B-44	Two-station electric field waveforms of flash 00436.	396
B-45	Two-station electric field waveforms of the RS1 of flash 00436.	397
B-46	Two-station electric field waveforms of flash 00438.	398
B-47	Two-station electric field waveforms of the RS1 of flash 00438.	399
B-48	Two-station electric field waveforms of flash 00453.	400
B-49	Two-station electric field waveforms of the RS1 of flash 00453.	401
B-50	Two-station electric field waveforms of flash 00456.	402
B-51	Two-station electric field waveforms of the RS1 of flash 00456.	403
B-52	Two-station electric field waveforms of flash 00477.	404
B-53	Two-station electric field waveforms of the RS1 of flash 00477.	405

B-54	Two-station electric field waveforms of flash 00577	406
B-55	Two-station electric field waveforms of the RS1 of flash 00577.....	407
B-56	Two-station electric field waveforms of flash 00580	408
B-57	Two-station electric field waveforms of the RS1 of flash 00580.....	409
B-58	Two-station electric field waveforms of flash 00590	410
B-59	Two-station electric field waveforms of the RS1 of flash 00590.....	411
B-60	Two-station electric field waveforms of flash 01162	412
B-61	Two-station electric field waveforms of the RS1 of flash 01162.....	413
B-62	Two-station electric field waveforms of the RS2 of flash 01162.....	414
B-63	Two-station electric field waveforms of flash 01163	415
B-64	Two-station electric field waveforms of the RS1 of flash 01163.....	416
C-1	Frames showing the first stroke of flash 1593.....	418
C-2	First two frames showing the second of flash 1593.....	419
C-3	Last two frames showing the second stroke of flash 1593.....	420
C-4	Frames showing the third stroke of flash 1593.....	421
C-5	First two frames showing the fourth stroke of flash 1593	422
C-6	Last two frames showing the fourth stroke of flash 1593.....	423
C-7	Frames showing the fifth stroke of flash 1593.....	424
C-8	First two frames showing the sixth stroke of flash 1593.....	425
C-9	Last two frames showing the sixth stroke of flash 1593.....	426
C-10	Frames showing the second stroke of flash 1594	427
C-11	Frames showing the third stroke of flash 1594	428

Abstract of Dissertation Presented to the Graduate School
of the University of Florida in Partial Fulfillment of the
Requirements for the Degree of Doctor of Philosophy

CHARACTERIZATION OF FLORIDA LIGHTNING WITH EMPHASIS ON THE
PRELIMINARY BREAKDOWN PROCESS, BIPOLAR LIGHTNING, AND LIGHTNING
INTERACTION WITH A 257-M TOWER

By

Yanan Zhu

December 2017

Chair: Vladimir A. Rakov

Cochair: Martin A. Uman

Major: Electrical and Computer Engineering

Various characteristics of Florida lightning were examined and the results were found to be consistent with previous studies. An automated data processing algorithm was developed for studying preliminary breakdown (PB) pulse trains in negative cloud-to-ground (CG) lightning. For more than 3000 high-intensity (≥ 50 kA first-stroke peak current) flashes, the time interval between PB and return stroke (RS) was found to decrease with increasing RS peak current. The largest PB pulse peak exhibited positive correlation with the RS peak current. It appears that the high-intensity negative CG is characterized by shorter (and by inference faster) stepped leaders and more pronounced PB pulse trains.

A highly unusual bipolar cloud-to-ground lightning flash was observed to start with a negative stroke followed by a positive stroke and bipolar continuing current, all in the same channel. This is the first observation of positive stroke in the channel of preceding negative stroke after not unduly-long (70 ms) time interval. The 2-D speed profile, for the positive leader in the previously-conditioned channel was examined for the first time.

Electric field and high-speed video records of two flashes that contained a total of 8 strokes terminated on a 257-m tower were obtained. All these strokes exhibited very similar and unusually narrow bipolar electric field waveforms with damped oscillatory tails. By using an engineering model of lightning striking a tall object, the measured electric field waveforms were reproduced using as the channel-base current a narrow pulse followed by a steady-current tail. The effects of the input parameters on model-predicted fields were examined.

The National Lightning Detection Network (NLDN) detection efficiency and classification accuracy for cloud discharge activity were evaluated (for the first time) using optical and electric field data acquired at LOG. A similar evaluation was also performed for natural CG flashes and the results were compared with previous evaluations based on rocket-triggered lightning data.

The performance characteristics of the Earth Network Total Lightning Network (ENTLN) were evaluated by using as ground-truth both natural lightning data (for the first time) recorded at LOG and rocket-triggered lightning data obtained at Camp Blanding.

CHAPTER 1 INTRODUCTION

1.1 Cloud-to-Ground Lightning

Based on the polarity of charge effectively lowered to the ground and the direction of initial leader propagation, four types of lightning can be identified. They are downward negative lightning, upward negative lightning, downward positive lightning, and upward positive lightning, as illustrated in Figure 1-1.

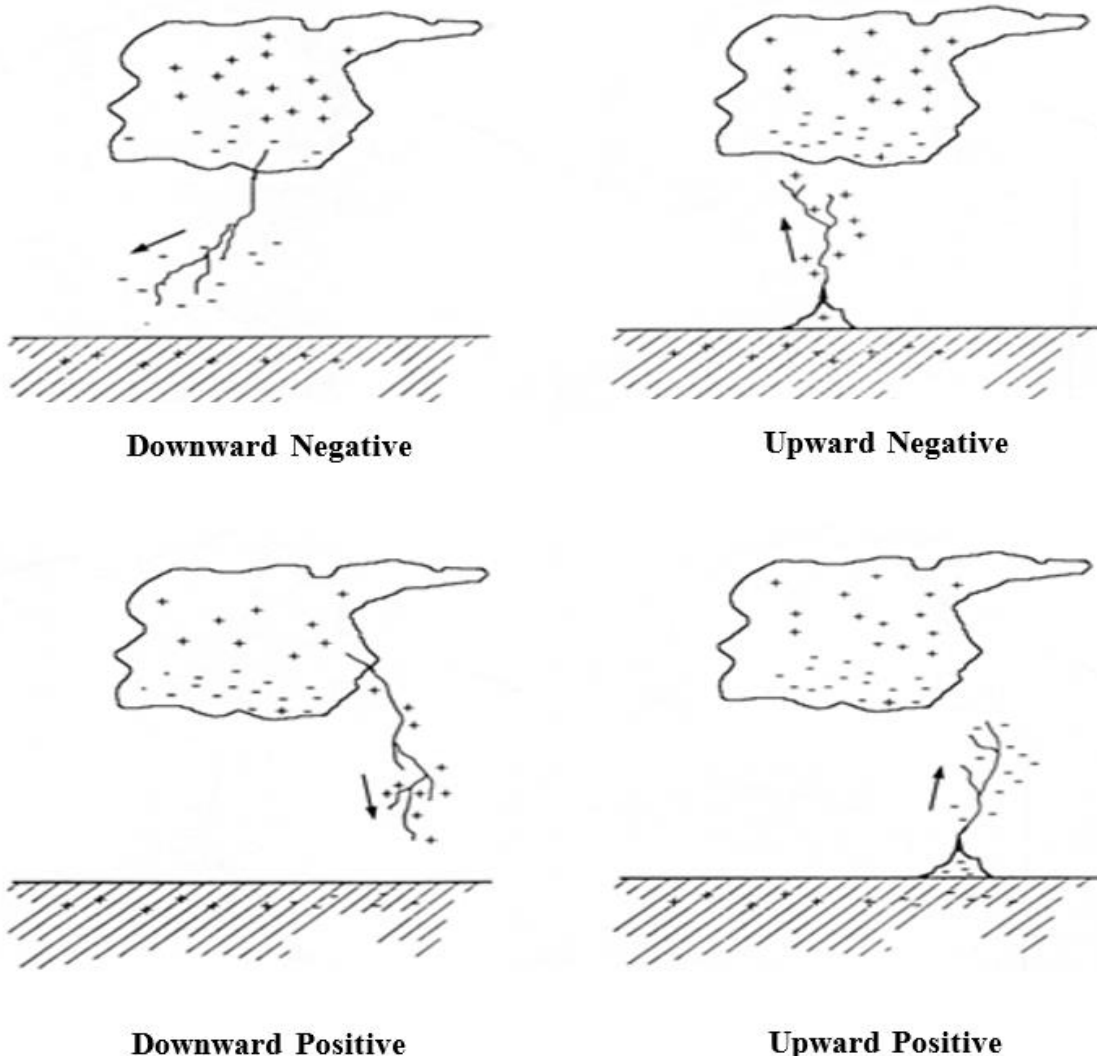


Figure 1-1. Four types of cloud-to-ground lightning. Adapted from *Rakov and Uman* [2003].

Downward negative lightning accounts for about 90% percent of cloud-to-ground lightning. A complete sequence of processes involved in a typical downward negative cloud-to-ground lightning will be introduced next and the corresponding illustration is shown in Figure 1-2. Thunderstorm charge structure usually can be simplified as a tripole model, which contains a main positive charge region, a main negative charge region, and a lower positive charge region. They are labeled P, N, and LP, respectively, in Figure 1-2. Although not shown in Figure 1-2, usually a negative charge region called upper screening layer is induced at the top of the thundercloud. Preliminary breakdown (PB) process is commonly viewed as the initiation of lightning. More detailed information on preliminary breakdown process will be given in section 1.3. Preliminary breakdown process serves to provide the condition for the formation of a stepped leader. The latter is a hot plasma channel which moves downward in a discrete manner (in the case of -CG). Each luminous step typically moves tens of meters in one microsecond or less, then there is a pause for 20 to 50 μ s, then another step is formed. Negative charges are effectively lowered from the negative charge region and distributed along the path of the stepped leader. When the stepped leader is close to ground, the positively charged upward leader will be initiated from the ground or protruding objects on the ground. When the upward leader makes contact with the branched downward negative leader, the most luminous process termed the return stroke starts, during which negative charges deposited on the stepped leader channel flow into the ground, resulting a current wave of tens of kA amplitude that travels from ground up the channel at the one-third to one-half of the speed of light. If a flash ceased after the first return stroke, this flash is called a single-stroke flash, otherwise a continuously propagating leader (as opposed to stepped leader), known as dart leader, will traverse the downward the first-stroke

channel and lead to a subsequent return stroke. About 80% negative cloud-to-ground flashes have multiple (usually 3-5) leader-return stroke sequence.

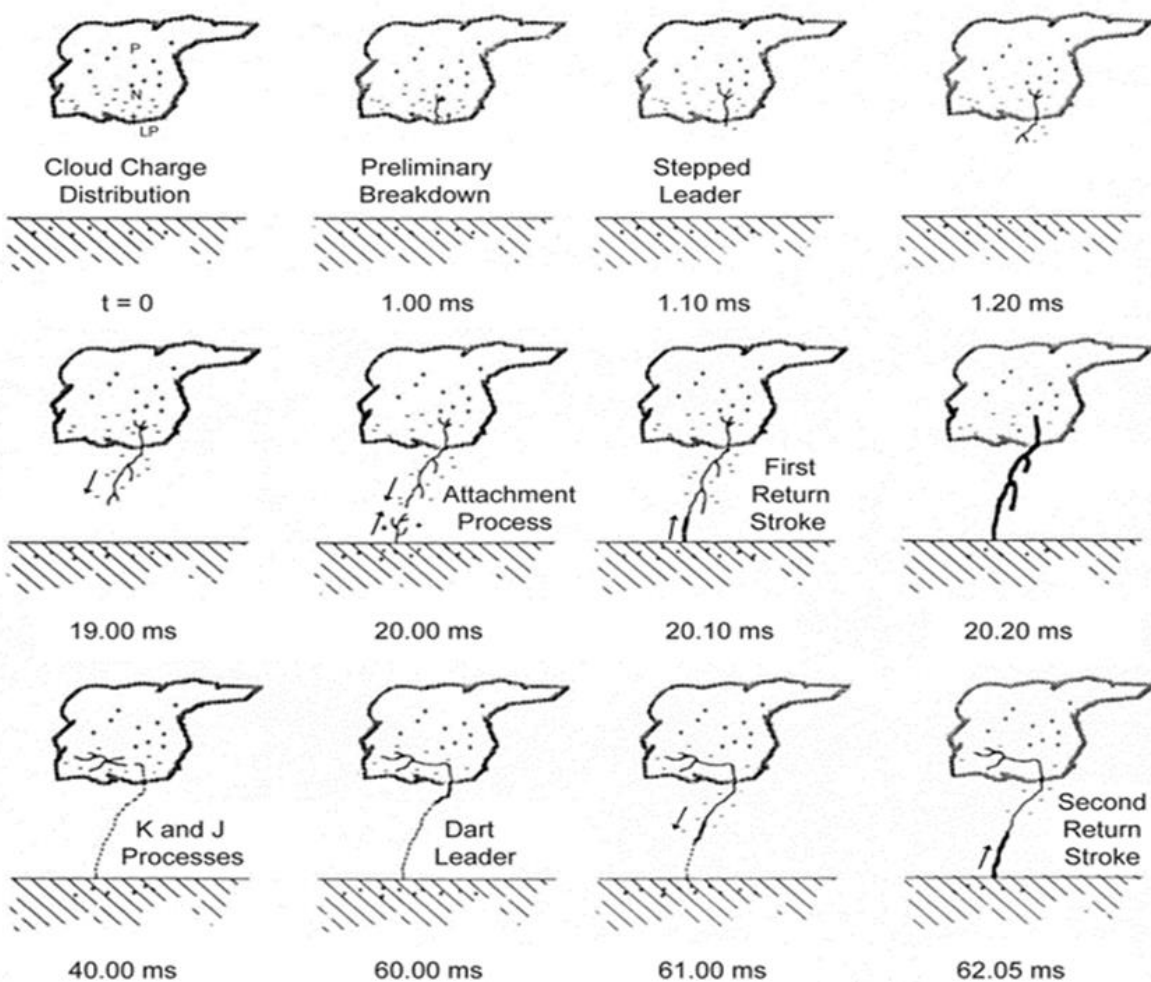


Figure 1-2. A nearly complete sequence of processes of a typical downward negative flash.
Adapted from Uman [1987].

1.2 Rocket-Triggered Lightning

Lightning can be triggered by launching a small rocket with a thin metallic trailing wire toward the thundercloud overhead. There are two techniques for triggering lightning, “classical” technique and “altitude” technique. Only the “classical” technique will be discussed in this section.

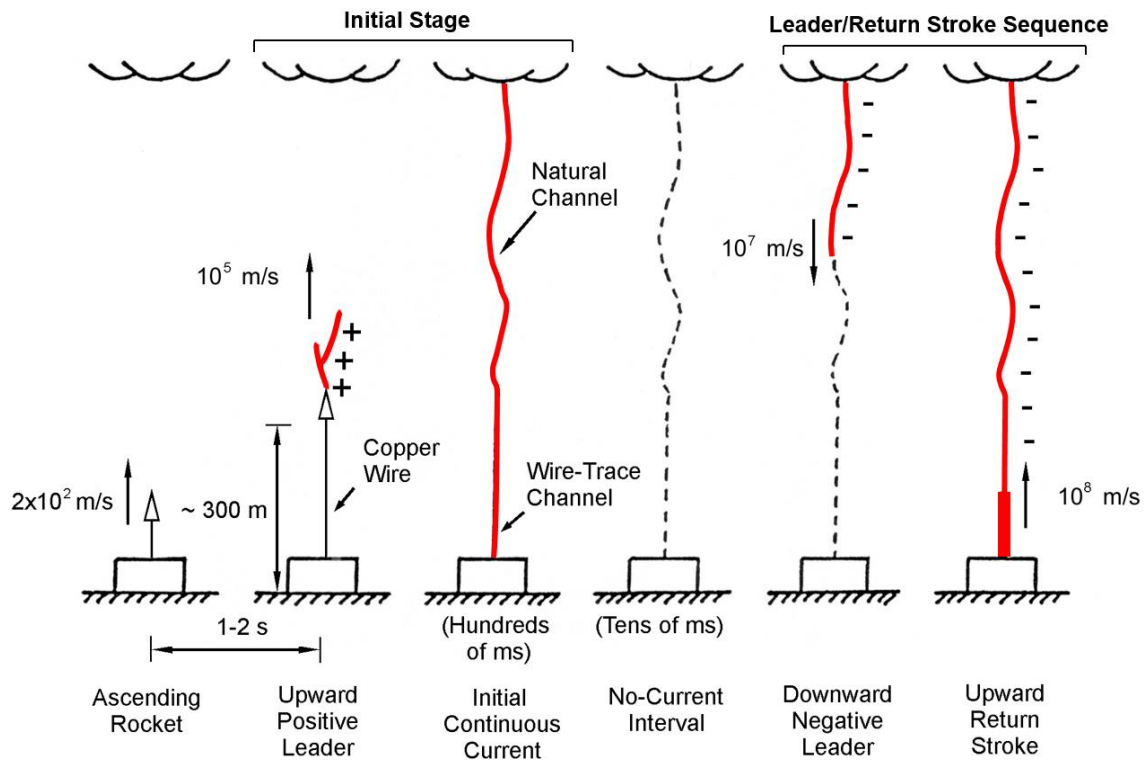


Figure 1-3. Sequence of events in classical triggered lightning. Adapted from *Rakov et al.* [1998].

In Figure 1-3, an illustration of six stages in the classical triggering process is shown. A rocket is launched when the quasi-static electric field measured at the ground level reaches some critical value. Also, it is usually launched during the dissipating stage of the thunderstorm that characterized by a low flash rate, since the occurrence of nearby natural lightning could reduce the electric field needed for a successful triggering. The rocket ascends at the speed of about 150-200 m/s. During the rocket ascent, small electrical breakdowns termed “precursors” are produced at the wire tip and typically extend a few meters ahead of the ascending rocket [Biagi *et al.*, 2011, 2012]. These precursors abort within several meters since the enhanced electric field at the tip of the wire is insufficient for sustained propagation. When the rocket reaches the height of 200-300 m, the enhanced electric field near the tip of the wire is strong enough to initiate a positive leader propagates upward toward the cloud at a speed of about 10^5 m/s, as shown in the

second stage in Figure 1-3. The increasing UPL current will vaporize the triggering wire, which will be quickly replaced by a plasma channel. The UPL will continue to extend toward the cloud. When the UPL reaches the negative charge region, initial continuous current (ICC) characterized by slowly varying current with duration of several hundreds of milliseconds and average current of the order of 100 A. Usually, the lightning channel is straight below the wire top while the channel above the wire top is tortuous. The precursors, UPL, and ICC form the initial stage (IS). After the end of the IS stage, the lightning channel decays and the current measured at the channel base falls to nearly zero. One or more downward dart leader/return stroke sequences may traverse the remnants of the decayed lightning channel established between the cloud and the triggering facility. The dart leader/return stroke sequences in rocket-triggered lightning are similar to the dart leader/return stroke sequences in natural lightning.

1.3 Preliminary Breakdown

Preliminary breakdown (PB) or initial breakdown process seems to be the most mysterious process of lightning. How lightning (or preliminary breakdown channel) is initiated and processes within the thundercloud that create the high electric field needed for lightning to be initiated remain some of the biggest unsolved problems in lightning physics [*Dwyer and Uman, 2013*].

Clarence and Malan [1957] suggested that PB is a vertical discharge between the main negative charge region and the lower positive charge region. However, *Krehbiel et al. [1979]*, from eight-station electric field measurements, found that breakdown events before the stepped leader involved considerable horizontal extent. *Rakov and Uman [2003]* concluded that the PB process can be viewed as a sequence of channels extending in seemingly random directions from the cloud source with one of them evolving into the stepped leader to the ground. More recently studies by *Stolzenburg et al. [2013, 2014]*, who used high speed video records of preliminary

breakdown, indicated that the luminosity bursts were correlated with the amplitude of the PB pulses and suggested that each PB pulse is caused by a substantial current surge traversing a channel segment that is hundreds of meters long. *Wilkes et al.* [2016] found that characteristics of luminosity pulses of preliminary (initial) breakdown processes in CG and IC are different and suggested that physics of the initiation process in each case either may inherently be different or may be the same but in different cloud environments.

Preliminary breakdown of negative cloud-to-ground lightning is characterized by a sequence of bipolar pulses typically occurring a few tens of milliseconds before the first return stroke with duration on the order of 1 ms and pulse width of 20-40 μ s [*Rakov et al.*, 1996]. The amplitude of PB pulse can be comparable to or even exceed the amplitude of the following return stroke (RS) pulse [*Brook*, 1992; *Nag and Rakov*, 2009a].

Nag and Rakov [2008] examined electric field records of negative cloud-to-ground lightning acquired in Gainesville, FL, in 2006 and found that only 18% of them had detectable PB pulses. However, *Baharudin et al.* [2012] and *Marshall et al.* [2014] found that 100% of flashes in each study had detectable PB pulse trains. *Marshall et al.* [2014] found that the noise level of recording system, record length, and distance to the observation point, can reduce the detectability of PB pulses. The amplitudes of preliminary breakdown pulses were found to be significantly higher at higher-latitude (temperate) regions than their counterparts at lower-latitude (tropical or subtropical) regions [*Gomes et al.*, 1998; *Nag and Rakov*, 2009b; *Marshall et al.*, 2014]. *Gomes et al.* [1998] and *Nag and Rakov* [2009b] attributed this difference to a more significant lower positive charge region at higher-latitude regions.

Brook [1992] found that PB pulses produced in winter storms were more intense than in summer storms. Also, the PB-RS interval was found to be a factor of 4 shorter for winter storms.

The shortest PB-RS interval was 2.5 ms, observed in winter. He attributed the disparity to the difference of precipitation mixes in summer and winter storms. However, *Heavner et al.* [2002] and *Kolmašová et al.* [2014] reported PB-RS intervals as short as a few milliseconds for summer storms and the inferred leader speed was on the order of 10^6 m/s, which is an order of magnitude greater than typical value of stepped leader. *Kolmašová et al.* [2014] suggested that unusually strong negative charge sources account for such fast leaders.

CHAPTER 2

RESEARCH FACILITIES

2.1 Lightning Observatory in Gainesville (LOG)

The Lightning Observatory in Gainesville (LOG), Florida is currently located on the roof of the five-story New Engineering Building on the campus of the University of Florida, which is 45 km from Camp Blanding. Sensors currently used at LOG include electric field (E) antennas, electric field derivative (dE/dt) antennas, magnetic field derivative (dB/dt) antennas, and an x-ray detector. Signals from the sensors are transmitted to digitizing oscilloscopes in the LOG cupola using fiber optic links. Trigger times are GPS time stamped on a computer.

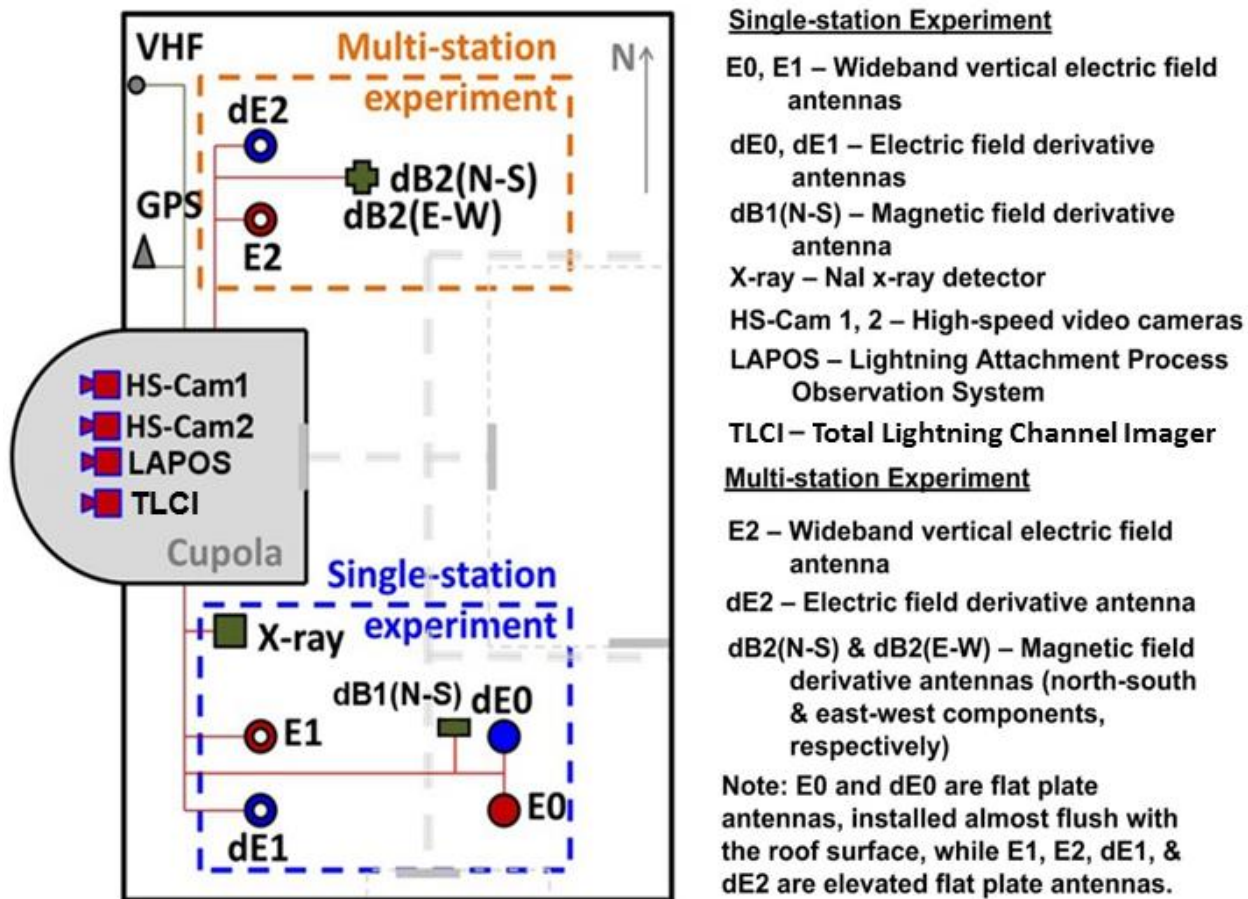


Figure 2-1. Overview of Lightning Observatory in Gainesville (LOG), Florida. Adapted from Mallick [2013] and Tran [2015].

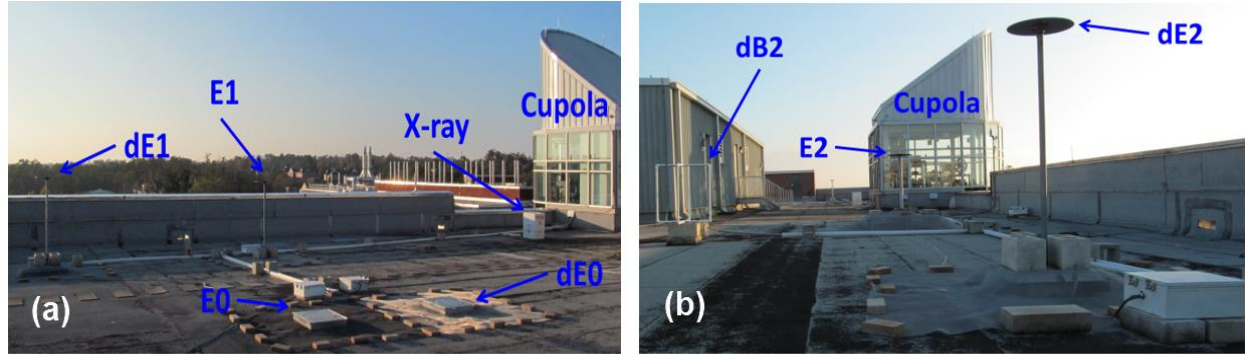


Figure 2-2. Photographs of Lightning Observatory in Gainesville. a) South-side and b) North-side. Adapted from *Mallick [2013]*.

Two high-speed cameras, Phantom V310 and HHC-X2, were installed at LOG in 2012 and 2013, respectively. Also, the Total-sky Lightning Channel Imager (TLCI) was installed at LOG in 2013 as part of our collaboration with the Chinese Academy of Meteorological Sciences. Additionally, Lightning Attachment Process Observation System (LAPOS) was installed in LOG in 2016 as part of our collaboration with the Gifu University, Japan. An overview of LOG is shown in Figure 2-1. Photographs of LOG are shown in Figure 2-2.

Two experiments - single-station experiment and multi-station experiment are performed at LOG. Single-station experiment is designed to study local natural lightning. Single-station system can record electromagnetic fields, optical images and x-rays/gamma rays produced by natural lightning over Gainesville area.

The electric field measuring systems in single-station experiment include a low-gain and a high-gain electric field measuring systems and an electric field derivative (dE/dt) measuring system. The low-gain electric field measuring system includes a circular flat-plate antenna, installed nearly flush with the roof surface, followed by an amplifier with an RC time constant of 10 ms. The high-gain electric field measuring system includes a similar but elevated flat-plate antenna followed by a different amplifier having a higher gain and a shorter RC time constant of 440 μ s, which allowed us to accentuate relatively small field pulses. The bandwidths are 16 Hz

to 10 MHz and 360 Hz to 10 MHz for the low-gain and high-gain systems, respectively. The upper frequency response of the dE/dt measuring system is 10 MHz.

Multi-station experiment is aimed at recording electromagnetic radiation produced by rocket-triggered lightning (RTL) at CB and natural lightning over the CB area. It can be further divided into three-station RTL experiment and two-station natural lightning experiment. When an RTL or onsite natural lightning occurs at ICLRT, a signal will be sent via a dedicated phone line to trigger the oscilloscope Yokogawa DL 850 at LOG, from where a signal is sent via Internet by an IP-addressed digital input and output device (ipIO) to trigger the oscilloscope Yokogawa DL 850 at Golf course site (GC) in Starke, which is a station 3 km west of CB. For the three-station experiment, electric field, the electric field derivative (dE/dt) and magnetic field derivative (dB/dt) produced by RTL or on-site natural lightning at CB were recorded at both LOG and GC from 2013 to 2015. When the electric field produced by natural lightning over CB area exceeds a preset value, the Lecroy 7100A oscilloscope at GC is triggered and a signal will be sent by ipIO to LOG via Internet to trigger the Lecroy 7100A oscilloscope at LOG. For two-station experiment, electric field and dE/dt produced by natural lightning over the Starke area were recorded from 2013 to 2014. With the upgrade in the summer of 2015 (the new oscilloscope Lecroy HDO 6034), GC can additionally record magnetic field derivative (dB/dt) produced by natural lightning over the CB area. Three-station and two-station trigger schemes are shown in Figure 2-3.

The multi-station electric field measuring system at LOG includes an elevated circular flat-plate antenna followed by an integrator/amplifier with a decay time constant of 10 ms. The frequency bandwidth was 16 Hz to 10 MHz. Signals from the antenna were relayed to an oscilloscope via a fiber optical link. The vertical resolution of the Lecroy 7100A oscilloscope

(dedicated for recording natural lightning from 2013 to 2014) was 8 bits and the sampling rate was 50 Msamples/s (sampling interval was 20 ns). The record length was 2 s. For the oscilloscope Yokogawa DL 850, which is dedicated for recording rocket-triggered lightning, the vertical resolution was 12 bit and the sampling rate was 100 Msamples/s (sampling interval was 10 ns). The record length was set to be 5 s.

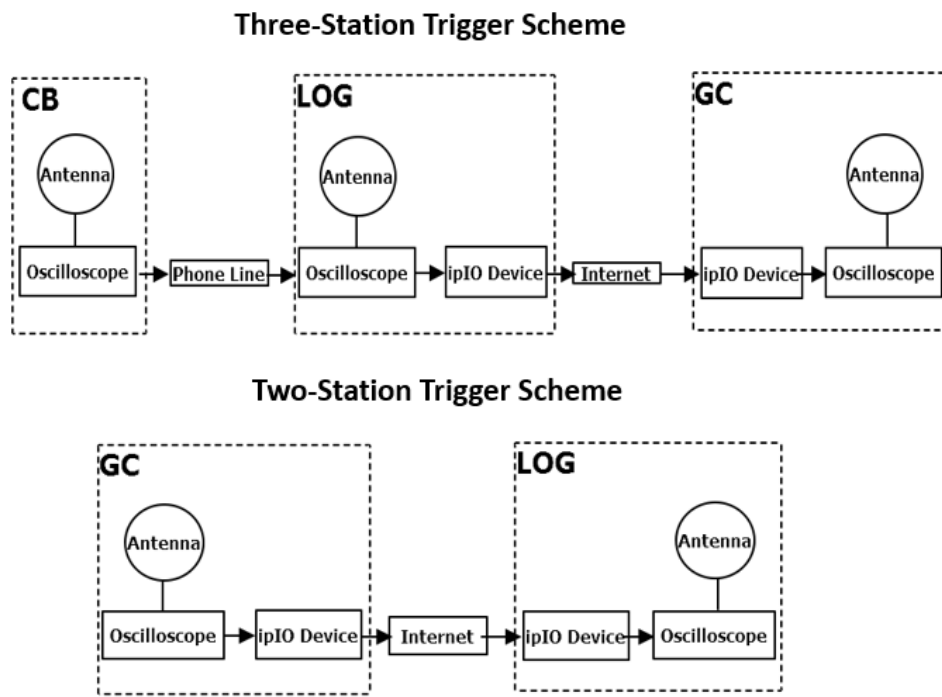


Figure 2-3. Three-station and two-station trigger schemes. The ipIO trigger scheme is designed by S. Mallick.

2.2 Golf Course Site in Starke (GC)

As one site of multi-station experiment, the Golf Course site (GC) at Starke is 3 km west of the ICLRT at Camp Blanding (CB). Two circular flat plate antennas and one square loop antenna were used at GC to measure the electric field, electric field derivative, and magnetic field derivative produced by rocket-triggered lightning and onsite natural lightning at CB, and close natural lightning over the CB area. All the signals from the antennas are transmitted via

fiber optical links to the digitizing oscilloscopes (Yokogawa DL850 and Lecroy 7100A) in the instrumentation truck (Figure 2-4b). All the recorded events are GPS time stamped on the computer in the truck. The field measuring system used at GC is very similar to the one used for multi-station experiment at LOG, except that RC time constant used for electric field measurement at GC is 1.36 s, while it is 10 ms for the one used at LOG. Additionally, after the upgrade in the summer of 2015, the new scope (Lecroy HDO 6034) allows the GC to record two orthogonal magnetic field derivatives for close natural lightning. For the oscilloscope Lecroy HDO 6034, the vertical resolution was 12 bit and the sampling rate was 50 Msamples/s (sampling interval was 20 ns). The record length was set to be 1 s. Figure 2-4 shows the overview and a photograph of GC. In order to avoid flood issue at GC during the thunderstorm season, limerock layer was installed to elevate the ground level by several inches in the summer of 2013.

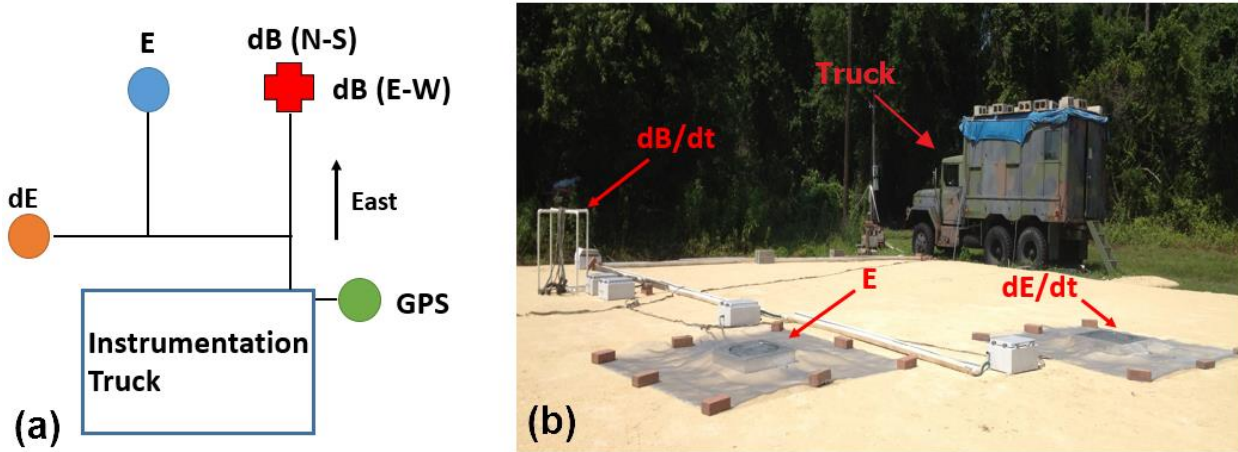


Figure 2-4. Overview of the Golf Course (GC) site. a) Layout of GC site. b) A photograph of GC site (2013). Photo courtesy of author.

2.3 Camp Blanding Facility (CB)

Rocket-triggered lightning experiments have been conducted at Camp Blanding (CB), Florida, since 1993. It is also referred to as the International Center for Lightning Research and

Testing (ICLRT) at CB, although it presently also includes LOG and GC. The satellite image of the ICLRT is shown in Figure 2-5. The buildings, measurement stations, and the rocket launcher are labeled. The CB facility occupies an area of roughly 1 km^2 , and includes a network of about one hundred measurements of lightning electric/magnetic fields and their derivatives, energetic radiation (x-rays and gamma rays). Additionally, lightning channels are optically imaged using a variety of high-speed video and still cameras. The launcher controls and the data acquisition systems are located inside the launch control trailer. Fiber-optic links are used to transmit data from the sensors to the data acquisition systems. An eight-station Lightning Mapping Array (LMA) network, a continuously operating system used to locate VHF radiation sources associated with lightning discharges, was installed in 2011 around CB. Natural lightning occurring on or very near the site are also recorded by CB facilities. Detailed descriptions of CB facilities can be found in *Gamerota [2014]*.

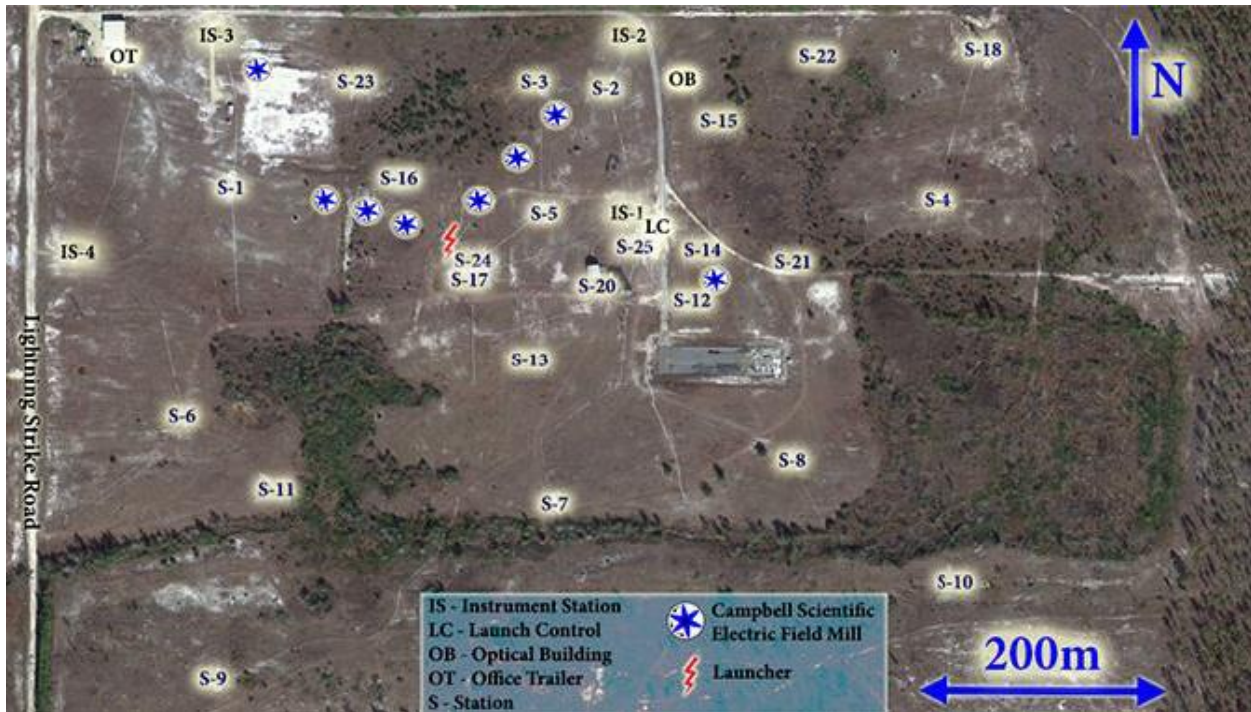


Figure 2-5. Overview of the ICLRT. Buildings and measurement stations are labeled. Taken from *Gamerota [2014]*.

The lightning-channel-base current was measured at the ground launcher using a $1\text{-m}\Omega$ current-viewing resistor (CVR) with bandwidth from DC to 8 MHz. The signal from the CVR was transmitted to four separate sets of electronics (channels with different measuring ranges), which could collectively measure currents ranging from 1 mA to 60 kA [Ngin *et al.*, 2014]. The channel-base currents are recorded on several oscilloscopes, each configured with different record lengths and sample intervals. When the current magnitude exceeded 6 kA, a GPS time stamp was produced, which was used as the ground-truth timing of the stroke. When the return-stroke current did not exceed the 6-kA threshold, the GPS timing of the stroke was determined from another current measuring system operated at CB by NASA.

CHAPTER 3

CHARACTERIZATION OF FLORIDA NEGATIVE CLOUD-TO-GROUND LIGHTNING

3.1 Literature Review

It is well known that lightning flash density and polarity dramatically vary with geographical location and season. However, it is still not certain if similar dependences exist for other lightning parameters. Clearly, lightning parameters can vary from one storm to another [Biagi *et al.*, 2007; Saraiva *et al.*, 2010], which may influence statistics, particularly in the case of small sample size. Before attributing any variation of lightning parameters to regional or meteorological peculiarities, one should rule out the influence of measuring and data processing techniques used in different locations, as well as methodology and limited sample size.

Many characteristics of negative cloud-to-ground lightning in Florida were studied by the University of Florida Lightning Research Group in the early 1990s [e.g., Rakov and Uman, 1990; Thottappillil *et al.*, 1992; Rakov *et al.*, 1994]. For 76 negative flashes recorded during 3 storms in Florida in 1979, Rakov *et al.* [1994] examined the number of strokes per flash (multiplicity) and percentage of single-stroke flashes. They used electric field and optical data and found that the percentage of single-stroke flashes was 17% and the arithmetic mean flash multiplicity was 4.6. Thottappillil *et al.* [1992] found that 15 (33%) of 46 multiple-stroke flashes had one or more subsequent return strokes with distance-normalized initial electric field peak greater than that of the corresponding first return stroke, and that the interstroke interval preceding these greater-than-first subsequent strokes were more than 1.7 times longer than the average preceding interstroke interval for all subsequent strokes in their dataset.

Nag et al. [2008] examined the ratio of electric field peaks of first and subsequent return strokes based on the data acquired in Florida, Austria, Brazil, and Sweden. They found that the electric field peak of first return strokes was on average 1.7 to 2.4 times larger than its counterpart for subsequent return strokes. For 239 negative cloud-to-ground flashes in Florida, the arithmetic and geometric means of first to subsequent return stroke field peak ratio were 2.1 and 1.7, respectively.

In this chapter, we will examine characteristics of negative cloud-to-ground lightning flashes using their electric field waveforms acquired at the Lightning Observatory in Gainesville (LOG), Florida in the summers of 2013 and 2014. Flash multiplicity, interstroke interval, flash duration, and first to subsequent stroke field peak ratio are determined for 478 flashes containing 2188 strokes and compared with previous results obtained in Florida.

3.2 Data

The dataset of 478 negative cloud-to-ground flashes in this study was acquired at LOG by using two-station (LOG-Golf Course site) trigger scheme. The Golf Course site (GC) is located in Starke, about 45 km from LOG. When electric field at GC exceeds the preset threshold, the measuring instrumentation at GC is triggered, and a trigger pulse is sent to LOG over the Internet by using an IP-addressed digital input and output device. Due to this trigger scheme, the majority of lightning flashes recorded at LOG were relatively close to GC. The distances from LOG to lightning strike points were in the range of 16-330 km and the geometric mean distance was 55 km. Over 73% of events were in the 20-60 km range.

The more detailed information on the multi-station electric field measuring system at LOG can be found in Section 2.2. Pretrigger time (time interval between the beginning of the record and the first RS) was not fixed because of the IP triggering scheme. The pretrigger times were in the range of 46-1879 ms. The average pretrigger time was 612 ms and over 97% of records had >100 ms pretrigger times. Additional information about LOG is found in *Rakov et al.* [2014] and in Section 2.1 and that about GC in Section 2.2.

All the electric field waveforms analyzed in this study were smoothed (filtered) by using a 50-point (1- μ s) moving time-averaging window in order to improve the signal/noise ratio. It was determined by trial and error that the 50-point window for our data is optimal in that it allows a significant reduction of noise, while keeping the distortion minimal. The reduction of field peaks caused by filtering was determined to be less than 5%. NLDN data were used to confirm that the first stroke of each flash was not missed by our system due to insufficient pretrigger time (assuming that first strokes are unlikely to be missed by the NLDN).

3.3 Results

3.3.1 Multiplicity and Percentage of Single-Stroke Flashes

Out of 478 flashes containing 2188 strokes recorded during 17 storms, 57 (12%) were single-stroke flashes. The average number of strokes per flash was 4.6 and the geometric mean was 3.7. A histogram of multiplicity is shown in Figure 3-1. In the previous study of *Rakov et al.* [1994], 76 flashes recorded during 3 storms on average had 4.6 strokes per flash, and the percentage of single-stroke flash was 17%. Our results are consistent with the previous findings. Information on multiplicity and percentage of single-stroke flashes in Florida and in other

regions is summarized in Table 3-1, from which it follows that these two parameters are probably not significantly influenced by location.

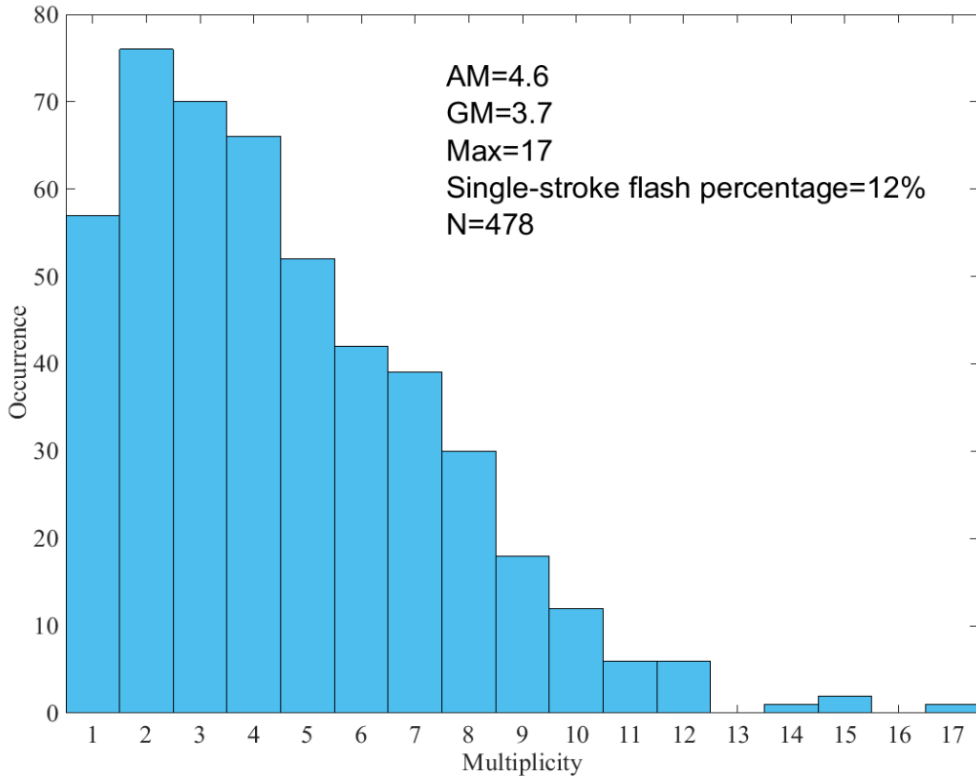


Figure 3-1. Histogram of the number of strokes per flash (multiplicity).

3.3.2 Interstroke Interval and Flash Duration

Figure 3-2 shows a histogram of the interstroke interval. The interstroke intervals were measured between the return-stroke field peaks. The arithmetic mean (AM) and geometric mean (GM) of all the interstroke intervals are 80 ms and 53 ms, respectively. *Thottappillil et al.* [1992] reported that GM of 199 interstroke intervals (46 flashes) was 57 ms. *Rakov et al.* [2014] reported that the GM of 270 interstroke intervals (76 flashes) was 60 ms. Our results are comparable with the corresponding values from the previous studies in Florida.

Figure 3-3 shows a histogram of the flash duration for multiple-stroke flashes only. We define here the flash duration as the time interval between the electric field peaks of the first stroke and the last subsequent stroke. The GM duration for 421 multiple-stroke flashes is 223 ms, which is close to 216 ms and 229 ms, which are GM flash durations of negative cloud-to-ground flashes observed in Arizona and Sao Paulo, respectively [Saraiva *et al.*, 2010]. We are not aware of previous flash duration measurements in Florida.

Information on interstroke intervals and flash durations in Florida and in other regions is summarized in Table 3-2, from which no significant variation from one region to another is seen.

Table 3-1. Summary of multiplicity of negative flashes and percentage of single-stroke flashes in different regions

Reference and Region	Average Number of Strokes per Flash (Multiplicity)	Percentage of Single-Stroke Flashes	Sample Size
Kitagawa et al. [1962], New Mexico	6.4	13%	83
Rakov et al. [1994], Florida	4.6	17%	76
Cooray and Jayaratne [1994], Sri Lanka	4.5	21%	81
Cooray and Pérez [1994], Sweden	3.4	18%	137
Saraiva et al. [2010], Arizona	3.9	19%	209
Ballarotti et al. [2012], Brazil	4.6	17%	883
Baharudin et al. [2014], Malaysia	4.0	16%	100
Present Study, Florida	4.6	12%	478

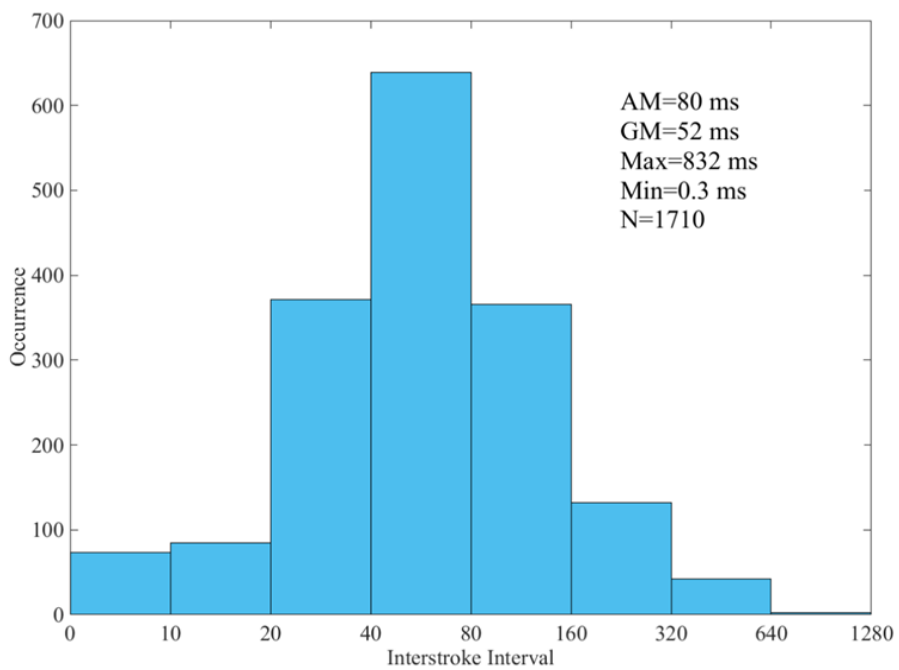


Figure 3-2. Histogram of the interstroke interval.

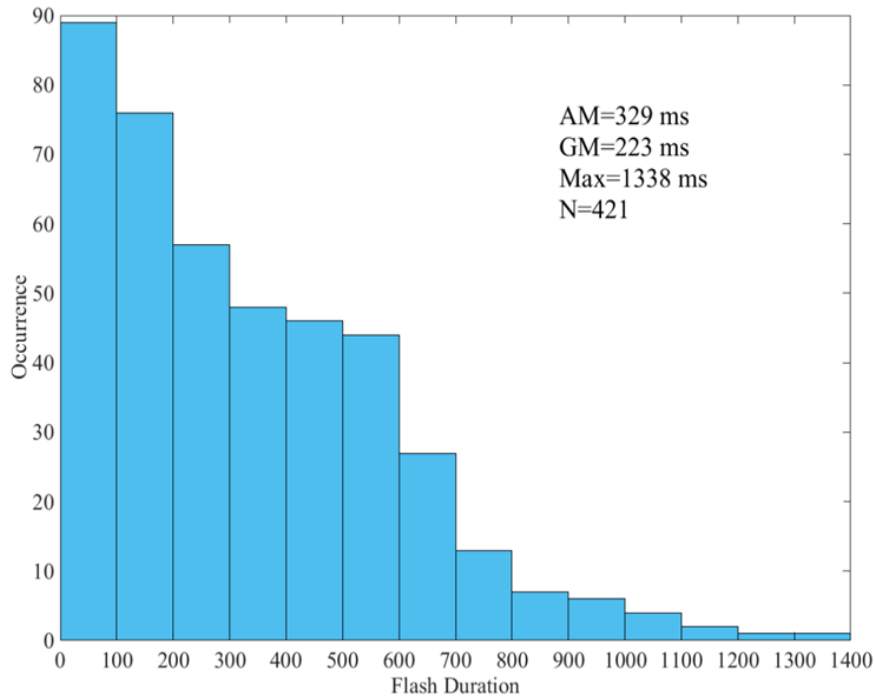


Figure 3-3. Histogram of the flash duration.

Table 3-2. Summary of geometric mean interstroke intervals and flash durations (sample sizes are given in the parentheses)

Reference and Region	Geometric Mean Interstroke Interval (ms)	Geometric Mean Flash Duration (ms)
Rakov et al. [1994], Florida	60 (270)	-
Cooray and Jayaratne [1994], Sri Lanka	57 (284)	-
Cooray and Pérez [1994], Sweden	48 (568)	-
Saraiva et al. [2010], Arizona	61 (598)	216 (169)
Saraiva et al. [2010], Brazil	62 (624)	229 (179)
Baharudin et al. [2014], Malaysia	67 (305)	-
Present Study, Florida	52 (1710)	223 (421)

3.3.3 First to Subsequent Return Stroke Field Peak Ratio

Figure 3-4 shows a histogram of the ratio of first to subsequent electric field peaks. For 1693 subsequent strokes (excluding saturated records), the ratio ranges from 0.3 to 28 with a GM of 2.4 and an AM of 3.1, which are somewhat higher than their counterparts reported for Florida and other regions by Nag *et al.* [2008] (Table 3-3). Higher ratios in this study are possibly a result of filtering, which allowed us to detect smaller amplitude strokes (many of them had NLDN-reported currents below 10 kA). It also could be a result of the fact that the electric field peaks of subsequent strokes got more attenuation along the path (longer in our study) of propagation since they contain more high frequency component. Out of 421 multiple-stroke flashes, 144 (34%) had at least one subsequent stroke whose field peak was greater than that of the first stroke, which is very close to 33% (15 of 46) reported by Thottappillil *et al.* [1992].

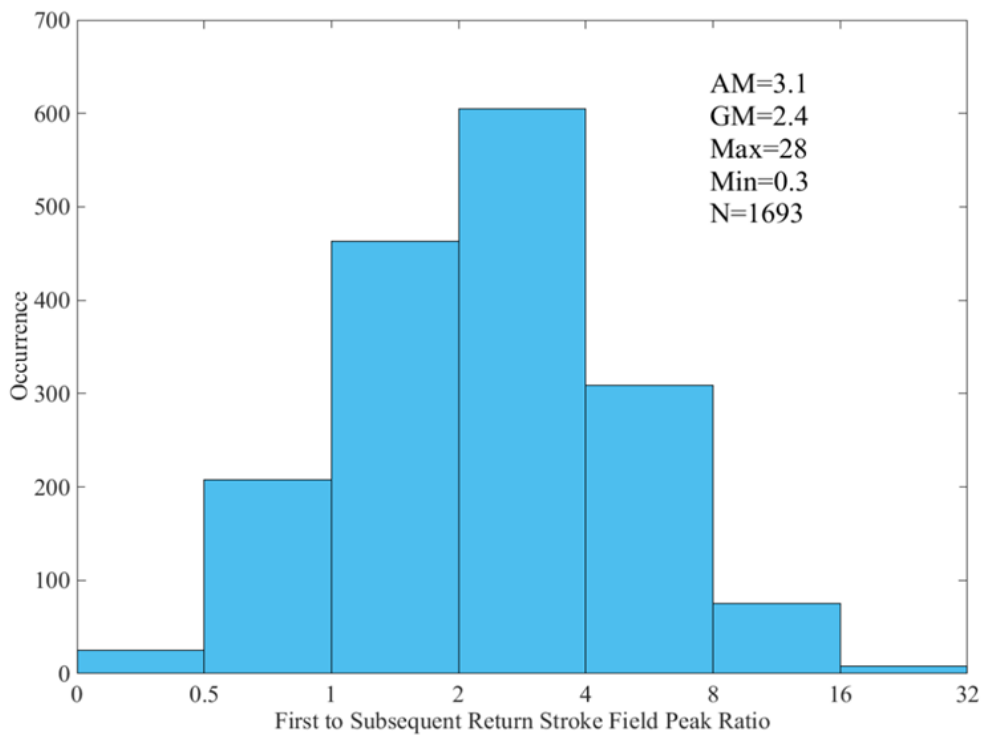


Figure 3-4. Histogram of the ratio of the first to subsequent return stroke field peaks.

Table 3-3. Summary of statistics on the ratio of the first to subsequent return stroke field peaks

Reference	Region	Arithmetic Mean	Geometric Mean	Sample Size
Nag et al. [2008]	Florida	2.1	1.7	239
	Austria	2.3	1.6	247
	Brazil	2.4	1.9	909
	Sweden	2.4	1.9	258
	Present Study	3.1	2.4	1693

Shown in Figure 3-5 are electric field peaks of subsequent strokes that are normalized to their corresponding first return stroke peaks and plotted versus stroke order. For strokes of order 2 to 10 (when sample sizes are greater than 20), the geometric mean of normalized electric field peak shows a relatively weak tendency to decrease with increasing stroke order. The range of variation of GM normalized electric field peak for strokes of order 2 to 15 is from 0.50 (stroke order 2) to 0.23 (stroke order 13).

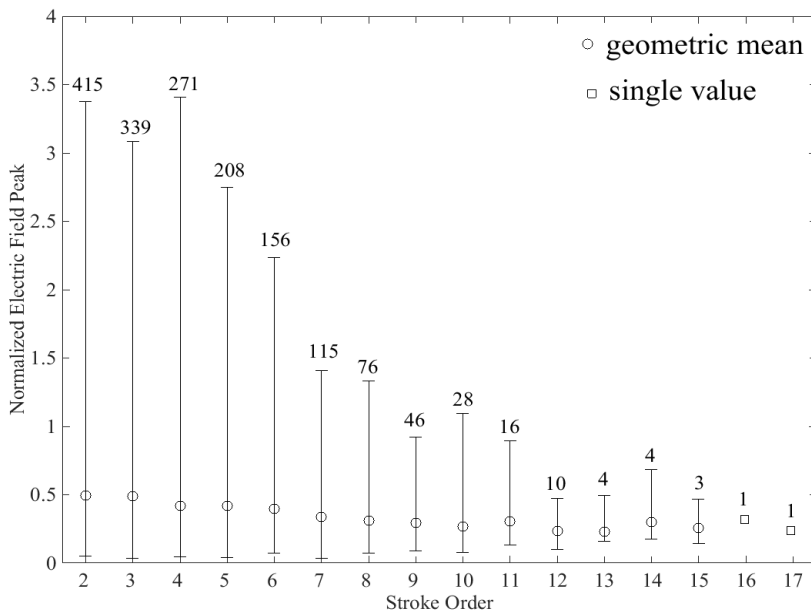


Figure 3-5. Normalized electric field peaks for strokes of different order. Ranges of variation (vertical bars) and sample sizes (at the top of vertical bars) for subsequent strokes of different order are given.

3.3.4 Variation of Lightning Parameters from One Storm to Another

Statistics on flash multiplicity, interstroke interval, flash duration, and ratio of first to subsequent electric field peak for 17 individual storms are presented in Table 3-4. Some significant differences were observed. For instance, the average multiplicity for the storm on 09/06/2013 was 3.5 ($N=17$) while its counterpart for the storm on 08/02/2014 was 6.1 ($N=24$). The GM interstroke interval and GM flash duration for the storm on 05/15/2014 were 38 ms ($N=48$) and 128 ms ($N=16$), respectively, 2-4 times smaller than 71 ms ($N=75$) and 554 ms ($N=14$) for the storm on 07/05/2014. The average ratio of first to subsequent return stroke electric field peak for the storm on 07/25/2014 was 5.5 ($N=61$), 2.8 times larger than 2.2 for the

storm on 06/08/2014 (N=114). However, the majority of storms had similar statistics for all the considered lightning parameters.

3.4 Summary

The characteristics of negative cloud-to-ground lightning were examined by analyzing the electric field waveforms of 478 flashes recorded during 17 storms in Florida. The percentage of single-stroke flashes is 12% and the average flash multiplicity is 4.6. The arithmetic mean (AM) and geometric mean (GM) of interstroke intervals are 80 ms and 52 ms. The AM and GM of flash durations are 329 ms and 223 ms. The ratios of first to subsequent stroke field peaks for 1693 subsequent strokes range from 0.3 to 28 with an AM of 3.1 and a GM of 2.4. The GM normalized electric field peaks of subsequent strokes show a slowly descending trend with increasing stroke order. Out of 421 multiple-stroke flashes, 144 (34%) had at least one subsequent stroke whose field peak was greater than that of the first stroke. Significant differences were observed in lightning parameters for different storms, however, the majority of storms had similar lightning parameter statistics. No significant disparities were found between characteristics of Florida negative cloud-to-ground lightning obtained in this study and their counterparts from previous studies.

Table 3-4. Variation of lightning parameters from one storm to another

Storm ID (mm/dd/yyyy)	Multiplicity			Interstroke Interval (ms)						Flash Duration for Multiple-Stroke Flashes (ms)						First to Subsequent Return Stroke Field Peak Ratio				
	Number of Flashes Recorded	AM	GM	Max	Sample Size	AM	GM	Max	Min	Sample Size	AM	GM	Max	Min	Sample Size	AM	GM	Max	Min	
08/17/2013	25	4.6	4.0	10	90	95	72	488	11	24	356	242	756	44	88	2.7	2.0	12.5	0.4	
08/22/2013	16	4.8	4.2	8	61	63	48	325	0.5	15	257	202	538	22	61	3.7	2.8	22.5	0.8	
08/31/2013	88	5.1	4.3	17	365	82	61	760	0.9	83	363	276	1199	31	365	2.4	2.0	15.6	0.3	
09/06/2013	17	3.5	2.8	8	43	82	63	345	7.5	12	294	219	601	51	41	3.1	1.9	25.1	0.4	
05/15/2014	17	3.8	3.4	7	48	51	38	217	6	16	152	128	320	31	48	3.7	3.0	13.7	0.7	
05/25/2014	19	4.5	4.0	8	66	74	52	450	13	18	273	208	644	38	66	3.5	2.8	11.3	0.3	
05/28/2014	21	3.7	2.8	12	56	77	57	399	9	16	271	143	943	9	56	3.1	2.5	13.6	0.7	
05/29/2014	21	3.7	2.7	11	56	76	48	42	0.8	15	284	138	1096	17	56	4.0	3.0	15.4	0.8	
06/08/2014	31	4.7	3.8	11	114	76	56	294	0.4	28	309	228	649	44	114	2.2	1.7	9.1	0.3	
07/03/2014	96	4.3	3.5	12	319	80	50	491	0.3	81	316	220	1016	0.7	319	3.0	2.3	14.9	0.3	
07/05/2014	16	5.7	4.6	15	75	127	71	832	0.7	14	684	554	1338	86	73	2.8	2.3	8.7	0.4	
07/07/2014	15	4.3	3.4	11	49	73	42	412	0.5	13	275	165	546	0.5	49	3.0	2.5	12.0	0.7	
07/10/2014	15	4.2	3.6	10	48	58	35	289	0.7	14	200	130	613	21	48	4.2	2.9	15.2	0.5	
07/25/2014	20	4.2	3.3	15	64	73	56	322	7.9	17	274	184	799	10	61	5.5	3.9	27	0.3	
08/02/2014	24	6.1	5.0	14	122	94	51	615	0.6	23	511	386	1229	73	117	3.6	2.8	28.2	0.5	
08/15/2014	20	4.7	3.8	11	74	58	41	236	0.6	18	237	139	777	0.6	71	4.7	3.8	16	0.6	
08/23/2014	17	4.5	3.4	12	60	92	55	509	1.1	14	401	310	837	45	60	2.7	2.1	8.1	0.5	
Total	478	4.6	3.7	17	1710	80	52	832	0.3	421	329	223	1338	0.5	1693	3.1	2.4	28.2	0.3	

CHAPTER 4

ELECTRIC FIELD SIGNATURES OF PRELIMINARY BREAKDOWN AND AUTOMATED ANALYSIS FOR HIGH-INTENSITY EVENTS

4.1 Literature Review

Nag and Rakov [2008] examined electric field records of negative cloud-to-ground flashes acquired in Gainesville, Florida, in 2006 and found that 18% of them had detectable preliminary breakdown (PB) pulse trains. However, from more recent studies of PB pulse trains in negative lightning in Florida, *Baharudin et al. [2012]* and *Marshall et al. [2014]* found that 100% of flashes in each study had detectable PB pulse trains. Possible reasons for the discrepancy, including differences in noise level, record length, and distance, were discussed by *Marshall et al. [2014]*.

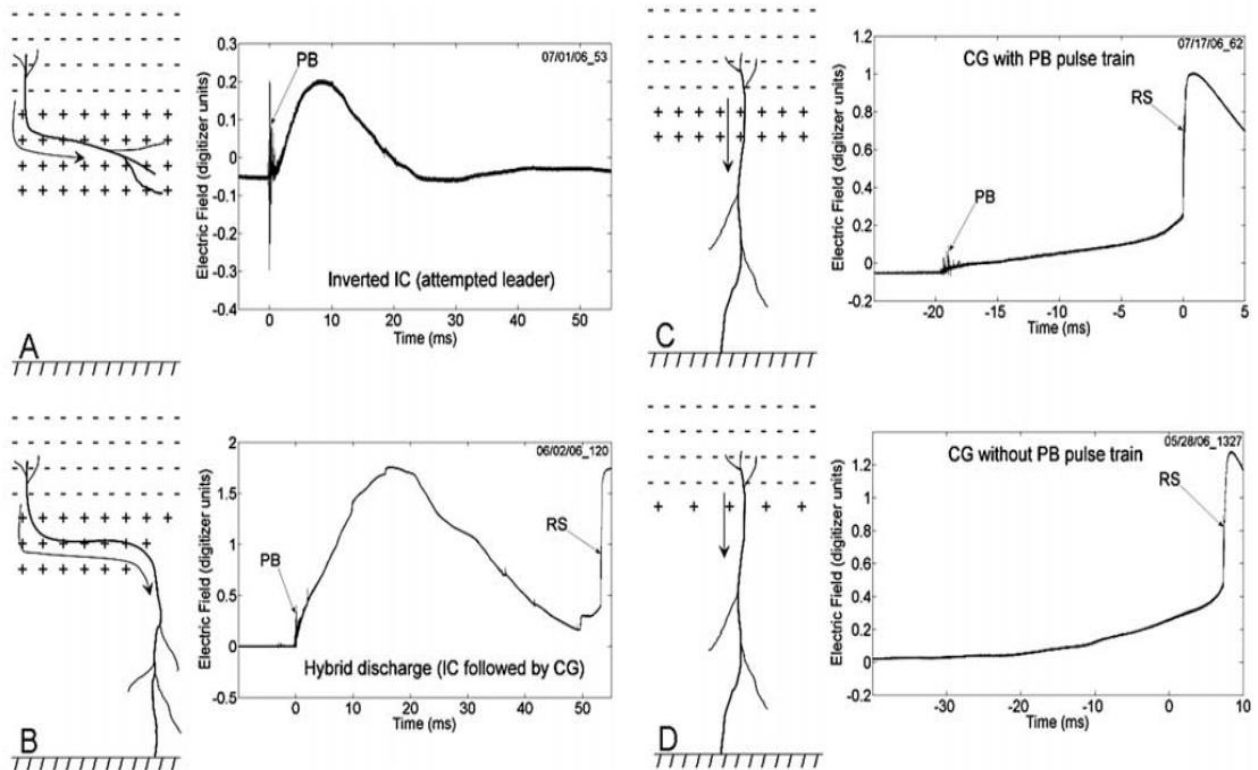


Figure 4-1. Schematic representation of four types of lightning (left) and the expected electric field waveforms (right). The charge configuration in each of the scenarios represents only its vertical profile. Adapted from *Nag and Rakov [2009b]*.

The amplitudes of preliminary breakdown pulses were found to be significantly higher at higher-latitude (temperate) regions than the counterparts at lower-latitude (tropical or subtropical) regions [Gomes *et al.*, 1998; Nag and Rakov, 2009b; Marshall *et al.*, 2014]. Gomes *et al.* [1998] and Nag and Rakov [2009b] attributed this difference to a more significant lower positive charge region at higher-latitude regions. Nag and Rakov [2009b] proposed that the preliminary breakdown pulses is a manifestation of the interaction of a downward extending negative leader channel with the lower positive charge region (LPCR). Depending on the magnitude of LPCR, four different scenarios of lightning development were inferred to exist. The expected electric field signatures for these scenarios are shown Figure 4-1.

Brook [1992] found that PB pulses produced in winter storms were more intense than in summer storms. Also, he found the time interval between the peaks of the first PB pulse and the first-return-stroke pulse (PB-RS interval) in winter storms to be a factor of four shorter than in summer storms. The shortest PB-RS interval in his study was 2.5 ms, observed in winter. He attributed the disparity to the difference in precipitation mixes in summer and winter thunderclouds. However, many researchers observed PB-RS intervals as short as a few milliseconds in summer storms [Heavner *et al.*, 2002; Frey *et al.*, 2005; Kolmašová *et al.*, 2014; Zhu *et al.*, 2015; Kotovsky *et al.*, 2016]. For the short PB-RS interval events, Heavner *et al.* [2002] inferred leader speeds of the order of 10^6 m/s, which is an order of magnitude greater than typical speeds of negative stepped leaders. Nag and Rakov [2009b] and Kolmašová *et al.* [2014] suggested that such unusually fast stepped leaders are produced by unusually strong negative charge sources. According to Nag and Rakov [2009b], only 5% of stepped leaders in Florida have durations shorter than 5 ms. The events with short PB-RS intervals were recently found by

Kotovsky et al. [2016] to be associated with long-lasting disturbances in the upper mesosphere and lower ionosphere.

In this chapter, the dataset of 478 negative flashes used in Chapter 3 was used to study the factors affecting detectability of PB pulse trains in negative cloud-to-ground lightning in Florida and the results are presented in section 4.2. The locations of these 478 flashes are shown in Figure 4-2. In section 4.3, distant (50 to 500 km) electric field waveforms of PB pulses in negative cloud-to-ground lightning flashes characterized by relatively high (≥ 50 kA) first-RS peak currents are analyzed by using an automated data processing algorithm. The following parameters are examined: PB-RS interval, the ratio of peaks of the largest PB pulse and the corresponding first-return-stroke pulse (PB/RS pulse peak ratio), range-normalized peak of the largest PB pulse, and PB pulse train duration.

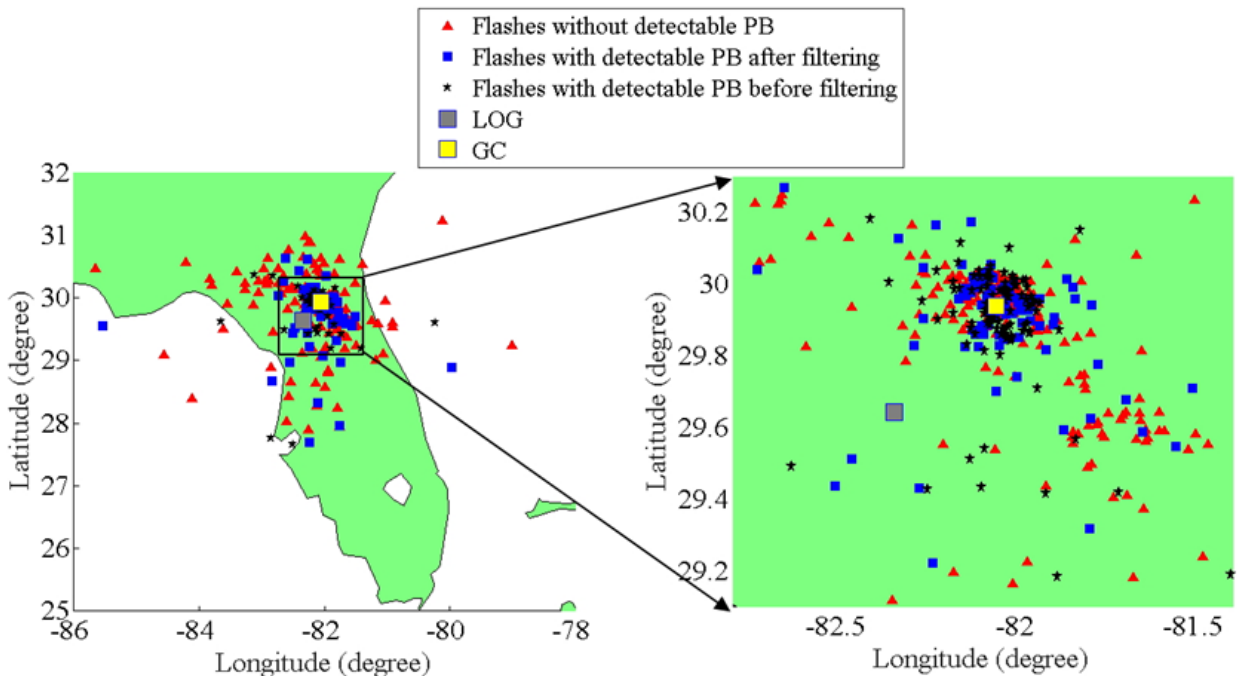


Figure 4-2. Locations of 478 flashes (first strokes only) recorded at LOG and reported by the NLDN. The expansion of the black box area in the left panel is shown in the right panel.

4.2 Factors Affecting Detectability of PB Pulse Trains

4.2.1 Signal/Noise Ratio of Recording System

The criteria for identifying the PB pulse trains described by *Nag and Rakov* [2008] were used in this study. For the raw data, the percentage of flashes with PB pulse train was 22%. However, after applying moving-average filtering to the data, the percentage increased to 46%, which means that the signal/noise ratio significantly affects the detectability of PB pulse trains. Figure 4-3 shows an example of records before and after filtering.

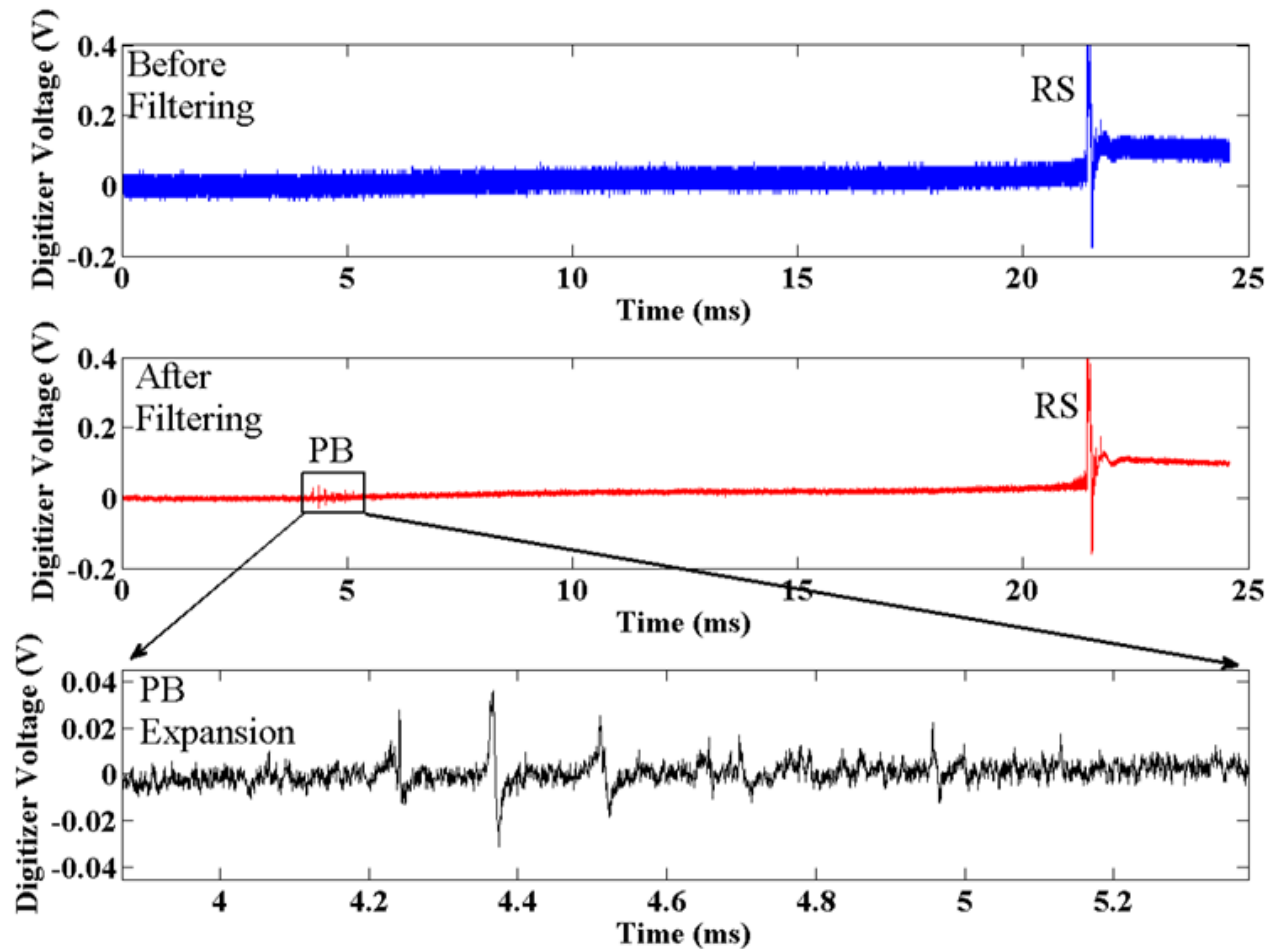


Figure 4-3. Comparison of the electric field waveforms before and after filtering. The top panel shows the waveform before filtering, in which no PB pulses can be seen. The same waveform after filtering, shown in the middle panel, exhibits a readily detectable PB pulse train around 5 ms. The bottom panel shows an expansion of the PB pulse train seen in the middle panel.

4.2.2 Type of Storm

The 478 flashes are grouped by storm in Table 4-1. For each storm, the percentage of flashes with detectable PB pulse train is given. It is clear from Table 4-1 that there is a significant variation of detectability from one storm to another, both before and after filtering. For example, before filtering, the storm on 07/03/2014 had only 6% of flashes with detectable PB pulse train, while this percentage for the storm on 07/10/2014 was 53%. After filtering, the percentages of flashes with detectable PB pulse train for these two storms increased to 28% and 100%, respectively, with the difference still being large.

Table 4-1. Percentages of flashes with detectable PB pulses before and after filtering for 17 storms

Storm ID mm/dd/yyyy	Number of Flashes Recorded	Percentage of flashes with detectable PB Pulses Train	
		Before Filtering	After Filtering
08/17/2013	25	20%	60%
08/22/2013	16	38%	56%
08/31/2013	88	13%	30%
09/06/2013	17	18%	47%
05/15/2014	17	41%	59%
05/25/2014	19	21%	37%
05/28/2014	21	29%	62%
05/29/2014	21	52%	81%
06/08/2014	31	16%	42%
07/03/2014	96	6%	28%
07/05/2014	16	31%	69%
07/07/2014	15	33%	47%
07/10/2014	15	53%	100%
07/25/2014	20	15%	55%
08/02/2014	24	42%	58%
08/15/2014	20	45%	55%
08/23/2014	17	18%	35%
Total	478	22%	46%

Cooray and Jayaratne [2000] found that the PB pulses produced by lightning in Sweden were much more intense than those in Sri Lanka. They attributed the difference to stronger lower positive charge region in thunderstorms in Sweden. Based on the hypothesis proposed by *Nag and Rakov* [2009b] that PB pulses are the manifestation of interaction between a negative stepped leader and the lower positive charge region , we speculate that storms with higher percentage of flashes with detectable PB pulse train may have a more significant lower positive charge region. We also observed that flashes with detectable PB pulses tend to occur close to each other temporally (cluster in time), which might indicate that PB intensity depends on the cloud charge structure that changes during the storm life cycle.

4.2.3 Prospective Return-Stroke Peak Current

We found that flashes with higher first return stroke peak currents (only current magnitudes are considered here) are more likely to have detectable PB pulse trains. The detectability of PB for all the 478 flashes is plotted versus first stroke peak current in Figure 4-4a, which shows a generally increasing trend. In order to reduce the effect of different distances to the LOG for different flashes, which will be examined in the next section, we chose 204 flashes in the relatively narrow 40-50 km distance range (which has the largest sample size compared to other ranges) to see the effect of the peak current more clearly. One can see from Figure 4-4b that the PB pulse train detectability tends to increase with the increasing prospective return-stroke peak current. If we combine some adjacent bins in Figure 4-4b, the percentages of flashes with detectable PB pulse train will be 44% for the 0-40 kA range ($N=133$), 63% for the 40-80 kA range ($N=59$), and 92% for the >80 kA range ($N=12$). Thus, flashes with higher first return stroke peak currents are generally more likely to have detectable PB pulse trains, although this trend can be countered by the distance dependence (discussed in the next section). In other

words, a less-intense event at a smaller distance can have the same probability of PB detection as a more distant event of higher intensity.

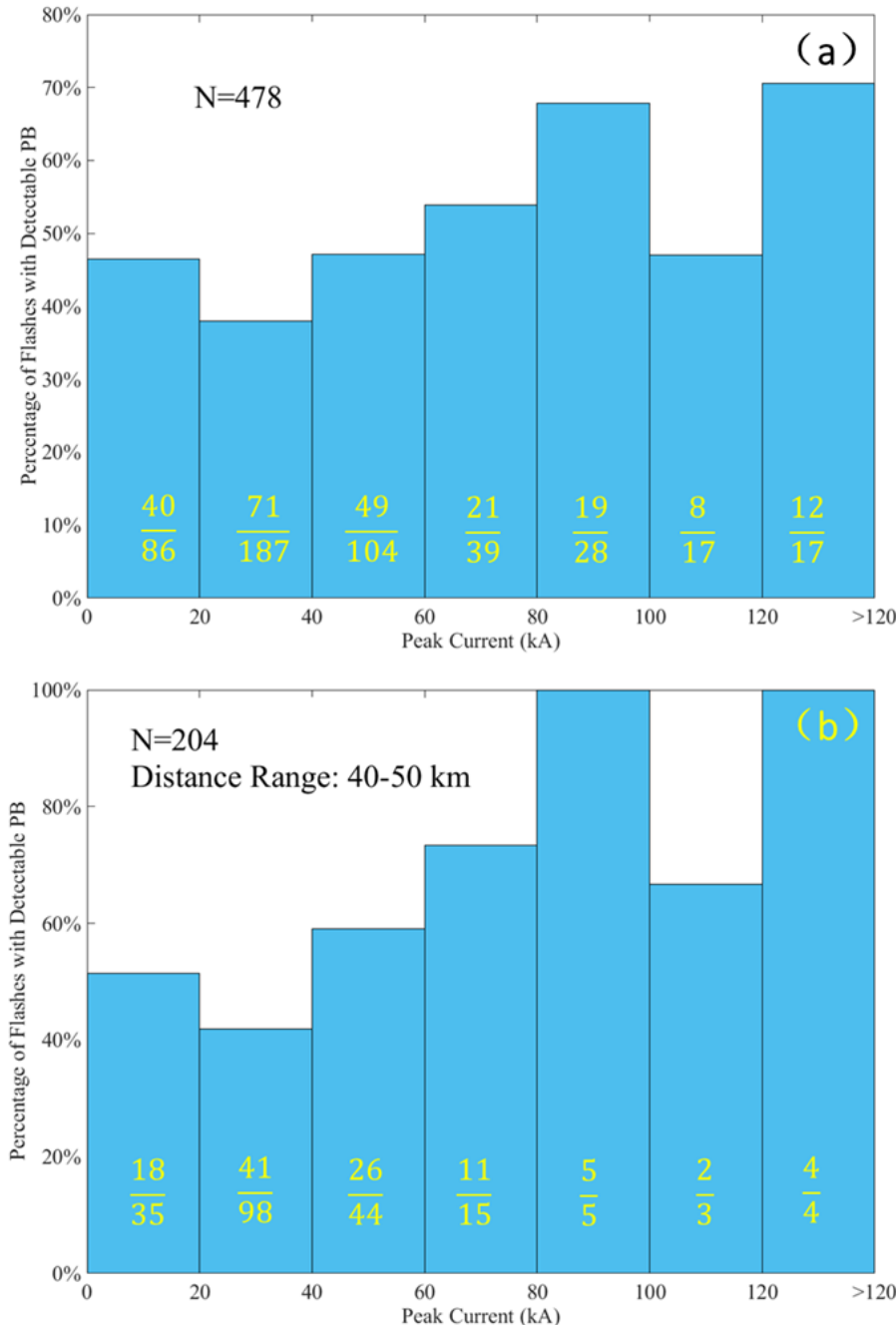


Figure 4-4. Percentage of flashes with detectable PB pulse trains versus peak current. a) The percentage of flashes with detectable PB pulse trains versus peak current of first return stroke reported by the NLDN for all 478 flashes. The denominator is the sample size and the numerator is the number of flashes with detectable PB pulse trains. b) The same as Figure 4-4a, but for 204 flashes at distances ranging from 40 to 50 km.

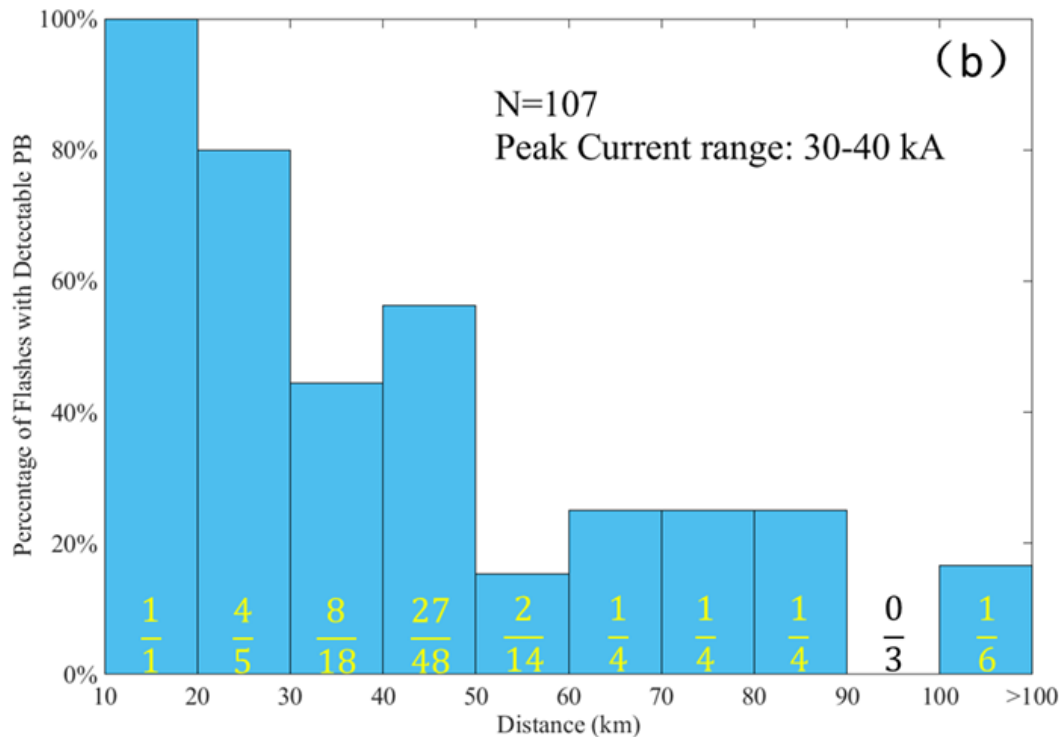
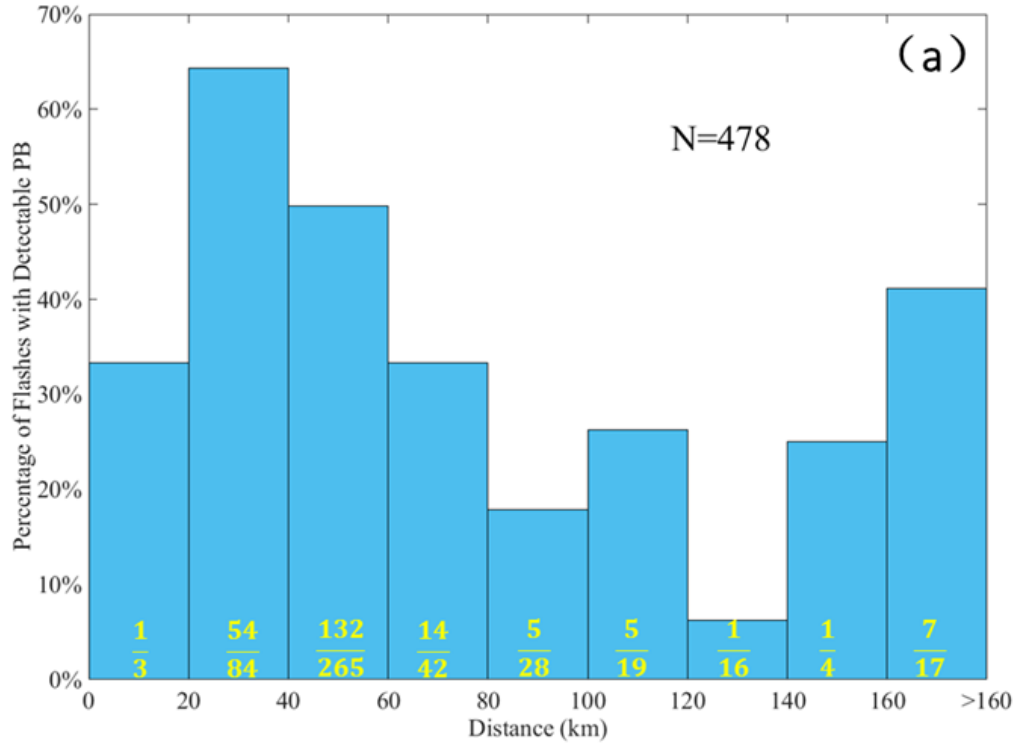


Figure 4-5. Percentage of flashes with detectable PB pulse trains versus distance. a) The percentage of flashes with detectable PB pulse trains versus distance from the strike point to the observation point for all 478 flashes. b) The same as Figure 4-5a, but for 107 flashes with first-stroke peak currents ranging from 30 to 40 kA.

4.2.4 Distance from the Strike-Point Location to the Observation Point

The effect of distance from the strike-point location of flash to the observation point on detectability of PB pulse trains is examined in this section. The PB detectability for all the 478 flashes is plotted versus distance in Figure 4-5a from which no clear dependence on distance can be seen, probably because of the effect of first-stroke peak current discussed in the previous section. In order to reduce that effect, we chose flashes with first-stroke peak currents in the relatively narrow 30-40 kA range (which has the largest sample size compared to other ranges) to examine the PB detectability variation versus distance. The results are shown in Figure 4-5b. Although the sample size in the first two bins and the last several bins are rather small, similar to the analysis of the effect of prospective peak current on detectability of PB pulse trains, a decreasing trend is evident. If we combine some adjacent bins, we can find that the PB detectability for flashes in the distance ranges 10-30 km (N=6), 30-60km (N=80), and more than 60 km (N=21) are 83%, 46%, and 19%, respectively. Also, one can see from Figure 4-2 that most flashes with detectable PB pulse train before filtering (black dots) are close to the LOG. Therefore, as expected, the detectability of PB pulse trains decreases significantly with increasing distance from the strike-point location to the observation point. However, this trend can be countered by a higher probability of recording larger-current events from larger distances, when measurements are performed at a single station with a fixed trigger threshold.

4.3 Automated Analysis of Preliminary Breakdown and Return Stroke Processes in High-Intensity Negative Lightning Discharges

4.3.1 Data

All the electric field records in this section were acquired at the Lightning Observatory in Gainesville (LOG), Florida, in 2014. In the late summer of 2014, the multi-station electric field measuring system was operated in single-station mode. The record length is 2s with 700 ms

pretrigger time. The system was triggered when the electric field change produced by lightning exceeded a fixed threshold. This triggering scheme resulted in some bias toward a larger fraction of higher-intensity events in the records from larger distances. Unfortunately, this bias did not allow us to meaningfully compare, for the same azimuth, the stroke intensity over land and over salt water, since the over-salt-water events were farther away from the LOG than the over-land events. The electric field measuring system at LOG was mostly triggered by first strokes in cloud-to-ground (CG) flashes, although triggering by other lightning processes occasionally occurred. Data from the U.S. National Lightning Detection Network (NLDN) were used to provide the location and first RS peak current for each flash. The median values of NLDN location error and absolute peak current estimation error were found by *Mallick et al.* [2014] to be 334 m and 14%, based on a comparison of NLDN responses to rocket-triggered lightning with ground-truth data.

4.3.2 Methodology

In order to process LOG electric field data more efficiently, an automated procedure was developed to match NLDN data and LOG electric field records (all GPS-time-stamped), process the electric field data, detect the PB pulse trains and corresponding first RS pulses, and measure parameters of those trains, as well as the PB-RS time interval. The automated procedure is described below and illustrated in Figure 4-6.

Step 1. Find LOG records containing NLDN-reported negative first strokes

For each LOG electric field record, we define a 3-ms time window centered at the GPS time stamp of the record. Then we search the NLDN negative flash dataset containing information only on the first stroke in each flash (subsequent strokes in multiple-stroke flashes are not included in this dataset) in the 50 to 500 km range of distances from the LOG to see if the NLDN detected a first stroke in that 3-ms window. If no NLDN-reported first stroke is found, the

electric field record is discarded. If the NLDN reported a first stroke within the 3-ms time window (within ± 1.5 ms of the LOG trigger) and within 50 to 500 km of LOG, we go to step 2. During step 1, LOG records triggered by subsequent strokes, cloud discharges, and close (<50 km) lightning events (which may contain significant non-radiation field components that make the automated detection of pulses difficult), as determined by the NLDN, are excluded from this study.

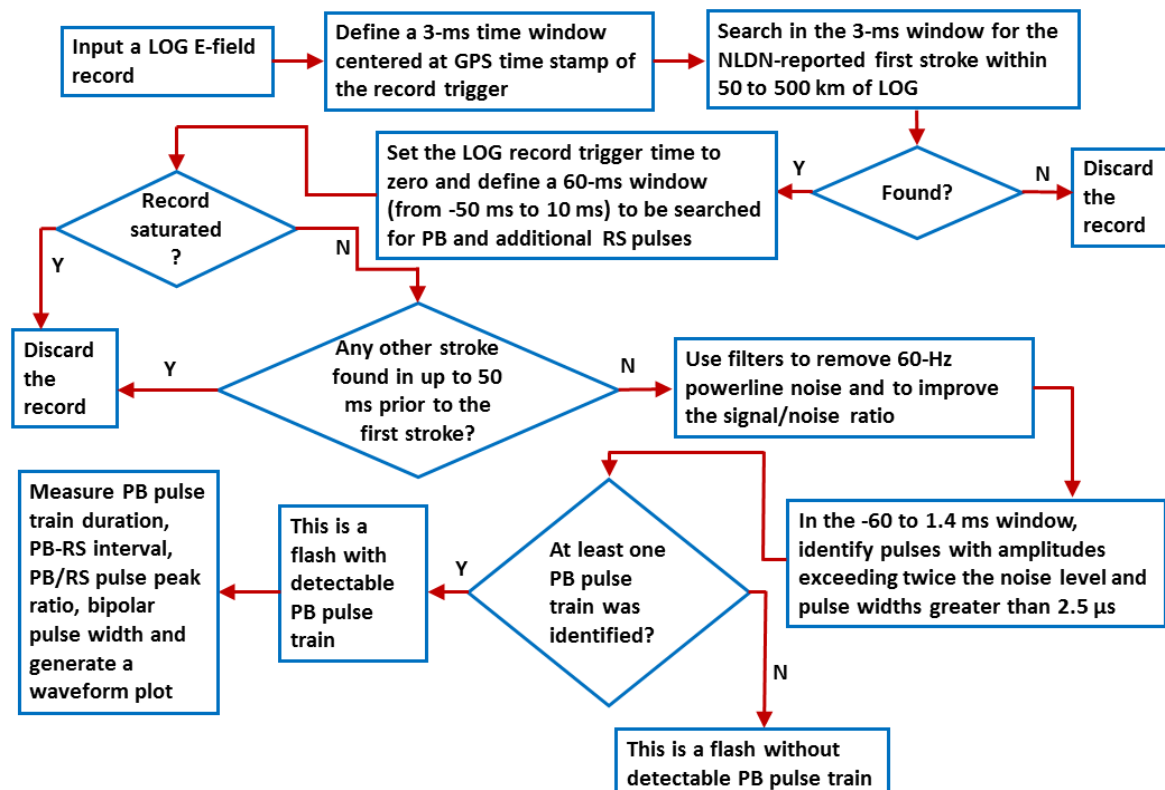


Figure 4-6. Flowchart of the automated data processing algorithm. LOG, Lightning Observatory in Gainesville, Florida; NLDN, U.S. National Lightning Detection Network; PB, preliminary breakdown; RS, return stroke.

Step 2. Exclude LOG records that are saturated or contain other strokes prior to the first stroke of interest

If an NLDN-reported first stroke is found in step 1, we further check, in a 60-ms window (within -50 ms to $+10$ ms relative to the record GPS time stamp) if (1) the field record is saturated or (2) one or more strokes are found up to 50 ms prior to the first return stroke. This is

accomplished by using another NLDN dataset which includes information on both first and subsequent strokes in each flash. The 50-ms pre-return-stroke interval was selected because 95% of PB-RS intervals in Florida negative CGs are less than 50 ms [*Baharudin et al., 2012; Zhu et al., 2015*]. Occurrence of other return strokes (e.g., from a different flash) less than 50 ms prior to the first return stroke would not allow us to adequately examine the PB-RS time interval. If the record is saturated or there are other return strokes within 50 ms prior to the first return stroke of interest, the record is discarded. Otherwise, we go to step 3.

Step 3. Reduce noise

At this point, ideally, we have a 60-ms (-50 ms to $+10$ ms) electric field records with the first return stroke at $t = 0$ and possibly cloud pulses before and after the first return stroke. Additionally, we allowed the occurrence of subsequent strokes (using the NLDN temporal and spatial criteria to group strokes into flashes) between 0 and $+10$ ms, which would not interfere with our analysis. The 60-ms records were passed through the moving-average and power-line-noise-removal filters to remove 60-Hz power-line noise and to improve the signal/noise ratio. The power-line-noise-removal filter generates a 60-Hz sinusoidal waveform, based on the phase and amplitude of the power-line signal found from the 60-ms record, and subtracts that sinusoidal waveform from the original record. The moving-average window was $0.6 \mu\text{s}$ (31 points). After reducing noise we go to step 4.

Step 4. Identify and characterize individual pulses

From the beginning of the 60-ms record to 1.4 ms prior to the first return stroke (from -60 ms to -1.4 ms), we search each record to identify all unipolar pulses wider than $2.5 \mu\text{s}$ and all bipolar pulses wider than $5 \mu\text{s}$ with amplitudes greater than three times the residual noise level. Bipolar pulses were defined as composites of two consecutive monopolar pulses of

opposite polarity separated by a time interval shorter than one-tenth of the width of the first pulse. The criteria used at this step were optimized by the trial-and-error method to achieve the best discrimination of lightning-generated pulses from residual noise. The -1.4 ms upper limit for the pulse search window was needed to exclude pulses generated by the stepped leader near ground; also, no PB-RS intervals shorter than 1.4 ms were reported for Florida lightning by *Baharudin et al.* [2012] and *Zhu et al.* [2015]. At the end of this step, we have amplitudes and widths of all pulses in the search window. Then we go to step 5.

Step 5. Identify PB pulse trains (if any) and measure parameters of the train

We consider as a pulse train a sequence of at least three detected bipolar pulses. Pulses that are separated from the last pulse of the train by more than 2 ms are considered not belonging to that train, which is the same criterion as that used in *Nag and Rakov* [2008] and *Zhu et al.* [2015]. If no PB pulse train is identified, the flash is labeled as having no detectable PB pulses and not included in further analysis. If one or more PB pulse trains are identified, the flash is considered as a flash with detectable PB pulses. In the following, we consider only pulses that belong to PB pulse trains. If a record contains one or more detected PB pulse trains, the automated data processing code will output a plot showing the 60-ms filtered electric field record, including the first-return-stroke pulse and all detected PB pulses, each marked by a box, along with all the pertinent information (given in a table above the plot) about this event, including the filename, date, location, NLDN-reported peak current, and all the PB pulse train parameters (including the PB-RS interval). An example of the output plot is shown in Figure 4-7.

From August to October 2014, during 31 storms, thousands of electric field records were obtained and processed using the automated algorithm described above. For a total of 5498 flashes with NLDN-reported first return strokes, 3496 (64%) had detectable PB pulse trains. The

NLDN-reported locations of all the 5498 first strokes are shown in Figure 4-8. Since (1) the algorithm excluded all flashes that occurred within 50 km of LOG and (2) the average distance to LOG for the 5498 accepted flashes was 235 km, our dataset is biased toward flashes with higher peak currents. Specifically, the arithmetic mean (AM) and geometric mean (GM) of NLDN-reported peak currents are 119 kA and 104 kA, respectively, for all the 5498 events, and 124 kA and 109 kA, respectively, for 3496 events with detectable PB pulse trains, which are considerably higher than the GM value of 30 kA for first strokes in negative lightning [Rakov and Uman, 2003]. A histogram of NLDN-reported peak currents for the 3496 events with detectable PB pulse trains is shown in Figure 4-9. In this study, we excluded 133 events with multiple PB pulse trains and considered only high-intensity events with the NLDN-reported first-stroke peak currents \geq 50 kA, for which the sample size was 3077 and the GM peak current was 122 kA.

Event ID: 2014-10207	Date and time: 2014/09/02 13:35:08.327 UT	Distance to LOG: 205 km	Distance to coastline: 93 km
Location: 30.408N, 80.408W	Occurred over land or salt water: salt water	Peak current: 77.4 kA	PB-RS interval: 10.8 ms
Largest PB pulse peak (d.u.): 0.03	Range-normalized largest PB pulse amplitude (d.u.): 0.062	PB/RS pulse peak ratio: 0.272	PB pulse train duration: 2.04 ms

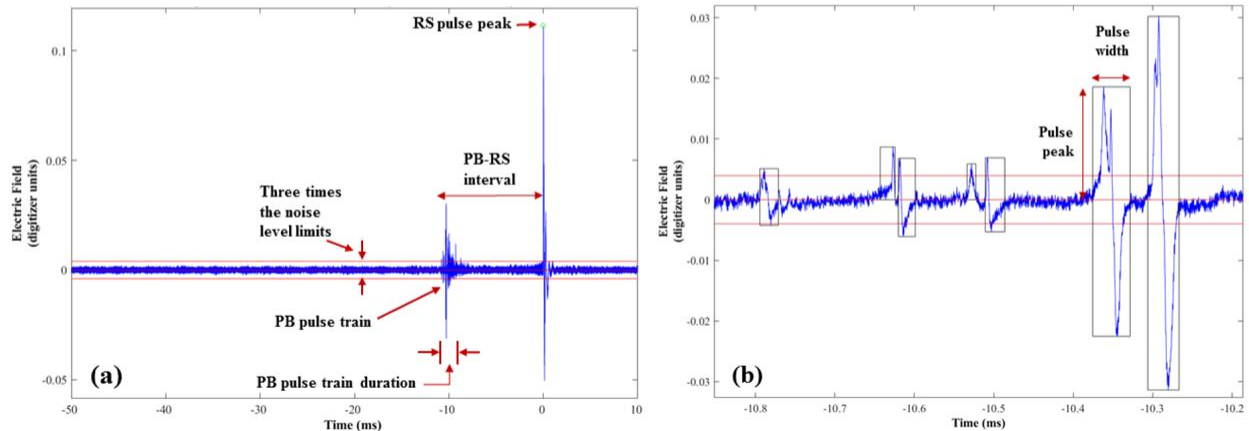


Figure 4-7. An example of the output figure produced by the automated data processing algorithm, a) An output figure and a table containing pertinent information about the flash; b) Expansion of the initial part of the PB pulse train shown in (a) with the detected PB pulses marked by boxes. The d.u. stands for digitizer units.

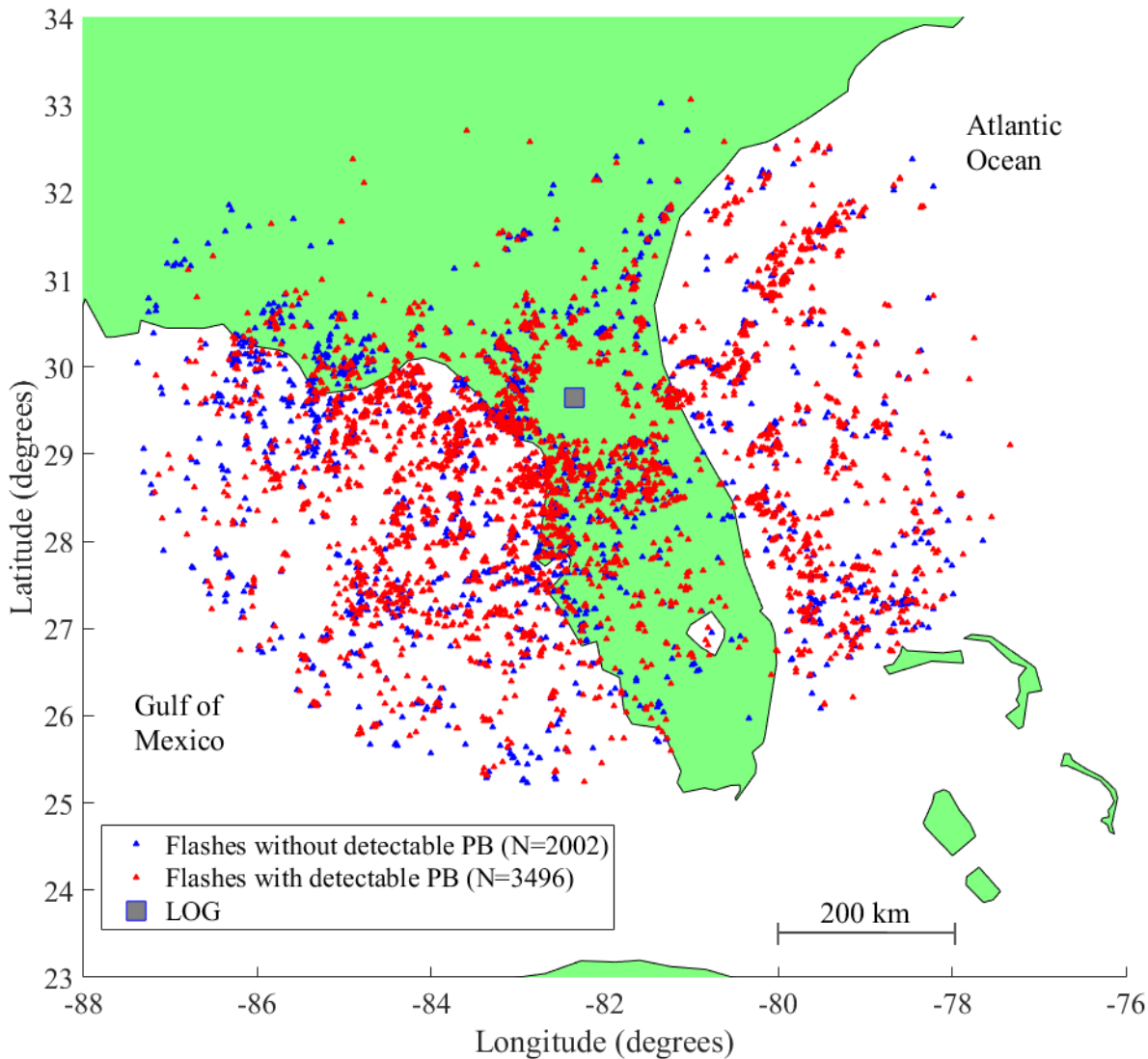


Figure 4-8. NLDN-reported locations of the 5498 negative first strokes within 50 to 500 km of LOG.

Table 4-2. Characterization of PB pulses in 3077 negative flashes each containing a single PB pulse train.

Parameters	AM	GM	Min	Max	Sample size
PB/RS pulse peak ratio	0.15	0.13	0.02	0.81	3077
PB-RS interval (ms)	8.8	7.5	1.7	49.9	3077
PB pulse train duration (ms)	2.7	2.2	0.19	26.8	3077
Bipolar pulse width (μ s)	25	21	5	170	43010
NLDN-reported peak current (kA)	134	122	14	432	3077
Distance to LOG (km)	246	222	51	495	3077

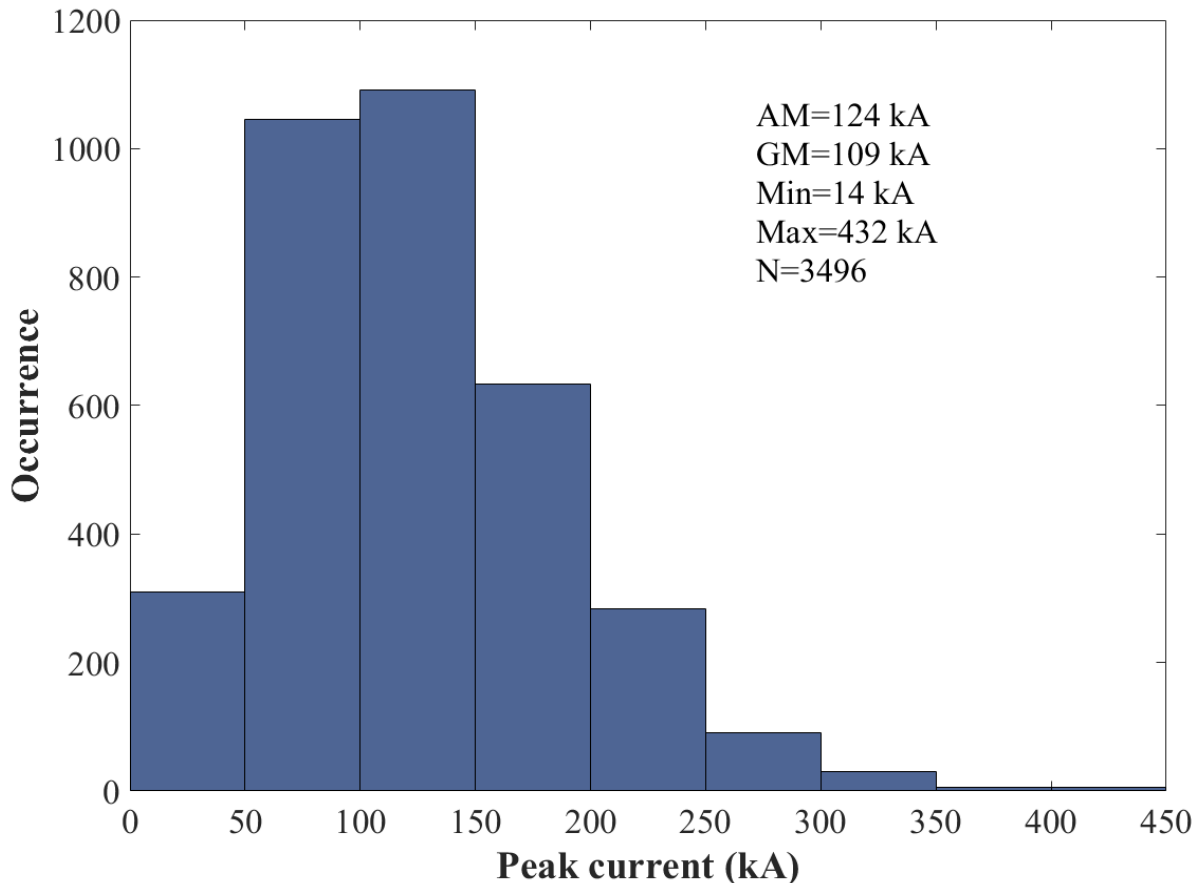


Figure 4-9. Histogram of NLDN-reported peak currents for the 3496 negative first strokes in flashes with detectable PB pulse trains. The arithmetic mean (AM) and geometric mean (GM) distances to LOG for the 3496 flashes are 229 and 201 km, respectively.

4.3.3 Characteristics of PB Pulse Trains in High-Intensity Negative Flashes

We found that 133 (3.8%) of 3496 flashes with detectable PB pulses had multiple PB pulse trains. In order to avoid ambiguity, these 133 events were excluded from the analysis presented in this section. Further, to limit our analysis to high-intensity events, we also excluded 286 (8.2%) events with NLDN-reported peak current < 50 kA, so that the sample size here is reduced to 3077 with the total number of bipolar pulses being 43,010. Statistics for the PB-RS interval, PB/RS pulse peak ratio, PB pulse train duration, and bipolar pulse width, as well as for the NLDN-reported current and distance are given in Table 4-2.

The AM PB/RS pulse peak ratio of 0.15 in Table 4-2 is comparable to the AM values of 0.20 to 0.29 reported in the literature [Baharudin *et al.*, 2012; Marshall *et al.*, 2014; Zhu *et al.*, 2015]. The AM PB-RS interval of 8.8 ms in Table 4-2 is more than a factor of two smaller than previously reported, this disparity being likely due to the very high AM peak current of 134 kA (GM = 122 kA) in our dataset. The AM and GM values of PB pulse train duration in Table 4-2 are somewhat longer than their counterparts, 2.2 and 1.7 ms, respectively, given in Zhu *et al.* [2015]. The AM and GM bipolar pulse widths in Table 4-2 are 25 μ s and 21 μ s, respectively, which are consistent with typical widths of 20–40 μ s reported by Rakov *et al.* [1996]. Histograms of the parameters of PB pulses summarized in Table 4-2 are shown in Figures 4-10 to 4-13.

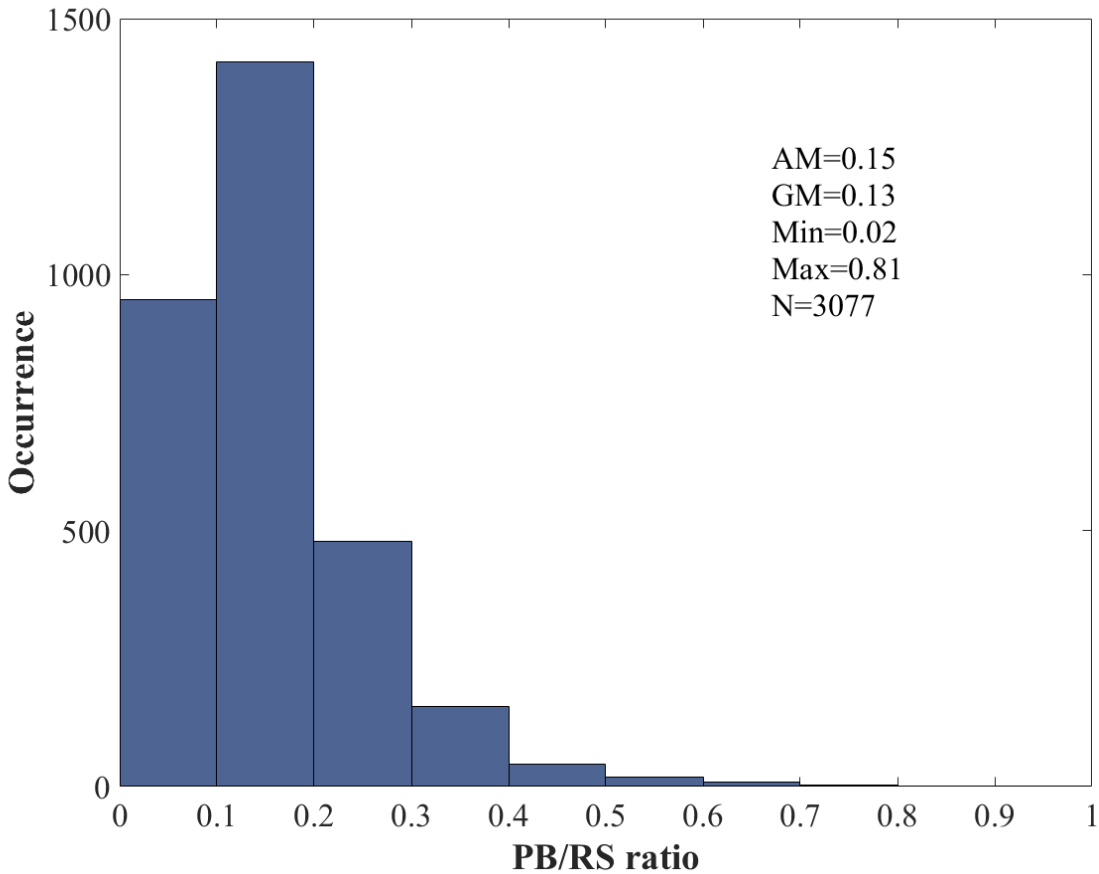


Figure 4-10. Histogram of PB/RS pulse peak ratio for the 3077 flashes.

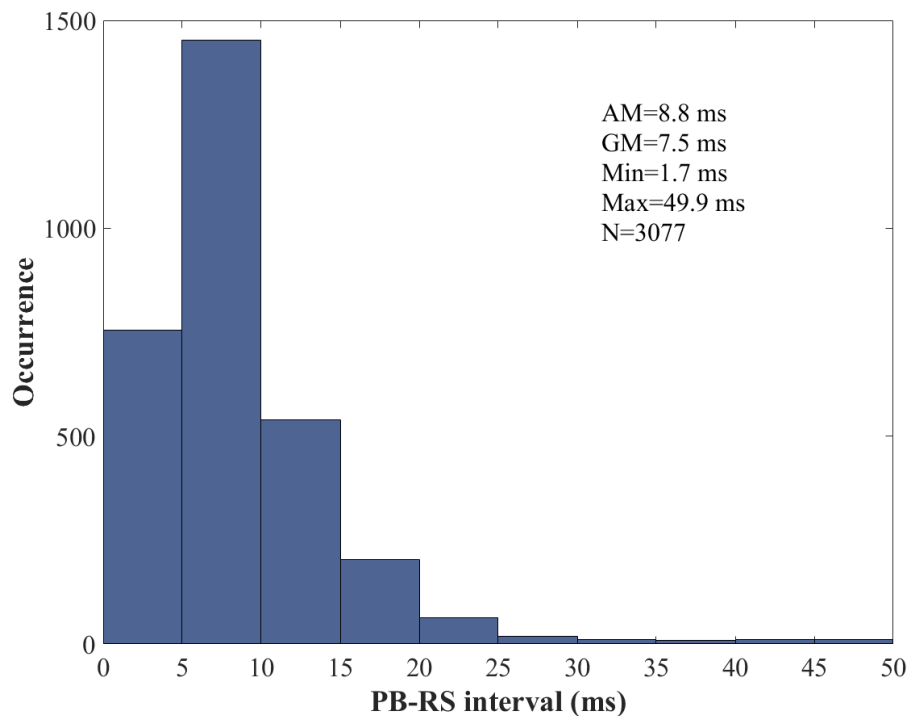


Figure 4-11. Histogram of PB-RS interval for the 3077 flashes.

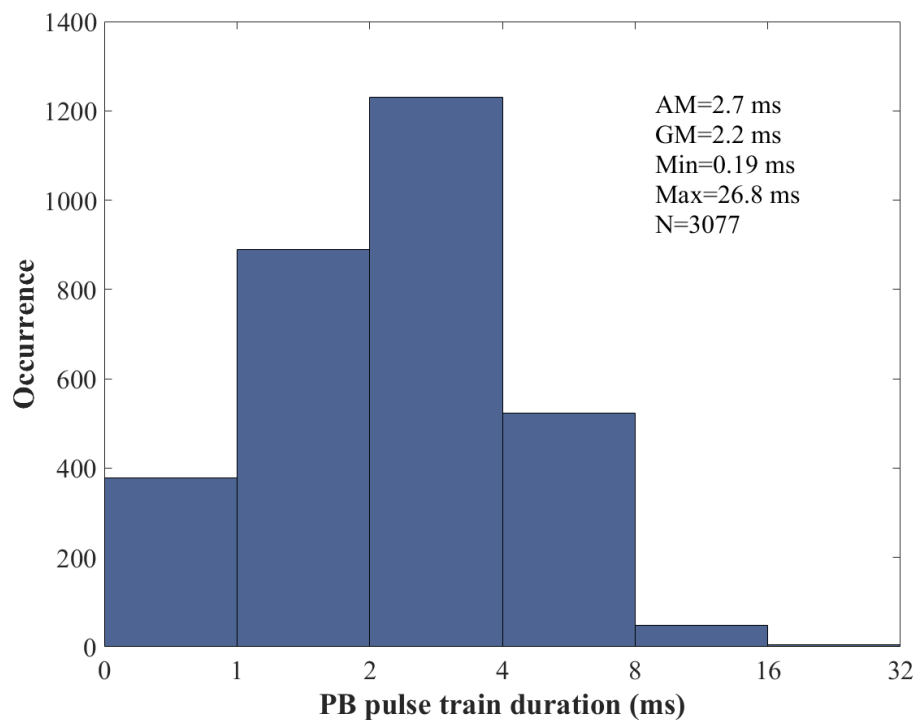


Figure 4-12. Histogram of PB pulse train duration for the 3077 flashes.

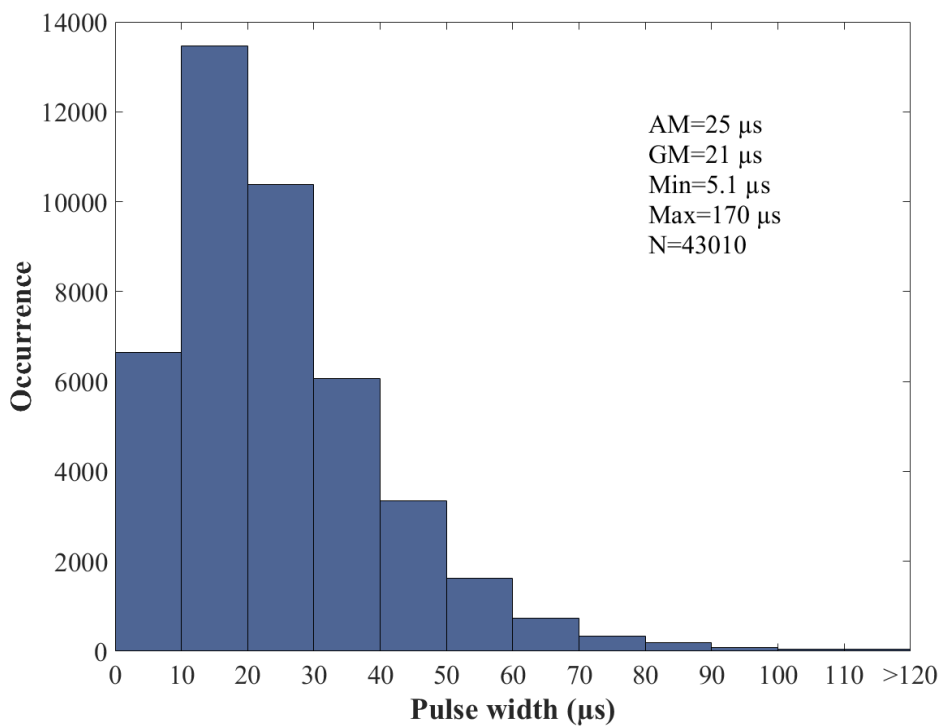


Figure 4-13. Histogram of bipolar pulse width in the 3077 flashes.

4.3.4 Correlation between Parameters of Preliminary Breakdown and Return Stroke Processes

In this section, besides showing the correlation plots for the dataset ($N=3077$) of high-intensity (≥ 50 kA) flashes, similar plots were shown for the dataset ($N=3363$) without excluding the flashes with first-stroke peak currents ranging from 0 to 50 kA. Figure 4-14a shows a scatter plot of PB-RS interval vs. NLDN-reported RS peak current. Clearly, the PB-RS interval tends to decrease with increasing peak current. The best fit curve, $y = 1560 \times x^{-1.12} - 0.694$, obtained by using the power law function in Matlab is also shown. The Spearman correlation coefficient between the PB-RS interval and the NLDN-reported peak current was determined to be -0.80 with the p-value less than 0.001; this indicates a strong negative correlation which is statistically significant at the 99.9% confidence level. Note that Spearman correlation coefficient is a non-parametric measure of rank correlation [MacDonald,

2008], which is used to assess monotonic relationships (not necessarily linear). Similar plot is also shown in Figure 4-15 for 3363 negative first strokes, in which the 0-50 kA events were not excluded. A stronger correlation could be found.

Zhu et al. [2014] reported nine negative flashes (Table 4-3) with short PB-RS intervals, all of which exhibited high ($AM = 131$ kA) NLDN-reported peak currents. For five of the nine events, the corresponding Lightning Mapping Array (LMA) data were available and showed that the first LMA source heights ranged from 4.8 to 6 km. Based on these observed flash initiation heights and corresponding PB-RS intervals (stepped leader durations), *Zhu et al.* [2014] estimated the average 1D stepped-leader speed to be 1.2×10^6 m/s, which (although an underestimate) is almost an order of magnitude higher than 2×10^5 m/s thought (e.g., *Rakov and Uman*, [2003], Chapter 4) to be typical for negative stepped leaders. Thus, the strong correlation seen in Figures 4-14a and b suggests that negative flashes with faster stepped leaders tend to have higher first RS peak currents. *Jordan et al.* [1992] found that the subsequent (dart or dart-stepped) leader speed and return-stroke peak current are positively correlated for both natural and rocket-triggered lightning. It is likely that this trend also holds for first strokes initiated by stepped leaders.

Table 4-3. Summary of short PB-RS interval events

Flash ID	Time Interval between PB and First Return Stroke (ms)	First Return Stroke Peak Current Reported by NLDN (kA)	Inferred Leader Speed* (m/s)
839	3.5	222	1.61×10^6
854	4.5	133	1.3×10^6
881	5.9	82	0.78×10^6
882	6.0	102	-
1138	4.4	129	-
1203	4.0	150	1.23×10^6
1204	3.6	172	1.28×10^6
1205	4.3	110	-
1215	5.0	128	-
GM	4.5	131	1.21×10^6

* Estimated as $v=H/T_{PB-RS}$, where H is the altitude of the first LMA source. This estimate should be considered as a lower bound because the actual (3D) channel length should be considerably larger than H .

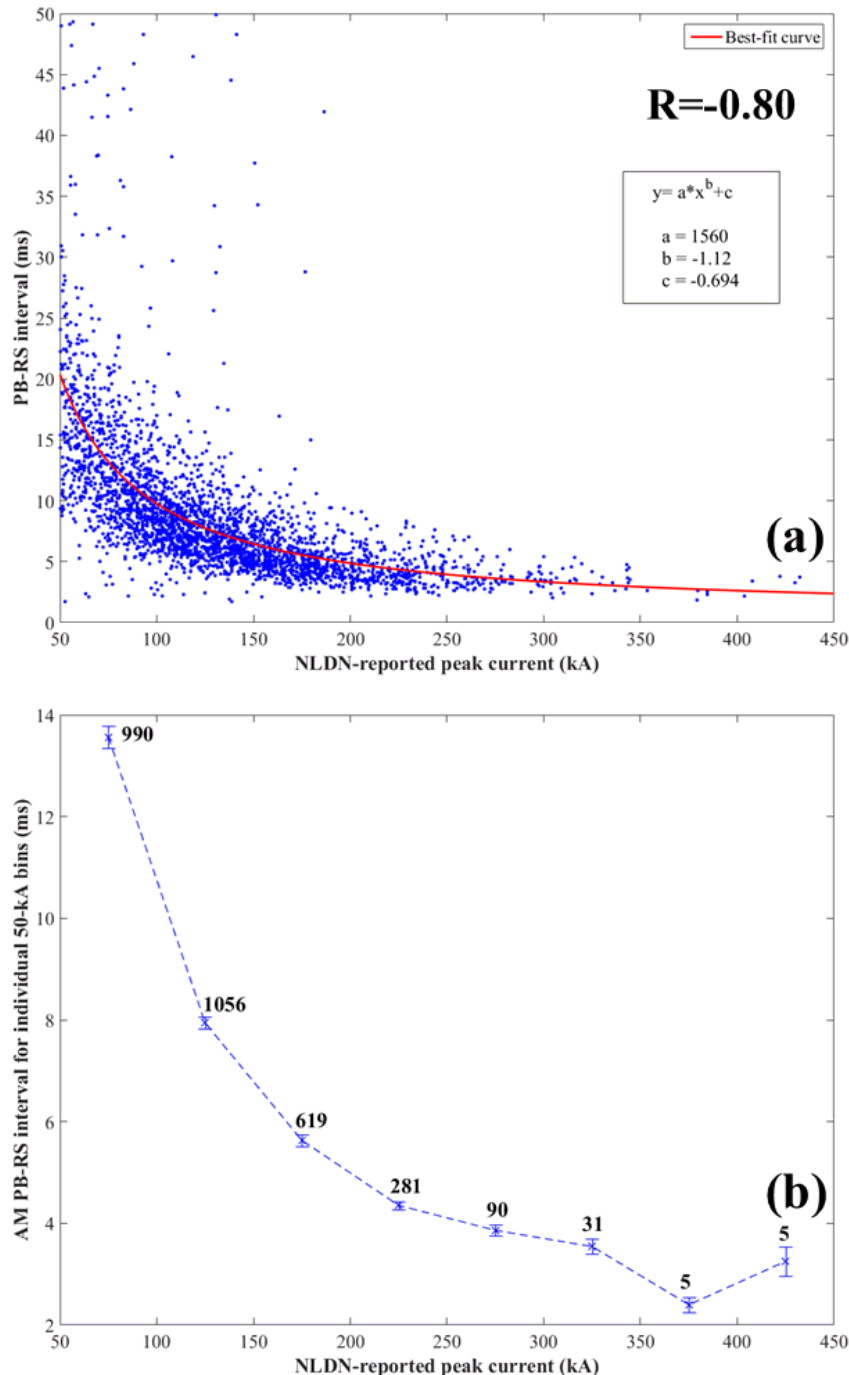


Figure 4-14. PB-RS interval versus NLDN-reported RS peak current for 3077 negative first strokes. a) Scatterplot of PB-RS interval versus NLDN-reported RS peak current for 3077 negative first strokes within 50 to 500 km of LOG. The best-fit curve, $y = 1560 * x^{-1.12} - 0.694$, is shown by solid red line. R is the Spearman correlation coefficient; b) AM values of PB-RS interval versus NLDN-reported RS peak current for individual 50-kA bins. The standard errors in mean values are shown by vertical bars and the corresponding sample sizes are given above them.

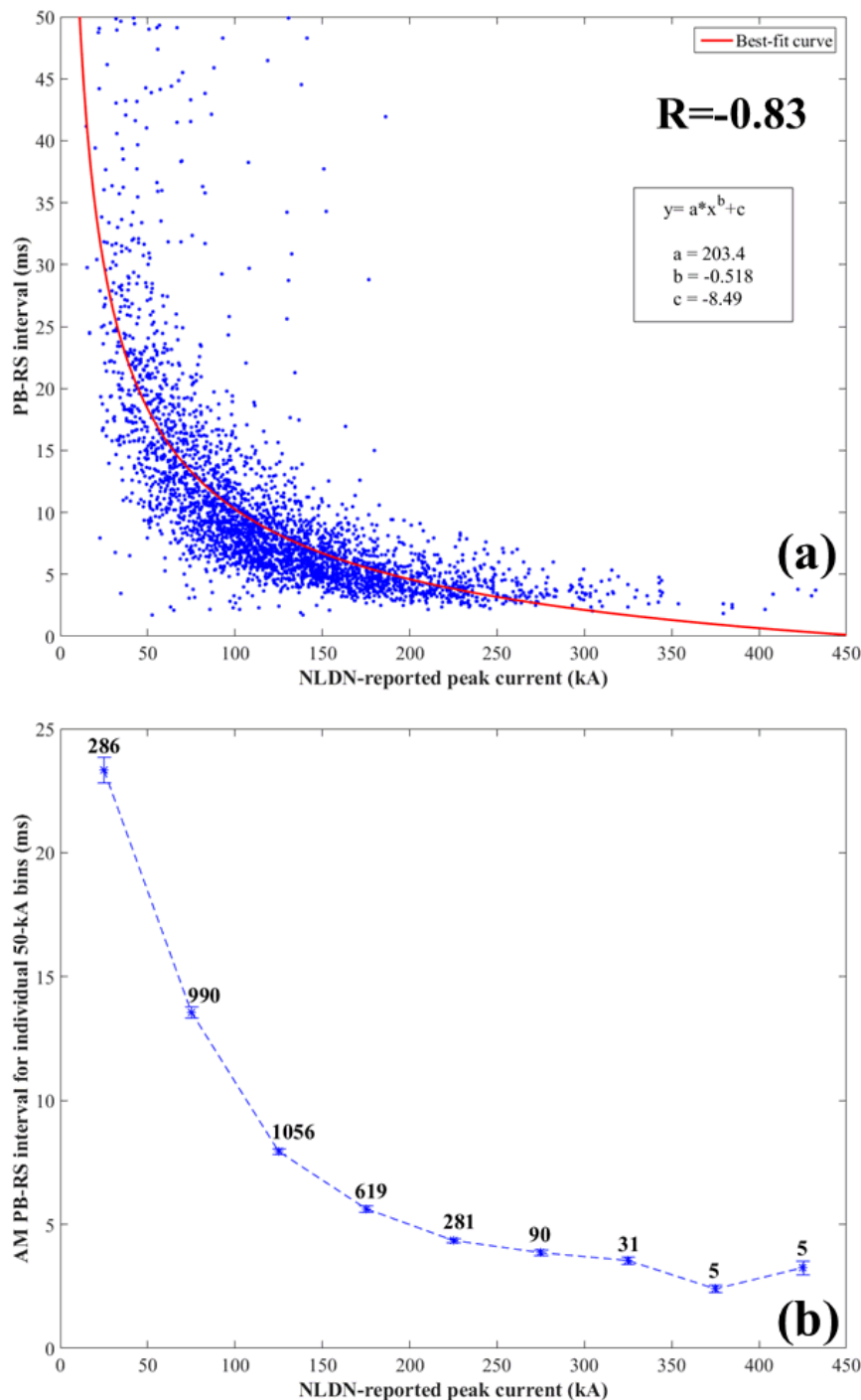


Figure 4-15. PB-RS interval versus NLDN-reported RS peak current for 3363 negative first strokes. a) Scatterplot of PB-RS interval versus NLDN-reported RS peak current for 3363 negative first strokes, within 50 to 500 km of LOG. The best-fit curve, $y=203.4 \cdot x^{-0.518} - 8.49$, is shown by solid line. R is the Spearman correlation coefficient. b) AM values of PB-RS versus NLDN-reported RS peak current interval for individual 50-kA bins. The standard errors in mean values are shown by vertical bars with the corresponding sample size shown above.

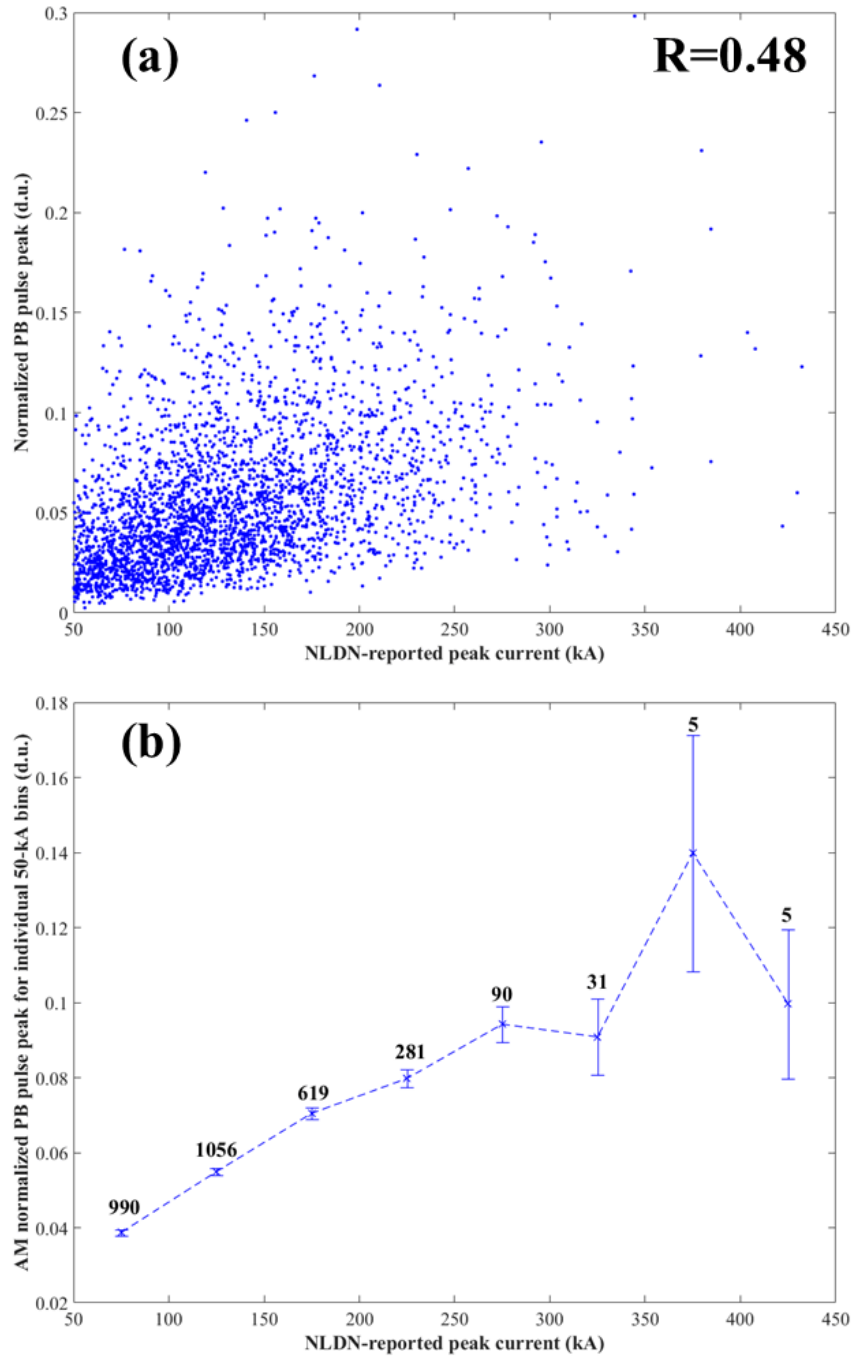


Figure 4-16. Peak of the largest PB pulse normalized to 100 km versus NLDN-reported RS peak current for the 3077 negative first strokes. a) Scatterplot of the peak of the largest PB pulse normalized to 100 km (in digitizer units) versus NLDN-reported RS peak current for the 3077 negative first strokes within 50 to 500 km of LOG. R is the Spearman correlation coefficient; b) AM values of normalized PB pulse peak versus NLDN-reported RS peak current for individual 50-kA bins. The standard errors in mean values are shown by vertical bars and the corresponding sample sizes are given above them.

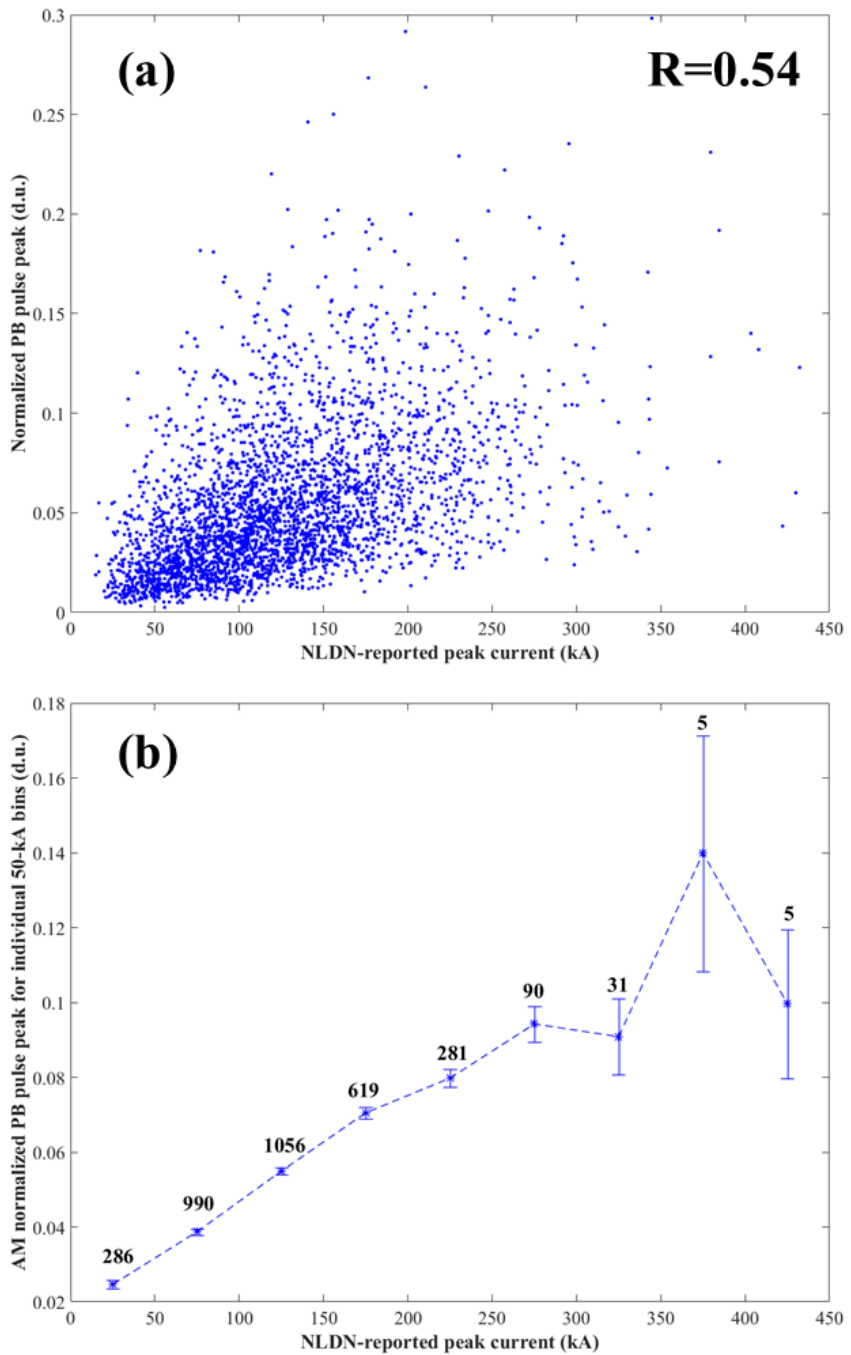


Figure 4-17. Peak of the largest PB pulse normalized to 100 km versus NLDN-reported RS peak current for the 3363 negative first strokes. a) Scatterplot of the peak of the largest PB pulse normalized to 100 km (in digitizer units) versus NLDN-reported RS peak current for the 3363 negative first strokes within 50 to 500 km of LOG. R is the Spearman correlation coefficient. b) AM values of normalized PB pulse peak versus NLDN-reported RS peak current for individual 50-kA bins. The standard errors in mean values are shown by vertical bars with the corresponding sample size shown above.

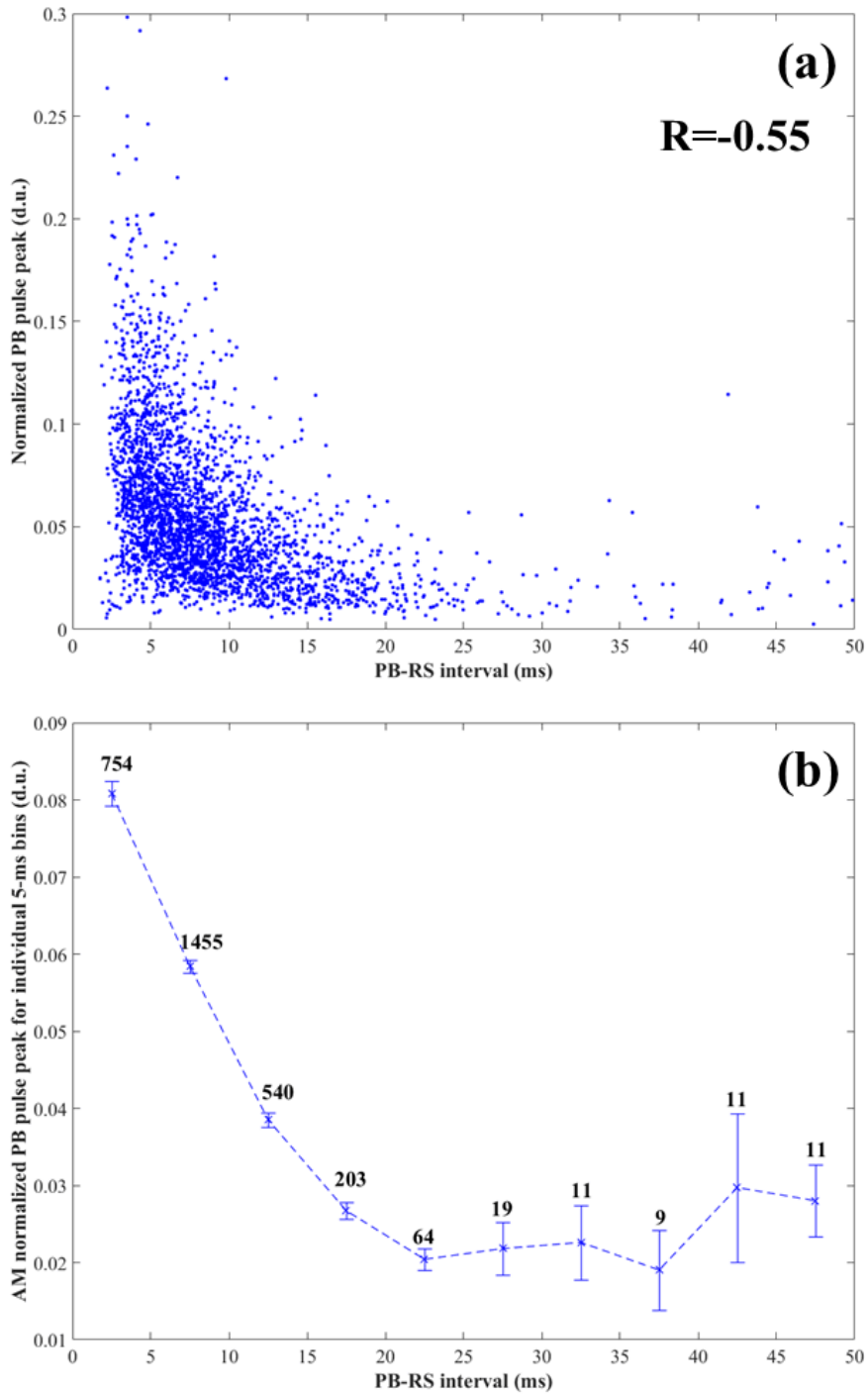


Figure 4-18. Peak of the largest PB pulse normalized to 100 km versus PB-RS interval for the 3077 negative first strokes. a) Scatterplot of the peak of the largest PB pulse normalized to 100 km (in digitizer units) versus PB-RS interval for the 3077 negative first strokes within 50 to 500 km of LOG. R is the Spearman correlation coefficient; b) AM values of normalized PB pulse peak versus PB-RS interval for individual 5-ms bins. The standard errors in mean values are shown by vertical bars and the corresponding sample sizes are given above them.

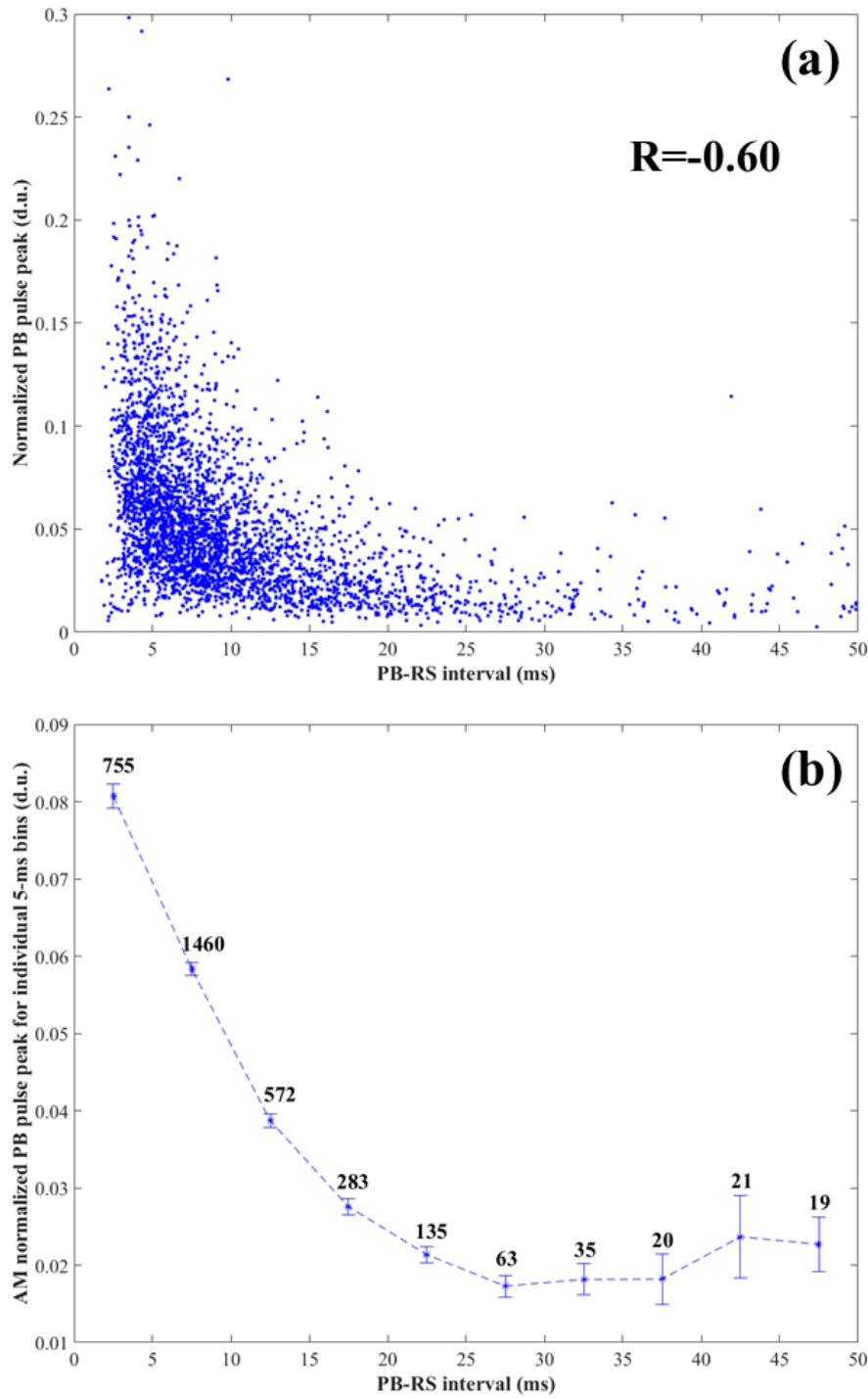


Figure 4-19. Peak of the largest PB pulse normalized to 100 km versus PB-RS interval for the 3363 negative first strokes. a) Scatterplot of the peak of the largest PB pulse normalized to 100 km (in digitizer units) versus PB-RS interval for the 3363 negative first strokes within 50 to 500 km of LOG. R is the Spearman correlation coefficient. b) AM values of normalized PB pulse peak versus PB-RS interval for individual 5-ms bins. The standard errors in mean values are shown by vertical bars with the corresponding sample size shown above.

Scatterplots of the peak of the largest PB pulse normalized to 100 km versus NLDN-reported peak current are shown in Figures 4-16a and 4-17a for datasets with peak currents from 50 to 450 kA and peak currents from 0 to 450 kA, respectively. Normalization was performed assuming that the electric field peak in the 50 to 500 km distance range varies as the inverse inclined distance from the elevated PB source to the LOG. The inclined distance was roughly estimated using the NLDN reported horizontal distance and the assumed source height of 6 km. One can see that the maximum normalized PB pulse peak tends to increase with increasing RS peak current. For the datasets with peak currents from 50 to 450 kA, the Spearman correlation coefficient between the maximum normalized PB pulse peak and NLDN-reported peak current is 0.48 and it is statistically significant at the 99.9% confidence level. It is difficult to discern any trend in Figure 4-16a where the individual data points are shown. However, there is a clear trend (Figure 4-16b) for the AM normalized PB pulse peak corresponding to individual 50-kA bins to increase with increasing RS peak current.

Scatterplots of the normalized PB pulse peak vs. PB-RS interval are shown in Figures 4-18a and 4-19a. The normalized PB pulse peak tends to decrease with increasing PB-RS interval and the corresponding Spearman coefficient are -0.55 for the dataset with peak currents from 50 to 450 kA and -0.6 for the dataset with peak currents from 0 to 450 kA. It is statistically significant at the 99.9% confidence level. Similar trends were previously observed in Florida [Marshall *et al.*, 2014], as well as in Japan [Wu *et al.*, 2013] and China [Wang *et al.*, 2016].

4.4 Summary

For 478 negative cloud-to-ground lightning flashes, factors that might affect detectability of PB pulse trains were examined. By using the moving average filtering, the percentage of flashes with detectable PB pulse trains increased from 22% to 46%. Thus, the detectability of PB

pulse train is significantly affected by the signal-to-noise ratio of the recording system. Further, PB pulse train detectability can vary from one storm to another. The PB pulse trains of flashes with higher peak currents of the first return stroke and smaller distances to the observation point are more likely to be detected.

Using an automated data processing algorithm, we have examined the characteristics of PB pulse trains and the following first return strokes (RSs) in negative cloud-to-ground lightning flashes in Florida. Out of 5498 flashes within 50 to 500 km of LOG, 3496 (64%) had PB pulse trains that were detected by the automated algorithm. For the 3077 flashes with one detectable PB pulse train and relatively high (≥ 50 kA) first-stroke peak current, the arithmetic (geometric) mean values of peak current, PB pulse train duration, PB-RS interval, PB/RS pulse peak ratio, and bipolar pulse width were 134 (122) kA, 2.7 (2.2) ms, 8.8 (7.5) ms, 0.15 (0.13), and 25 (21) μ s, respectively. The PB-RS interval was found to decrease with increasing NLDN-reported first-stroke peak current, with the corresponding Spearman correlation coefficient being -0.80 (statistically significant at the 99.9% confidence level). Since shorter PB-RS intervals were found to correspond to faster leaders [Zhu *et al.*, 2014], the latter result suggests that negative flashes with faster stepped leaders tend to have higher first-stroke peak currents. The largest range-normalized PB pulse peak exhibited positive correlation with the RS peak current, with Spearman correlation coefficient of 0.48 (statistically significant at the 99.9% confidence level). Thus, it appears that the high-intensity (≥ 50 kA) negative lightning is characterized by shorter (and, by inference, faster) stepped leaders and more pronounced PB pulse trains. The range-normalized PB pulse peak tended to decrease with increasing the PB-RS interval (Spearman correlation coefficient = -0.55 ; statistically significant at the 99.9% confidence level).

CHAPTER 5

A SUBSEQUENT POSITIVE STROKE DEVELOPING IN THE CHANNEL OF PRECEEDING NEGATIVE STROKE AND CONTAINING BIPOLAR CONTINUING CURRENT

5.1 Literature Review

Correlated optical and electric field records of natural downward cloud-to-ground bipolar flashes are rarely reported. Based on video observations and multi-station field measurements, *Jerauld et al.* [2009] gave the first well-documented description of a natural downward bipolar flash containing two initial positive strokes with strike points separated by about 800 m, followed by four negative strokes that traversed the same channel as the second positive stroke. *Fleenor et al.* [2009] reported four bipolar flashes that all started with a positive stroke followed by one or two negative strokes. Out of five subsequent negative strokes in the four flashes, two followed the pre-existing but decayed channel of the first (positive) stroke. *Saba et al.* [2013] presented five natural downward, “single-channel” bipolar flashes in which two strokes of different polarity occurred in the same channel, although there could have been other strokes in different channels. Each of their bipolar flashes started with a positive stroke and all the second (negative) strokes were initiated by optically imaged recoil leaders in decayed upper-level branches of the first downward positive leader. *Saraiva et al.* [2014] observed one single-channel downward bipolar flash and one multi-channel downward bipolar flash. Each of these two started with a positive stroke and all the negative subsequent strokes occurred as a result of recoil leaders, in the manner described above. *Chen et al.* [2015] reported a downward bipolar flash with a first (positive) stroke followed by five negative strokes, all occurring in the same channel terminated on a 90-m tall structure. *Tian et al.* [2016] reported a downward bipolar flash in which the first (positive) stroke was followed by three negative strokes along the same channel. Similarly to *Saba et al.* [2013] and *Saraiva et al.* [2014], they found that the three subsequent

negative strokes were initiated by recoil leaders. There is only one case found in the literature, in which a subsequent positive stroke developed in the channel of preceding negative stroke. It was recently reported by *Xue et al.* [2015] who attributed the polarity change to some intracloud process that altered the cloud charge structure during the relatively long time interval (136 ms) between the two strokes.

In this chapter, we present correlated electric field and high-speed video records of a natural four-stroke cloud-to-ground flash having a negative first stroke followed by a positive stroke in the same channel whose 2D length was 4.2 km. As follows from the literature review given above, this scenario is highly unusual. The second (positive) stroke was followed by bipolar continuing current (with the initial positive charge transfer to ground followed by negative charge transfer to ground), so that the flash exhibited the features of both Type 1 and Type 3b bipolar discharges identified by *Rakov* [2003]. The third and fourth strokes in our flash were negative and followed a newly created channel, different from the one of the first and second strokes. The atmospheric electricity sign convention, according to which the downward-directed electric field change vector produced by a negative return stroke is positive, is used throughout this chapter.

5.2 Instrumentation

The bipolar flash (labeled 2117) was recorded at 01:55:20 UT on Aug. 22nd (at 21:55:20 local time on Aug. 21st), 2014 at the Lightning Observatory in Gainesville (LOG), Florida, by two high-speed video cameras, Phantom V310 and Megaspeed HHC-X2, and by electric field measuring systems. Additionally, the event was recorded by the Total-sky Lightning Channel Imager (TLCI) installed at LOG as part of our collaboration with the Chinese Academy of Meteorological Sciences. The electric field measuring systems include the low-gain and high-gain electric field measuring systems and the electric field derivative (dE/dt) measuring system.

The record length for the field measuring systems was 1 s with 200 ms pretrigger time. The Phantom V310 was operated at 3200 frames per second (fps) with 80 μ s exposure time (232.5 μ s deadtime) and resolution of 1280×800 pixels. The HHC-X2, equipped with a fish-eye lens to provide a wider field of view, was operated at 1000 fps with 1 ms exposure time (essentially no deadtime) and resolution of 832×600 pixels. The electric field records and high-speed video records were GPS time stamped. The synchronization accuracy between the Phantom records and electric field records was better than 1.3 μ s. The spatial resolution of Phantom records used in this study was 5 m. The TLCI had a fish-eye lens and was operated at 40 fps with 25 ms exposure time [Lu *et al.*, 2014]. Outputs of all three optical instruments are generally consistent with each other. Only Phantom images are presented in this chapter. Additionally, U.S. National Lightning Detection Network (NLDN) data, including locations and peak current estimates for lightning strokes, were used in this study.

5.3 Observations and Analysis

5.3.1 General Description

According to the NLDN, flash 2117 contained four strokes with peak currents, in the order of occurrence, of -101 kA, 16 kA, -20 kA, and -32 kA. Based on the locations of strike points provided by the NLDN, the distances between the 1st and 2nd strokes, 2nd and 3rd strokes, and 3rd and 4th strokes were 0.14 km, 1.87 km, and 0.12 km, respectively. The corresponding interstroke intervals (measured between return-stroke field peaks) were 70 ms, 210 ms, and 65 ms. The distance between the strike-point of the first (negative) stroke and LOG was 5 km. This distance was used for estimating all the heights, as well as 2D distances and speeds presented in this chapter. The Phantom high-speed video camera captured all the strokes of this flash. The Megaspeed HHC-X2 high-speed video camera and TLCI captured only the first and second strokes, with the third and fourth strokes being outside their fields of view.

From all the video records, it was unambiguously determined that the second stroke followed the same channel as the first stroke, except for the bottom 115 m, where the channels of the first two strokes were found, from the Phantom record, to be slightly different from each other. It appears that the second-stroke, positive leader, after extending from 3.9 km (the upper limit of the Phantom camera's field of view) to 115 m above ground along the path of the first (negative) stroke, deviated from that path and contacted ground 40 m from the first-stroke termination point. About 210 ms after the second return stroke, the third, negative stroke occurred. It exhibited branching and created an entirely new channel whose termination point was about 1.87 km from that of the second stroke. The fourth stroke was not branched and followed the main channel of the third one. Leaders of the third and fourth strokes had propagation speeds that were characteristic of stepped and dart leaders, respectively. In the field of view of Phantom camera, no clear relation was seen between the former two strokes and the latter two strokes, but they all do satisfy the spatial and temporal stroke grouping into flash criteria used by the NLDN [Cummins *et al.*, 1998]. The third and fourth strokes are not further discussed in this chapter.

Composite images of the first two leader-return stroke sequences are shown in Figure 5-1. As noted above, within about 115 m of the ground, the first and second strokes followed slightly different paths and formed separate ground terminations, which were 40 m apart (2-D distance estimated from the Phantom camera record). The separate terminations are clearly seen in the magnified superposition of the bottom portions of the channels of the first and second strokes shown in the inset in Figure 5-1. As discussed below, the bottom part of the second-stroke channel could be actually created by the first-stroke leader. Based on the Phantom camera

record, the durations of continuing currents (CCs) following the first (negative) stroke and the second (positive) stroke were 5 ms and 122 ms, respectively.

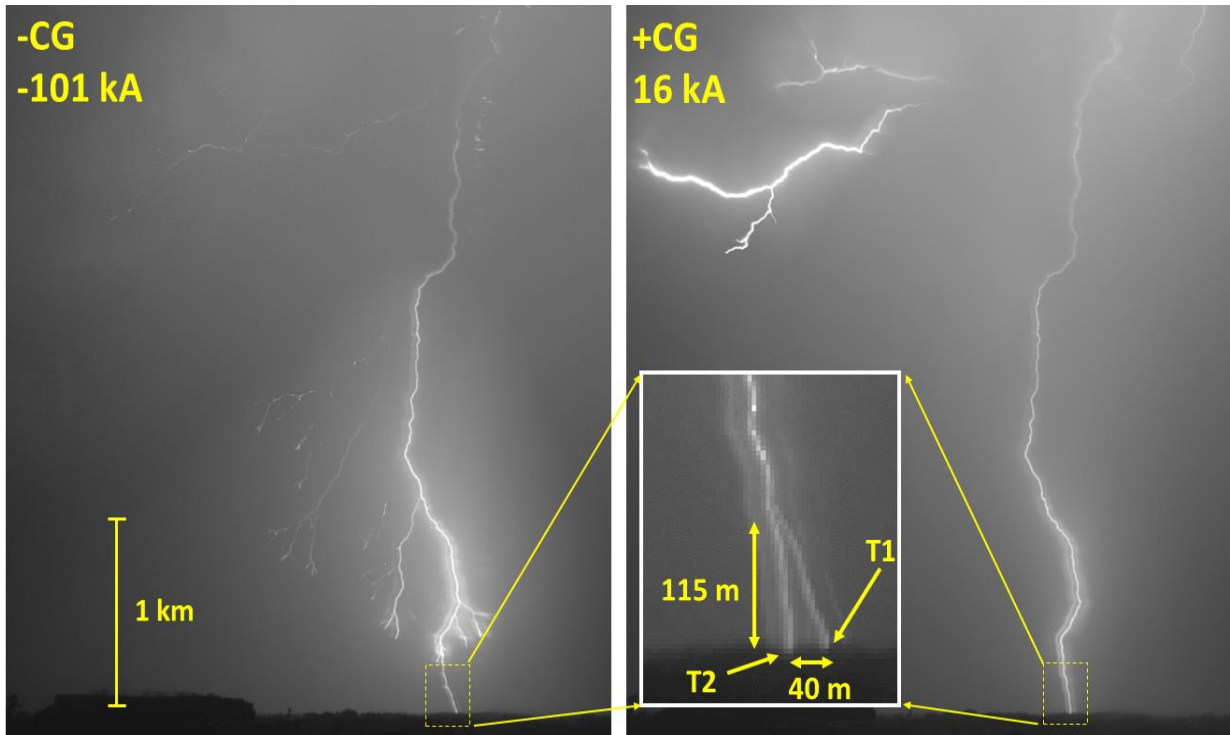


Figure 5-1. Composite Phantom images of the negative first stroke (left panel labeled -CG) and the positive second stroke (right panel labeled +CG). The images were produced using all the frames (except for one and three saturated ones for the negative and positive strokes, respectively) corresponding to the leader, return stroke, and continuing current processes. The top of the imaged channel was about 3.9 km above ground. The inset shows the magnified composite image of the bottom portions of the channels of the first and second strokes. T1 and T2 mark the ground terminations of the first and second strokes, respectively. The predominantly horizontal branches seen in the upper left corner of the right panel were repeatedly illuminated before and during the development of downward positive leader, as well as during and after the continuing current following the positive return stroke. These branches were apparently associated with concurrent in-cloud discharge activity and were possibly connected to the faintly luminous channel segment in the upper right corner (to the right from the main channel) of the right panel, although the connection was obscured by cloud debris. The faintly luminous channel segment (maybe indiscernible in the reproduction) probably had intermittent connection to the main channel to ground.

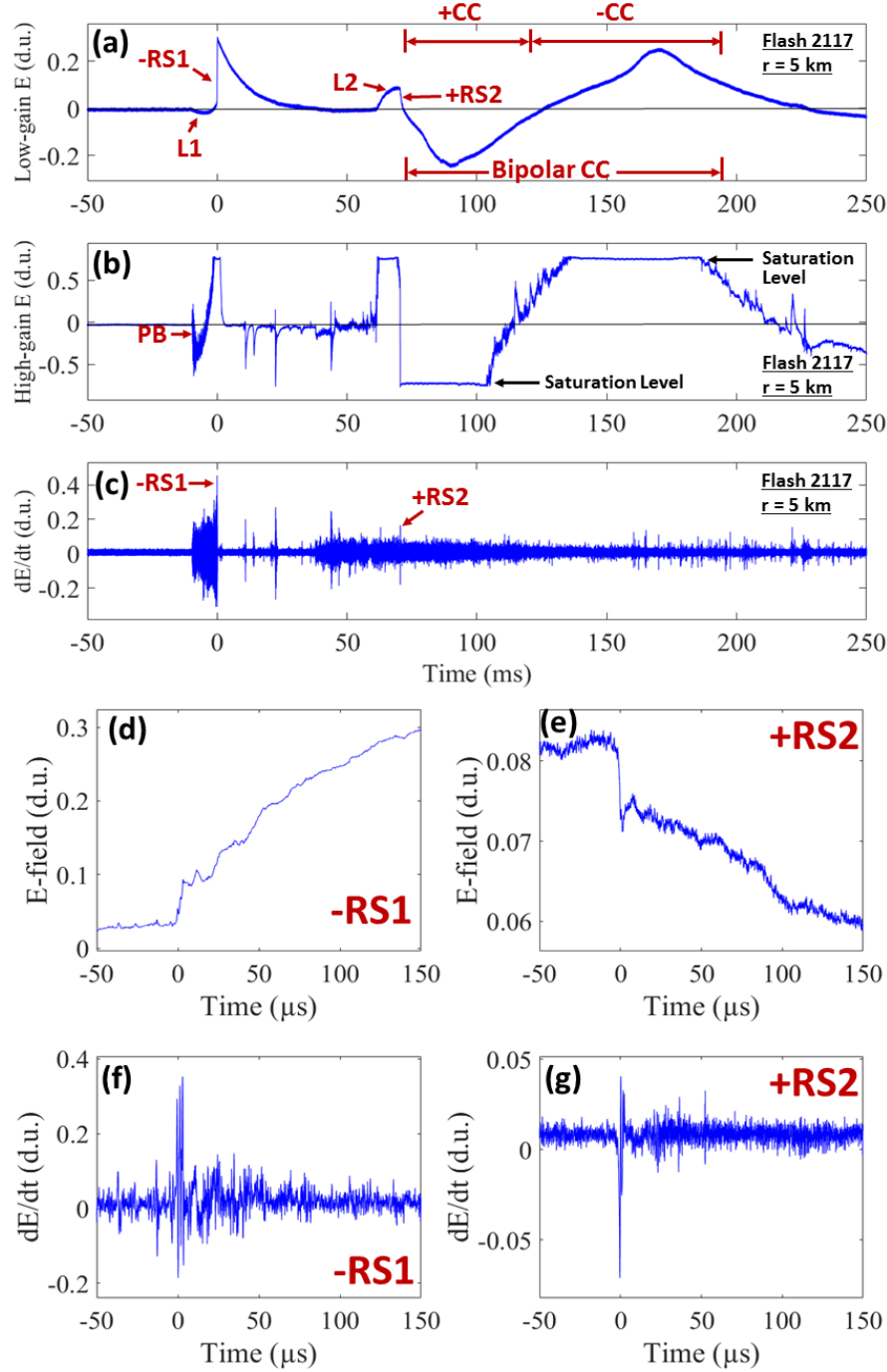


Figure 5-2. Electric field and dE/dt records of the bipolar flash. Panels a) to c) show simultaneous low-gain electric field, high-gain electric field, and dE/dt records of the initial part of the bipolar flash, including the preliminary breakdown (PB), the first and the second leader (L) /return stroke (RS) sequences and bipolar continuing current (CC). Duration of the bipolar CC was estimated from the Phantom camera record. In panels d) to g), the low-gain electric field (panels d) and e)) and electric field derivative (panels f) and g)) waveforms of the negative first and positive second return strokes are shown on a 200- μs time scale. All records have been obtained at a distance of 5 km from the lightning channel.

Figures 5-2a to 5-2c show simultaneous low-gain electric field, high-gain electric field, and dE/dt records of the two strokes of interest. The time interval between the negative first return stroke and the positive second return stroke is 70 ms, which is comparable to the typical interstroke interval in negative flashes of 60 ms [e.g., *Rakov and Uman*, 2003, p. 7]. The leader durations (measured in the low-gain electric field record) for the first and second strokes are similar, 9.5 ms and 9.4 ms, respectively. The net electric field change produced by the leader of the first stroke has the same polarity as the corresponding return-stroke field change, while for the second stroke the net electric field changes due to the leader and return stroke have opposite polarities. This disparity is likely to be caused by different horizontal displacements of the negative and positive charge sources relative to the observer and the channel to ground, as discussed by *Rakov et al.* [1990], with the positive charge being considerably farther from both the observer and channel to ground than the negative one. If so and in view of another polarity change during the continuing current after RS2, the cloud charge structure was far from “classical” (see, for example, *Rakov and Uman* [2003, Ch. 3] and references therein), which could be possibly related to the fact that the thunderstorm was in its dissipating stage.

Based on the high-gain electric field record, the first preliminary breakdown (PB) pulse, which had the same polarity as the negative return stroke pulse, occurred 9.5 ms before the negative first return stroke onset, which is consistent with the stepped-leader duration obtained by measuring the duration of leader electric field waveform in the low-gain record. The expansions of the negative and positive return-stroke electric field and dE/dt waveforms are shown in Figures 5-2d to 5-2g. Note that the first (negative) return stroke exhibited a double-peak electric field waveform (Figure 5-2d), which might be indicative of two channel terminations on ground created by the forked first-stroke leader (e.g., *Thottappillil et al.*, 1992;

Rakov and Uman, 1994; Ballarotti et al., 2005), even though this can't be confirmed by our optical records. It is possible that the ground termination labeled T2 in the inset of Figure 5-1 was one of the terminations formed by the first (negative) stroke leader, but appeared only in the first frame containing the return stroke, which was saturated, and was too faint to be imaged in the following frames. If so, the apparent deviation of the second-stroke leader from the first-stroke channel at height of 115 above ground level could actually be the second-stroke leader following one of the decayed paths to ground created by the forked first-stroke leader.

The RC decay time constants of the low-gain and high-gain electric field measuring systems were 10 ms and 440 μ s, respectively, so that only field changes occurring on the time scale shorter than 1 ms or so (for example, Figures 5-2d and 5-2e) were faithfully reproduced by the low-gain electric field measuring system and only shorter than 44 μ s or so by the high-gain electric field measuring system. The instrumental decay can be compensated for using the method proposed by *Rubinstein et al. [2012]*. We have used this method in determining the CC polarity-reversal point in our low-gain field record (Figure 5-2a). In practice, the late part of the signals that have decayed to the level that is close to the noise may not be accurately reproduced, so determination of the moment that polarity change occur is a rough estimation. Our approach was as follows. We assumed that 1) the electric field change produced by CC is essentially electrostatic, 2) the electrostatic field change is proportional to the charge transfer Q, and 3) the corresponding current I is given by dQ/dt . Under these assumptions, the CC polarity change should correspond to the zero rate of change (negative maximum) of the bipolar CC electric field signature, after its compensation for instrumental decay. Using the compensated electric field waveform, in which the negative maximum occurred considerably later than seen in Figure 5-2a, we found that the initial 44-ms long portion of the CC following the second return stroke was

positive (positive charge transported to ground) and the following 78-ms long portion was negative (negative charge transported to ground). The average luminosity of the main channel during the positive CC was 3.7 times higher than that during the negative CC, which is likely indicative of about 3.7 times higher current of the positive CC. For comparison, average currents associated with upward negative leaders (positive charge transported to ground) initiated from tall objects are considerably higher than their counterparts associated with upward positive leaders. For example, the average current for negative charge transfer to ground at the Gaisberg tower (Austria) was 113 A [Diendorfer *et al.*, 2011], while for positive charge transfer to ground it was 707 A [Zhou *et al.*, 2012]. It is likely that upward negative leaders are more heavily branched inside the cloud than the upward positive ones, which makes the upward negative leaders more efficient in collecting the cloud charges and funneling them to the channel to ground.

5.3.2 Characteristics of the Negative and Positive Leaders

One can see from the left panel of Figure 5-1 that the stepped leader (labeled L1 in Figure 2a) initiating the negative first stroke, like most negative stepped leaders, was branched. Its 26 frame-to-frame speeds range from 2.6×10^5 m/s to 13.1×10^5 m/s with an arithmetic mean of 4.7×10^5 m/s, which is equal to the average speed calculated by dividing the entire 2D length of the channel by the time it took the leader to traverse that channel. This average speed is somewhat higher than the typical negative stepped-leader speed of 2×10^5 m/s given in *Rakov and Uman* [2003, Chapter 4], possibly because the stroke was of higher than typical intensity. Variation of the frame-to-frame speed of the negative stepped leader versus height of the leader tip above ground is shown in red in Figure 5-3. The speed varied irregularly between 2.6 and 6.4×10^5 m/s at heights ranging from 3600 m to 1000 m above ground and then significantly increased in the last few frames before the leader attachment to ground.

The positive leader (labeled L2 in Figure 5-2a) initiating the second stroke exhibited no low-level branches. It was fainter than L1 and became clearly visible only when it was at the height of 3.2 km above ground. For comparison, the typical cloud-base height during summer thunderstorms in Florida is about 1.5 km above ground. Variation of the frame-to-frame 2D speed vs. height for the positive leader is shown in blue in Figure 5-3. Similar to L1, L2 accelerated as it was approaching the ground. The minimum, maximum, and mean values of 14 frame-to-frame speeds are 4.8×10^5 m/s, 12×10^5 m/s, and 7.2×10^5 m/s, respectively.

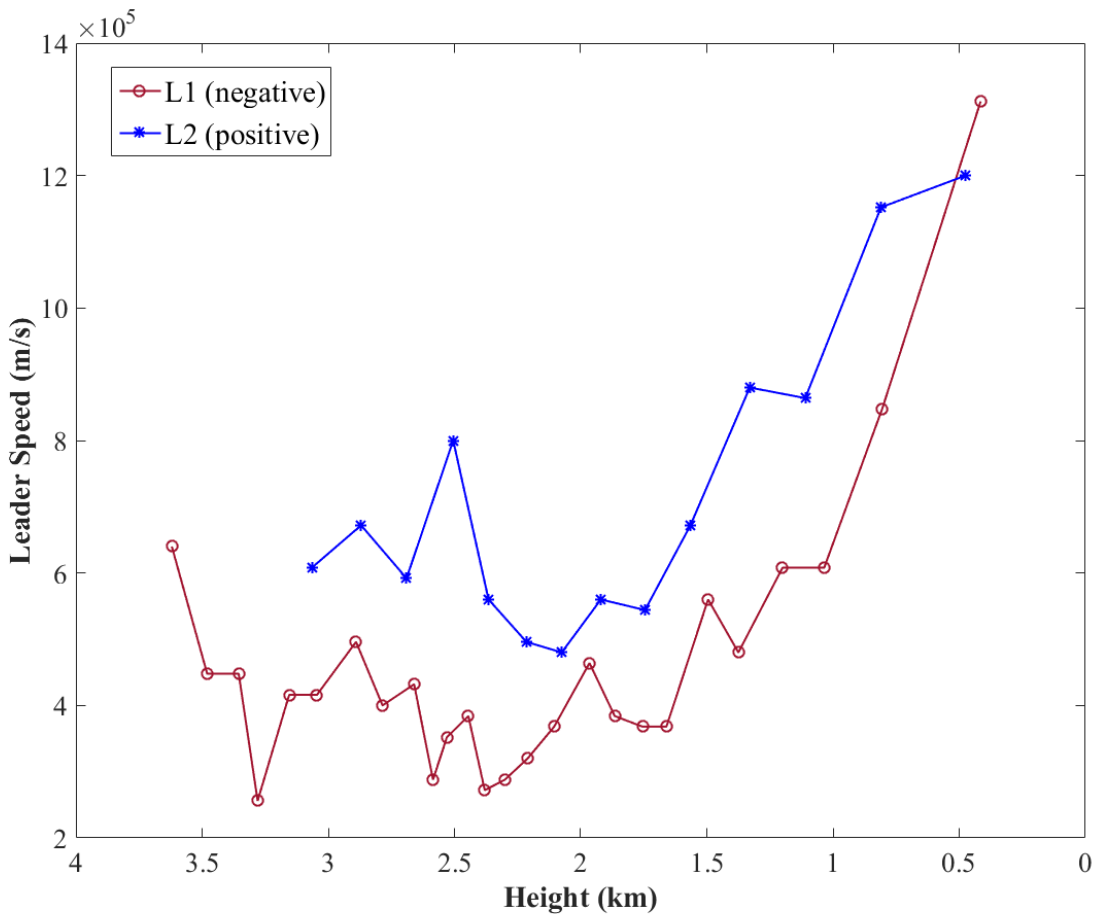


Figure 5-3. The frame-to-frame 2D speeds of the negative stepped leader (L1) and the following positive leader (L2) versus height of the leader tip above ground. Both leaders developed in the same channel and significantly accelerated below 2 km above ground.

5.4 Discussion

Some researchers, based on the various observations of “polarity asymmetry” (for example, Ch. 5 of *Rakov and Uman* [2003] and references therein), believe that subsequent strokes never transport positive charge to ground along the previously created channel. For example, for the case of channel created by a negative stroke, *Saba et al.* [2013] stated that “a positive subsequent return stroke following a negative return stroke is likely not viable given that recoil leaders (RL) would be required to retrace the horizontal channels created by negative leaders. To date, RLs forming on decayed negative leader branches have not been reported.” The mechanism proposed by *Saba et al.* [2013] for natural bipolar cloud-to-ground flashes, in which negative stroke follows the path of positive stroke, is illustrated in Figure 5-4. In this suggested mechanism, the leader develops bidirectionally with the positive end propagating toward the ground and heavily branched negative end developing inside the cloud. Although the positive leader developed nearly vertical near ground, it has some horizontal branches near the cloud base, which cut off from the main channel as the positive leader is approaching the ground. After the cessation of the positive stroke, the recoil leader is initiated in decayed horizontal positive channel and propagates bidirectionally. When their negative end gets connection to the decayed main channel, a subsequent negative return stroke is initiated.

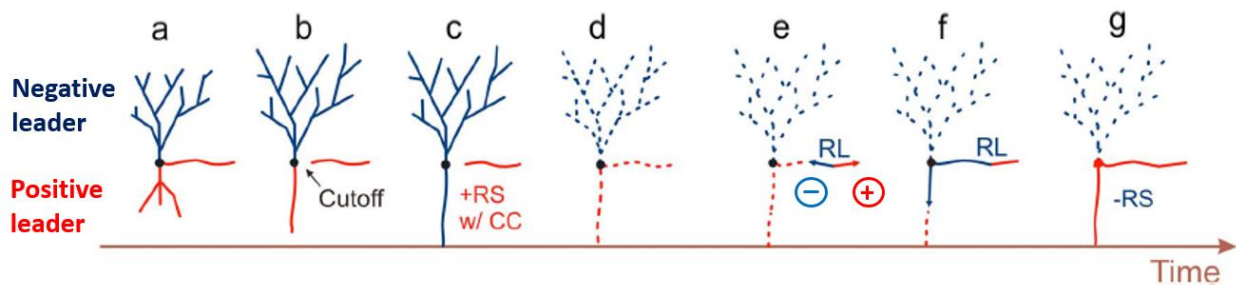


Figure 5-4. Sequence of events that lead to a bipolar flash with the negative second stroke initiated in a decayed branch of positive leader. RL is the bidirectional recoil leader. Adapted from *Saba et al.* [2013].

However, this generalizing statement is not supported by our observations and those of *Xue et al.* [2015] who presented correlated high-speed video and electric field records of a two-stroke bipolar cloud-to-ground flash with the positive second stroke retracing the channel of the negative first stroke. Additionally, the occurrence of recoil-leader-like processes that formed in decayed negative leader branches was recently reported by *Montanyà et al.* [2014] and *Stolzenburg et al.* [2015]. In our view, a recoil leader is an electrical breakdown in warm, low-density air which the decayed lightning channel branches are filled with. The polarities of its ends should be determined by the direction of local electric field or electric field change vector. It is not clear how the conditions for occurrence of this breakdown can be influenced by the sign of charge previously hosted by the branches.

The average speed of L2 is about 1.5 times higher than that of L1. For negative lightning, it is expected (e.g., *Rakov and Uman*, 2003, Ch. 4) that a leader traversing previously-created channel is considerably (1 to 2 orders of magnitude) faster than the stepped leader that created the channel. For positive strokes traversing previously-created channels, such information is not available. Prior to this writing, the speed of positive leader that traversed the pre-existing channel (regardless of preceding-stroke polarity) was reported only for one event by *Xue et al.* [2015]. They optically observed a bipolar flash with only two video frames being recorded for each the negative stepped leader and the subsequent positive leader, with both leaders following the same channel. The corresponding frame-to-frame 2D speeds were 3.6×10^5 m/s and 1.7×10^6 m/s and the interstroke interval was 136 ms. The typical speeds of negative dart-stepped and dart leaders are $(1-2) \times 10^6$ m/s and $(1-2) \times 10^7$ m/s, respectively [*Rakov and Uman*, 2003, Ch.4], and, hence, the subsequent, positive leader speed reported by *Xue et al.* [2015] is similar to that expected for negative dart-stepped leaders. In our case, the 7.2×10^5 m/s value is

lower than expected for negative subsequent leaders in the previously formed channel. As noted above, the interstroke interval between the first two strokes in our bipolar flash was not too long (in contrast with the event reported by *Xue et al.* [2015]), 70 ms, which is not much different from the median value of 60 ms for interstroke intervals in negative flashes. Further, the magnitude of NLDN-reported first-stroke peak current was very large (101 kA). Thus, the lightning channel traversed by the positive leader might be expected to be warm enough to allow faster than observed leader propagation.

Saba et al. [2010] reported that the average speeds of 29 positive leaders (it is not specified if all of them were developing in virgin air) ranged from 0.24 to 11.8×10^5 m/s with the arithmetic mean of 2.76×10^5 m/s, which is about 2.5 times lower than the average speed of the subsequent positive leader observed in our study. Considering that positive flashes normally contain a single stroke or have subsequent strokes following newly-created channels, the majority of the 29 positive leaders studied in *Saba et al.* [2010] probably propagated through virgin air, and hence, are not directly comparable to our positive leader traversing the previously conditioned channel.

Additional data on positive leaders developing in warm air are needed to help interpret our observations. One possible explanation of the relatively low speed of our positive subsequent leader is the relatively low (but rather typical for negative subsequent strokes) magnitude of corresponding return-stroke peak current, only 16 kA vs. 101 kA for the preceding negative stroke. Indeed, *Jordan et al.* [1992] reported positive correlation between the subsequent-leader speed and return-stroke peak current in both natural and triggered negative lightning. Also, *Zhu et al.* [2015] found a tendency for negative first return strokes with higher peak current to be preceded by faster stepped leaders. Another possible factor is the height above sea level, 2496 m

in the work of *Xue et al.* [2015] vs. 52 m in our study. Detailed comparison of our flash with that of *Xue et al.* [2015] is given in Table 5-1. Clearly, further research of this rare phenomenon is needed.

Table 5-1. Comparison of bipolar flashes with a positive stroke following the negative-stroke channel

	Xue et al. [2015]	This study
Location	Qinghai, China	Florida, U.S.
Season	Summer	Summer
Altitude above sea level (m)	2496	52
Storm stage	Dissipation	Dissipation
Channel height in the camera's field of view (km)	unknown	3.9
Interstroke interval (ms)	136	70
Peak current of R1 (kA)	unknown	-101
Peak current of R2 (kA)	unknown	16
R1/R2 peak current ratio	1.6*	6.3
Leader speed of L1 (10^5 m/s) **	3.6	4.7
Leader speed of L2 (10^5 m/s) **	17	7.2
L2/L1 speed ratio	4.7	1.5

*Peak currents are not available in the study of *Xue et al.* [2015], so that the electric field peak ratio is used instead.

**Each of the leader speeds in the study of *Xue et al.* [2015] was the frame-to-frame speed based on two frames only, while our speeds are average values based on 27 and 15 frames for the negative leader and the positive leader, respectively.

5.5 Summary

Using simultaneous high-speed video camera records and electric field measurements, we examined a bipolar flash that started with a negative stroke with a peak current of -101 kA, which was followed by a positive stroke with a peak current of 16 kA. From the leader electric

field waveforms, the positive charge source is inferred to be located considerably farther from both the observer and the channel to ground than the negative charge source. The second (positive) stroke was followed by a bipolar continuing current. The average luminosity of the main channel during the positive CC was 3.7 times higher than that during the negative CC, which is likely indicative of significantly higher current of the positive CC. It is likely that upward negative leaders are more heavily branched inside the cloud than the upward positive ones, which makes the upward negative leaders more efficient in collecting the cloud charges and funneling them to the channel to ground.

In our view, a recoil leader is an electrical breakdown in warm, low-density air which the decayed lightning channel branches are filled with. The polarities of its ends should be determined by the direction of local electric field or electric field change vector. It is unlikely that the conditions for occurrence of this breakdown can be influenced by the sign of charge previously hosted by the branches.

The first two strokes (including the continuing current) followed the same channel to ground, whose imaged 2D length was 4.2 km, except for the bottom 115 m, where the paths of the two strokes were slightly different. As of this writing, there is only one previously documented case of positive leader following the path of preceding negative stroke. We presented the first leader speed versus height profiles for such an unusual sequence. The average leader speeds for the first (negative) and second (positive) strokes were 4.7×10^5 m/s and 7.2×10^5 m/s, respectively. The speed of the positive leader traversing the previous-stroke channel after not-unduly-long (70 ms) interstroke interval is lower than typical speeds of negative leaders following previously formed channels. The speeds of both the negative leader and the positive leader increased as they approached the ground.

CHAPTER 6

OPTICAL AND ELECTRIC FIELD SIGNATURES OF LIGHTNING INTERACTION WITH THE 257-M TOWER IN FLORIDA

6.1 Literature Review

Several research groups reported narrow bipolar electric field pulses (initial-half-cycle durations ranging from 5 to 15 μ s or so), most of which, if not all, being associated with lightning strikes to tall towers. *Pavanello et al.* [2007] observed that for lightning striking the 553-m tall CN tower (Canada), the electric and magnetic field waveforms measured at 16.8 km and 50.9 km exhibited a very short first zero-crossing time of about 5 μ s followed by a narrow ($<5 \mu$ s) opposite-polarity overshoot (Figure 6-1). They attributed these unusual field signatures to the transient process excited by lightning along the tower. The CN-tower observations were performed in summer. *Ishii and Saito* [2009] reported bipolar electric field waveforms produced by 21 negative “ground-to-cloud (GC) discharges” in winter storms in Japan. Examples of those waveforms are shown in Figure 6-2. *Ishii and Saito* [2009] suggested that GC discharges involved an upward leader making contact with a horizontal in-cloud channel, as illustrated in the left panel of Figure 6-2b. In this scenario, the source is located in the cloud, as opposed to being located at ground level in the case of normal cloud-to-ground (CG) lightning (right panel of Figure 6-2b). *Pichler et al.* [2010] presented simultaneous current and electric field records of 73 subsequent return strokes terminated on the 100-m Gaisberg tower (Austria) and found that the arithmetic mean zero-crossing time of the electric field waveforms of those strokes was 11.2 μ s, which is more than a factor of 3 shorter than that for “normal” subsequent strokes not involving tall objects. Examples of current and electric field waveforms of a stroke terminated on the Gaisberg tower are shown in Figure 6-3. Most of the Gaisberg-tower events occurred during the cold season. *Wu et al.* [2014], using a low-frequency lightning location network, observed

374 electric field waveforms, which they termed “large bipolar events (LBEs)”, in winter storms in Japan. They speculated that LBEs involved tall grounded objects and occurred when the negative charge layer in the cloud was very close to the top of the strike object. The LBE label was also used for the discharge giving rise to the observed electric field waveforms, examples of which are shown in Figure 6-4. *Ishii et al.* [2013] and *Saito et al.* [2015] reported unusually narrow electric field waveforms produced by return strokes in upward and downward lightning discharges to the 634-m high Tokyo Skytree in Japan, observed in spring and summer. Observed and calculated electric field waveforms for one subsequent return stroke recorded at three stations, along with their causative current waveform, are shown in Figure 6-5. Note that the current waveform measured at the tower is similar to those typical for normal negative return strokes (relatively fast rise to peak and relatively slow decay).

Chen et al. [2015a] simulated far-field waveforms (Figure 6-6) characteristic of LBEs observed by *Wu et al.* [2014] assuming that they occurred in relatively short channels (500-1000 m) attached to strike objects of 100 to 300 m in height. They used the bouncing-wave model for two different positions of the source representing the RS-like and ICC-pulse-like processes and found that the electric field waveforms observed by *Wu et al.* [2014] could be reproduced in either case, but only when the injected current waveform was a symmetric Gaussian pulse. Note that *Chen et al.* [2015a] used the field sign convention that is opposite to the one used by *Wu et al.* [2014].

In this chapter, we present two lightning flashes containing a total of eight negative strokes that terminated on a 257-m tower and produced unusually narrow bipolar electric field waveforms with damped oscillatory tails. High-speed video camera records were also obtained for these two flashes. The observed electric field waveforms exhibit some similarities to the

events reviewed above. In the camera's field of view, the 257-m tower was obscured by trees, but the azimuth of the 8 strokes and NLDN data clearly indicate that all of them terminated on the tower.

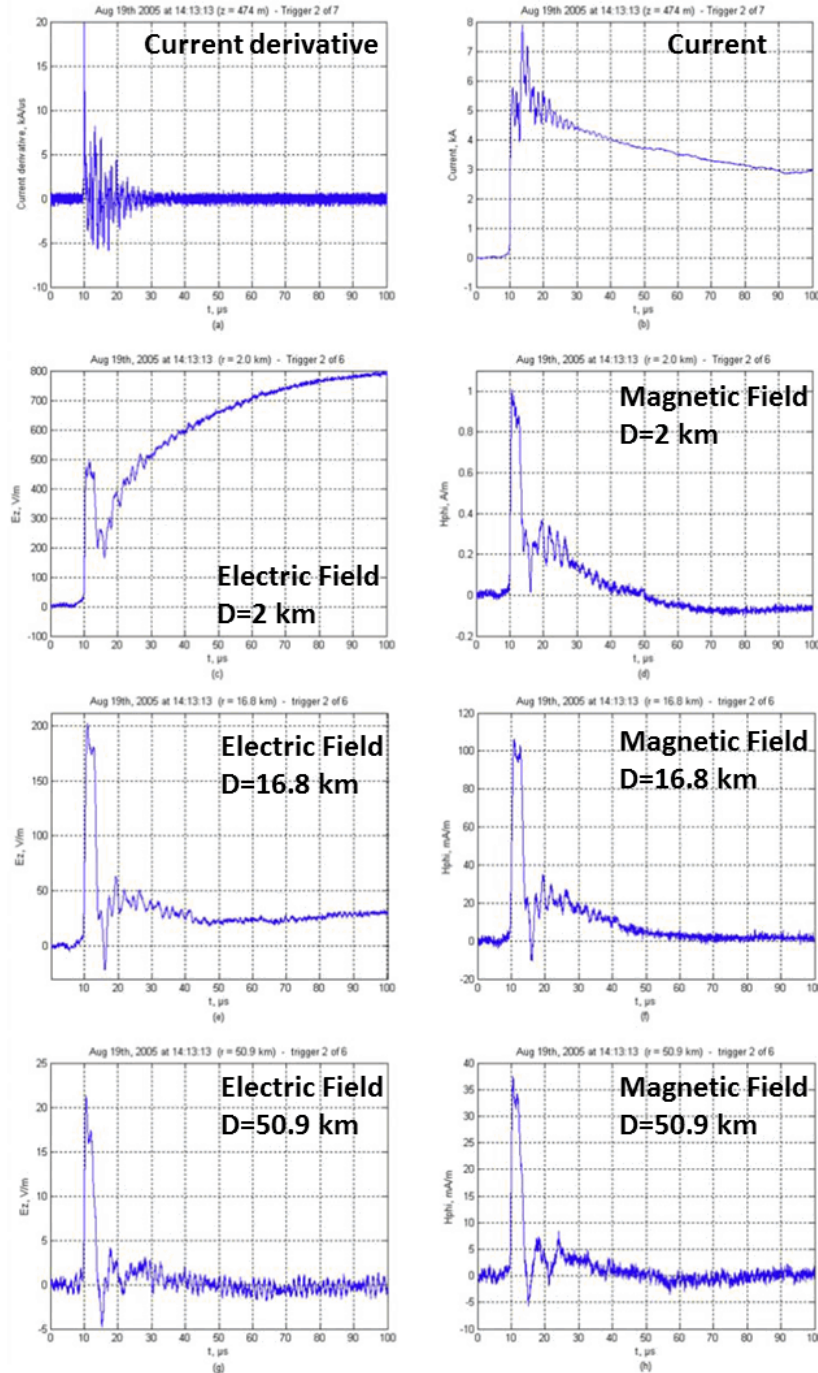


Figure 6-1. Current derivative, current, electric field, and magnetic field records of the 2nd stroke of the flash striking the 553-m CN tower on August 19th, 2015. The current was measured at the height of 474 m. Adapted from Pavanello *et al.* [2007].

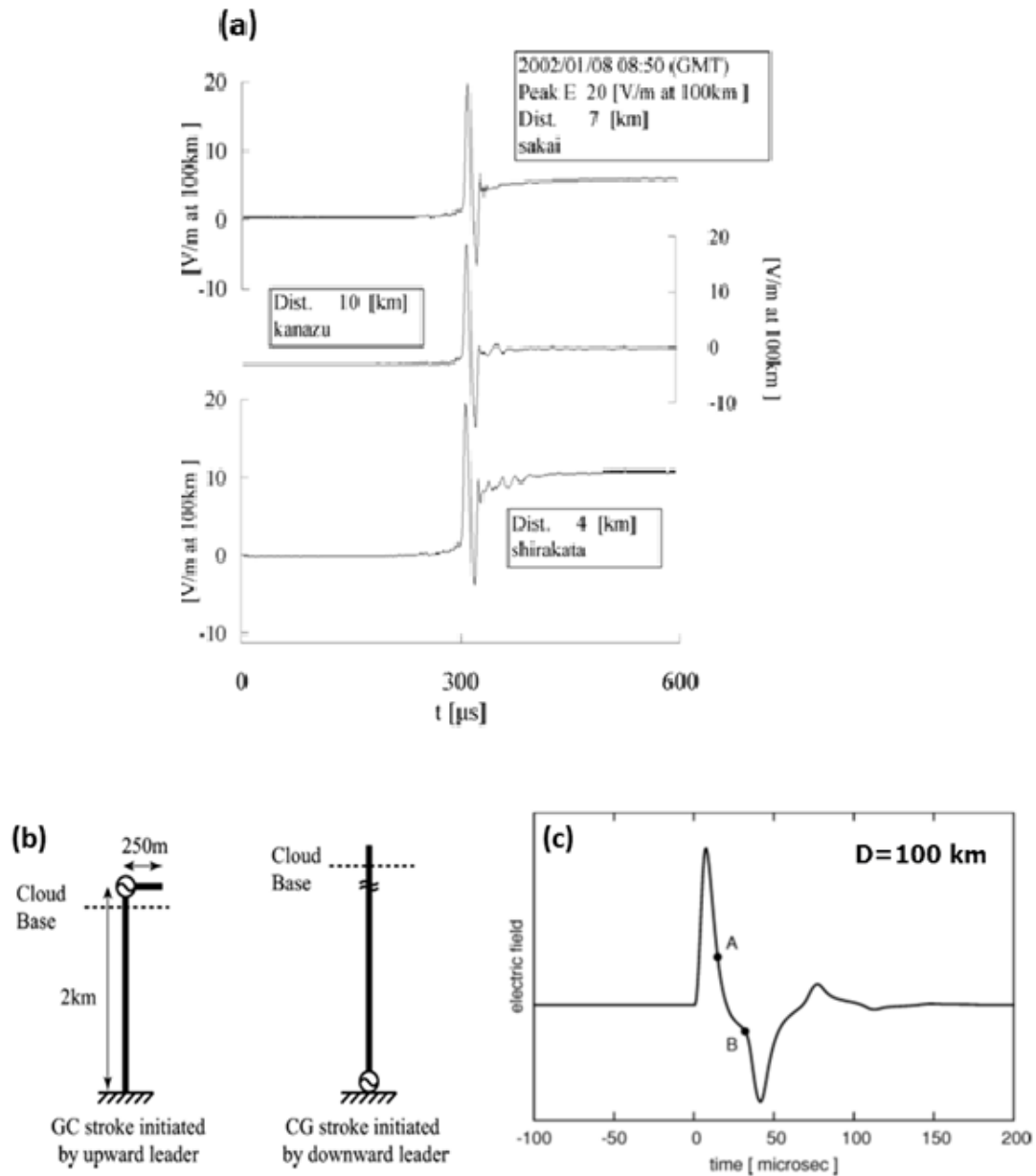


Figure 6-2. The observed and simulated “ground-to-cloud” (GC) discharge. a) Electric field waveforms simultaneously recorded at three different stations in winter in Japan and attributed to a GC discharge. b) Models of -GC stroke initiated by an upward positive leader (left) and normal return stroke initiated by a downward negative leader (right). In the latter case the source is placed at the channel base and the channel is vertical, while in the former case the source is placed at the junction point between a 2-km vertical, grounded channel section and a 250-m horizontal, in-cloud section. c) Electric field waveform calculated at 100 km using the model shown in the left panel of b). Ground reflection occurred at A and reflection from the upper end of the vertical channel occurred at B. The calculated electric field waveform shown in c) resembles the GC stroke waveform measured at 10 km shown in a) (middle trace). Adapted from *Ishii and Saito [2009]*.

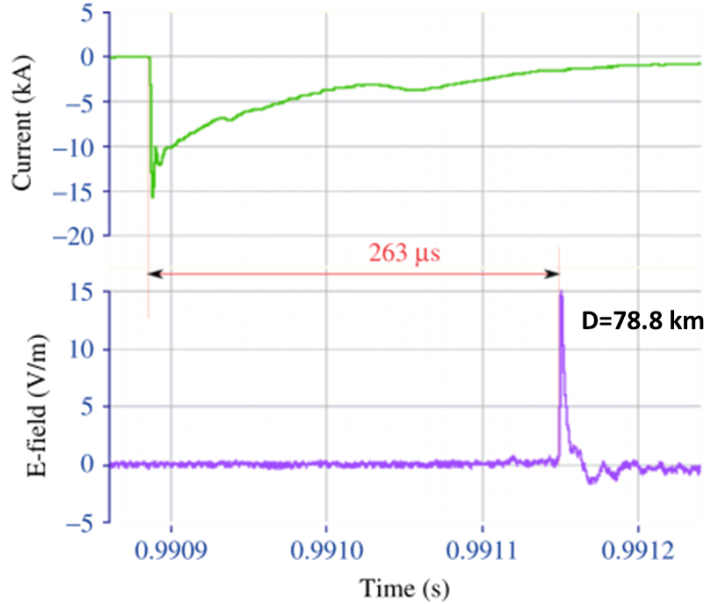


Figure 6-3. Current and electric field records of a negative lightning stroke terminated on the 100-m Gaisberg tower. The current was measured at the top of the tower. The peak current of this event is 15.9 kA. Adapted from Pichler *et al.* [2010].

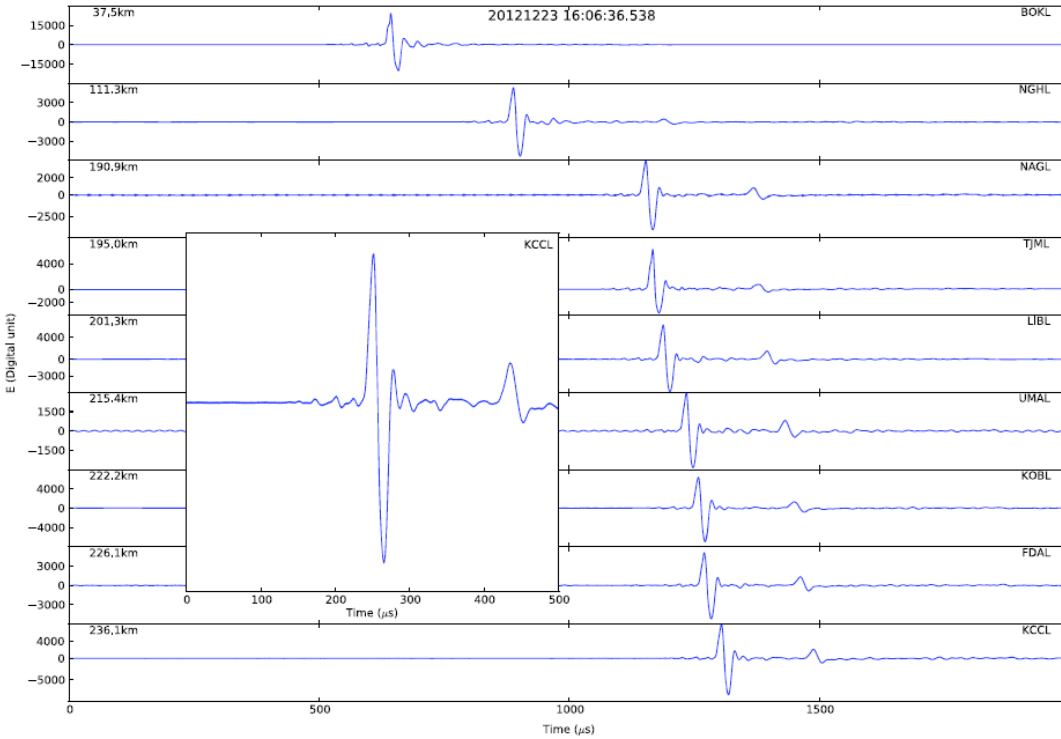


Figure 6-4. Electric field waveforms of a typical LBE recorded by nine stations at distances ranging from 37.5 to 236.1 km in winter in Japan. The waveform recorded at 236.1 km is shown on the expanded time scale in the inset (the second, smaller pulse between 400 and 500 μ s is the ionospheric reflection). The typical initial half-cycle width was 15 μ s. Adapted from Wu *et al.* [2014].

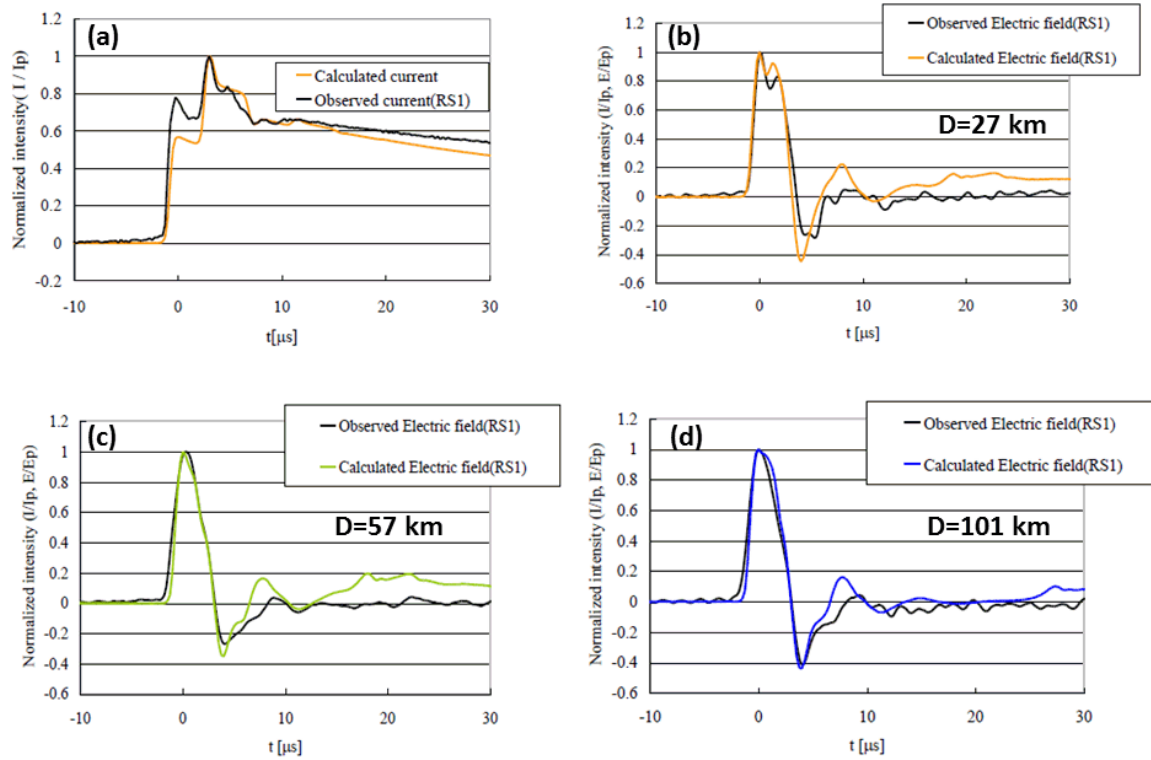


Figure 6-5. A subsequent return stroke terminated on the Tokoyo Skytree showing the narrow bipolar signature in electric field records. a) Observed and calculated current waveforms for a subsequent return stroke of an upward negative flash terminated on the 634-m high Tokyo Skytree in May of 2012 (Flash 2012-1). The current was measured at the height of 497 m. b)-d) Corresponding observed and calculated electric field waveforms at three distances ranging from 27 to 101 km. The initial half-cycle width of electric field waveforms is about 5 μ s, which is considerably smaller than the duration of current waveform shown in a). The measured current peak is 16 kA. Adapted from Ishii *et al.* [2013].

6.2 Observations and Analysis

The two flashes presented in this chapter were recorded at the Lightning Observatory in Gainesville (LOG), Florida, by electric field measuring systems and Megaspeed HHC-X2 high-speed video camera in the summer of 2014. The detailed information of the field measuring systems at LOG can be found in Section 2.2. In this study, the record length for the field measuring systems was 1 s with 200 ms pretrigger. The Megaspeed HHC-X2 camera, equipped with a fish-eye lens to provide a wider field of view (about 185°), was operated at 1000 frames

per second (fps) with 1 ms exposure time (essentially no deadtime) and resolution of 832×600 pixels. The record length of the camera was 1.2 s with 200 ms pretrigger. No processing of optical images was done to remove the fish-eye effect. Since the imaged channels were near the lens center, the distortion was not significant. All the records were GPS time stamped. The field measuring system was synchronized with the high-speed video camera with precision better than 1 ms. The measuring system and high-speed camera were triggered when the electric field exceeded a preset threshold. More detailed information on LOG can be found in Section 2.2 and the review paper by *Rakov et al.* [2014].

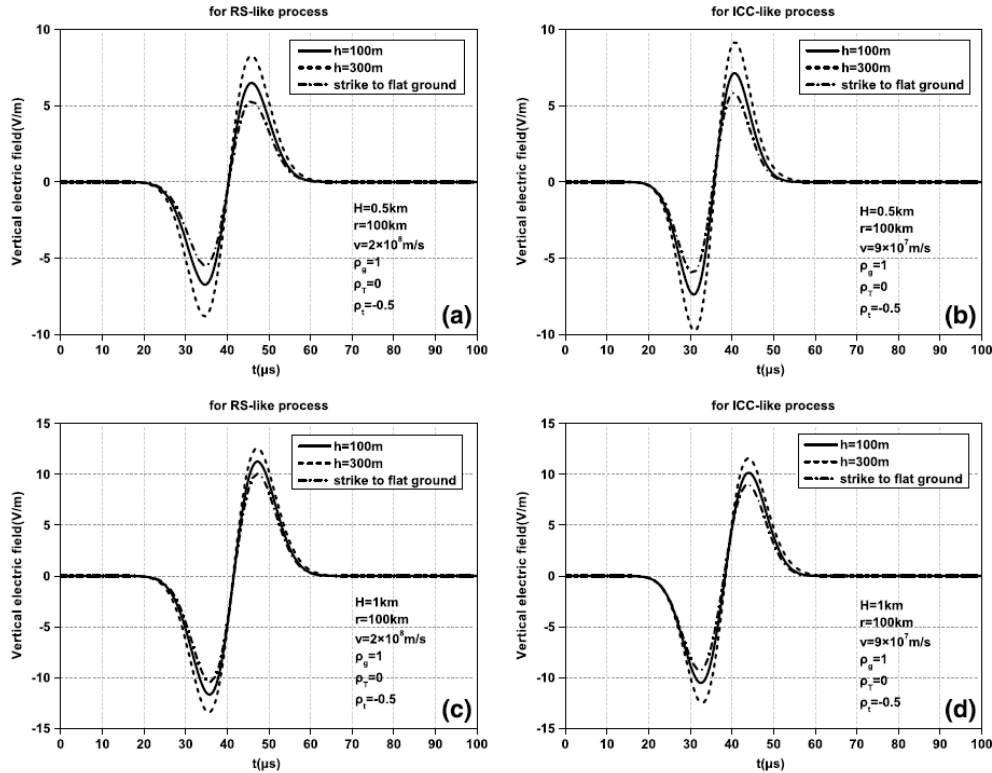


Figure 6-6. Simulated electric field waveforms of LBEs at 100 km. Panels a) and c) for RS-like process and panels b) and d) for ICC-pulse-like process. H , h , r , and v are the lightning channel length, strike object height, horizontal distance from the lightning strike point, and current-wave speed, respectively. ρ_g , ρ_T , and ρ_t are the reflection coefficients at the ground level, at the channel top, and at the strike object top, respectively. Physics sign convention (a downward directed electric field or field change vector is considered to be negative) is used in this figure. Adapted from *Chen et al.* [2015a].

6.2.1 General Description of two Flashes Terminated on the 257-m and 60-m Towers in Florida

Flash 1593 was recorded at 12:10:58 UT (at 08:10:58 local time) on July 16th, 2014. It was an upward negative flash whose upward positive leader initiated from the 257-m high tower (located 8.8 km from the LOG). This upward leader was clearly seen in six consecutive frames (for about 6 ms) moving at an average 2D frame-to-frame speed of 3.2×10^5 m/s. It was optically detectable up to a height of 1.9 km. Flash 1593 contained 6 negative strokes, all of which terminated on the 257-m tower. This flash occurred after and possibly was initiated by a nearby intracloud discharge. Flash 1594 was a downward bipolar flash that occurred 8 minutes after flash 1593. Natural downward bipolar flashes are rare with only several observations being found in the literature [*Fleenor et al.*, 2009; *Jerauld et al.*, 2009; *Nag and Rakov*, 2012; *Saba et al.*, 2013; *Chen et al.*, 2015b; *Xue et al.*, 2015; *Tian et al.*, 2016; *Zhu et al.*, 2016b]. During the 8-minute interval between flashes 1593 and 1594, only one cloud discharge was reported by the NLDN within 40 km of the LOG. The first stroke of flash 1594 was positive and terminated on the 60-m tower located 3.6 km from the 257-m tower and 8.9 km from the LOG. It was followed by two negative strokes that terminated on the same 257-m tower as the 6 strokes of flash 1593. All of the 8 negative strokes that terminated on the 257-m tower exhibited very similar electric field waveforms, characterized by a narrow bipolar pulse with a damped oscillatory tail. The electric field waveform of the positive stroke terminated on the 60-m tower was unipolar and exhibited initial, predominately radiation field peak followed by a large electrostatic ramp.

Table 6-1. NLDN data on 8 negative strokes in flashes 1593 and 1594 terminated on the 257-m tower.

Flash Type	Stroke ID	Peak Current (kA)	Preceding Interstroke Interval (ms)	NLDN Classification (C for cloud events and G for cloud-to-ground events)	Semi-Major Axis Length (m)	Semi-Minor Axis Length (m)	Number of Reporting Sensors	Distance between the NLDN-Reported Location and the 257-m Tower (m)
Upward Negative Flash	1593-1	7.6	-	C	200	200	4	110
	1593-2	5.7	18	C	200	200	5	50
	1593-3	20.7	64	G	200	100	5	40
	1593-4	6.5	56	G	200	200	4	80
	1593-5	6.6	18	C	200	200	4	60
	1593-6	6.7	14	C	200	200	5	90
Downward Bipolar Flash*	1594-2	6.5	148	C	200	200	5	70
	1594-3	10.2	20	C	200	200	5	140
	Mean	8.8	42	-	200	200	5	80

* Information on the first, positive stroke of this bipolar flash is given in Table 6-2.

Table 6-2. NLDN data on the first, positive stroke of bipolar flash 1594, which terminated on the 60-m tower, located 3.6 km from the 257-m tower.

Flash Type	Stroke ID	Peak Current (kA)	Preceding Interstroke Interval (ms)	NLDN Classification (C for cloud events and G for cloud-to-ground events)	Semi-Major Axis Length (m)	Semi-Minor Axis Length (m)	Number of Reporting Sensors	Distance between the NLDN-Reported Location and the 60-m Tower (m)
Downward Bipolar Flash*	1594-1	193	-	G	100	100	20	30

* Information on the second and third strokes of this bipolar flash is given in Table 6-1

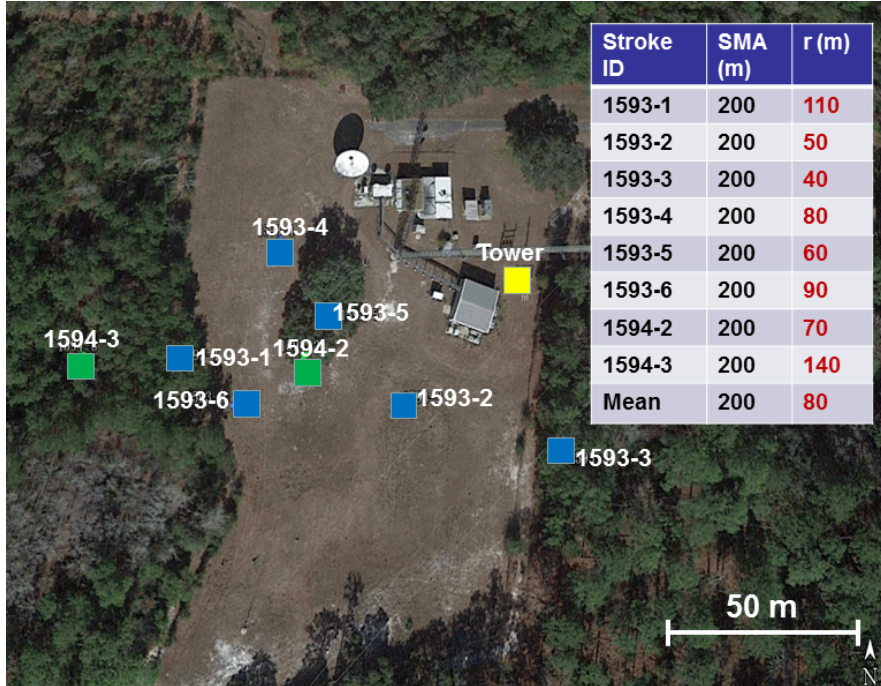


Figure 6-7. Locations of strike points reported by the NLDN for 8 negative strokes terminated on the 257-m tower. Blue squares are the reported strike points for 6 strokes of flash 1593 and green squares are the reported strike points for 2 strokes of flash 1594. The yellow square is the location of the tower and the ground-truth location of the 8 strokes. SMA stands for the semi-major axis length and r is the NLDN location error defined as the distance from the NLDN-reported location to the ground-truth location (yellow square). Note that the yellow square, whose position is determined by the geographical coordinates of the tower (available from <http://www.cellreception.com/towers/details.php?id=1029807>), is about 25 m from the location of the tower base seen in the Google Earth map. The reason for this offset is unknown.

6.2.2 NLDN Responses to the 257-m and 60-m Tower Strokes

The NLDN information for the two flashes is summarized in Table 6-1 (negative strokes) and Table 6-2 (positive stroke). The 8 negative strokes had NLDN-reported peak currents ranging from 5.7 to 20.7 kA with a geometric mean of 8 kA and an arithmetic mean of 8.8 kA. Out of the 8 negative strokes, 6 were misclassified by the NLDN as cloud discharges. The peak currents for the 2 correctly classified events were 20.7 and 6.5 kA. *Warner et al. [2012]* reported that the NLDN misclassified as cloud discharges 30% (46/151) of “subsequent events” (leader/return stroke sequences and ICC pulses) in upward flashes initiated from towers in South

Dakota. They found that the peak-to-zero times and pulse durations of electric field pulses produced by misclassified events were smaller than those for the correctly-classified events. The NLDN-reported locations for the 8 negative strokes and the 257-m tower location are shown in Figure 6-7. The distances between NLDN-reported locations and the tower location ranged from 40 m to 140 m, all being less than 200 m, the median error (assumed to be equal to the semi-major axis length of the location error ellipse) reported by the NLDN for each located event.

For the first, positive stroke of the bipolar flash 1594, the NLDN-reported peak current was 193 kA and the distance between the NLDN-reported location and the 60-m tower was 30 m. The positive stroke is not further discussed in this chapter.

6.2.3 High-Speed Camera and Electric Field Data for Eight Negative Strokes of Flashes 1593 and 1594

First frames showing the channels (including the upper parts normally hidden inside the cloud) of the eight negative return strokes from the two flashes are shown in Figure 6-8. Multiple frames showing the evolution of luminous channels (not discussed in this chapter) are presented for each event in Appendix C. From the high-speed video camera data, the time interval between the initiation of upward positive leader and the first return stroke in flash 1593 was 184 ms. There was no initial continuous current detectable in either optical or electric field records after the upward positive leader. The channel length for individual strokes progressively increased (extended upward) with increasing stroke order. The corresponding electric field waveforms on a 30- μ s time scale are shown in Figure 6-9. They are very similar to each other. Except for 1593-R4 having a shoulder in its field waveform, all the eight strokes had very fast rise and fall times (<2 μ s) of the field initial half-cycle. The field waveforms of all eight strokes show damped oscillatory tails. The similarity of field waveforms for different strokes in two different flashes suggest that they are largely determined by the transient response of the tower. The field

waveform parameters are defined in Figure 6-10, in the same manner as in *Wu et al.* [2014], and summarized in Table 6-3. Electric field waveforms on a longer time scale (not discussed in this paper) are presented in Appendix C.

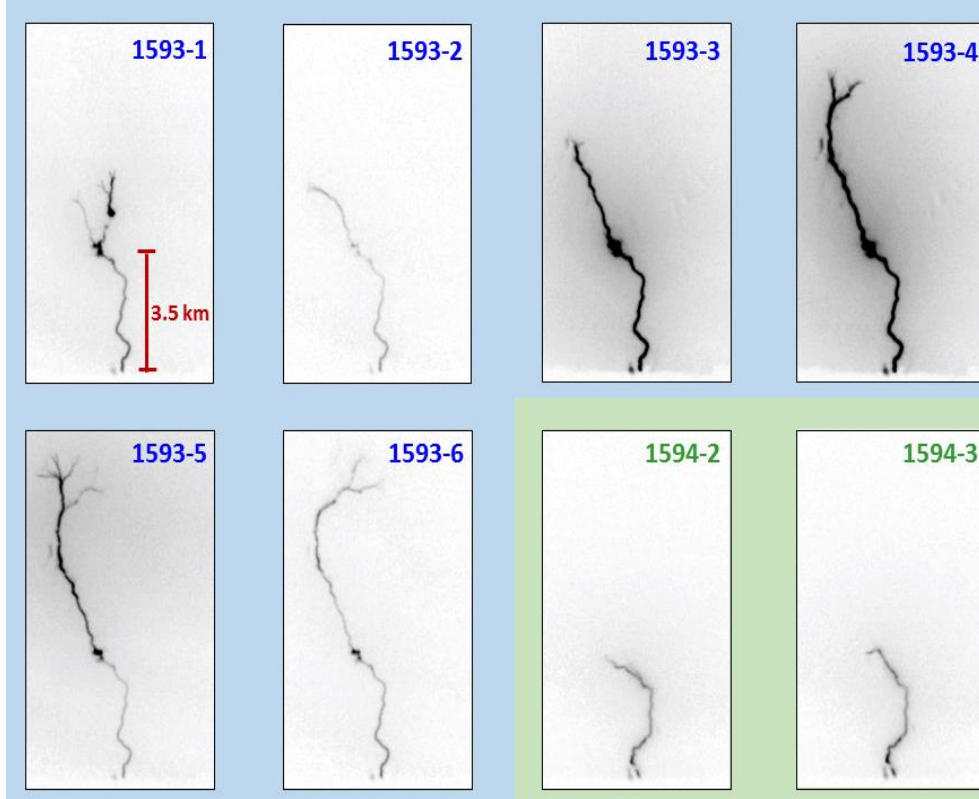


Figure 6-8. First video frames showing the channel of each of the eight negative strokes terminated on the 257-m tower.

Table 6-4 compares the field waveform parameters obtained in the present study with the parameters of similar field waveforms found in the literature [*Pavanello et al.*, 2007; *Ishii and Saito*, 2009; *Pichler et al.*, 2010; *Ishii et al.*, 2013; *Wu et al.*, 2014]. Our events have the narrowest average electric field initial-half-cycle width (T_p) of 2.44 μ s. It is significantly smaller than its counterparts reported by *Ishii and Saito* [2009], *Pichler et al.* [2010], and *Wu et al.* [2014], but only a factor of two smaller than those reported by *Pavanello et al.* [2007] and *Ishii et al.* [2013]. The NLDN-reported peak currents for our events are considerably smaller than those reported by *Ishii and Saito* [2009] and *Wu et al.* [2014], but are rather similar to those

reported by *Pavanello et al.* [2007], *Pichler et al.* [2010], and *Ishii et al.* [2013]. Note that direct current measurements are available only for the events presented by *Pavanello et al.* [2007], *Pichler et al.* [2010], and *Ishii et al.* [2013]. For the events presented in this chapter, as well as for those studied by *Ishii and Saito* [2009] and *Wu et al.* [2014], the peak currents were estimated from measured fields. The ratio of the first (positive) and the second (negative) field half-cycles for our events is about a factor of 4 to 5 larger than those for LBEs studied by *Wu et al.* [2014] and GC events reported by *Ishii and Saito* [2009], but very close to those reported by *Pavanello et al.* [2007] and *Ishii et al.* [2013].

Further observations and associated modeling are needed to better understand the nature of narrow bipolar field waveforms observed both in winter and in summer with strike-object heights ranging from 100 m or less to 634 m. Modeling of our events is presented in Chapter 7.

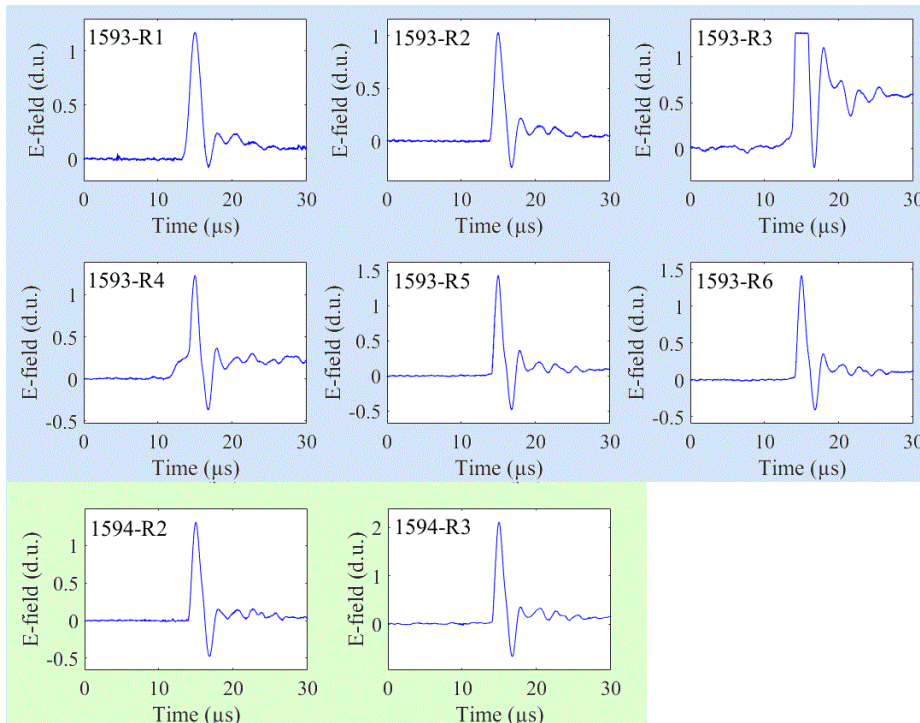


Figure 6-9. Electric field waveforms of 8 negative strokes terminated on the 257-m tower. The electric field waveform of 1593-R3 is saturated. Atmospheric electricity sign convention (a downward directed electric field or field change vector is considered to be positive) is used in this figure and in all other figures in this chapter showing electric field waveforms, except for Figure 6-6.

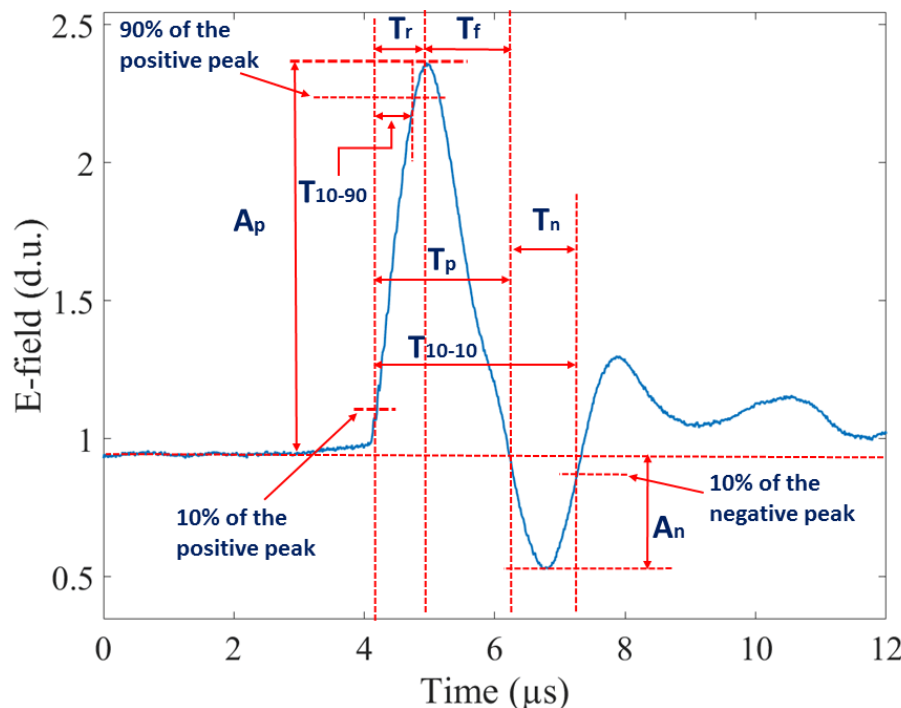


Figure 6-10. Measurements (definitions) of electric field waveform parameters.

Table 6-3. Electric field waveform parameters for the seven negative strokes terminated on the 257-m tower.

Stroke ID	T_p (μs)	T_{10-90} (μs)	T_{10-10} (μs)	T_r (μs)	T_f (μs)	T_r/T_f	T_n (μs)	T_p/T_n	A_p/A_n	A_p	A_n
1593-1	2.82	0.98	3.43	1.24	1.58	0.78	0.61	4.60	19.5	1.17	0.06
1593-2	2.25	0.80	3.22	0.93	1.32	0.70	0.97	2.32	4.1	1.03	0.25
1593-3	- ^a	-	-	-	-	-	0.51	-	-	-	0.19
1593-4	3.91	2.45	5.08	2.71	1.20	2.26	1.17	3.34	3.3	1.2	0.36
1593-5	1.92	0.55	3.06	0.72	1.20	0.60	1.14	1.68	2.7	1.39	0.51
1593-6	2.04	0.59	3.12	0.79	1.25	0.63	1.08	1.89	3.0	1.37	0.44
1594-2	2.10	0.62	3.33	0.85	1.25	0.68	1.23	1.71	2.7	1.30	0.48
1594-3	2.02	0.57	2.95	0.82	1.20	0.68	1.14	1.78	2.9	2.06	0.71
AM ^b	2.44	0.94	3.46	1.15	1.29	0.90	0.98	2.47	5.5	1.36	0.38
Coefficient of variation ^c	0.29	0.73	0.21	0.61	0.11	0.66	0.28	0.45	1.14	0.24	0.51

^a T_p of 1593-3 can't be accurately measured due the saturation of the positive peak, but it is close to 5 μs, which is the time interval between first and second zero-crossing

^b May be biased due to exclusion of the largest event (1593-R3)

^c The ratio of the standard deviation to the arithmetic mean

6.3 Summary

Simultaneous electric field and high-speed video camera records of two flashes, labeled 1593 and 1594, were acquired at the Lightning Observatory in Gainesville (LOG), Florida, in the summer of 2014. Flash 1593 was an upward negative flash whose upward positive leader initiated from a 257-m high tower after a nearby intracloud discharge and propagated with an average 2D frame-to-frame speed of 3.2×10^5 m/s. It contained 6 downward leader/return stroke sequences, all of which terminated on the tower following the upward positive leader path. Flash 1594 was a downward bipolar flash, the first stroke of which was positive and terminated on a 60-m tower, while two subsequent strokes were negative and terminated on the same 257-m tower as the six strokes of flash 1593. The first negative stroke of 1594 created a new path to the 257-m tower and, hence, was likely stepped. The peak current reported by the NLDN for the 8 negative strokes ranged from 5.7 to 20.7 kA, with a geometric mean of 8 kA and an arithmetic mean of 8.8 kA. Out of the 8 negative strokes, 6 were misclassified by the NLDN as cloud discharges. All the 8 negative strokes that terminated on the 257-m tower (located 8.8 km from LOG) exhibited very similar narrow (2.44 μ s on average) bipolar electric field pulses with damped oscillatory tails.

From comparison with similar narrow bipolar electric field waveforms observed in different studies, we found that our events have the narrowest average electric field pulse width. It is significantly smaller than its counterparts reported by Ishii and Saito [2009], Pichler et al. [2010], and Wu et al. [2014], but only a factor of two smaller than those reported by Pavanello et al. [2007] and Ishii et al. [2013]. The NLDN-reported peak currents for our events are considerably smaller than those reported by Ishii and Saito [2009], and Wu et al. [2014], but are rather similar to those reported by Pavanello et al. [2007], Pichler et al. [2010], and Ishii et al. [2013]. The ratio of the amplitudes of first and the second field half-cycles for our events is

about a factor of 4 to 5 larger than those for LBEs studied by Wu et al. [2014] and GC events reported by Ishii and Saito [2009], but very close to those observed by Pavanello et al. [2007] and Ishii et al. [2013]. It is not clear if all the lightning events producing narrow bipolar electric field waveforms discussed in this chapter are of the same nature or not. Further research is needed.

Table 6-4. Characteristics of narrow bipolar electric field waveforms observed in different studies

References	Location and season	Strike object height (m)	Sample size	Tp (μs)	T ₁₀₋₉₀ (μs)	T ₁₀₋₁₀ (μs)	Peak current (kA)	Tr/Tf	Tp/Tn	Ap/An
Pavanello et al. [2007]	Toronto, Canada, summer	553	1	Around 5	-	-	5.5	-	2 ^a	4.4 ^a
Ishii and Saito [2009]	Hokuriku region, Japan, winter	unknown	21	-	AM=12.3	AM=53	>70	-	-	1.3 ^b
Pichler et al. [2010]	Salzburg, Austria, mostly at cold season	100	73	AM=11.2	AM=1.8	-	AM=10.6	-	-	-
Wu et al. [2014]	Western Japan, winter	unknown	356	AM=15.1	-	-	AM=68.8	>1 for 92.4% of events	Median around 1	Median around 1
Ishii et al. [2013]	Tokyo, Japan, summer	634	1	4.5 ^c	-	-	16	-	1.6 ^c	4 ^c
This study	Florida, USA, summer	257	7	AM=2.4	AM=0.9	AM=3.5	AM=7.1	AM=0.9	AM=2.47	AM=5.5

^aMeasured in Figure 4g of Pavanello et al. [2007].

^bMeasured in Figure 2 of Ishii and Saito [2009].

^cMeasured in Figure 13b of Ishii et al. [2013].

CHAPTER 7

MODELING OF LIGHTNING INTERACTION WITH THE TOWER

7.1 Literature Review

Rakov and Uman, [1998] categorized lightning return stroke models into four classes based on the types of governing equations. The first class models are gas dynamic models, which involve the solution of gas dynamic equations (conservation of mass, momentum, and energy) coupled to two equations of state. In contrast with the other three classes of return stroke models, it is primarily concerned with the radial evolution the lightning channel. The gas dynamic model developed by *Paxton et al.* [1986] could output the profiles of temperature, mass density, pressure, and conductivity versus channel radius at different times. The second class models are electromagnetic models, in which the lightning channels are often represented by loaded or unloaded conducting wires. Electromagnetic models, using numerical techniques, such as Finite Difference Time Domain (FDTD) method or Method of Moment (MoM), solve Maxwell's equations to produce the current distribution along the lightning channel, which could be used to calculate the radiated electric and magnetic fields. The third class models are distributed-circuit models, in which the lightning channel is considered as an RLC transmission line, where R, L, C are the series resistance, series inductance, and shunt capacitance, all per unit, respectively. By solving the telegrapher's equations, the profiles of current and voltage along the channel as a function of time and height can be obtained. Note that the telegrapher's equations can be derived from Maxwell's equations assuming that the electromagnetic waves guided by the lightning channel have the transverse electromagnetic (TEM) field structure. The fourth class models are engineering models, which are equations relating the longitudinal current along the lightning channel at any height and any time to the current at the channel base. Engineering models can be further grouped in two categories: traveling-current-source-type models and transmission-line-

type models. In the traveling-current-source-type models, the return stroke may be viewed as being generated at the upward-moving-return stroke front and then propagating downward, while in the transmission-line-type models, a current source is placed at the channel base to inject current into the channel. The current wave propagates upward without attenuation for the original transmission line model [*Uman and McLain*, 1969] and with specified height-dependent attenuation terms for different modified transmission line models [*Rakov and Dulzon*, 1987, 1991; *Nucci et al.*, 1988]. The current equations for the four widely used transmission-line-type models are summarized in Table 7-1. Those models included (1) the transmission line (TL) model, (2) the modified TL model with linear current decay with height (MTLL), (3) the modified TL model with exponential current decay with height (MTLE), and (4) the modified transmission line model with parabolic current decay with height (MTLP).

Table 7-1. Current equations for transmission-line-type return stroke models

Type	Equation
TL [Uman and McLain, 1969]	$I(z', t) = I(0, t)$
MTLL [Rakov and Dulzon, 1987]	$I(z', t) = \left(1 - \frac{z'}{H}\right) I(0, t)$
MTLE [Nucci et al., 1988]	$I(z', t) = e^{-z'/\lambda} I(0, t)$
MTLP [Rakov and Dulzon, 1991; Maslowski and Rakov, 2006]	$I(z', t) = \left(1 - \frac{z'}{H}\right)^2 I(0, t)$

As discussed in Chapter 6, lightning striking tall objects can produce electric field waveforms with first zero-crossing times ranging from 2 μ s to 15 μ s or so [*Pavanello et al.*, 2007; *Ishii and Saito*, 2009; *Pichler et al.*, 2010; *Wu et al.*, 2014; *Zhu et al.*, 2016c], which are significantly smaller than the typical values ranging from 30 to 50 μ s [*Rakov and Uman*, 2003, chapter 4]. Some researchers attempted to model such narrow electric field waveforms.

Saito et al. [2015a, 2015b] obtained multiple-station measurements of very narrow (first zero-crossing time is about 2.5 μ s) bipolar electric field waveforms produced by a stroke in

upward lightning striking the Tokyo Skytree (634-m) in Japan. The corresponding current measured at the height of 497 m showed fast rise followed by a slow decay, which is the characteristic of a normal return stroke. Numerical Electromagnetics Code (NEC-4) based on the method of moments was used for numerical analysis by *Saito et al.* [2015a, 2015b]. In the model, lightning channel and tower were represented as thin wires and the voltage source was placed at the top of the tower. The observed electric field was reproduced by using the measured current waveform and channel geometry reconstructed from high-speed camera images. The channel was not vertical, and the authors noted that the channel tilt was an important factor in achieving a good match with measured field waveforms.

Chen et al. [2015] used a bouncing-wave model to simulate far-field waveforms of large bipolar events (LBEs) observed by *Wu et al.* [2014]. In the model, the lightning channel was assumed to be very short (hundreds of meters) and the tower height ranged from 100 to 300 m. Reflections at the channel top, tower top, and tower bottom were considered. They found that the LBE-like waveform can be reproduced only when the injected current was characterized with a symmetric Gaussian pulse. Also, they found that the simulated electric field waveforms for RS-like events (current injected at the top of the tower) and ICC-pulse-like processes (current injected at the top of the channel) were very similar.

Azadifar et al. [2017] measured a narrow bipolar current waveform recorded at the height of 82 m of the 124-m Santis Tower in Switzerland, which was associated with the first stroke in a downward negative 4-stroke flash striking the tower. The peak current was as high as 102 kA. The recorded current waveform, shown in Figure 7-1, is very similar to a symmetric Gaussian pulse, except that it was followed by a small opposite-polarity overshoot. Neglecting the presence of the tower and using the MTLE model, *Azadifar et al.* [2017] calculated the

corresponding electric field waveform at a distance of 100 km that showed the characteristics similar to those of LBEs observed by *Wu et al.* [2014].

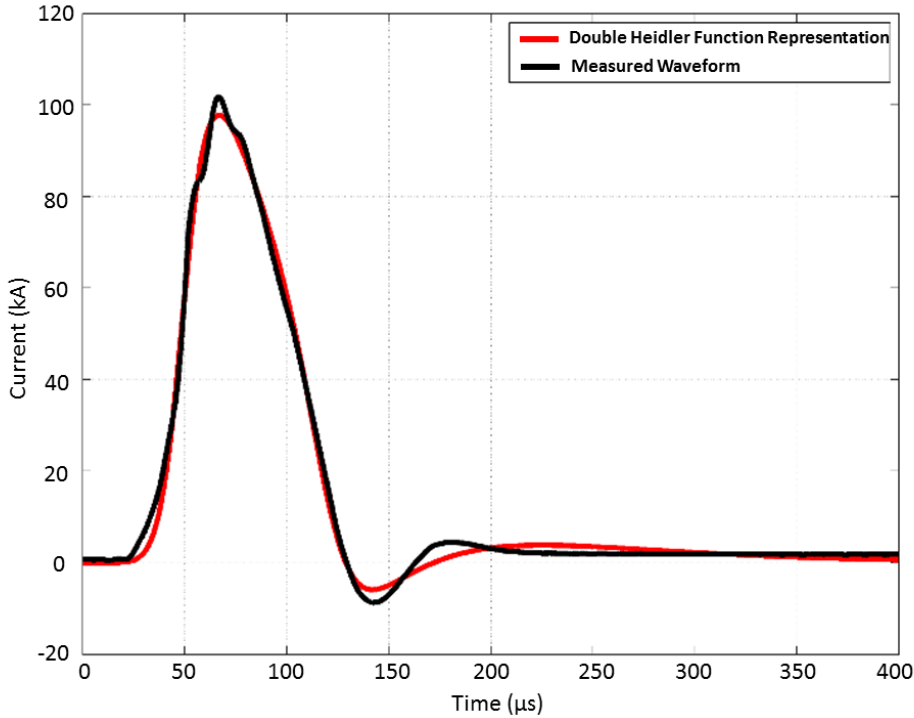


Figure 7-1. Measured current waveform (black line) associated with the first return stroke in a downward flash recorded at the Santis tower. The red line is the analytical representation using Heidler's function. Adapted from *Azadifar et al.* [2017].

In this chapter, we will try to reproduce the narrow bipolar electric field waveforms produced by lightning striking the 257-m tower in Florida and presented in Chapter 6. Effects of each model parameter on the vertical electric field waveform will be investigated.

7.2 Model Description

The engineering return stroke models were originally introduced for lightning strikes to flat ground. For lightning striking tall towers, reflections at tower extremities have to be taken into consideration. Rachidi et al. [2002], based on a distributed-current-source representation of the lightning channel, extended several engineering lightning return stroke models to include the effect of transient processes in tower. Baba and Rakov [2005] used the lumped voltage source (illustrated in Figure 7-2) in order to extend the TL model to the case of lightning strike to the

tall object. The approach proposed by Baba and Rakov [2005] will be used here for all four models. The distributions of current along the tower and along the lightning channel are given by equations 7-1 and 7-2.

Along the tower,

$$I(z', t) = \frac{1-\rho_t}{2} \sum_{n=0}^{\infty} \left[\rho_g^n \rho_t^n I_{sc} \left(h, t - \frac{h-z'}{c} - \frac{2nh}{c} \right) + \rho_g^{n+1} \rho_t^n I_{sc} \left(h, t - \frac{h+z'}{c} - \frac{2nh}{c} \right) \right] \quad 0 \leq z' \leq h \quad (7-1)$$

Along the lightning channel,

$$I(z', t) = \frac{1}{2} \left[I_{sc} \left(h, t - \frac{z'-h}{v} \right) - \rho_t I_{sc} \left(h, t - \frac{z'-h}{v} \right) + (1 - \rho_t)(1 + \rho_t) \sum_{n=1}^{\infty} \rho_g^n \rho_t^{n-1} I_{sc} \left(h, t - \frac{z'-h}{v} - \frac{2nh}{c} \right) \right] \quad z' \geq h \quad (7-2)$$

where n is the number of reflections occurring between the top and bottom of the tower and h is the height of the tower. v is the speed of current wave traveling upward in the lightning channel. I_{sc} is the lightning short-circuit current, which is defined by *Baba and Rakov* [2005] as the lightning current that would be measured at an ideally grounded object of negligible height. ρ_g and ρ_t are the current reflection coefficients at the tower bottom and tower top, respectively, which could be expressed as

$$\rho_g = \frac{Z_t - Z_g}{Z_t + Z_g} \quad (7-3)$$

$$\rho_t = \frac{Z_t - Z_{ch}}{Z_t + Z_{ch}} \quad (7-4)$$

where Z_t , Z_g , Z_{ch} are the characteristic impedance of the tower, grounding impedance, and the equivalent impedance of the lightning channel.

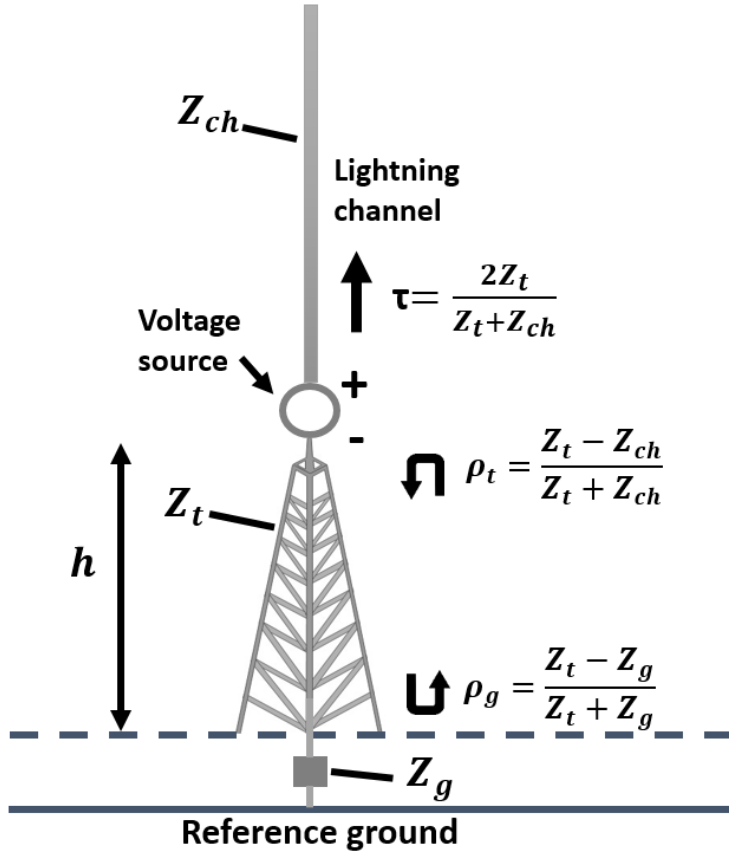


Figure 7-2. Transmission line representation of lightning strike to a tall object.

The derived expression for current along the tower (equation 7-1) is same as its counterpart in *Rachidi et al.* [2002]. However, the expression for current along the channel (equation 7-2) slightly differs from its counterpart derived by *Rachidi et al.* [2002]. In the latter case, the ground-reflected current wave transmitted into the lightning channel was set to propagate upward along the lightning channel at the speed of light, while *Baba and Rakov* [2005] assumed the corresponding value of speed to be $v < c$, which is more physical (does not allow the higher-order waves to catch up with the original upward-moving front). As noted above, the model proposed by *Baba and Rakov* [2005] will be used in this study. Several assumptions were used in this model. The reflection coefficients at the top and bottom of the towers are assumed to be constants. The lightning channel and the tower are simplified as vertical conductors above a

perfectly conducting ground. The lightning channel extending from the tower top to the cloud is assumed to be very long so that there is no need to consider the reflection at the channel top.

The expression (equation 7-5) for electric field produced by infinitesimal vertical dipole in cylindrical coordinate system given by *Thottappillil et al.* [1997] and integration over the channel length will be used to compute the vertical electric field. The code developed in this study to compute the fields was first validated with the example given by *Uman et al.* [1975, Fig. 3].

$$E_Z(r, t) = \frac{1}{2\pi\epsilon_0} \int_0^{H(t)} \left[\frac{2z'^2 - r^2}{R^5(z')} \int_{\frac{z'}{v_f} + \frac{R(z')}{c}}^t I\left(z', \tau - \frac{R(z')}{c}\right) d\tau + \frac{2z'^2 - r^2}{cR^4(z')} I\left(z', \tau - \frac{R(z')}{c}\right) - \frac{r^2}{c^2 R^3(z')} \frac{\partial I\left(z', t - \frac{R(z')}{c}\right)}{\partial t} \right] dz' - \frac{1}{2\pi\epsilon_0} \frac{r^2}{c^2 R^3(H(t))} I(H(t), \frac{H(t)}{v_f}) \frac{dH(t)}{dt} \quad (7-5)$$

The last term in equation 7-5 is no-zero when the current waveform has a discontinuity at its front.

7.3 Sensitivity Analysis

In this section, we will first vary the value of each model parameter (e.g. rise and fall times of current waveform, reflection coefficients, tower height) to study their effects on the resultant electric field waveforms. In Section 7.4, we will try to reproduce the narrow bipolar electric field waveform associated with all (except one for which the measured electric field waveform was saturated) of the Florida tower strokes presented in Chapter 7.

Current measurements for LBE-like events were rarely reported. For a stroke terminated on the Tokyo Skytree that produced narrow bipolar electric field waveforms at multiple stations, the measured current (Figure 6-5) was very similar to the typical current waveform of subsequent return stroke [*Saito et al.*, 2015a, 2015b]. However, for another presumed LBE-like event observed at the Santis tower, the measured current waveform was like a Gaussian pulse with a

small opposite-polarity overshoot (Figure 7-1). Both types of current waveform were used here as I_{sc} to simulate the resultant vertical electric field. Figure 7-3 shows the typical current waveform of a subsequent stroke (left panel) and the resultant electric field (right panel) at 10 km from the tower. The current waveform is expressed by the Heidler function. Parameters for the Heidler function (given in the left panel) were the same as specified by *Rakov* [2003], except for the peak of the current, which was reduced here to 10 kA from 50 kA. The tower was assumed to be 300 m in height and the current reflection coefficients at the top and the bottom of the tower were assumed to be -0.5 and 1, respectively. One-half of the speed of light was used as the return-stroke speed. The transmission-line return stroke model was used. It appears from Figure 8-2, that the use of current waveform typical of subsequent stroke does not allow reproduction of the narrow bipolar electric field waveform. However, the periodic field variation caused by current bouncing between the tower ends is clearly seen in Figure 7-3. In Figure 7-4, the symmetric Gaussian waveform was used as the input current. The function for the Gaussian waveform is given in Equation 7-6, where a and t_1 determine the magnitude and time of the pulse peak. The g_1 and g_2 determine the steepness of the rising and falling edges (i.e., rise and fall times). As seen from the right panel of Figure 7-4, the narrow bipolar field waveform followed by the oscillatory tail is produced. In this case, the Gaussian waveform was symmetric since g_1 is equal to g_2 . The electric field contributions from the tower and from the lightning channel are shown in the right panel in Figure 7-4. The electric field waveform produced by current along the tower is a narrow bipolar pulse, while that produced by current along the lightning channel is a unipolar pulse that is very similar to the current pulse. It follows that the presence of tower causes the total electric field to become narrower because of the opposite-polarity (negative) overshoot in the electric field contribution from the tower. It can also be observed that the initial

half cycles of the field contributions from the tower and from the lightning channel have comparable magnitudes.

$$i_0(t) = \begin{cases} ae^{-(g_1(t-t_1))^2} & t \leq t_1 \\ ae^{-(g_2(t-t_1))^2} & t > t_1 \end{cases} \quad (7-6)$$

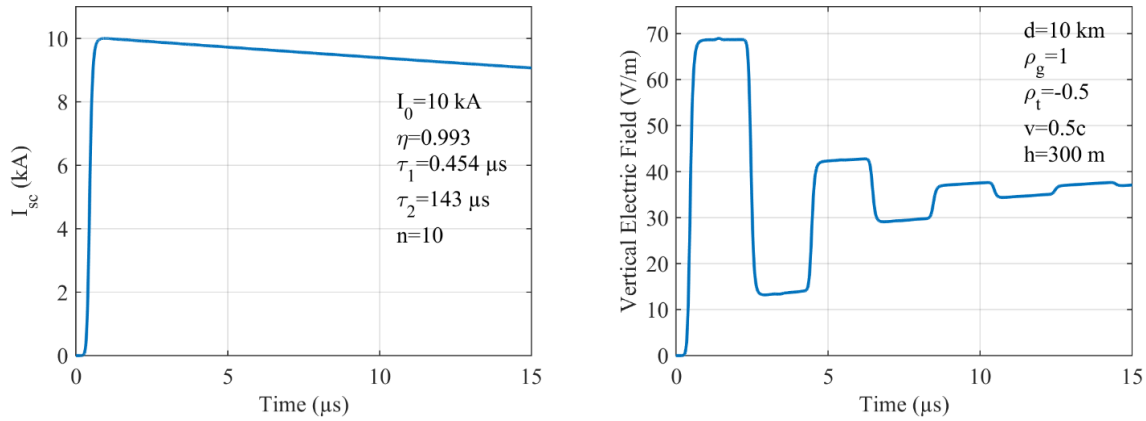


Figure 7-3. Typical current waveform of subsequent stroke (left panel) and the computed electric field (right panel) at a distance of 10 km from the tower. The time axis in right panel is shifted by $-d/c$, where d is the distance from tower to the observation point and c is the speed of light.

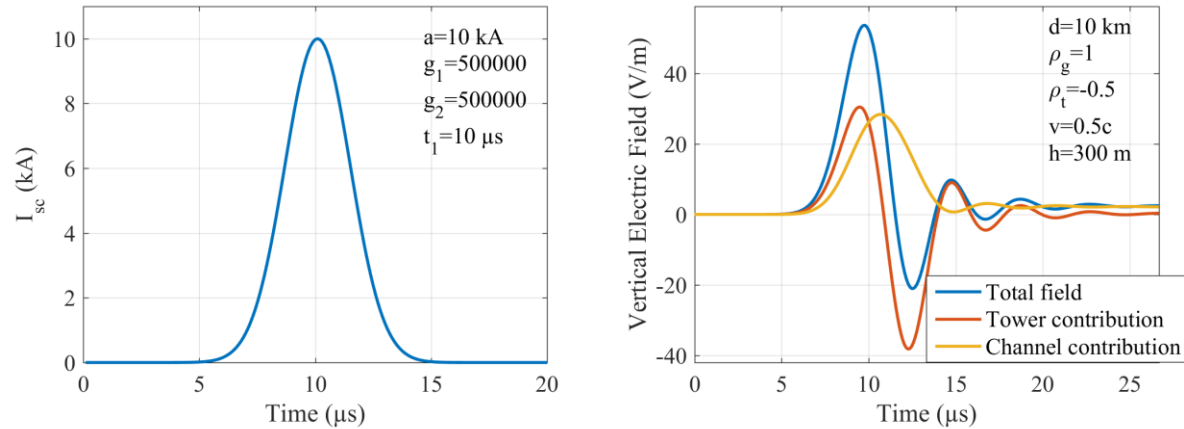


Figure 7-4. Similar to Figure 7-3, but for symmetric Gaussian waveform. In the right panel, the electric field contributions from the tower and from the lightning channel are indicated.

The effects of rise and fall times of Gaussian waveform were investigated as well. The results are shown in Figure 7-5. With decreasing the rise time of the current waveform, the width of the initial half cycle of the electric field waveform becomes smaller and the peaks of both the initial-half cycle and the first opposite-polarity overshoot become greater. The magnitude of the first opposite-polarity overshoot and the following oscillations become larger as the sharpness of the falling edge increases.

In the following, the effects of reflection coefficients, strike-object height, return-stroke speed, and return-stroke model will be tested by using the current waveform shown in Figure 7-4 (left panel). Except for the variable to be tested, all other parameters remain the same, as specified in Figure 7-4. The reflection coefficients at the tower top (ρ_t) and bottom (ρ_g) determine the magnitudes of current waves bouncing along the tower and transmitted into the lightning channel, which in turn affects the electric field waveform, as shown in Figure 7-6. As expected, the magnitudes of the initial half cycle and the following oscillations are increasing with increasing (in absolute value) ρ_t or increasing ρ_g , due to more energy being trapped within the tower. When $\rho_t=0$ (characteristic impedances of the tower and the lightning channel are the same), there is no reflection at the tower top and oscillations in electric field waveform disappear (blue curve in Figure 8-5, left panel). When $\rho_g=1$ (perfectly conducting ground), there is full reflection, and the reflection becomes smaller as ρ_g decreases.

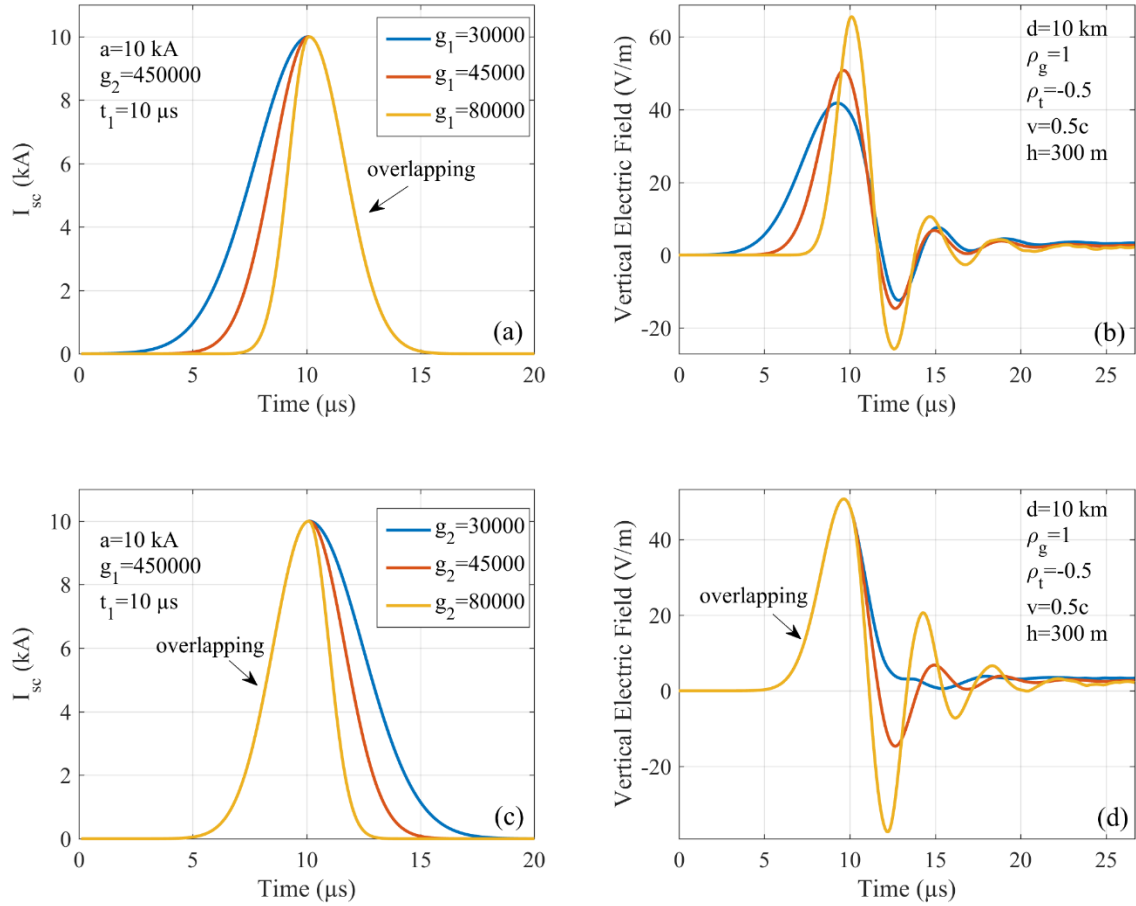


Figure 7-5. The asymmetric Gaussian waveforms with different rise times and fall times and their corresponding simulated electric field waveforms.

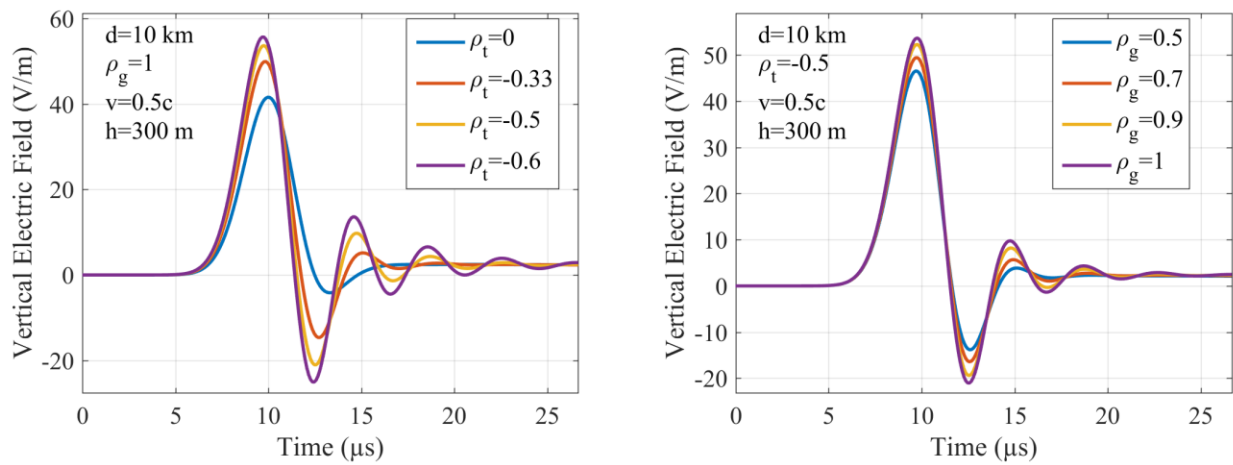


Figure 7-6. Electric field waveforms computed for different reflection coefficients at the tower top (ρ_t) and tower bottom (ρ_g).

The effects of the height of the strike object and return-stroke speed on the electric field waveform can be seen in Figures 7-7 and 7-8, respectively. For taller strike objects, the electric field is more enhanced and the width of the initial cycle and period of the following oscillations are larger. For shorter strike objects, the overshoot and oscillations become less pronounced and eventually disappear (blue curve in Figure 7-7). The return-stroke speed controls the ratio of magnitudes of the initial and second half-cycles. For larger return-stroke speeds, the magnitude of the initial half-cycle of the electric field waveform becomes larger, while the magnitude of the overshoot becomes smaller. The return-stroke speed has little effect on the following oscillations.

Four return-stroke models, TL, MTLE, MTL, and MTLP, were compared and the results are shown in Figure 7-9. The attenuation constant was set to 1 km for the MTLE model. For all return-stroke models, the peak of the initial half-cycle of the electric field waveforms, which is attained within a few microseconds, is almost the same. The peak of the opposite-polarity overshoot appears to increase with increasing the current attenuation with height along the channel (from no attenuation for the TL model to the strongest for the MTLE model). Note that in this study we used only the transmission-line-type return-stroke models that were developed and tested for “normal” lightning striking ground or a short grounded object. However, the 8 strokes examined here are far from “normal” and can be associated with stronger attenuation of current with height predicted by the existing models. An attenuation of more than 30% in the lower portion of lightning channels was inferred from luminosity pulses produced by return strokes in rocket-triggered lightning [e.g. *Wang et al.*, 1999; *Carvalho et al.*, 2015]. A stronger attenuation of current along the lightning channel (also changing channel geometry from predominantly vertical to predominantly horizontal) could affect the contribution from the

lightning channel (yellow curve in the right panel of Figure 7-4) to the total electric field waveform.

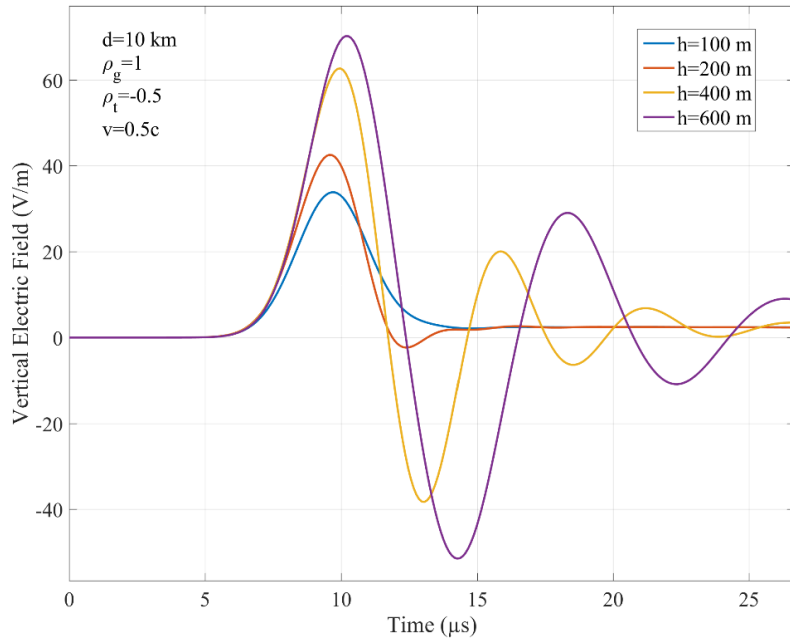


Figure 7-7. Electric field waveforms computed for different heights of the strike object.

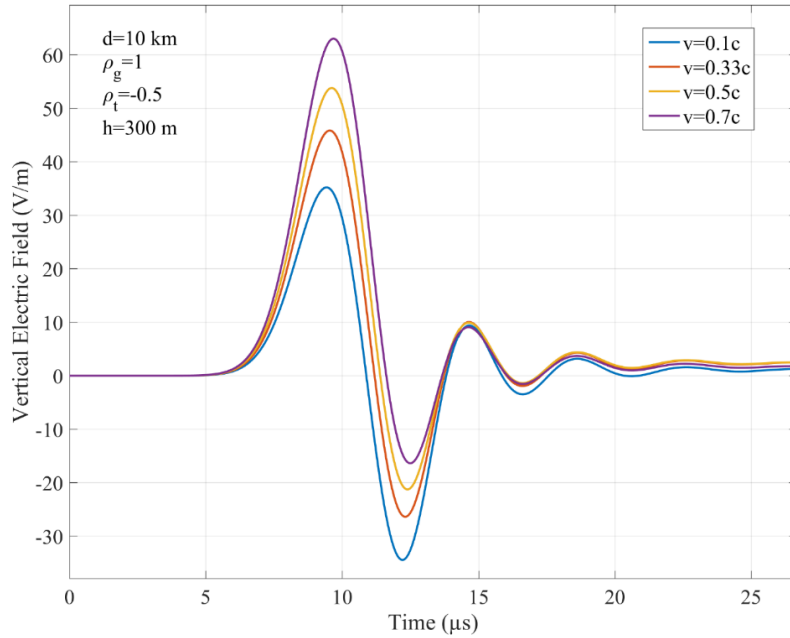


Figure 7-8. Electric field waveforms computed for different return-stroke speeds.

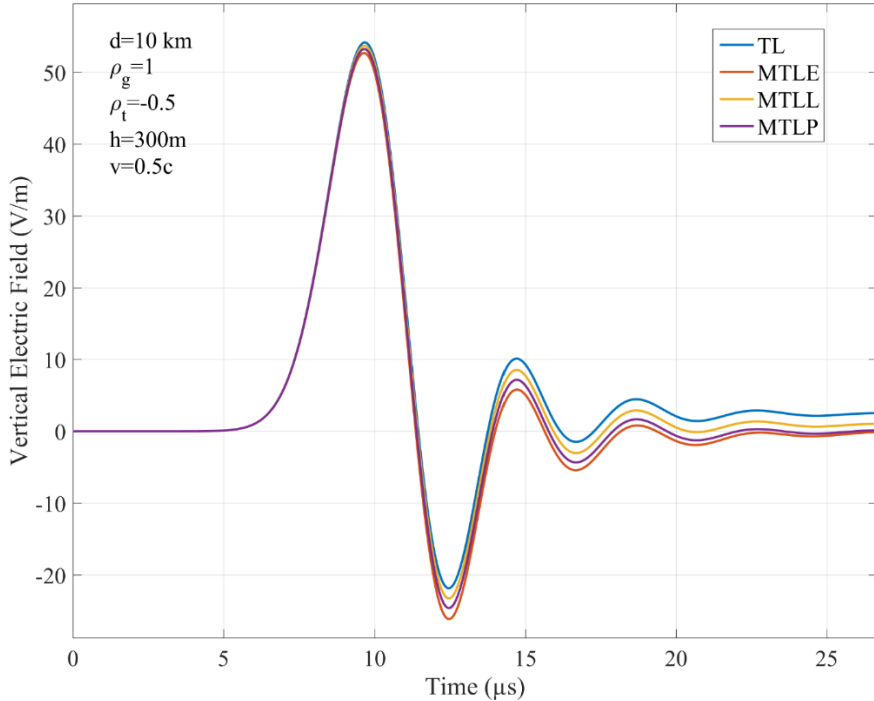


Figure 7-9. Electric field waveforms computed for different return-stroke models.

7.4 Modeling of Lightning Events Terminated on the 257-m Tower

As described in Chapter 6, we obtained optical and electric field records for 8 strokes terminated on the 257-m tower in Florida. Electric field waveforms for 7 strokes (excluding one stroke with saturated field measurement) were computed by using the model described above. Asymmetric Gaussian pulses shown in Figure 7-10 was used as the short-circuit current (I_{sc}). Asymmetric Gaussian pulses were used to represent current waveforms in modeling preliminary breakdown pulses and compact intracloud discharges [e.g., *Shao and Heavner, 2006; Nag and Rakov, 2010a, 2010b; Karunarathne et al., 2014*]. Also, in Section 7.3, we used asymmetric Gaussian pulse to reproduce the opposite-polarity overshoot in the measured electric field waveform, which could not be achieved using the typical return-stroke current waveform. The computed and measured electric field waveforms for 7 strokes at 8.8 km are shown in Figure 7-11. The MTLL return-stroke model was used for all the 7 strokes. The model parameters used to

compute electric fields waveforms shown in Figure 7-11 are summarized in Table 7-2. The model parameters were determined by using trial and error method to achieve the best matching between the computed and measured electric field waveforms. The first step is to roughly match the positive peak and the rising edge of the electric field waveform by varying the rise time and magnitude of the current waveform. After that, efforts were made to roughly match the opposite-polarity overshoot by choosing appropriate values of reflection coefficients, g_2 , and return-stroke speed. When the rough matching was achieved, some further small tunings would be made to polish the matching.

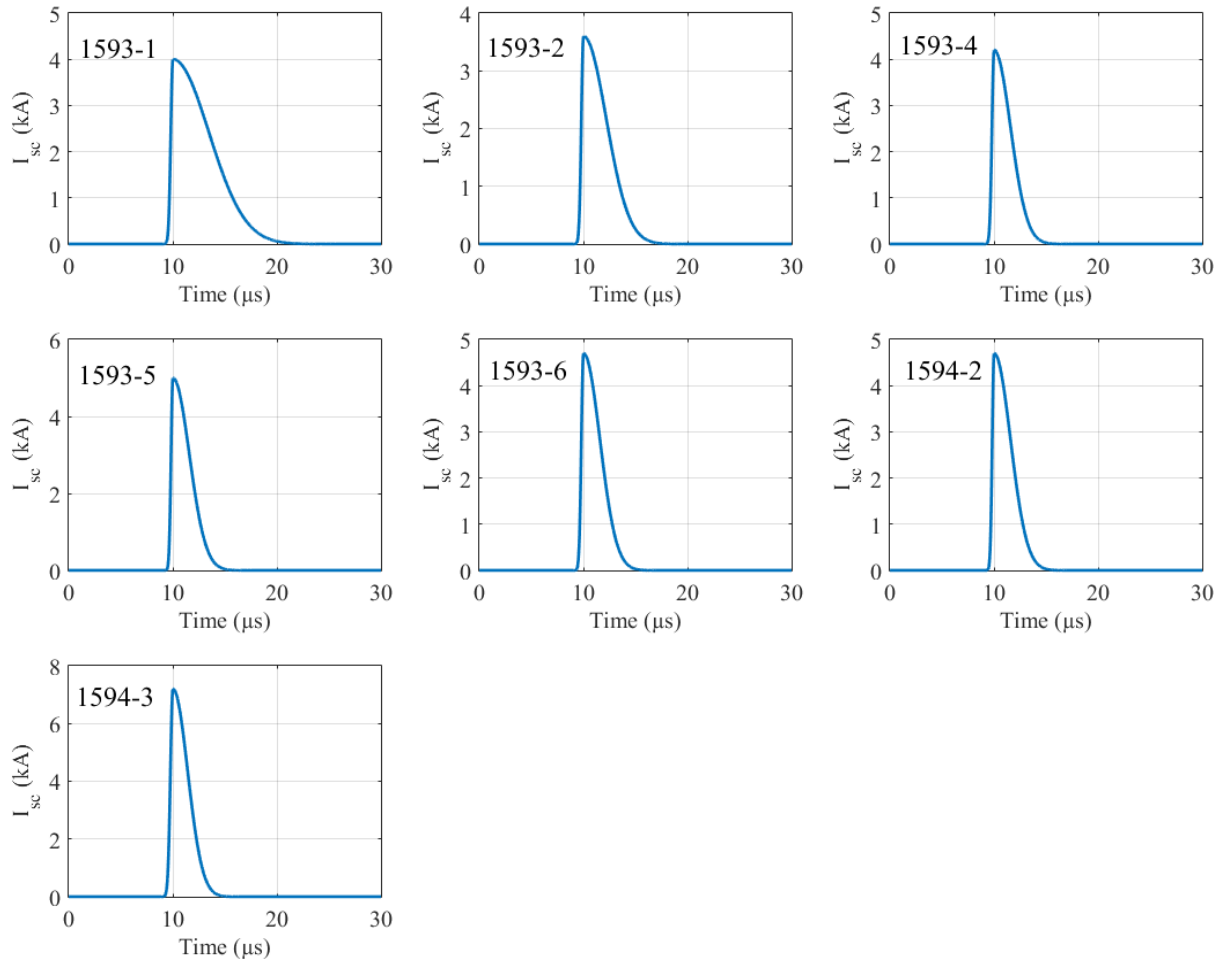


Figure 7-10. The current waveforms used for computing the electric field waveforms shown in Figure 7-11.

Table 7-2. Model input parameters used for computing electric field waveforms shown in Figure 7-11

	a (kA)	$g_1 (\times 10^5)$	$g_2 (\times 10^5)$	ρ_t	ρ_g	v
1593-1	4.0	35	4.1	-0.3	1	0.90c
1593-2	3.6	35	6.5	-0.3	1	0.90c
1593-4	4.2	35	9.0	-0.3	1	0.90c
1593-5	5.0	40	9.0	-0.3	1	0.85c
1593-6	4.7	35	9.0	-0.3	1	0.95c
1594-2	4.7	40	9.0	-0.3	1	0.80c
1594-3	7.2	30	10	-0.3	1	0.90c

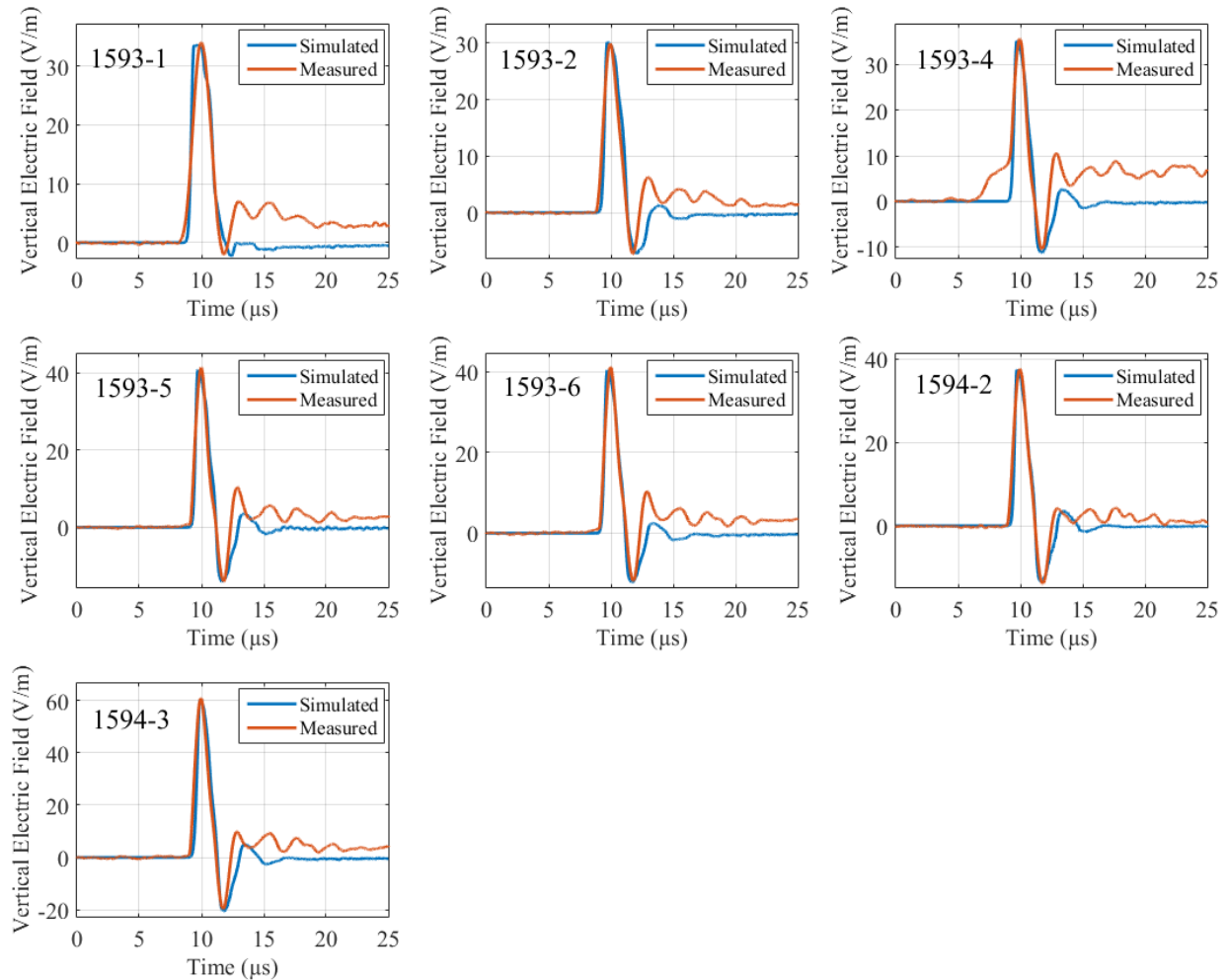


Figure 7-11. The measured and computed electric field waveforms. The corresponding I_{sc} for each event is shown in Figure 7-10.

In the process of matching (by trial and error) the model predictions to measurements, it was found that the width of the opposite-polarity overshoot is mainly determined by the fall time of the current and the height of strike object (fixed at 257 m in this case). However, a shorter fall time results in larger oscillations (Figure 7-5b). In order to match the peak of the opposite-polarity overshoot, a smaller reflection coefficient ($\rho_t = -0.3$) at the tower top had to be chosen for all the 7 events. Because of such a smaller value of ρ_t , current in the tower is significantly reduced, which results in no observable oscillations after 15 μs (Figure 7-11) in the computed electric field waveform, in contrast with the measurements..

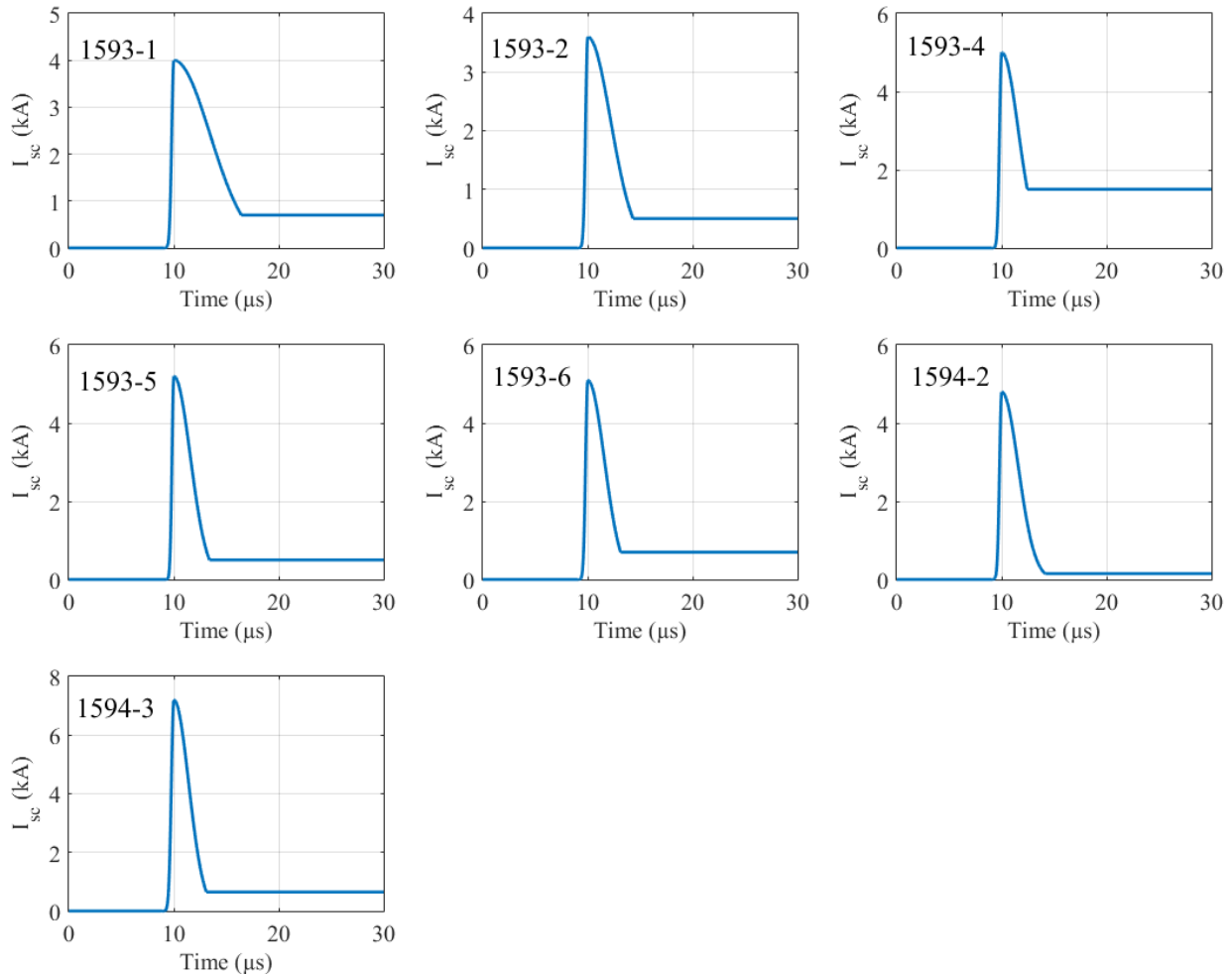


Figure 7-12. The current waveforms (with continuing current components) used for computing the electric field waveforms shown in Figure 7-13.

In Figure 7-11, there are offsets roughly ranging from 1 to 6 V/m between the tails of computed and measured electric field waveforms, which result from the insufficiently large electrostatic component in the computed electric field waveforms. In order to better reproduce the electrostatic field component, we added continuing-current like components to the input current waveforms, as shown in Figure 7-12. Calculations of fields were repeated with the modified current waveforms, and the results are shown in Figure 7-13 with the model parameters being summarized in Table 7-3. For the initial half cycle and the opposite-polarity overshoot, there is a good agreement between the computed electric field waveforms and their corresponding measured electric field waveforms. On the other hand, the following oscillatory tail is not well produced (it is less pronounced in the computed waveforms), although the offset seen in Figure 7-11 is largely eliminated in Figure 7-13.

Table 7-3. Model input parameters used for computing electric field waveforms shown in Figure 7-13 and NLDN-reported peak current for the 7 strokes

	a (kA)	g_1 ($\times 10^5$)	$g_2 (\times 10^5)$	ρ_t	ρ_g	v	I_{cc} (A)	NLDN-reported peak current (kA)
1593-1	4.0	35	4.1	-0.3	1	0.90c	700	7.6
1593-2	3.6	35	6.5	-0.3	1	0.85c	500	5.7
1593-4	5.0	35	9.0	-0.3	1	0.55c	1500	6.5
1593-5	5.2	40	9.0	-0.3	1	0.80c	500	6.6
1593-6	5.1	35	9.0	-0.3	1	0.80c	700	6.7
1594-2	4.8	35	9.0	-0.3	1	0.80c	150	6.5
1594-3	7.2	30	10	-0.3	1	0.90c	650	10.2

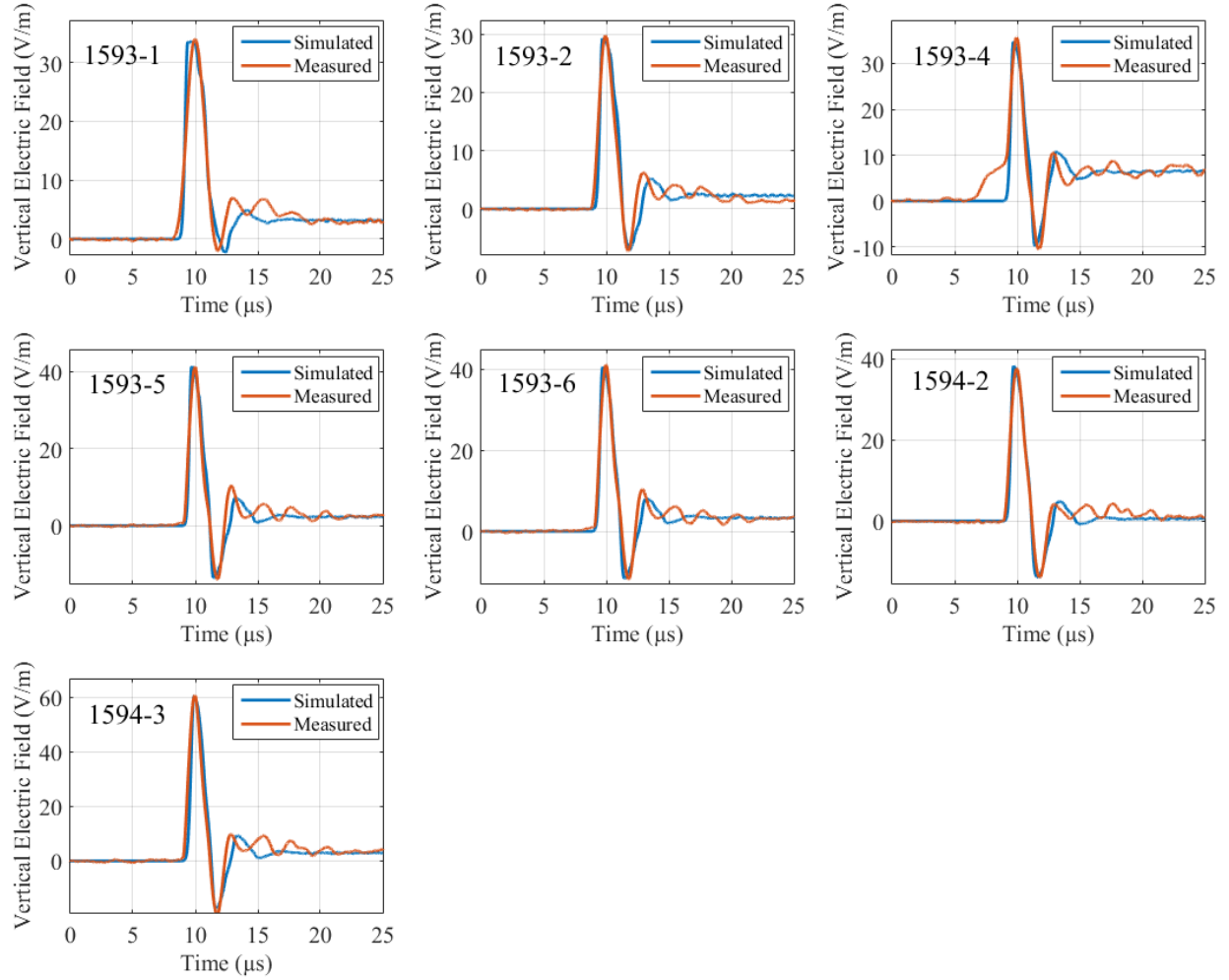


Figure 7-13. The measured and computed electric field waveforms. The corresponding I_{sc} for each event is shown in Figure 7-12.

As seen from Figure 7-13, the time interval between the peaks (period) of the oscillatory tail in the measured electric field waveform is not constant. The varying period of oscillations could be caused by the presence of guy-wires or/and impedance discontinuities within the tower, which are not reproduced in our simplified model. It is also conceivable that the lightning channel could be involved. The NLDN-reported peak current for the seven strokes are also listed in Table 7-3 for comparison with the peak currents of I_{sc} . For all the events, the NLDN overestimated the peak current and the overestimation range from 27% to 90% with an average of 45%.

7.4 Summary

The model proposed by *Baba and Rakov* [2005] was used to compute the electric field waveforms produced by lightning strike to tower. Effects of each model parameter on the electric field waveform were examined. It was found that the narrow bipolar electric field waveform for lightning strikes to tower can be produced by using asymmetric Gaussian pulse as channel-base current, rather than the typical return-stroke current waveform. The rise and fall times had significant impacts on the electric field waveform. With decreasing the rise time of the current waveform, the width of the initial half cycle of the electric field waveform becomes smaller and the peaks of both the initial-half cycle and the first opposite-polarity overshoot become greater. The magnitude of the first opposite-polarity overshoot and the following oscillations become larger as the sharpness of the falling edge increases. The magnitudes of the initial half cycle and the following oscillations are increasing with increasing reflection coefficients at tower top and bottom. For the taller strike objects, the electric field is more enhanced and the width of the initial cycle and period of the following oscillations are larger. As the return-stroke speed become larger, the ratio of magnitudes of the initial and second half-cycles become larger. Compared to other model parameters, return-stroke model had relatively small effect on the electric field waveforms.

We also tried to reproduce the narrow bipolar electric field waveforms for lightning striking the 257-m tower in Florida. Using asymmetric Gaussian pulses with continuing-current-like components superposed on the tails, the computed electric field waveforms matched well the corresponding measured waveforms for the initial half cycle and the opposite-polarity overshoot, as well as for the late-time electrostatic field offset. However, due to the selection of the small reflection coefficient at the tower top, the current in the tower is significantly reduced, which

results in no observable oscillations. Compared to the peak currents of I_{sc} , the NLDN-reported peak currents for the 7 strokes striking tower were 45% higher on average.

CHAPTER 8

NATIONAL LIGHTNING DETECTION NETWORK RESPONSES TO NATURAL LIGHTNING BASED ON GROUND-TRUTH DATA ACQUIRED AT LOG

8.1 Literature Review

The U.S. National Lightning Detection Network (NLDN) has more than 100 sensors installed in the contiguous USA with the typical separation distance of 300-350 km [*Cummins and Murphy, 2009*]. Both the time of arrival (TOA) and magnetic direction finding (MDF) techniques are used. The NLDN reports both cloud (IC) and cloud-to-ground (CG) lightning discharges, which are classified based on the magnetic field waveform criteria. In general terms, pulses wider than a certain threshold are interpreted as being produced by return strokes (RSs) in CG flashes and labeled “G”, while narrower pulses are attributed to cloud flashes and labeled “C”, although a new multi-parameter classification method was implemented in the course of the 2013 upgrade. Since any CG flash involves some cloud discharge activity (notably the preliminary breakdown process), both “G” and “C” pulses can be reported by the NLDN during CG flashes. Due to a large variation of pulse parameters for either cloud or ground discharges, some pulses produced by return strokes are misclassified as “C” and some of those produced by cloud discharge activity as “G”.

The detection efficiency is usually defined as the percentage of total ground-truth events that were detected by the lightning locating system. For the CG lightning, estimation of the stroke detection efficiency is straightforward, since each stroke involves a cloud-to-ground channel, which can be observed in optical records. However, for cloud discharges, the detection efficiency is more difficult to define since they mainly occur inside the cloud and do not have readily identifiable features. *Rakov [2013]* stated that “if all cloud discharge pulses are accepted as “counts,” the number of detected cloud discharges may be largely determined by the local noise level and lightning locating system’s signal transmission rate limit.”

Biagi et al. [2007], using video camera records, studied the performance characteristics of the NLDN in Southern Arizona, Oklahoma, and Texas. The ground-flash detection efficiency was found to be 93% in Southern Arizona and 92% in Texas/Oklahoma, with the corresponding stroke detection efficiency being 76% and 85%. *Fleenor et al.* [2009], who additionally used electric field records from Los Alamos Sferic Array (LASA), conducted a similar field campaign in the region of Colorado-Kansas-Nebraska (U.S. Central Great Plains). They found, based on the LASA field waveforms, that 54% of NLDN-reported CG strokes were actually cloud pulses. *Cummins and Murphy* [2009] found that the NLDN classification accuracy varies from region to region and that for regions with higher frequency of positive lightning the classification accuracy tends to be lower. Also, rocket-triggered lightning data have been used to evaluate the NLDN performance characteristics in the Florida region [*Jerauld et al.*, 2005; *Nag et al.*, 2011; *Mallick et al.*, 2014]. For 2004-2014, *Mallick et al.* [2014] found the ground-flash and stroke detection efficiencies to be 94% and 75%, respectively. The strokes in rocket-triggered lightning are similar to regular subsequent strokes in natural lightning. Hence, the 75% stroke detection efficiency value cited above should be an underestimate for natural lightning, since the first strokes in natural lightning tend to be larger than subsequent ones.

Information about NLDN responses to cloud discharge activity is rather limited compared to cloud-to-ground lightning and may be outdated due to system upgrades (particularly the latest one completed in 2013 [*Nag et al.*, 2014]). As reported by *Cummins and Murphy* [2009], in 2006 the NLDN cloud-flash detection efficiency was in the range of 10–20%. *Wilson et al.* [2013] reported that the NLDN typically detected 1–3 cloud pulses per flash prior to the 2013 upgrade. *Zhang et al.* [2015], who used video and VHF lightning mapping array (LMA) observations, reported that the NLDN cloud-flash detection efficiency in 2012 was 29% and

increased to 41% in 2013, after the upgrade. From a more recent study based on using LMA data as reference, *Murphy and Nag* [2015] reported the cloud-flash detection efficiency in 2014 to be in the 50-60% range. *Nag et al.* [2010] found that the NLDN detection efficiency and classification accuracy for 157 compact intracloud discharges (CIDs) were 96% and 95%, respectively. Note that CIDs produce VLF/LF field pulses that are comparable in magnitude to higher-intensity return-stroke pulses.

The focus of this chapter is on the NLDN detection efficiency (DE) and classification accuracy (CA) of cloud discharge activity based on the ground-truth dataset containing 153 IC events (identified by sequences of electric field pulses not accompanied by channels to ground) recorded at the Lightning Observatory in Gainesville (LOG), Florida. Additionally, a ground-truth dataset of 367 CG strokes recorded at LOG will be used to evaluate the NLDN DE and CA for CGs after the 2013 upgrade. In this upgrade, the previous IMPACT (Improved Accuracy through Combined Technology) and LS7001 sensors were replaced by Vaisala's LS7002 sensors with enhanced sensitivity to low-amplitude signals. By using pulse onset corrections, the LS7002 can better determine the arrival time of electromagnetic pulse, which improves the location accuracy. Further, as noted above, a multi-parameter classification method was implemented. Also, a new algorithm, called burst processing, is presently used to locate individual pulses in the pulse train. More detailed information on this upgrade can be found in the works of *Buck et al.* [2014] and *Nag et al.* [2014].

8.2 Data and Methodology

Simultaneous electric field, electric field derivative (dE/dt), and high-speed (HS) video camera records were used in this study. All the records were obtained at the LOG, Florida, in the summer of 2014. The experimental setup in this study was same as the one that was introduced in Section 6.2.

We identified the “cloud discharge activity” or “IC event” by a sequence of electric field pulses produced by either IC or CG flash that (1) had waveshapes clearly different from those characteristic of close return strokes and (2) were not associated with channels to ground in the corresponding HS video camera record (the camera had about 185° wide field of view). The characteristic features of close RS electric field waveform include the initial (predominantly radiation) peak and the following electrostatic ramp. In order to be counted as a pulse in a given sequence, the pulse had to meet two requirements: 1) the amplitude of the pulse exceeds twice the noise level and 2) the time separation from the preceding pulse is less than 200 ms. We assumed that the interpulse interval in an IC event was unlikely to exceed 200 ms since the total cloud flash duration is usually less than some hundreds of milliseconds [Rakov and Uman, 2003, chapter 8]. Particularly in the case of CG flashes, there could be multiple IC events in a single 1-s record, when they contained multiple strokes. In the latter case, pulse sequences occurring between the return strokes and after the last stroke were treated as individual IC events after the first return stroke. In the case of IC flashes, there was always a single “IC” event in a 1-s record. Our ground-truth “IC events” (Table 8-1) include 26 “isolated IC events” that can be viewed as complete IC flashes and 127 IC events that occurred in 76 CG flashes (70 negative and 6 positive). Out of the latter 127 IC events, 58 were “IC events before first RS” and 69 were “IC events after first RS” (including pulses occurring between strokes and after the last stroke).

We additionally identified 24 preliminary breakdown (PB) pulse trains within “IC events before first return stroke” and 19 regular pulse bursts (RPBs), studied by *Krider et al.* [1975] and *Rakov et al.* [1996], within “IC events after first return stroke” and “Isolated IC events”. The DE and CA for these two types of IC events were computed separately, in addition to the three main

“IC event” categories; that is, PB pulse trains and RPBs were not treated as separate “IC events” in calculating the DE and CA of “IC events”.

Examples of isolated IC events, PB pulse trains, and regular pulse bursts are shown in Figures 8-1, 8-2, and 8-3, respectively.

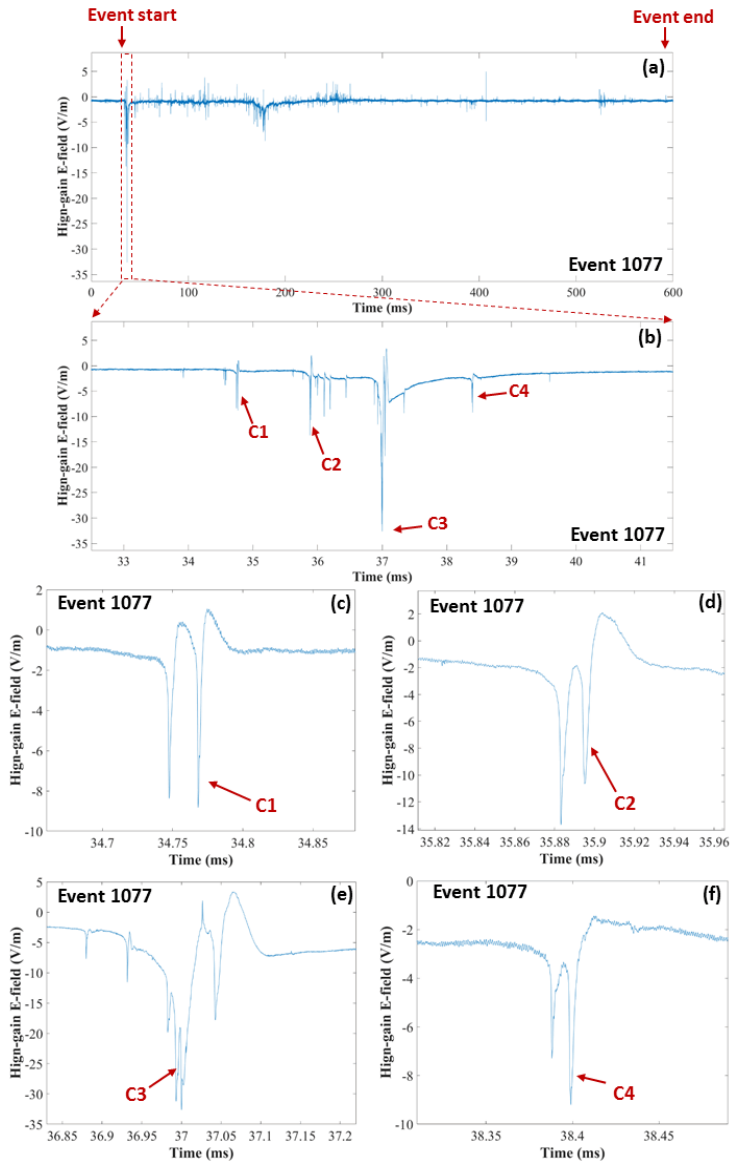


Figure 8-1. Example of an isolated IC event. No channel to ground was observed in the corresponding high-speed video camera record. The overall record of the event is shown in panel a). Four NLDN-detected cloud pulses, labeled C1 to C4, clustered in the initial portion of the event, whose expansion is shown in panel b). Expansions of the four NLDN-detected pulses are shown in panels c) to f). The pulses were located by the NLDN at distances of 22 to 28 km from the LOG.

Table 8-1. Summary of the Ground-Truth Dataset for IC Events

Event Type	Isolated IC Events	IC Events Before First RS	IC Events After First RS	All IC Events	PB Pulse Trains	Regular Pulse Bursts (RPBs)
Sample Size	26	58	69	153	24	19
Geometric Mean Duration (ms)	504	23	69	64	2.7	1.3

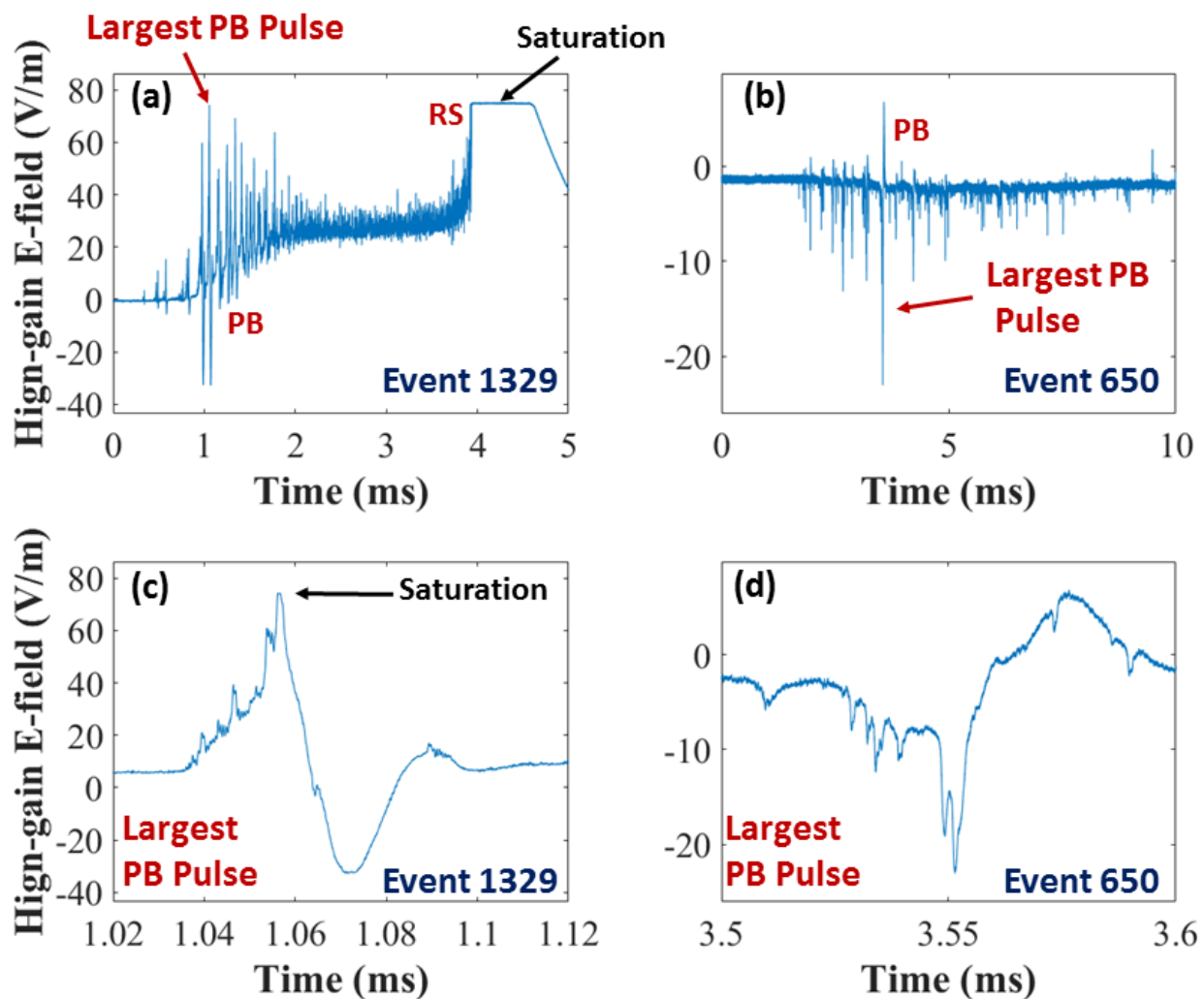


Figure 8-2. Examples of PB pulse trains in negative (left panels) and positive (right panels) CG flashes. The top panels show the PB pulse trains in their entirety. The bottom panels show the largest pulses in those two trains on an expanded (100- μ s) time scale. The pulses shown in c) and d) were located by the NLDN at 20 and 30 km from LOG, respectively, and were both misclassified as CGs.

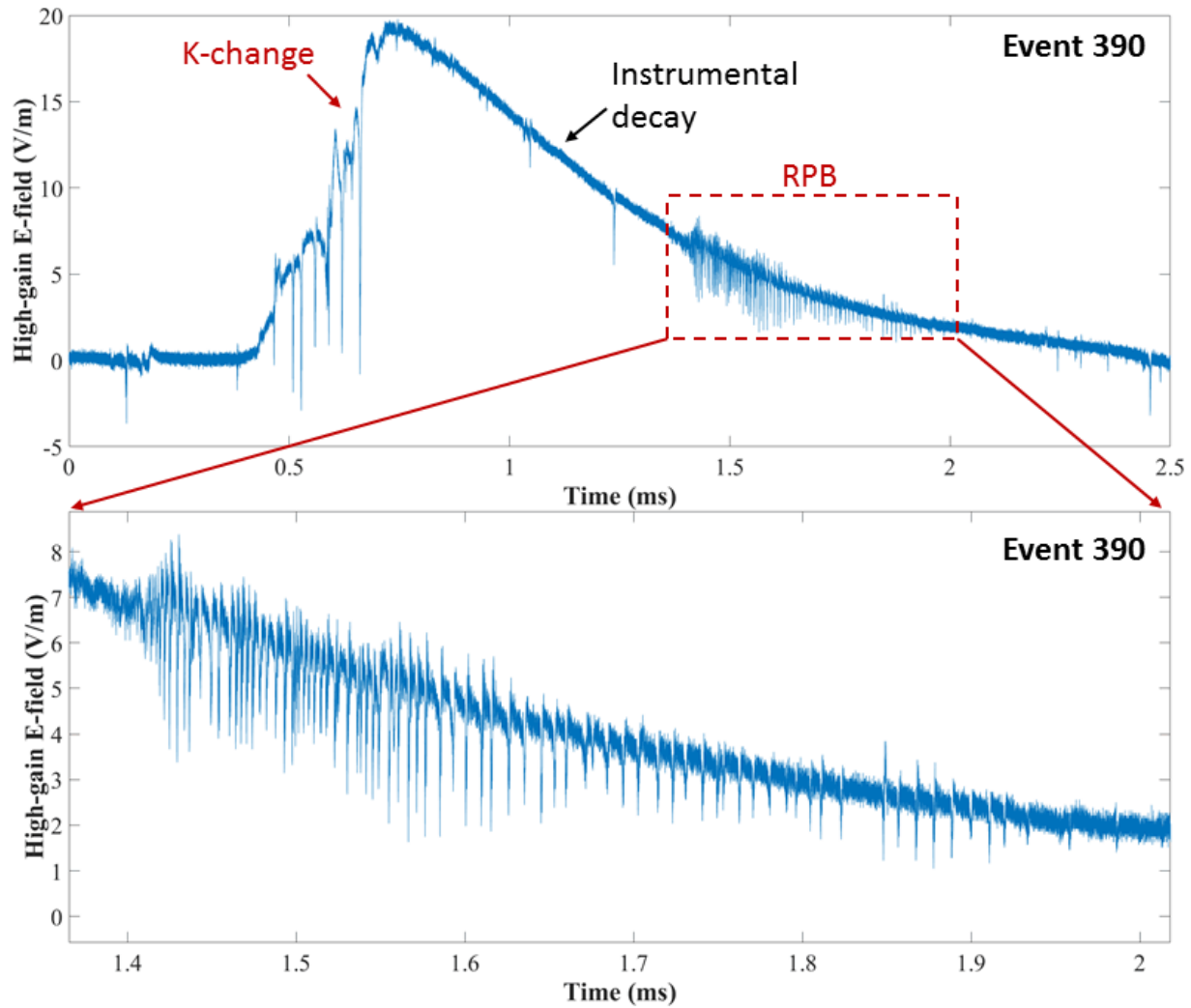


Figure 8-3. An example of regular pulse burst (RPB) that occurred in the later stage of a K-change. No RPBs were recorded by the NLDN.

As seen in Table 8-1, geometric mean durations for “isolated IC events”, “IC events before first RS”, and “IC events after first RS” were 504 ms, 23 ms, and 69 ms, respectively. The geometric mean duration for all the 153 “IC events” combined was 64 ms. For 24 PB pulse trains it was 2.7 ms and 1.3 ms for 19 RPBs. The IC event duration was limited by the electric field record length, which was 1 s. The histogram of event duration is shown in Figure 8-4. Sources of most (85%) of the cloud pulses were reported by the NLDN to be at distances less than 30 km from the LOG. Note, however, that no ground-truth information on source locations was

available and, hence, the NLDN location accuracy for IC events could not be evaluated. Also, we do not know the distribution of source intensities for the events in our ground-truth dataset.

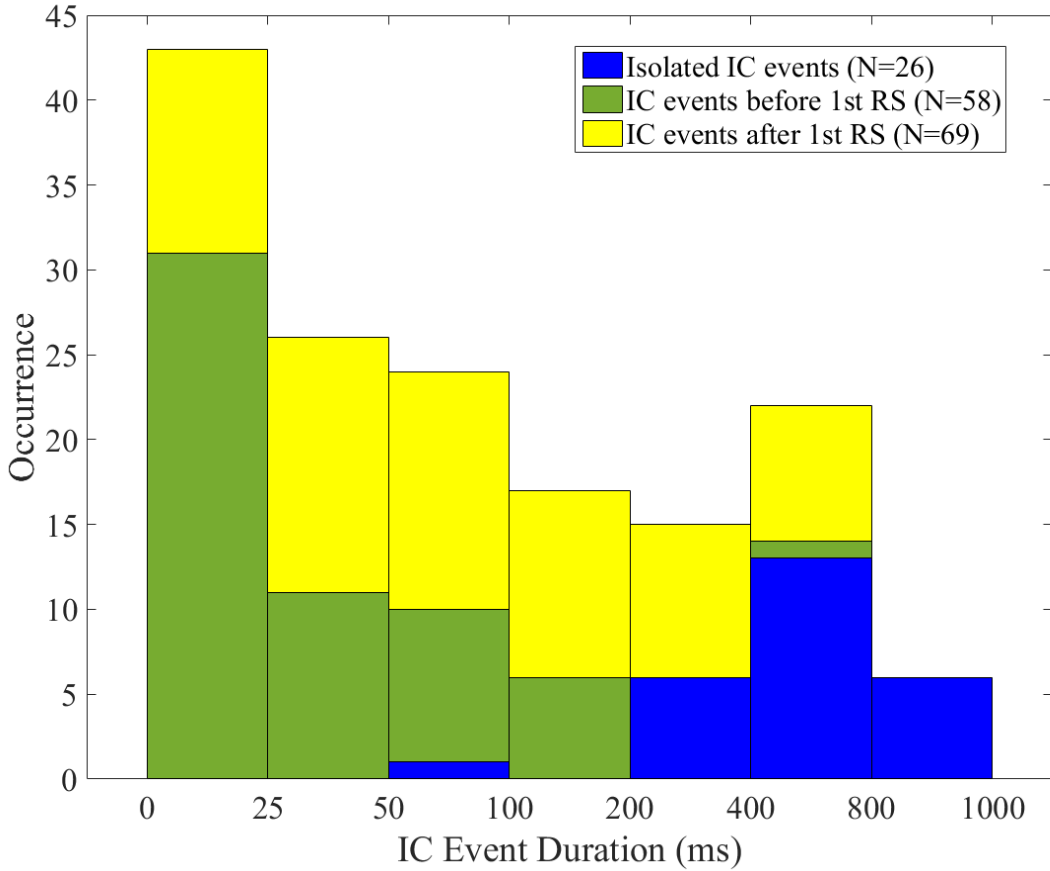


Figure 8-4. Histogram of durations of 153 IC events.

Our methodology was as follows (Figure 8-5). We first identified in our 1-s long electric field records the start and the end of an “IC event” (a sequence of non-return-stroke-type pulses, for which no channel to ground was observed by our HS video camera). The onset of the first pulse and the end of the last pulse (each exceeding twice the noise level) in the pulse sequence were considered as the start and the end of the “IC event”, respectively (see an example in Figure 8-1a). Then we searched NLDN data within that time window (between the start and the end of the IC event) and within 40 km of the LOG. If the NLDN reported no pulses corresponding to

the “IC event”, we regarded such an “IC event” as missed. If only “C” pulses (at least one) were reported, we regarded such “IC event” as correctly classified. If one or more “G” pulses were reported, we regarded such “IC event” as misclassified. The detection efficiency (DE) for “IC events” was defined as the fraction of LOG-observed “IC events” having as least one pulse reported by the NLDN (even if it was misclassified). The classification accuracy (CA) for “IC events” was defined as the fraction of NLDN-detected “IC events” for which the NLDN reported only “C” pulses and no “G” pulses.

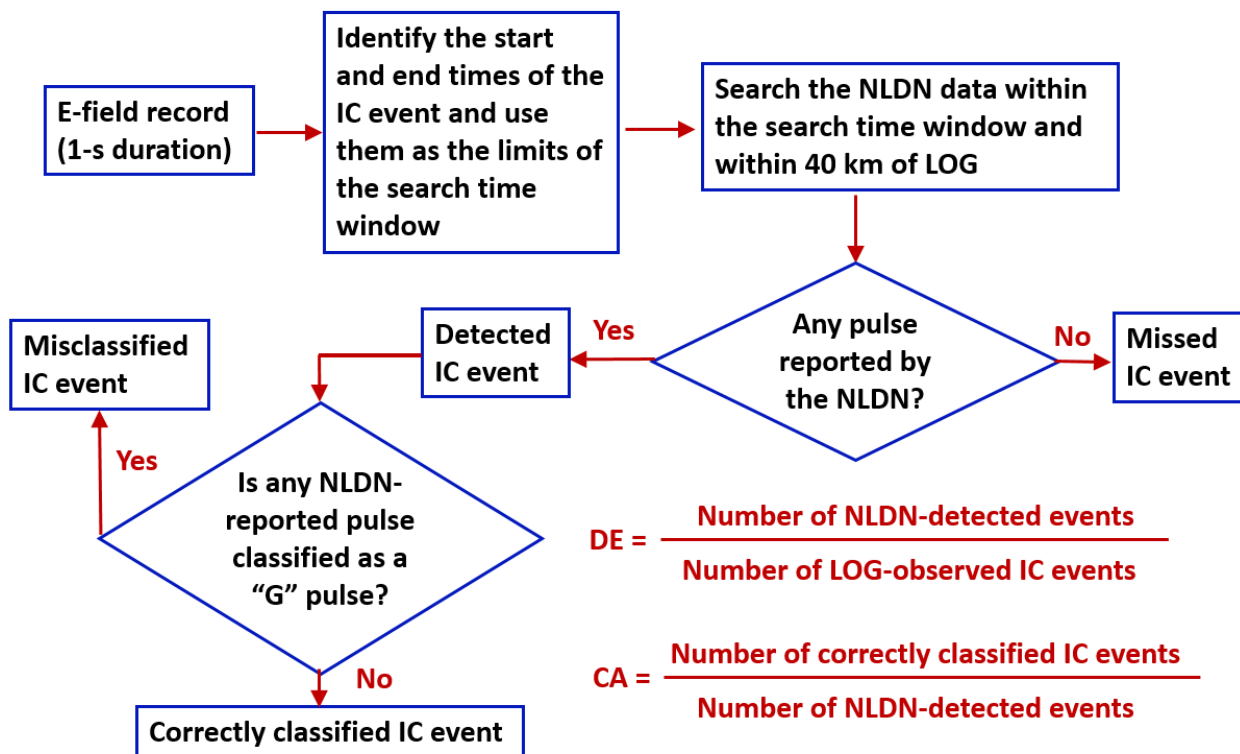


Figure 8-5. Flow chart used to determine the detection efficiency and classification accuracy for IC events.

NLDN responses to individual pulses in IC events were not evaluated in this study, since the number of ground-truth events would be less certain than in the case of more readily identifiable multi-pulse IC events (pulse sequences). Such identification is particularly straightforward for PB pulse trains (Figure 8-2) and RPBs (Figure 8-3). Note that the NLDN data

used in this study contained information for individual cloud pulses and CG strokes, and that the NLDN did not group individual pulses into flashes or other multi-pulse events; this was done by us in the ground-truth data and then NLDN responses (or lack of them) to those flashes/events were determined. Note also that our pulse-grouping algorithm, described at the beginning of this section, is different from that used by *Murphy and Nag* [2015].

Table 8-2. Summary of the Ground-Truth Dataset for CG Strokes

Stroke Type	Negative First Strokes	Negative Subsequent Strokes	All Strokes	Positive First Strokes	Positive Subsequent Strokes	All Positive Strokes	Total
Sample Size	84	257	341	21	5	26	367

The ground-truth dataset for CGs includes 367 strokes recorded by both the electric field measuring systems and HS video camera. The channel to ground was unambiguously documented for each of those strokes. Similar to IC events, no independent information on actual source location and its intensity was available. We believe that our requirement of simultaneous capturing of CGs by both optical and electric field measuring systems serves to reduce any potential bias. Most of the CG strokes were reported by the NLDN within 20 km of LOG. A summary of the CG dataset is given in Table 8-2. The 367 strokes were from 112 negative, 20 positive, and 2 bipolar CG flashes. The percentage of positive flashes was 15%, higher than average for summer thunderstorms. Note that the number of negative first strokes (84) is smaller than the number of negative flashes (112) due to the fact that some first return strokes were not included in the ground-truth dataset since they were outside the field of view of our HS video camera, even though they were identified in our electric field data. An example of ground-truth negative CG flash (both video and electric field records) is shown in Figure 8-6. Out of the 367

strokes, 39 were from single-stroke flashes and the other 328 strokes were from multiple-stroke flashes. Single-stroke flashes constituted 20% of -CGs and 85% of +CGs.

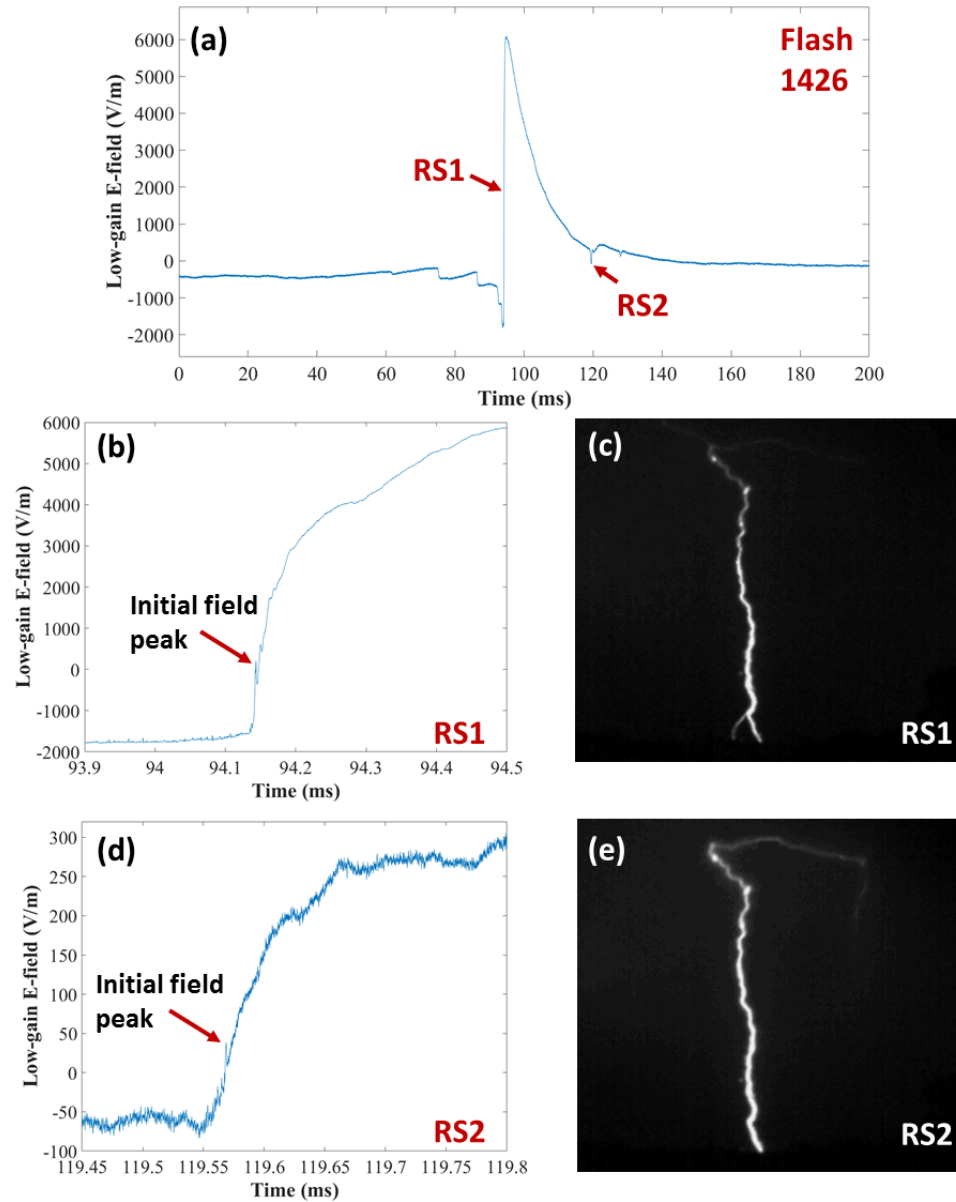


Figure 8-6. An example of ground-truth data for a two-stroke CG flash. The overall flash electric field record is shown in a) and expansions for the two strokes (RS1 and RS2) are shown in b) and d) on 600 μ s and 350 μ s scales, respectively. The corresponding video images (single frames) are shown in c) and e). For the first stroke (RS1), the second frame is shown because the first frame is saturated. The NLDN reported that the RS1 occurred at 1.7 km and had peak current of -78 kA, while the second stroke (RS2) was missed. The peak current of RS2 was estimated to be -3.4 kA based on its field peak relative to that of RS1.

By using a 2-ms time window (± 1 ms relative to the GPS time of ground-truth stroke), we identified all the NLDN-reported events (if any) in that time window and within 40 km of the LOG. If no events were reported by the NLDN in the search window, we regarded this stroke as a missed event. If a G pulse was reported in the window, we regarded this stroke as a correctly classified event. If a C pulse was reported in this window or the reported G pulse was assigned incorrect (opposite) polarity, we regarded this stroke as a misclassified event. For the rare cases of multiple pulses reported by the NLDN in the 2-ms window, we used the pulse whose timing was closest to that of the ground-truth stroke.

It is worth making a comment regarding our selected 40-km search radius. Strictly speaking, we cannot rule out the situation when the source that produced the electric field pulse in our record was farther than 40 km from LOG. The trigger threshold of our electric field measuring system was empirically set to provide triggering by lightning events within 20 km or so. We have chosen the 40 km search radius to cover the expected source locations with a significant “safety margin”. But it is still possible that some intense events could have occurred outside the 40 km search radius. If this did happen and the event was reported by the NLDN, the detection efficiency estimated in our study would be somewhat underestimated.

8.3 Analysis and Discussion

8.3.1 Detection Efficiency and Classification Accuracy of IC Events

Out of the total of 153 IC events, 26 were isolated IC events that could be viewed as complete IC flashes, one example of which is shown in Figure 8-1, 58 were IC events before first return stroke, and 69 were IC events after first return stroke. The overall detection efficiency and classification accuracy of IC events were 33% and 86%, respectively. More detailed results for the DE, CA, and the average numbers of NLDN-reported cloud pulses per detected IC event (minimum number of pulses is one) are given in Table 8-3. DE for isolated IC events was 73%,

which is 2-3 times higher than that for the other two IC-event categories. The DE for cloud flashes reported by *Murphy and Nag* [2015] was about 50-60%, which is somewhat lower than the 73% found for our complete IC flashes, but higher than the 33% for all IC events in our study. The average number of NLDN-reported cloud pulses per detected IC event was found to be 2.1.

Table 8-3. Summary of the NLDN Detection Efficiency (DE) and Classification Accuracy (CA) for IC Events

Type of IC Event	DE	CA	AM Number of NLDN-Reported Cloud Pulses per Detected Event	Maximum Number of NLDN-Reported Cloud Pulses per Detected Event
Isolated IC Events	73% (19/26)	95% (18/19)	2.9	12
IC Events Before First RS	28% (16/58)	88% (14/16)	1.4	7
IC Events After First RS	22% (15/69)	73% (11/15)	1.9	7
All IC Events	33% (50/153)	86% (43/50)	2.1	12
PB Pulse Trains	46% (11/24)	82% (9/11)	1.0	4
RPBs	0% (0/19)	-	-	-

For complete IC flashes, the average number of NLDN-reported cloud pulses was 2.9 per detected event, and the maximum number of reported pulses was 12, these numbers being higher than their counterparts for the other two IC-event categories. Classification accuracies for isolated IC events, IC events before first RS, and IC events after first RS are 95%, 88%, and 73%, respectively. Note that our sample sizes are not very large, especially for isolated IC events, so further studies are needed to reduce statistical uncertainties.

Due to very small pulse amplitudes, none of the 19 regular pulse bursts (in both IC and CG flashes) was detected by the NLDN. Out of the 24 preliminary breakdown pulse trains in CG flashes, 11 (46%) were detected and 9 (82%) of the 11 were correctly classified as cloud events. The two misclassified events are relatively high-intensity PB pulse trains, one of which preceded

the negative return stroke and the other one occurred before the positive return stroke. Those misclassified PB pulse trains are shown in Figures 8-2a and 8-2b. The largest pulses (shown in Figures 8-2c and 8-2d) were incorrectly reported by the NLDN as a 45-kA -CG stroke and a 30-kA +CG stroke, respectively.

Table 8-4. Summary of the NLDN Detection Efficiency (DE) and Classification Accuracy (CA) for CG Strokes

Stroke Type	DE	CA
Negative first strokes	98% (82/84)	96% (79/82)
Negative subsequent strokes	90% (231/257)	90% (208/231)
Positive first strokes	100% (21/21)	95% (20/21)
Positive subsequent strokes	100% (5/5)	100% (5/5)
All negative strokes	92% (313/341)	92% (287/313)
All positive strokes	100% (26/26)	96% (25/26)
All first strokes	98% (103/105)	96% (99/103)
All subsequent strokes	90% (236/262)	90% (213/236)
All strokes combined	92% (339/367)	92% (312/339)

8.3.2 Detection Efficiency and Classification Accuracy of CG Strokes

Out of the 367 positive and negative CG strokes, 28 were missed by the NLDN. For the 339 detected strokes, 312 were correctly classified as CGs with correct polarity and 27 were misclassified as cloud pulses. No CG strokes were reported with incorrect polarity. The resultant stroke detection efficiency (DE) is 92% and classification accuracy (CA) is 92%. Our results for DE and CA for different categories of CG strokes are summarized in Table 8-4. One can see from the table that both DE and CA of +CGs are higher than those of -CGs, and that DE and CA of first strokes are higher than those of subsequent strokes. Both DE and CA for the only strokes in single-stroke flashes are 100% (N=39), while for first strokes (N=78) in multiple-stroke

flashes they are 97% and 93%, respectively. For all strokes (first and subsequent strokes combined) in multiple-stroke flashes, the DE and CA are 92% and 91%, respectively.

NLDN DE and CA for CG strokes obtained in different studies are summarized in Table 8-5. Our results for negative subsequent strokes, DE = 90% and CA = 90%, can be compared with their counterparts (75% and 96%) for negative strokes in rocket-and-wire triggered lightning [*Mallick et al.* 2014], which are thought to be similar to subsequent strokes in natural lightning. For 231 NLDN-detected negative subsequent strokes in this study, the GM NLDN-reported peak current was 17 kA vs. 12 kA for 290 strokes in rocket-triggered lightning studied by *Mallick et al.* [2014]. Thus, the higher DE in our study can be, at least in part, associated with higher peak currents in our ground-truth dataset. Another possible reason for this discrepancy is the fact that the NLDN was upgraded between 2004-2012 (the study of *Mallick et al.* [2014]) and 2014 (this study).

Note that the classification accuracy for CG strokes found in this study cannot be generalized to the entire NLDN since it is known to vary by region and by storm [e.g., *Cummins and Murphy*, 2009].

8.4 Summary

The NLDN detection efficiency (DE) and classification accuracy (CA) for cloud discharge activity (IC events) and CG strokes in Florida were estimated by using the electric field and optical data acquired at LOG. For 153 ground-truth IC events, the DE and CA were 33% (50/153) and 86% (43/50), respectively. The average number of NLDN-reported cloud pulses per detected IC event was 2.1. Compared to IC events associated with CG flashes, isolated IC events (complete IC flashes) were found to have higher DE (73%), CA (95%), and average number of NLDN-reported cloud pulses (2.9). Out of the 24 preliminary breakdown pulse trains

in CG flashes, 11 (46%) were detected and 9 (82%) of the 11 were correctly classified as cloud events. None of the 19 regular pulse bursts was detected.

For CG strokes, the DE and CA were 92% (339/367) and 92% (312/339), respectively. Both DE and CA for +CGs are higher than those of -CGs, and DE and CA for first strokes are higher than those for subsequent strokes. The DE for negative subsequent strokes was 90% (GM peak current=17 kA), which is appreciably higher than the 75% estimated based on the rocket-and-wire triggered-lightning data (GM peak current=12 kA). The CA for negative subsequent strokes in our study was 90%, which is somewhat lower than the 96% estimated using the triggered-lightning data.

Note that the results of the present study correspond to the Florida region and to the NLDN configuration and settings that existed in the summer of 2014.

Table 8-5. NLDN DE and CA for CG strokes obtained in different studies

Reference	Jerauld et al. [2005]	Biagi et al. [2007]	Biagi et al. [2007]	Fleenor et al. [2009]	Nag et al. [2011]	Mallick et al. [2014]	This study
Type of lightning	Triggered	Natural	Natural	Natural	Triggered	Triggered	Natural
Time period	2001-2003	2003-2004	2003-2004	2005	2004-2009	2004-2012	2014
Region	Florida	Arizona	Texas-Oklahoma	Colorado-Kansas-Nebraska	Florida	Florida	Florida
Number of strokes	159 (negative subsequent*)	3620 (positive and negative, first and subsequent)	882 (positive and negative, first and subsequent)	547 (positive and negative, first and subsequent)	139 (negative subsequent)	326 (negative subsequent)	367 (positive and negative, first and subsequent)
Stroke DE	60%	68%	77%	84%	76%	75%	92%
Stroke CA	-	-	-	44%	-	96%	92%

* Except for one positive subsequent stroke

All triggered-lightning strokes are classified as subsequent

CHAPTER 9

EVALUATION OF ENTLN PERFORMANCE CHARACTERISTICS BASED ON THE NATURAL AND ROCKET-TRIGGERED LIGHTNING DATA ACQUIRED IN FLORIDA

9.1 Literature Review

The Earth Networks Total Lightning Detection Network (ENTLN) consists of more than 1500 wideband (1 Hz to 12 MHz) sensors deployed in more than 40 countries around the world, including North and South America, Europe, Africa, Asia, and Australia. More than 900 hundred sensors are presently installed in the contiguous United States. The sensors record electric field waveforms produced by lightning and send them to the central server via the Internet. By using the time-of-arrival technique, the ENTLN can report location and time of each lightning-produced pulse it detects. For each pulse, the polarity and type of discharge (either CG or IC) are determined based on the electric field pulse polarity (initial half-cycle for bipolar pulses) and waveshape. All waveforms from ENTLN sensors are saved and can be used for reprocessing in the future. More information on the ENTLN can be found in *Liu and Heckman* [2011].

Mallick et al. [2015] evaluated the ENTLN performance by using as ground-truth rocket-triggered lightning data acquired in Florida in 2009 to 2012. Two different ENTLN datasets were evaluated in that study. The first dataset was produced by the old processor that was in service in June 2009 to August 2012. The second dataset was produced by rerunning the same raw data (saved electric field waveforms) through the new processor that was put in service in November 2012. They found that the stroke detection efficiency and classification accuracy were 49% and 40% for the old processor and 67% and 48% for the new one. For the new processor, the medians of the location error and peak current estimation error were found to be 760 m and 19%, respectively.

In this study, the term “old processor” is used to denote the ENTLN processor introduced in June 2014. Compared to previous ENTLN processors, this one had a decreased time window

for searching for pulses, which served to increase the number of events seen by the ENTLN. The term “new processor” in this study refers to the ENTLN processor that was put in service in August 2015. This latter (currently operating) processor features a new lightning classification algorithm, which uses multiple waveform parameters to distinguish between CGs and ICs.

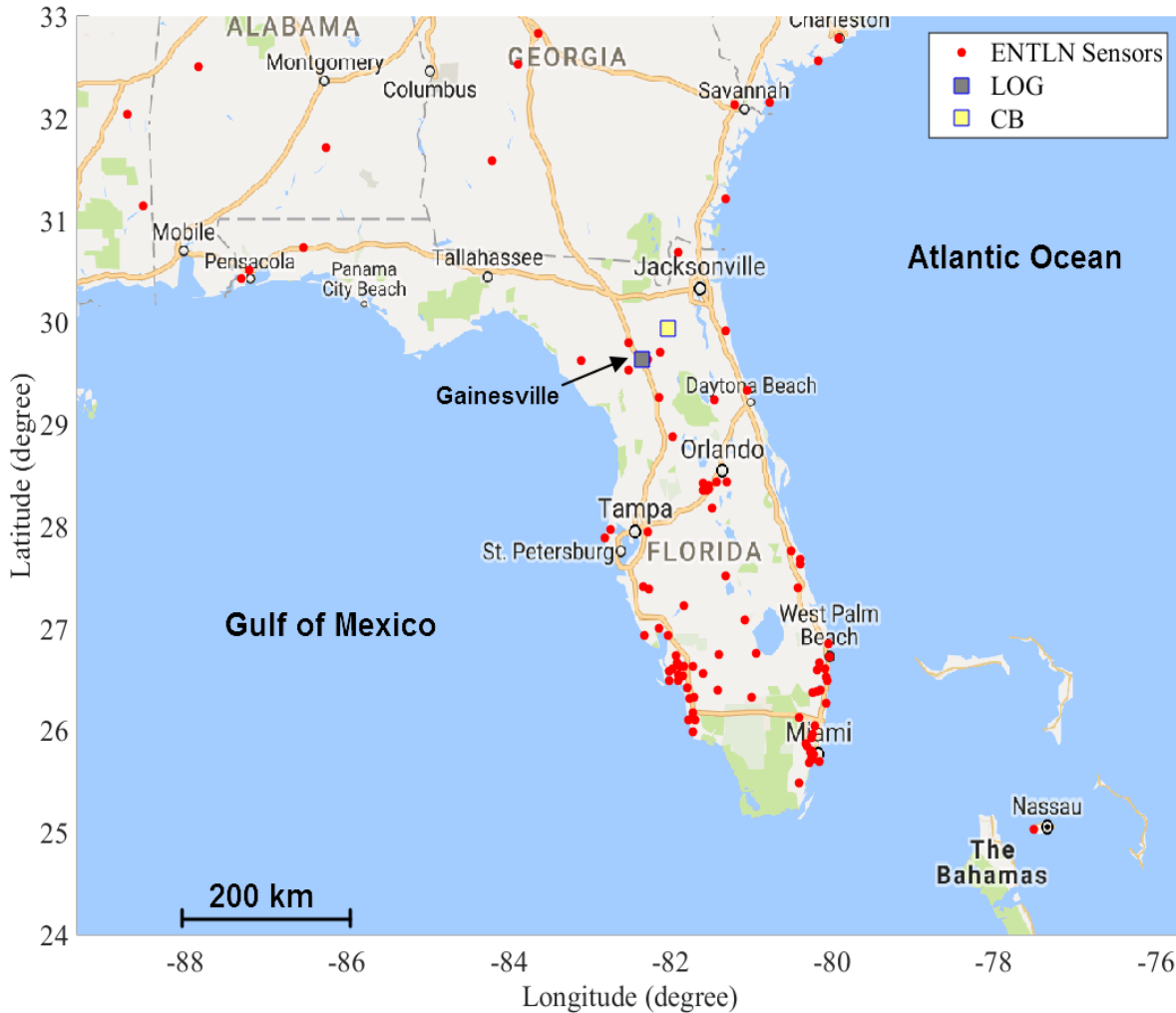


Figure 9-1. Locations of LOG (gray square), CB (yellow square) and ENTLN sensors (red circles) in the Florida region.

In this paper, the ENTLN performance in the Florida region is evaluated by using natural cloud-to-ground lightning data recorded at the Lightning Observatory in Gainesville (LOG), Florida, in 2014 and 2015. Additionally, rocket-triggered lightning data acquired at Camp

Blanding (CB), Florida, during the same time period were used for evaluation. The locations of LOG and CB (45 km apart) are shown in Figure 9-1. Also shown are the locations of ENTLN sensors deployed in the Florida region. The total number of sensors in Figure 9-1 is 84. Similar to the work of *Mallick et al.* [2015], two datasets produced using two processors were evaluated. The same originally recorded field waveforms were used as input to the two processors. The flash detection efficiency (DE), flash classification accuracy (CA), stroke DE, and stroke CA were examined for both natural lightning and rocket-triggered lightning, while the location errors and peak current estimation errors could be estimated only for rocket-triggered lightning. The results are important for proper interpretation of ENTLN data that are used in a variety of meteorological and geophysical studies and amount to the calibration of the network against the ground-truth data. The developed methodology can be applied to other lightning locating systems.

9.2 Data and Methodology

Simultaneous electric field, electric field derivative (dE/dt), and high-speed (HS) video camera records, obtained at LOG, Florida from 2014 and 2015, were used as ground-truth natural lightning data in this study. The experimental setup at LOG in this study was same as the one that was introduced in Section 6.2. For rocket-triggered lightning, channel-base currents measured at Camp Blanding and their GPS timing were used as ground-truth data in this study. Also, the position of the rocket launcher (lightning termination point on ground) was known precisely and was used as ground-truth for estimating location errors. The lightning triggering process is described in *Rakov and Uman* [2003, Chapter 7]. More information of channel-base current measurements at CB can be found in Section 2.3. For this study, the high-current channel (with highest measuring range) was used to record currents up to 60 kA with a resolution of 3 A,

sampling interval of 10 ns, and record length of 2 s. Records from this channel were used to measure the peak current of each return stroke in this study.

The ground-truth datasets for both natural lightning and rocket-triggered lightning are summarized in Table 9-1. In the summers of 2014 and 2015, electric fields for a total of 219 natural cloud-to-ground lightning flashes (175 negative, 39 positive, and 5 bipolar flashes) containing 608 strokes were recorded at LOG. The channel to ground was unambiguously documented for each of those strokes, although the termination point could be obscured by trees. No ground-truth information on the strike point nor on peak current is available for natural lightning. Note that strokes with characteristic CG electric field waveforms but occurring outside of the field of view of our camera are not included in this study.

Table 9-1. Summary of ground-truth datasets for natural and rocket-triggered lightning acquired in Florida and used in this study

Year	Natural lightning		Rocket-triggered lightning	
	Number of flashes	Number of strokes	Number of flashes	Number of strokes
2014	134	367	18	78
2015	85	241	18	97
Total	219	608	36	175

A total of 36 flashes containing 175 negative strokes were triggered at Camp Blanding in the summers of 2014 and 2015. Channel-base current records are available for 171 strokes. For one flash containing 4 strokes that were obtained from an altitude trigger [Lalande *et al.*, 1998; Rakov *et al.*, 1998] due to the breakage of the wire, no current record is available since the lightning channel did not attach to the instrumented launcher. These 4 strokes are not included in the evaluation of either current estimation errors or location errors. The histogram of ground-

truth peak currents for the 171 strokes in triggered lightning is shown in Figure 9-2. As noted in Section 2.2, the position of the rocket launcher was used as the ground-truth location of the channel termination point on the ground.

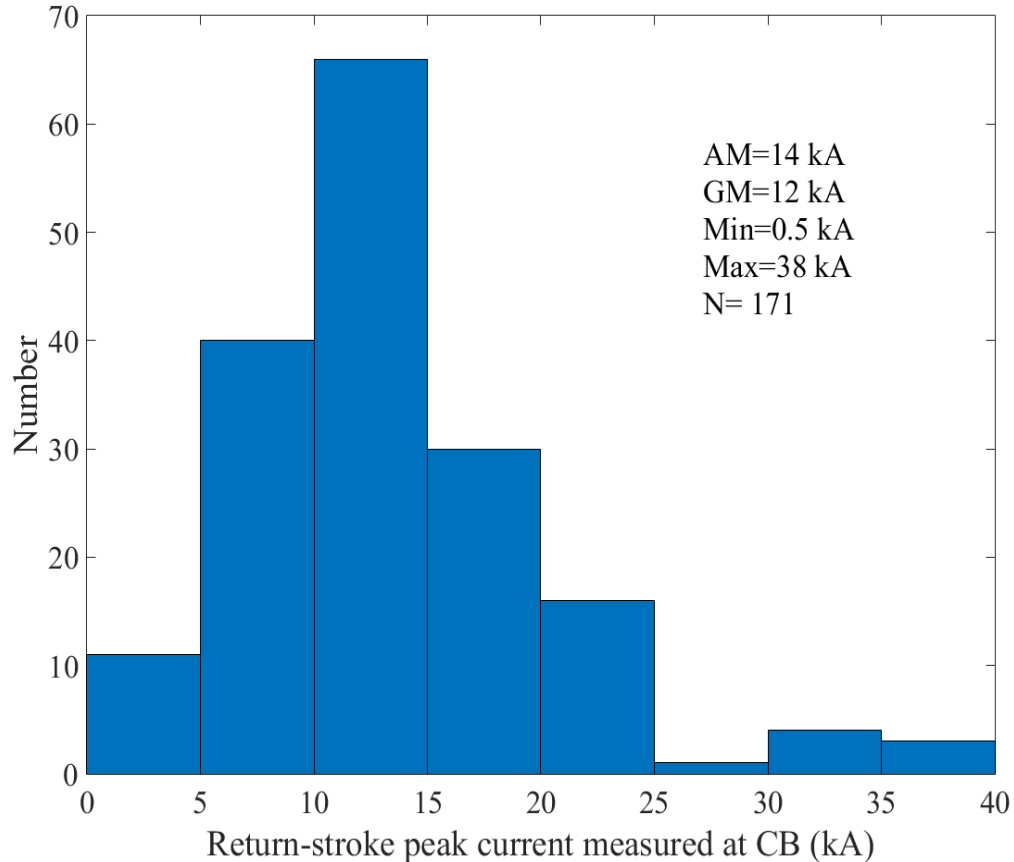


Figure 9-2. Histogram of peak currents for 171 return strokes in 18 flashes triggered using the rocket-and-wire technique at Camp Blanding, Florida.

The methodology to determine the detection efficiency and classification accuracy for natural CGs used here has been developed by *Zhu et al. [2016]* and is shown in the form of a flowchart in Figure 9-3. Each ground-truth natural CG had clearly identified cloud-to-ground channel in the high-speed video record and characteristic features of cloud-to-ground stroke in the corresponding electric field waveform. Since most our strokes were within 20 km of LOG, the return-stroke electric field waveforms had an initial (radiation) peak followed by an

electrostatic ramp. The timing of the return stroke was determined by using the time of the pulse peak relative to the trigger time of the record, which was GPS time stamped. By using a 2-ms time window (± 1 ms relative to the GPS time of ground-truth stroke), we identified all the ENTLN-reported events (if any) in that time window and within 40 km of the LOG. If no events were reported by the ENTLN in the search window, we regarded this stroke as a missed event. If a CG was reported in the window, we regarded this stroke as a correctly classified event. If a cloud pulse was reported in this window or the reported stroke was assigned incorrect (opposite) polarity, we regarded this stroke as a misclassified event. For the rare cases of multiple pulses reported by the ENTLN in the 2-ms window, we used the pulse whose timing was closest to that of the ground-truth stroke. A similar methodology was used for the rocket-triggered lightning dataset, except that the channel-base current records were used and the search area was centered at CB. Stroke DE is the percentage of ground-truth strokes that were detected by the ENTLN. Flash DE is defined as the percentage of ground-truth flashes in which at least one stroke was detected. The stroke CA is the percentage of ENTLN-detected ground-truth strokes that were correctly reported as CGs. Flash CA is the percentage of ENTLN-detected ground-truth flashes in which at least one stroke was correctly classified as a CG.

As noted above, two different ENTLN processors were evaluated in this study. The ENTLN datasets for evaluation were produced by running the old/new processor with previously saved waveforms as input, as if each of those processors was in service during the time period when our ground-truth data were collected.

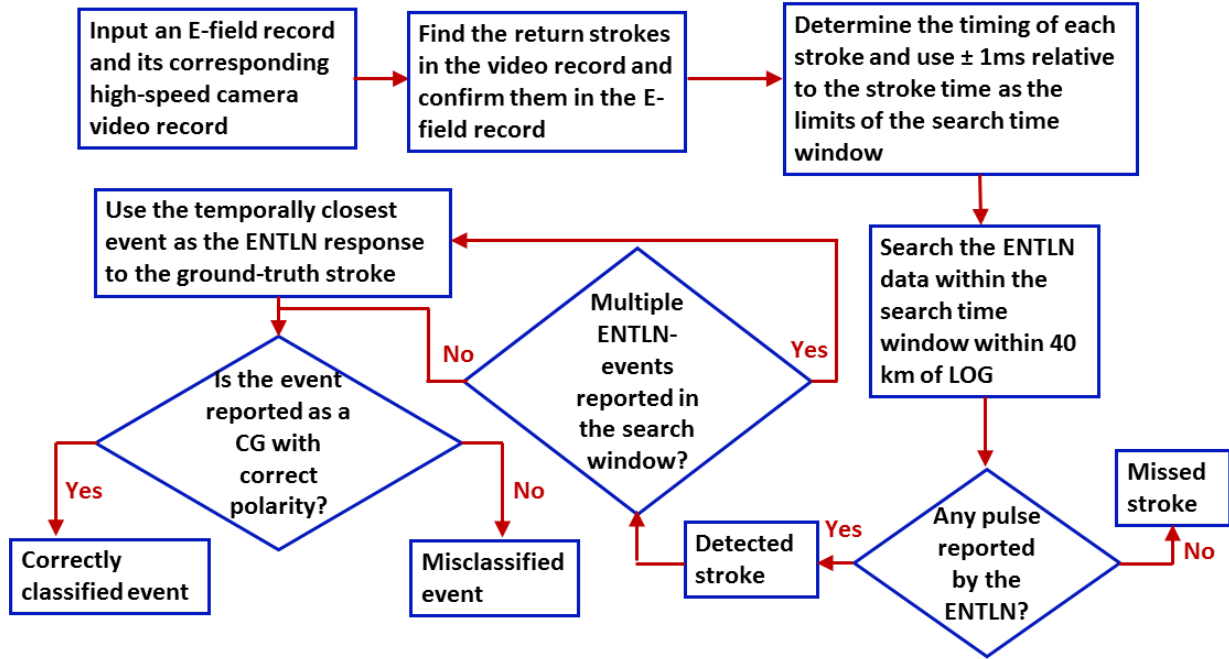


Figure 9-3. Flowchart showing the methodology to determine the detection efficiency and classification accuracy for natural cloud-to-ground lightning.

9.3 Analysis and Discussion

9.3.1 Natural Lightning

Following the procedure outline in Figure 9-3, flash DE, flash CA, stroke DE, and stroke CA were estimated using ground-truth data for 219 natural lightning flashes containing 608 strokes for old and new ENTLN processors. The results are summarized in Table 9-2. For the old processor, the ENTLN flash DE, flash CA, stroke DE, and stroke CA were found to be 99%, 91%, 97%, and 68%, respectively, and for the new processor they were 99%, 97%, 96%, and 91%. Note significant improvement in the flash/stroke CA, while the flash/stroke DEs remain essentially the same. The average number of strokes per flash for ground-truth natural lightning dataset is 2.8, which is smaller than the 4.6 reported for negative CG flashes in Florida by *Rakov and Uman* [1990].

Table 9-2. Summary of the ENTLN performance characteristics evaluated using natural lightning data

Processor	Old	New
Number of flashes	219	219
Number of strokes	608	608
Flash DE	99%	99%
Flash CA	91%	97%
Stroke DE	97%	96%
Stroke CA	68%	91%

Table 9-3. Summary of the estimated values of ENTLN stroke DE and CA for different types of strokes in natural lightning

Stroke type	Number of strokes	Stroke DE		Stroke CA		GM Peak current for ENTLN-detected strokes (kA)	
		Old processor	New processor	Old processor	New processor	Old processor	New processor
First negative strokes	139	99%	99%	86%	96%	31	30
First positive strokes	40	98%	98%	85%	90%	47	47
Subsequent negative strokes	419	96%	95%	60%	91%	18	18
Subsequent positive strokes	10	100%	100%	60%	60%	26	25
All first strokes	179	99%	99%	86%	95%	33	34
All subsequent strokes	429	96%	95%	60%	90%	18	18
All negative strokes	558	97%	96%	67%	92%	20	21
All positive strokes	50	98%	98%	80%	84%	41	41
All strokes combined	608	97%	96%	68%	91%	21	22

Stroke DE and stroke CA for different types of strokes in natural lightning are summarized in Table 9-3. Also given in Table 9-3 is the geometric mean (GM) peak current reported by the ENTLN for detected strokes (including misclassified ones). Both DE and CA for first strokes (positive and negative strokes combined) are higher than those for subsequent strokes (positive and negative strokes combined), which is likely due to the higher peak current for the first strokes. For the new processor, the GM peak currents for ENTLN-detected first strokes and subsequent strokes are 34 kA and 18 kA, respectively. The GM ENTLN-reported peak currents for misclassified strokes were 11 kA ($N=189$) for the old processor and 8 kA ($N=52$) for the new processor, while the corresponding values for correctly classified strokes were 30 kA ($N=399$) and 24 kA ($N=532$). It appears that strokes with higher peak current (inferred from measured electric field peak) are more likely to be both detected and correctly classified by the ENTLN. One possible reason could be that return strokes with higher peak current have wider field waveforms at the measurement threshold level. Also, field waveforms of strokes with higher peak currents are less affected by noise, so that more accurate waveform characteristics can be obtained, which should improve classification accuracy.

9.3.2 Rocket-Triggered Lightning

Flash DE, flash CA, stroke DE, and stroke CA were examined for 36 rocket-triggered lightning flashes containing 175 strokes. The results are summarized in Table 9-4. The ENTLN detected all the flashes for both old and new processors. For the new processor, only one flash was misclassified vs. three for the old processor. Compared to the old processor, the new processor stroke DE increased from 94% to 97% and the stroke CA increased from 42% to 86%. It is known that negative strokes in rocket-triggered lightning are similar to regular subsequent negative strokes in natural cloud-to-ground lightning [Rakov and Uman, 2003, chapter 7]. The new-processor stroke DE (97%) for rocket-triggered lightning is slightly higher than that (95%)

for subsequent negative strokes in natural lightning, as seen in Table 9-3. The new-processor stroke CA for rocket-triggered lightning is 86%, which is lower than 91% for the subsequent negative strokes in natural lightning. As seen from Table 9-4, the GM ground-truth peak current for detected strokes is about a factor of 5 greater than that for undetected strokes. Similarly, the GM ground-truth peak current for correctly classified strokes is about twice higher than that for misclassified strokes.

Table 9-4. Summary of the ENTLN performance characteristics evaluated using rocket-triggered lightning data

Processor	Old	New
Number of flashes	36	36
Number of strokes	175	175
GM channel-base peak current (kA)	11.6	11.6
Number of detected flashes	36	36
Number of correctly classified flashes	33	35
Number of detected strokes	169	169
Number of correctly classified strokes	71	145
Flash DE	100%	100%
Flash CA	92%	97%
Stroke DE	97%	97%
Stroke CA	42%	86%
GM ground-truth peak current for undetected strokes (kA)	2.6	2.4
GM ground-truth peak current for detected strokes (kA)	12.2	12.3
GM ground-truth peak current for misclassified strokes (kA)	9.8	6.5
GM ground-truth peak current for correctly classified strokes (kA)	16.5	13.6
Median absolute current estimation error	15%	15%
Median location error (m)	205	215

For rocket-triggered lightning strokes, peak current estimation errors and location errors were also examined. The histograms for absolute (unsigned) peak current estimation error ($|I_{ENTLN} - I_{CB}|/I_{CB}$), and signed peak current estimation error ($(I_{ENTLN} - I_{CB})/I_{CB}$), are shown in Figure 9-4. Figure 9-5 shows the scatterplots of the absolute current estimated by the ENTLN versus ground-truth peak current measured at CB, from which one can also see that the majority of misclassified events had peak currents < 20 kA for the old processor and < 10 kA for the new

processor. Histograms for location error and ENTLN-reported stroke locations are shown in Figures 9-6 and 9-7, respectively. The median location errors for old and new processors are 205 m and 215 m, respectively. Note that in Figures 9-4 to 9-7, the type (-CG, -IC, or +IC) for each event was designated by the ENTLN and that the ground-truth type for all the events is negative return stroke (-CG).

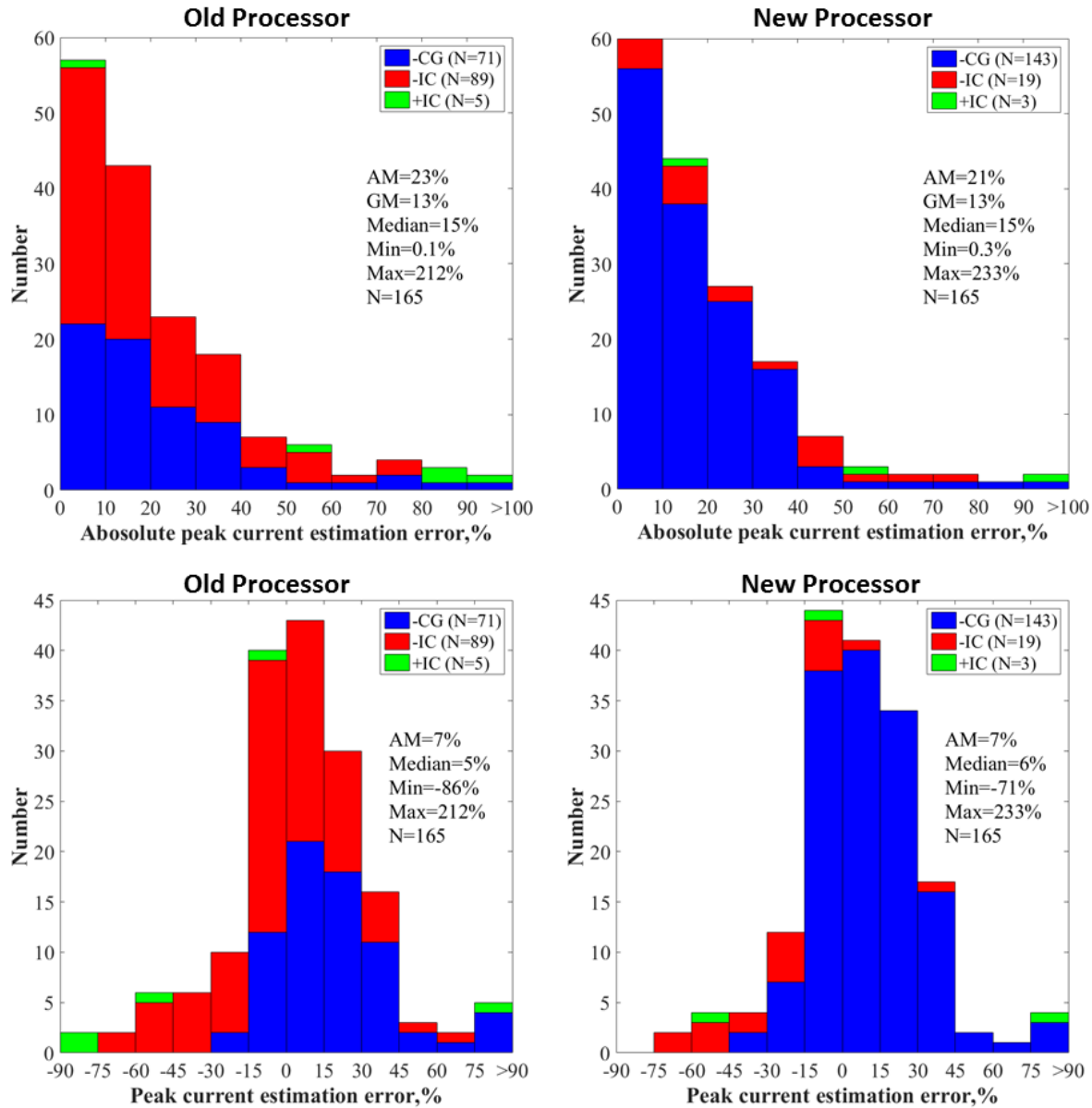


Figure 9-4. Histograms of absolute (upper panels) and signed (lower panels) peak current estimation errors for old (left panels) and new (right panels) processors.

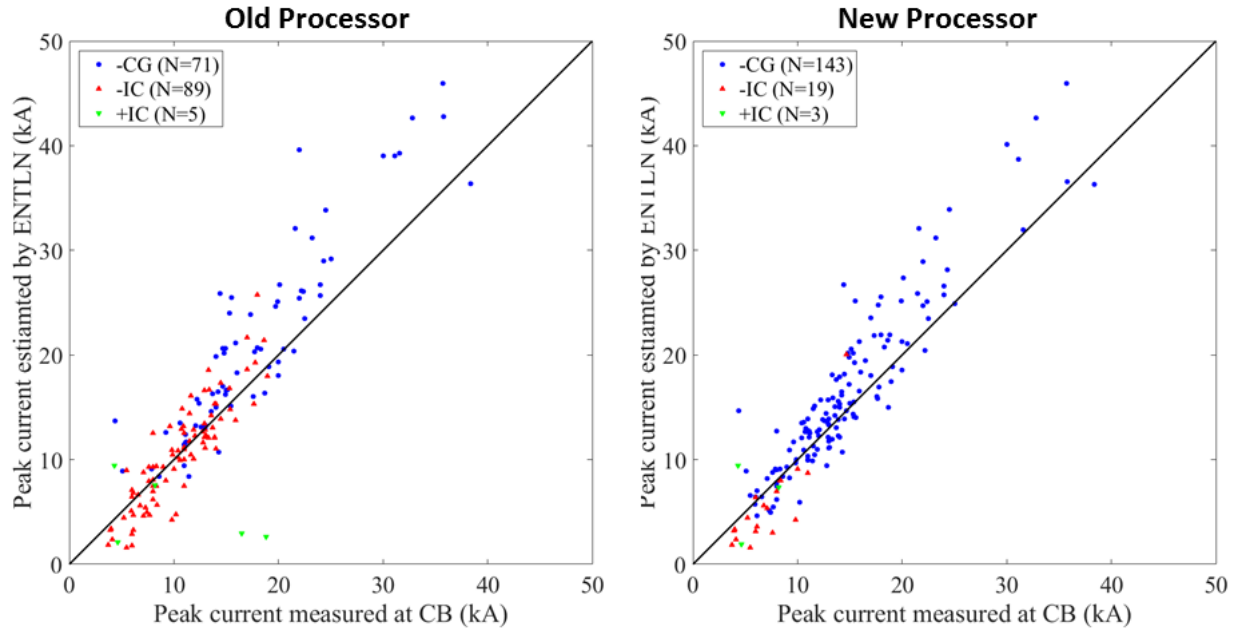


Figure 9-5. Scatterplots of peak current estimated by the ENTLN vs. ground-truth peak current measured at CB for old (left panel) and new (right panel) processors. Note that the type (-CG, -IC, or +IC) for each event was designated by the ENTLN and that the ground-truth type for all the events is negative return stroke (-CG).

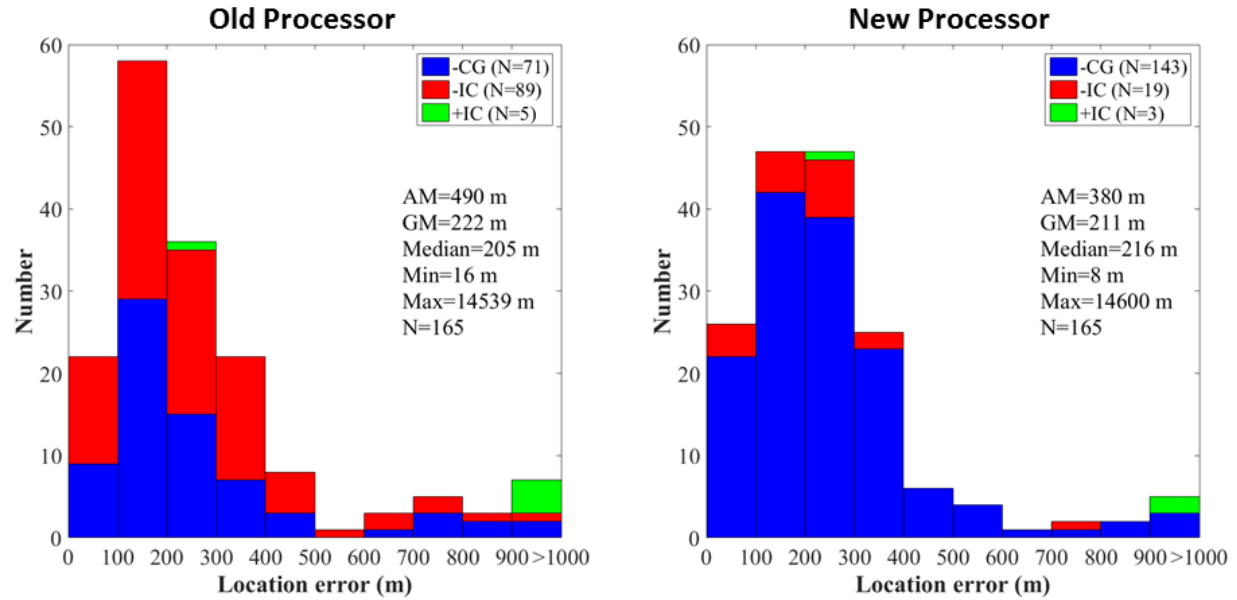


Figure 9-6. Histograms of location error for the old (left panel) and new (right panel) processors.

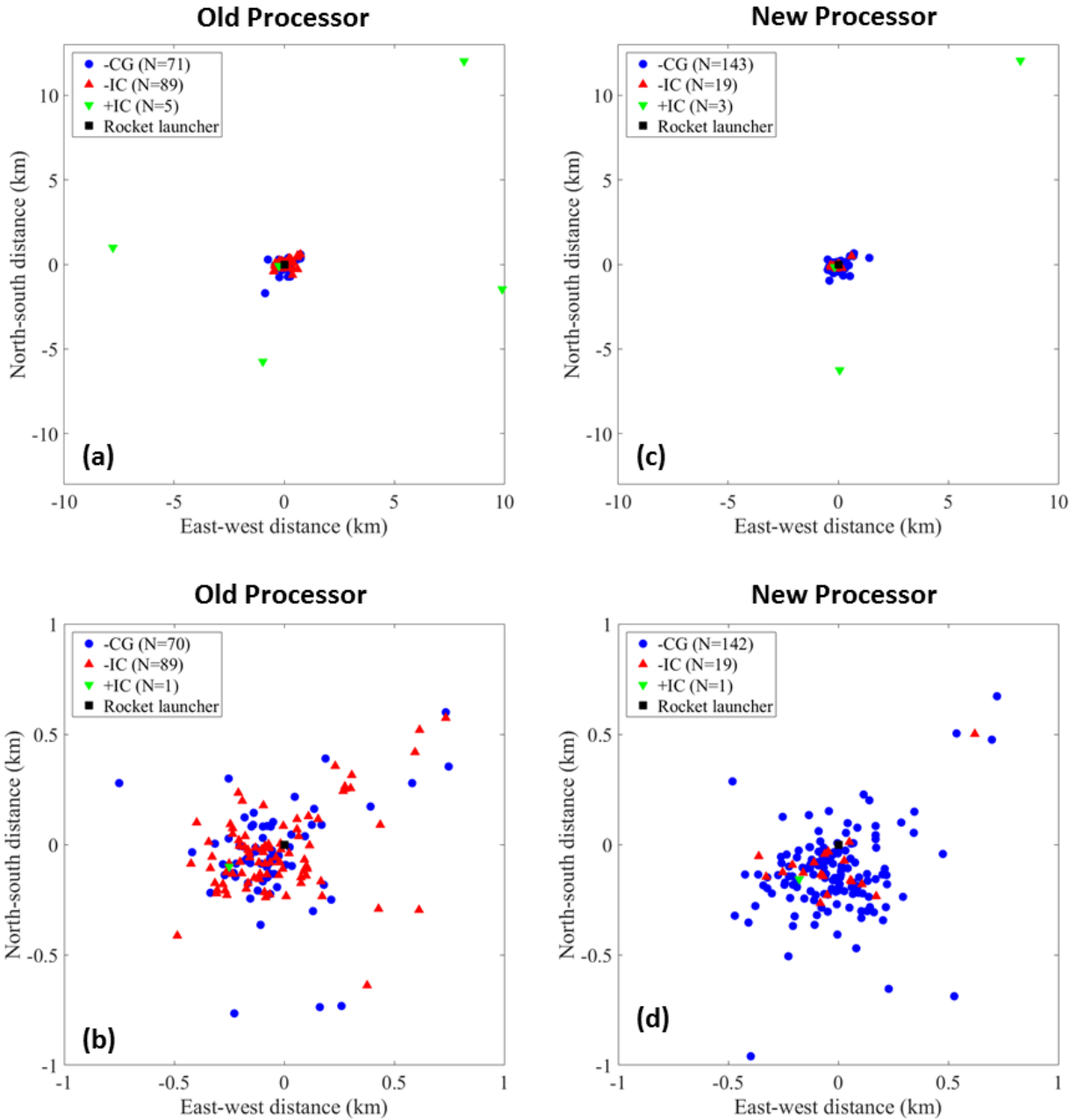


Figure 9-7. Plots of ENTLN-reported locations for old (left panels) and new (right panels) processors. The lower panels are 2 km by 2 km expansions of the upper panels. The ground-truth location (the position of the rocket launcher) is at the origin of coordinates [0,0].

In Table 9-5, the ENTLN performance characteristics evaluated using rocket-triggered lightning data in this study are compared with the results found in *Mallick et al. [2015]*. Note that

a total of four processors are compared in that table. One can see from Table 9-5 that the upgrade in November 2012 significantly decreased the current estimation error, which resulted from calibration of ENTLN peak-current evaluation formula against directly measured currents for rocket-triggered lightning [Mallick *et al.*, 2013]. Further, the upgrade in June 2014 greatly improved the detection efficiency and location accuracy. Finally, the upgrade in August 2015 notably increased the classification accuracy, due to the implementation of new multi-parameter classification algorithm.

Table 9-5. Comparison of ENTLN performance characteristics evaluated for four different processors using rocket-triggered lightning data

Reference	<i>Mallick et al. [2015]</i>		This study	
Processor service time period	2009 to Nov. 2012	Nov. 2012 to June 2014	June 2014 to Aug. 2015	Aug. 2015 to present
Time period of ground-truth data collection	2009-2012	2009-2012	2014-2015	2014-2015
Number of flashes	57	57	36	36
Number of strokes	245	245	175	175
Flash DE	77%	89%	100%	100%
Flash CA	-	-	92%	97%
Stroke DE	49%	67%	97%	97%
Stroke CA	39%	46%	42%	86%
Median location error (m)	631	760	205	215
Median absolute current estimation error	51%	19%	15%	15%

9.4 Summary

The performance characteristics of the ENTLN were evaluated by using as ground-truth natural lightning data recorded at LOG and rocket-triggered lightning recorded at CB in 2014 and 2015. For 219 natural CG lightning flashes containing 608 strokes and for the new

processor, the flash DE, flash CA, stroke DE, and stroke CA were 99%, 97%, 96%, and 91%, respectively, while they were 99%, 91%, 97%, and 68% for the old processor. The stroke DE and stroke CA for first strokes are higher than those for subsequent strokes. For 36 rocket-triggered lightning flashes containing 175 strokes and for the old processor, the flash DE, flash CA, stroke DE, and stroke CA were 100%, 92%, 97%, and 42%, respectively, while their counterparts for the new processor were 100%, 97%, 97%, and 86%. The median values of location error and absolute peak current estimation error were 205 m and 15% for the old processor and 215 m and 15% for the new processor. For both natural and triggered lightning, strokes with higher peak currents (inferred or directly measured, respectively) were more likely to be detected and correctly classified by the ENTLN. Note that the results of the present study correspond to the Florida region and might not be generalized to the entire ENTLN.

CHAPTER 10

SUMMARY OF RESULTS AND RECOMMENDATIONS FOR FUTURE RESEARCH

10.1 Summary of Results

1. Based on the electric field records of 478 negative cloud-to-ground lightning flashes acquired at Lightning Observatory in Gainesville (LOG), Florida, we found that the average number of strokes per flash is 4.6 and the percentage of single-stroke flashes is 12%. The geometric means of interstroke interval, flash duration, and first to subsequent stroke field peak ratio are 52 ms, 223 ms, and 2.4, respectively. It was found that the detectability of preliminary breakdown pulse trains is affected by the signal/noise ratio, distance, type of storm, and return-stroke peak current. The dependences on storm type and peak current were studied for the first time.

2. The study on preliminary breakdown process was extended to 5498 negative high-intensity (≥ 50 kA first-stroke peak currents) cloud-to-ground flashes using an original automated data processing algorithm. For 3077 flashes with detectable PB pulse trains, the arithmetic mean values of PB pulse train duration, PB-RS interval, and PB/RS pulse peak ratio were 2.7 ms, 8.8 ms, and 0.15, respectively. The PB-RS interval was found to decrease with increasing RS peak current (Spearman correlation coefficient was statistically significant and equal to -0.80). The range-normalized PB pulse peak exhibited statistically significant positive correlation with the RS peak current, with the Spearman correlation coefficient being 0.48. Thus, it appears that the high-intensity negative lightning is characterized by shorter (and, by inference, faster) stepped leaders and more pronounced PB pulse trains.

3. Using simultaneous high-speed video camera records and electric field measurements, we examined a bipolar flash that started with a negative stroke with a peak current of -101 kA, which was followed by a positive stroke with a peak current of 16 kA. From the leader electric

field waveforms, the positive charge source is inferred to be located considerably farther from both the observer and the channel to ground than the negative charge source. The second (positive) stroke was followed by a bipolar continuing current. The average luminosity of the main channel during the positive CC was 3.7 times higher than that during the negative CC, which is likely indicative of about 3.7 times higher current of the positive CC. It is likely that upward negative leaders are more heavily branched inside the cloud than the upward positive ones, which makes the upward negative leaders more efficient in collecting the cloud charges and funneling them to the channel to ground. The first two strokes (including the continuing current) followed the same channel to ground, whose imaged 2D length was 4.2 km, except for the bottom 115 m, where the paths of the two strokes were slightly different. As of this writing, there is only one previously documented case of positive leader following the path of preceding negative stroke. We presented the first leader speed versus height profiles for such an unusual sequence. The average leader speeds for the first (negative) and second (positive) strokes were 4.7×10^5 m/s and 7.2×10^5 m/s, respectively. The speed of the positive leader traversing the previous-stroke channel after not-unduly-long (70 ms) interstroke interval is lower than typical speeds of negative leaders following previously formed channels. The speeds of both the negative leader and the positive leader increased as they approached the ground.

4. Simultaneous electric field and high-speed video camera records of two flashes, terminating on a 257-m tower were obtained at LOG. One of the flashes was an upward negative flash whose upward positive leader initiated from the 257-m tower, located 8.8 km from LOG. It contained six leader/return-stroke sequences, all of which developed along the upward leader path and terminated on the 257-m tower. The other flash was a three-stroke downward bipolar flash whose first stroke was positive and terminated on a 60-m tower. The two subsequent

strokes were negative and terminated on the same 257-m tower as the six strokes of the first flash. All strokes terminated on the 257-m tower exhibited very similar and unusually narrow bipolar electric field waveforms with damped oscillatory tails. Characteristics of those electric field waveforms are examined and compared to similar observations found in the literature.

5. By using the an engineering model developed by *Baba and Rakov* [2005], the electric field waveform produced at LOG by 7 of the 8 strokes (for one stroke the electric field signature was saturated) terminated on the 257-m tower was computed using a narrow pulse followed by a steady current tail as the channel-base current. Also, the effects of each model parameter (current waveform, return-stroke speed, and return-stroke model) on the electric field waveform were investigated.

6. The NLDN detection efficiency and classification accuracy for cloud discharge activity (IC events) and natural CG strokes in Florida were estimated (for the first time) by using the electric field and optical data acquired at LOG. For 153 ground truth IC events, the DE and CA were 33% (50/153) and 86% (43/50), respectively. The average number of NLDN-reported cloud pulses per detected IC event was 2.1. Compared to IC events associated with CG flashes, isolated IC events (complete IC flashes) were found to have higher DE (73%), CA (95%), and average number of NLDN-reported cloud pulses (2.9). For 366 CG strokes, the DE and CA were both 92%. Both DE and CA for positive CGs were higher than those of negative CGs, and DE and CA for first strokes were higher than those for subsequent strokes. The DE for negative subsequent strokes was 90% (GM peak current=17 kA), which is appreciably higher than the 75% estimated based on the rocket-and-wire-triggered lightning data (GM peak current=12 kA). The CA for negative subsequent strokes in our study was 90%, which is somewhat lower than the 96% estimated using the triggered lightning data.

7. The performance characteristics of the ENTLN were evaluated by using as ground-truth natural lightning data (for the first time) recorded at LOG and rocket-triggered lightning recorded at CB in 2014 and 2015. For 219 natural CG lightning flashes containing 608 strokes and for the new processor, the flash DE, flash CA, stroke DE, and stroke CA were 99%, 97%, 96%, and 91%, respectively, while they were 99%, 91%, 97%, and 68% for the old processor. The stroke DE and stroke CA for first strokes are higher than those for subsequent strokes. For 36 rocket-triggered lightning flashes containing 175 strokes and for the old processor, the flash DE, flash CA, stroke DE, and stroke CA were 100%, 92%, 97%, and 42%, respectively, while their counterparts for the new processor were 100%, 97%, 97%, and 86%. The median values of location error and absolute peak current estimation error were 205 m and 15% for the old processor and 215 m and 15% for the new processor. For both natural and triggered lightning, strokes with higher peak currents (inferred or directly measured, respectively) were more likely to be detected and correctly classified by the ENTLN.

10.2 Recommendations for Future Research

1. Use of LMA and high-speed video cameras at CB to study the fast stepped-leader events and the charge structure of the parent thunderstorm.
2. Characterization of two-station (LOG and GC) electric field waveforms of different types of natural lightning (-CG, +CG) with a view toward testing return-stroke models.
3. Further analysis of the bidirectional leader development in the two tower flashes terminated on the 257-m tower and look for additional data (high-speed video, current, and field records) on lightning striking towers to improve our understanding of the lightning interaction with tall objects.
4. Modeling of narrow electric field waveforms associated with lightning strikes to different towers for which measured currents are available. Consider different rates of current attenuation

along the lightning channel, possible reflection at the channel top, and no-vertical channel geometry.

5. Comparison of wideband electric field waveforms produced by return strokes in natural and rocket-triggered lightning, which has important implications for evaluating the performance characteristics of lightning locating systems.

APPENDIX A
TWO-STATION MEASUREMENTS OF ROCKET-TRIGGERED LIGHTNING ELECTRIC
FIELD WAVEFORMS (2013-2016)

Electric field waveforms produced by rocket-triggered lightning at Camp Blanding in 2013-2016 and measured at two stations (LOG-GC) are shown in this appendix. Two-station field measurements are available for a total of 29 flashes containing 153 strokes. All strokes were negative. Flash ID and number of return strokes are listed in Table A-1. For each stroke, the complete field record of the flash is shown first, and followed by expansions on 1-ms and 200- μ s time scales for each stroke. For all rocket-triggered lightning flashes, the distances to GC and LOG are 3 km and 45 km, respectively. The LOG electric fields produced by return strokes in rocket-triggered seem to have a faster decay after the peak and shorter zero-crossing time compared with those for negative strokes in natural lightning, also recorded at LOG (see Appendix B), which is consistent with the findings reported by *Mallick and Rakov [2014]*.

Table A-1. Inventory of two-station (LOG-GC) field measurements for rocket-triggered lightning flashes from 2013 to 2016

Flash ID	Number of Return Strokes
UF 13-31	11
UF 13-33	6
UF 13-34	4
UF 14-01	1
UF 14-05	5
UF 14-06	2
UF 14-07	3
UF 14-08	4
UF 14-11	8

Table A-1. Continued

Flash ID	Number of Return Strokes
UF 14-12	7
UF 14-35	4
UF 14-36	2
UF 14-43	7
UF 14-51	8
UF 14-52	5
UF 14-53	5
UF 15-11	2
UF 15-12	5
UF 15-15	8
UF 15-20	2
UF 15-25	4
UF 15-26	8
UF 15-38	5
UF 15-39	6
UF 15-41	5
UF 15-42	6
UF 15-43	5
UF 16-04	1
Total Number of Flashes: 29	Total Number of Strokes: 153

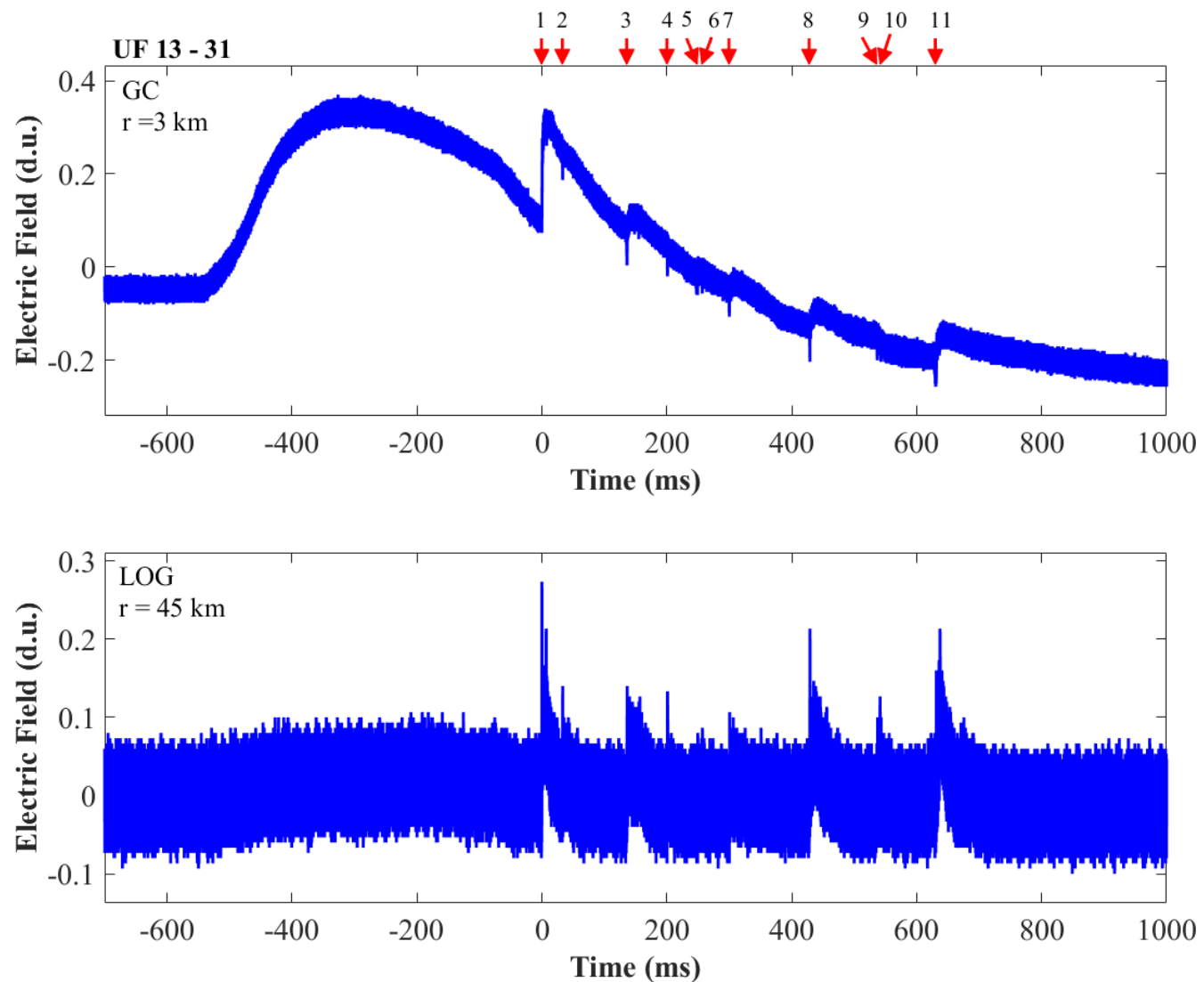


Figure A-1. Two-station electric field waveforms of flash UF 13-31.

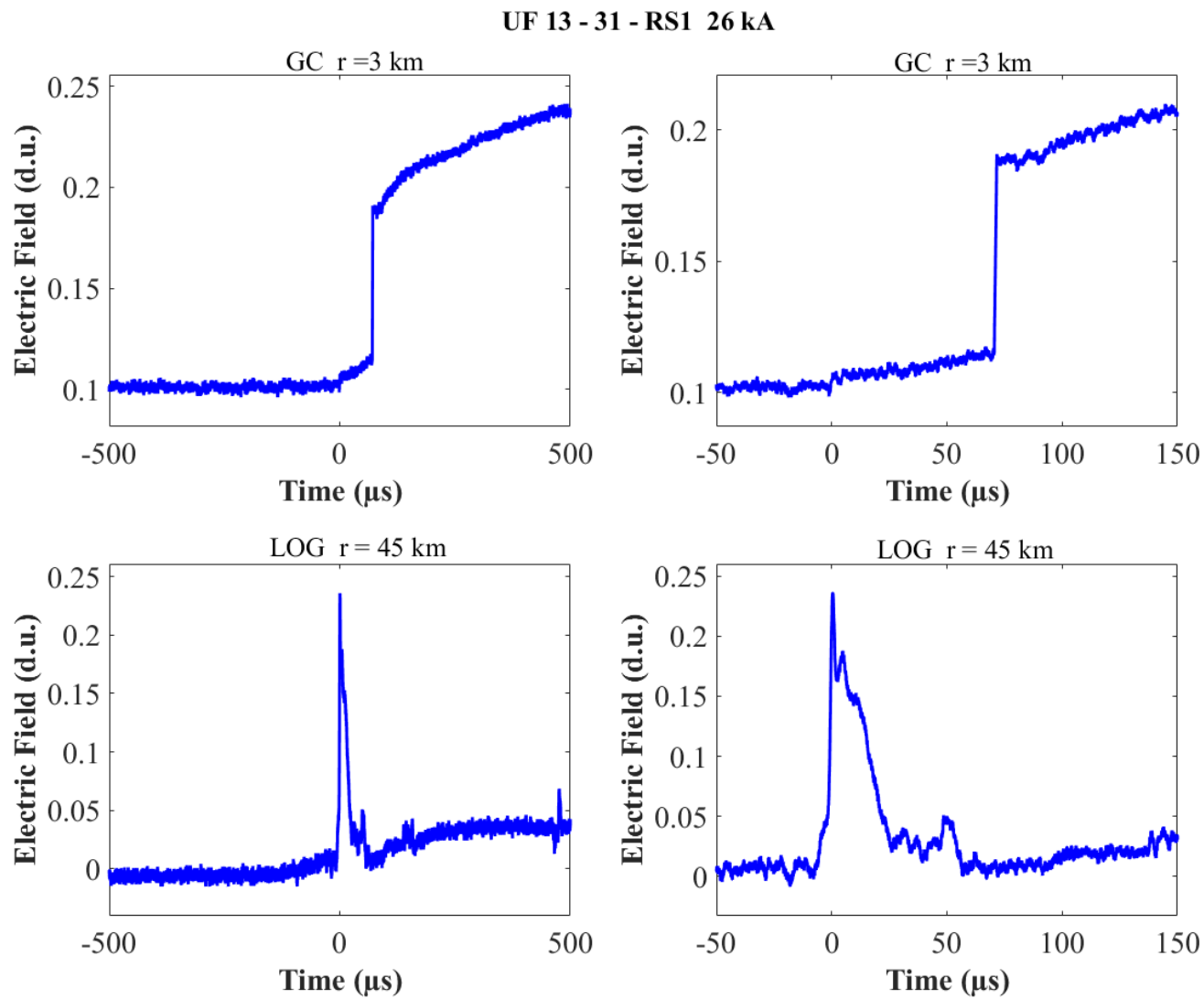


Figure A-2. Two-station electric field waveforms of the RS1 of flash UF 13-31. The timing offset between GC and LOG records is an artifact caused by electronics.

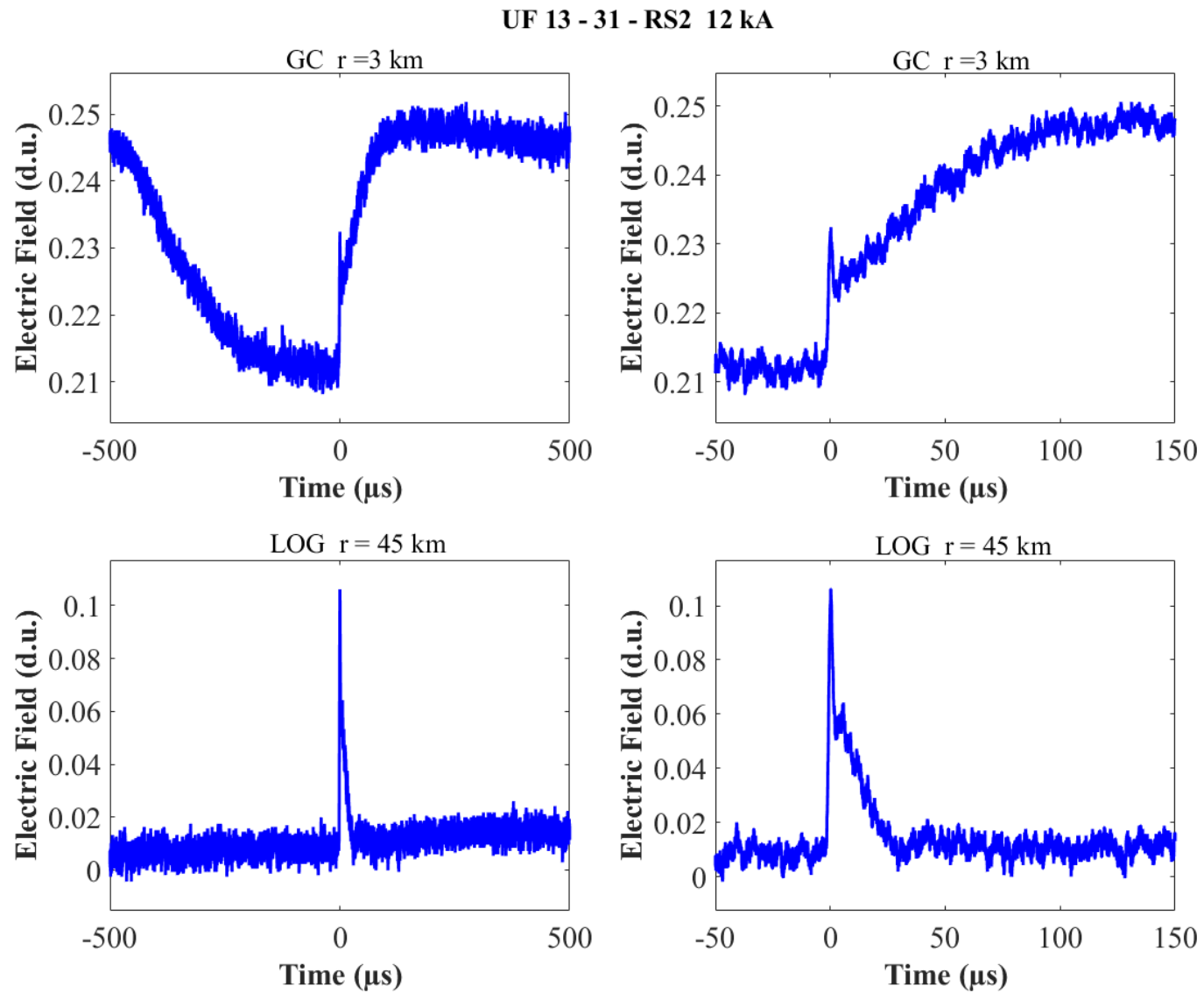


Figure A-3. Two-station electric field waveforms of the RS2 of flash UF 13-31.

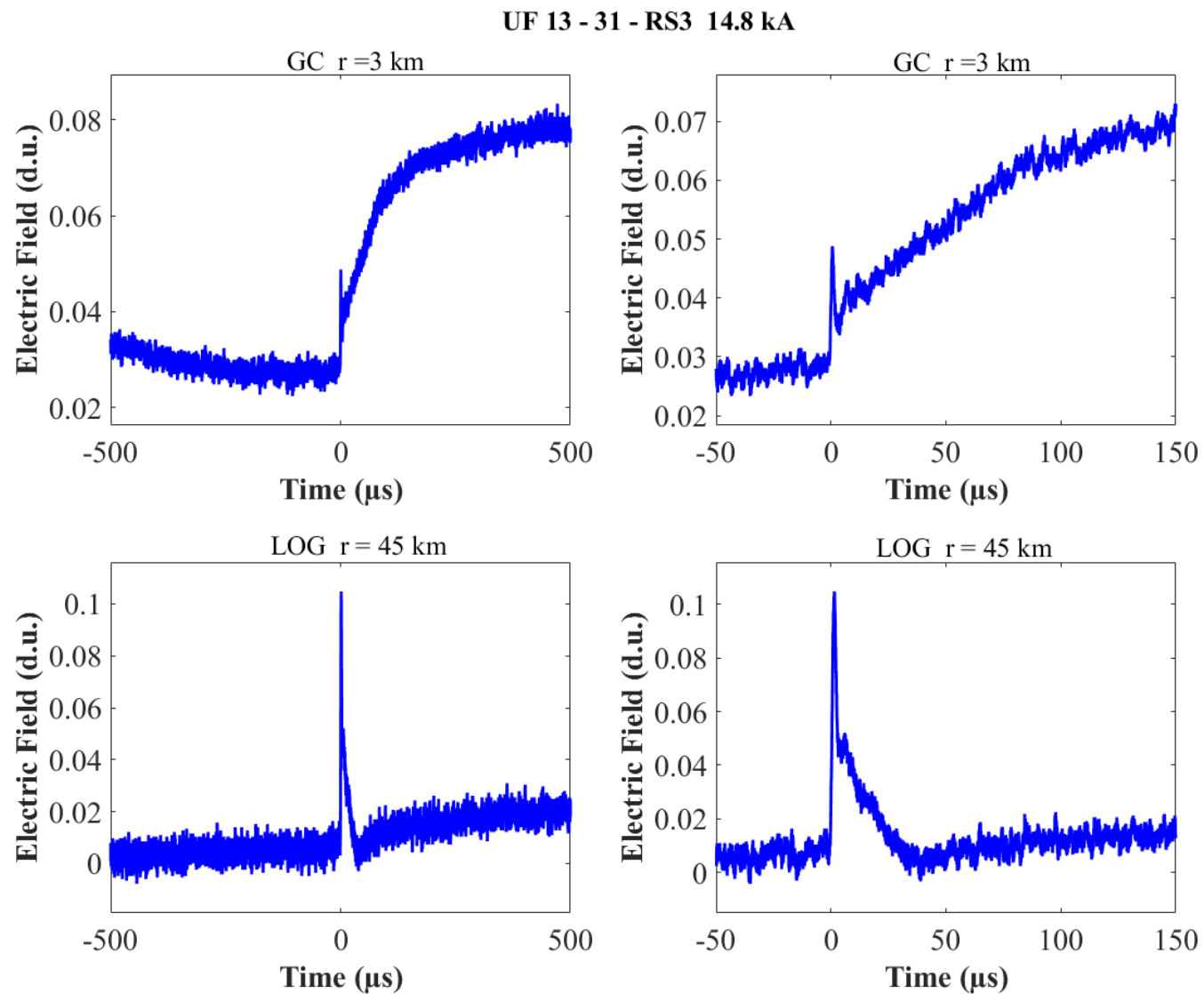


Figure A-4. Two-station electric field waveforms of the RS3 of flash UF 13-31.

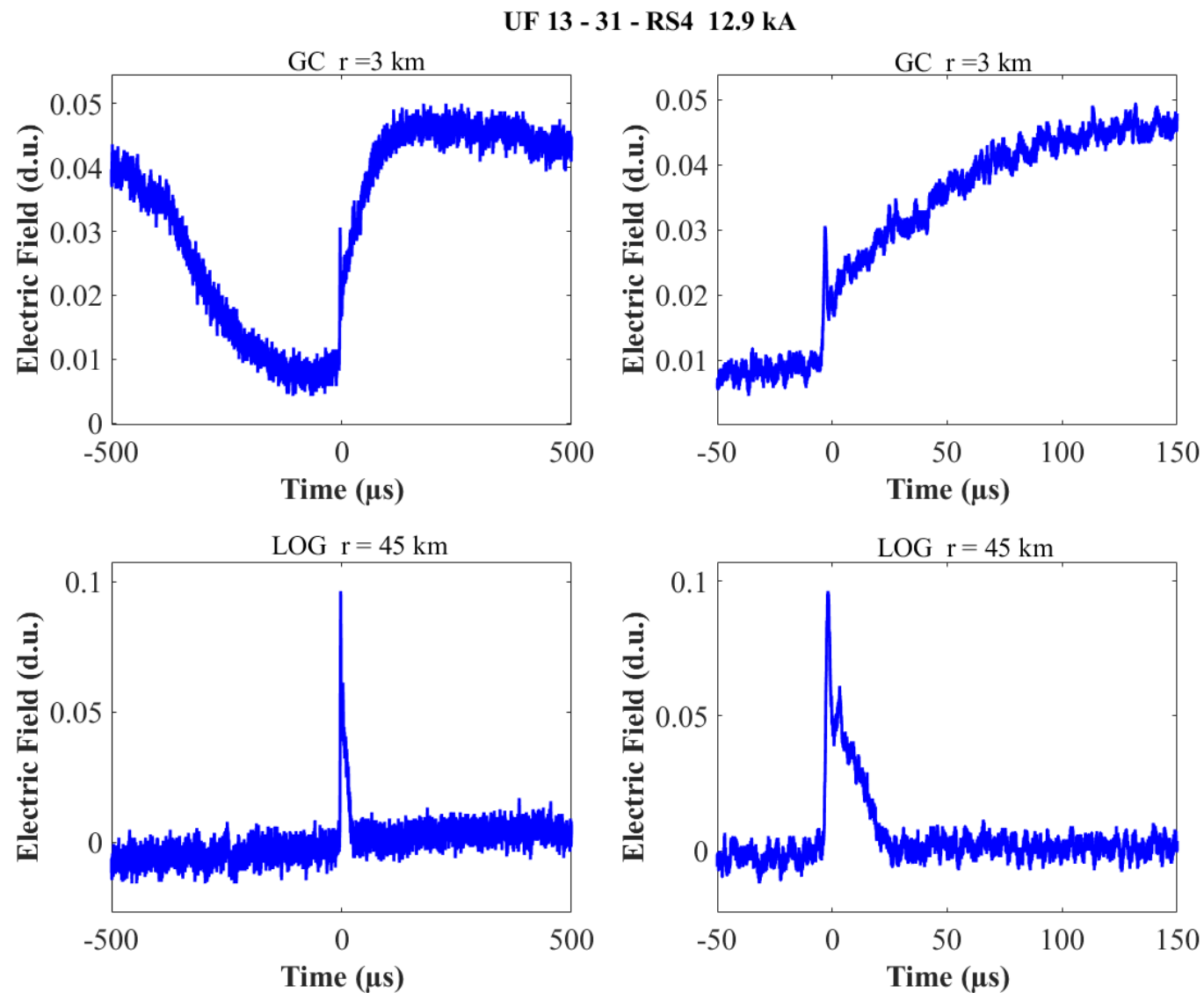


Figure A-5. Two-station electric field waveforms of the RS4 of flash UF 13-31.

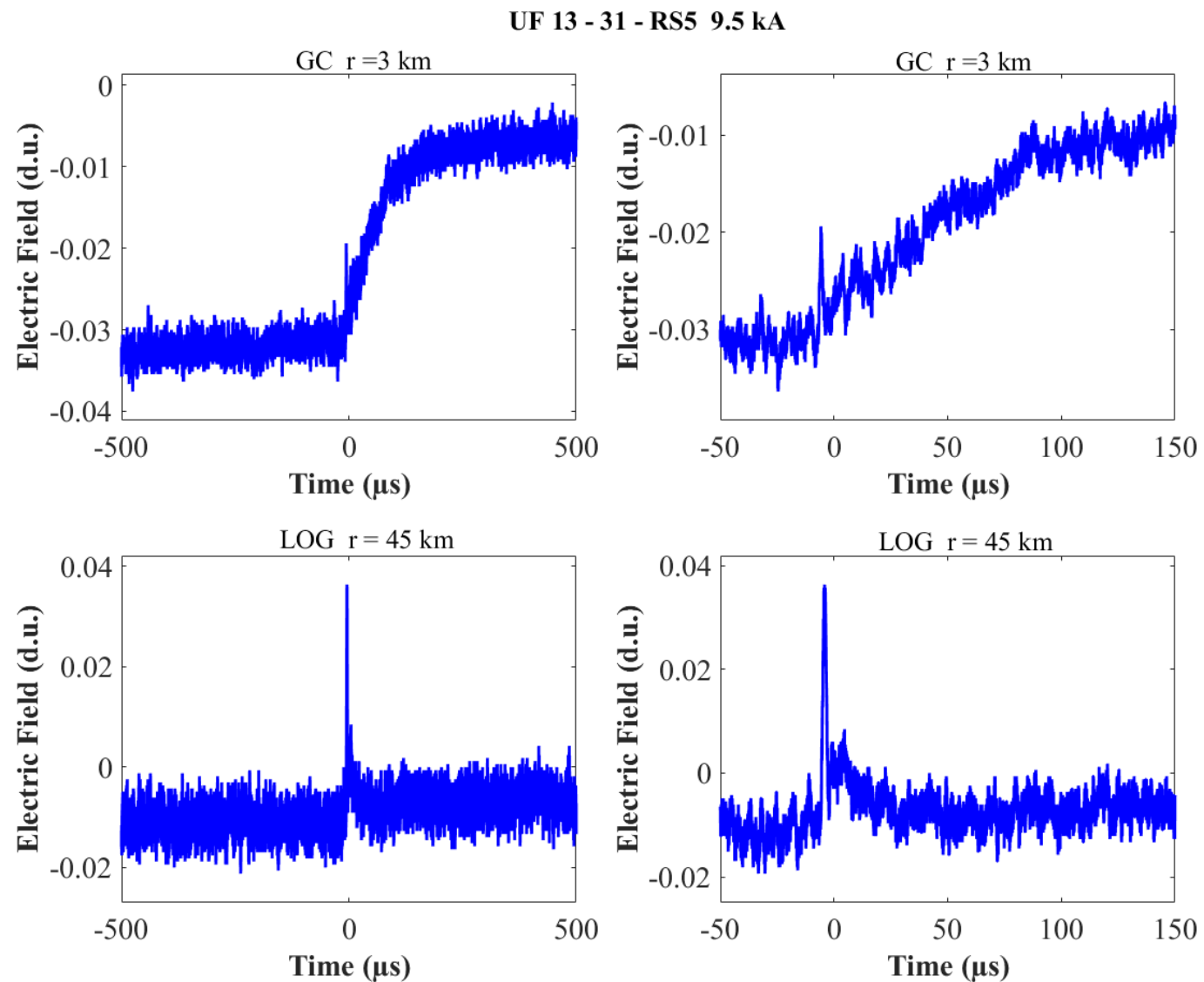


Figure A-6. Two-station electric field waveforms of the RS5 of flash UF 13-31.

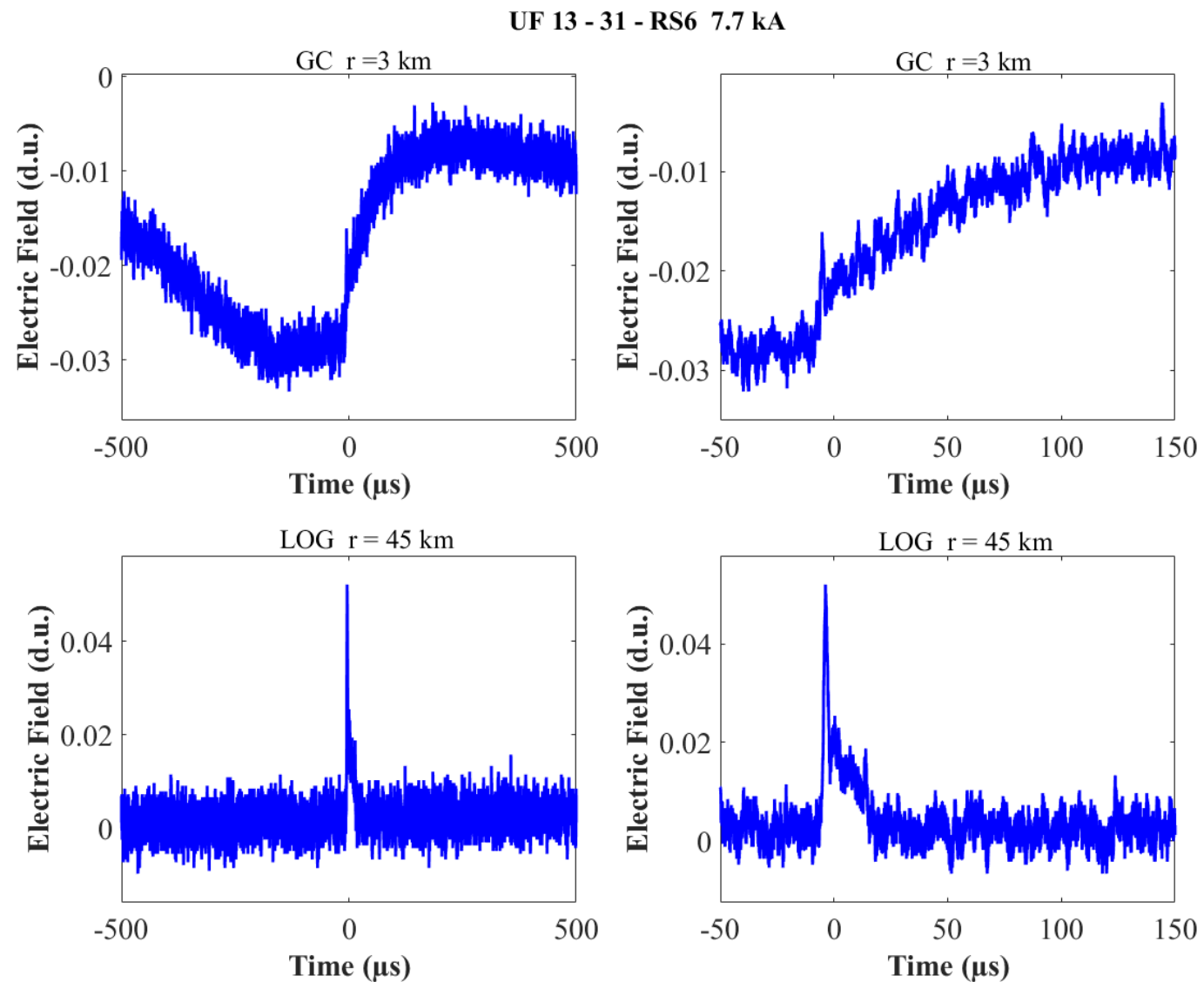


Figure A-7. Two-station electric field waveforms of the RS6 of flash UF 13-31.

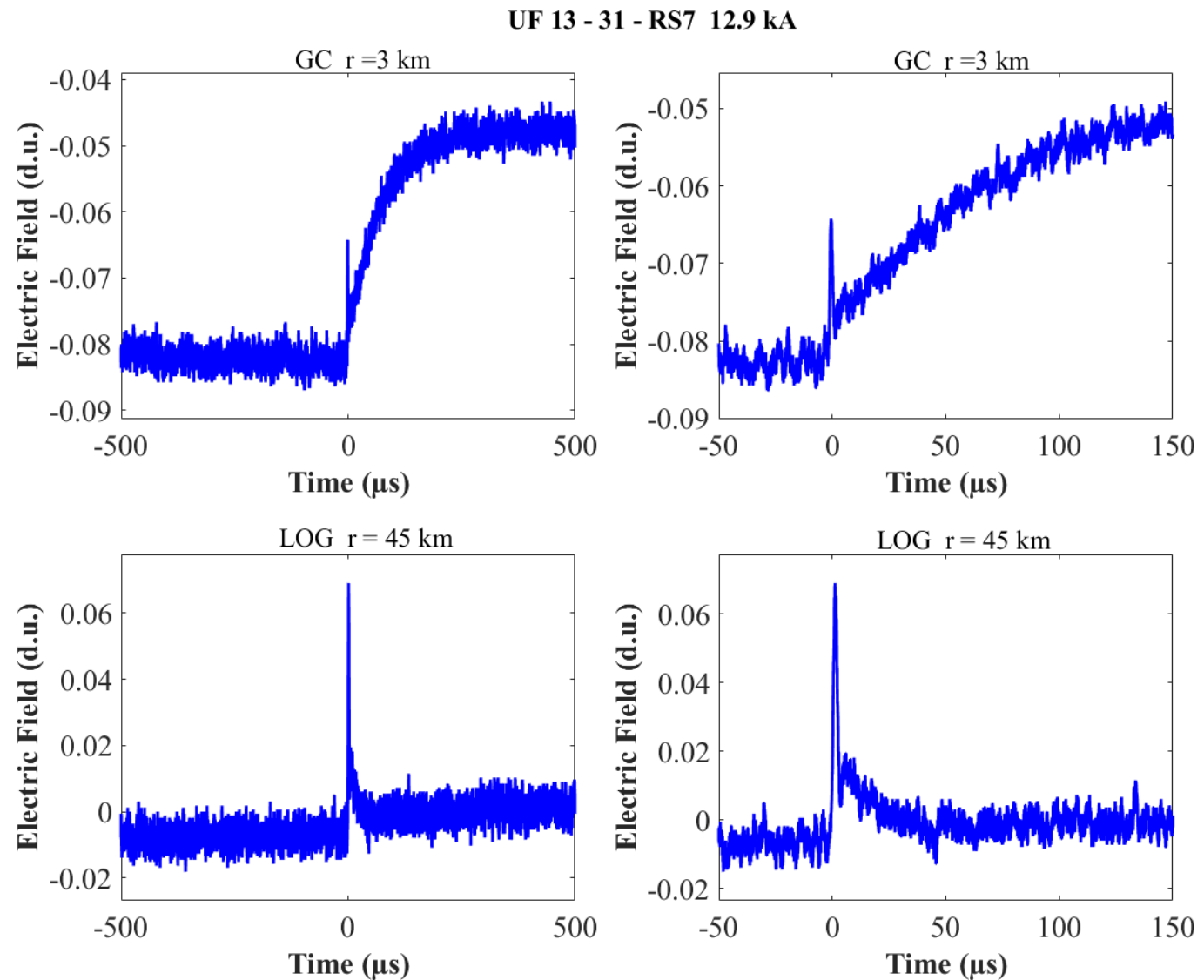


Figure A-8. Two-station electric field waveforms of the RS7 of flash UF 13-31.

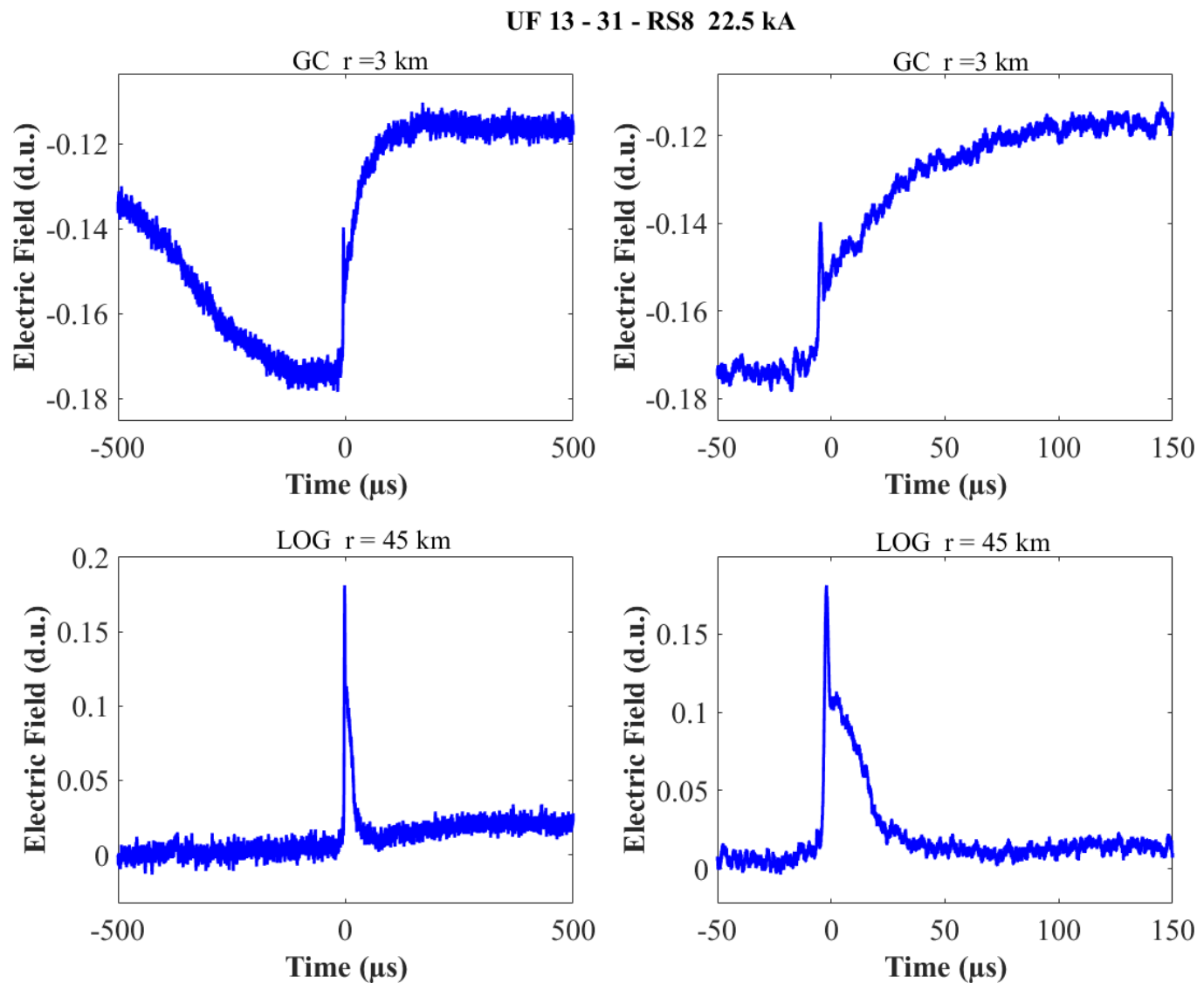


Figure A-9. Two-station electric field waveforms of the RS8 of flash UF 13-31.

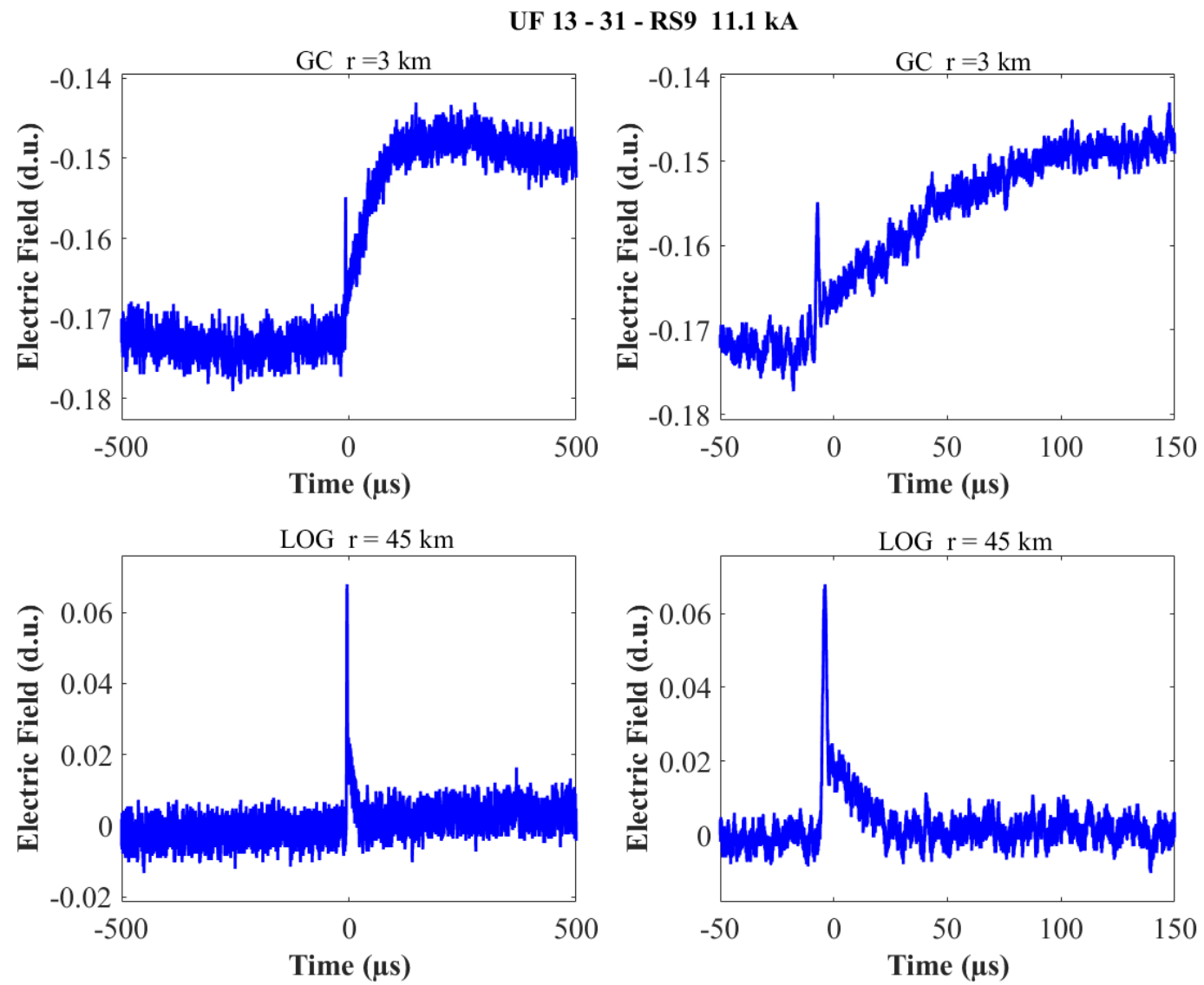


Figure A-10. Two-station electric field waveforms of the RS9 of flash UF 13-31.

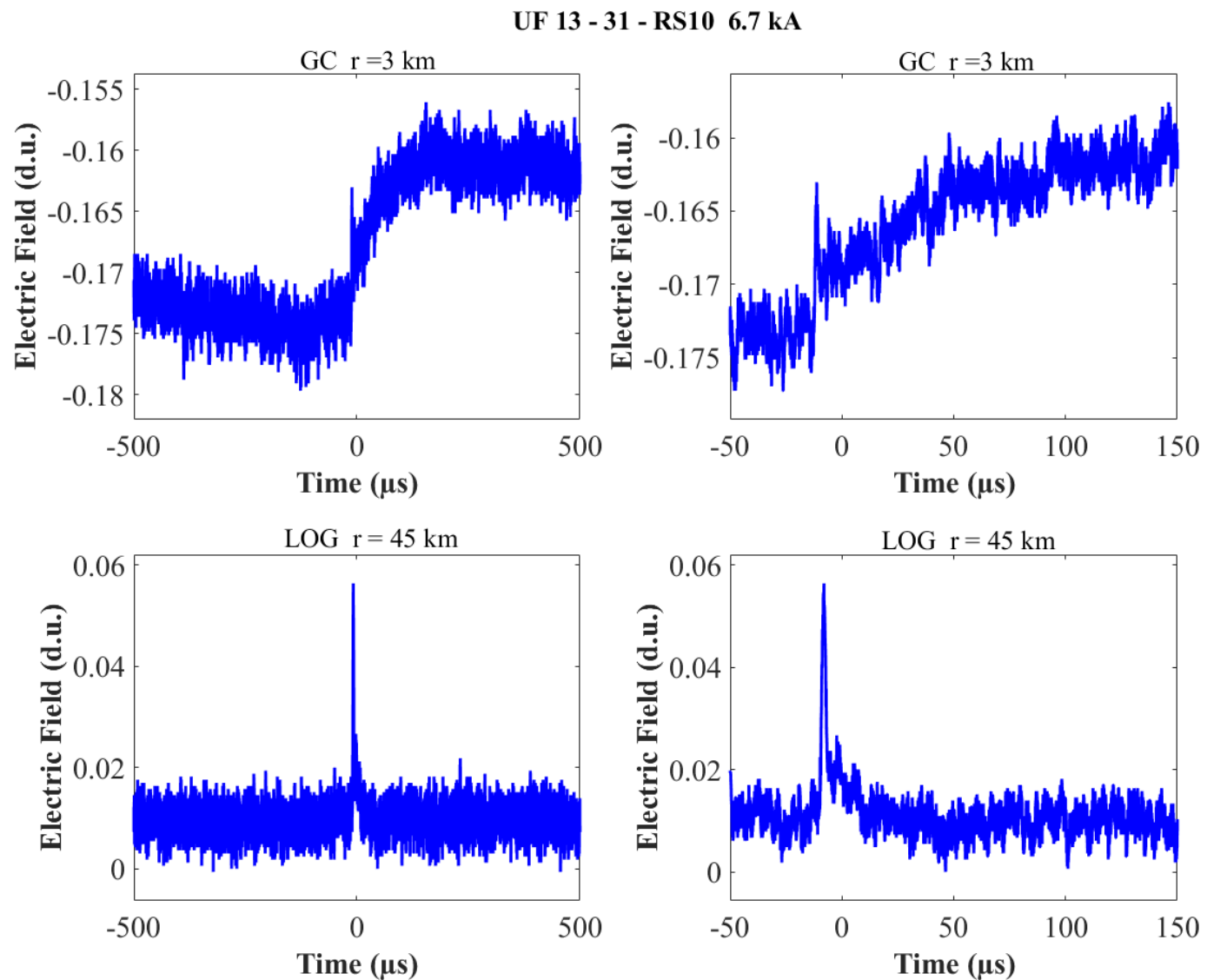


Figure A-11. Two-station electric field waveforms of the RS10 of flash UF 13-31.

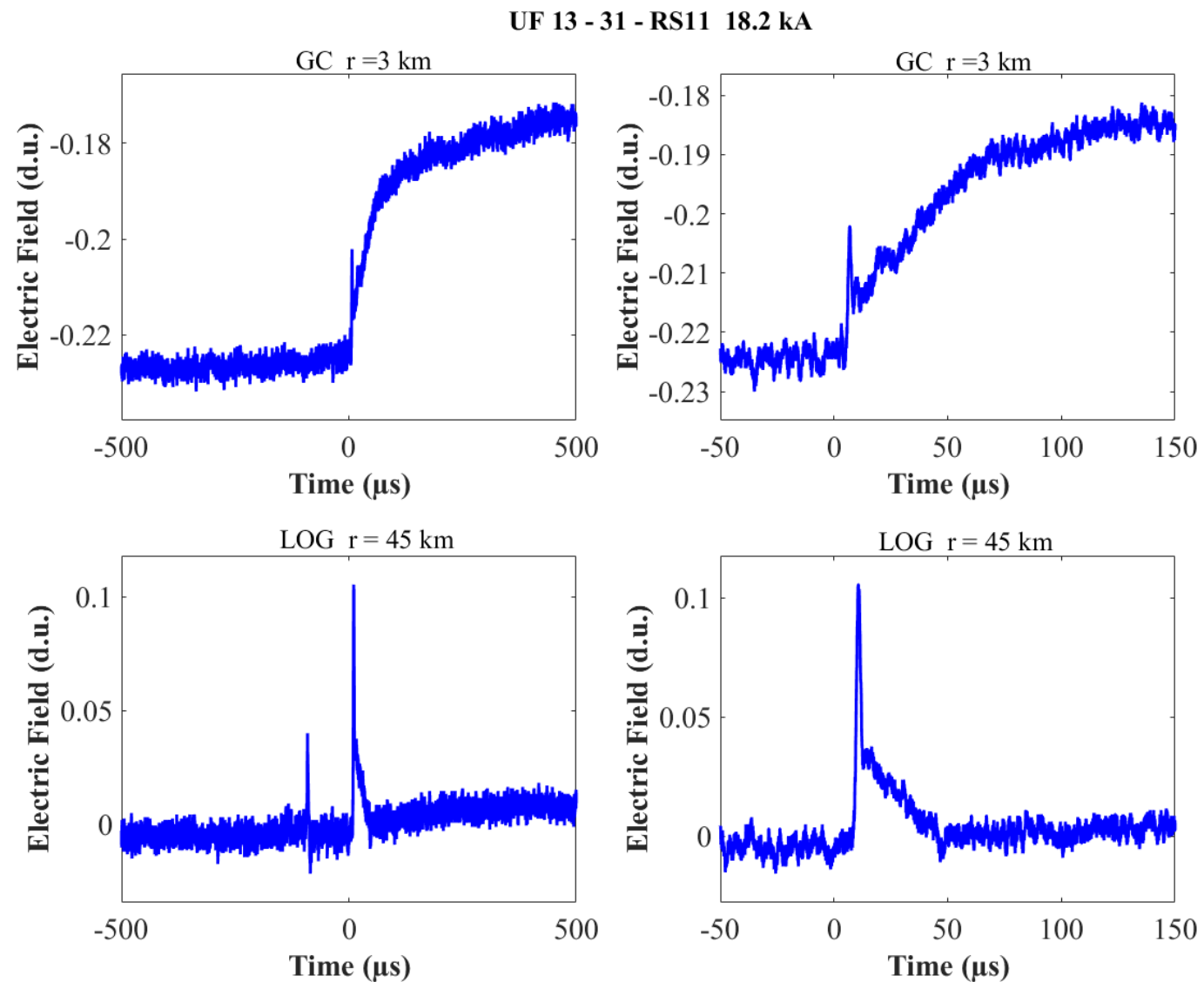


Figure A-12. Two-station electric field waveforms of the RS11 of flash UF 13-31.

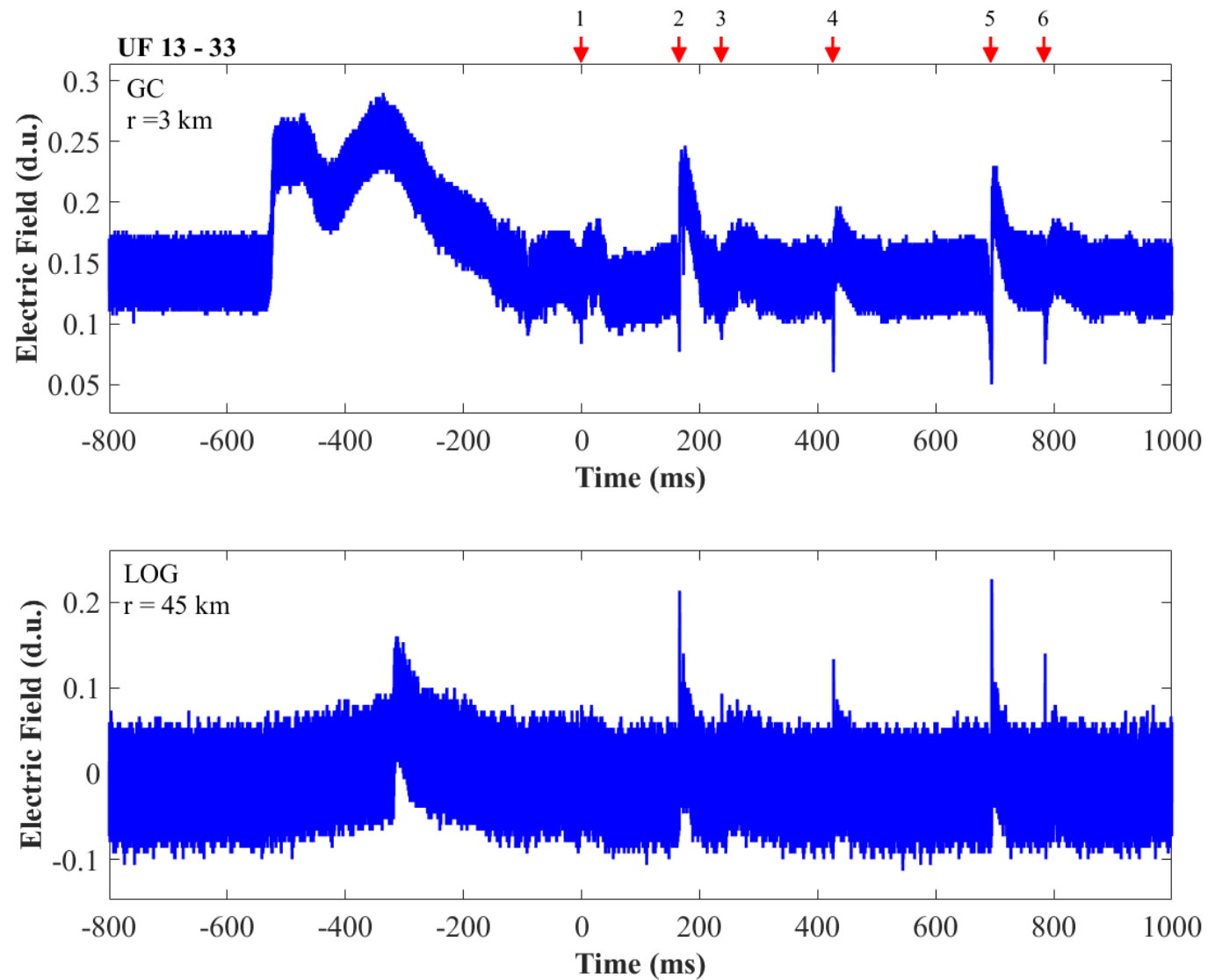


Figure A-13. Two-station electric field waveforms of flash UF 13-33.

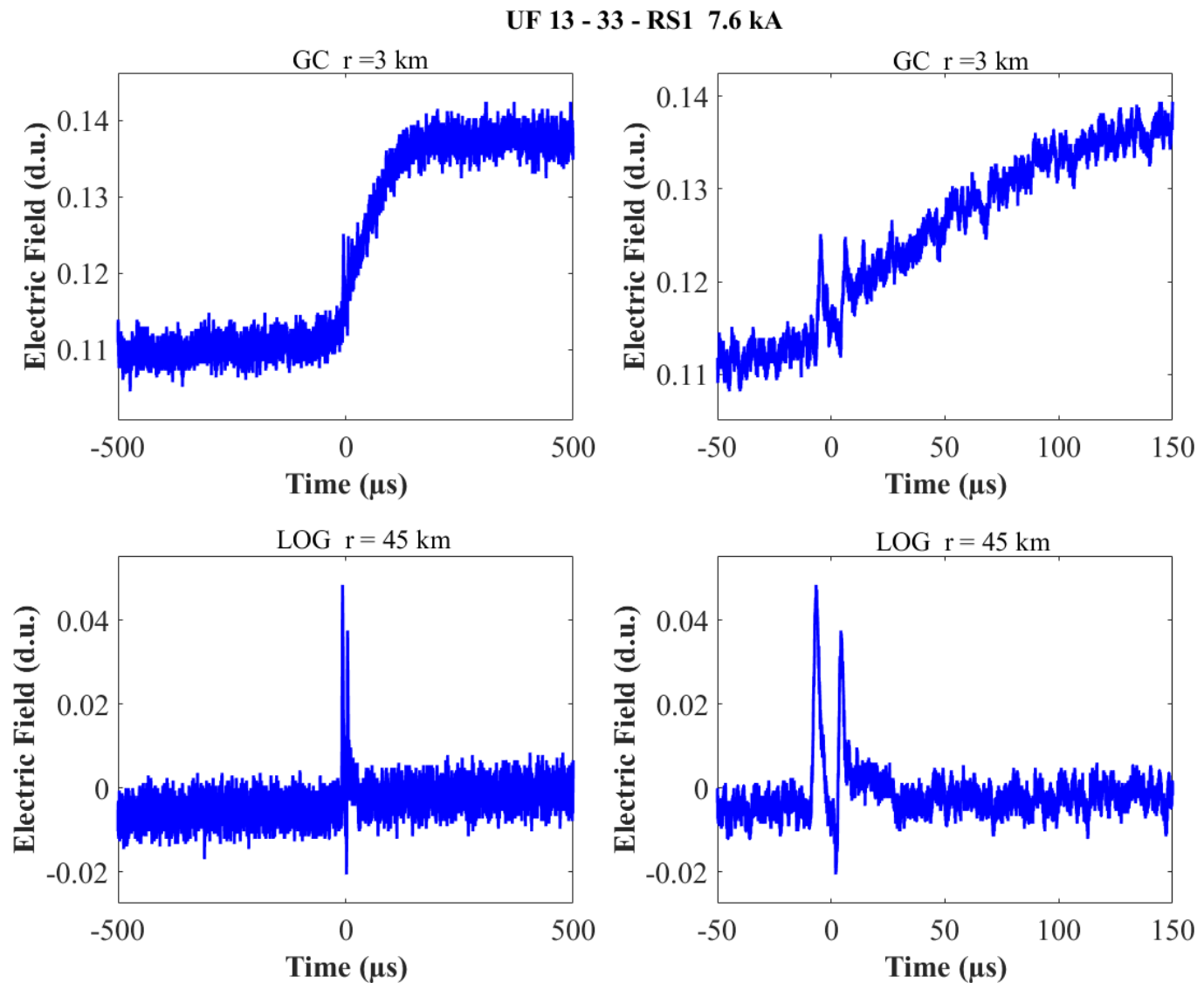


Figure A-14. Two-station electric field waveforms of the RS1 of flash UF 13-33.

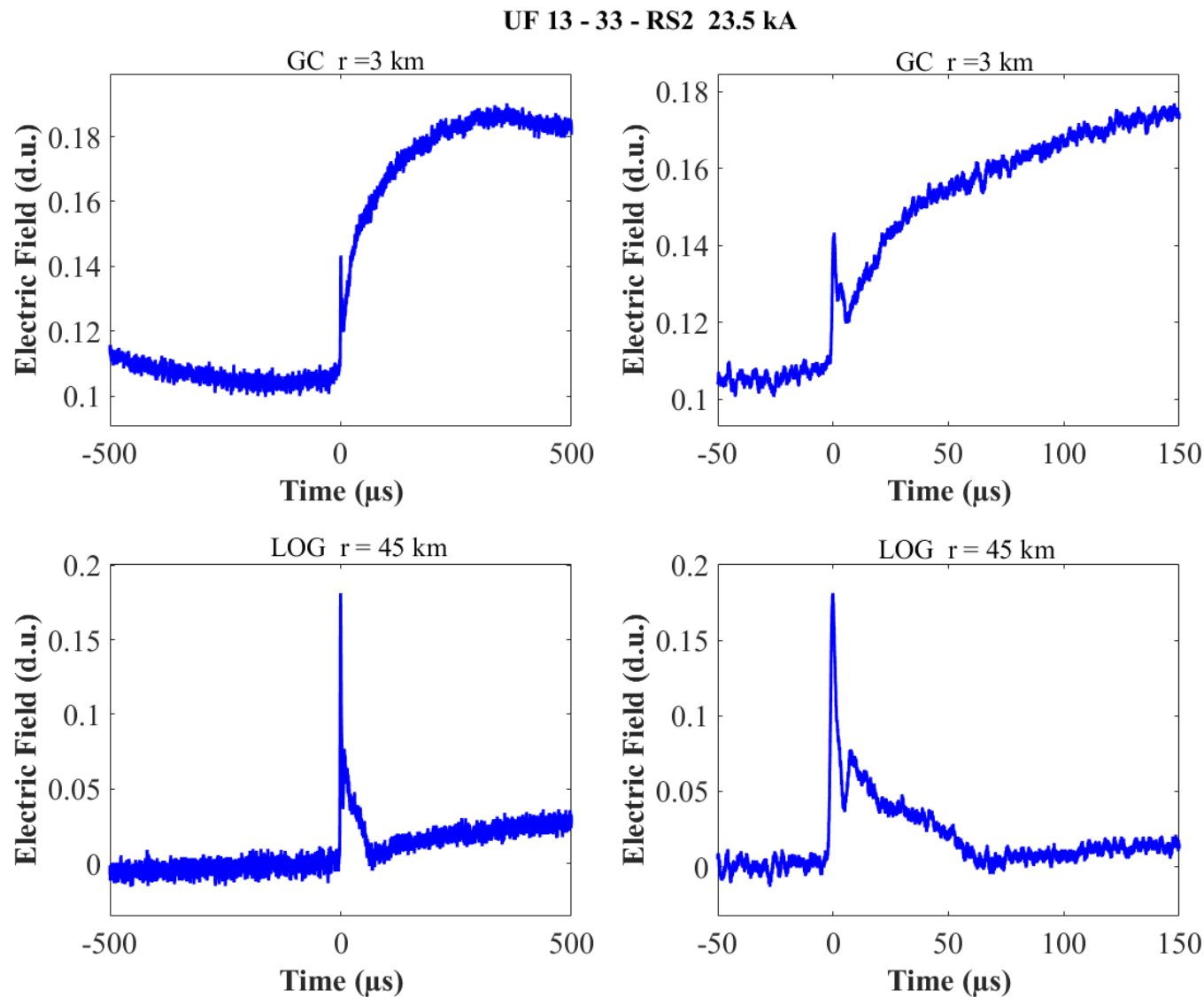


Figure A-15. Two-station electric field waveforms of the RS2 of flash UF 13-33.

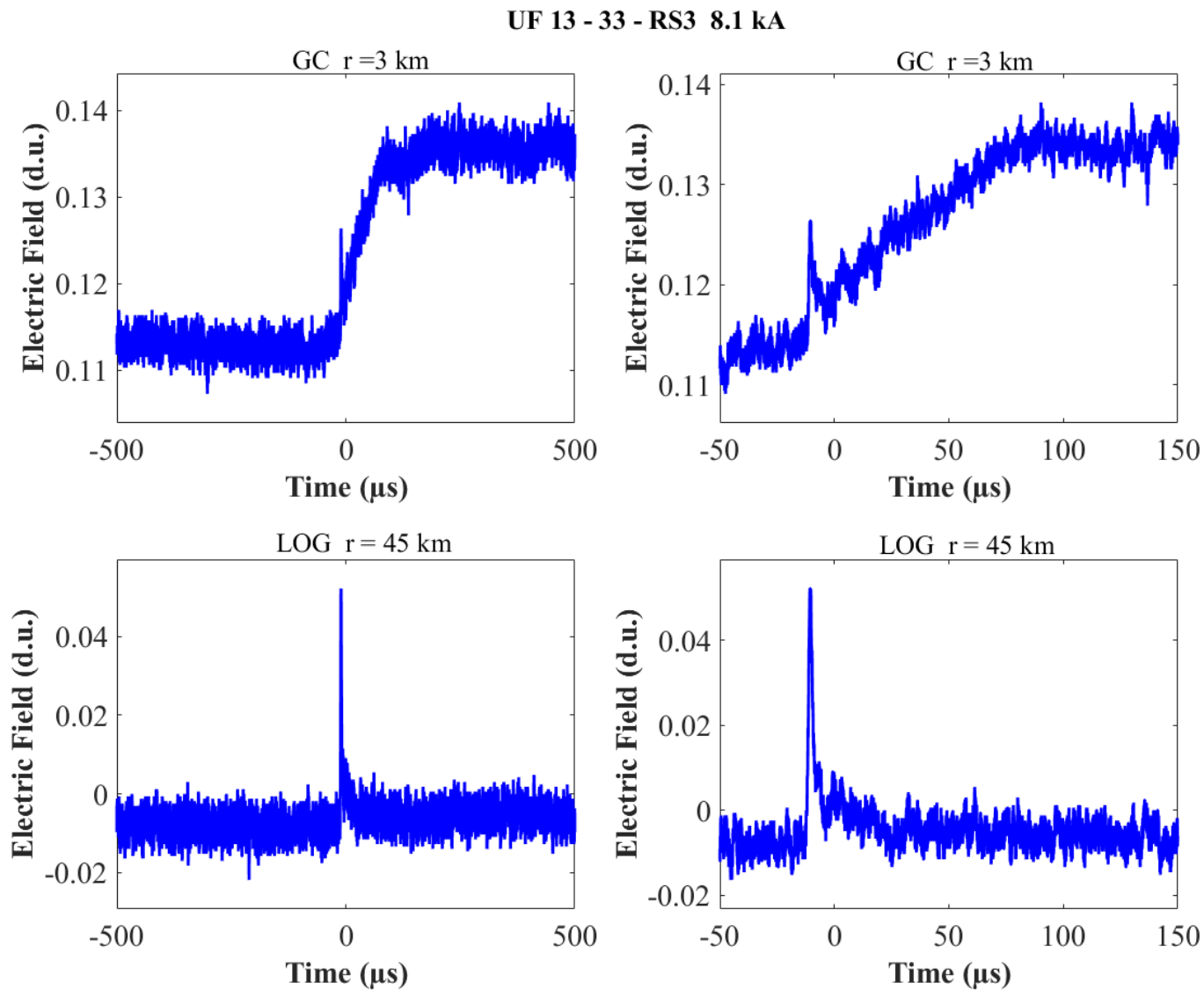


Figure A-16. Two-station electric field waveforms of the RS3 of flash UF 13-33.

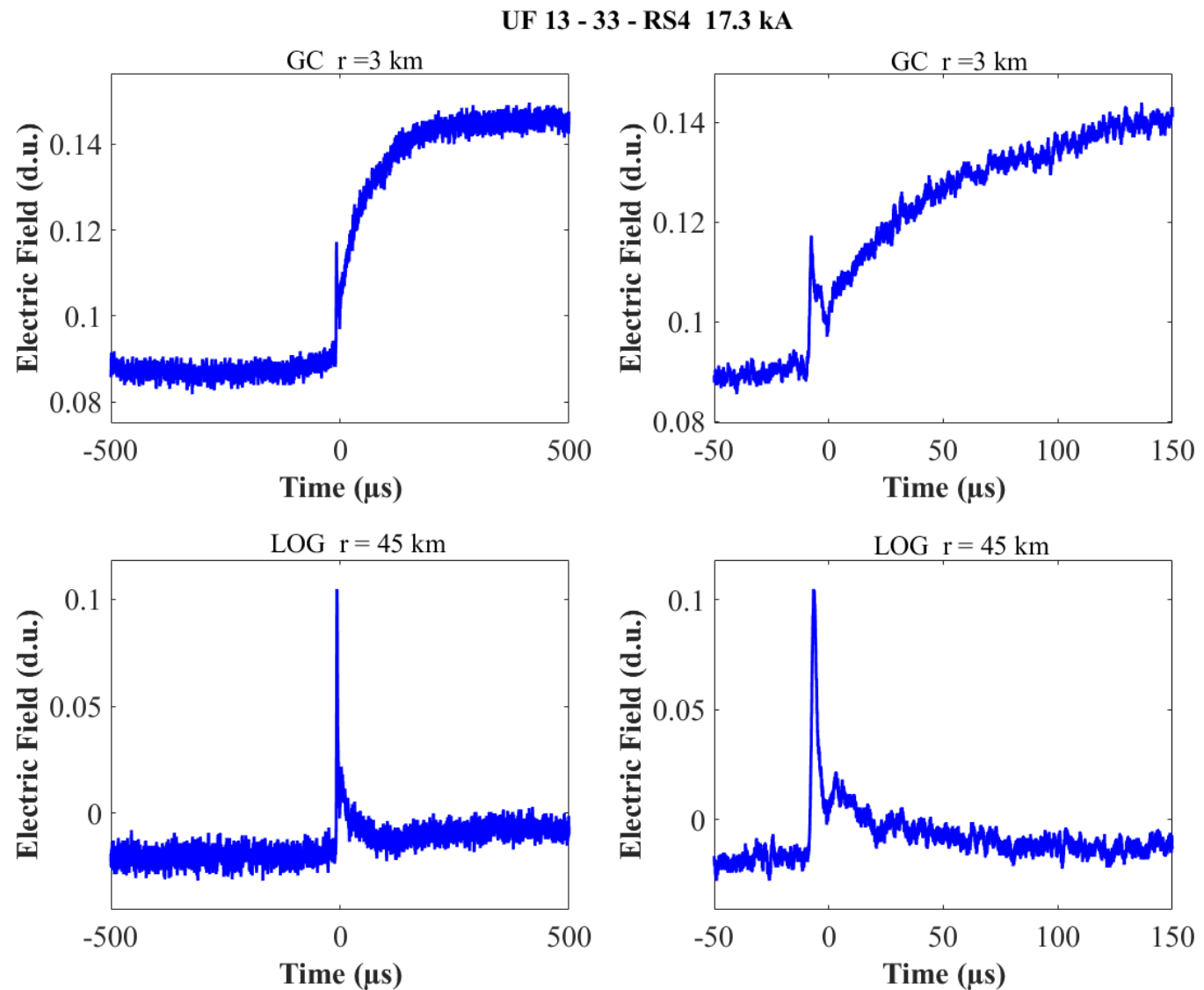


Figure A-17. Two-station electric field waveforms of the RS4 of flash UF 13-33.

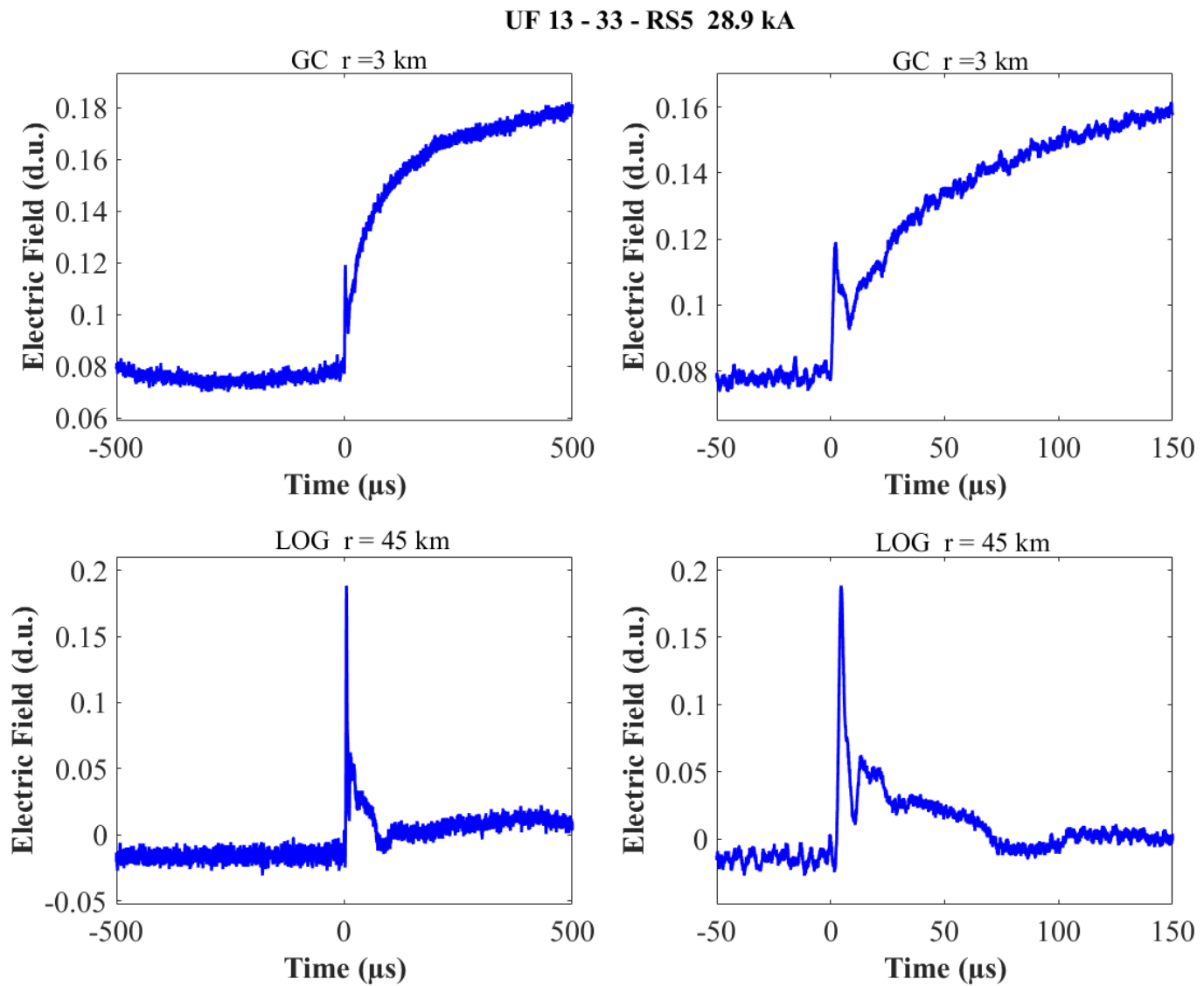


Figure A-18. Two-station electric field waveforms of the RS5 of flash UF 13-33.

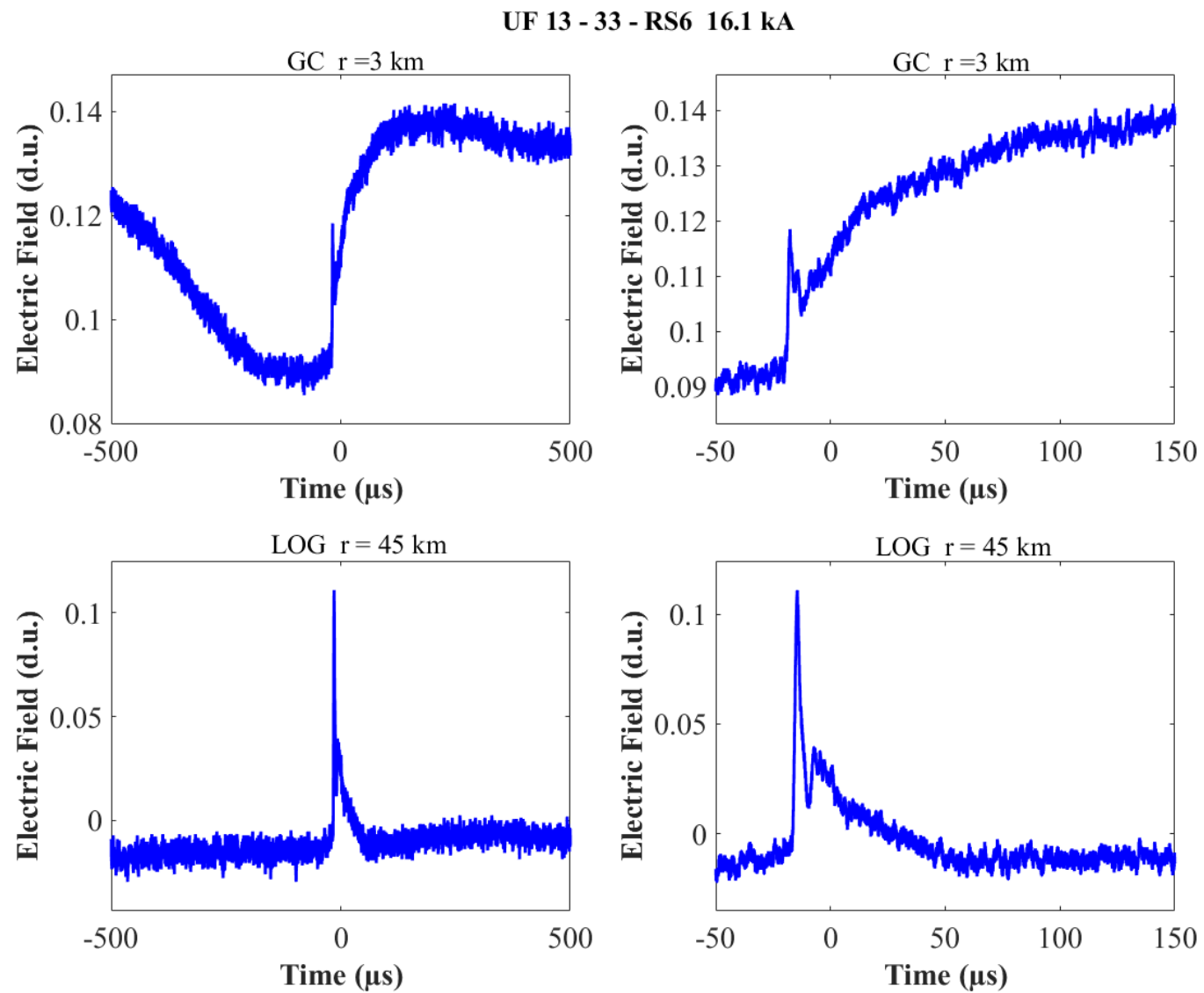


Figure A-19. Two-station electric field waveforms of the RS6 of flash UF 13-33.

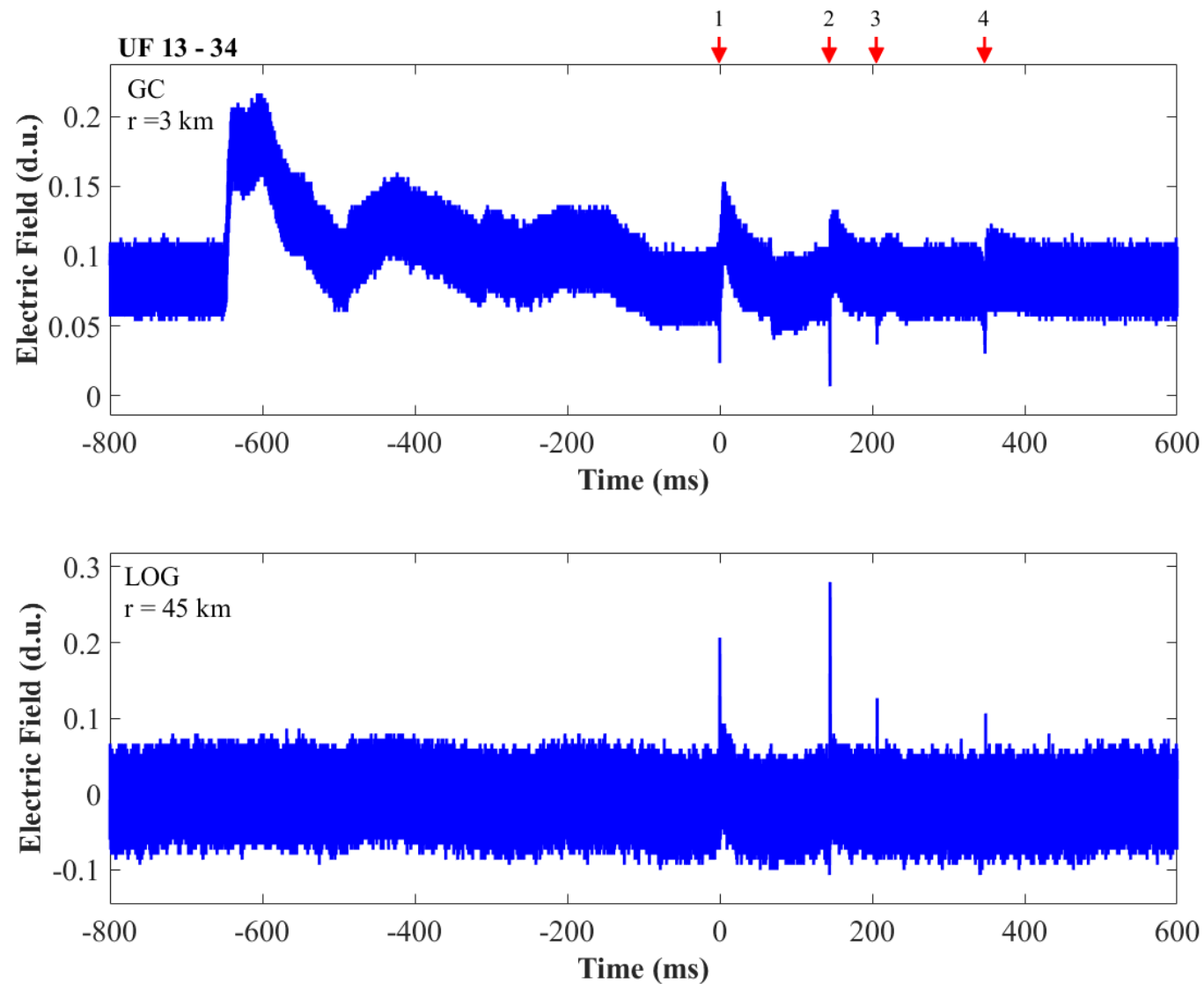


Figure A-20. Two-station electric field waveforms of flash UF 13-34.

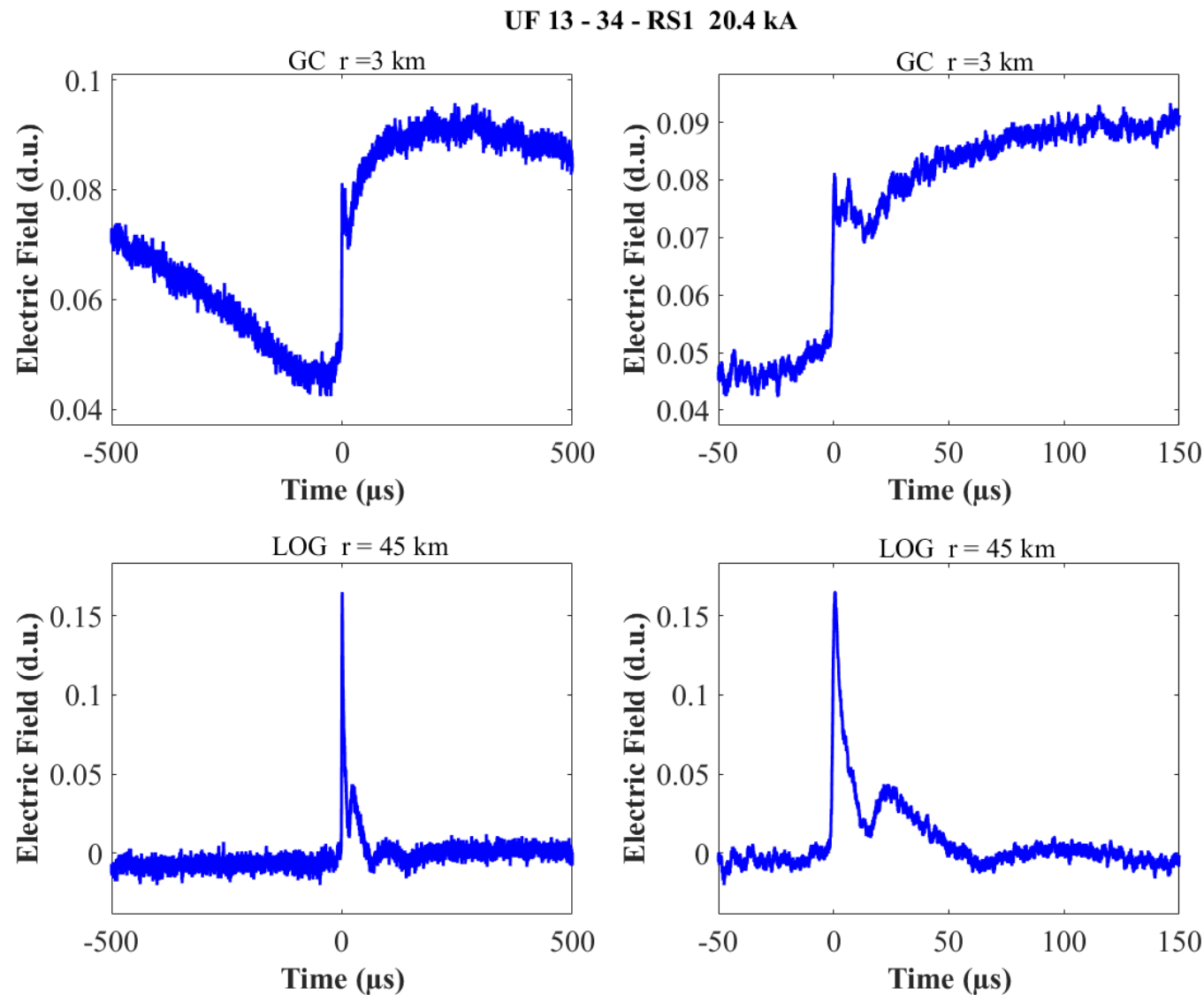


Figure A-21. Two-station electric field waveforms of the RS1 of flash UF 13-34.

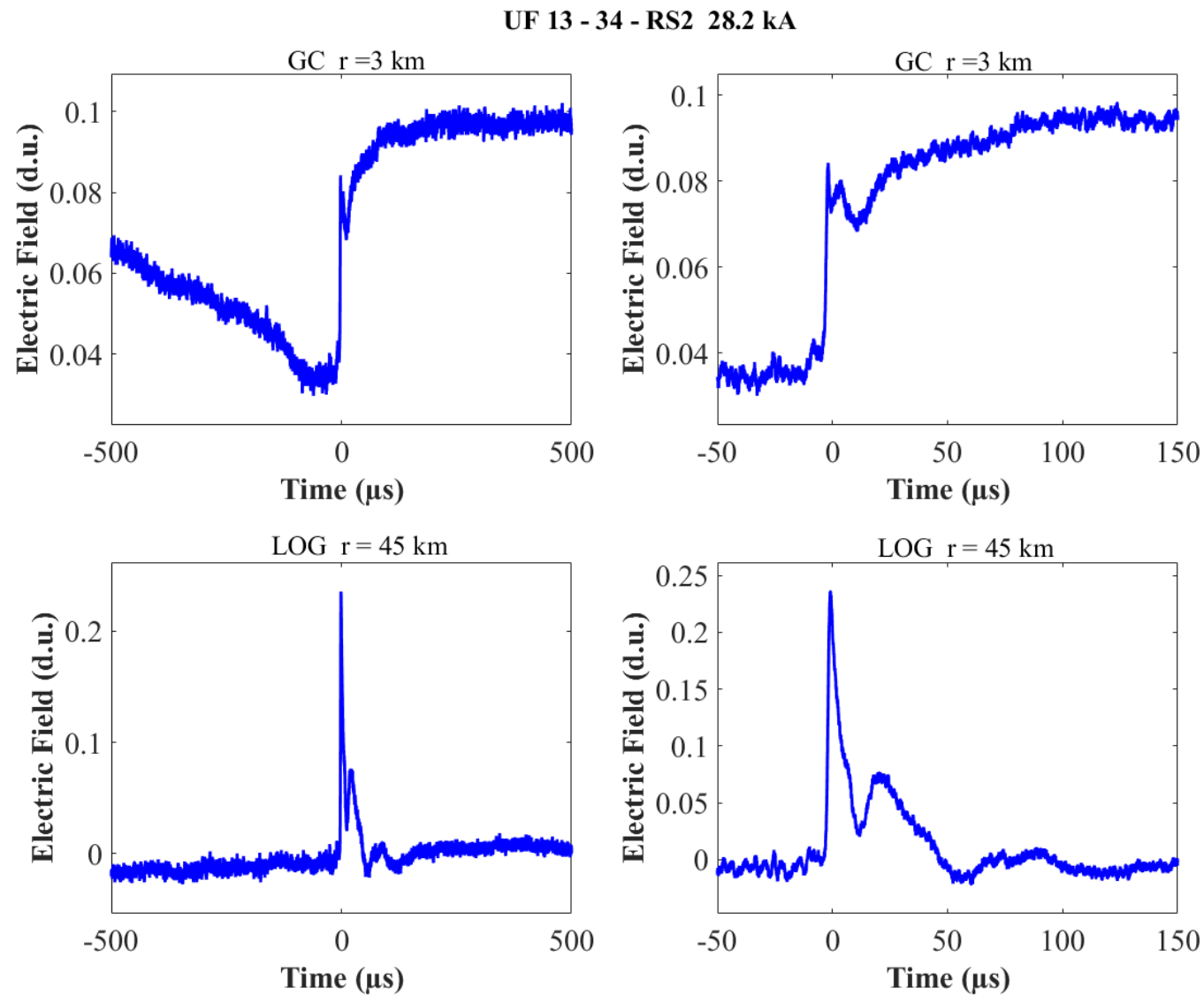


Figure A-22. Two-station electric field waveforms of the RS2 of flash UF 13-34.

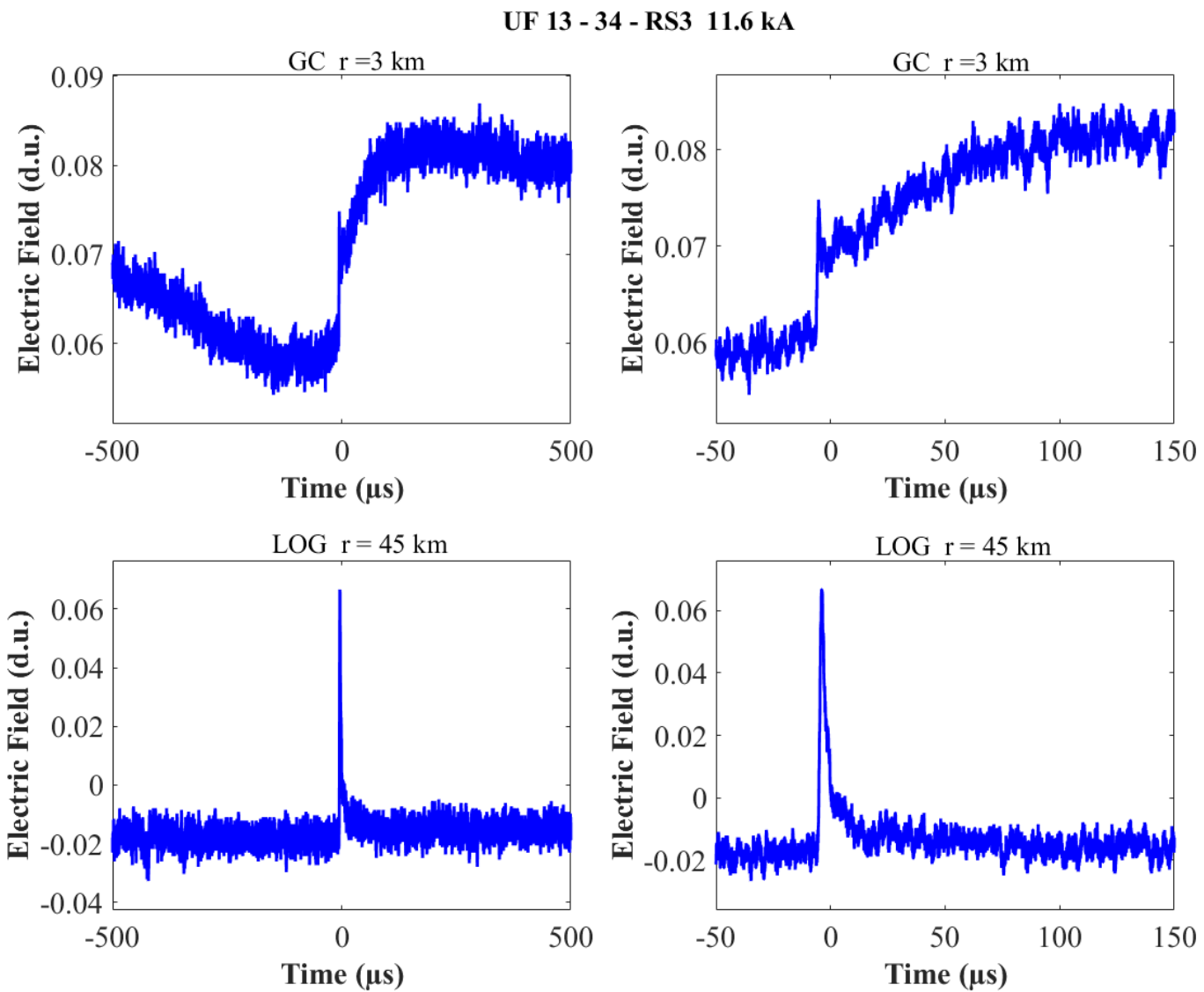


Figure A-23. Two-station electric field waveforms of the RS3 of flash UF 13-34.

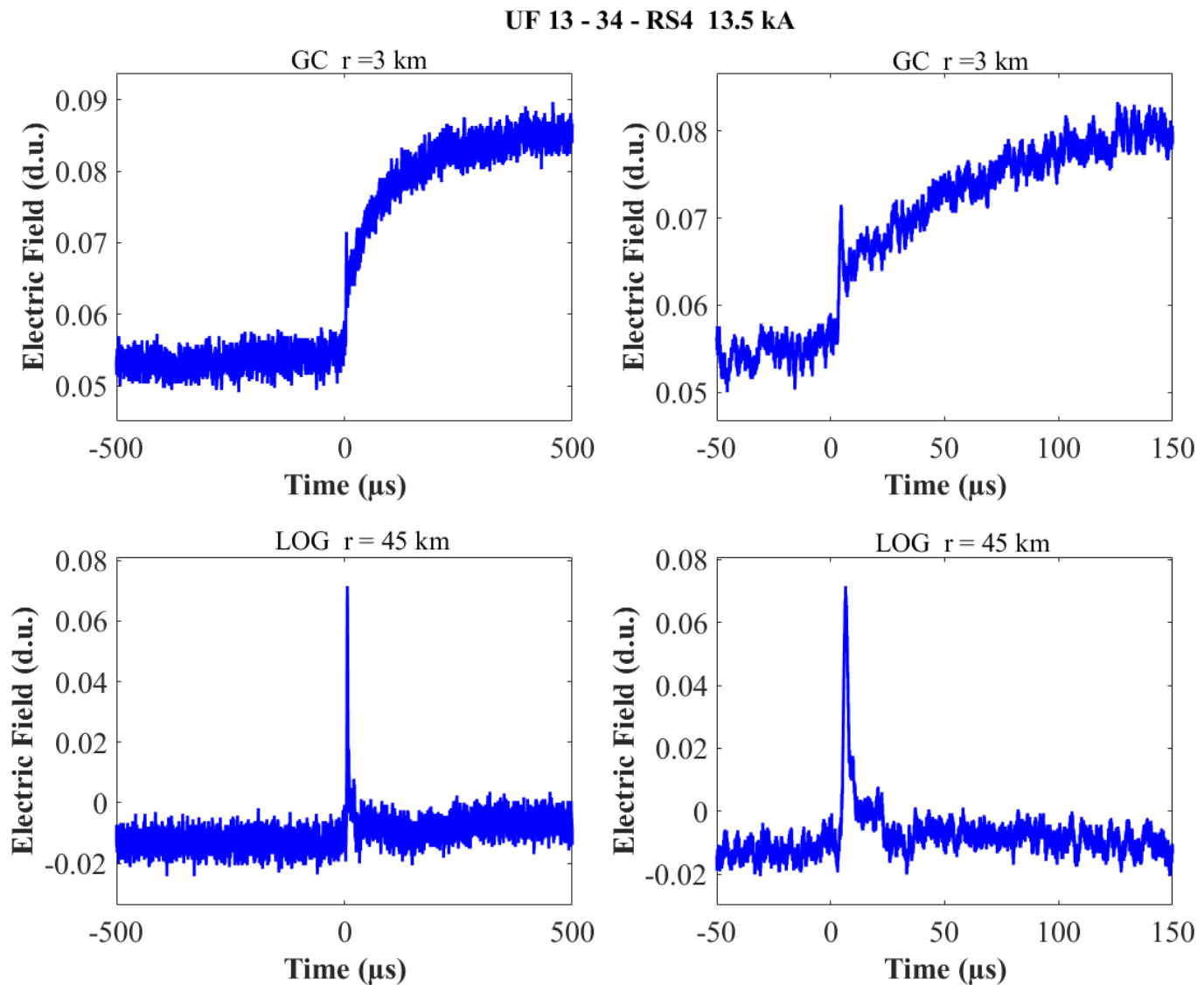


Figure A-24. Two-station electric field waveforms of the RS4 of flash UF 13-34.

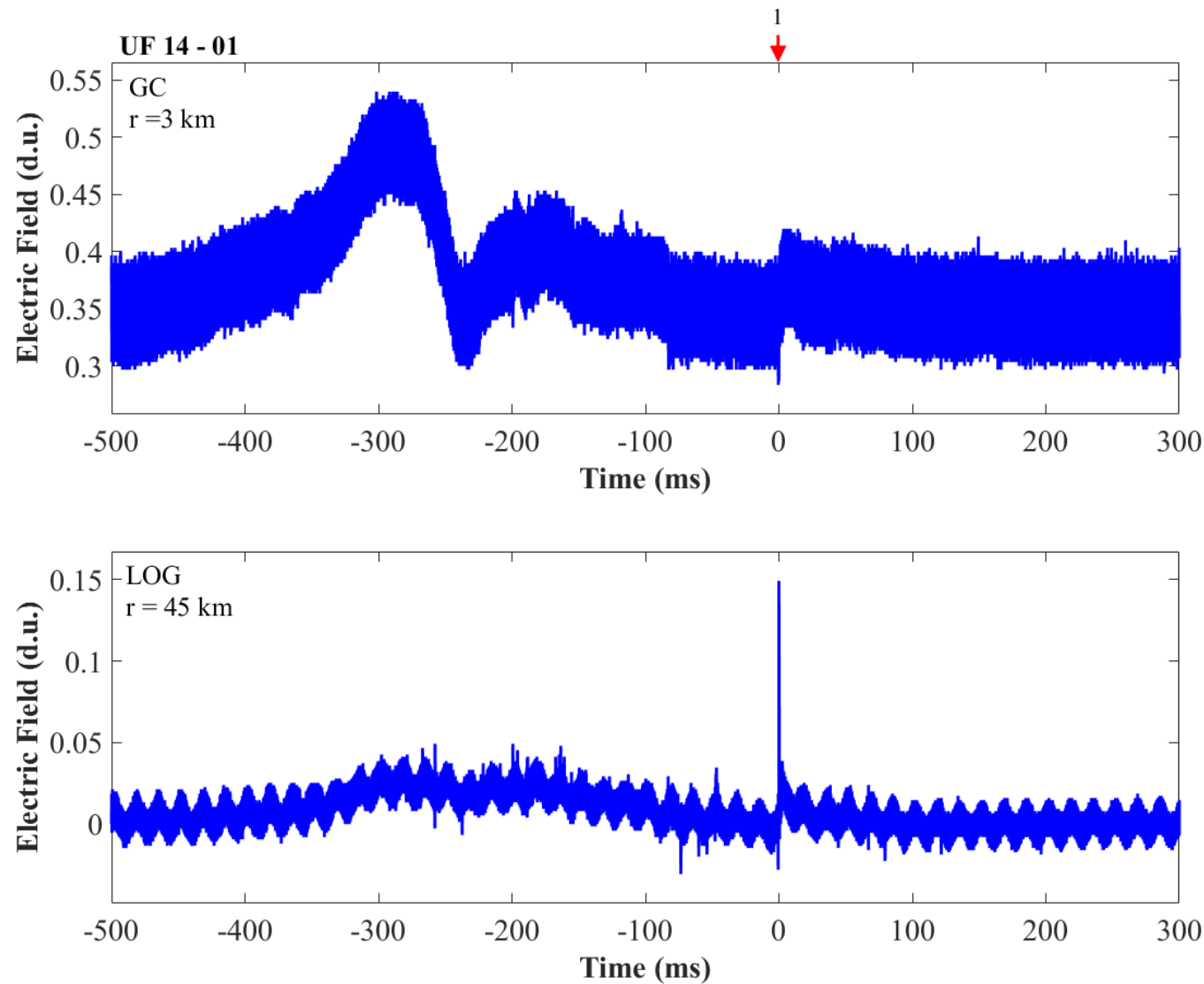


Figure A-25. Two-station electric field waveforms of flash UF 14-01.

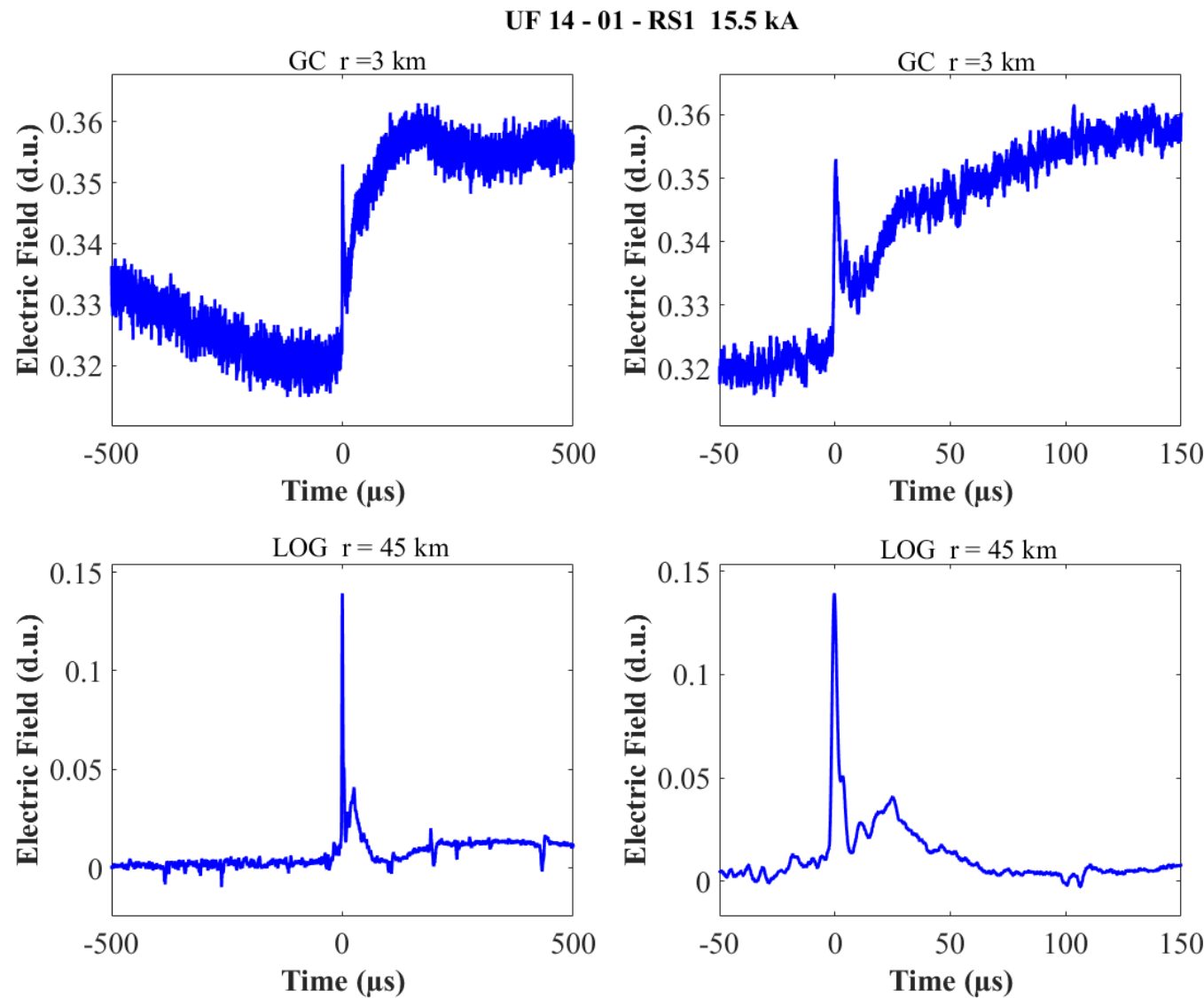


Figure A-26. Two-station electric field waveforms of the RS1 of flash UF 14-01.

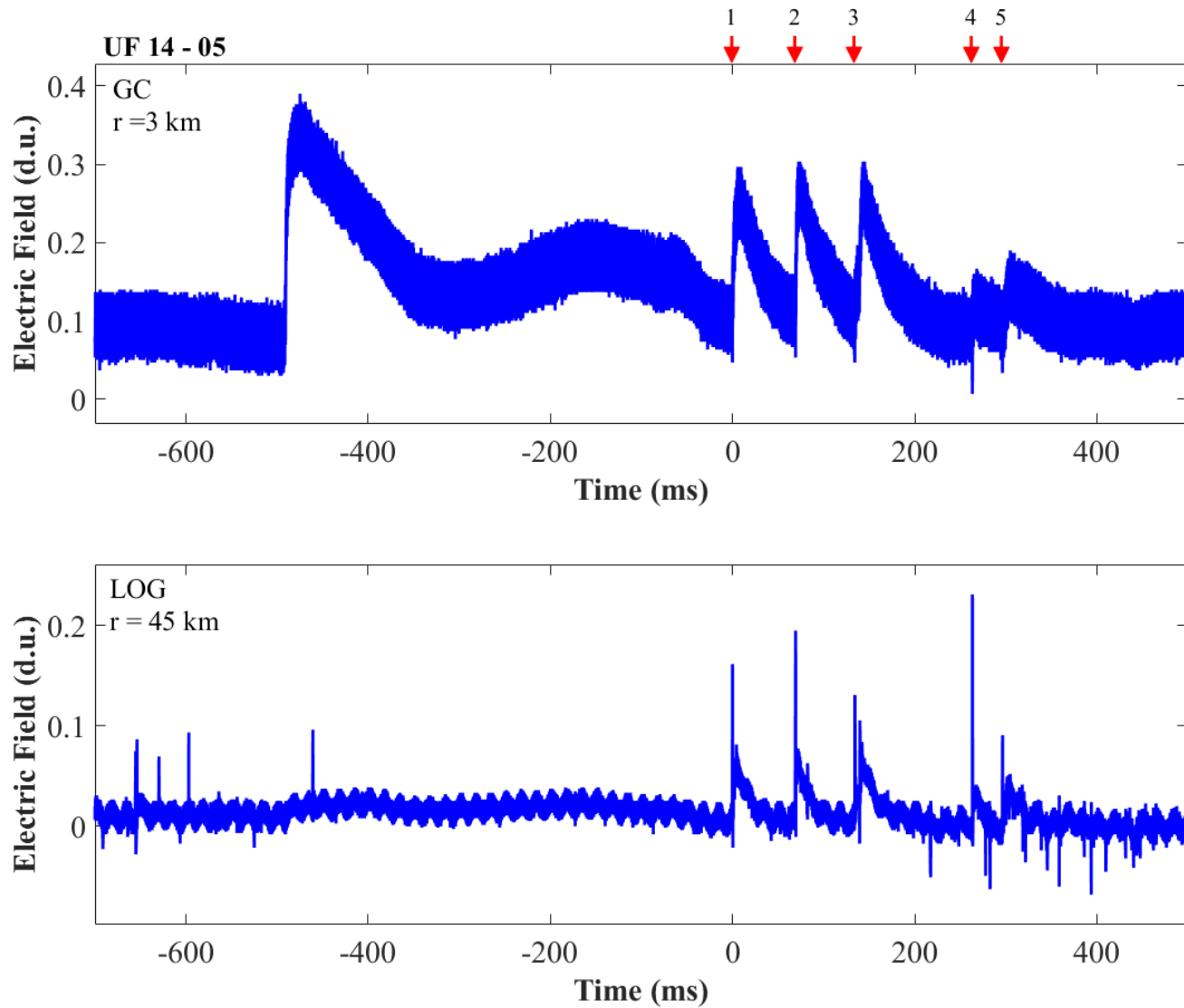


Figure A-27. Two-station electric field waveforms of flash UF 14-05.

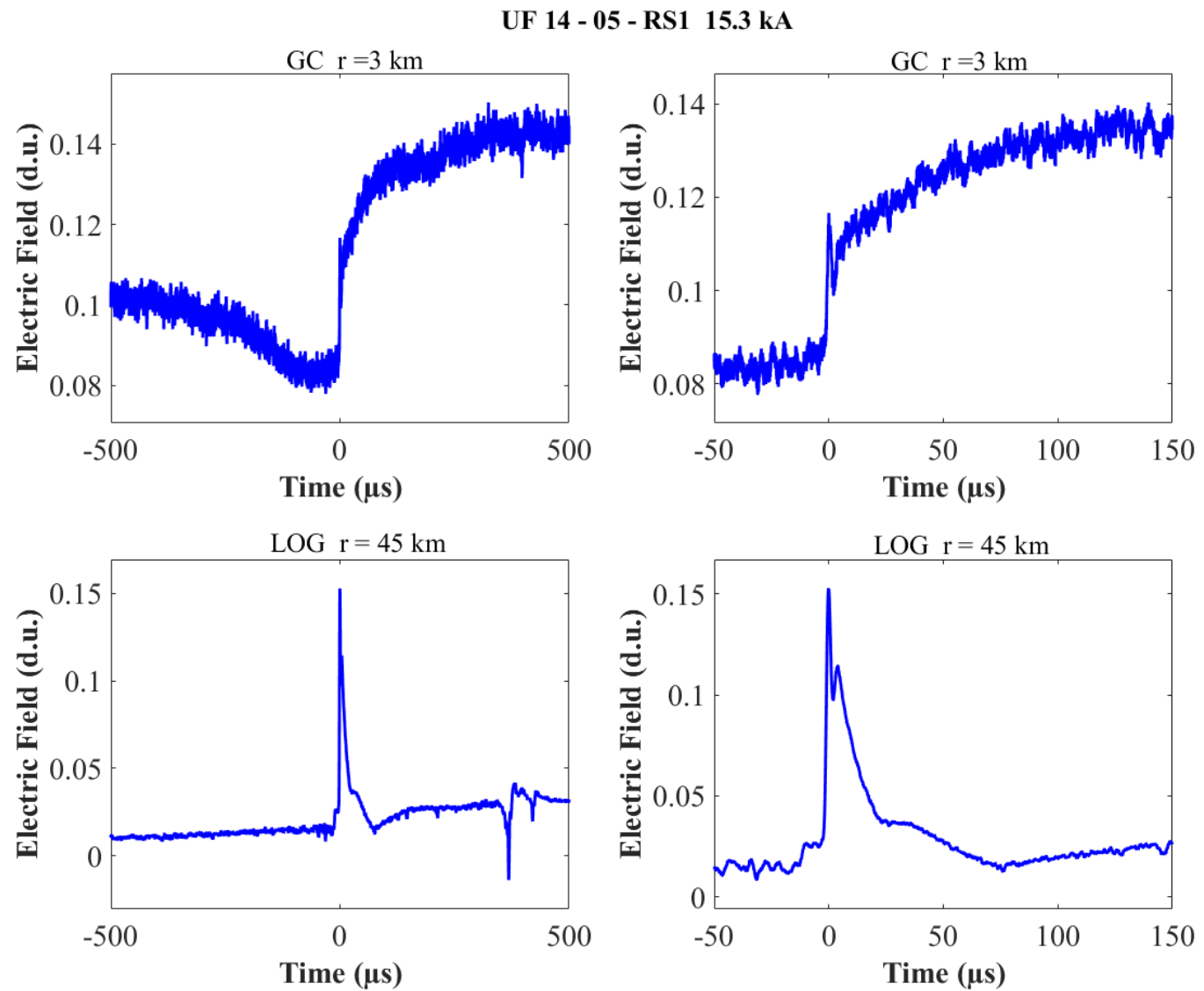


Figure A-28. Two-station electric field waveforms of the RS1 of flash UF 14-05.

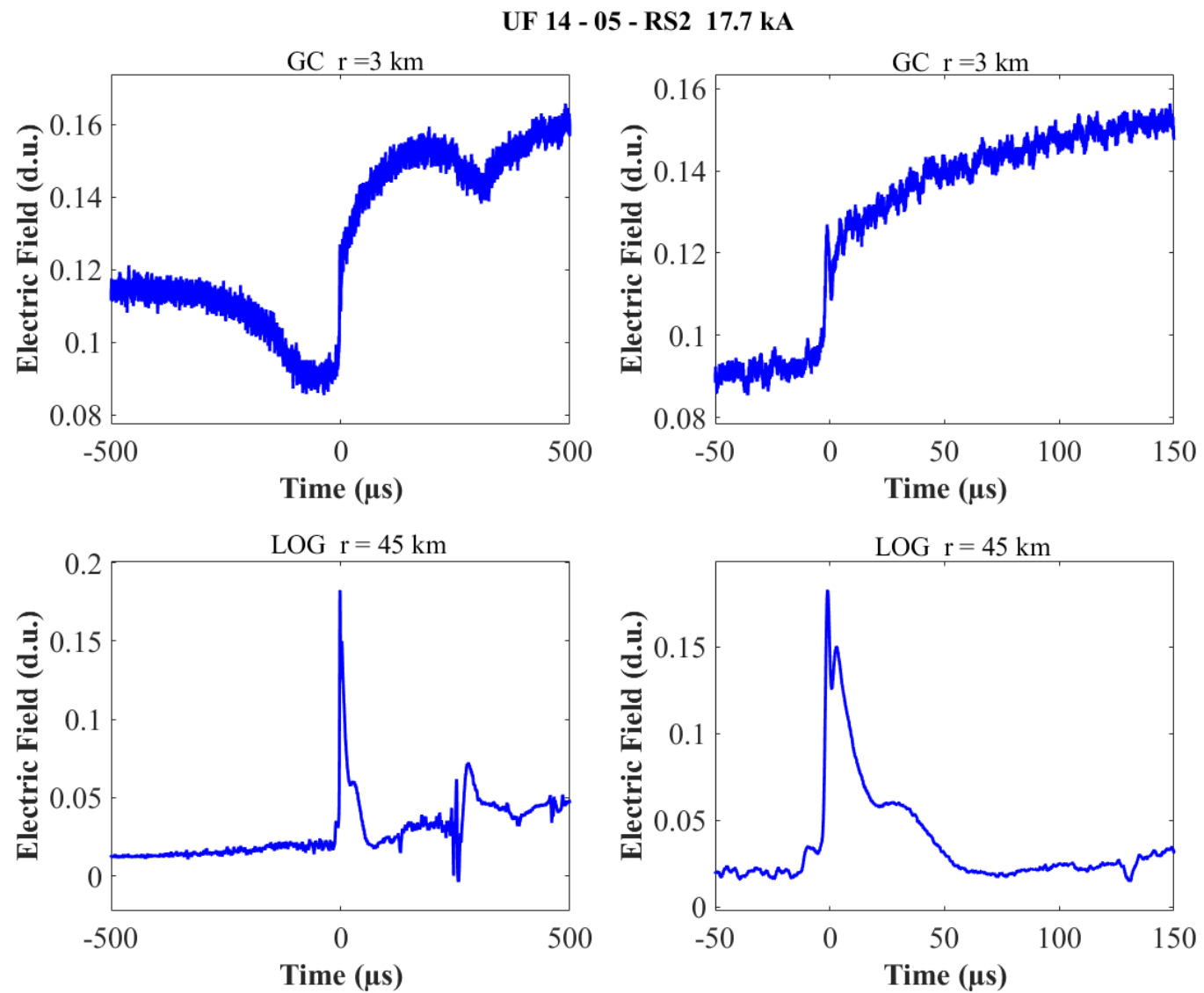


Figure A-29. Two-station electric field waveforms of the RS2 of flash UF 14-05.

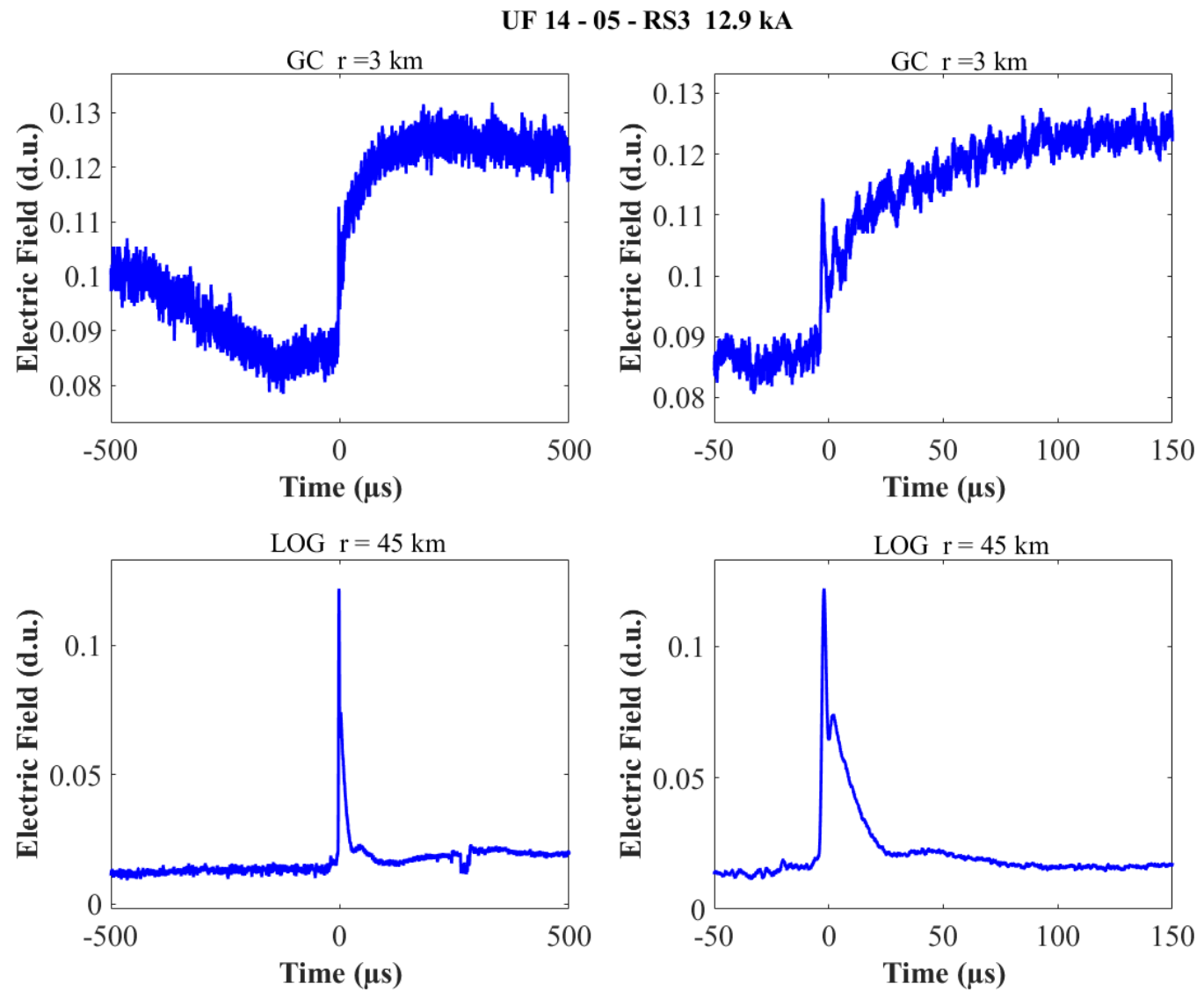


Figure A-30. Two-station electric field waveforms of the RS3 of flash UF 14-05.

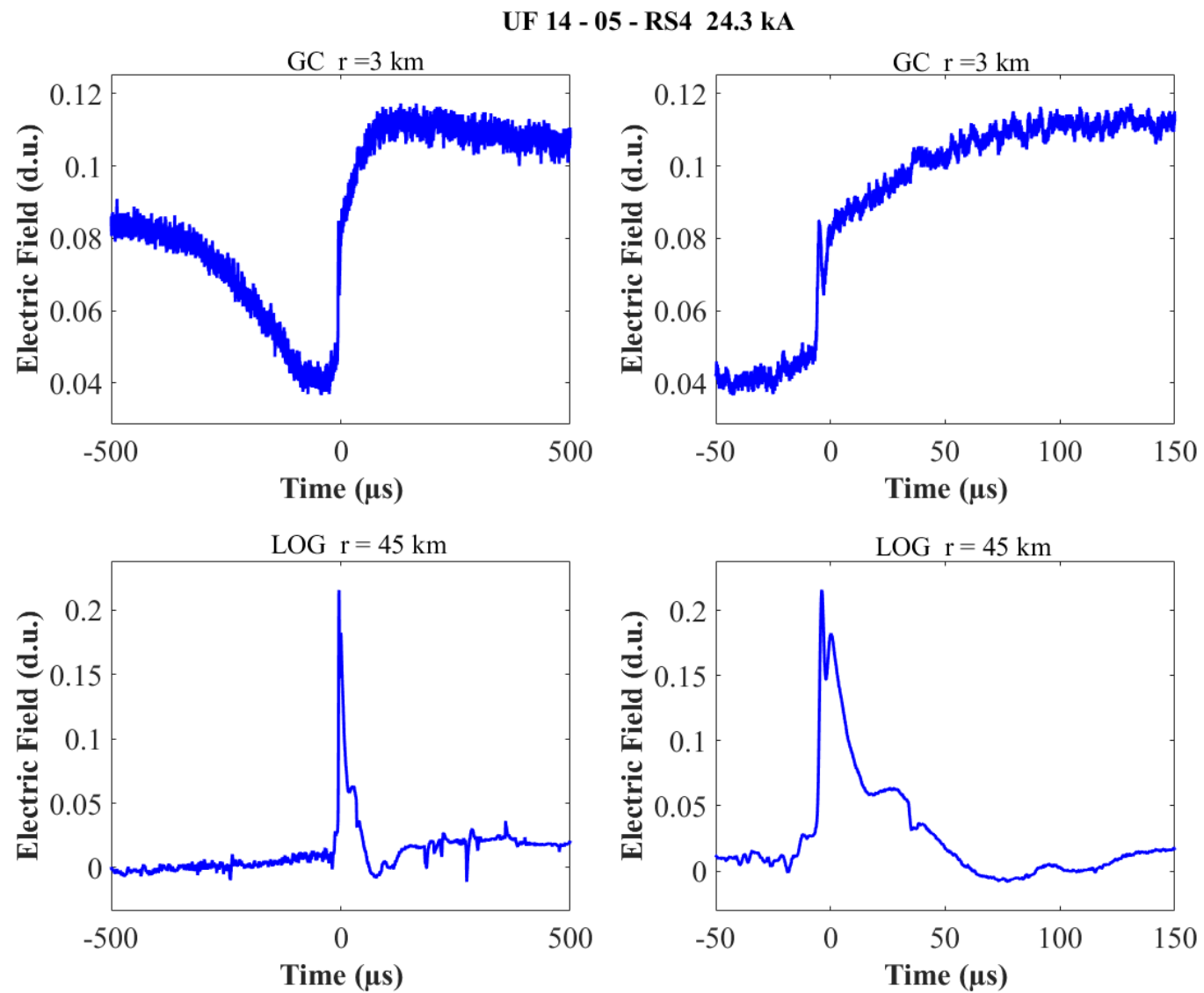


Figure A-31. Two-station electric field waveforms of the RS4 of flash UF 14-05.

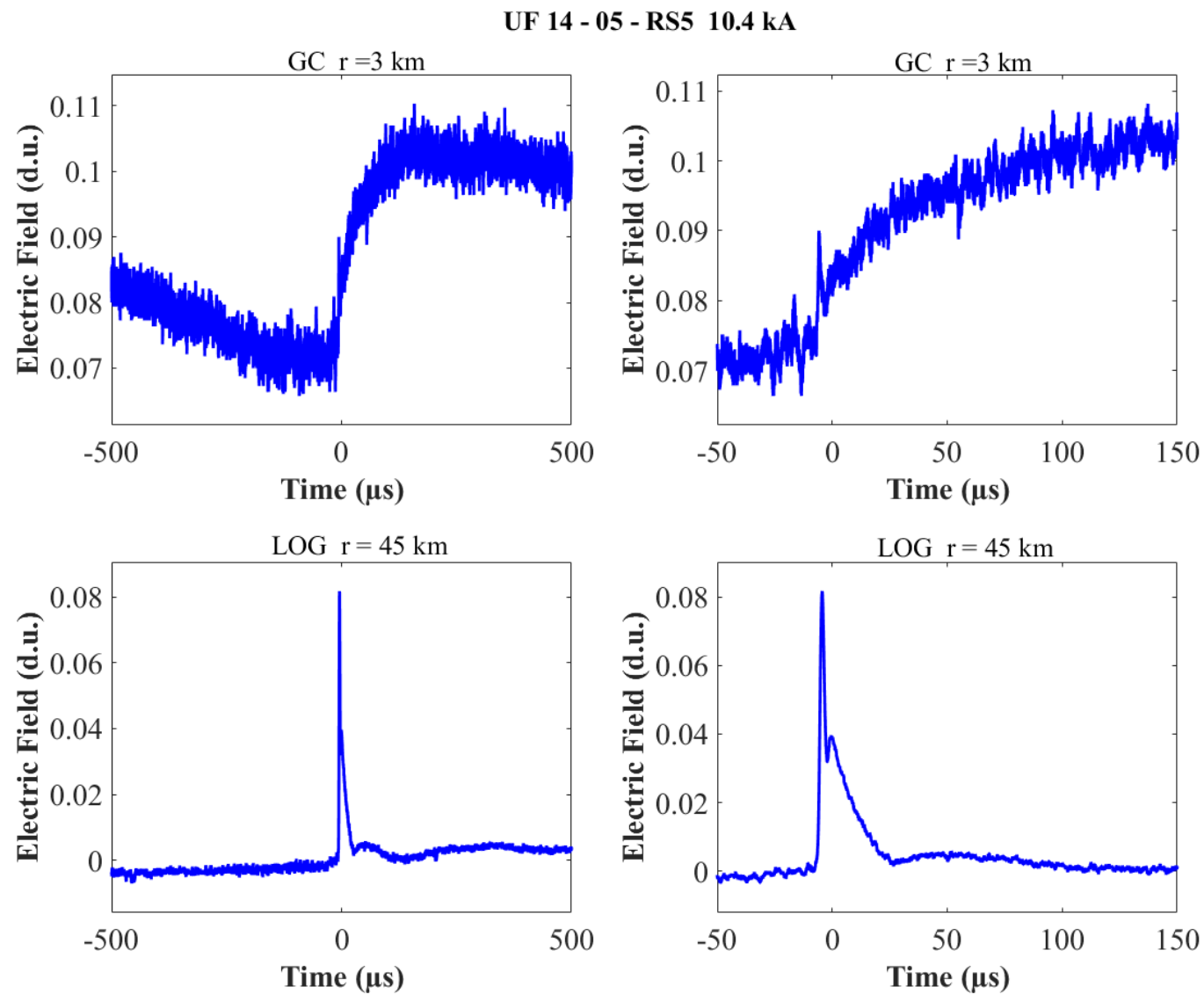


Figure A-32. Two-station electric field waveforms of the RS5 of flash UF 14-05.

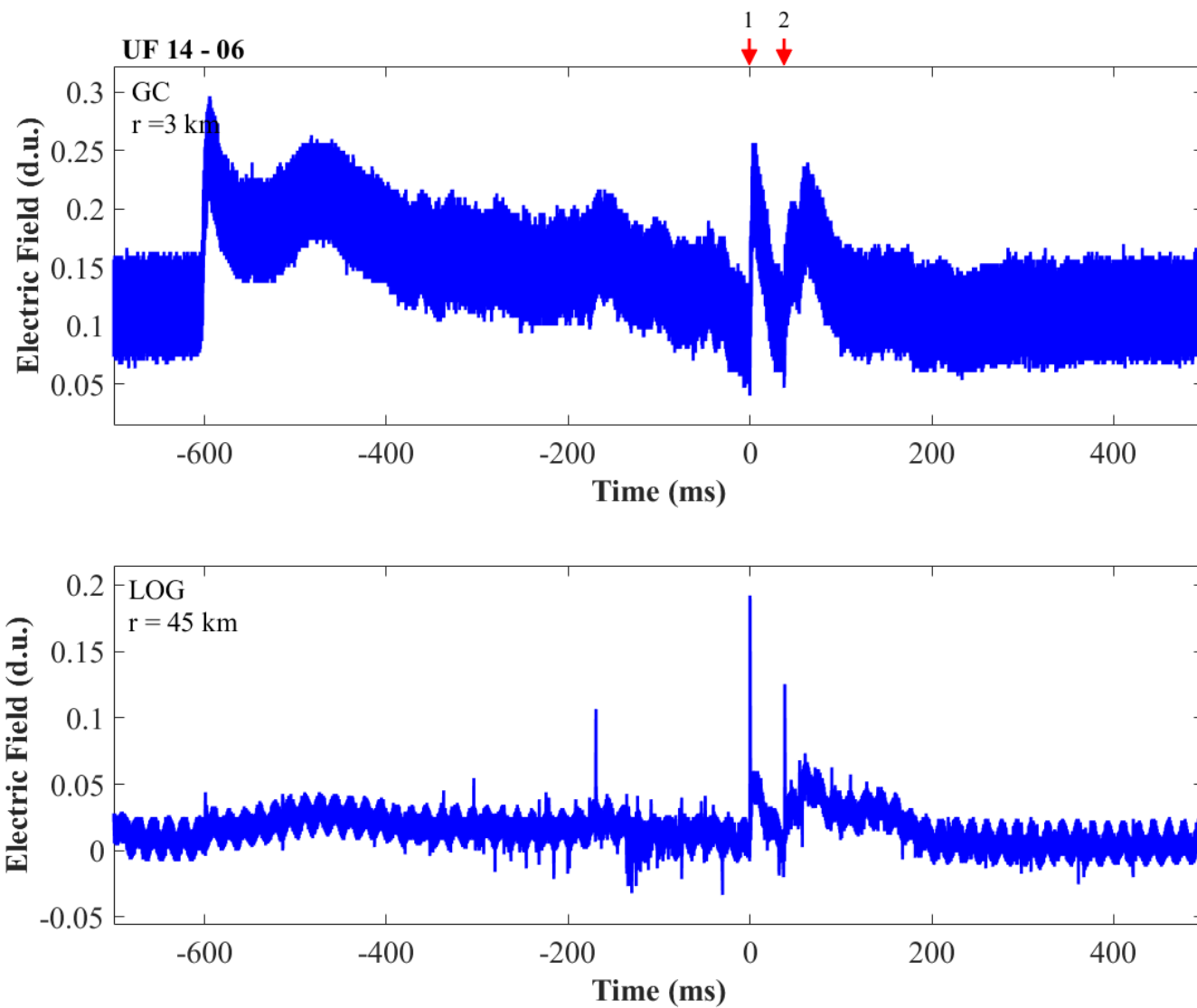


Figure A-33. Two-station electric field waveforms of flash UF 14-06.

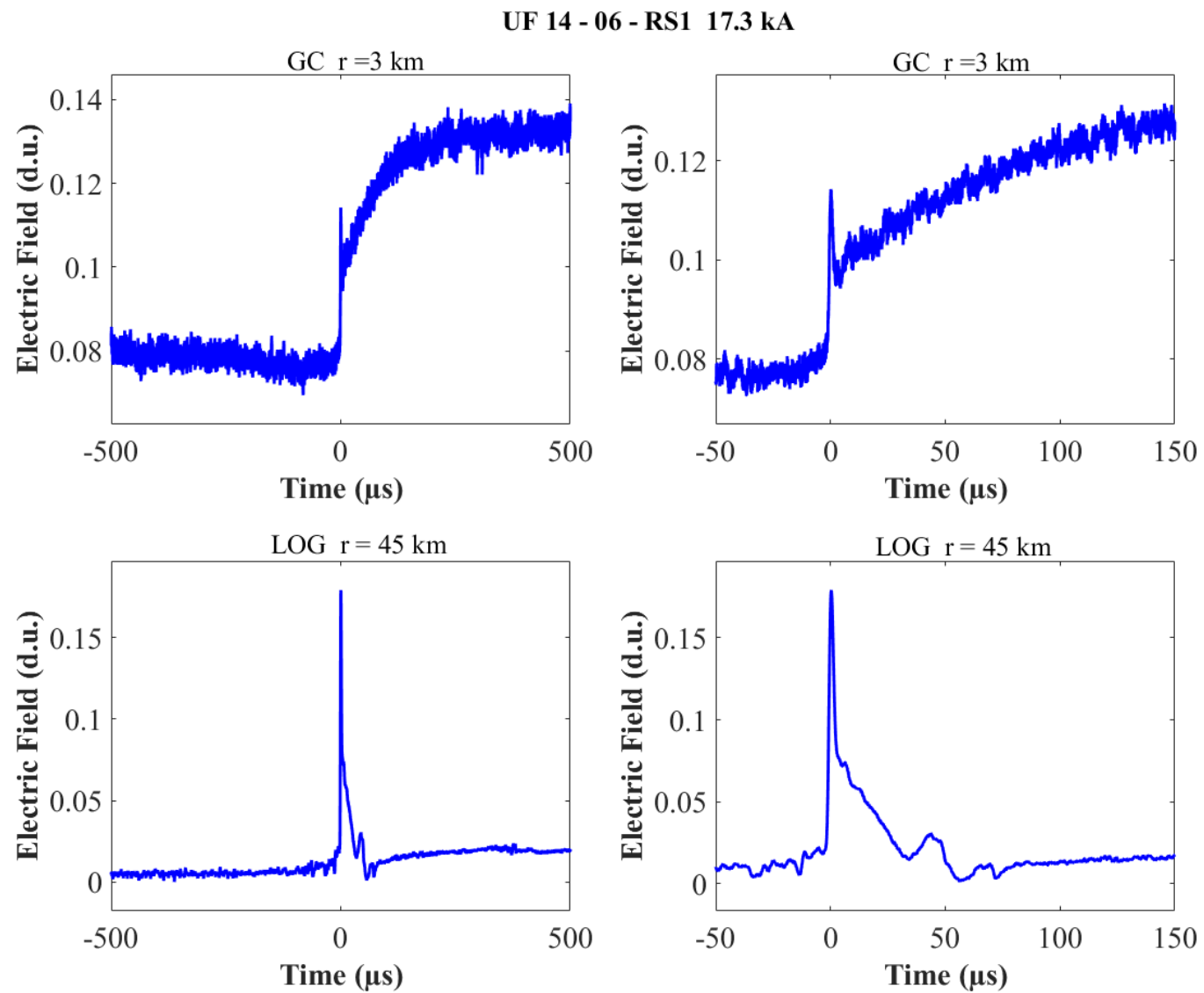


Figure A-34. Two-station electric field waveforms of the RS1 of flash UF 14-06.

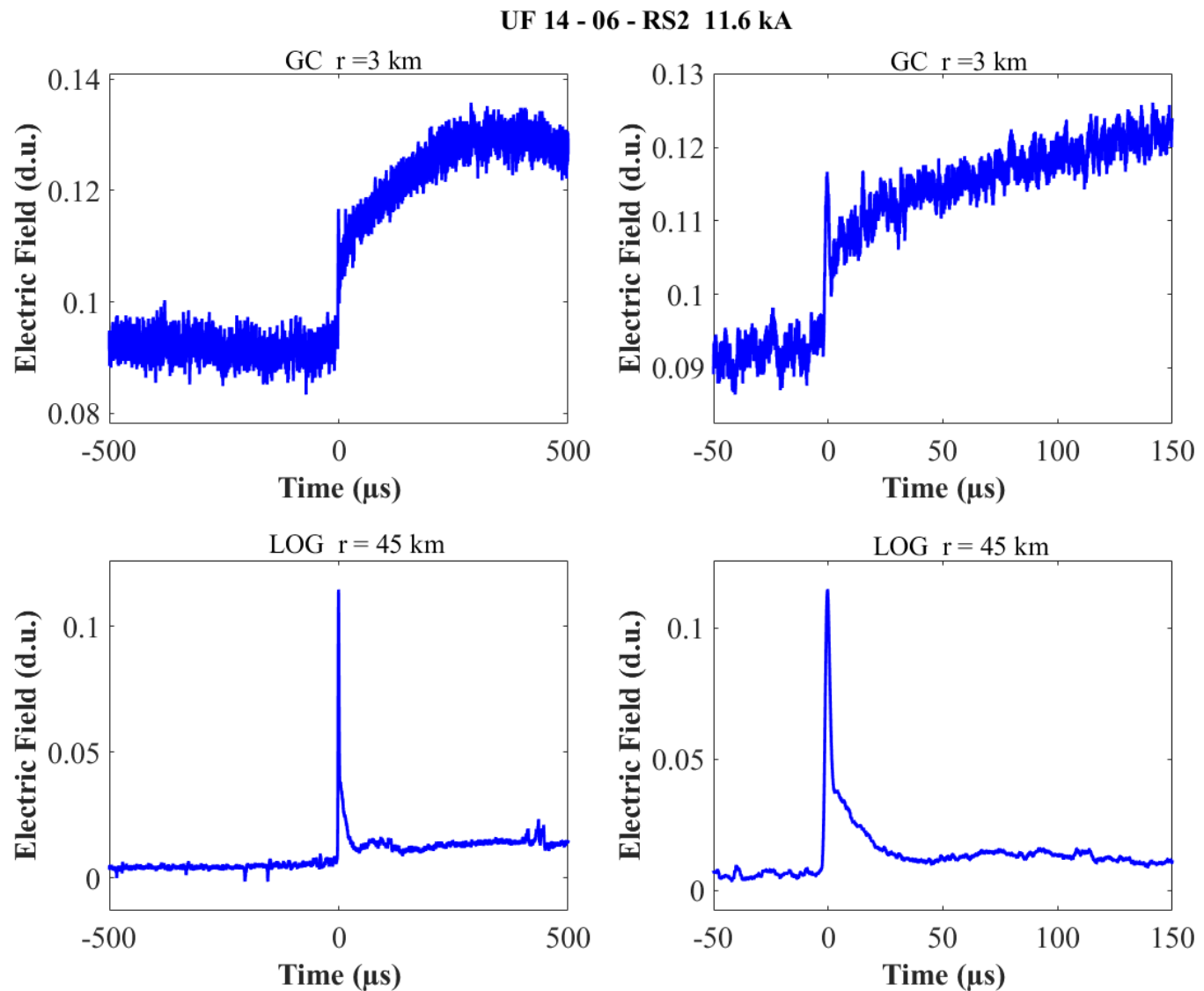


Figure A-35. Two-station electric field waveforms of the RS2 of flash UF 14-06.

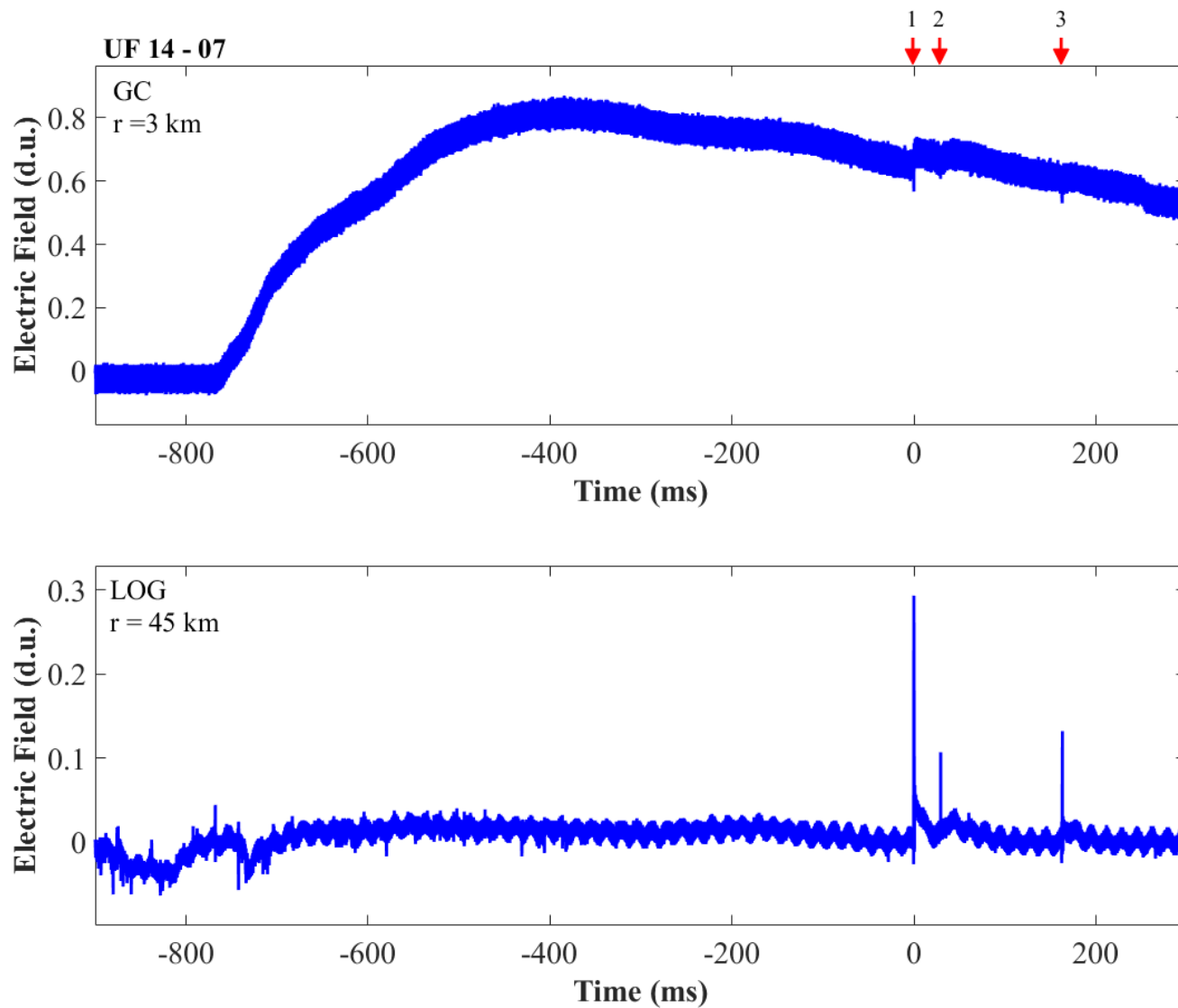


Figure A-36. Two-station electric field waveforms of flash UF 14-07.

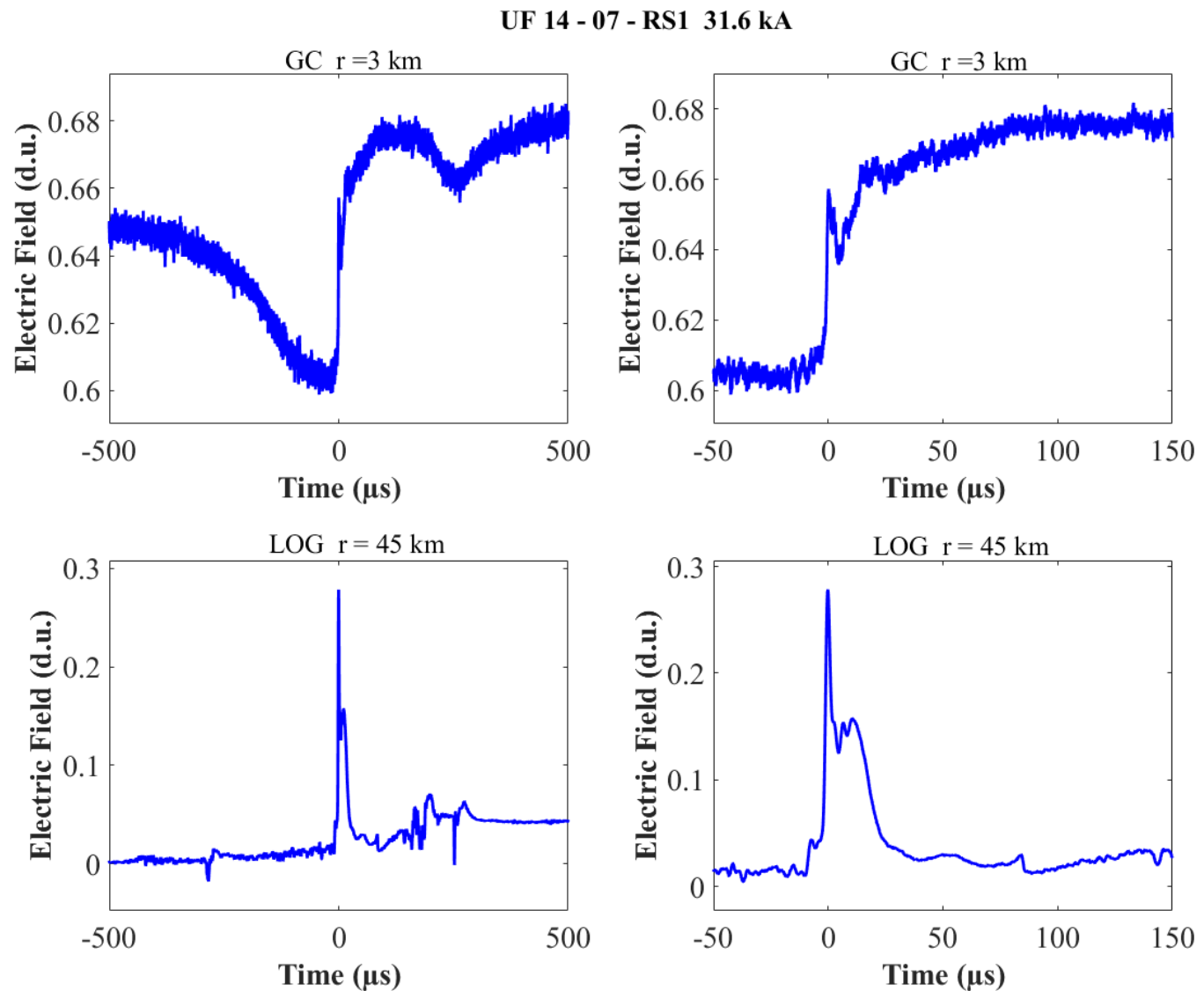


Figure A-37. Two-station electric field waveforms of the RS1 of flash UF 14-07.

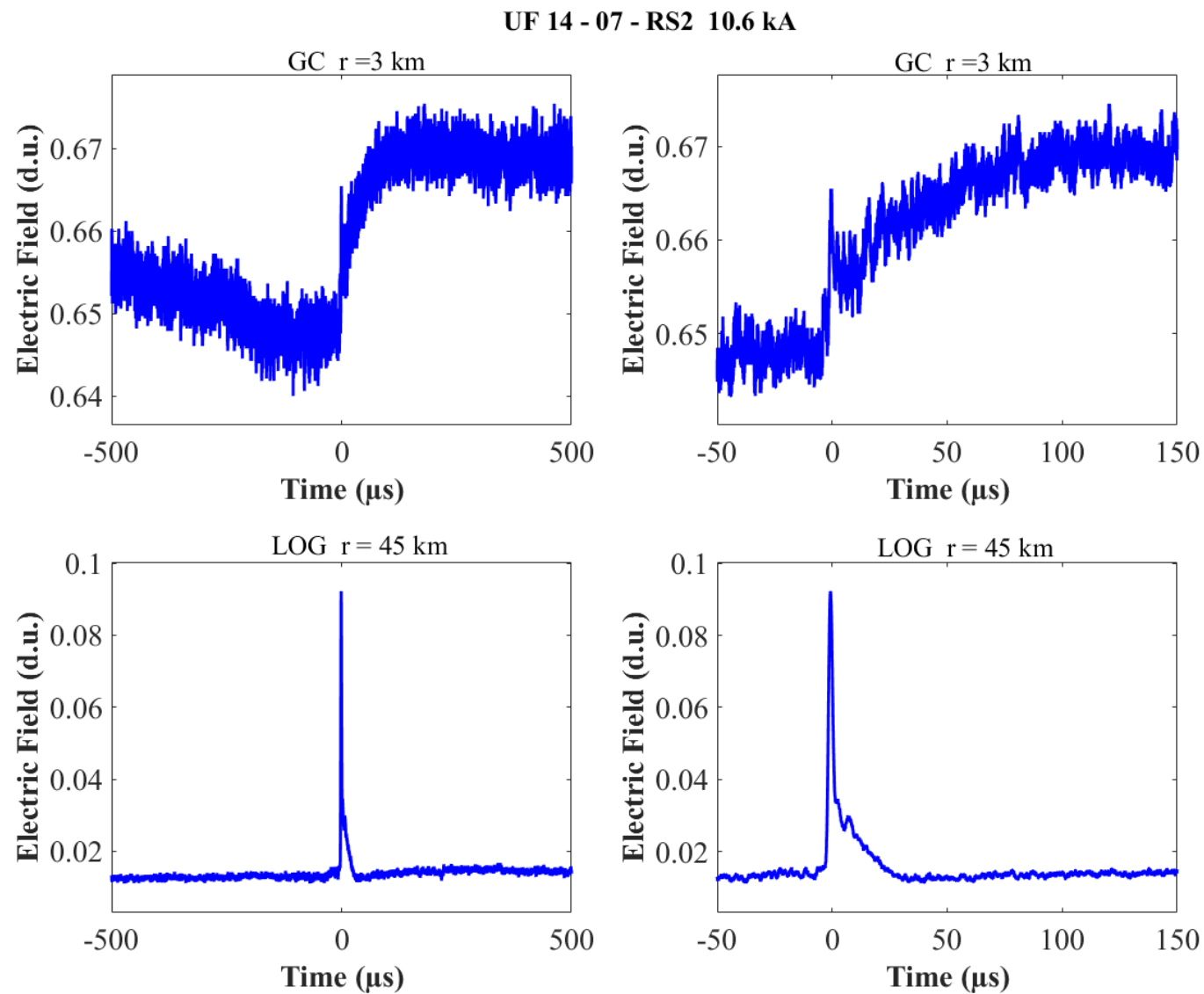


Figure A-38. Two-station electric field waveforms of the RS2 of flash UF 14-07.

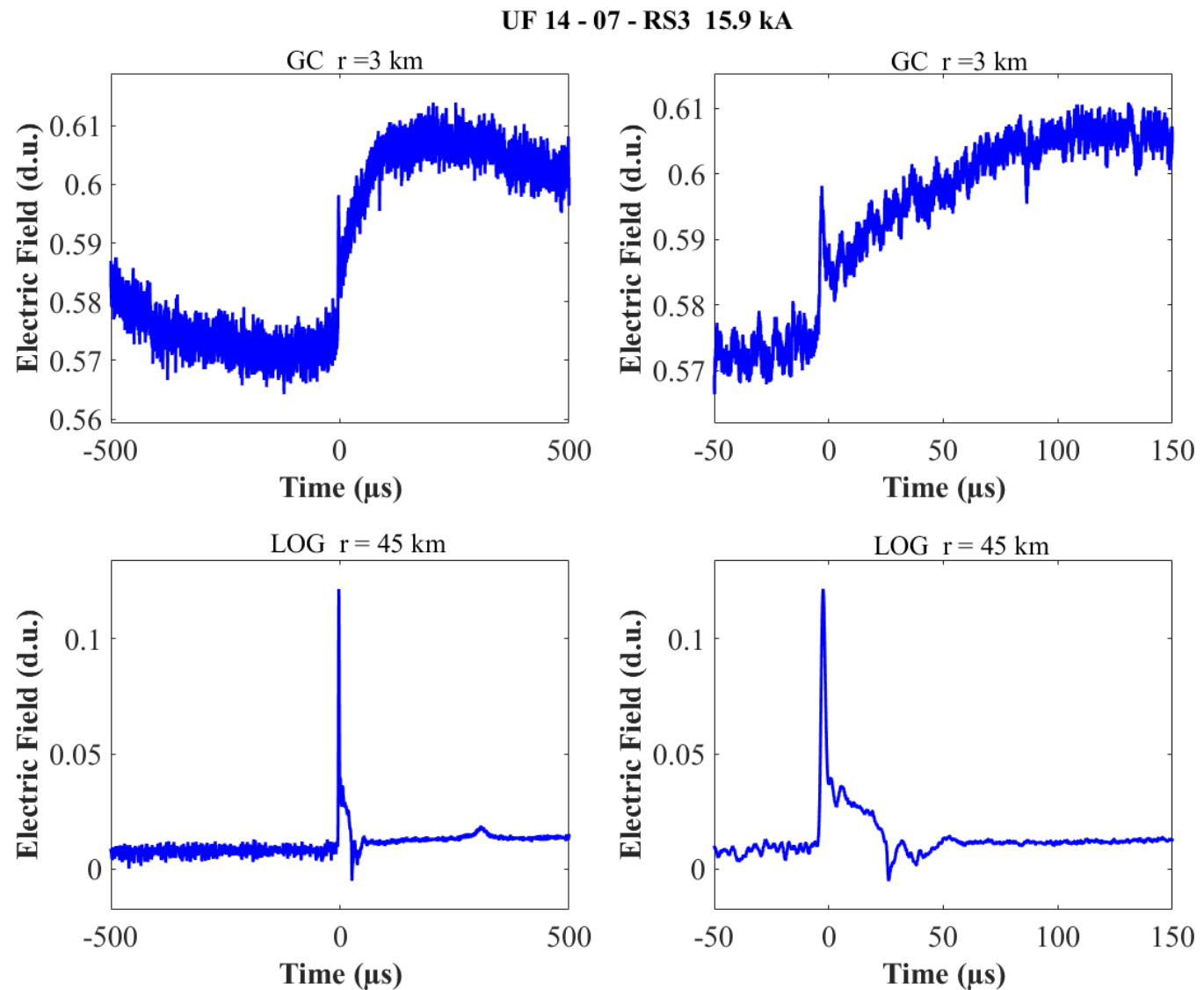


Figure A-39. Two-station electric field waveforms of the RS3 of flash UF 14-07.

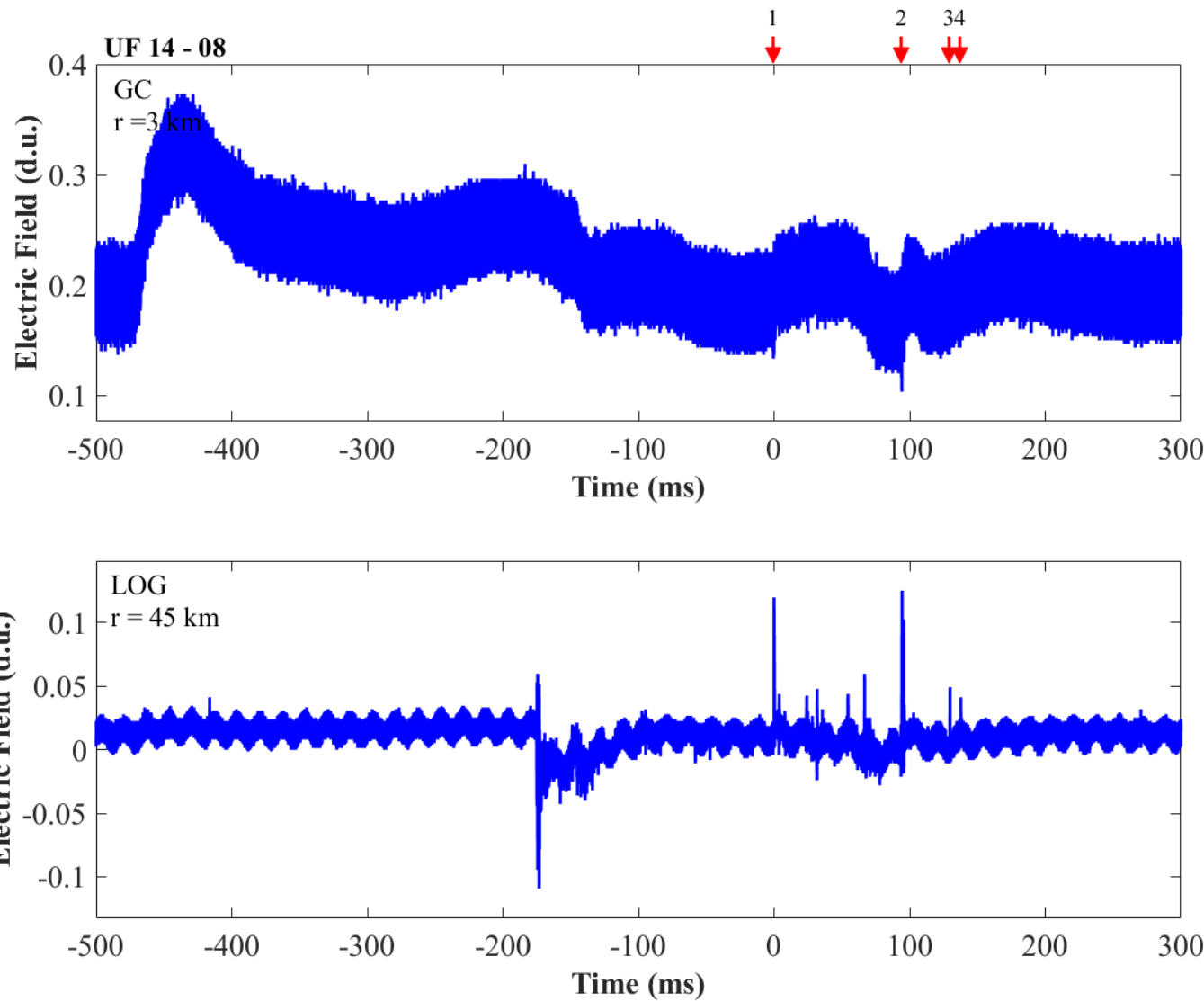


Figure A-40. Two-station electric field waveforms of flash UF 14-08.

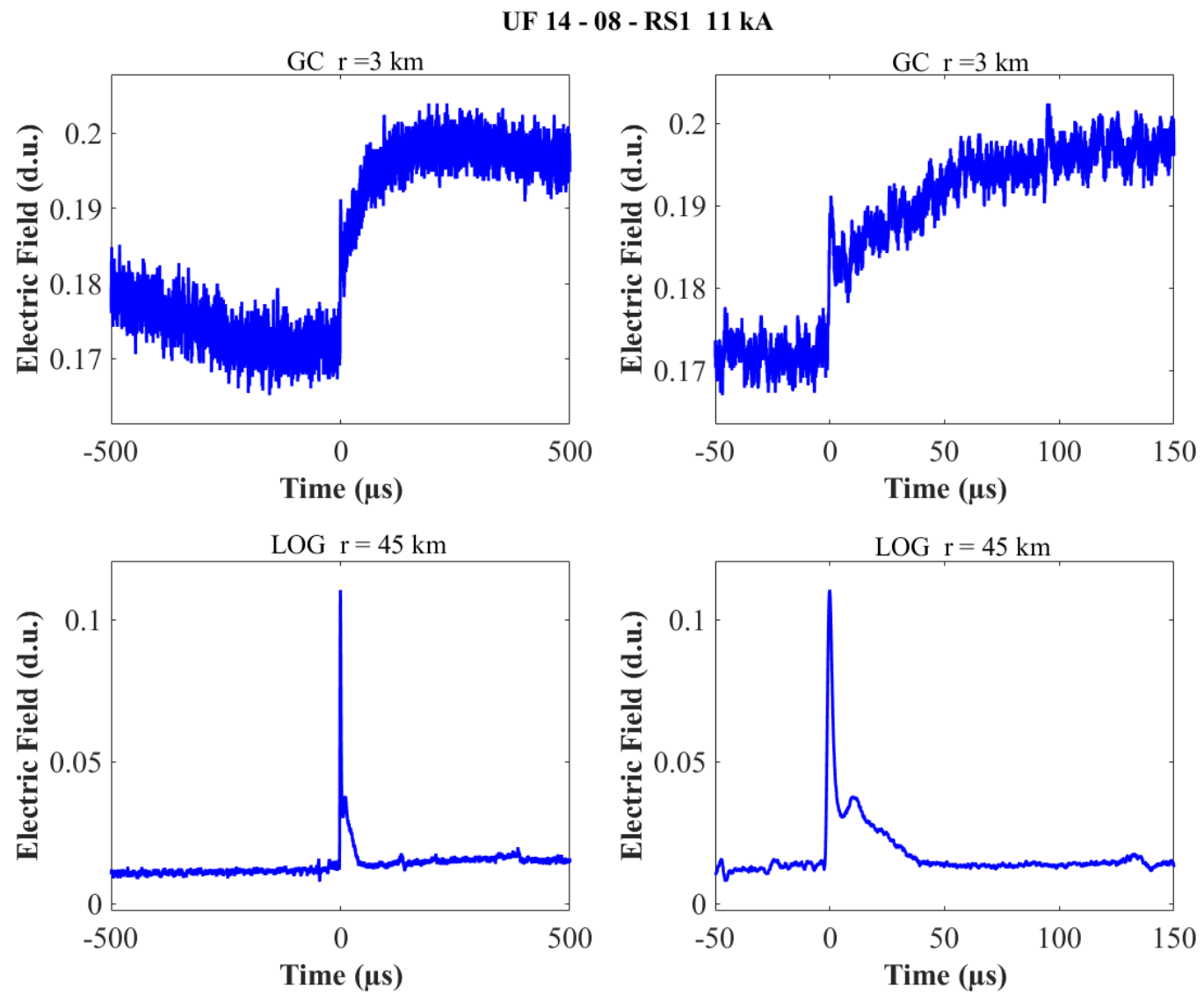


Figure A-41. Two-station electric field waveforms of the RS1 of flash UF 14-08.

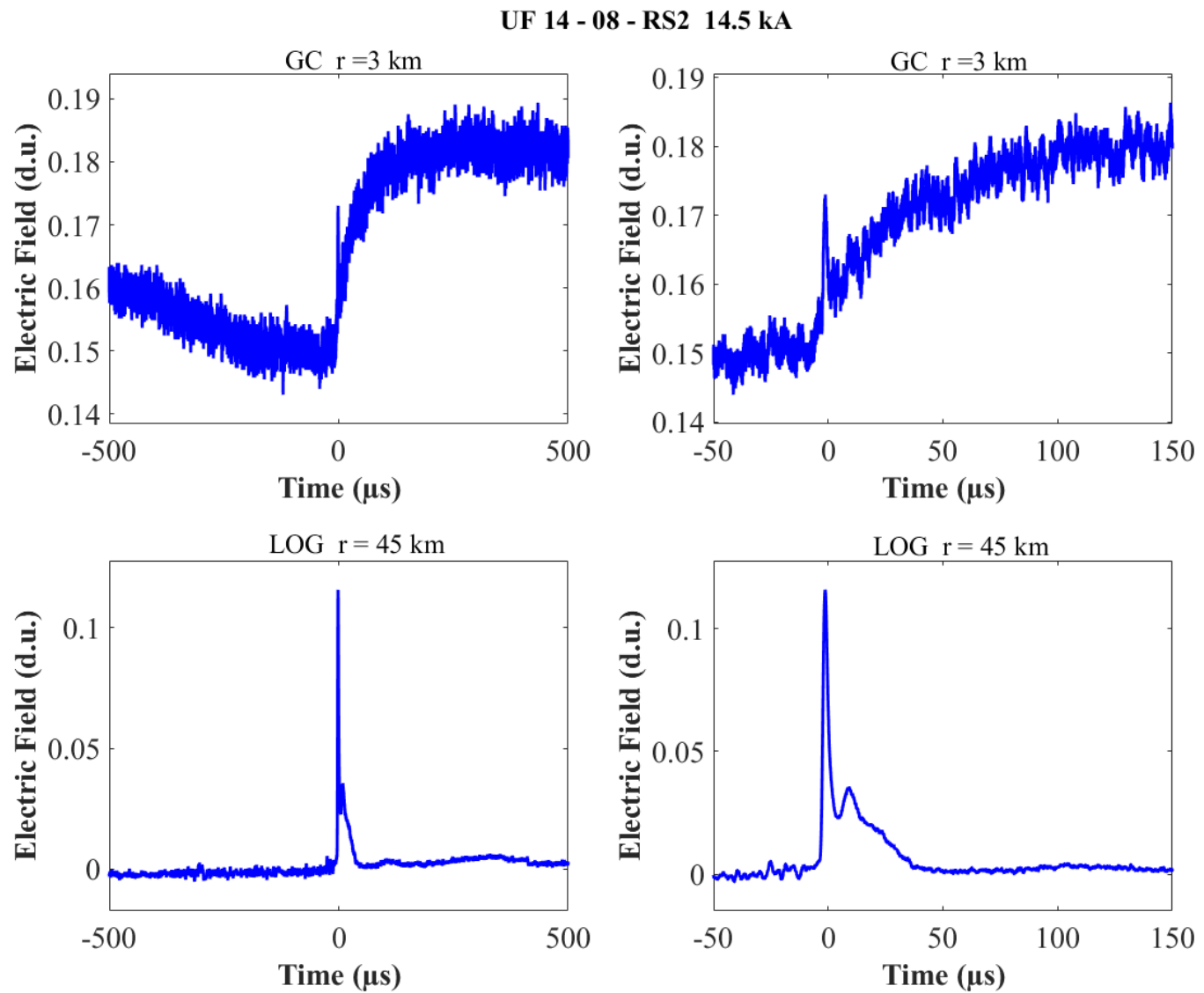


Figure A-42. Two-station electric field waveforms of the RS2 of flash UF 14-08.

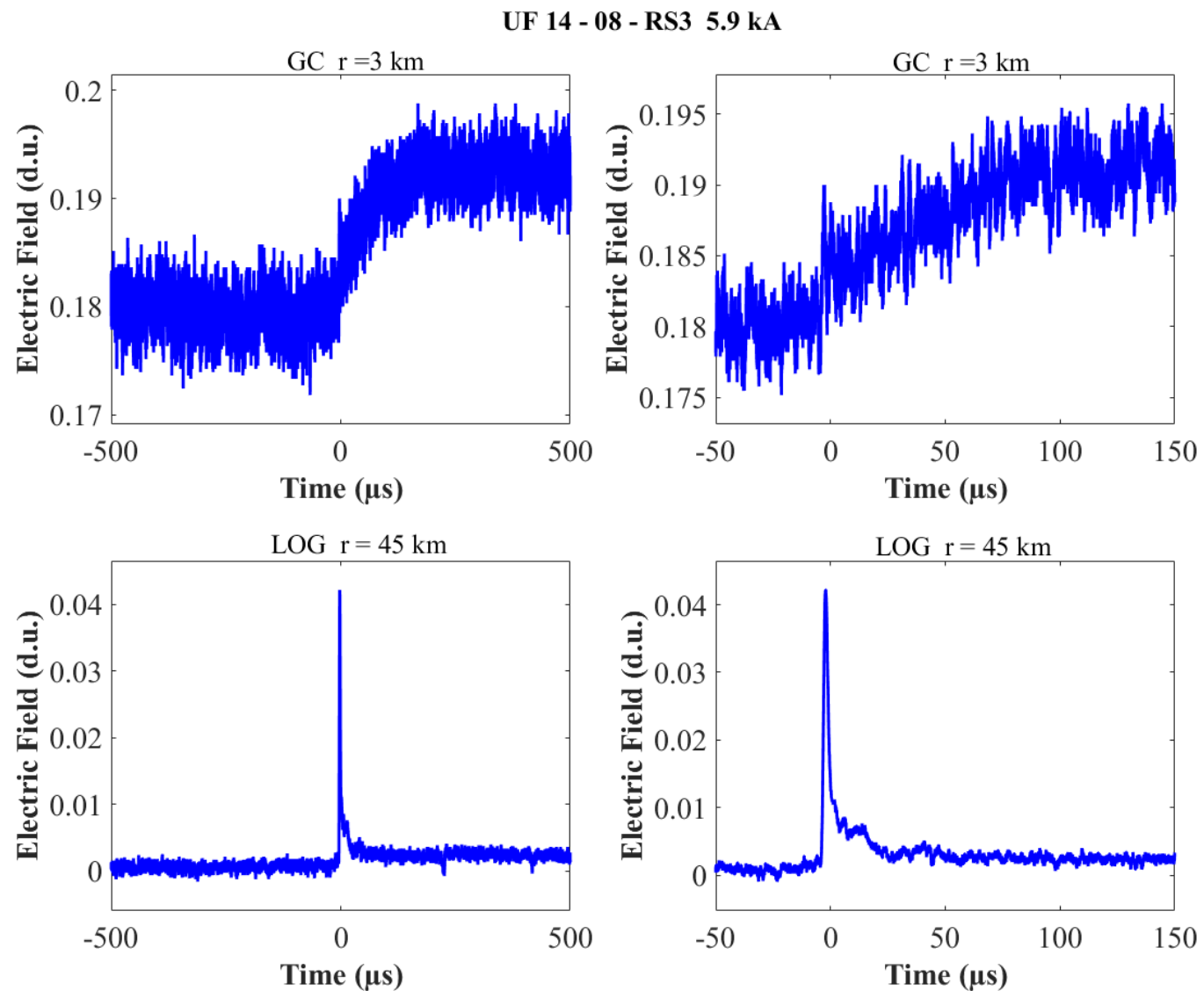


Figure A-43. Two-station electric field waveforms of the RS3 of flash UF 14-08.

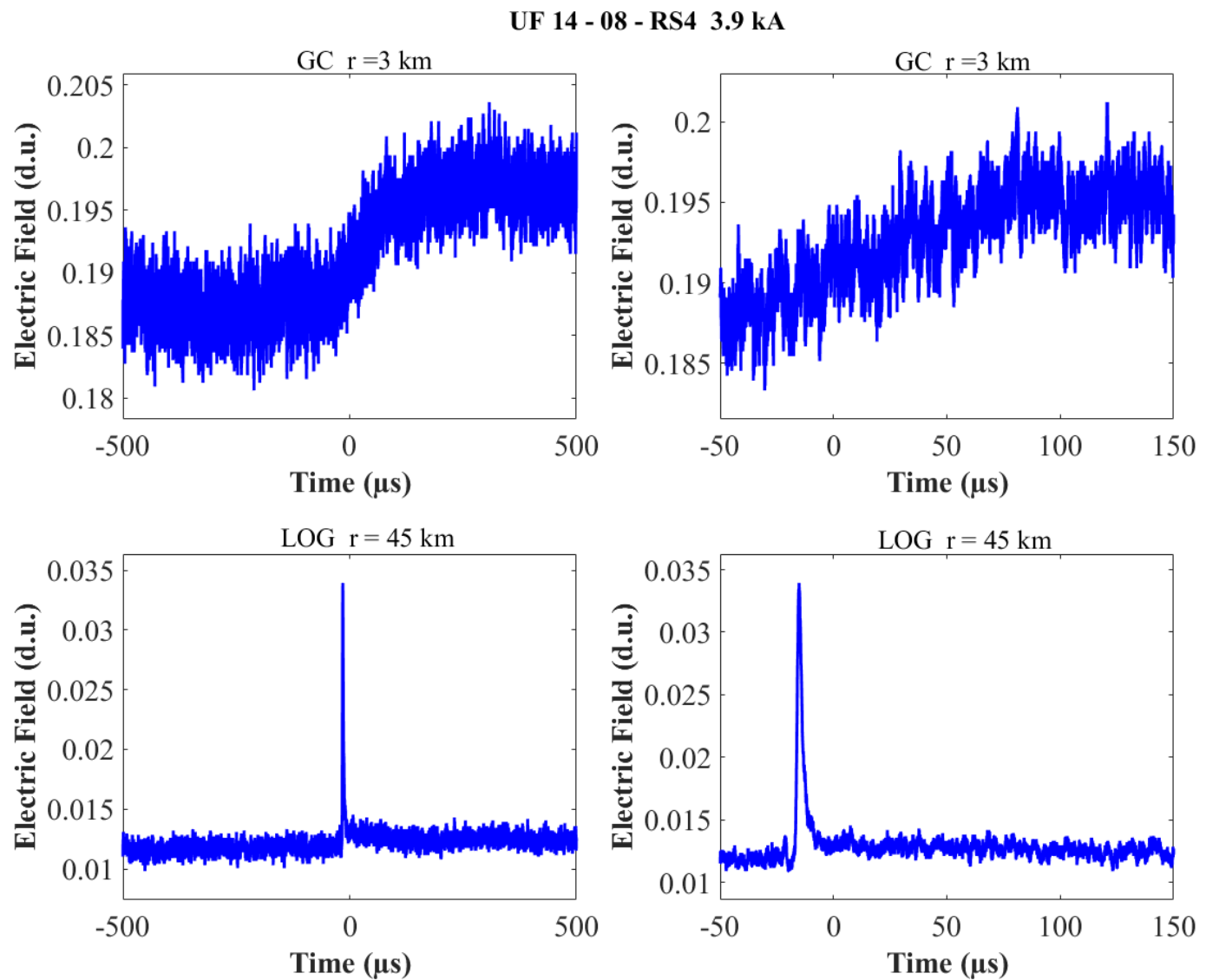


Figure A-44. Two-station electric field waveforms of the RS4 of flash UF 14-08.

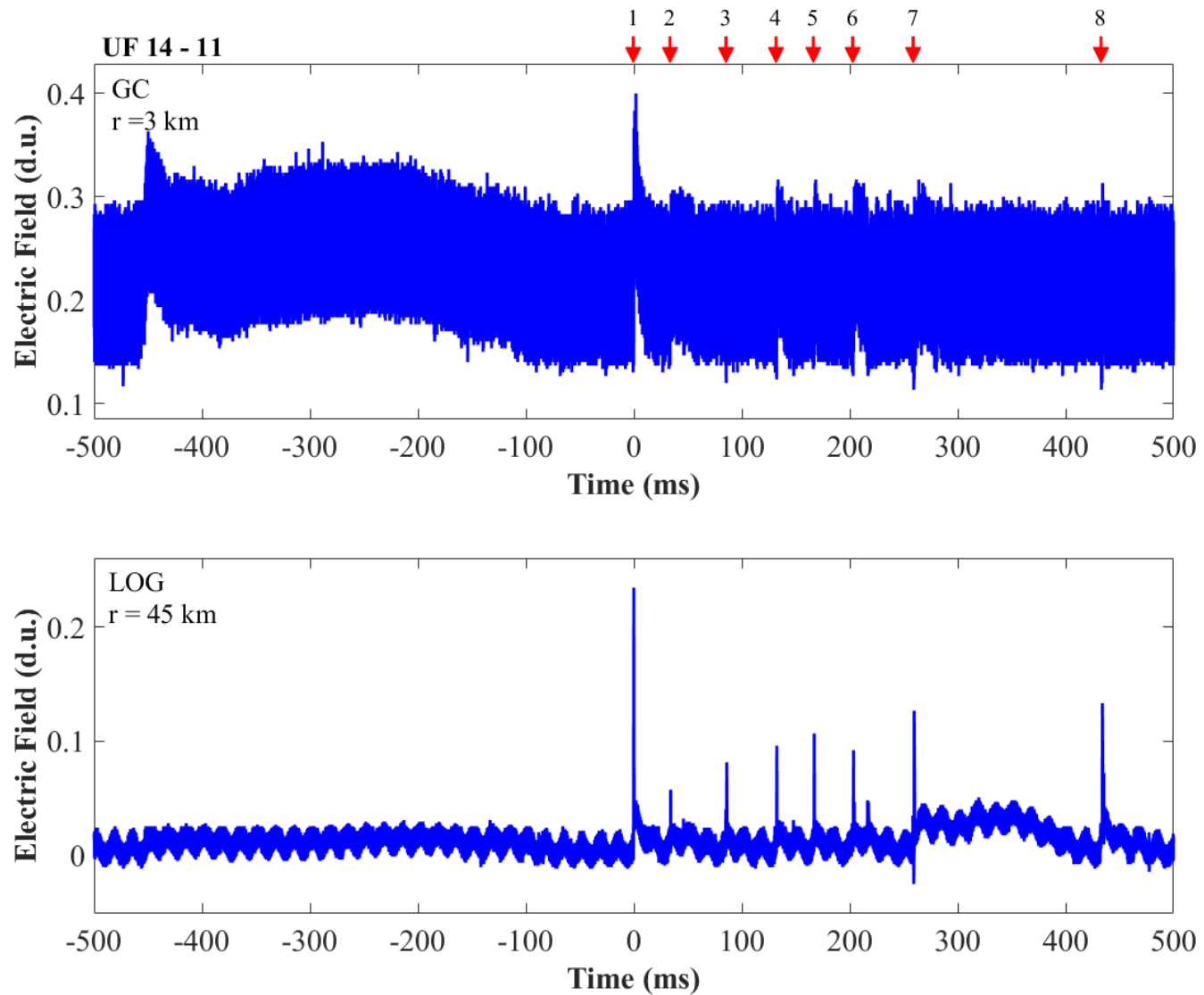


Figure A-45. Two-station electric field waveforms of flash UF 14-11.

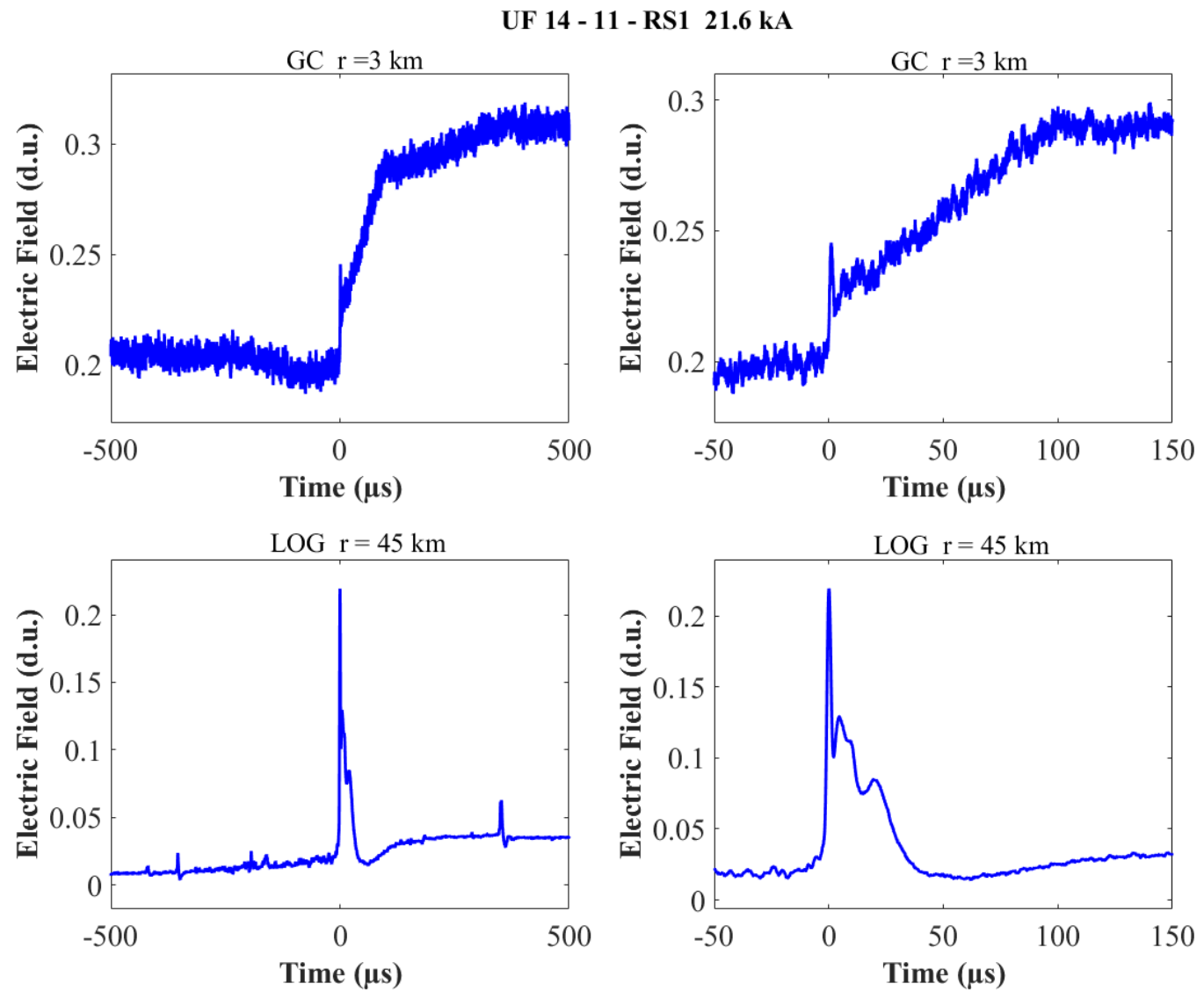


Figure A-46. Two-station electric field waveforms of the RS1 of flash UF 14-11.

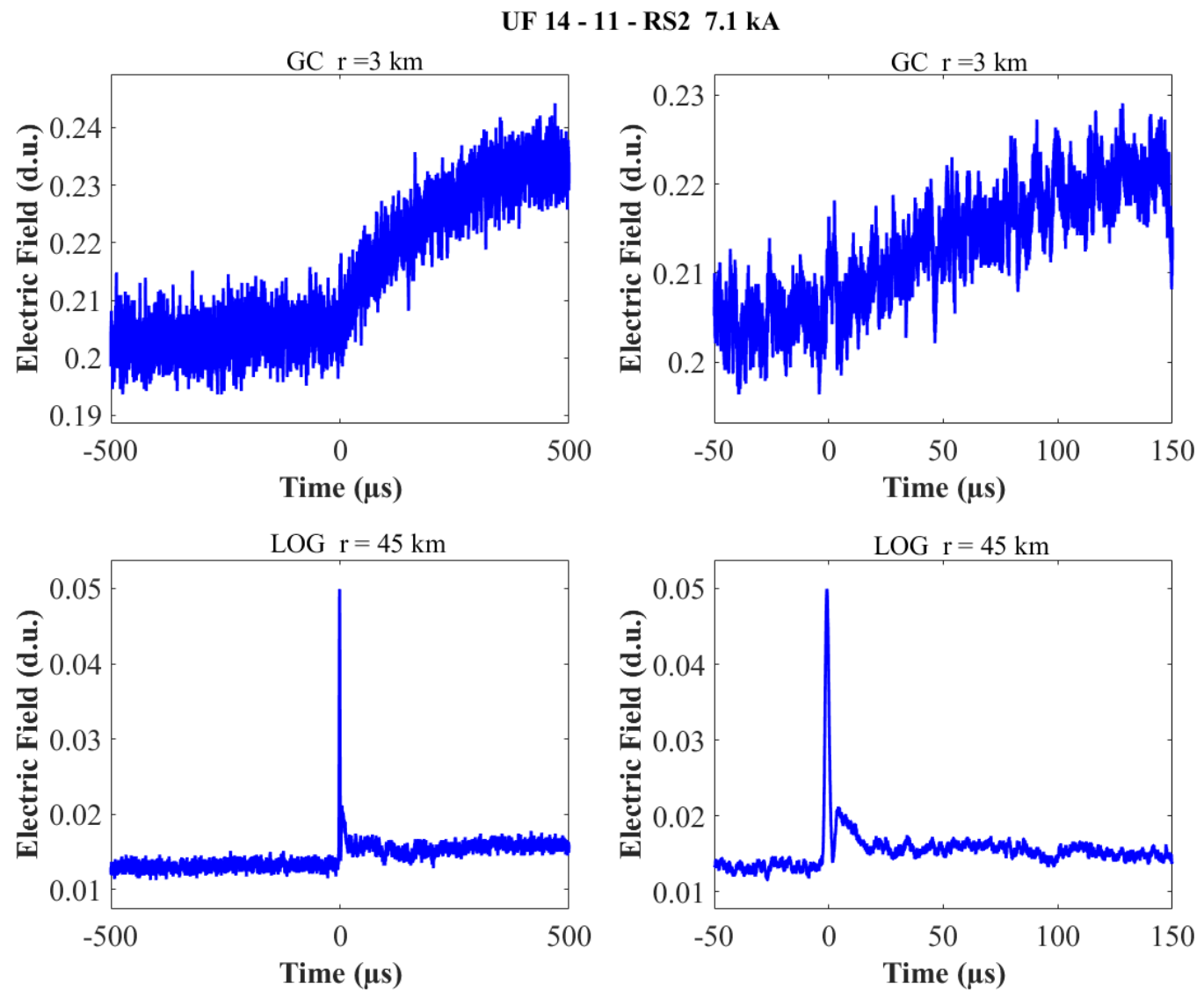


Figure A-47. Two-station electric field waveforms of the RS2 of flash UF 14-11.

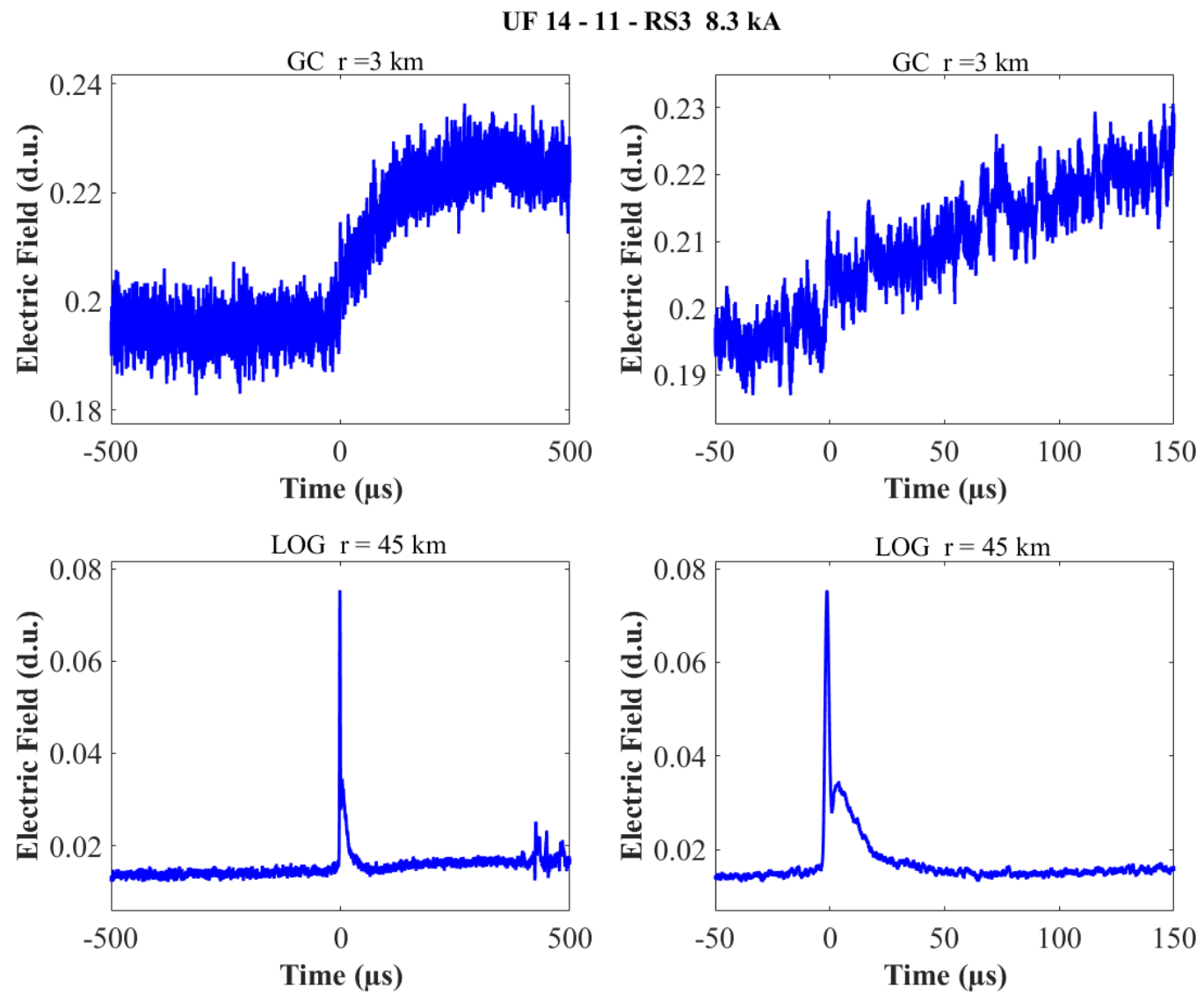


Figure A-48. Two-station electric field waveforms of the RS3 of flash UF 14-11.

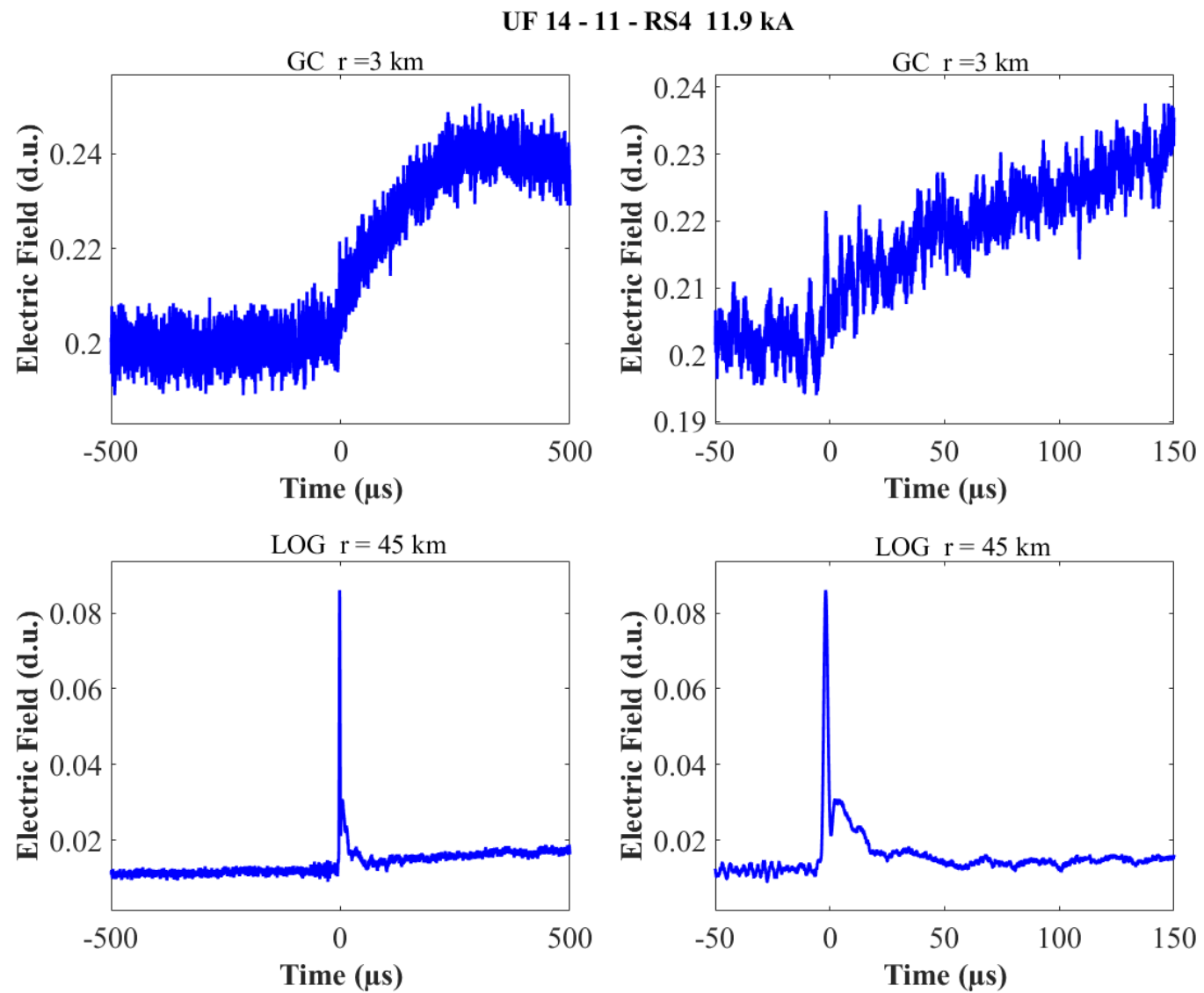


Figure A-49. Two-station electric field waveforms of the RS4 of flash UF 14-11.

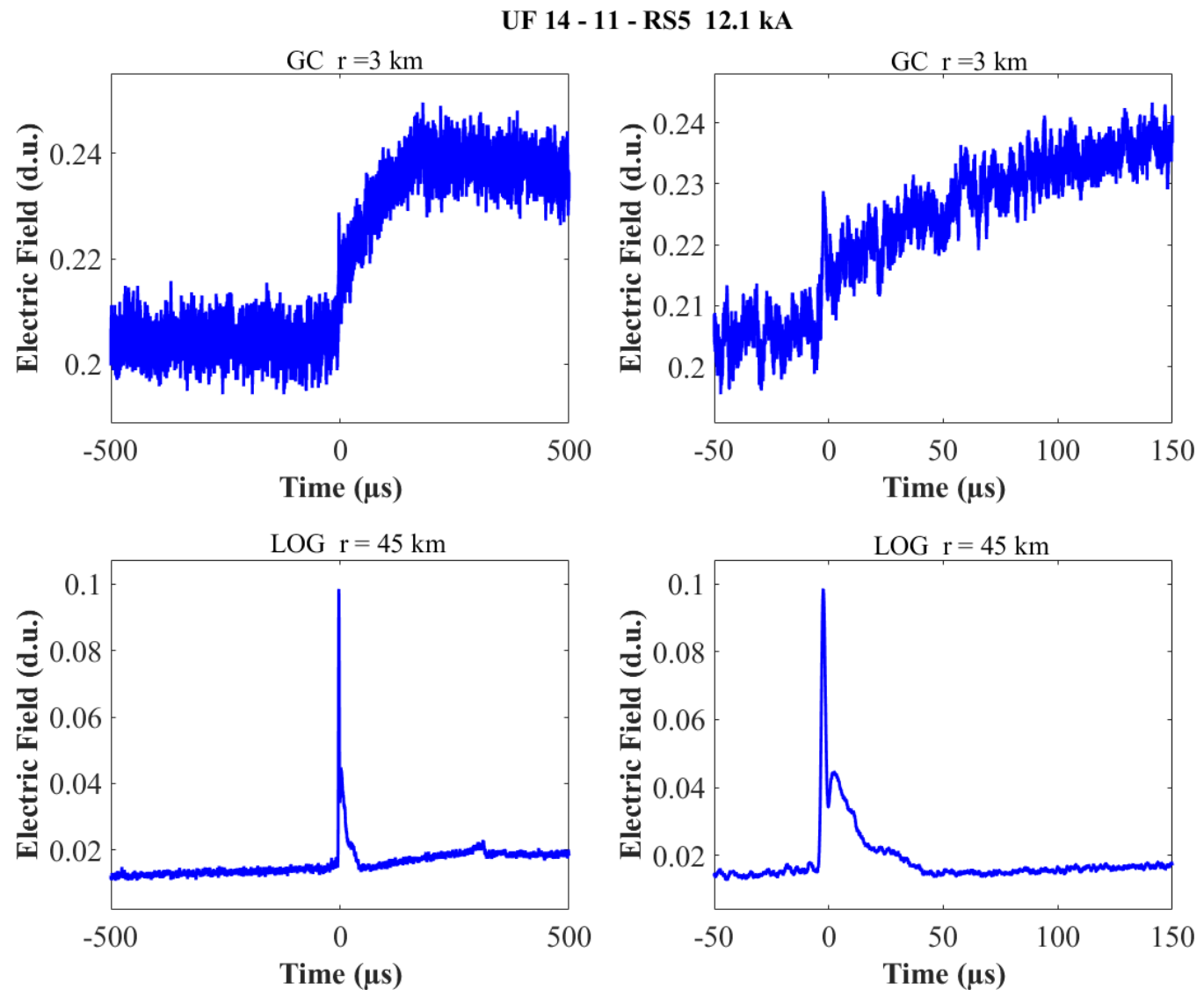


Figure A-50. Two-station electric field waveforms of the RS5 of flash UF 14-11.

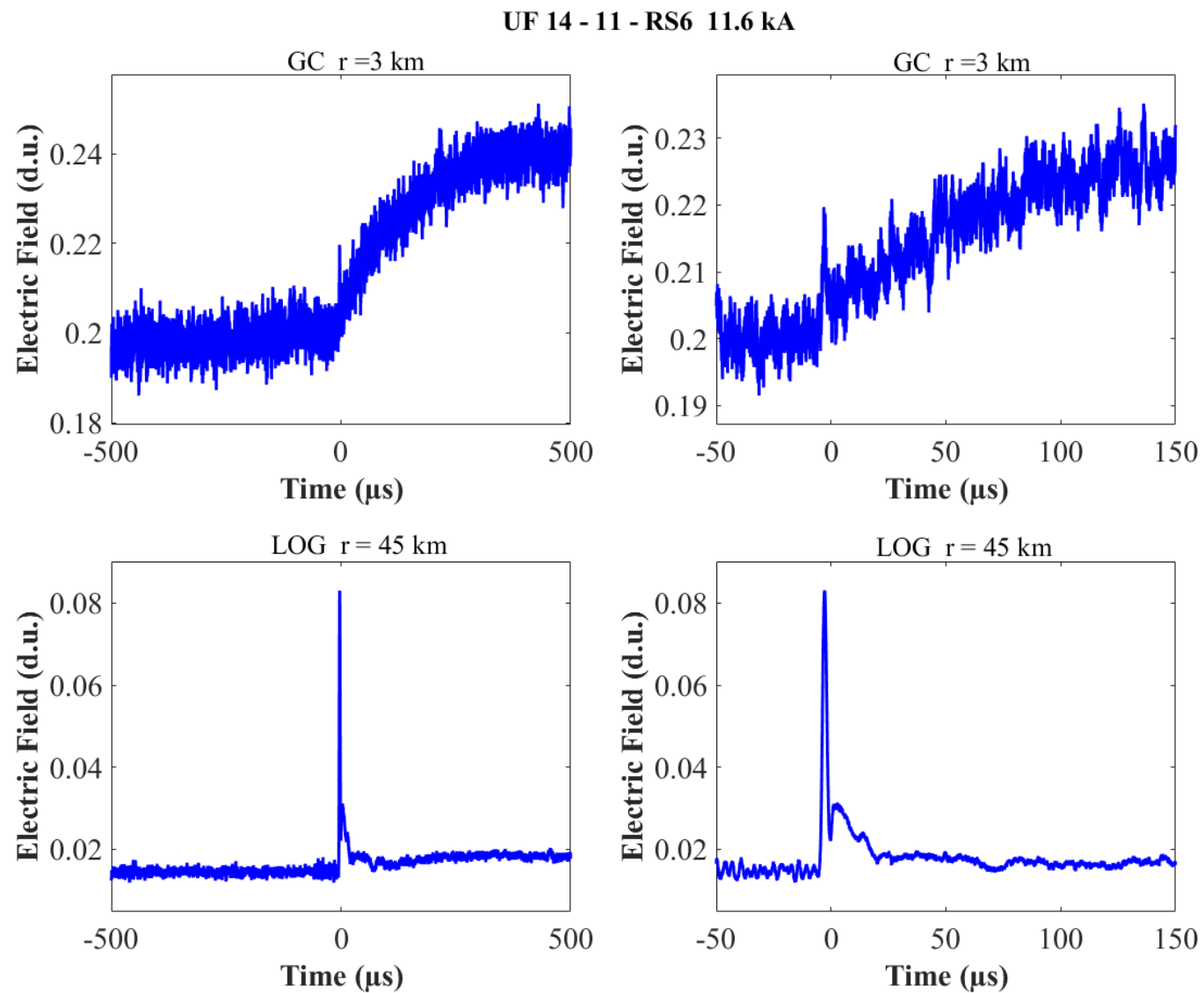


Figure A-51. Two-station electric field waveforms of the RS6 of flash UF 14-11.

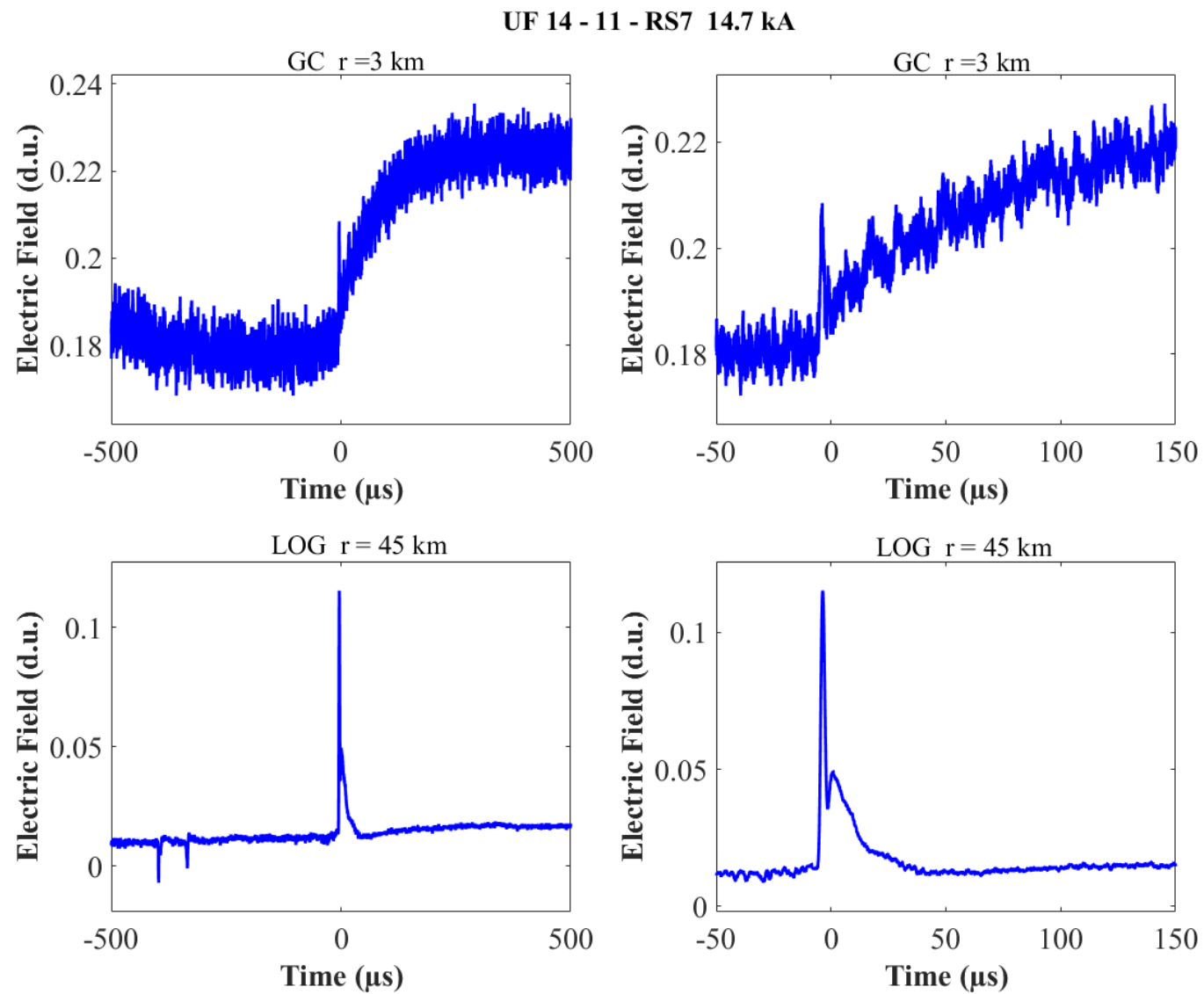


Figure A-52. Two-station electric field waveforms of the RS7 of flash UF 14-11.

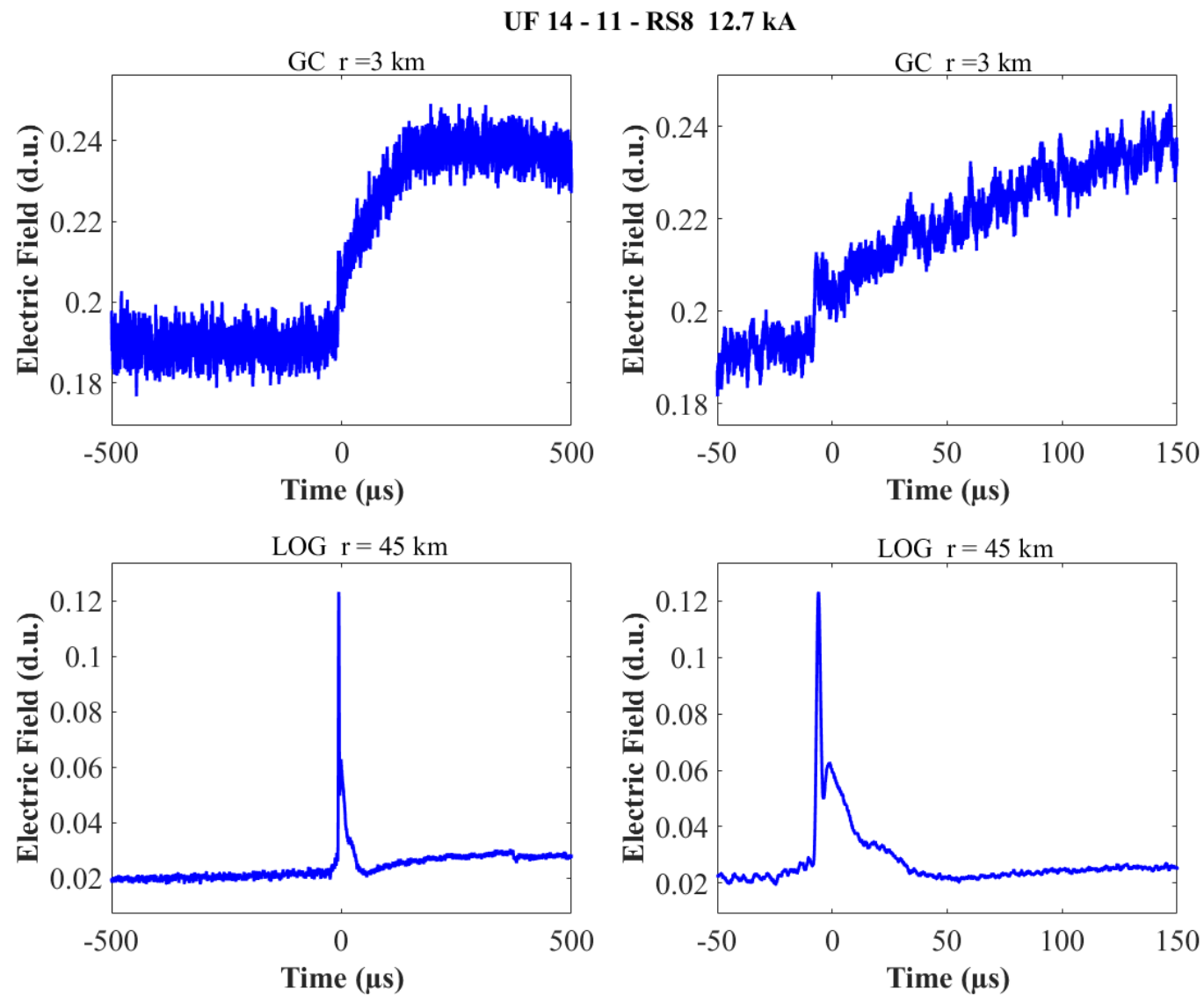


Figure A-53. Two-station electric field waveforms of the RS8 of flash UF 14-11.

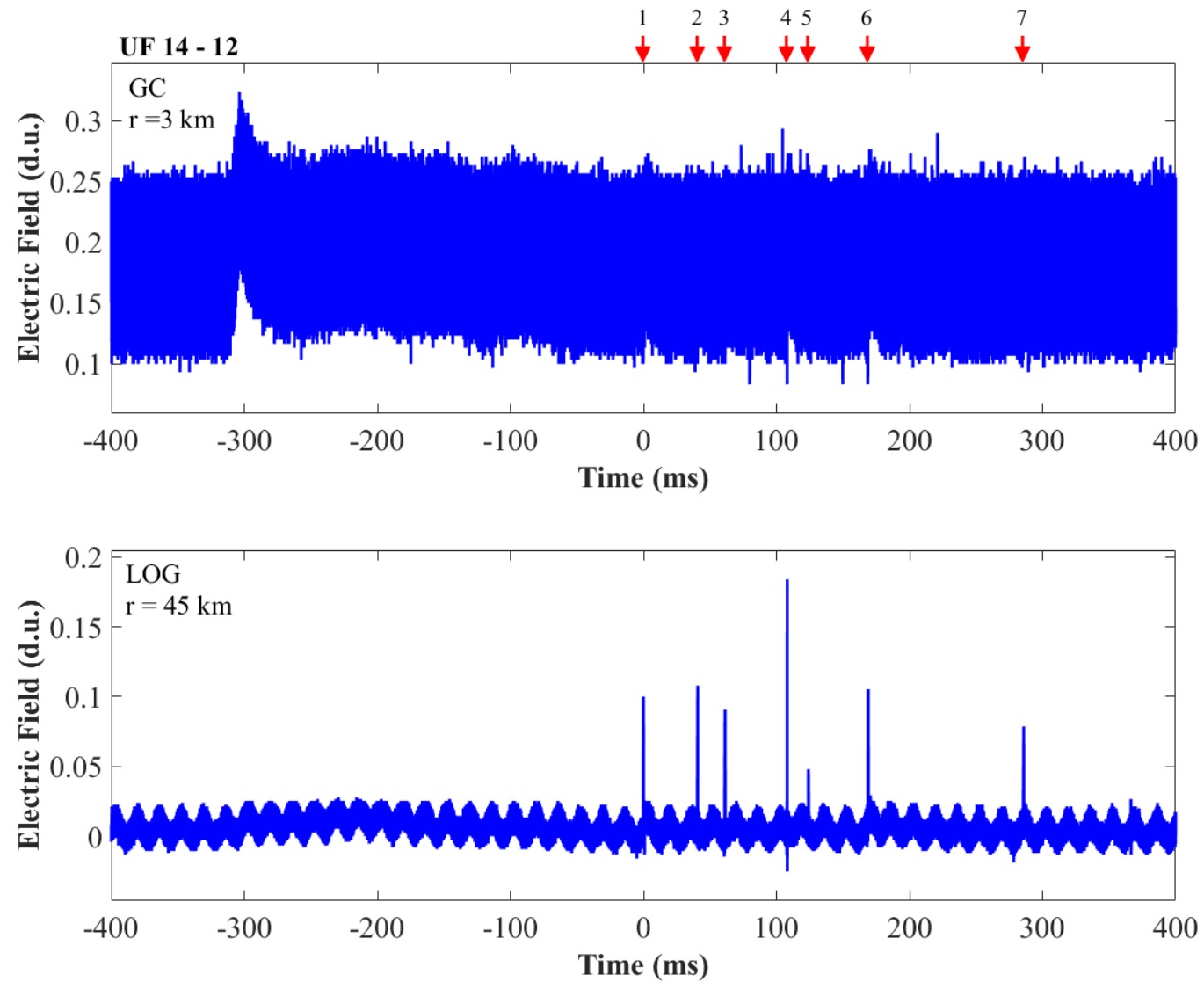


Figure A-54. Two-station electric field waveforms of flash UF 14-12.

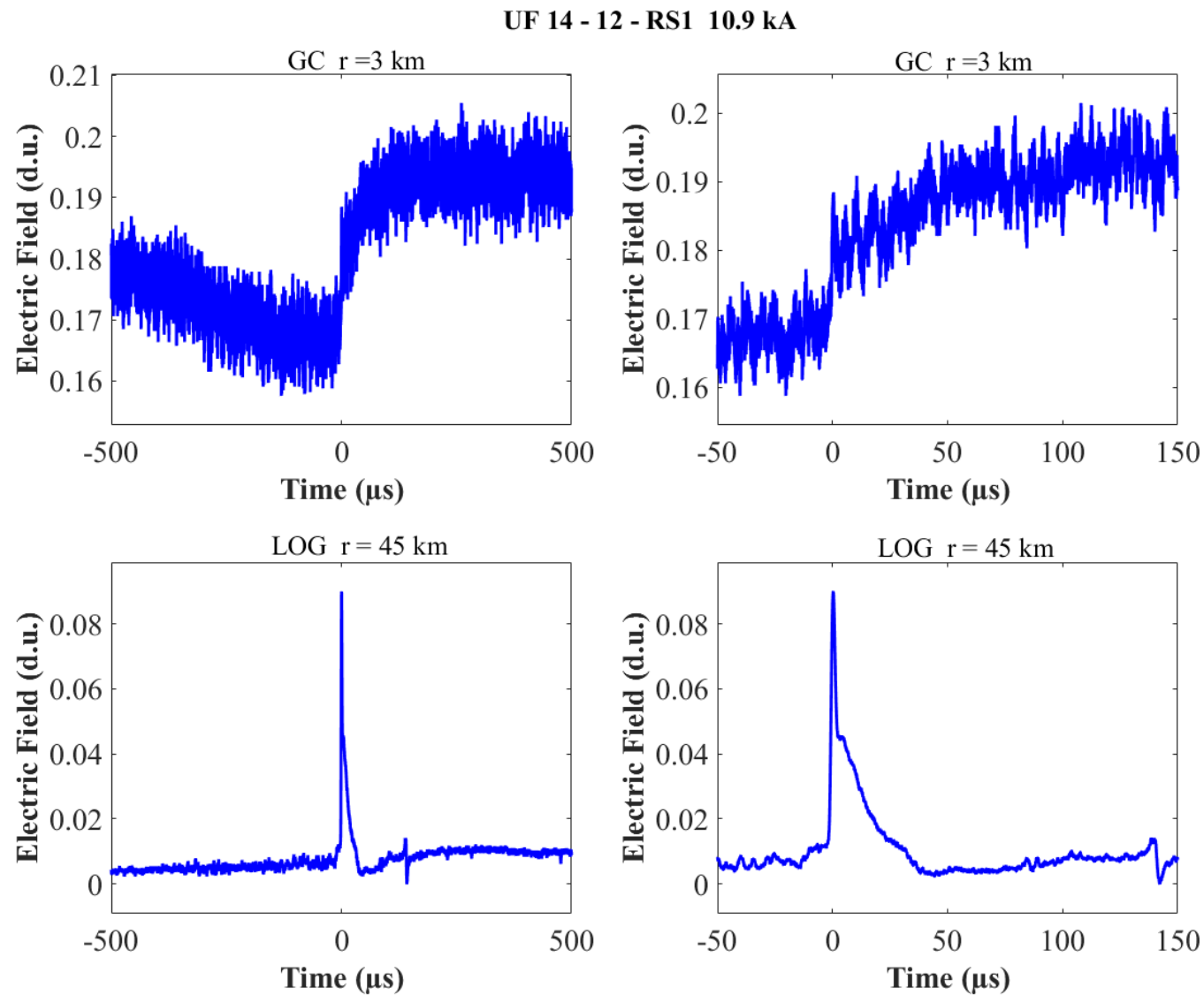


Figure A-55. Two-station electric field waveforms of the RS1 of flash UF 14-12.

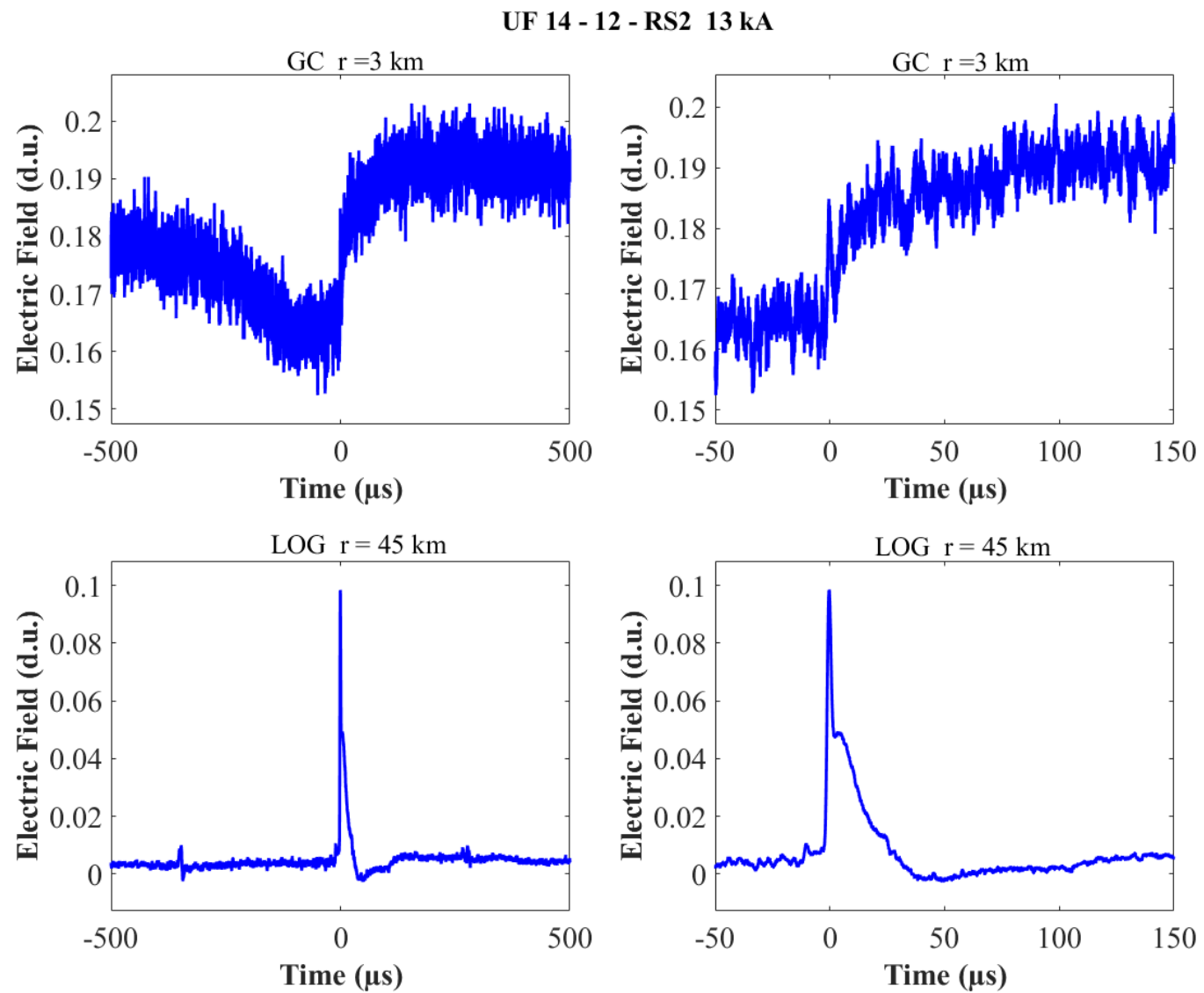


Figure A-56. Two-station electric field waveforms of the RS2 of flash UF 14-12.

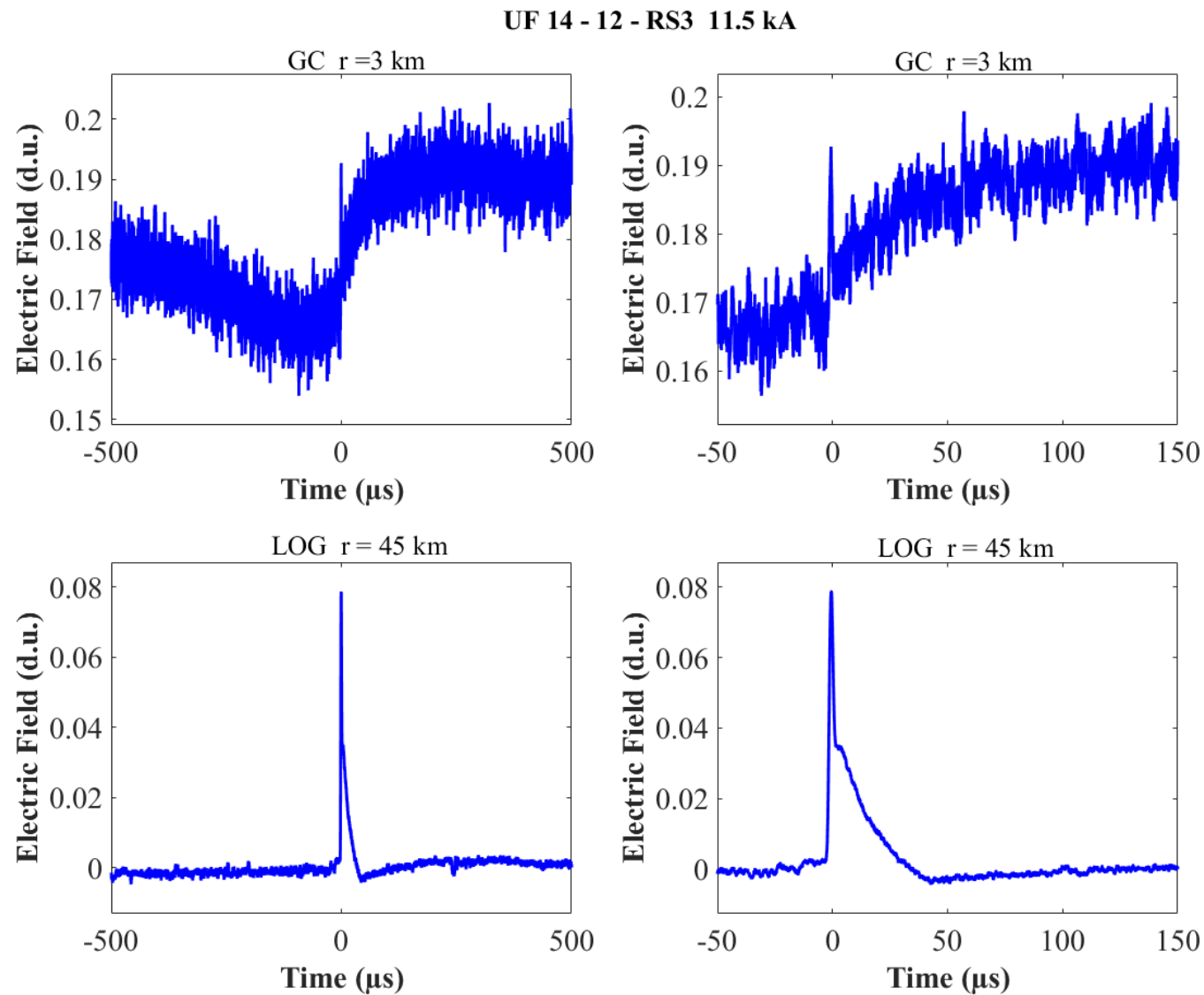


Figure A-57. Two-station electric field waveforms of the RS3 of flash UF 14-12.

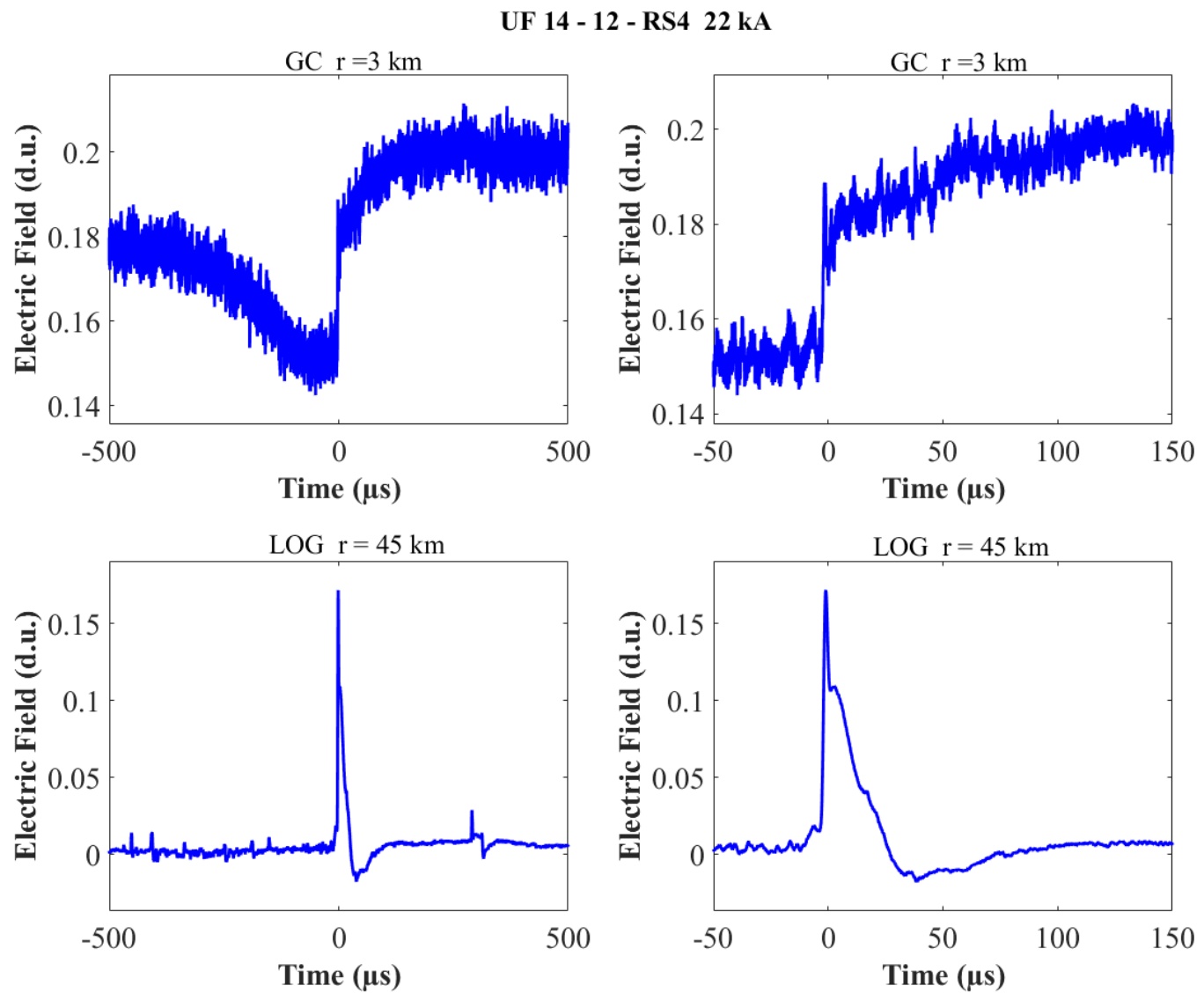


Figure A-58. Two-station electric field waveforms of the RS4 of flash UF 14-12.

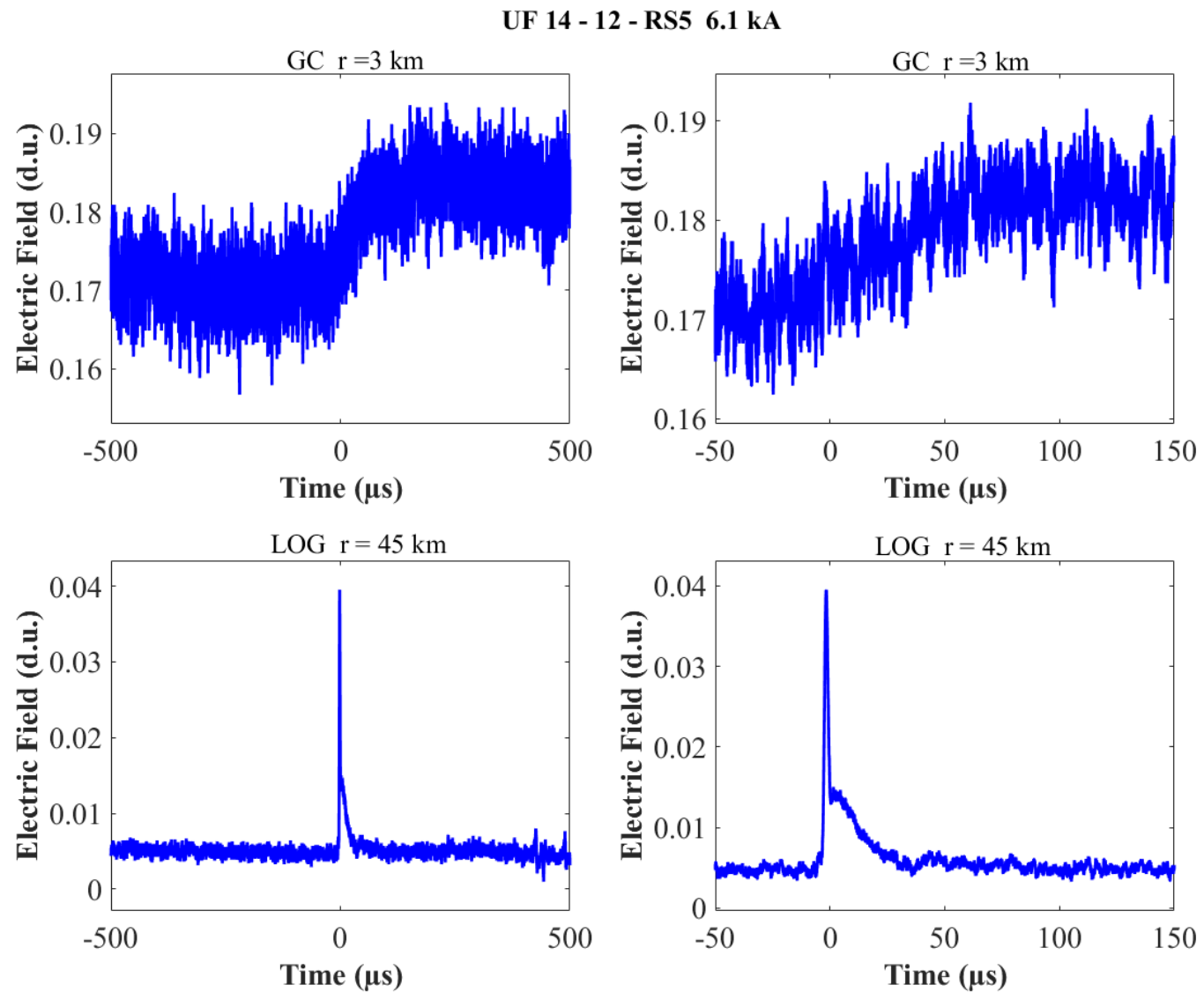


Figure A-59. Two-station electric field waveforms of the RS5 of flash UF 14-12.

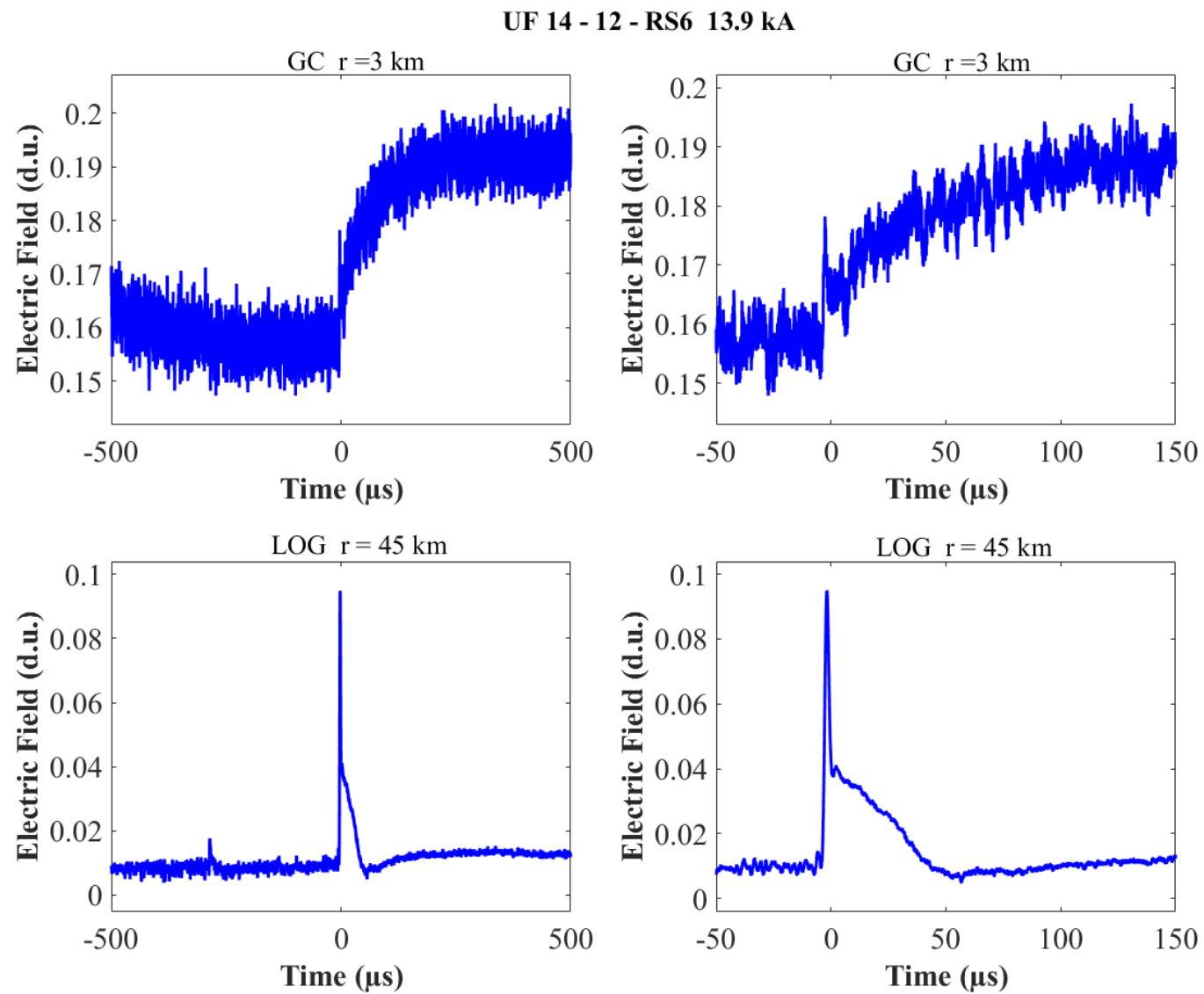


Figure A-60. Two-station electric field waveforms of the RS6 of flash UF 14-12.

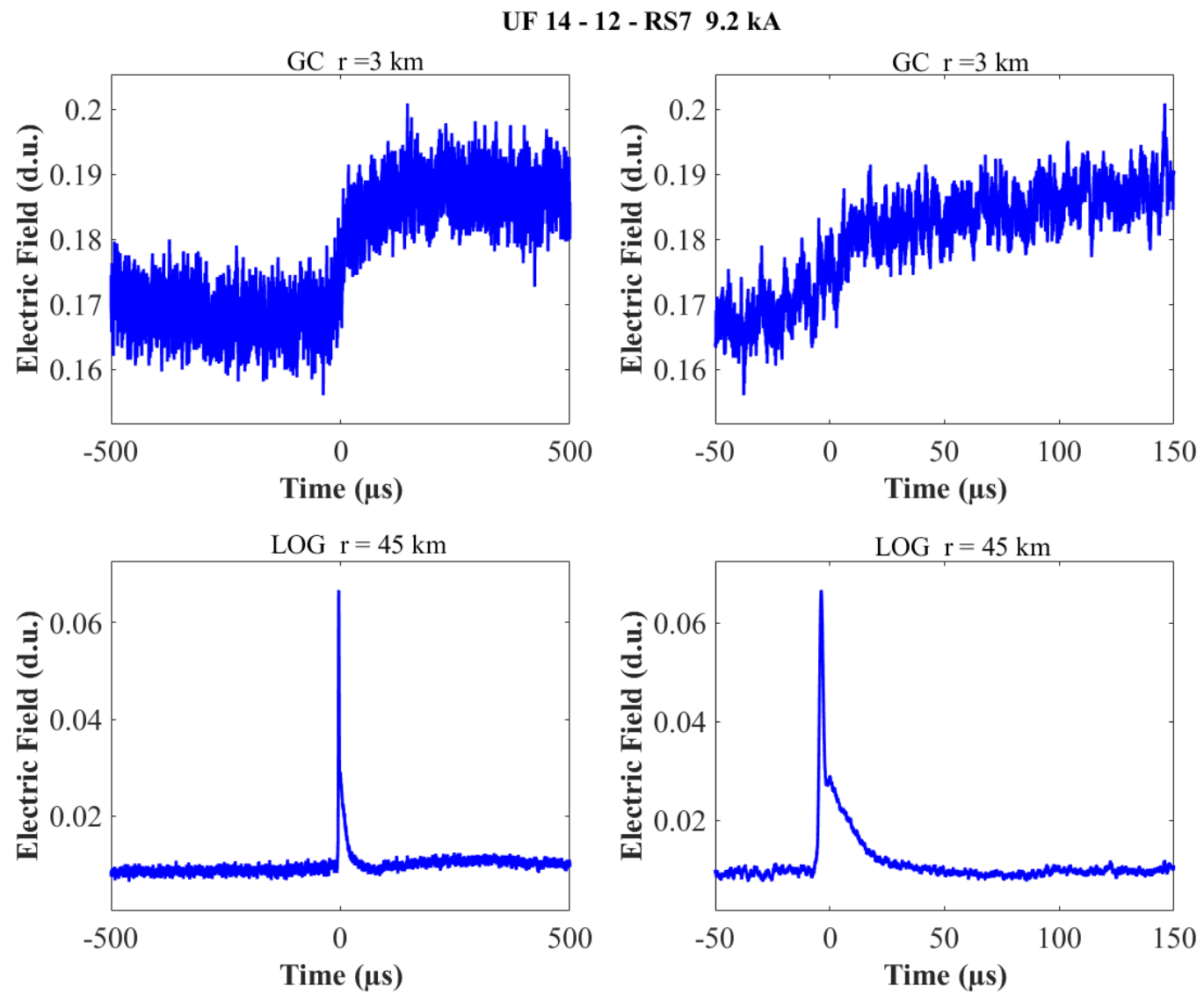


Figure A-61. Two-station electric field waveforms of the RS7 of flash UF 14-12.

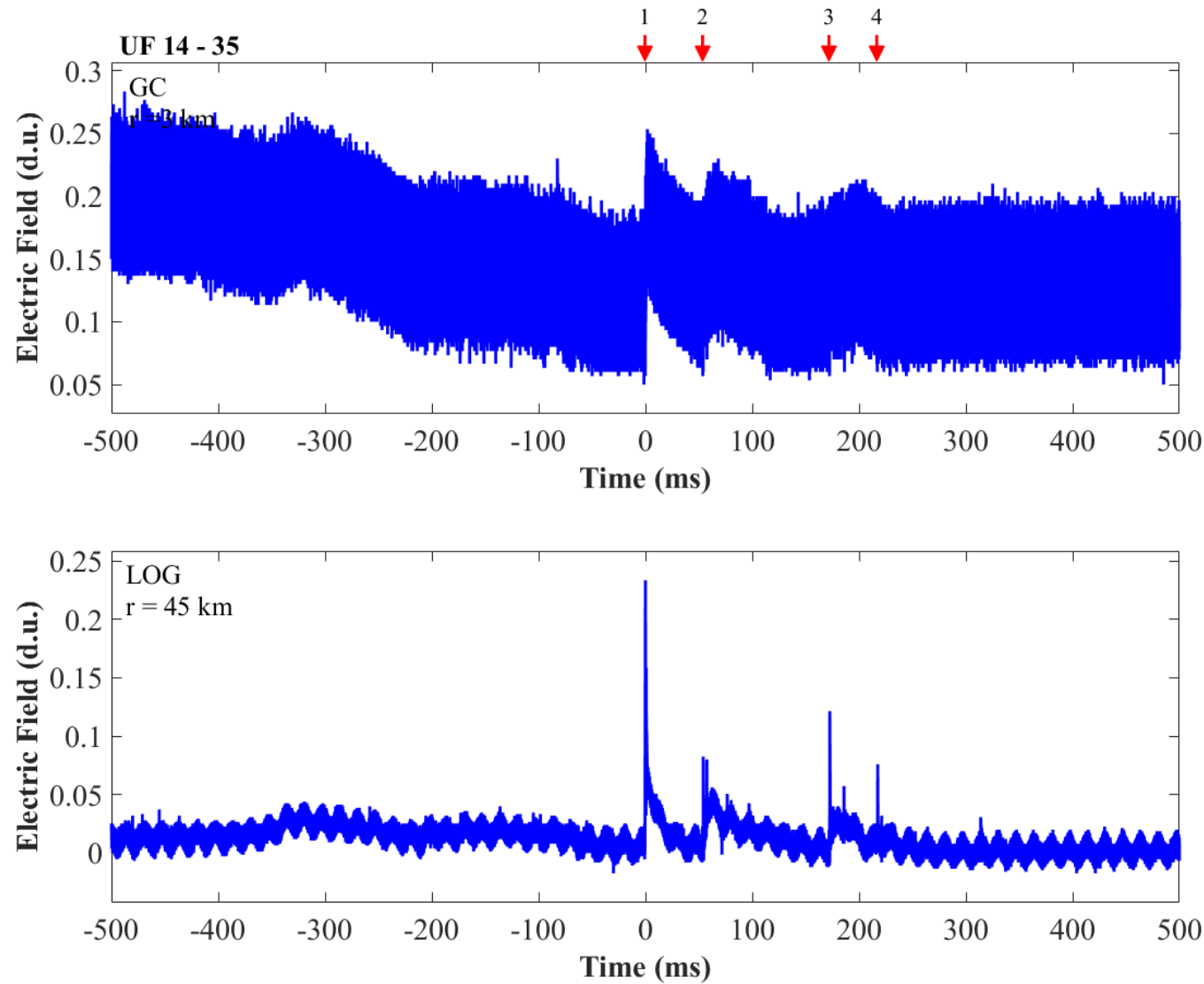


Figure A-62. Two-station electric field waveforms of flash UF 14-35.

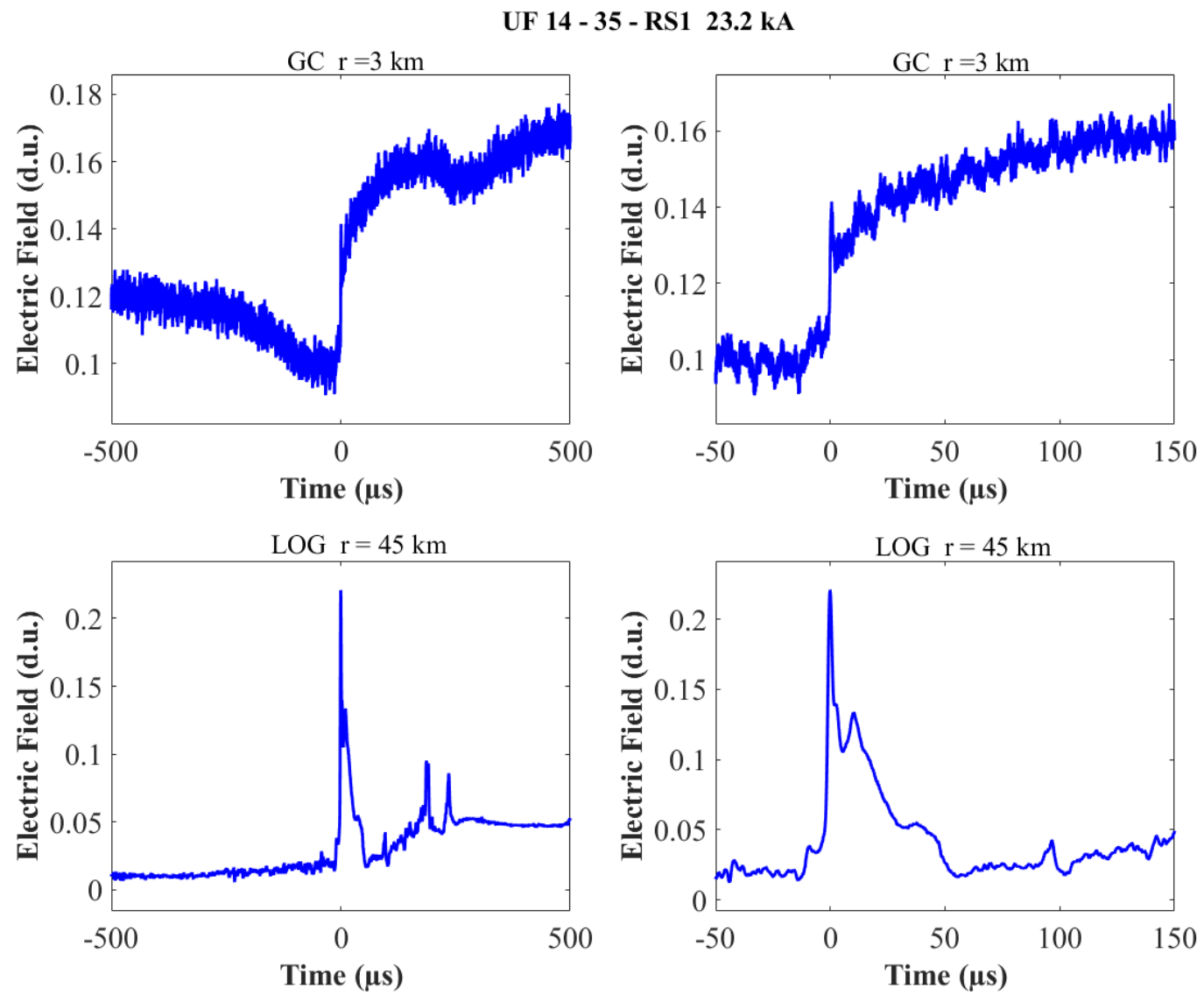


Figure A-63. Two-station electric field waveforms of the RS1 of flash UF 14-35.

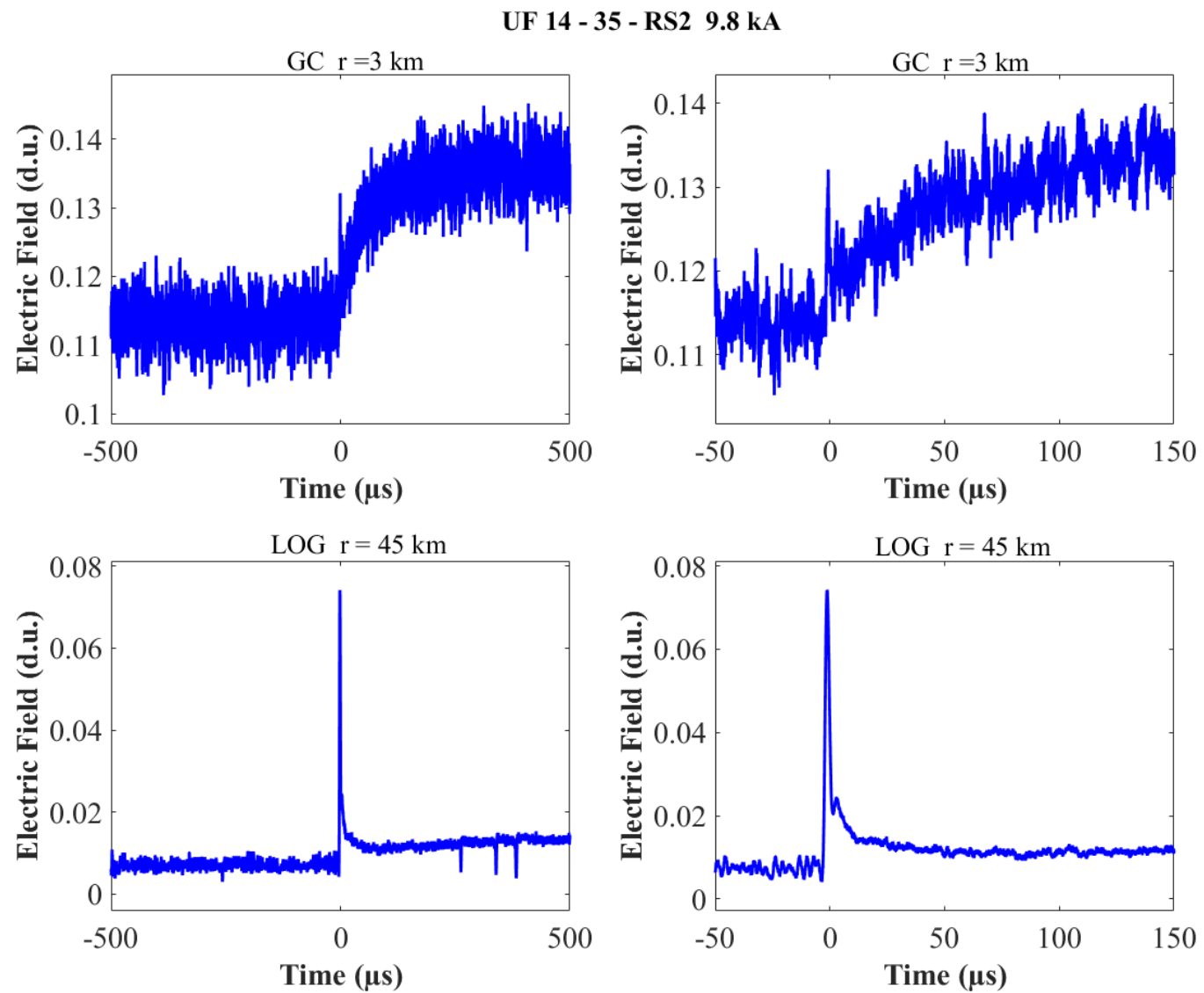


Figure A-64. Two-station electric field waveforms of the RS2 of flash UF 14-35.

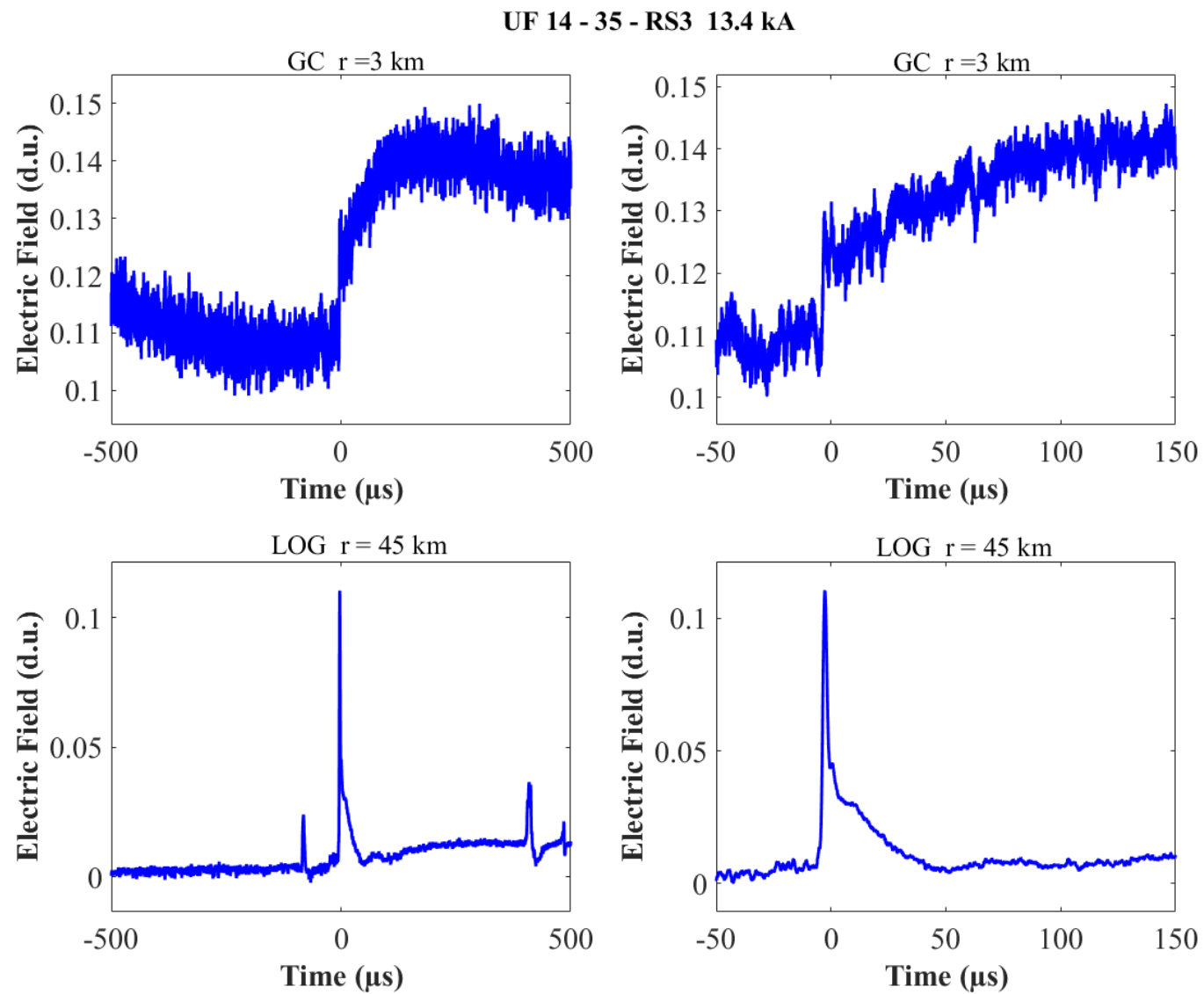


Figure A-65. Two-station electric field waveforms of the RS3 of flash UF 14-35.

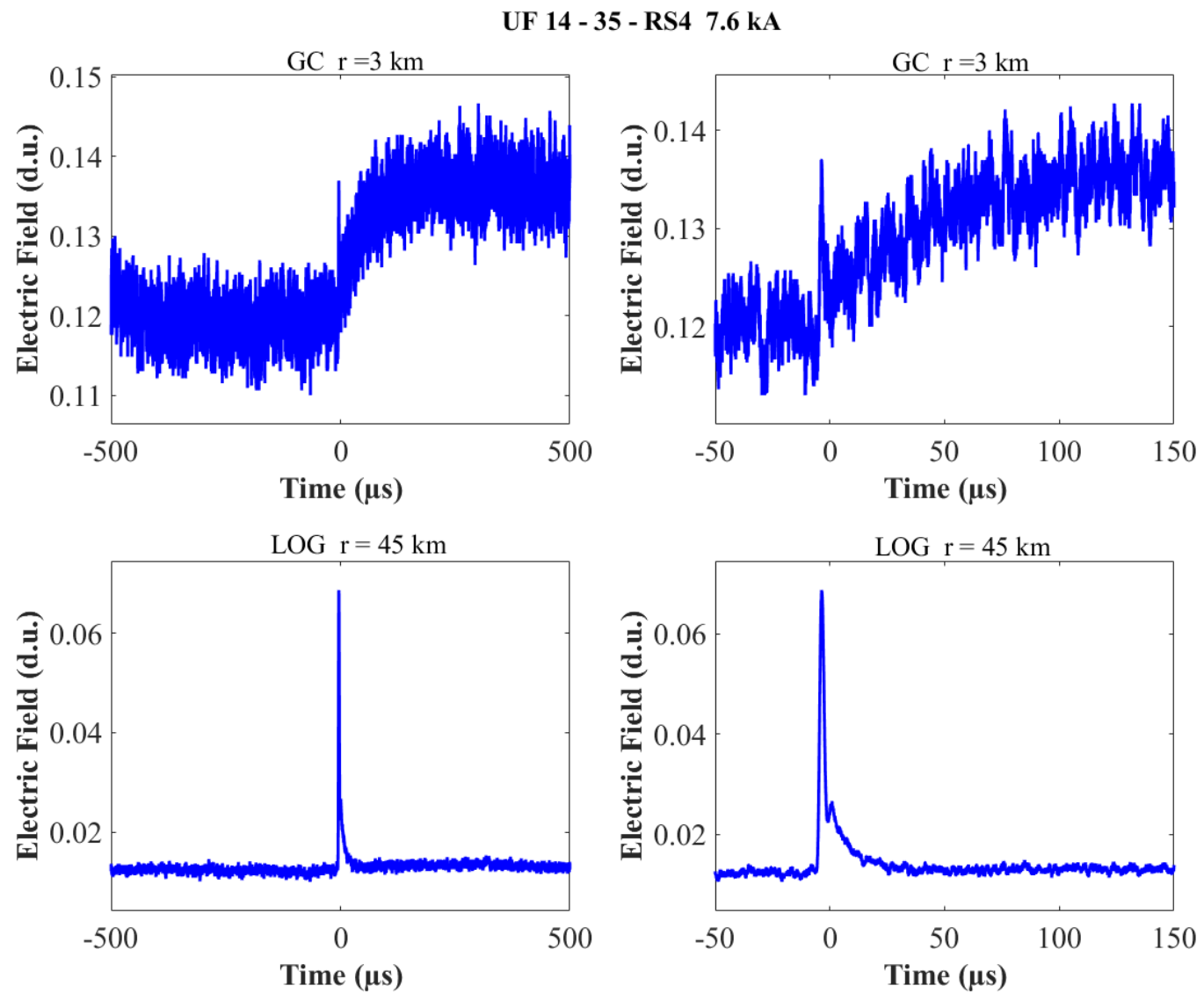


Figure A-66. Two-station electric field waveforms of the RS4 of flash UF 14-35.

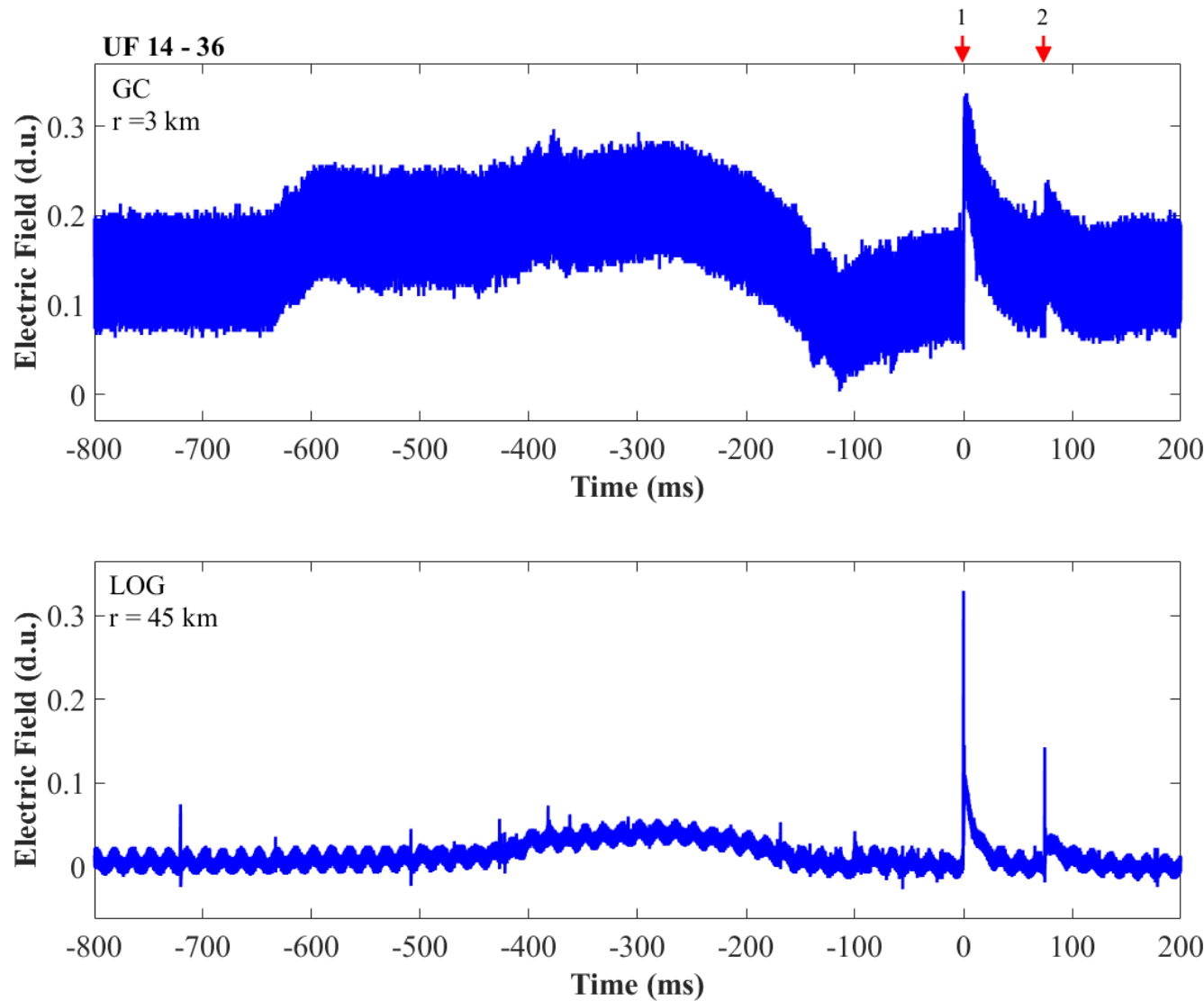


Figure A-67. Two-station electric field waveforms of flash UF 14-36.

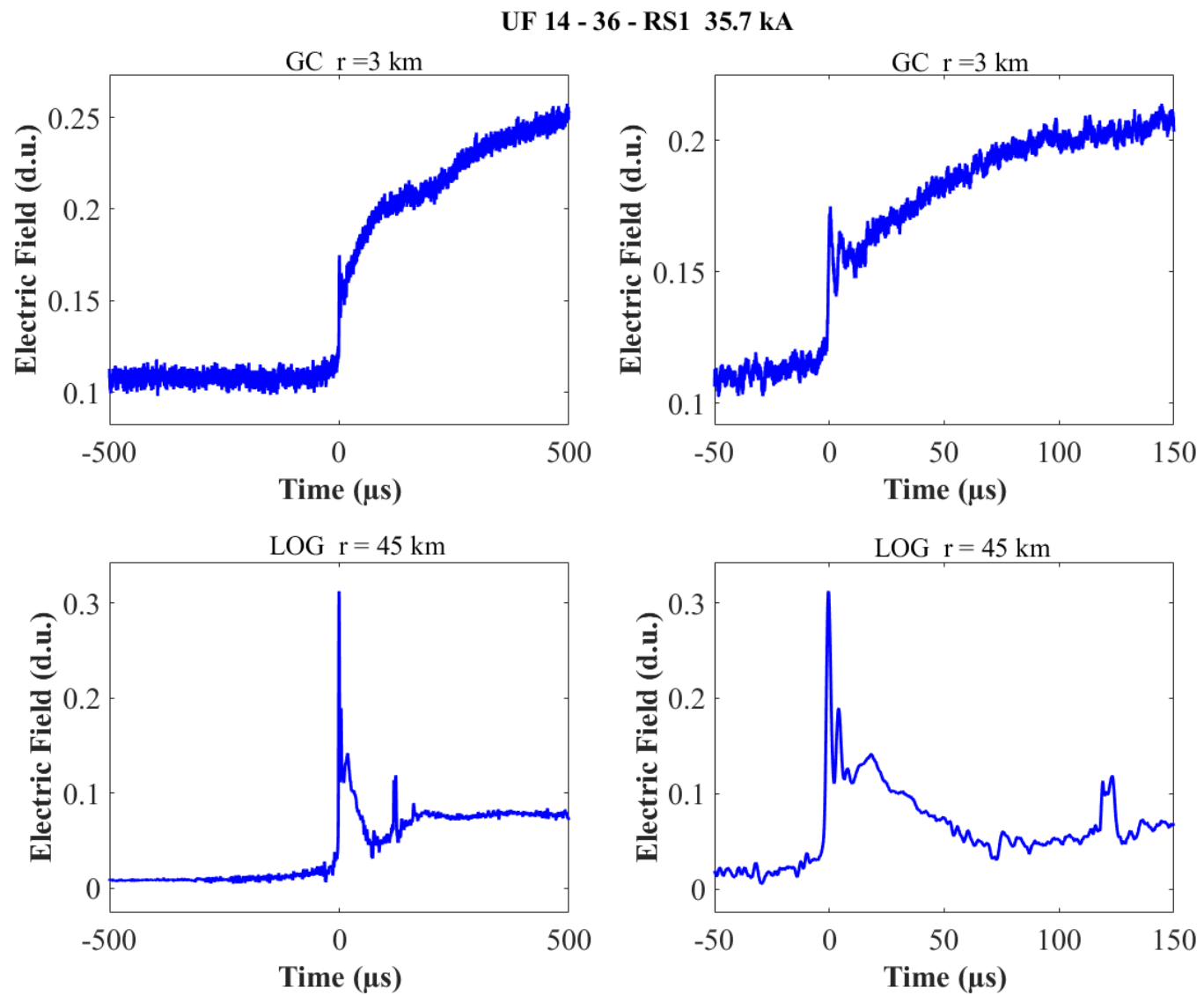


Figure A-68. Two-station electric field waveforms of the RS1 of flash UF 14-36.

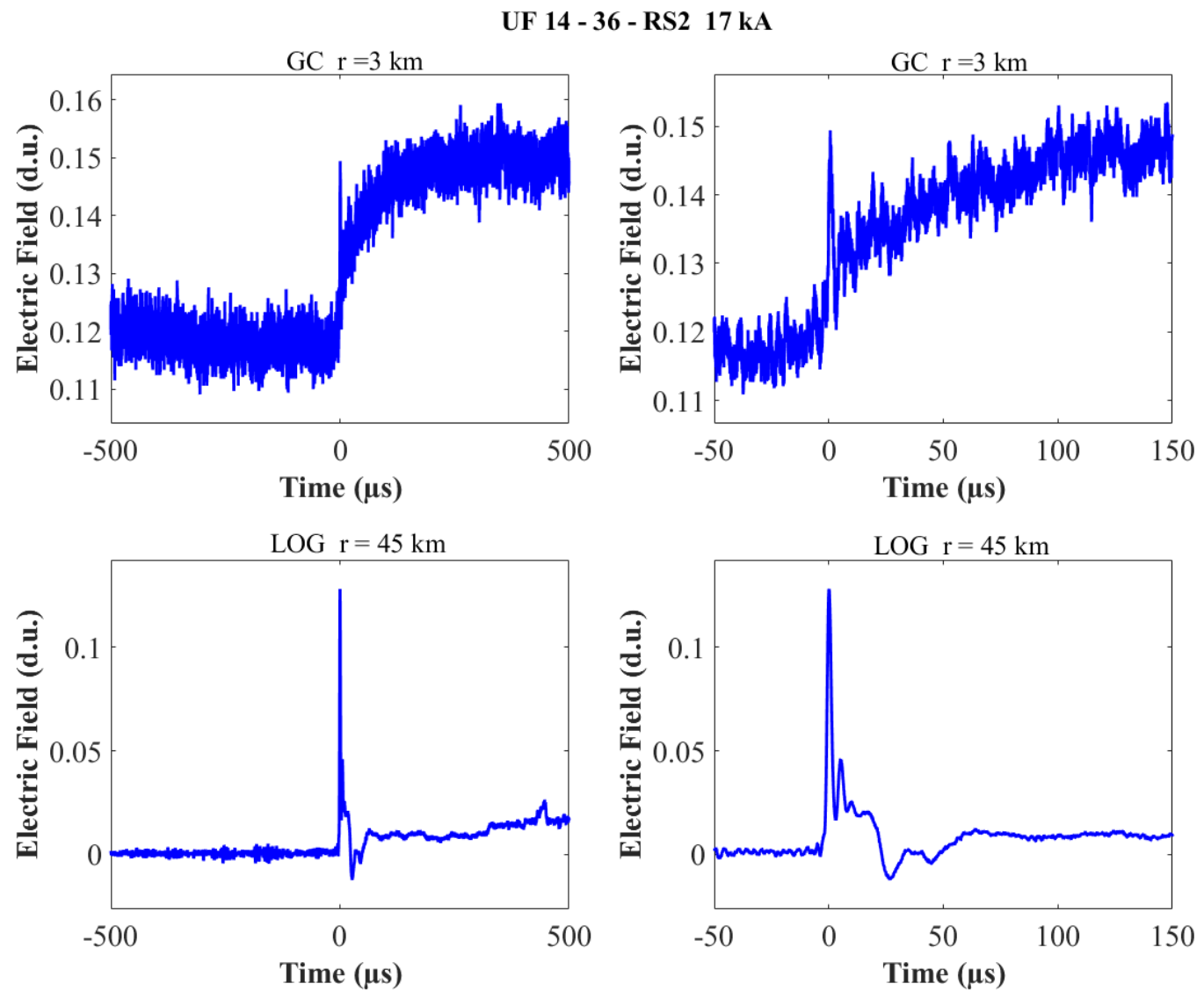


Figure A-69. Two-station electric field waveforms of the RS2 of flash UF 14-36.

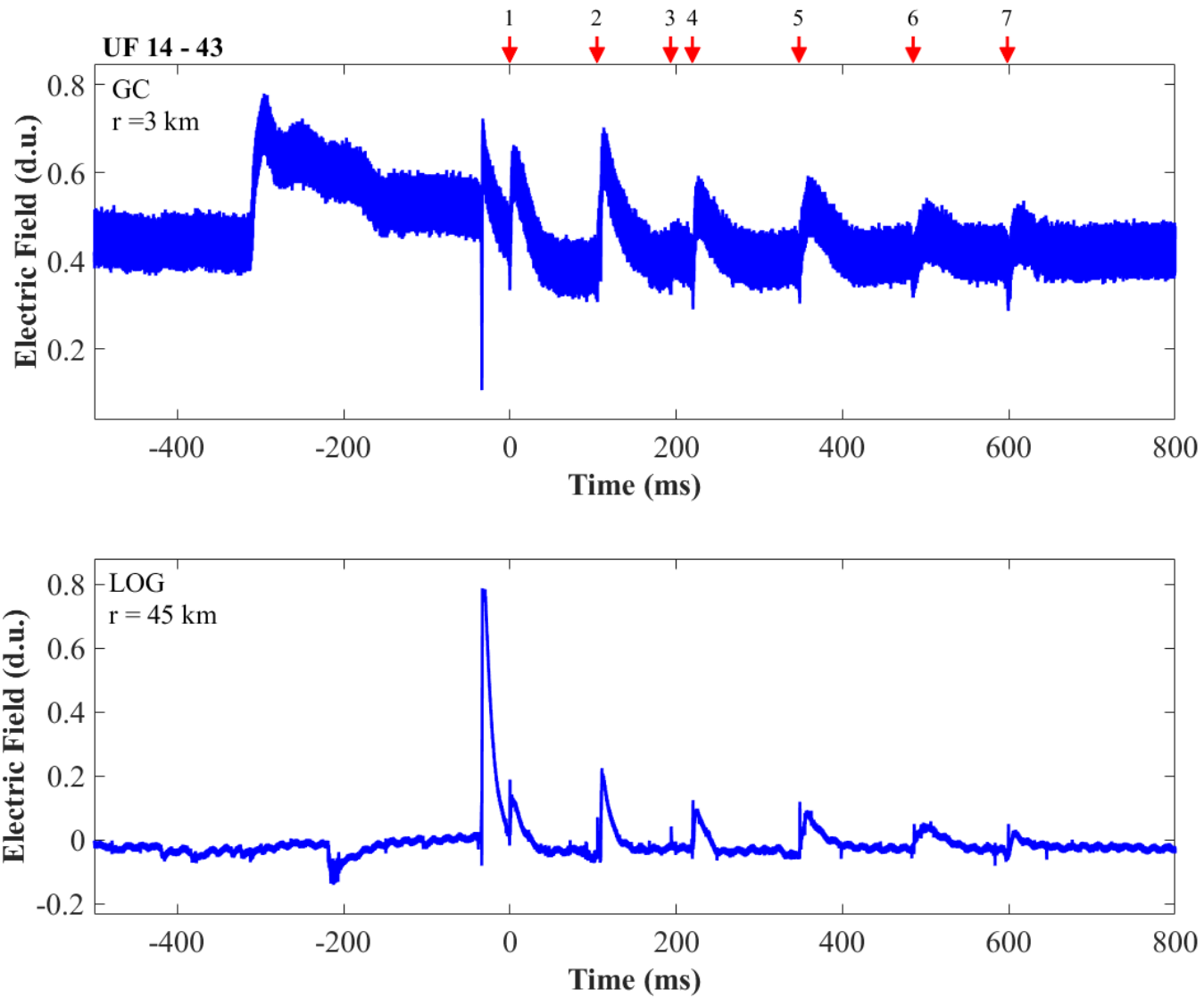


Figure A-70. Two-station electric field waveforms of flash UF 14-43.

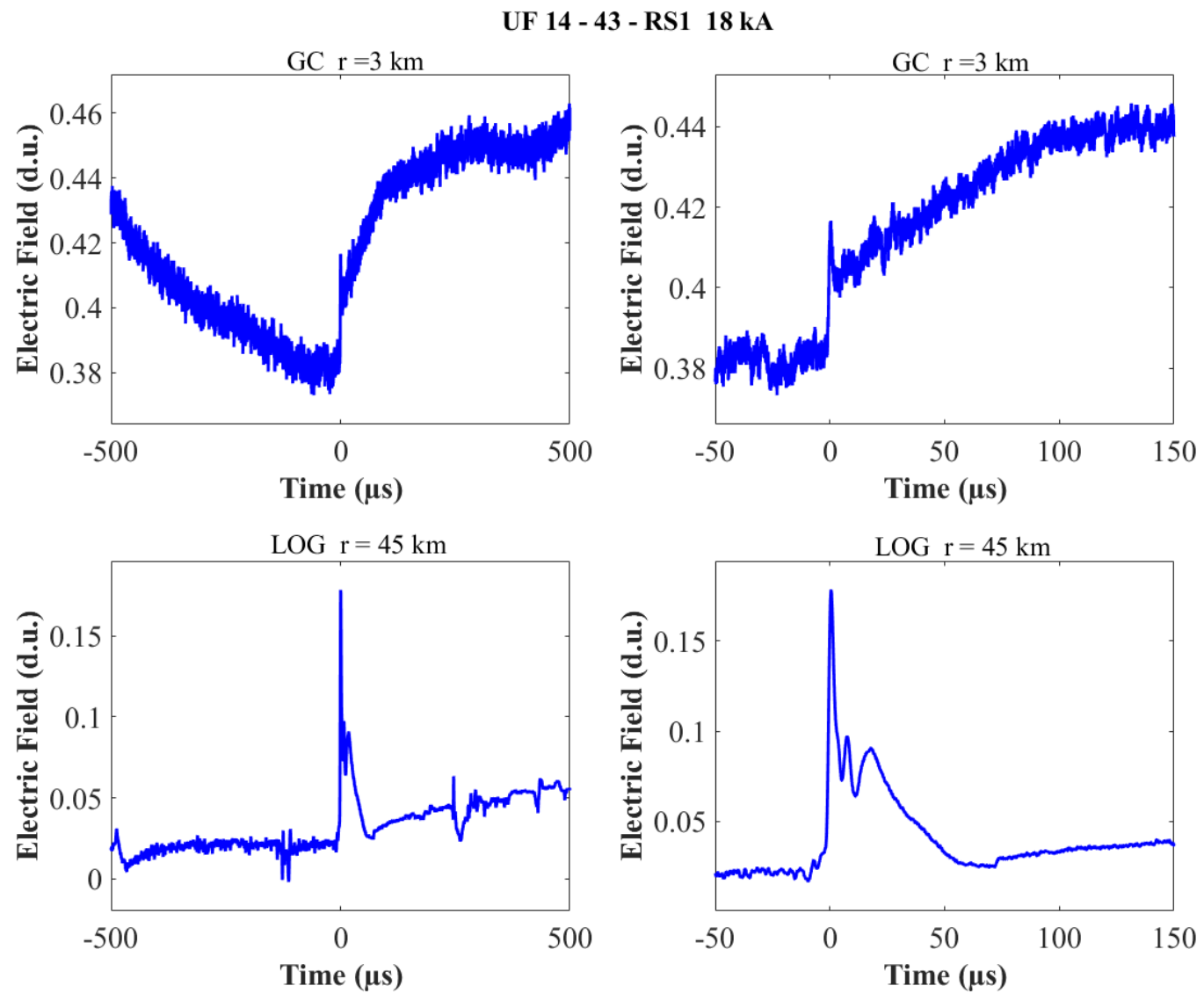


Figure A-71. Two-station electric field waveforms of the RS1 of flash UF 14-43.

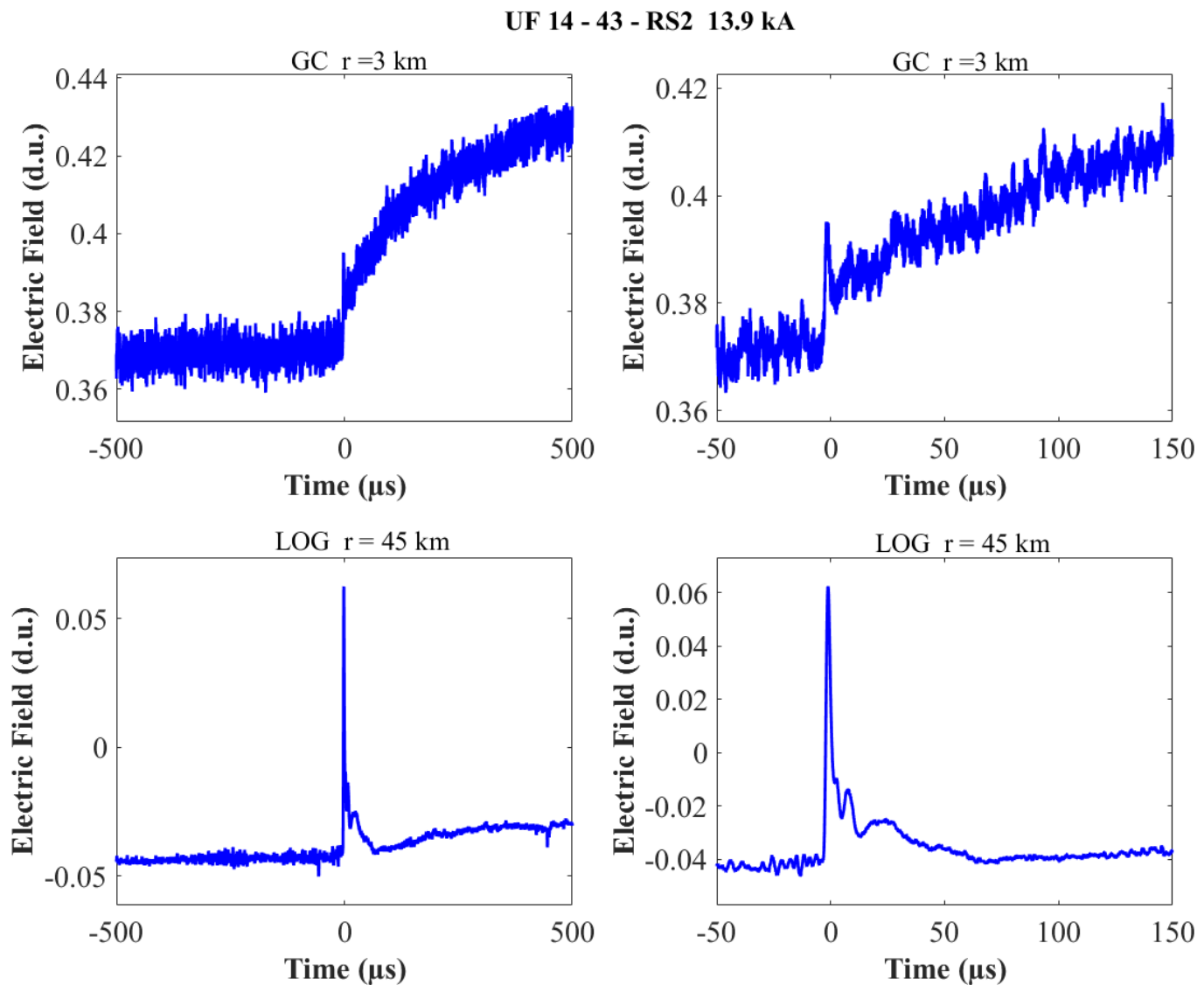


Figure A-72. Two-station electric field waveforms of the RS2 of flash UF 14-43.

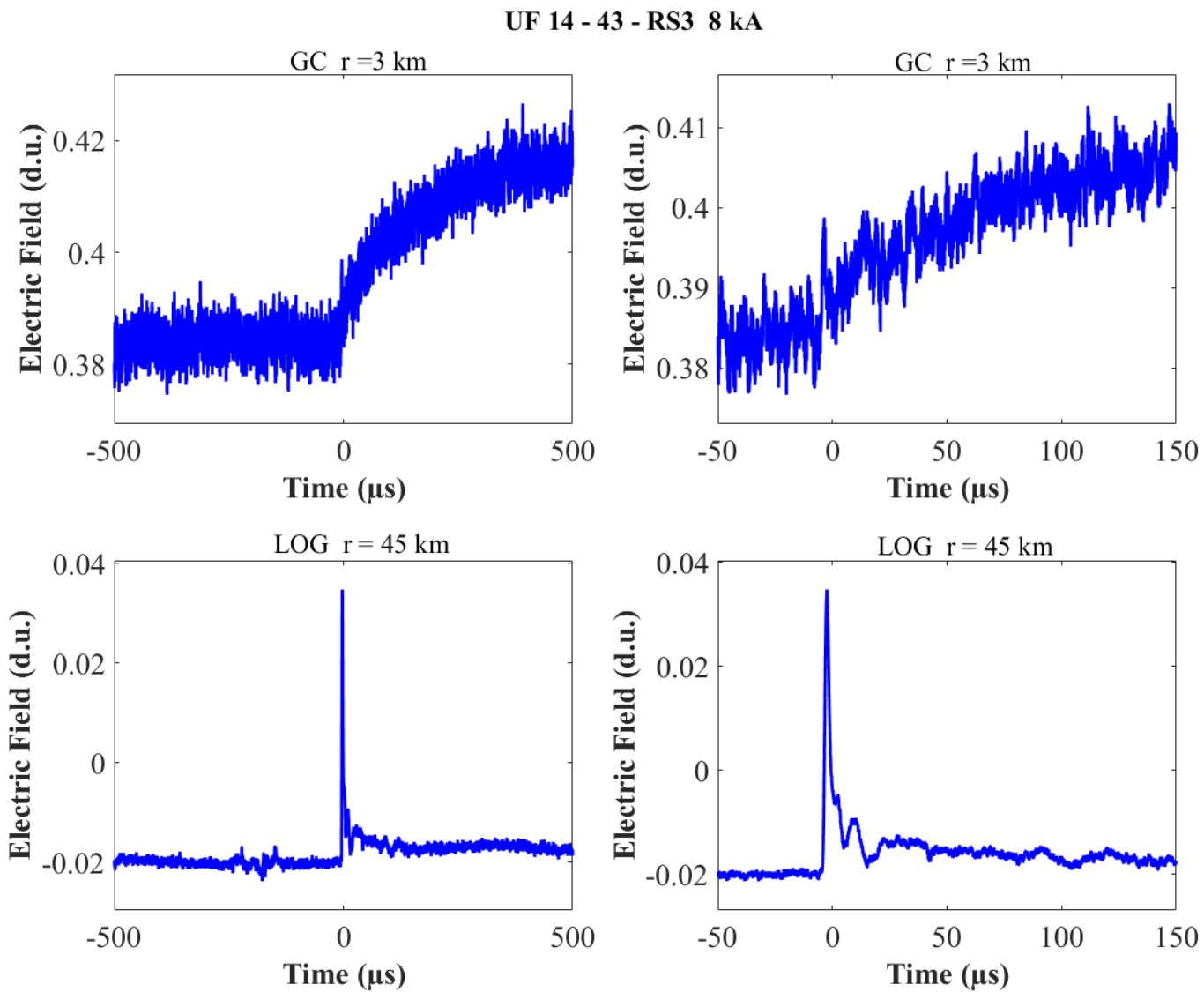


Figure A-73. Two-station electric field waveforms of the RS3 of flash UF 14-43.

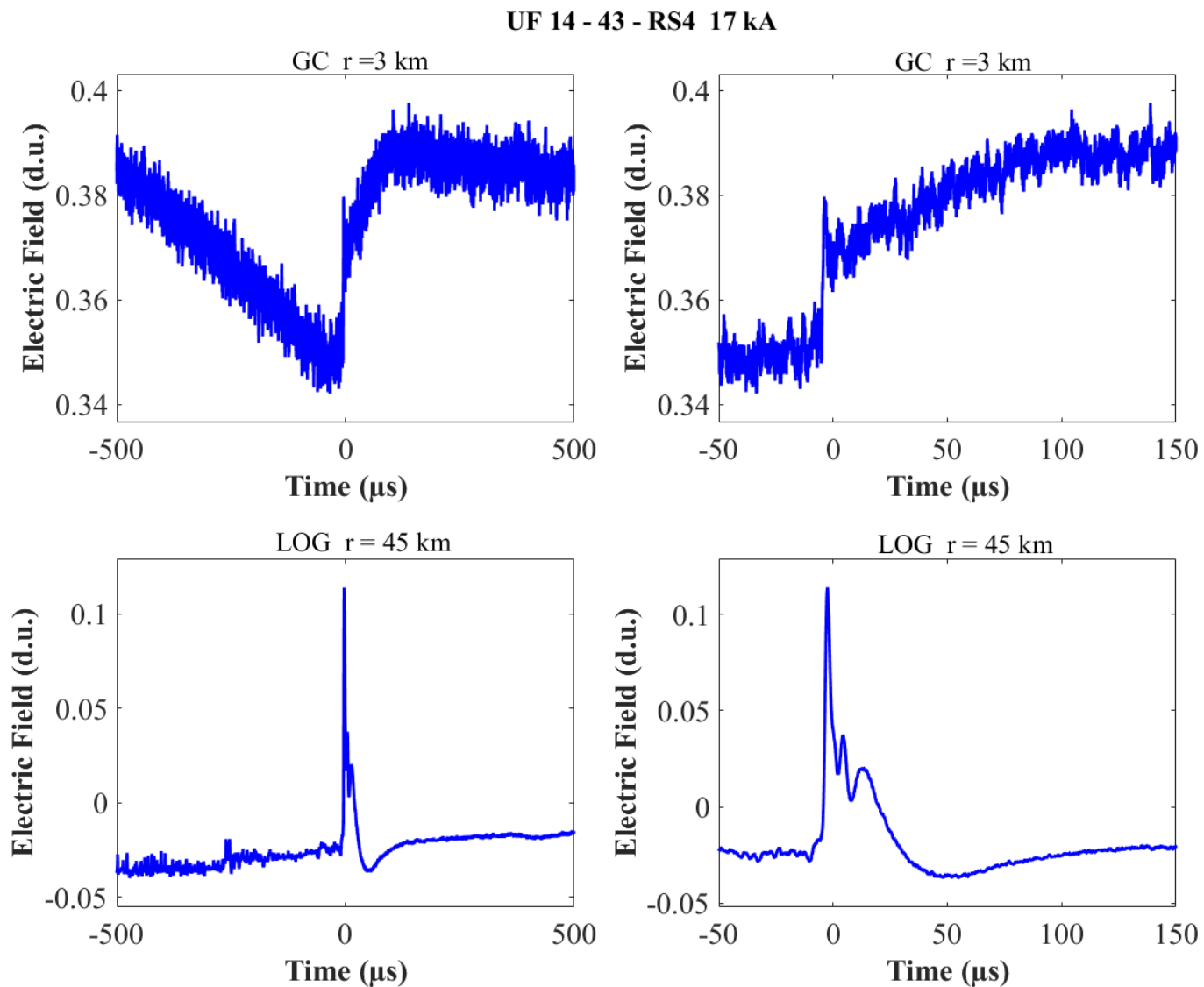


Figure A-74. Two-station electric field waveforms of the RS4 of flash UF 14-43.

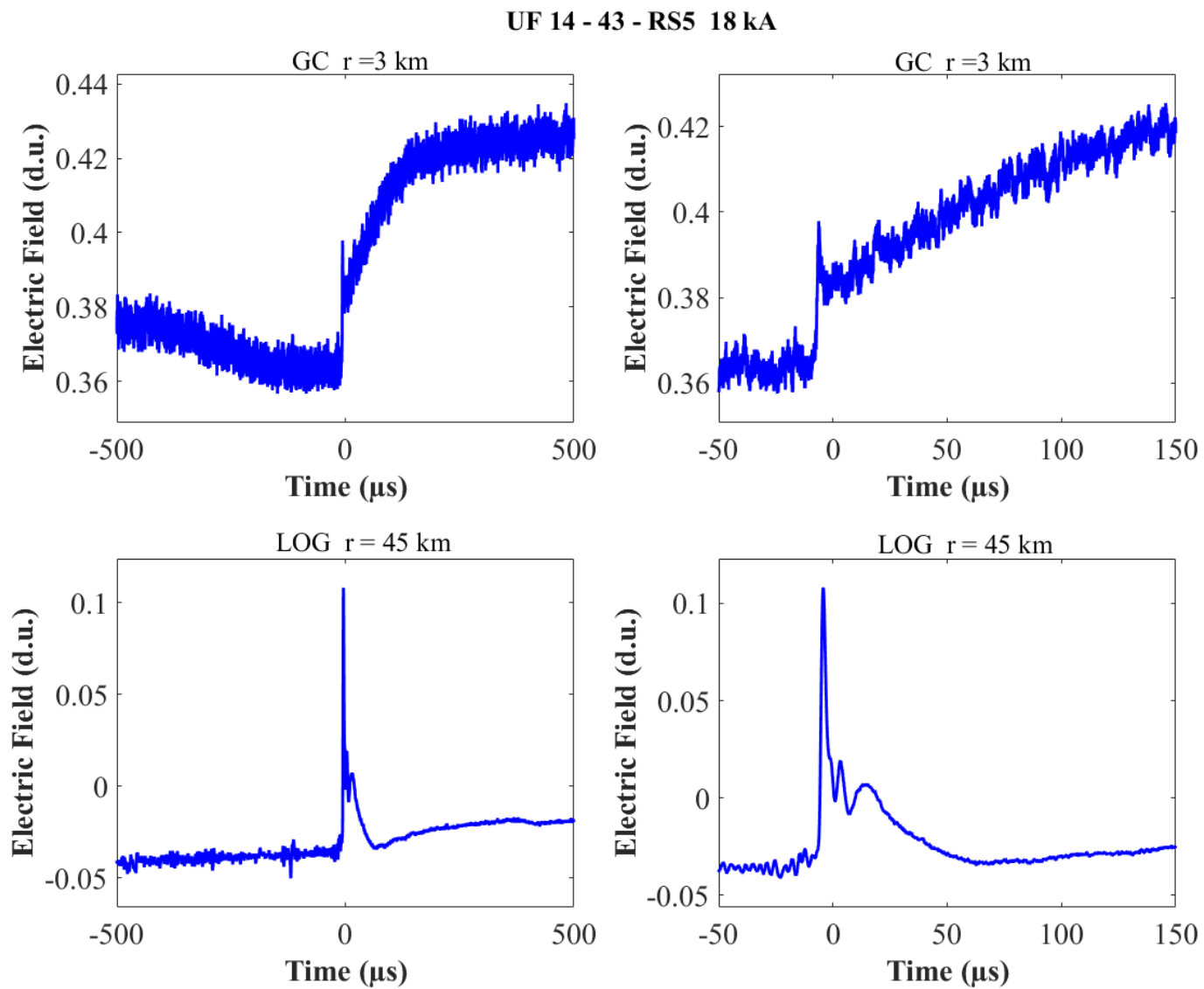


Figure A-75. Two-station electric field waveforms of the RS5 of flash UF 14-43.

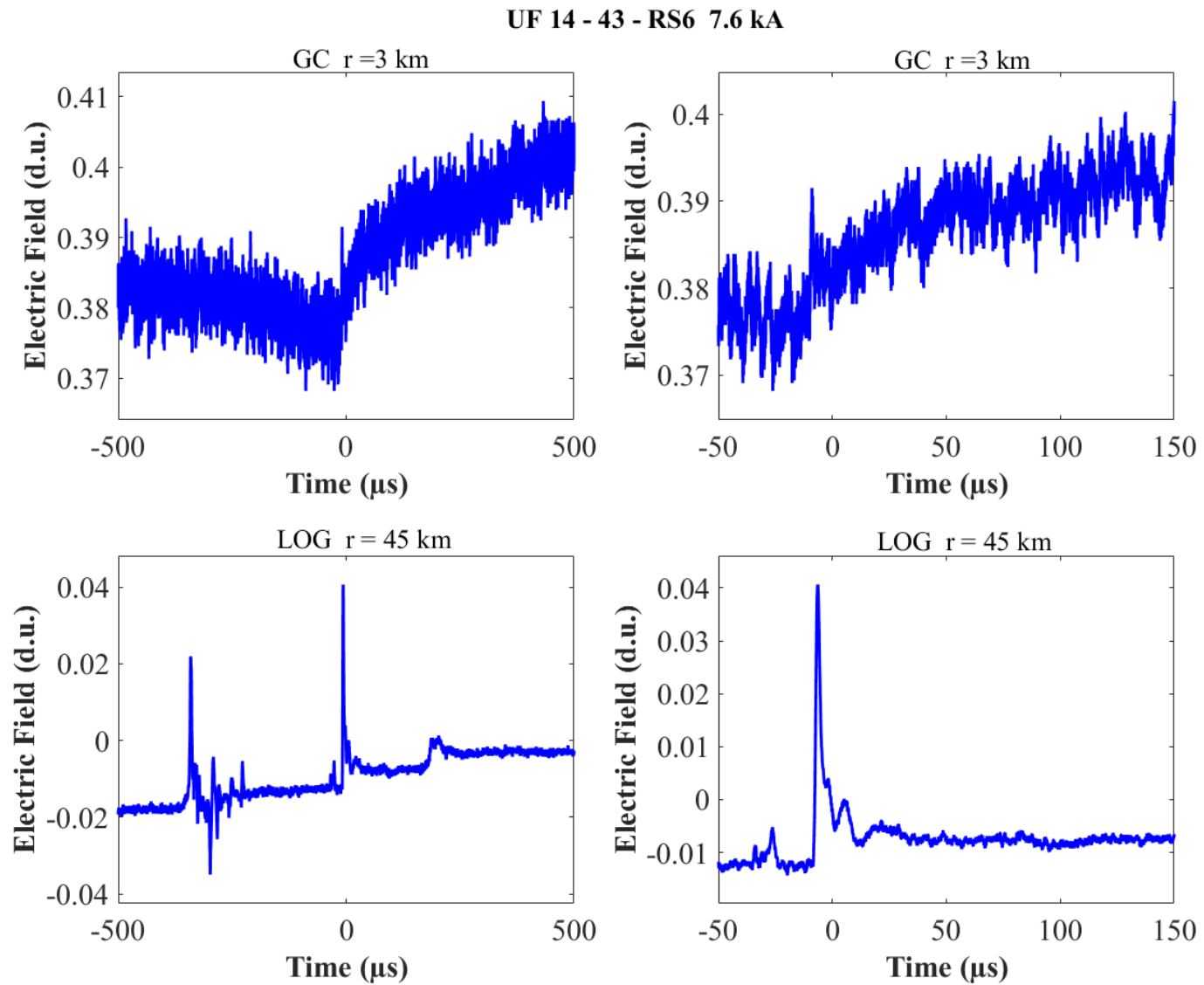


Figure A-76. Two-station electric field waveforms of the RS6 of flash UF 14-43.

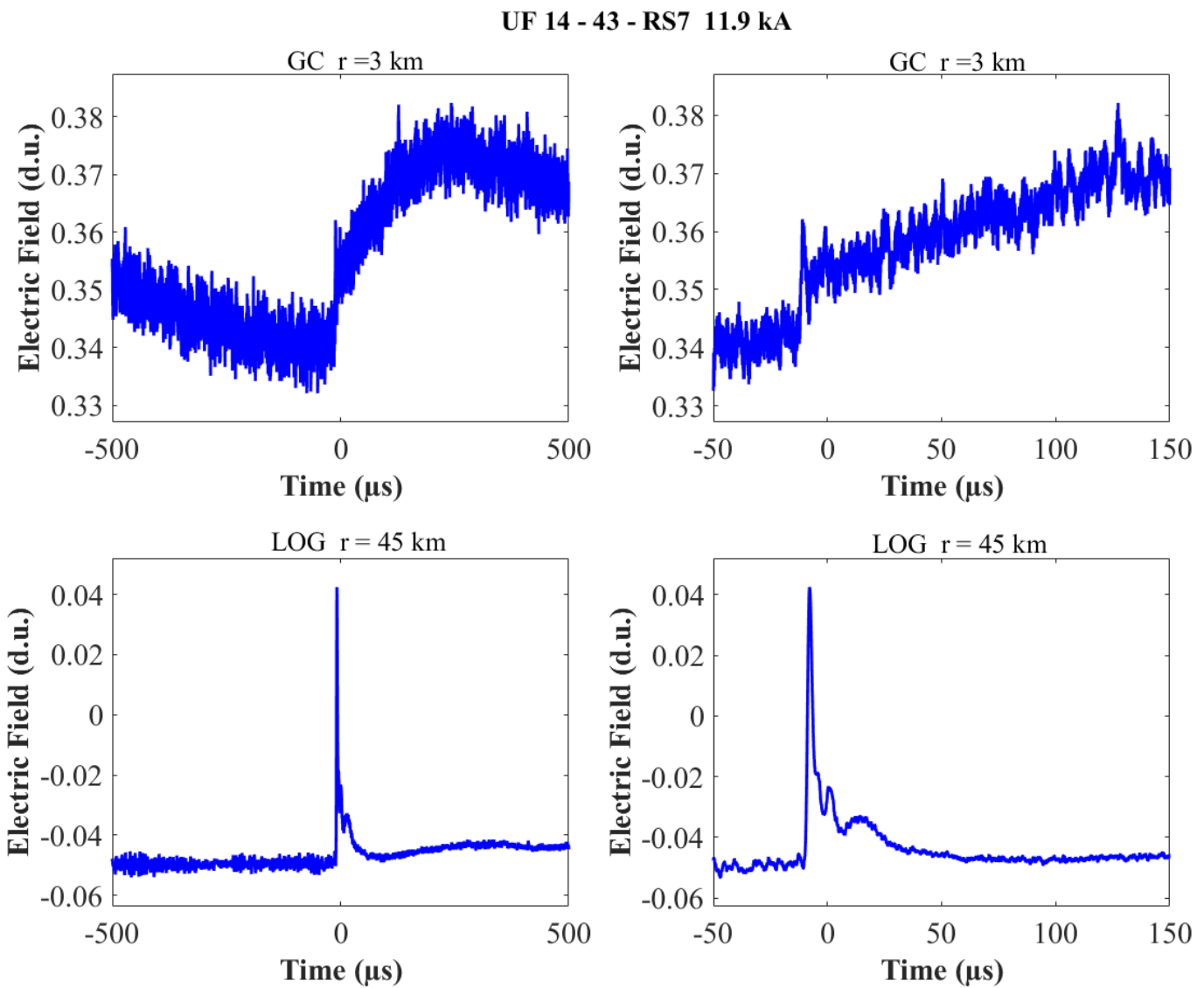


Figure A-77. Two-station electric field waveforms of the RS7 of flash UF 14-43.

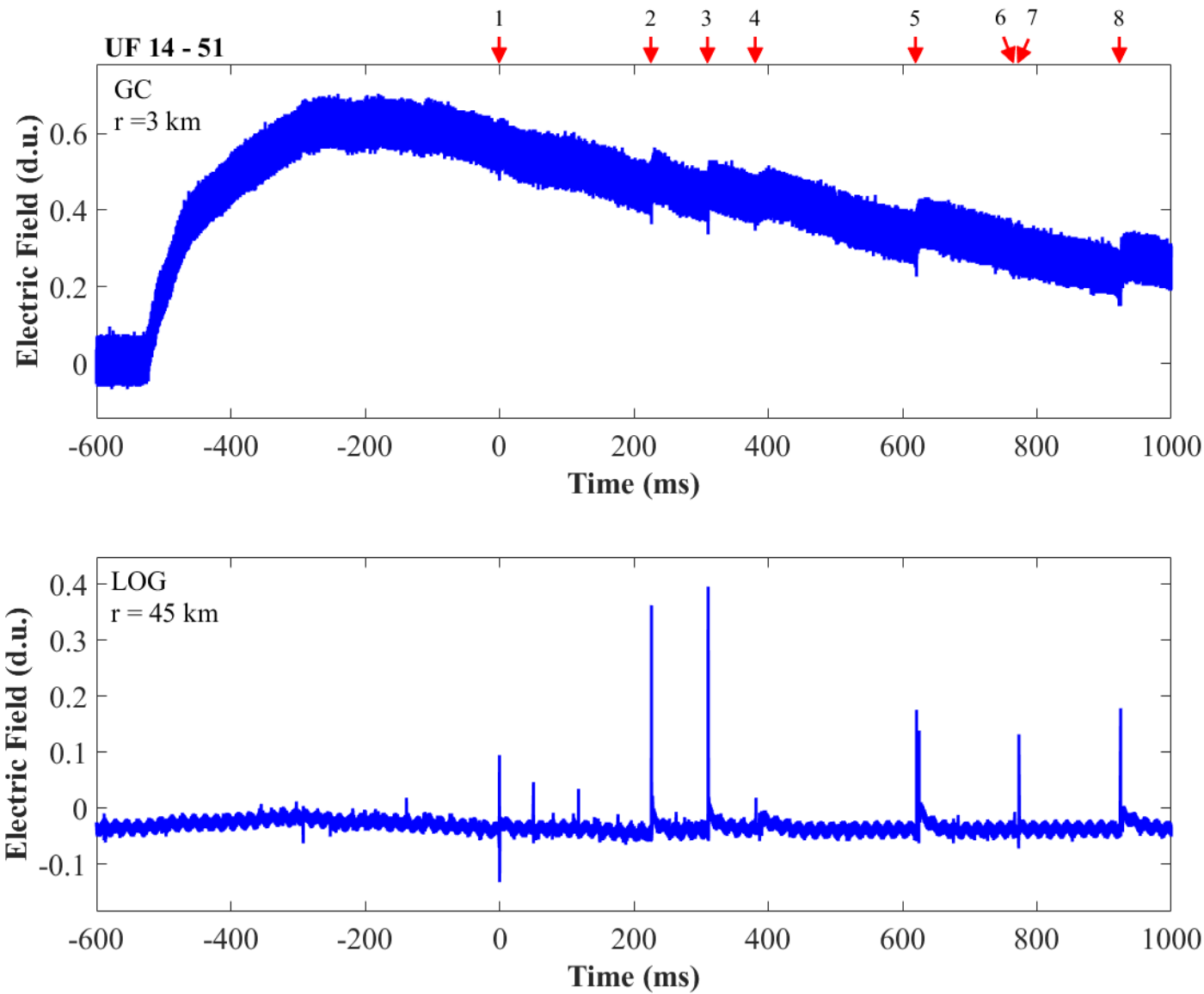


Figure A-78. Two-station electric field waveforms of flash UF 14-51.

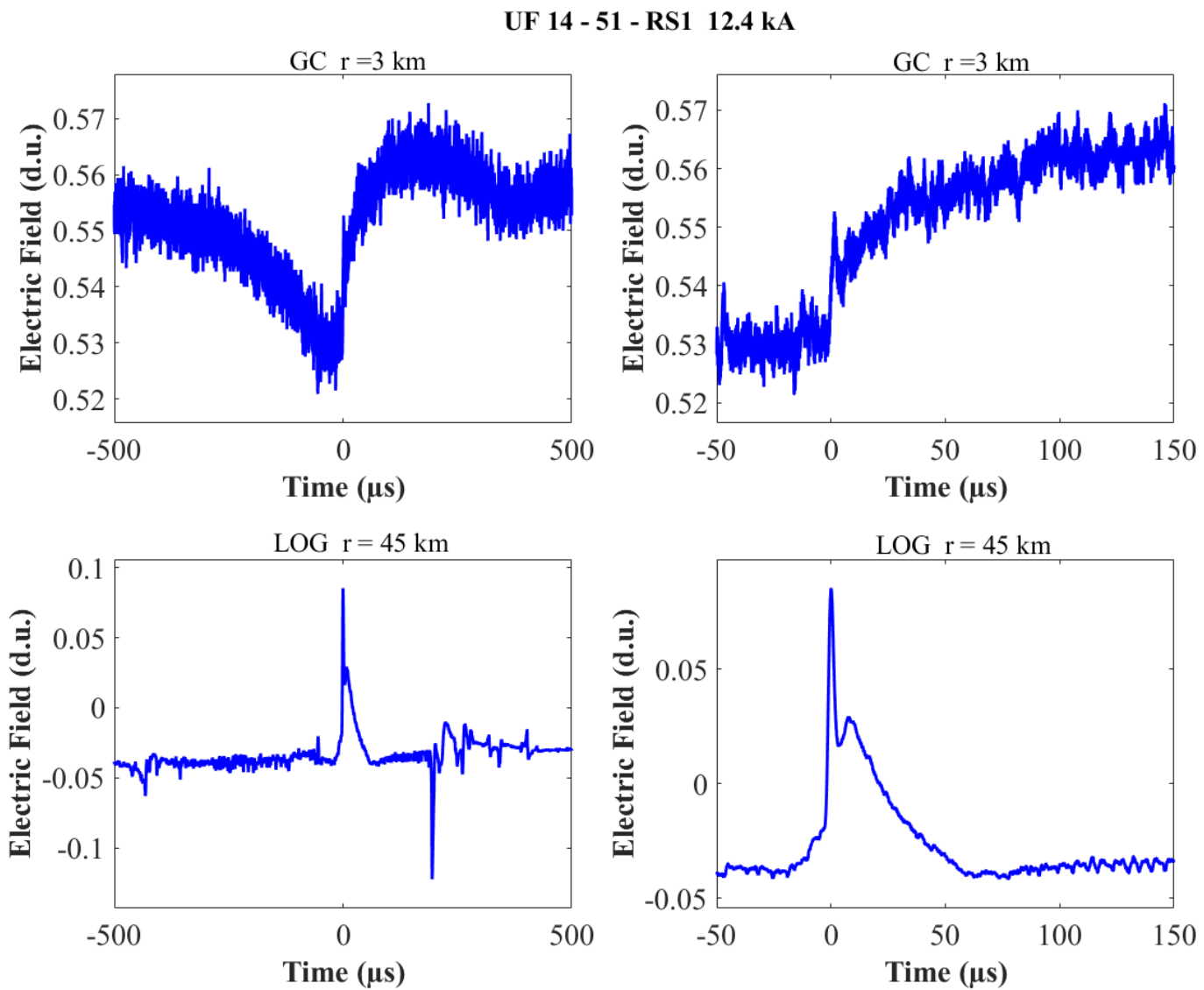


Figure A-79. Two-station electric field waveforms of the RS1 of flash UF 14-51.

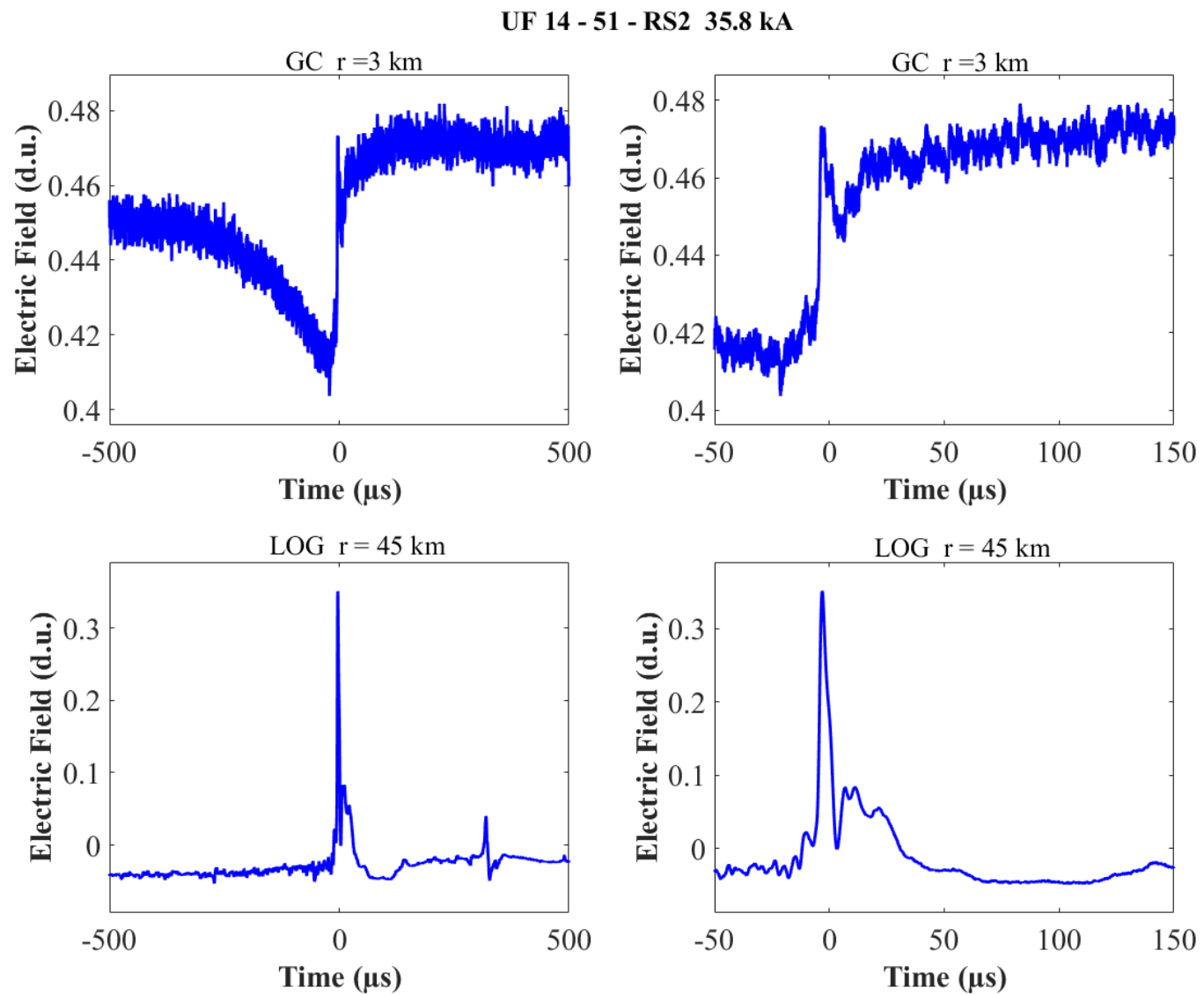


Figure A-80. Two-station electric field waveforms of the RS2 of flash UF 14-51.

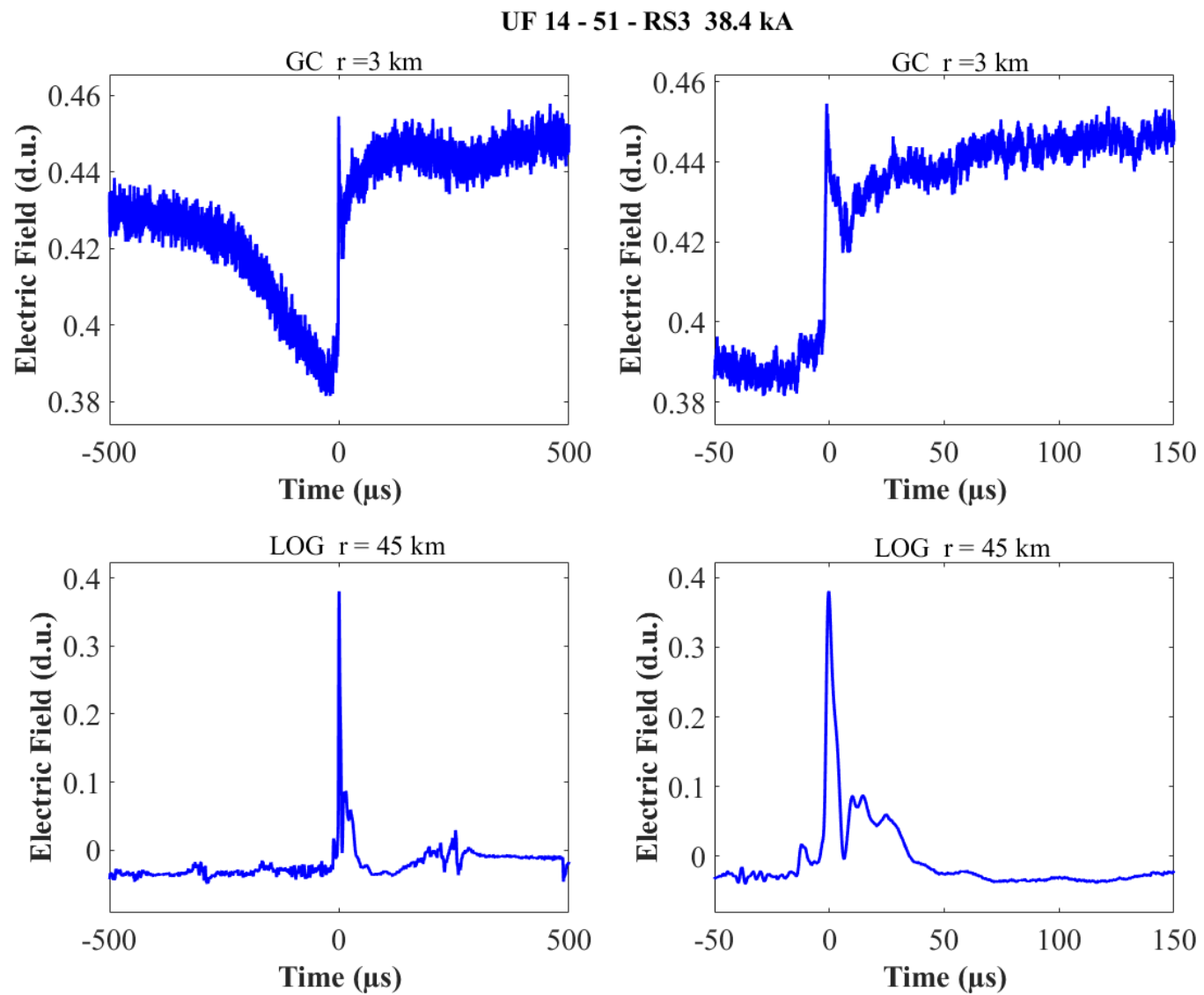


Figure A-81. Two-station electric field waveforms of the RS3 of flash UF 14-51.

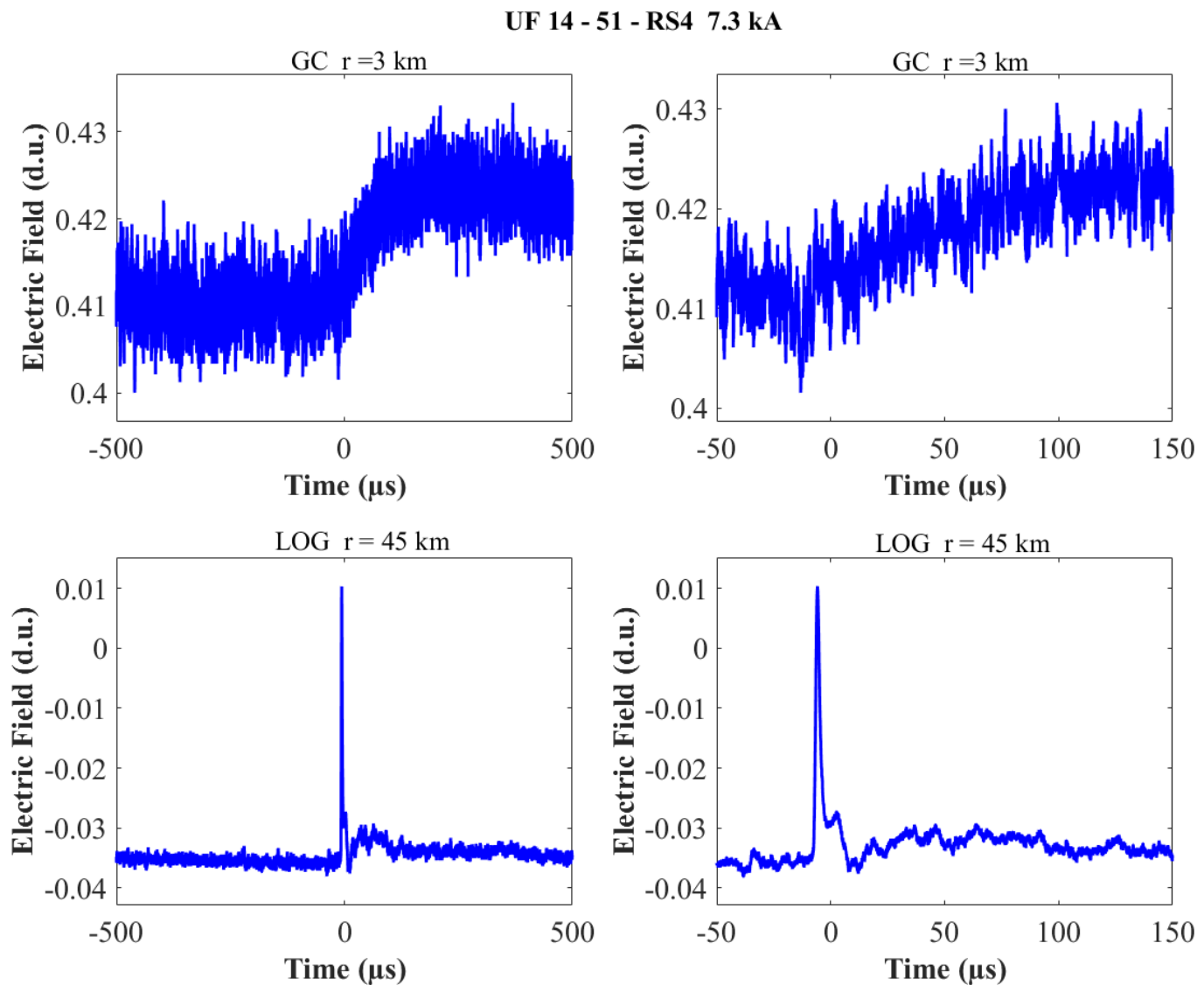


Figure A-82. Two-station electric field waveforms of the RS4 of flash UF 14-51.

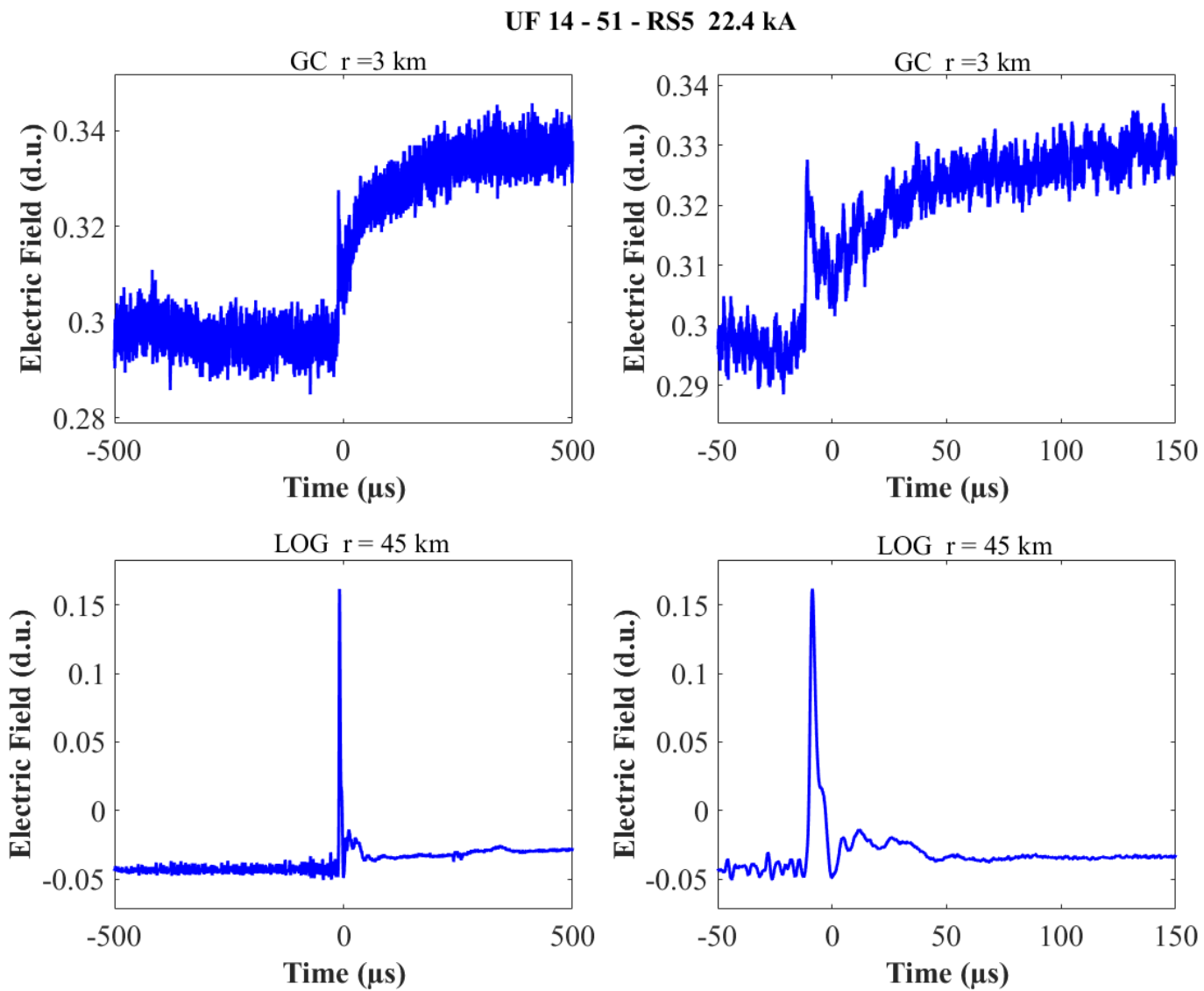


Figure A-83. Two-station electric field waveforms of the RS5 of flash UF 14-51.

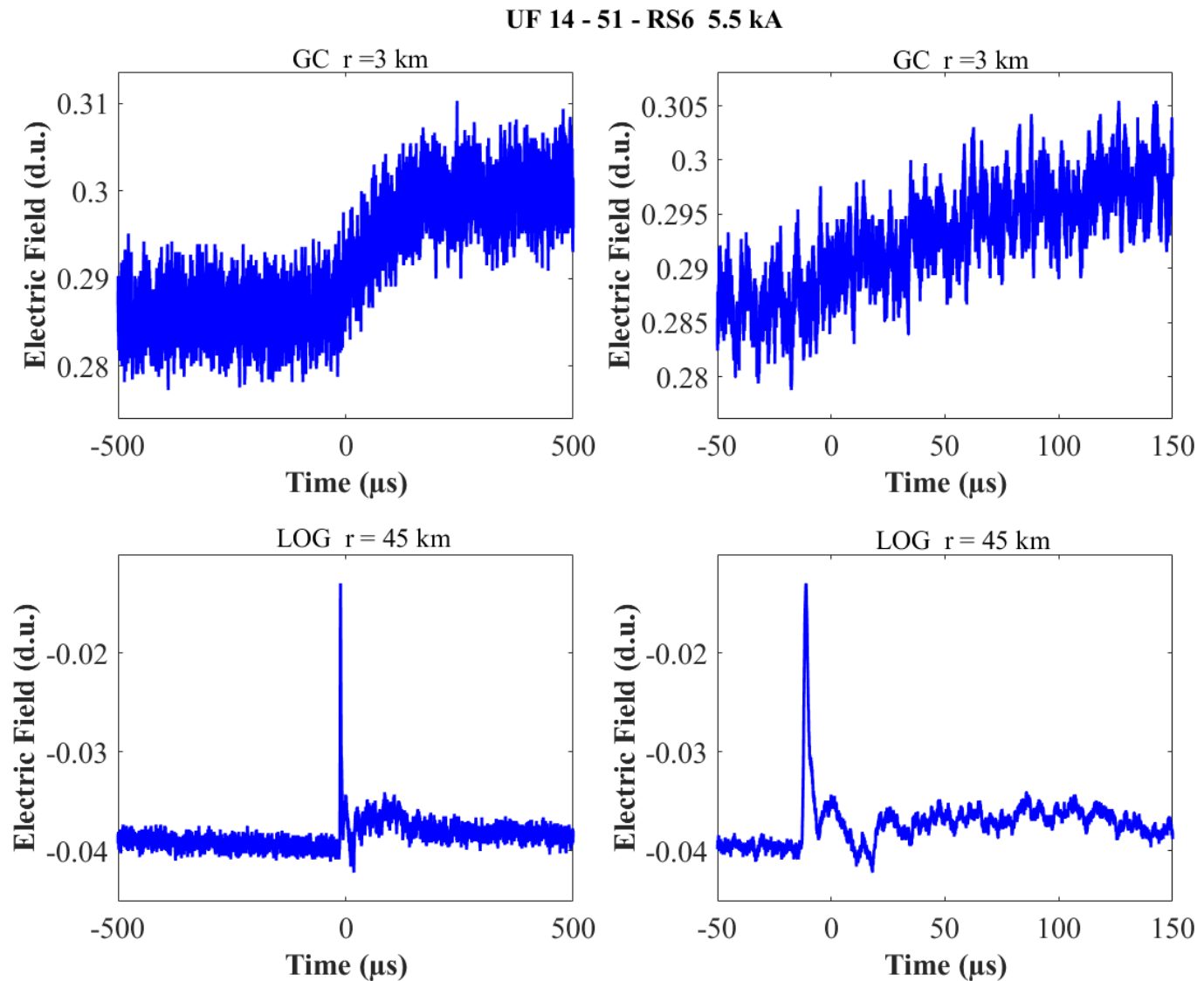


Figure A-84. Two-station electric field waveforms of the RS6 of flash UF 14-51.

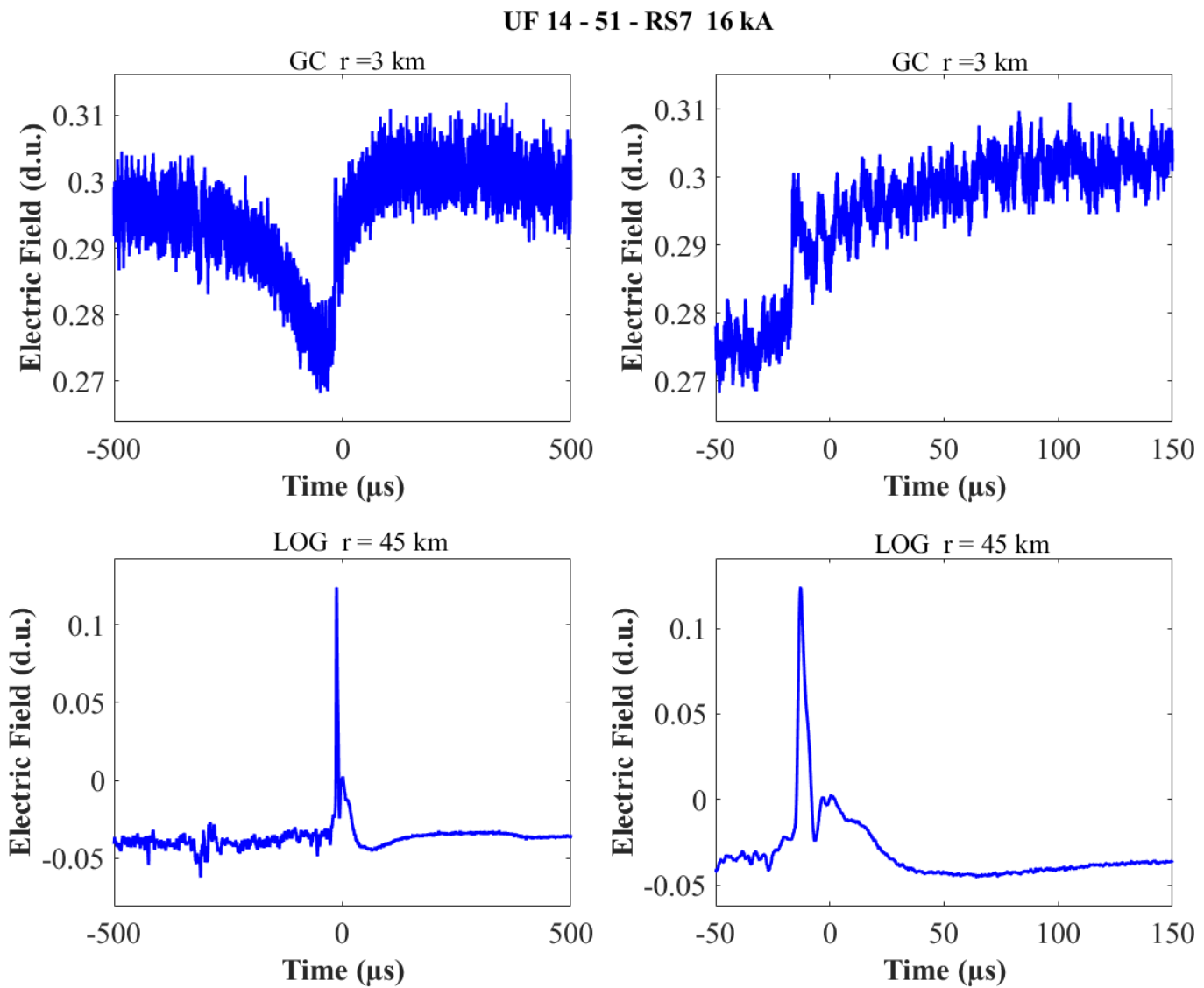


Figure A-85. Two-station electric field waveforms of the RS7 of flash UF 14-51.

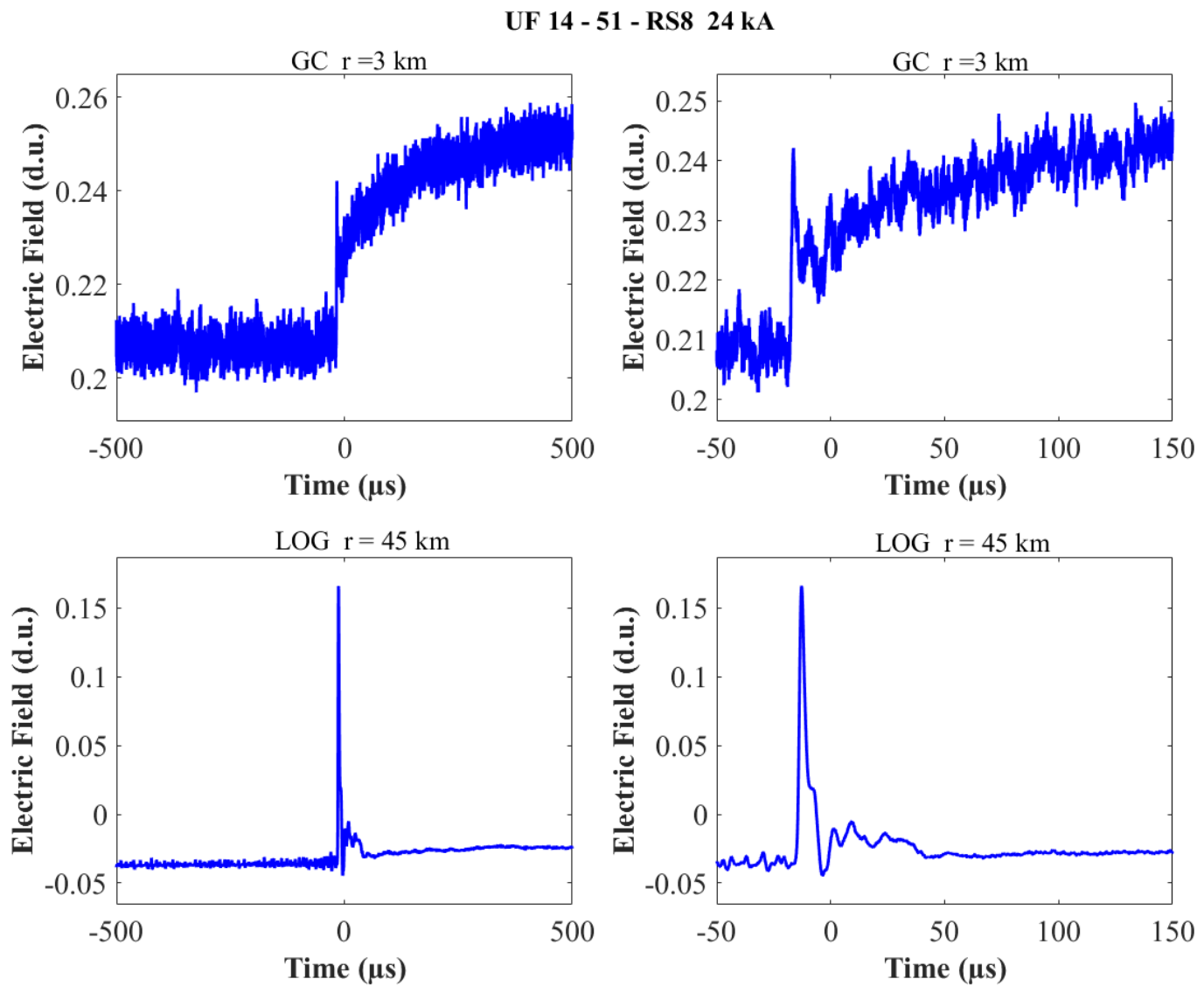


Figure A-86. Two-station electric field waveforms of the RS8 of flash UF 14-51.

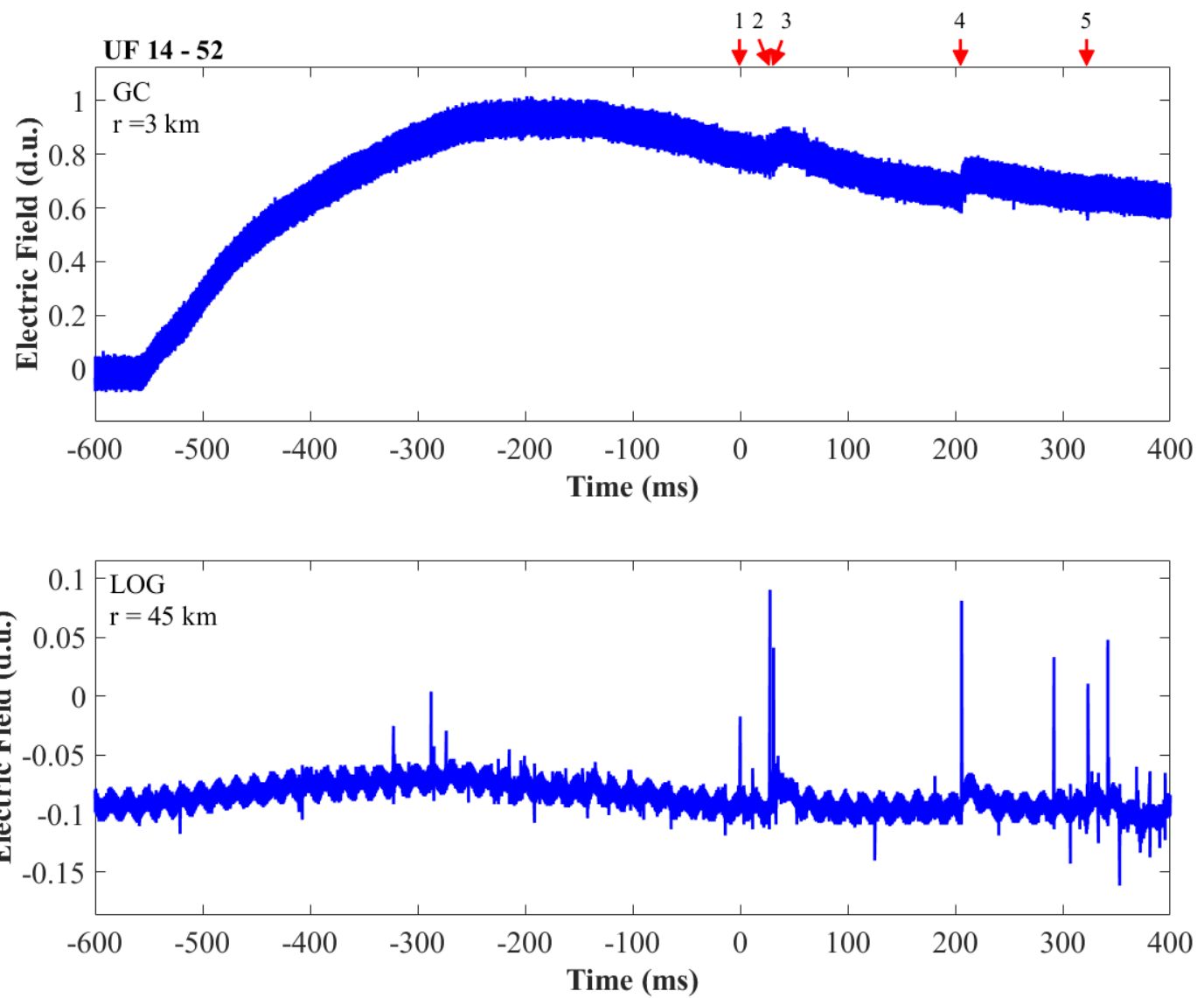


Figure A-87. Two-station electric field waveforms of flash UF 14-52.

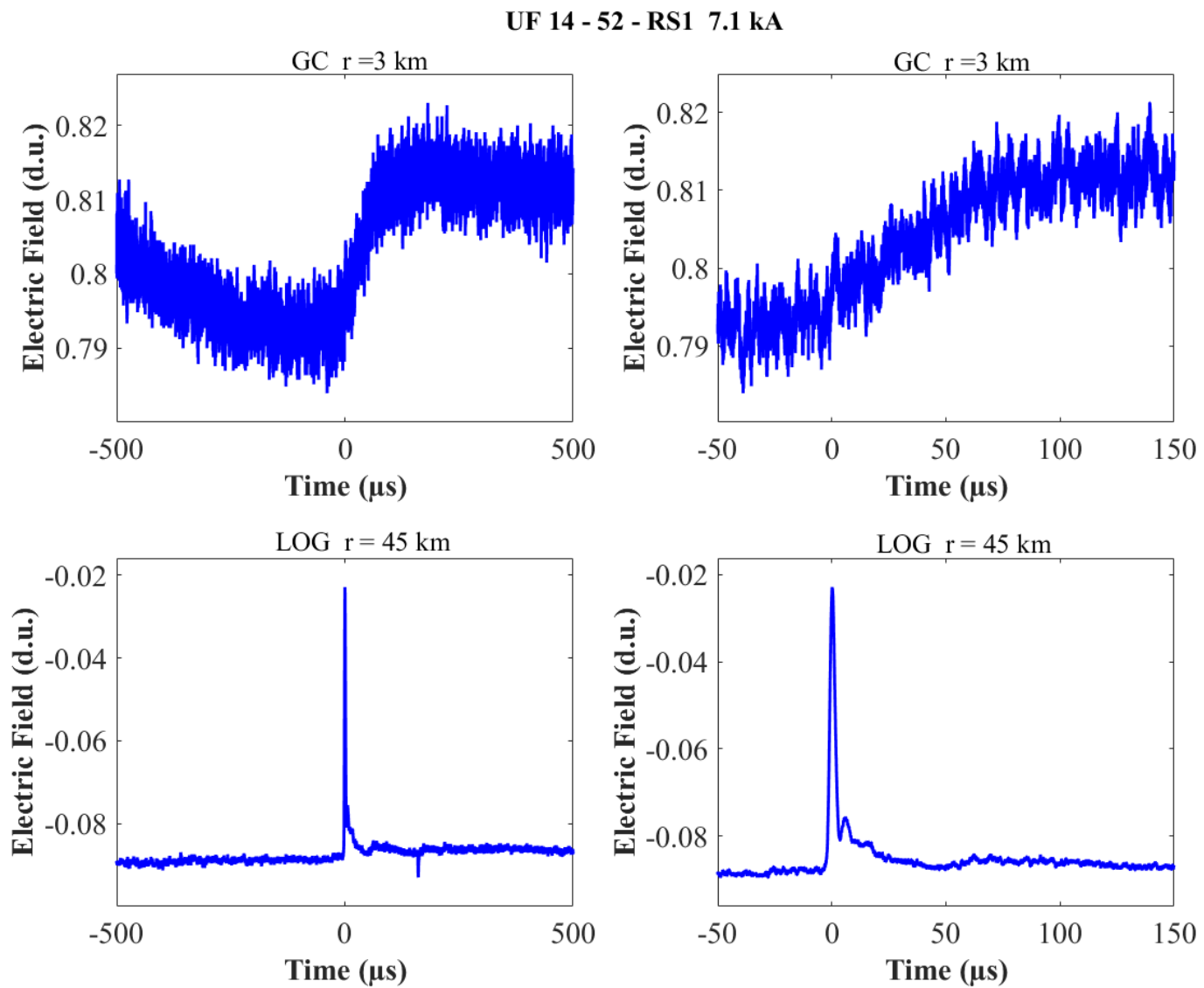


Figure A-88. Two-station electric field waveforms of the RS1 of flash UF 14-52.

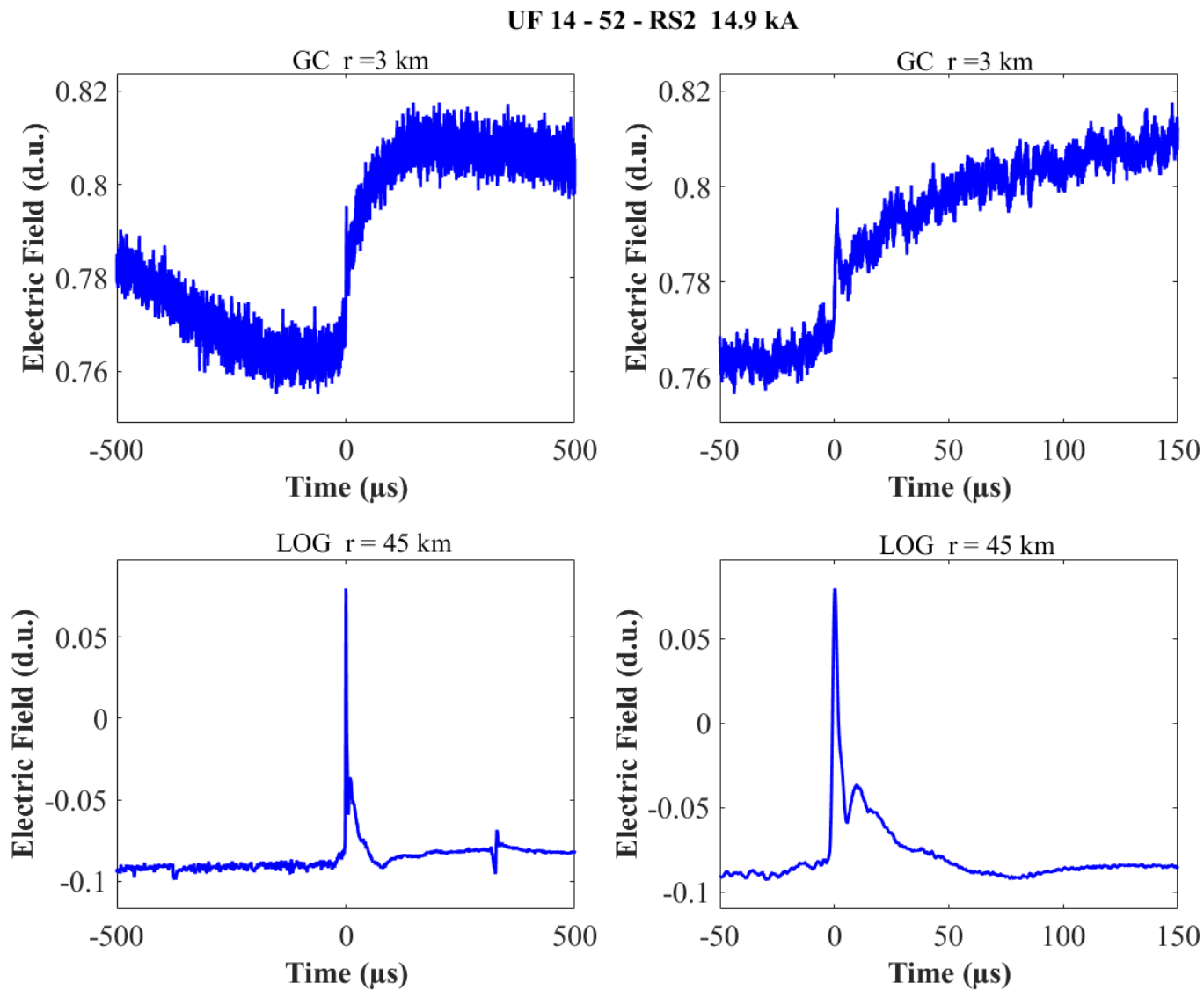


Figure A-89. Two-station electric field waveforms of the RS2 of flash UF 14-52.

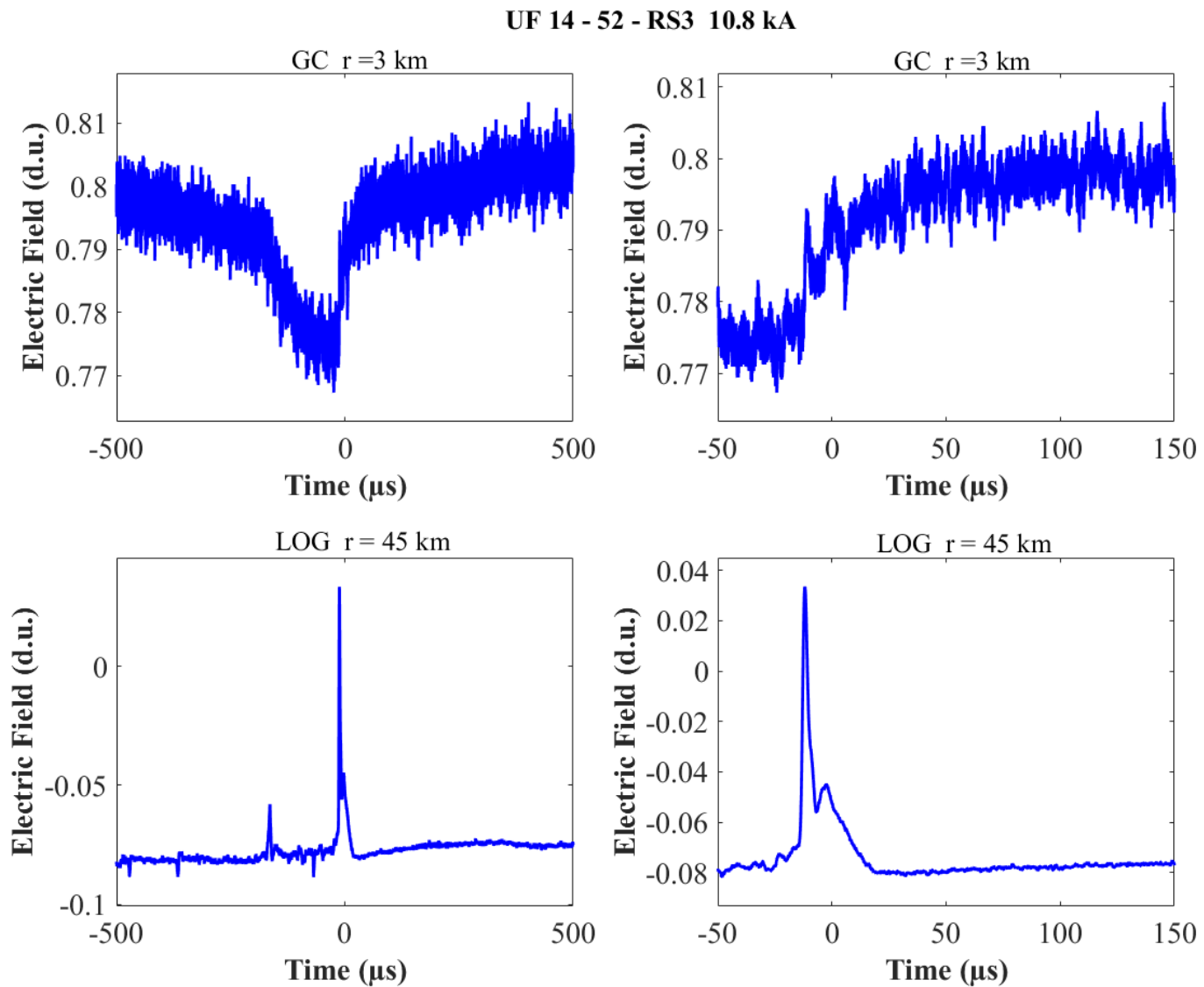


Figure A-90. Two-station electric field waveforms of the RS3 of flash UF 14-52.

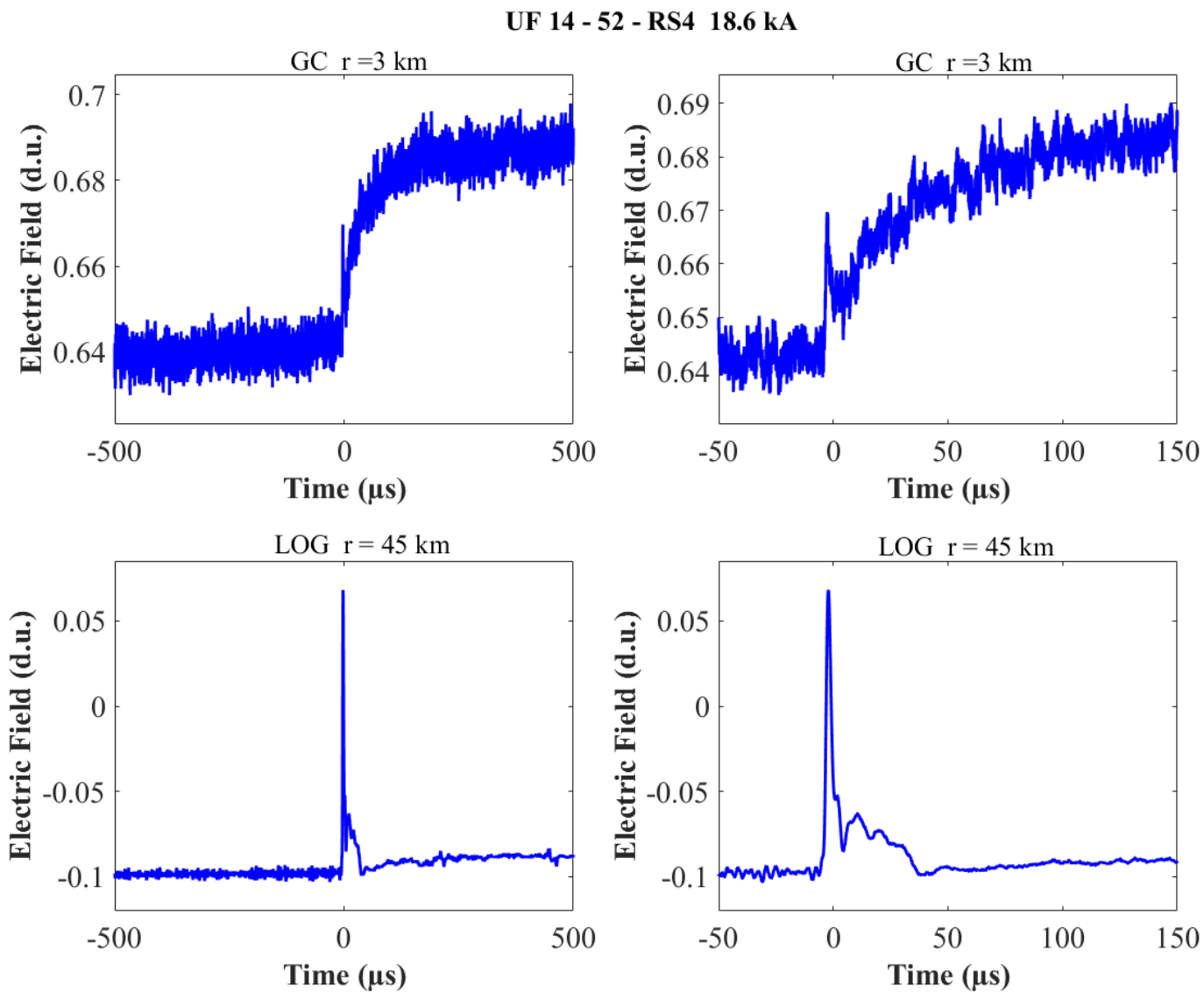


Figure A-91. Two-station electric field waveforms of the RS4 of flash UF 14-52.

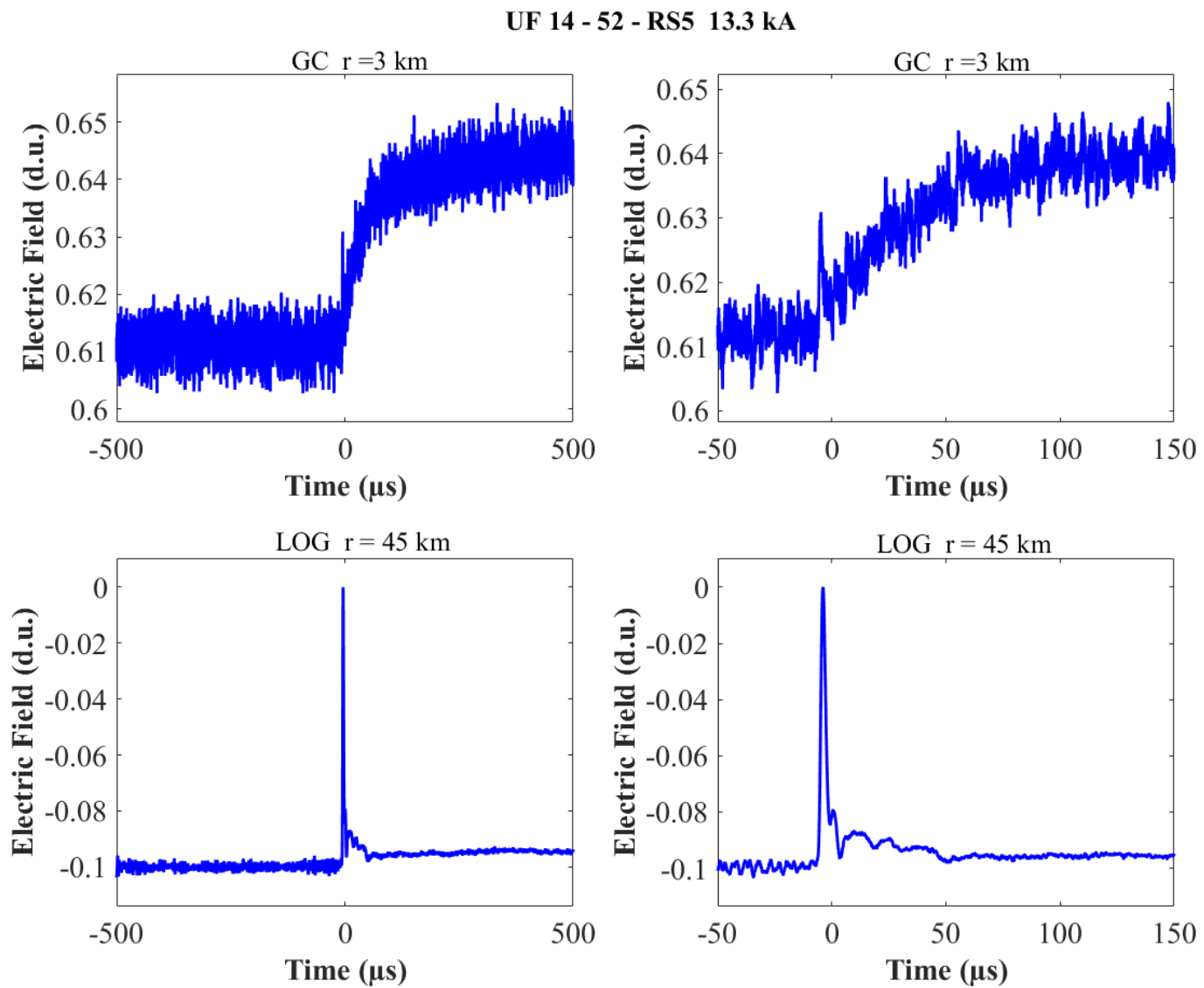


Figure A-92. Two-station electric field waveforms of the RS5 of flash UF 14-52.

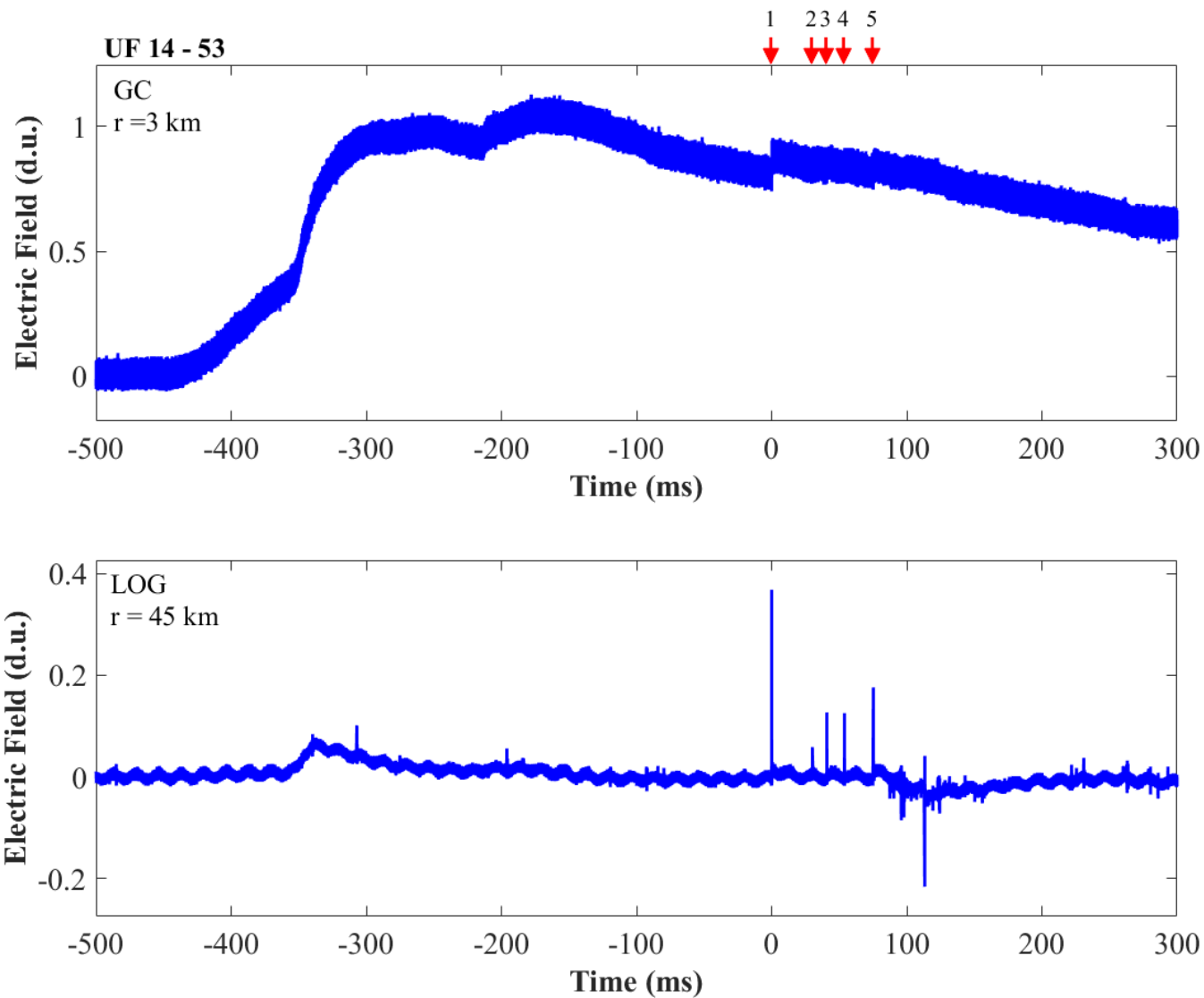


Figure A-93. Two-station electric field waveforms of flash UF 14-53.

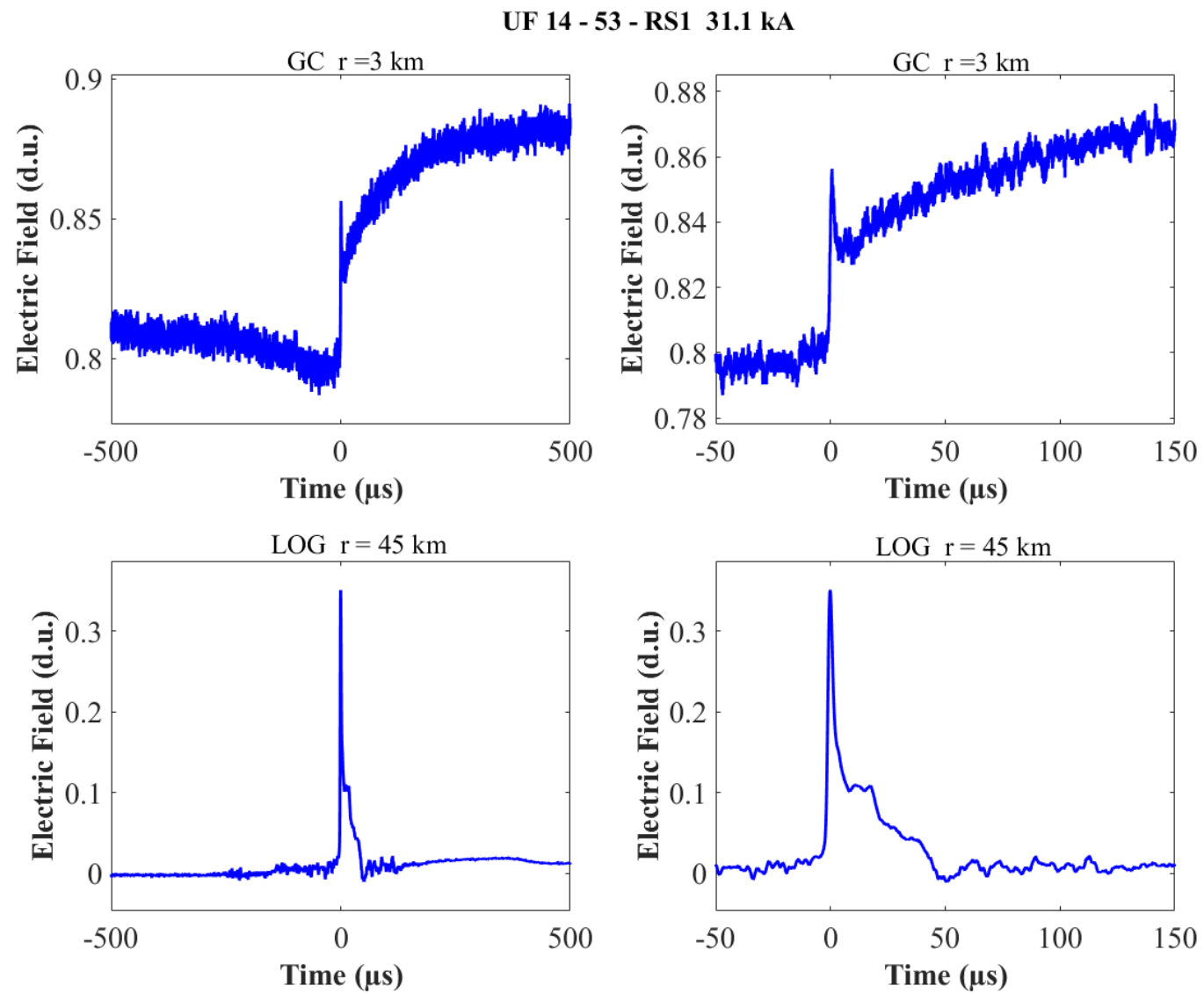


Figure A-94. Two-station electric field waveforms of the RS1 of flash UF 14-53.

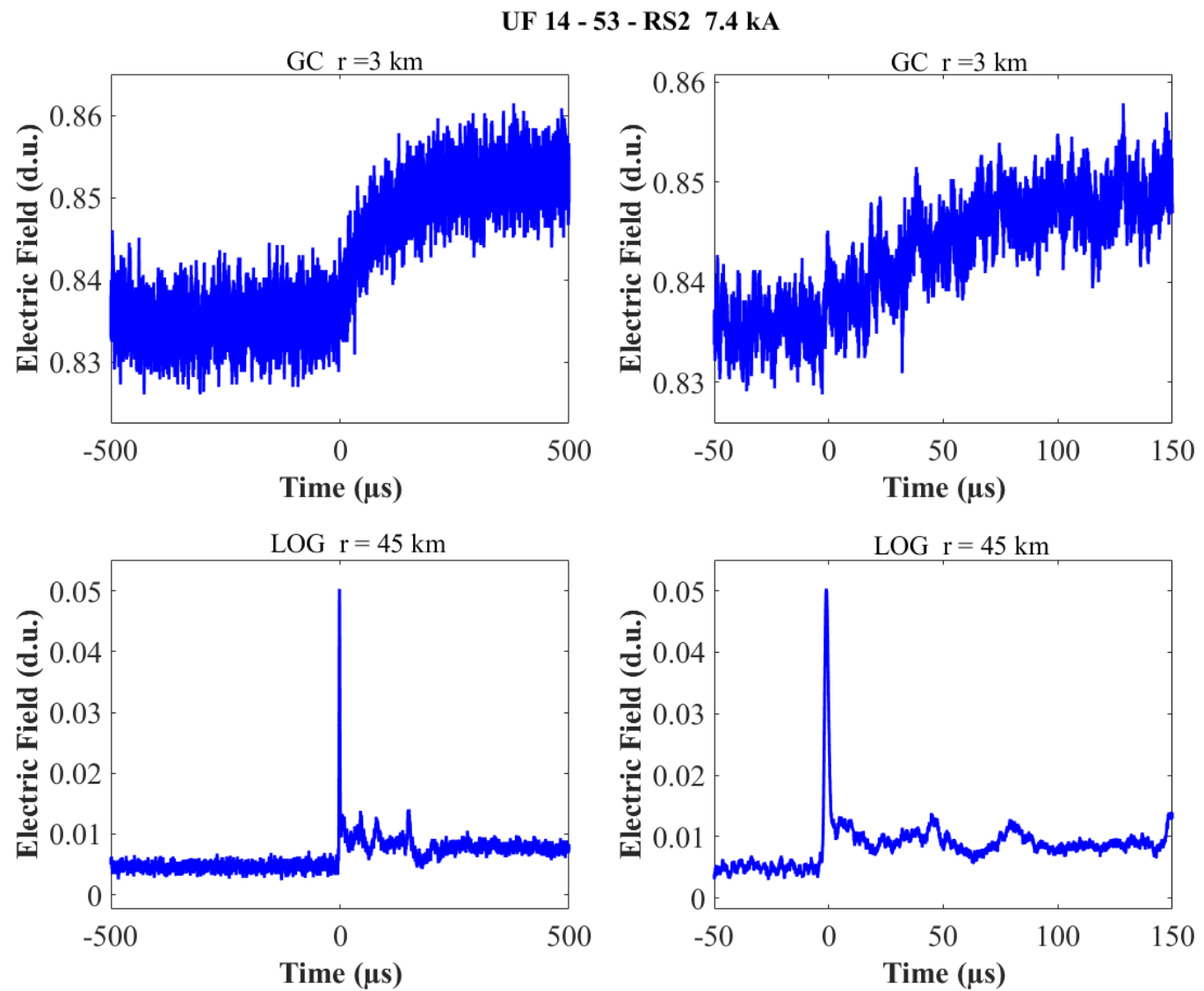


Figure A-95. Two-station electric field waveforms of the RS2 of flash UF 14-53.

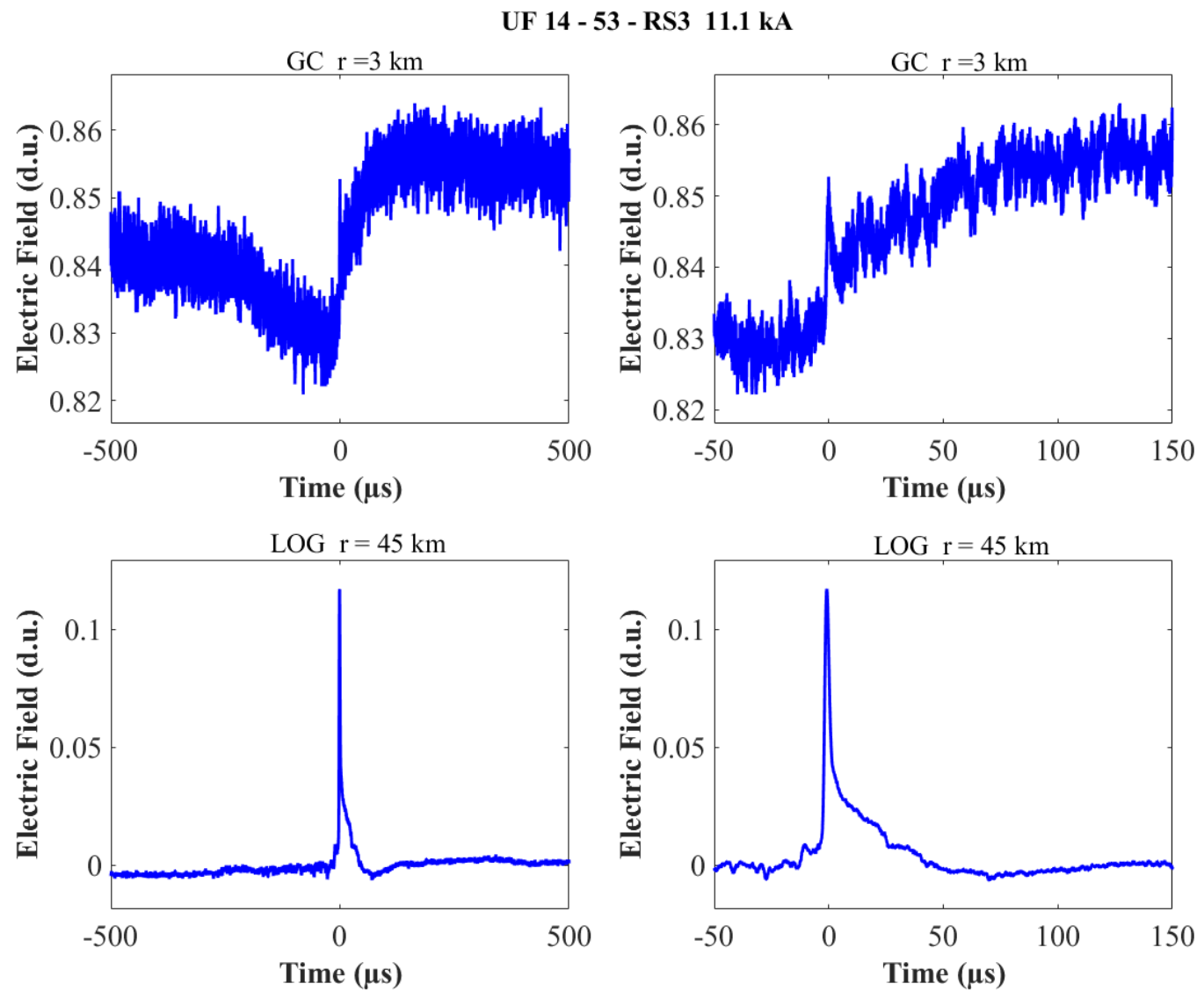


Figure A-96. Two-station electric field waveforms of the RS3 of flash UF 14-53.

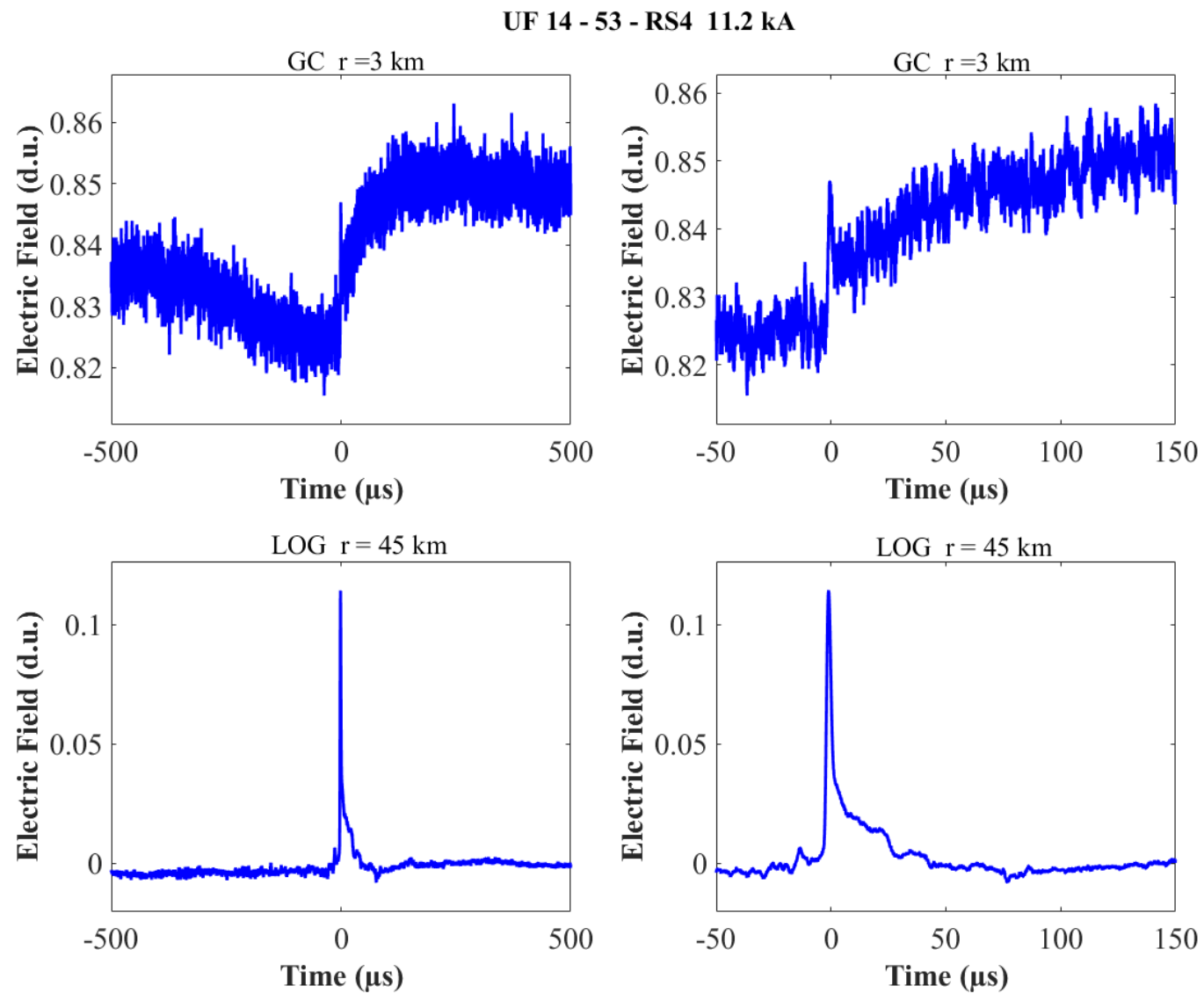


Figure A-97. Two-station electric field waveforms of the RS4 of flash UF 14-53.

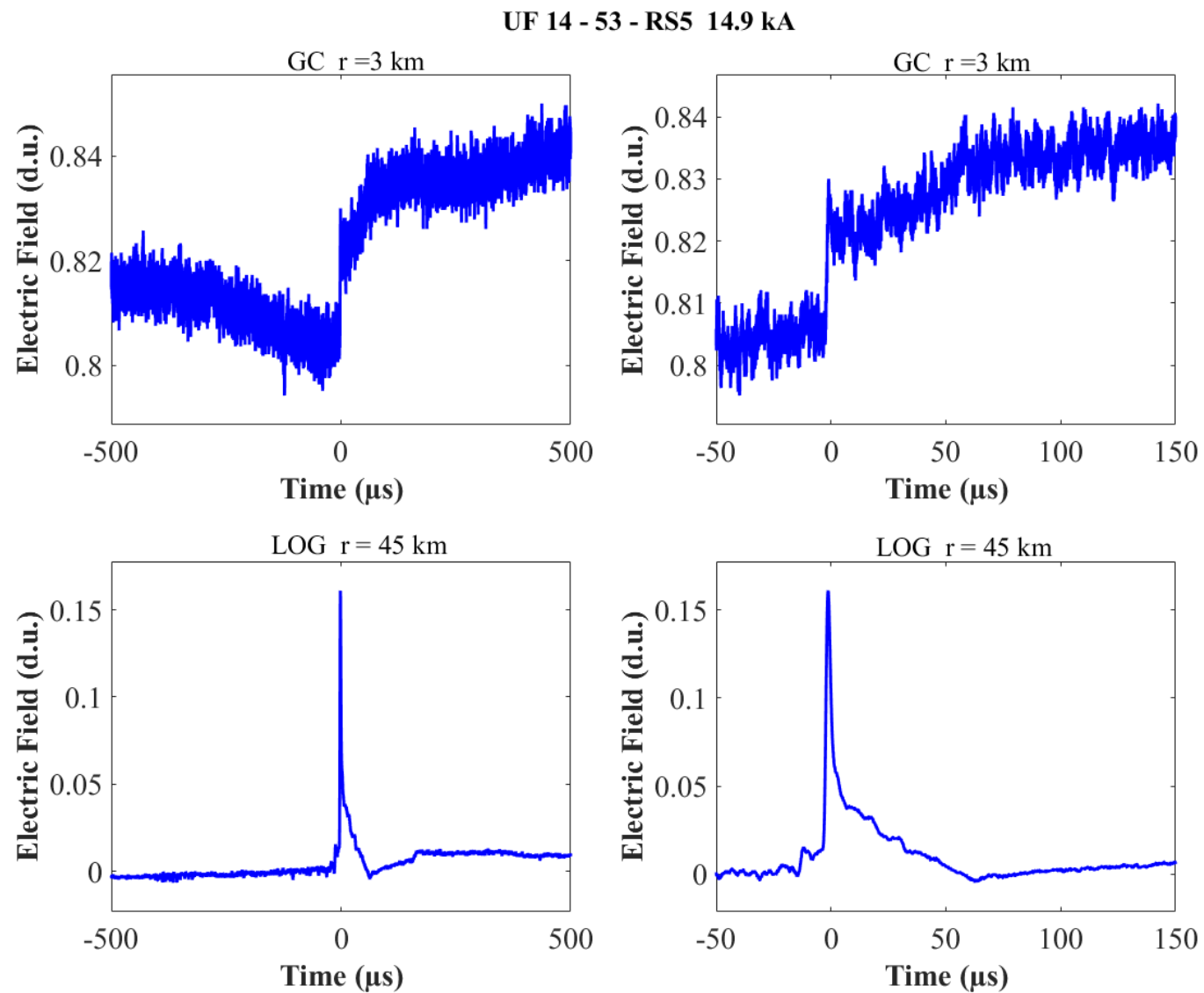


Figure A-98. Two-station electric field waveforms of the RS5 of flash UF 14-53.

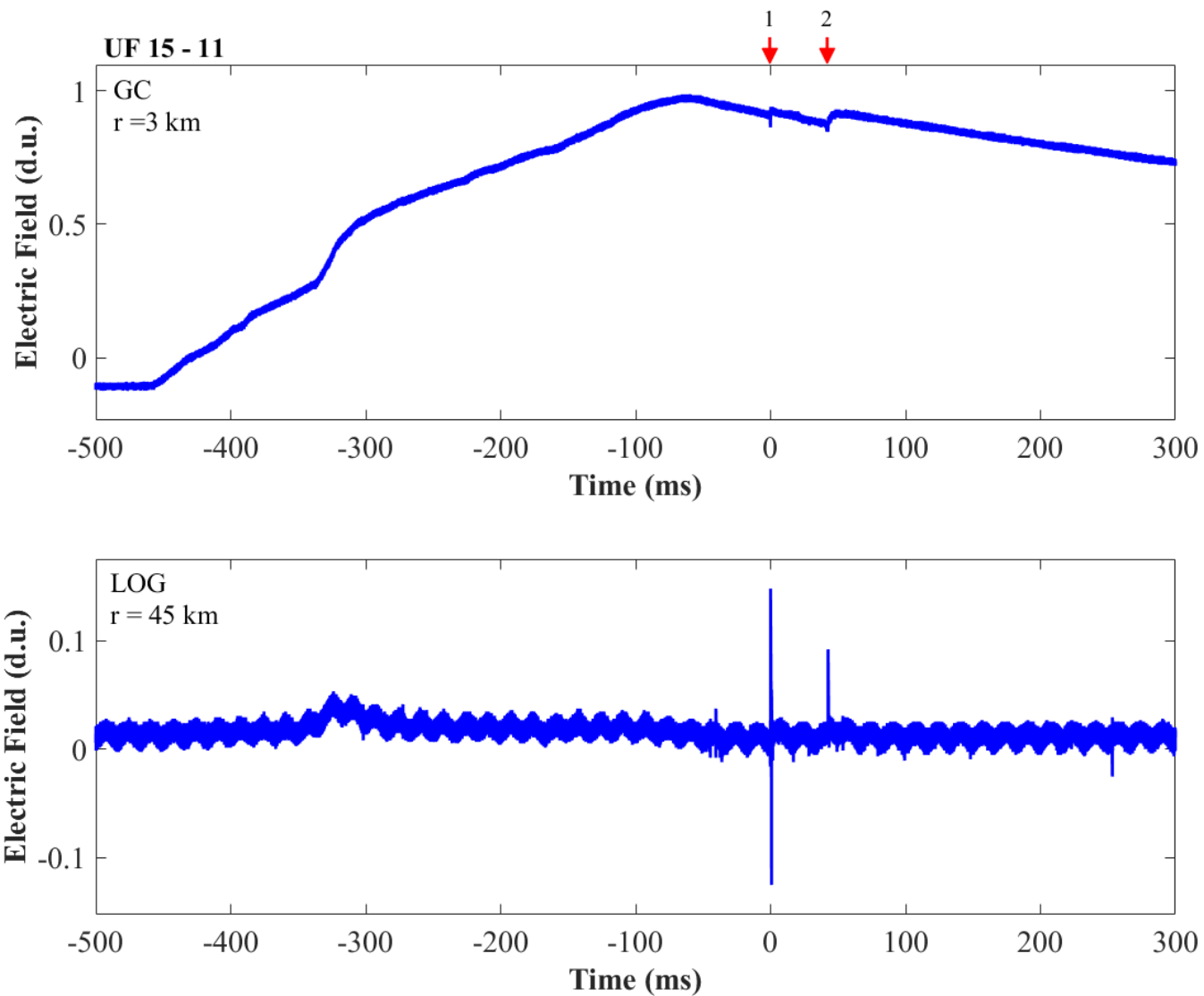


Figure A-99. Two-station electric field waveforms of flash UF 15-11.

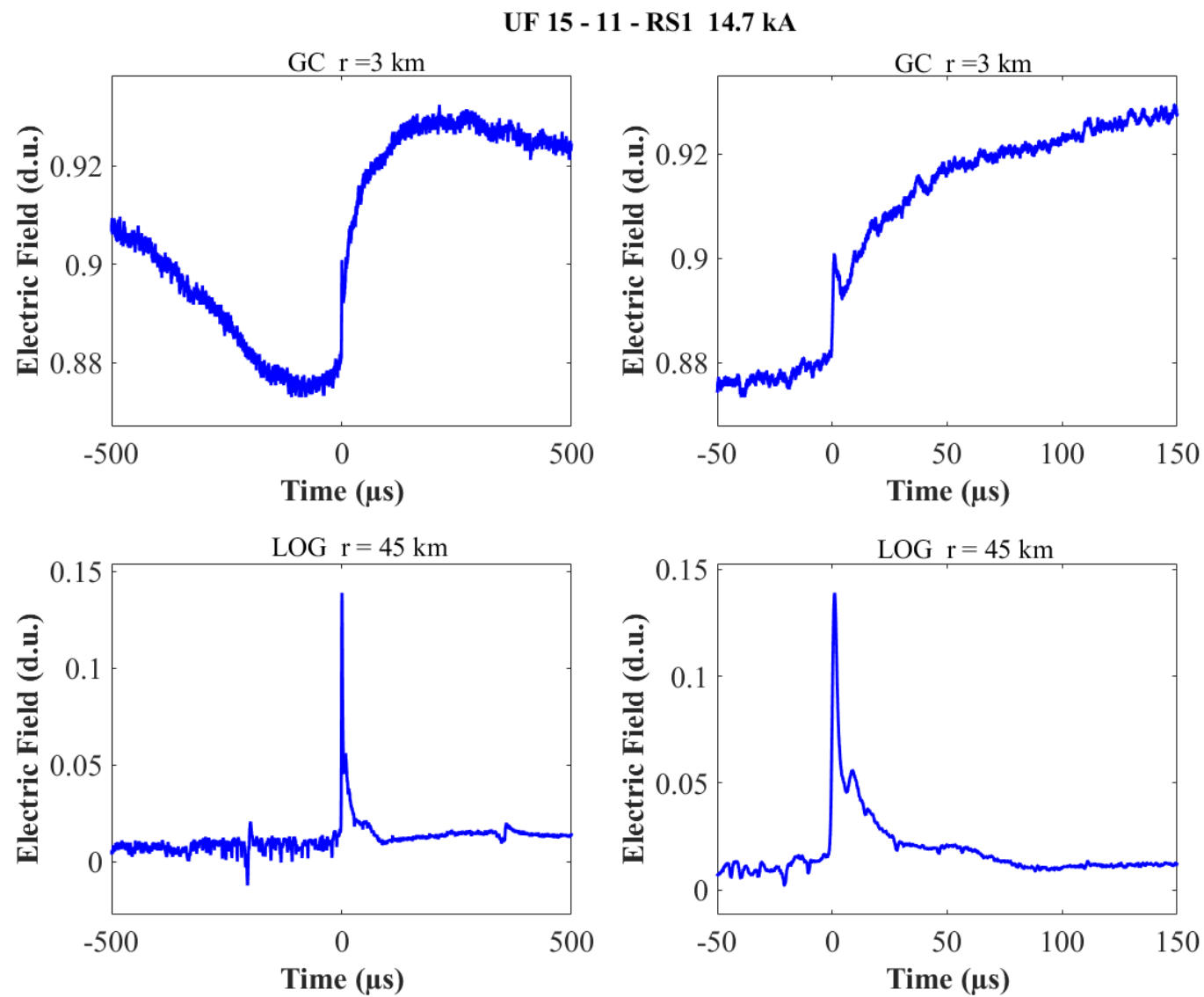


Figure A-100. Two-station electric field waveforms of the RS1 of flash UF 15-11.

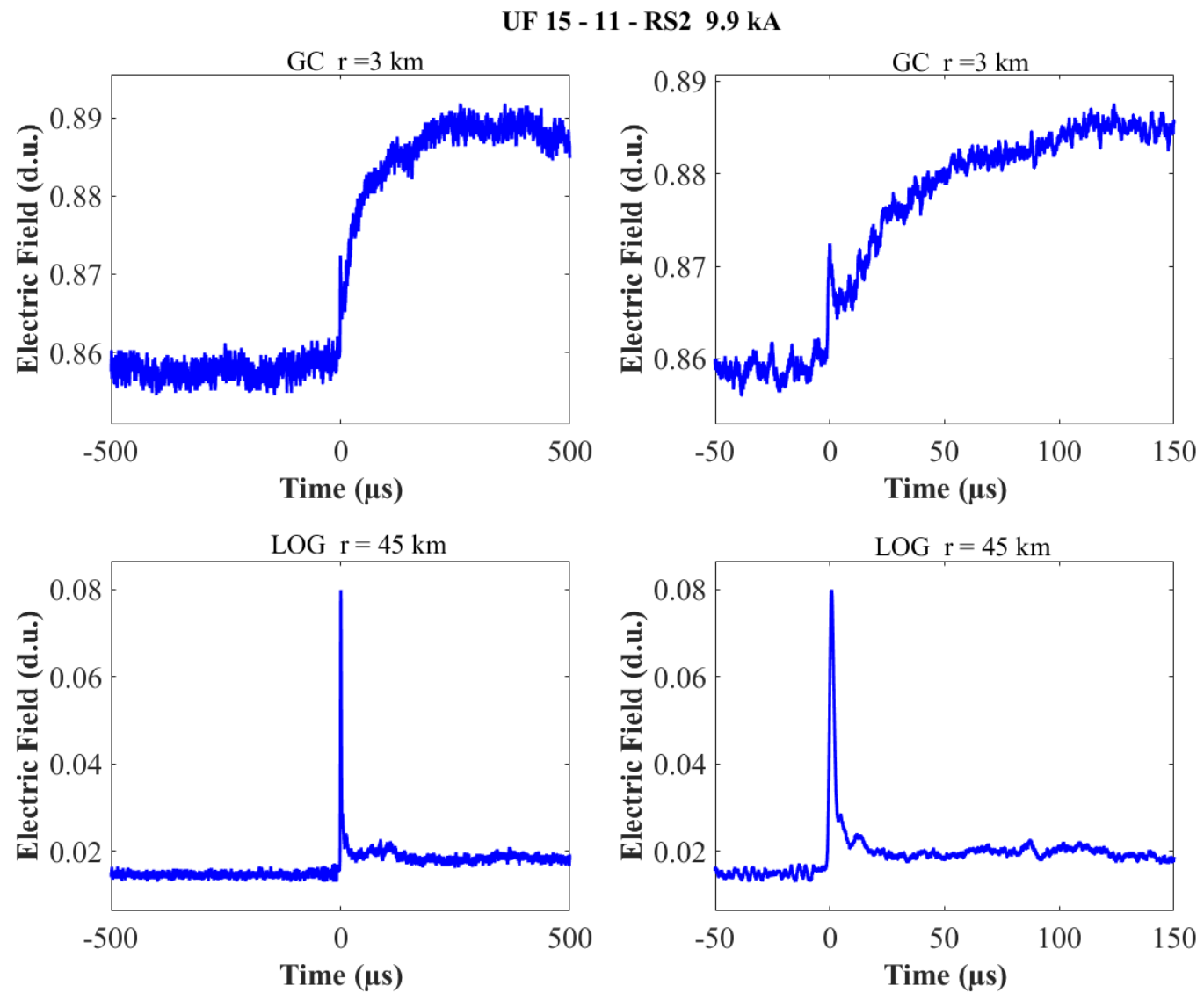


Figure A-101. Two-station electric field waveforms of the RS2 of flash UF 15-11.

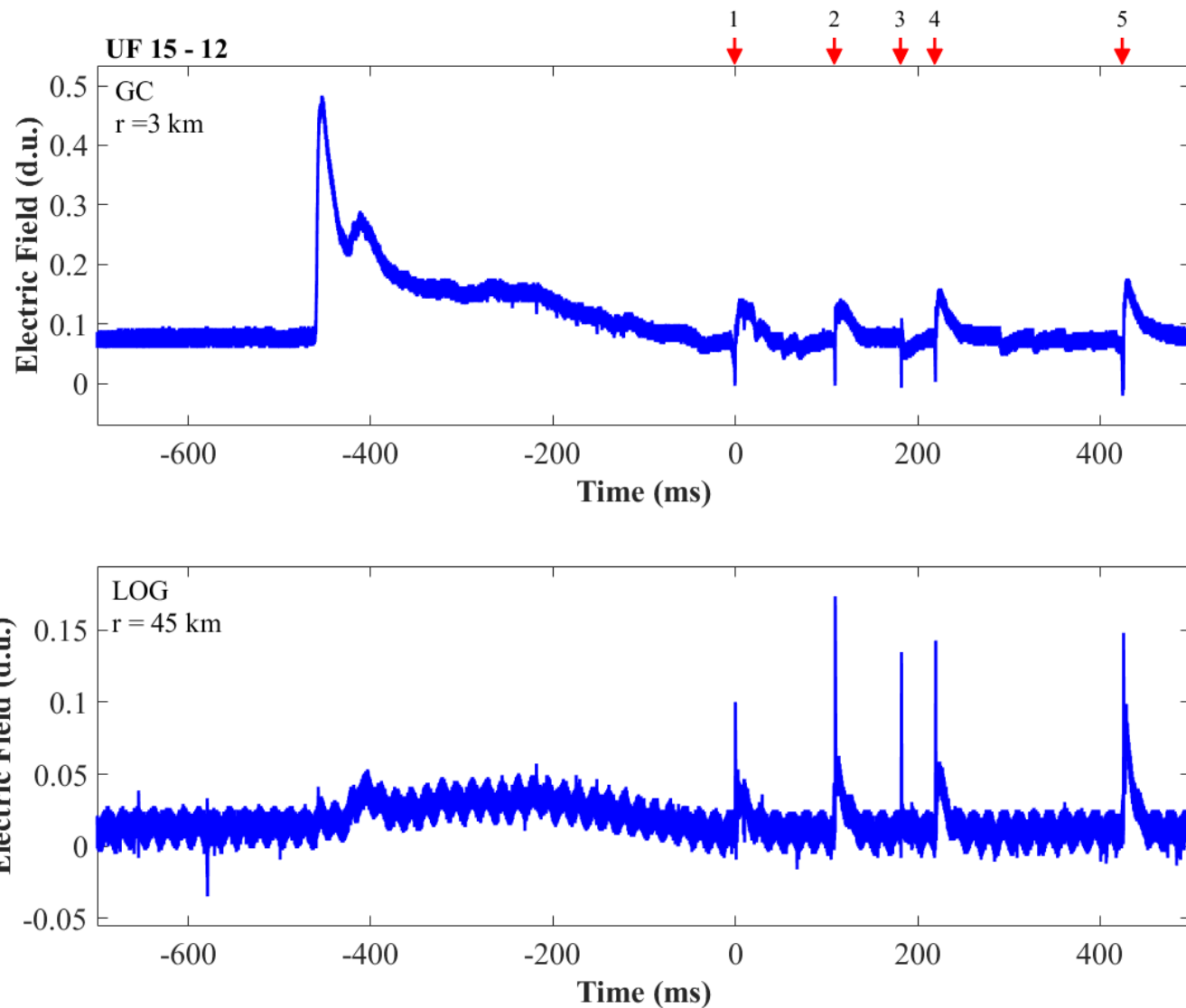


Figure A-102. Two-station electric field waveforms of flash UF 15-12.

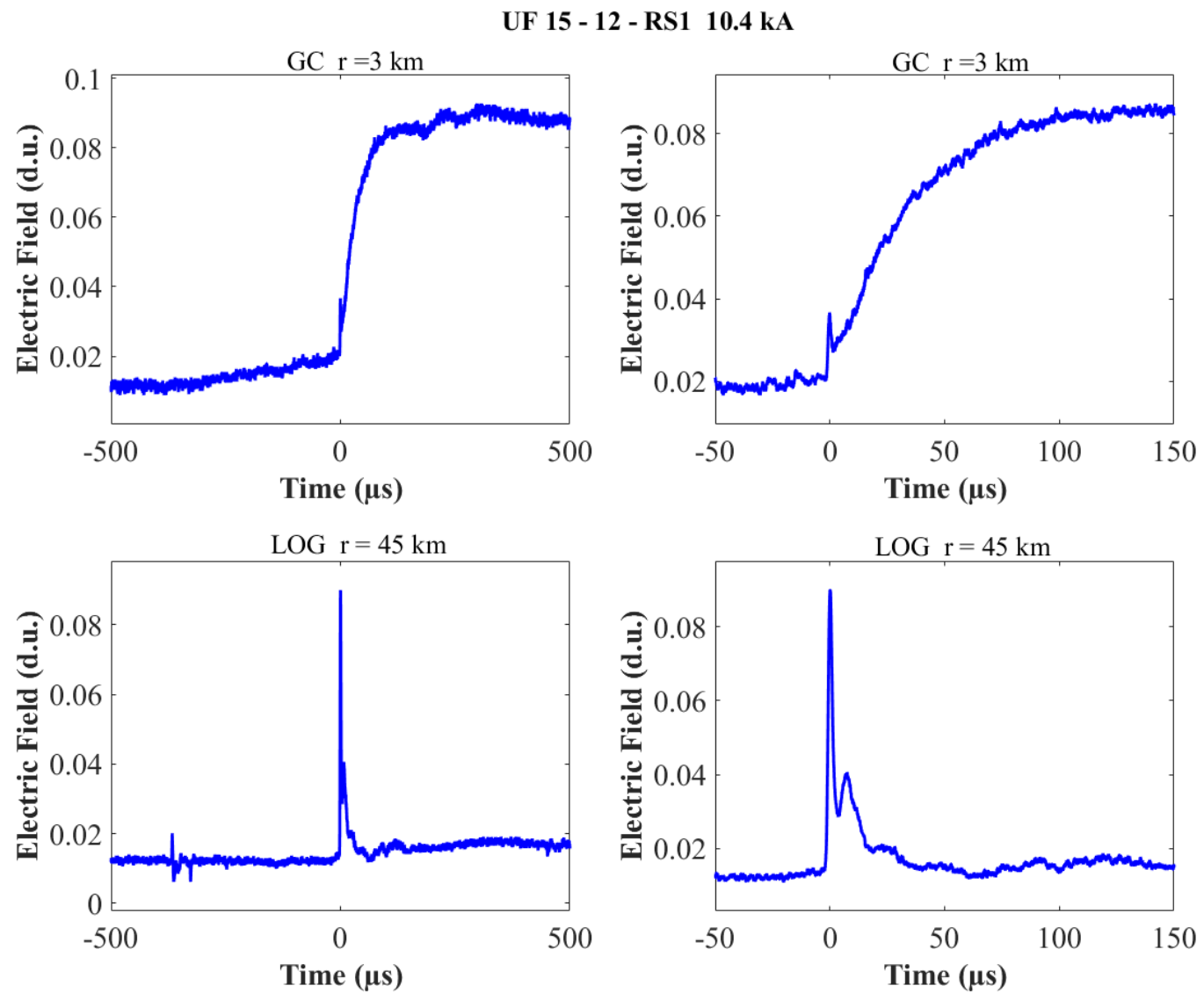


Figure A-103. Two-station electric field waveforms of the RS1 of flash UF 15-12.

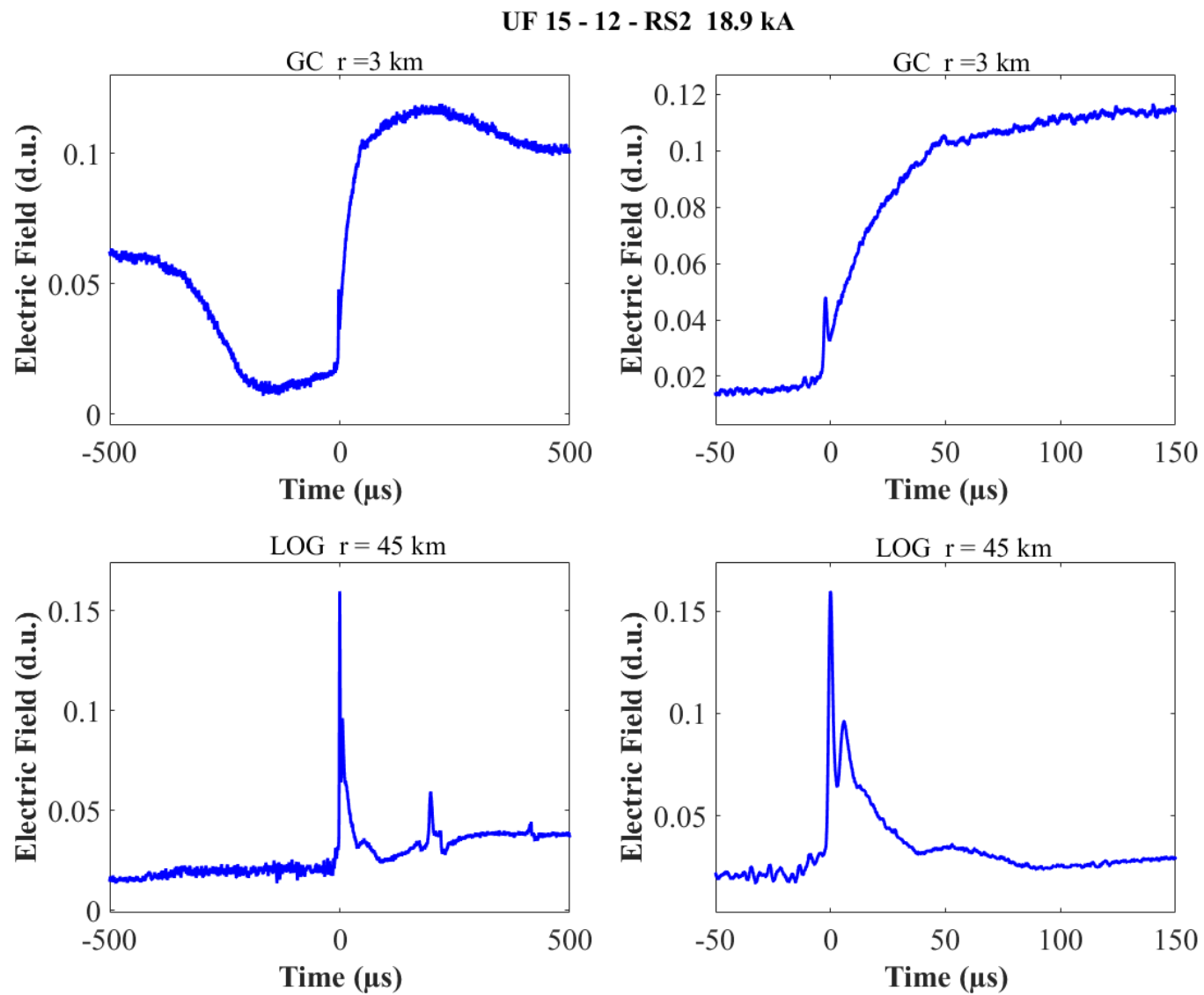


Figure A-104. Two-station electric field waveforms of the RS2 of flash UF 15-12.

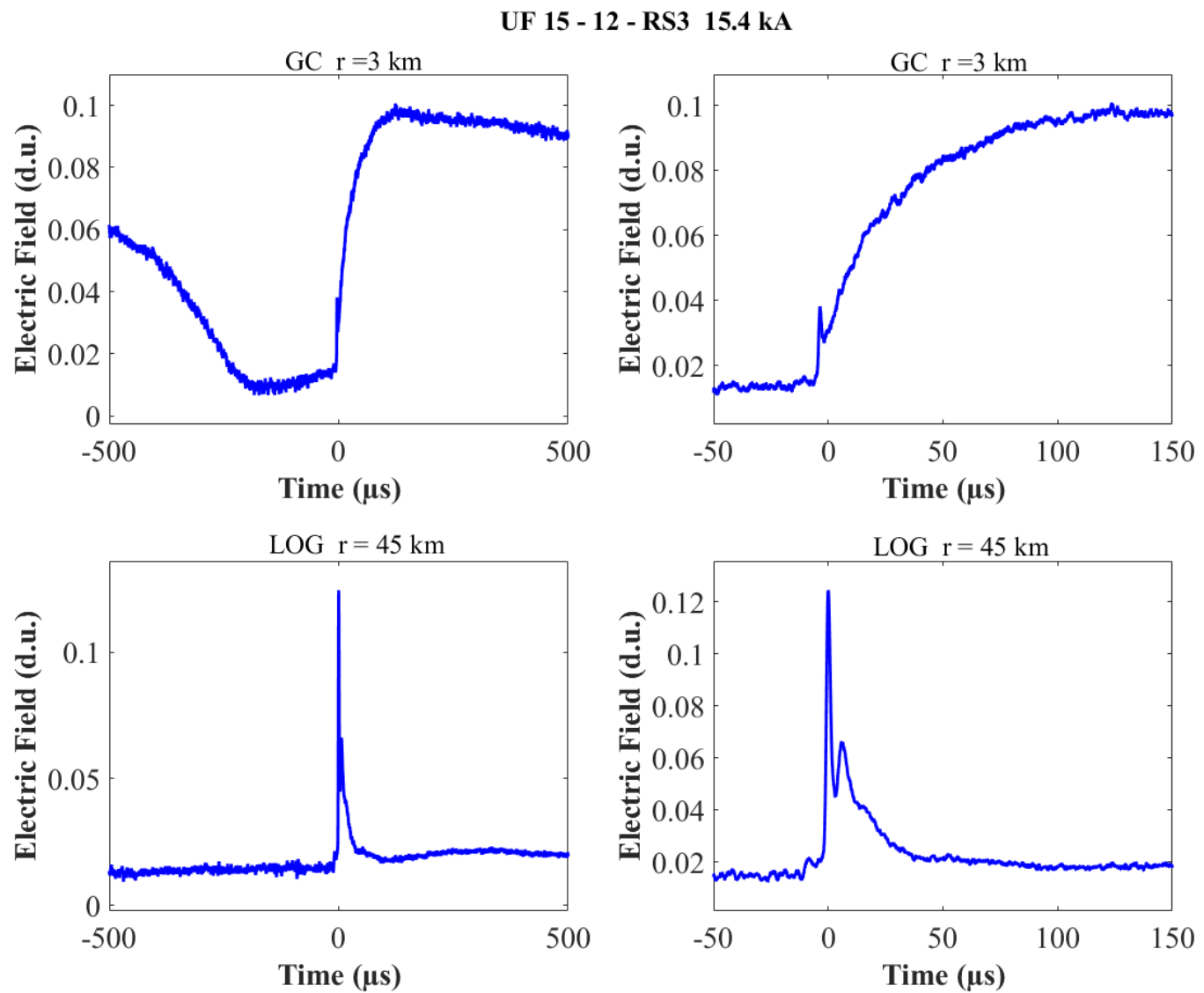


Figure A-105. Two-station electric field waveforms of the RS3 of flash UF 15-12.

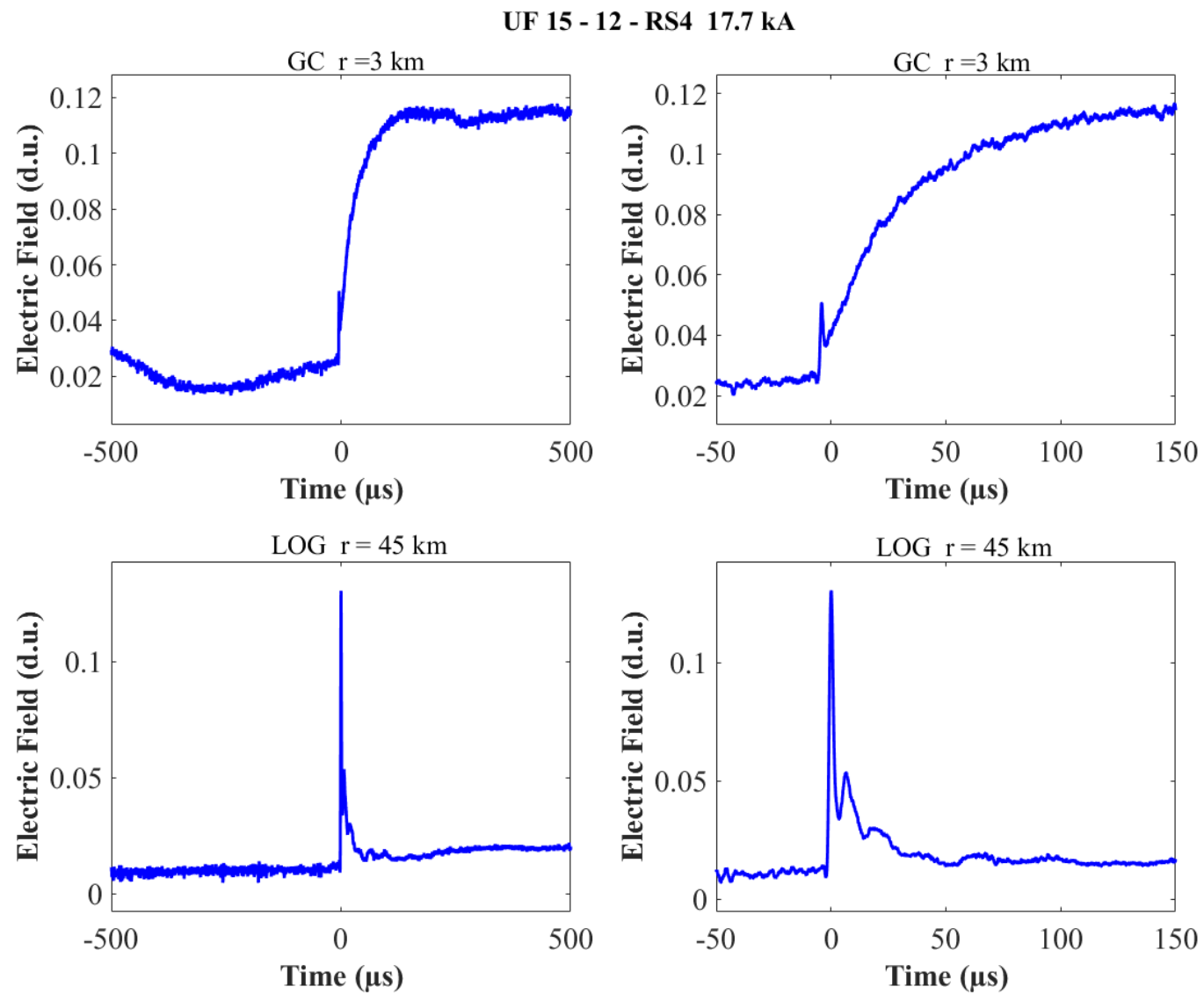


Figure A-106. Two-station electric field waveforms of the RS4 of flash UF 15-12.

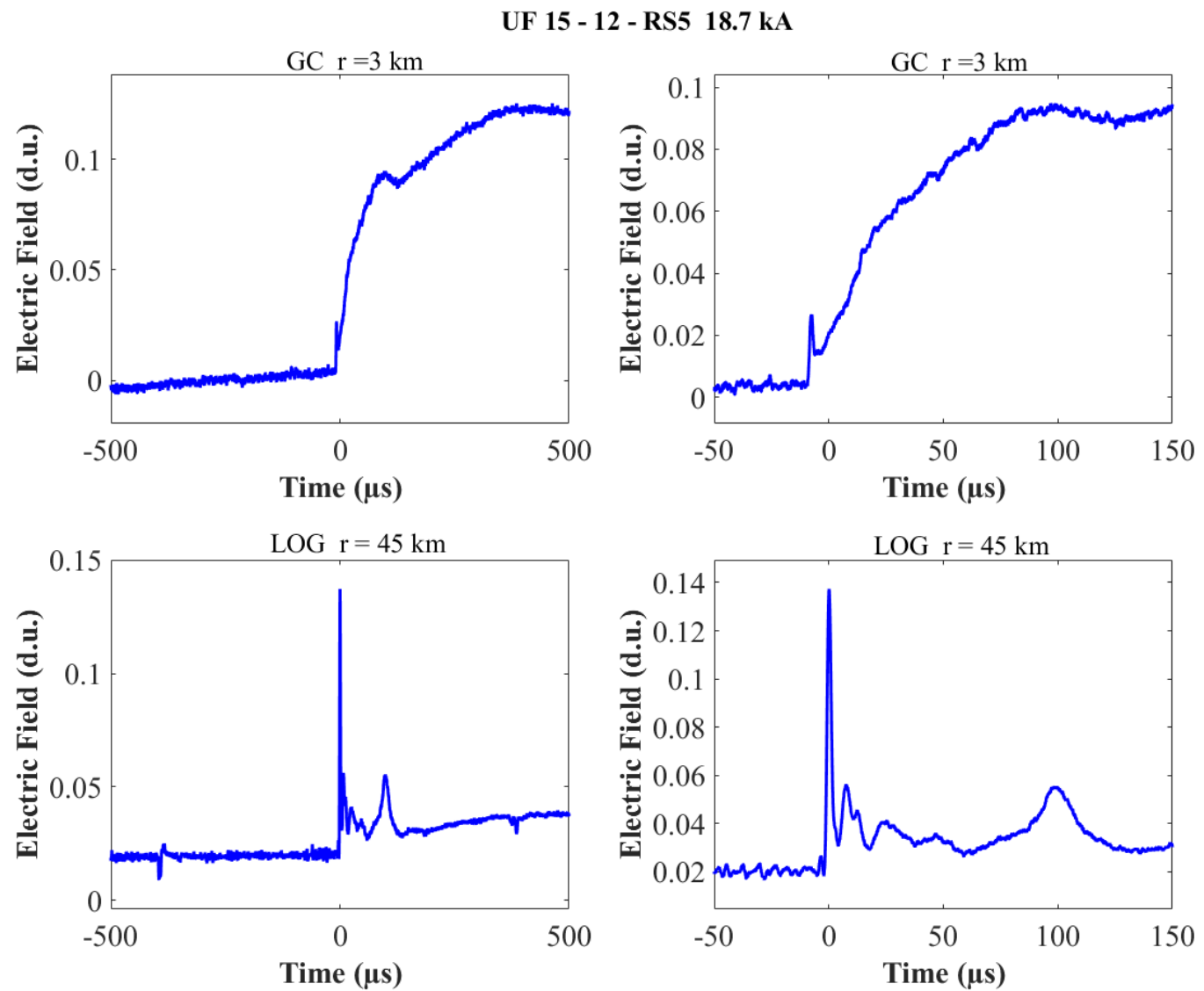


Figure A-107. Two-station electric field waveforms of the RS5 of flash UF 15-12.

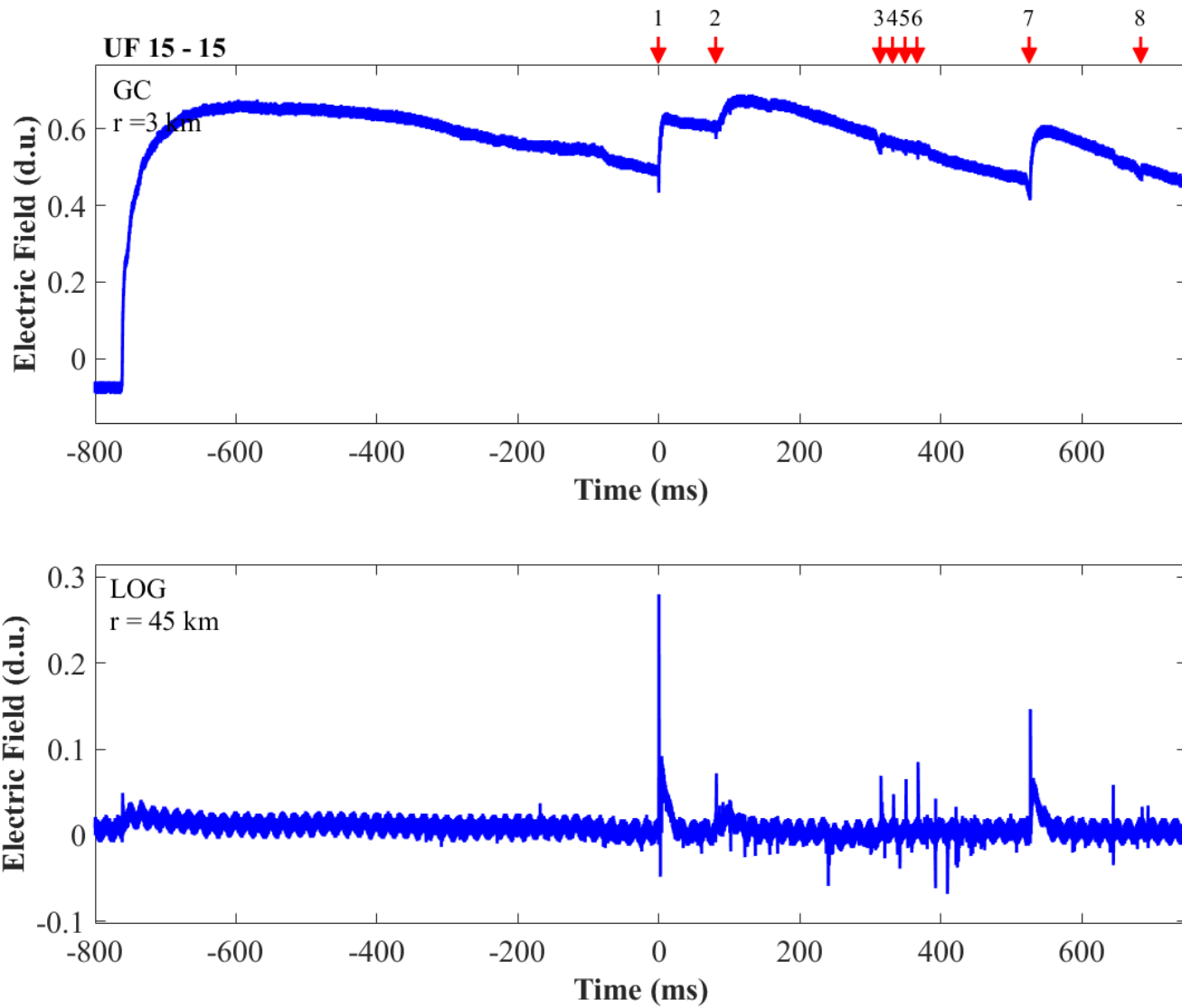


Figure A-108. Two-station electric field waveforms of flash UF 15-15.

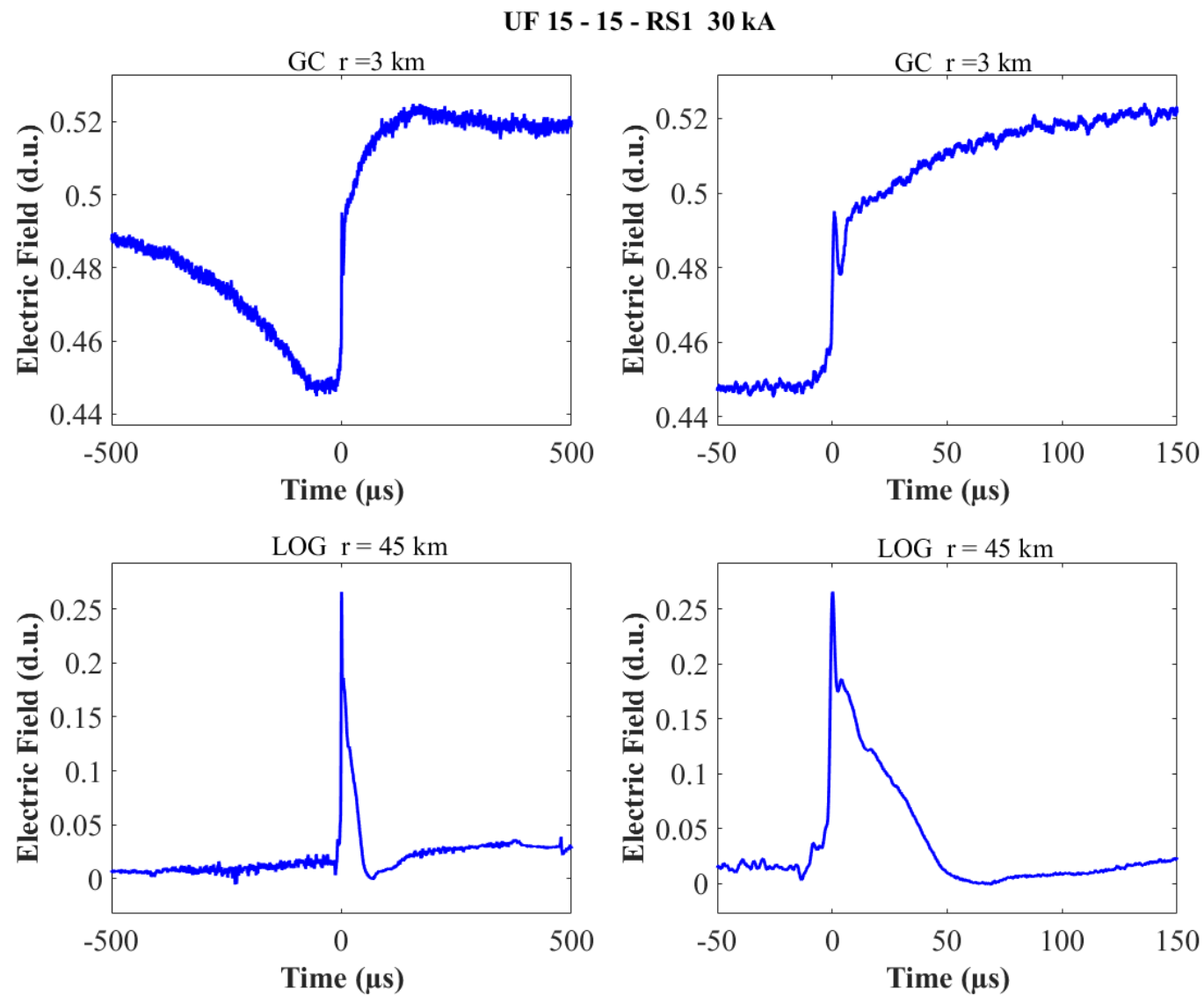


Figure A-109. Two-station electric field waveforms of the RS1 of flash UF 15-15.

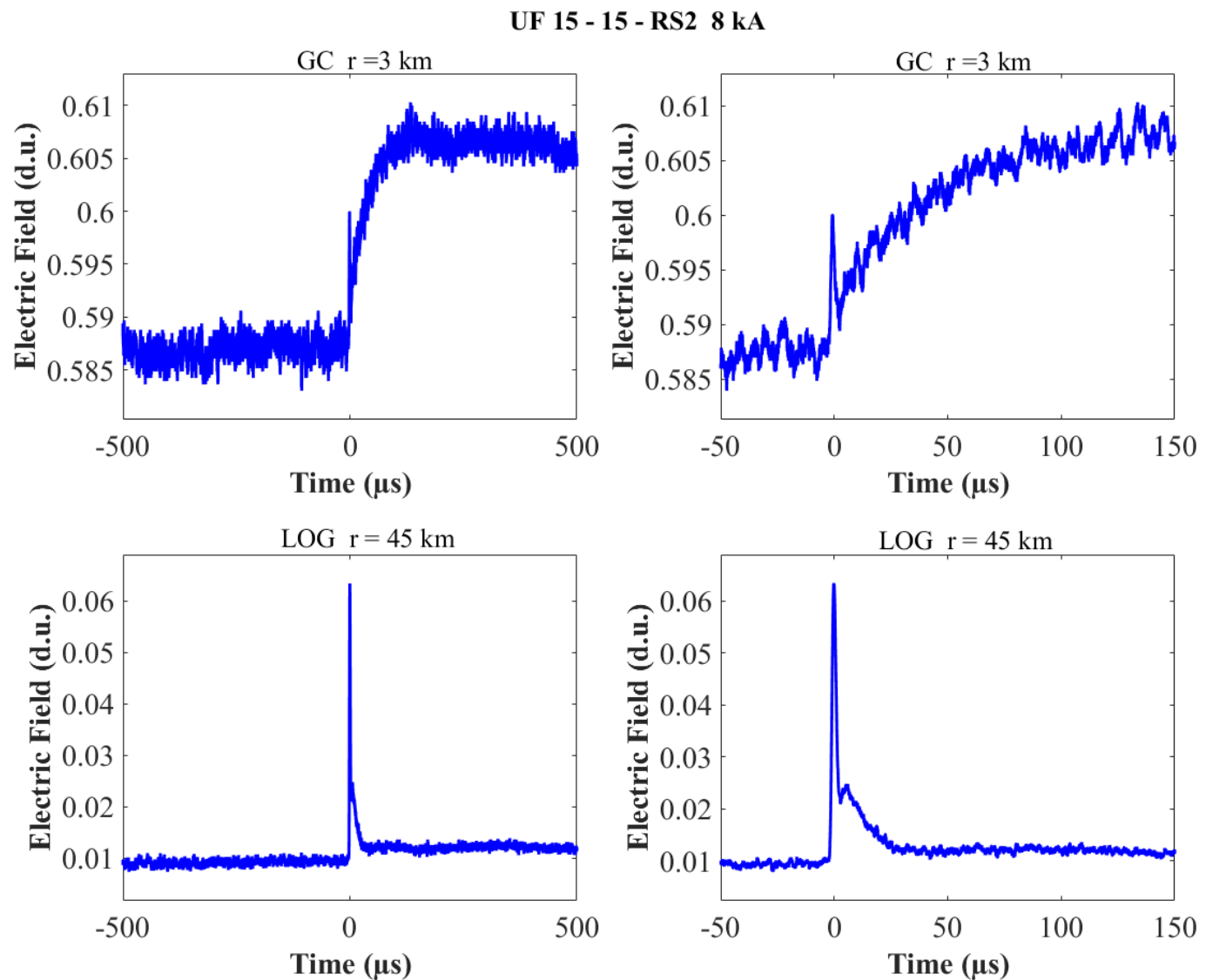


Figure A-110. Two-station electric field waveforms of the RS2 of flash UF 15-15.

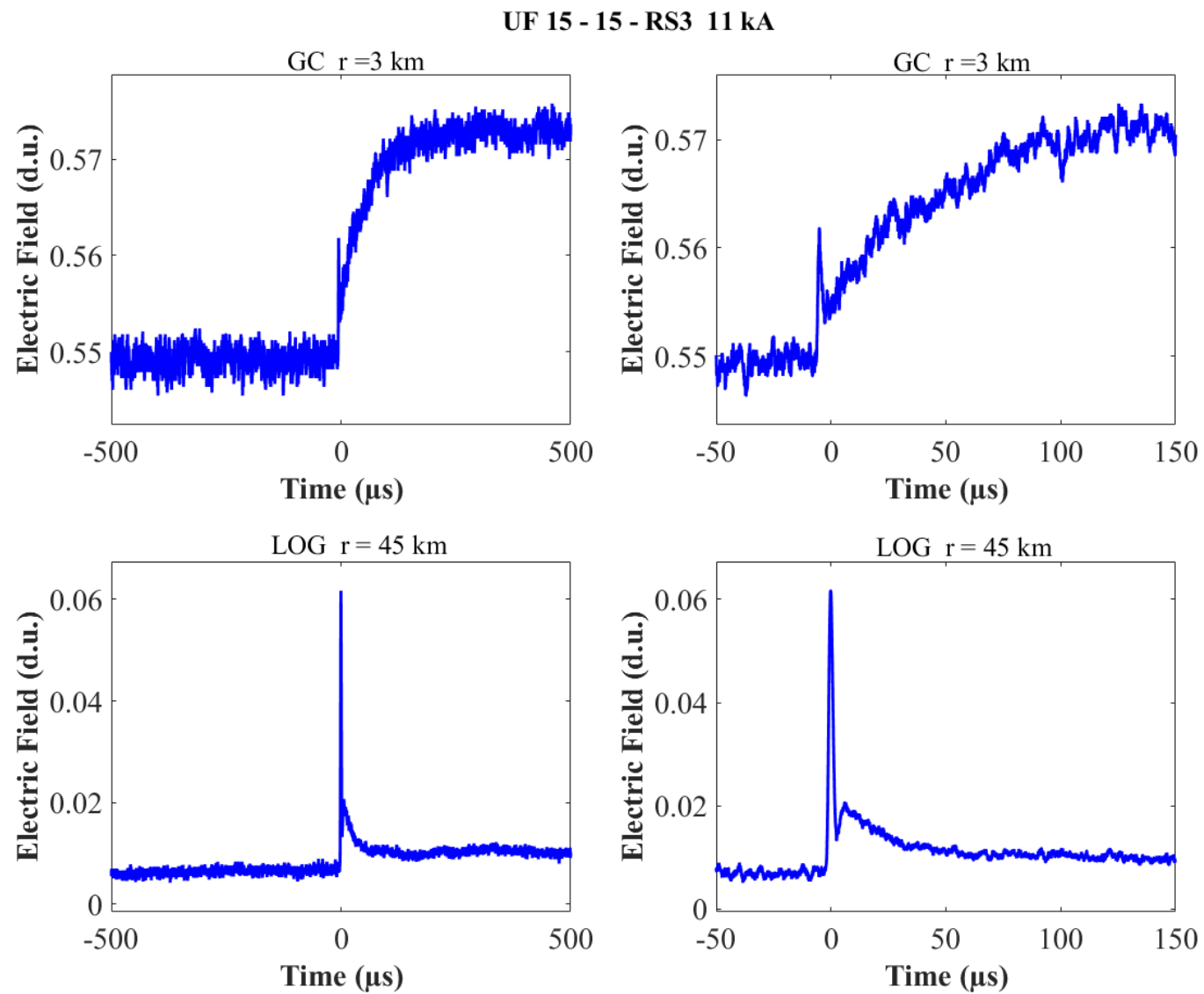


Figure A-111. Two-station electric field waveforms of the RS3 of flash UF 15-15.

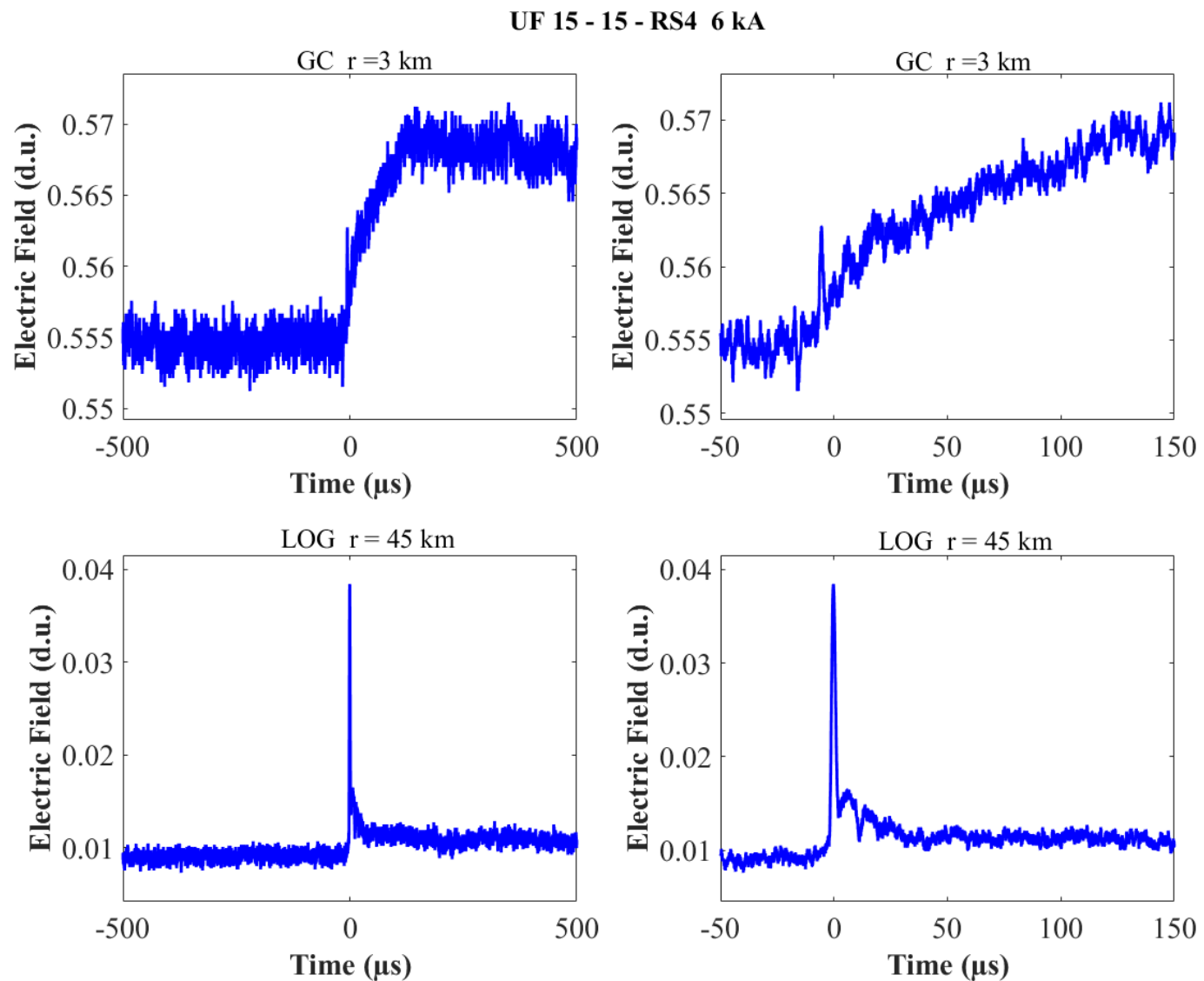


Figure A-112. Two-station electric field waveforms of the RS4 of flash UF 15-15.

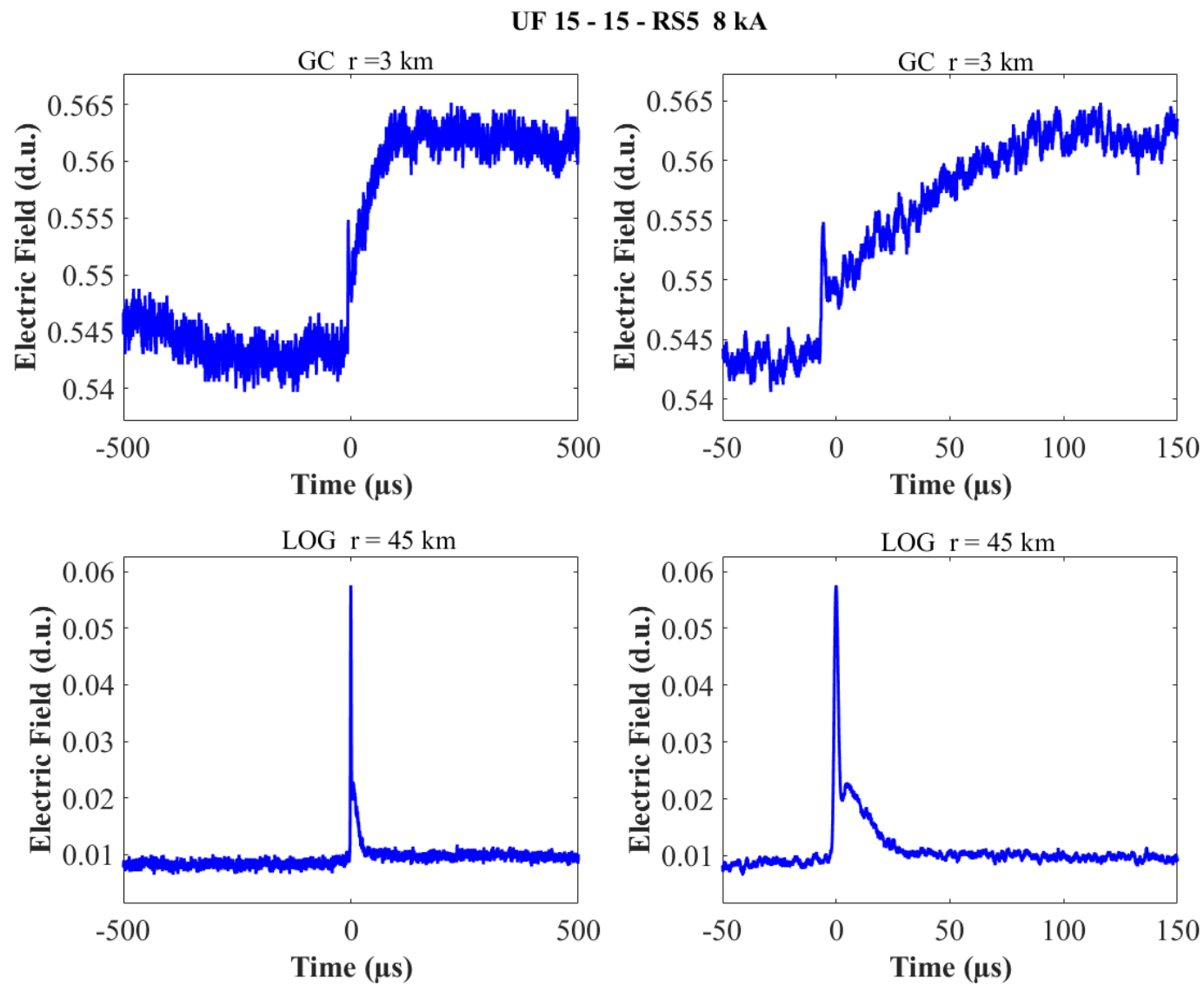


Figure A-113. Two-station electric field waveforms of the RS5 of flash UF 15-15.

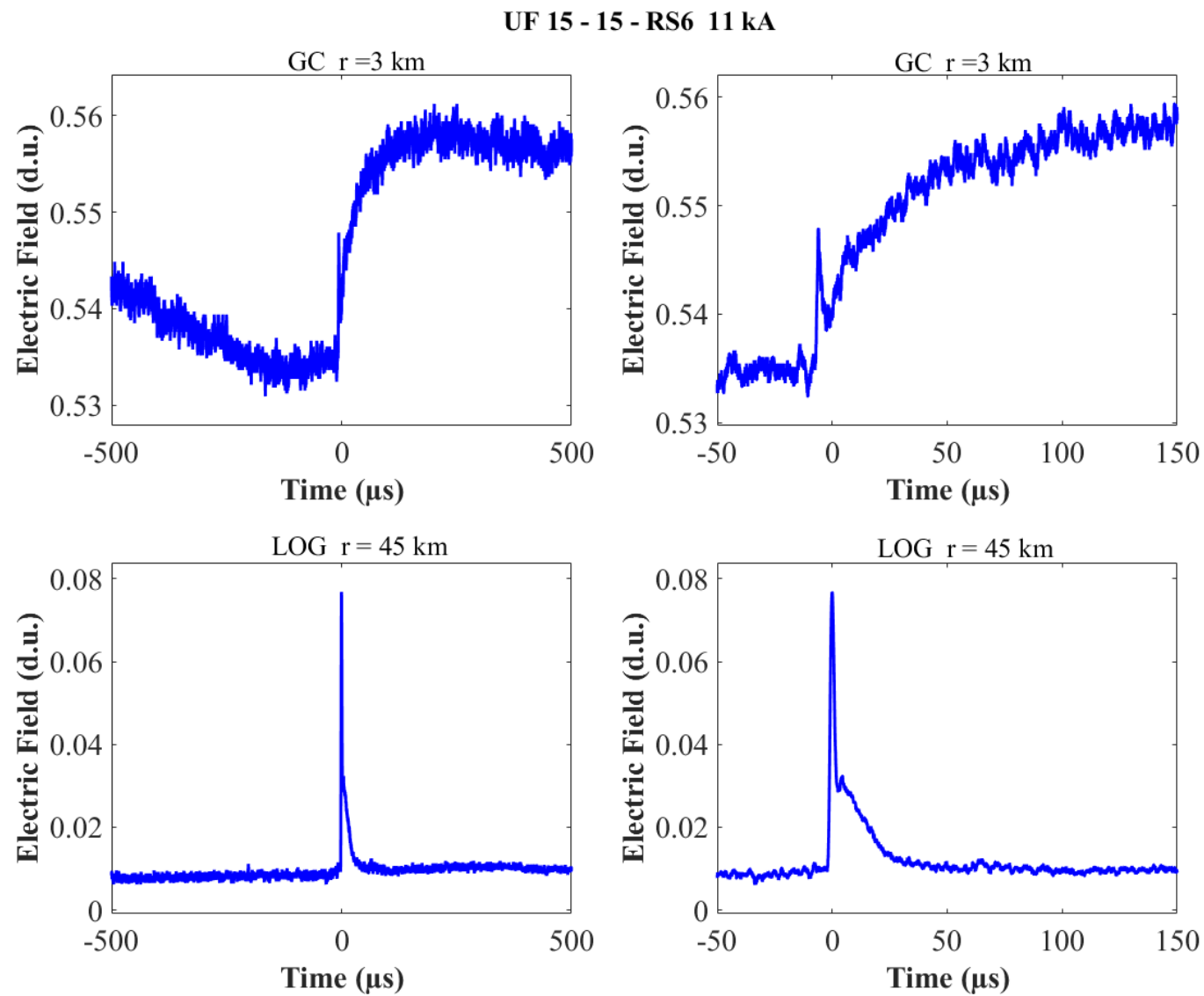


Figure A-114. Two-station electric field waveforms of the RS6 of flash UF 15-15.

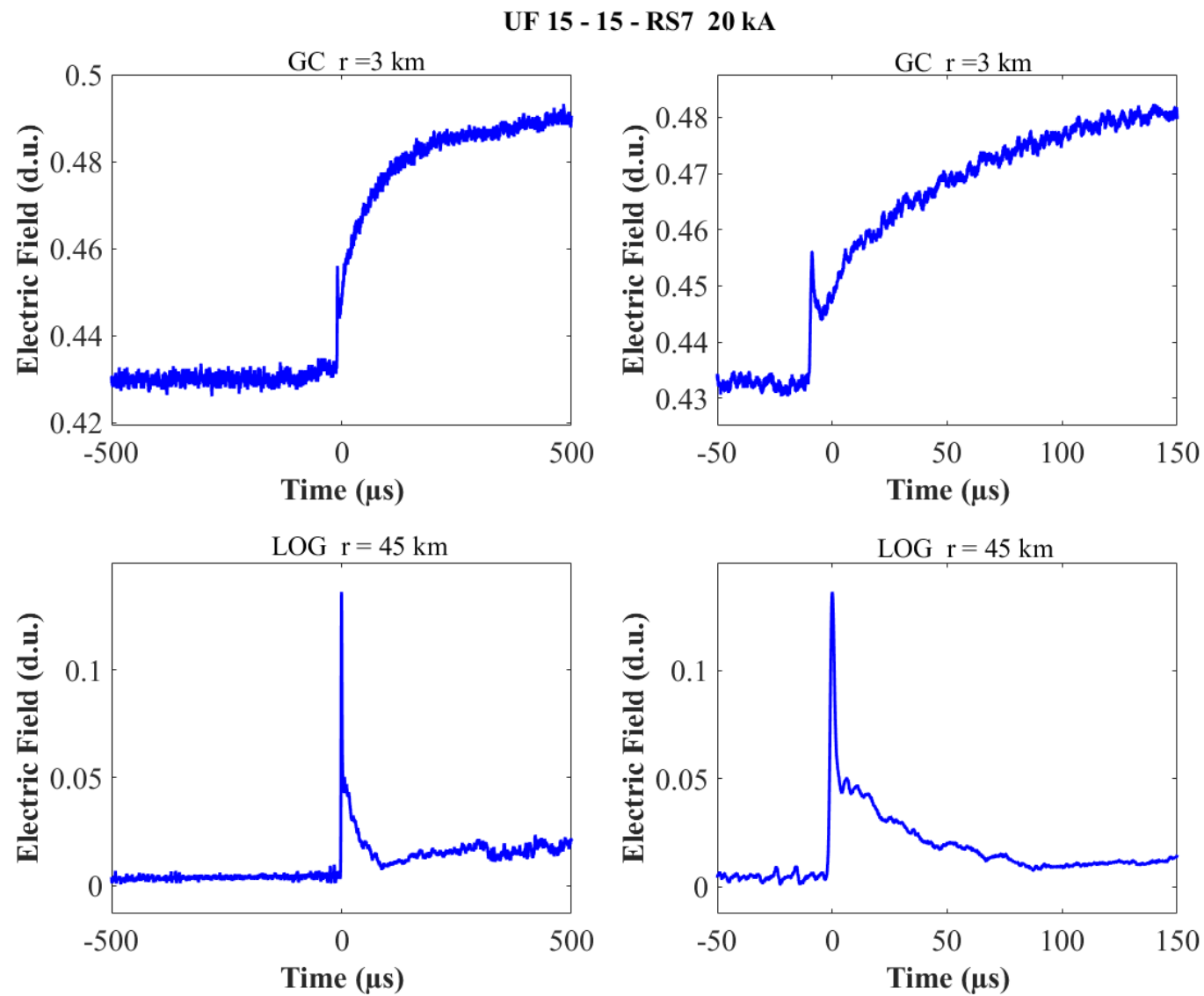


Figure A-115. Two-station electric field waveforms of the RS7 of flash UF 15-15.

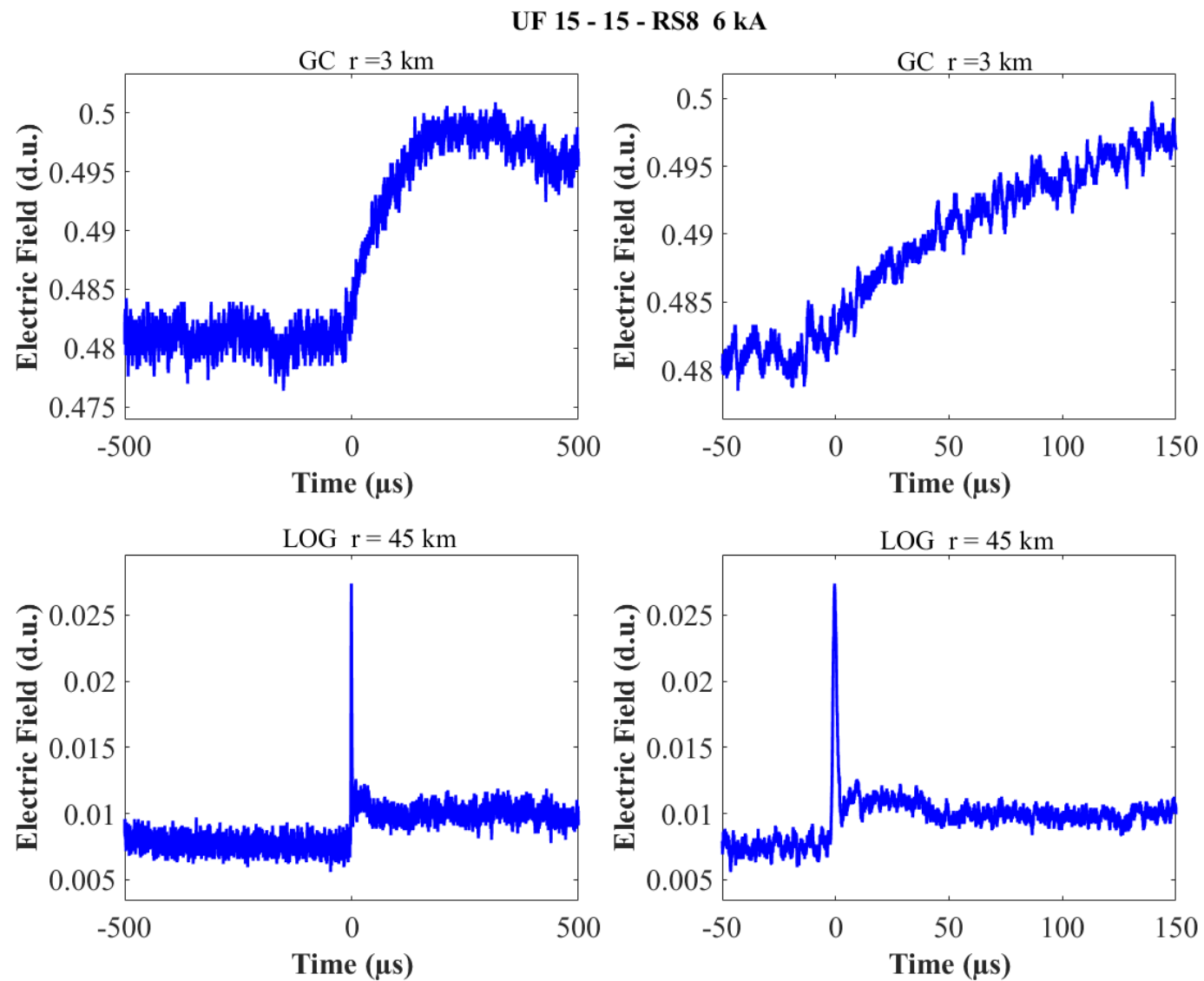


Figure A-116. Two-station electric field waveforms of the RS8 of flash UF 15-15.

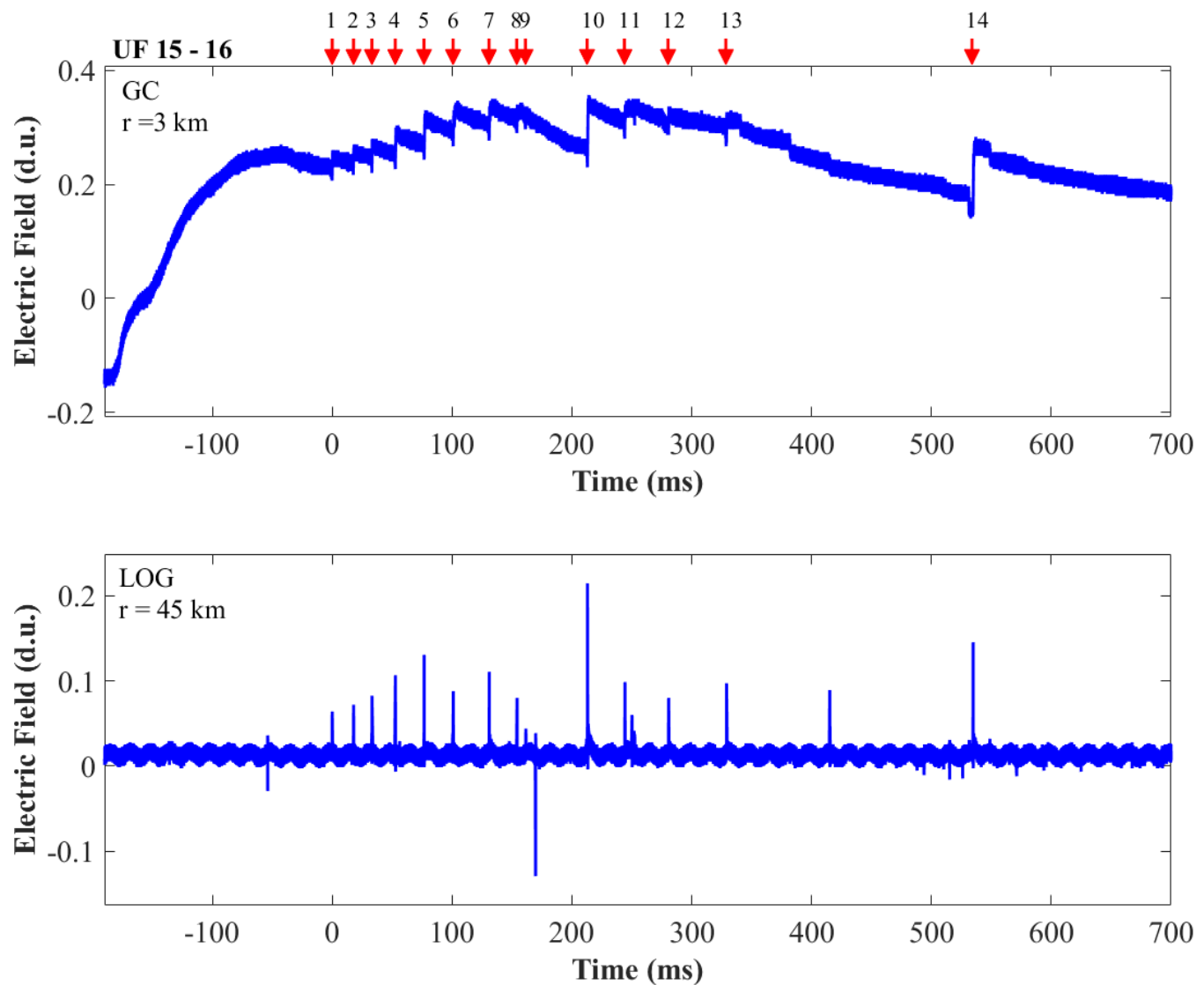


Figure A-117. Two-station electric field waveforms of flash UF 15-16.

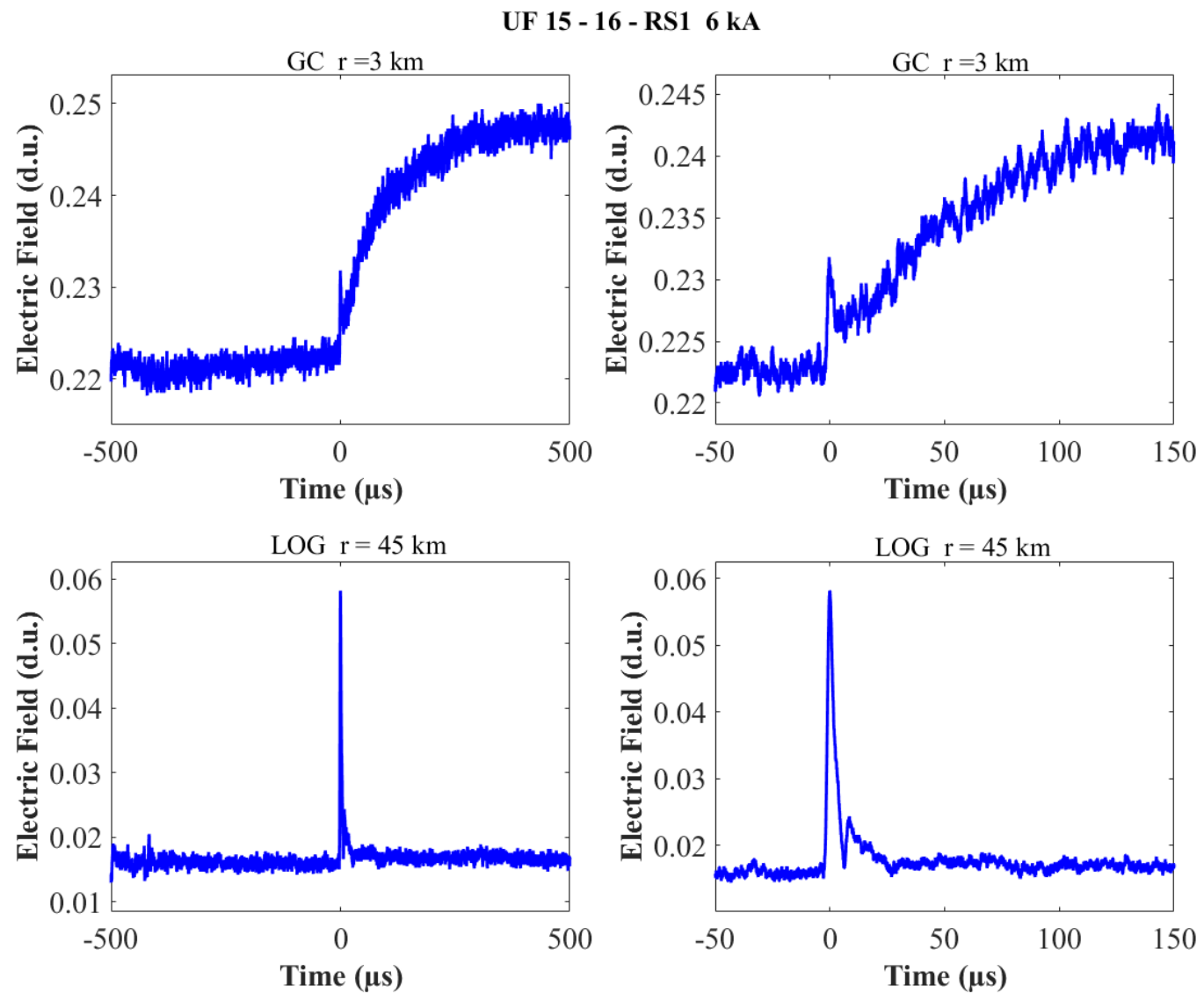


Figure A-118. Two-station electric field waveforms of the RS1 of flash UF 15-16.

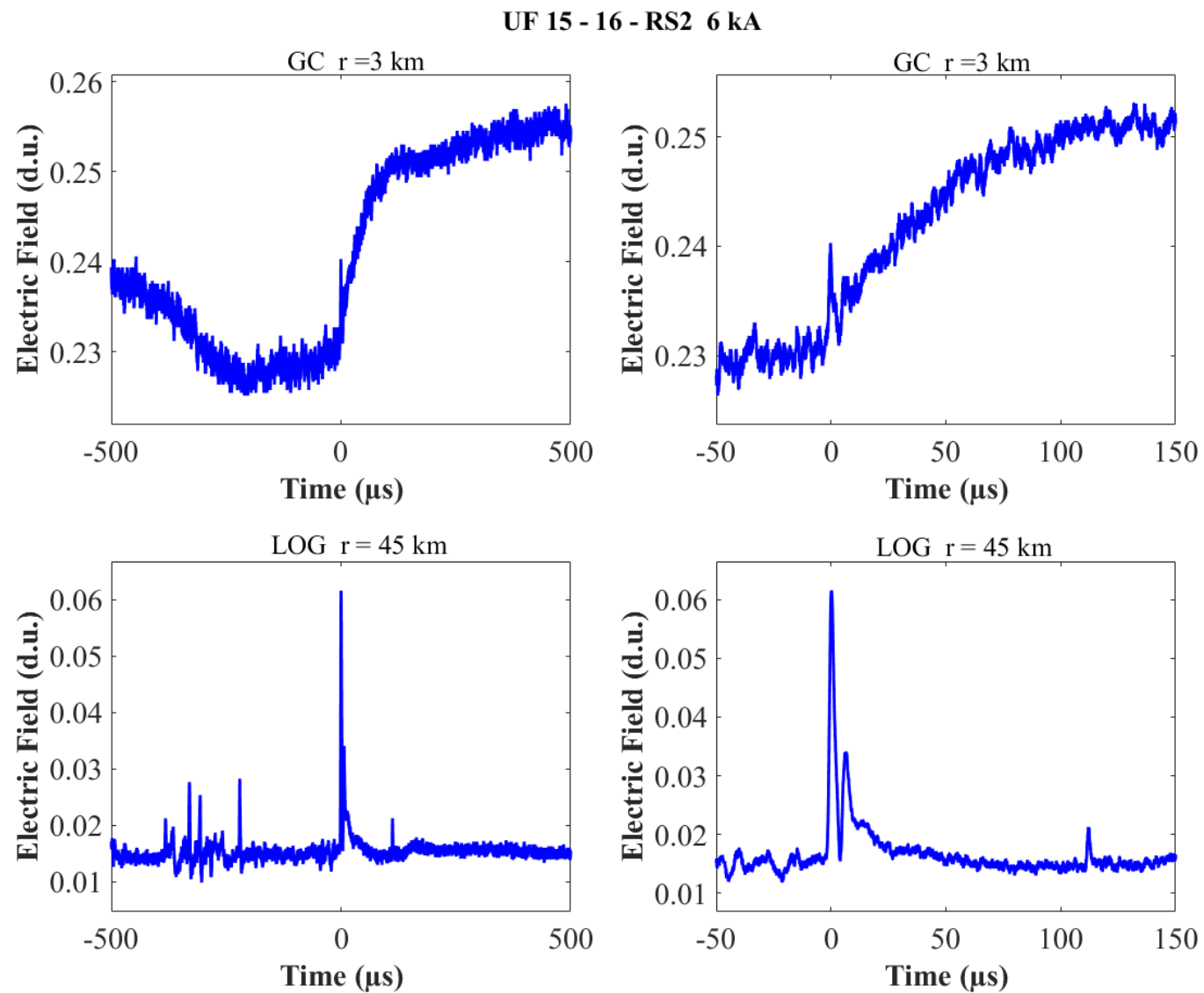


Figure A-119. Two-station electric field waveforms of the RS2 of flash UF 15-16.

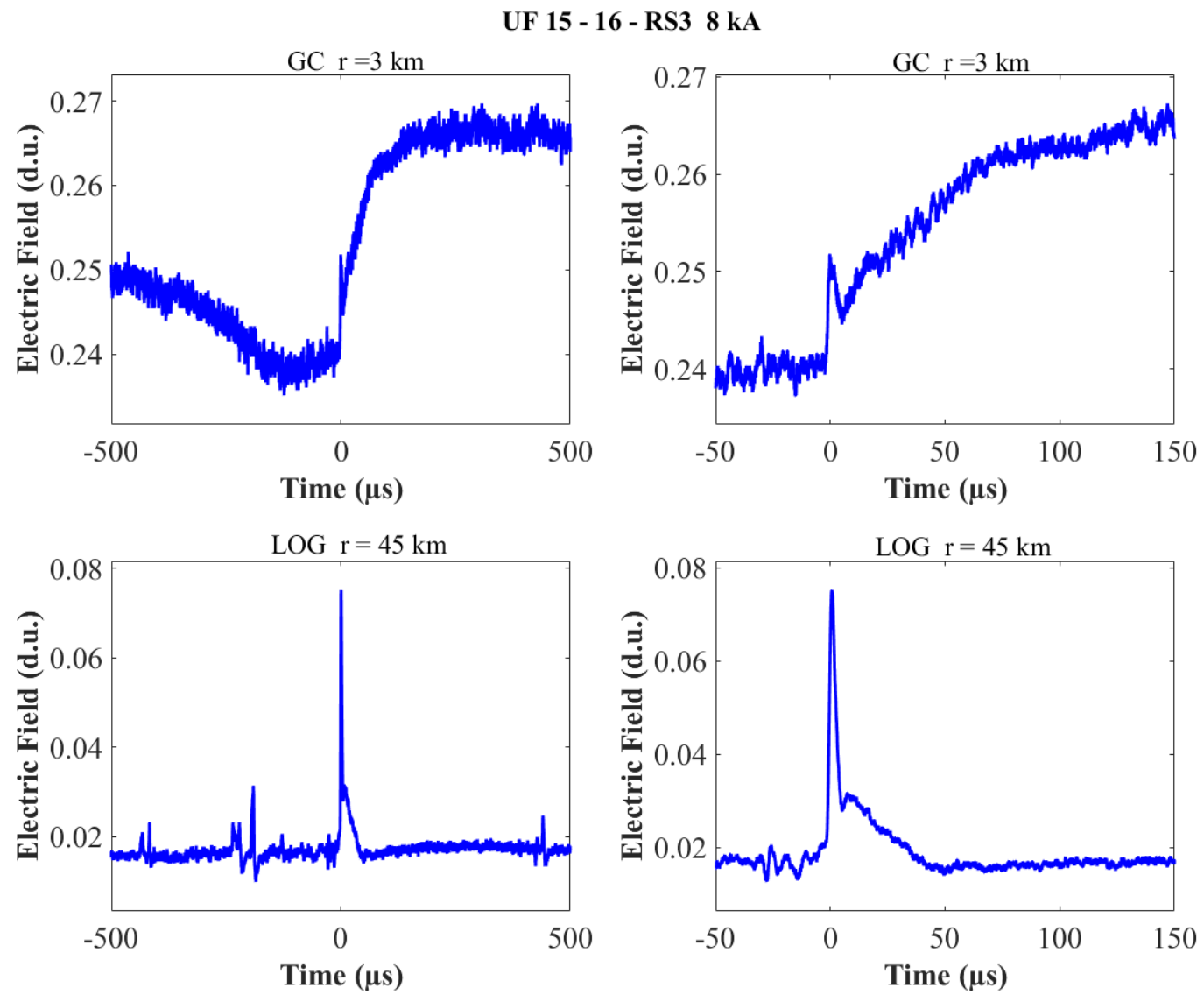


Figure A-120. Two-station electric field waveforms of the RS3 of flash UF 15-16.

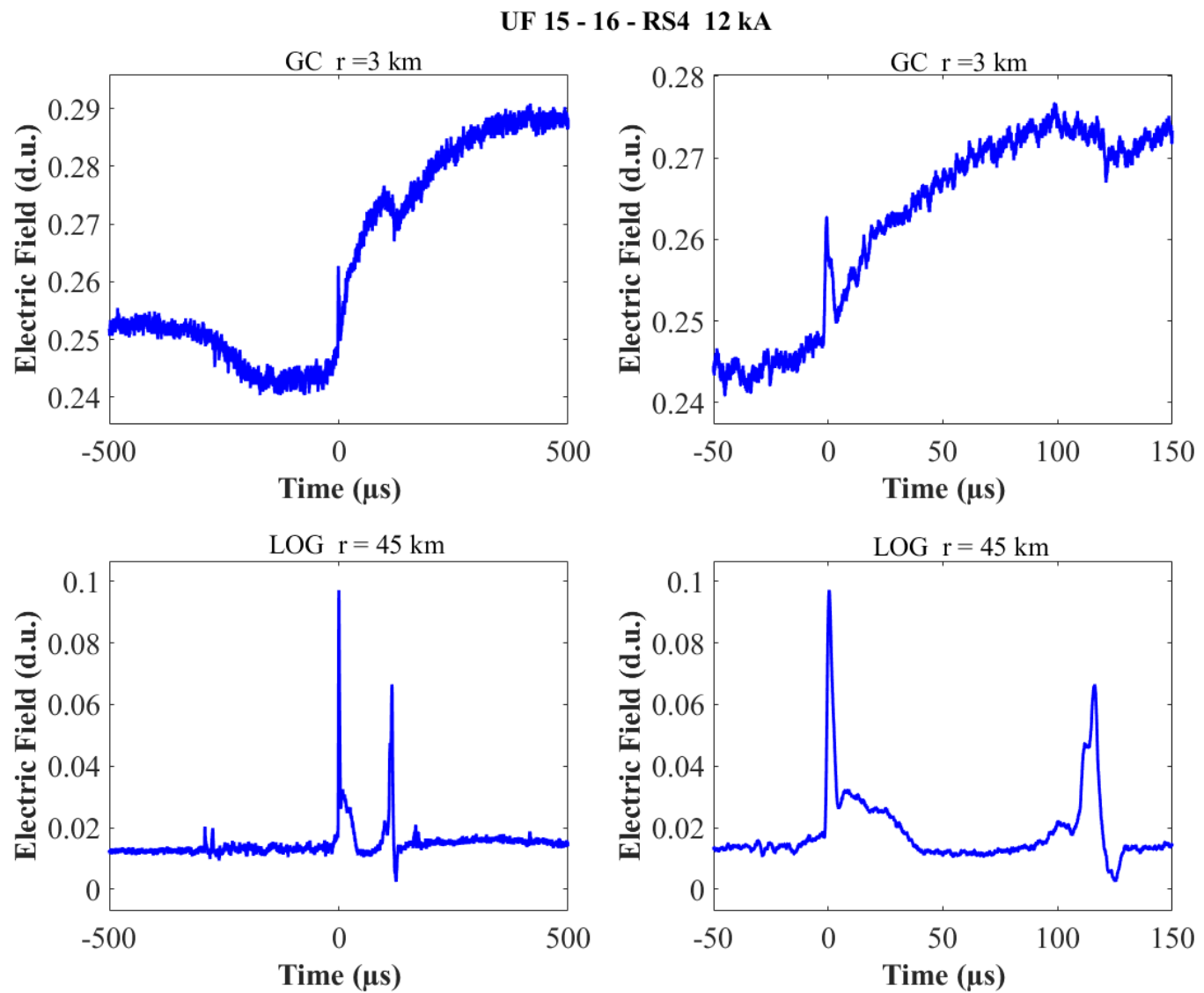


Figure A-121. Two-station electric field waveforms of the RS4 of flash UF 15-16.

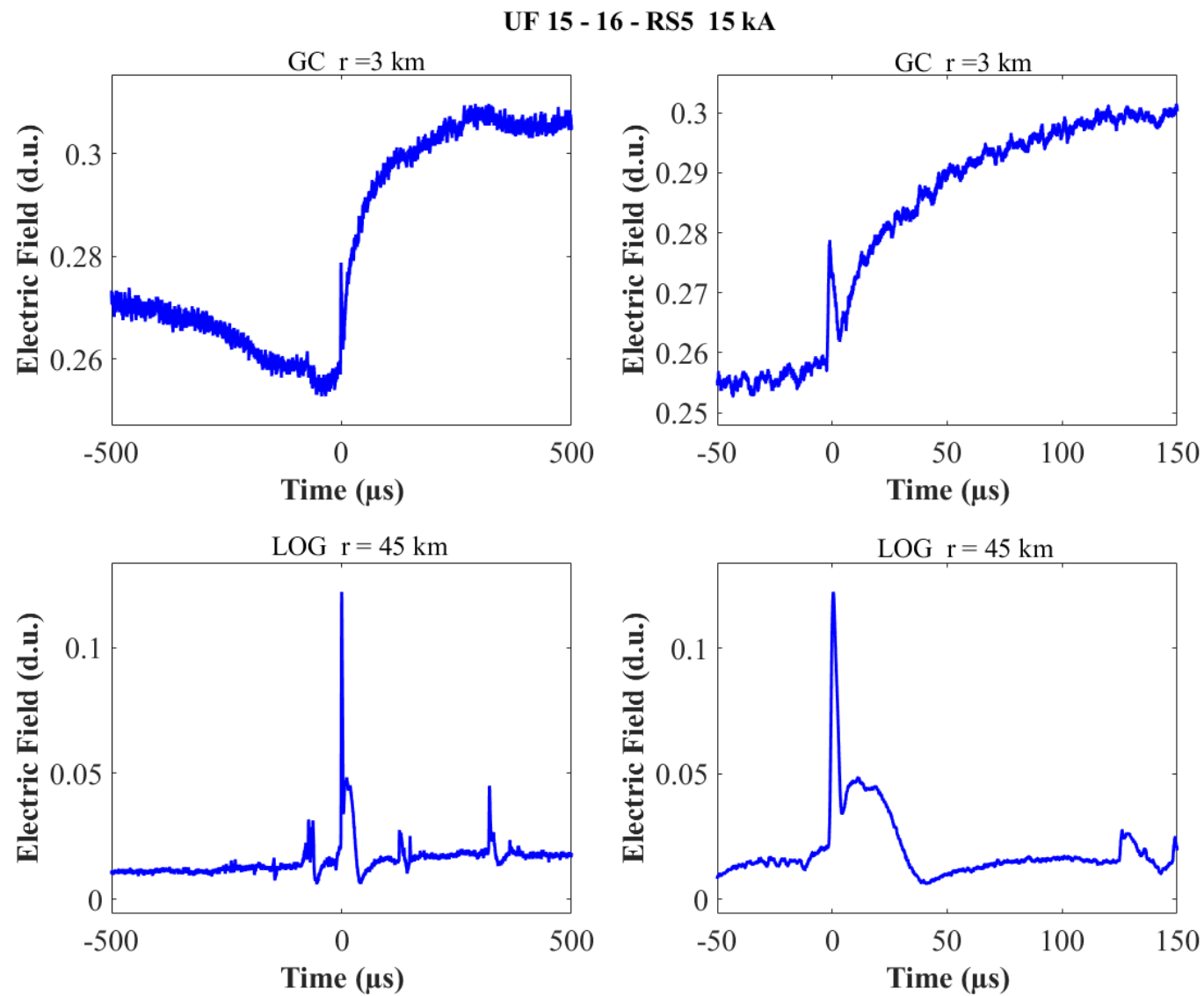


Figure A-122. Two-station electric field waveforms of the RS5 of flash UF 15-16.

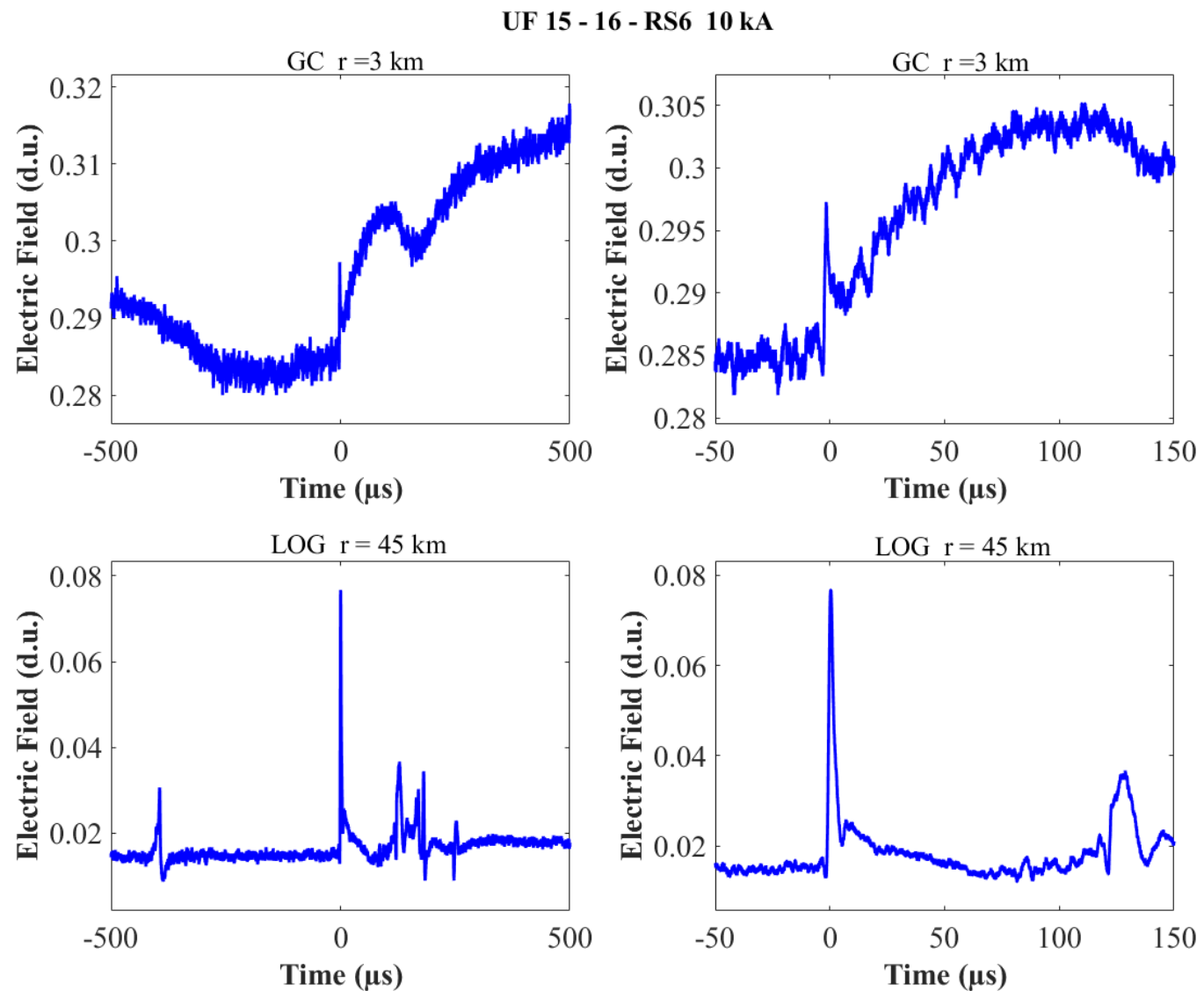


Figure A-123. Two-station electric field waveforms of the RS6 of flash UF 15-16.

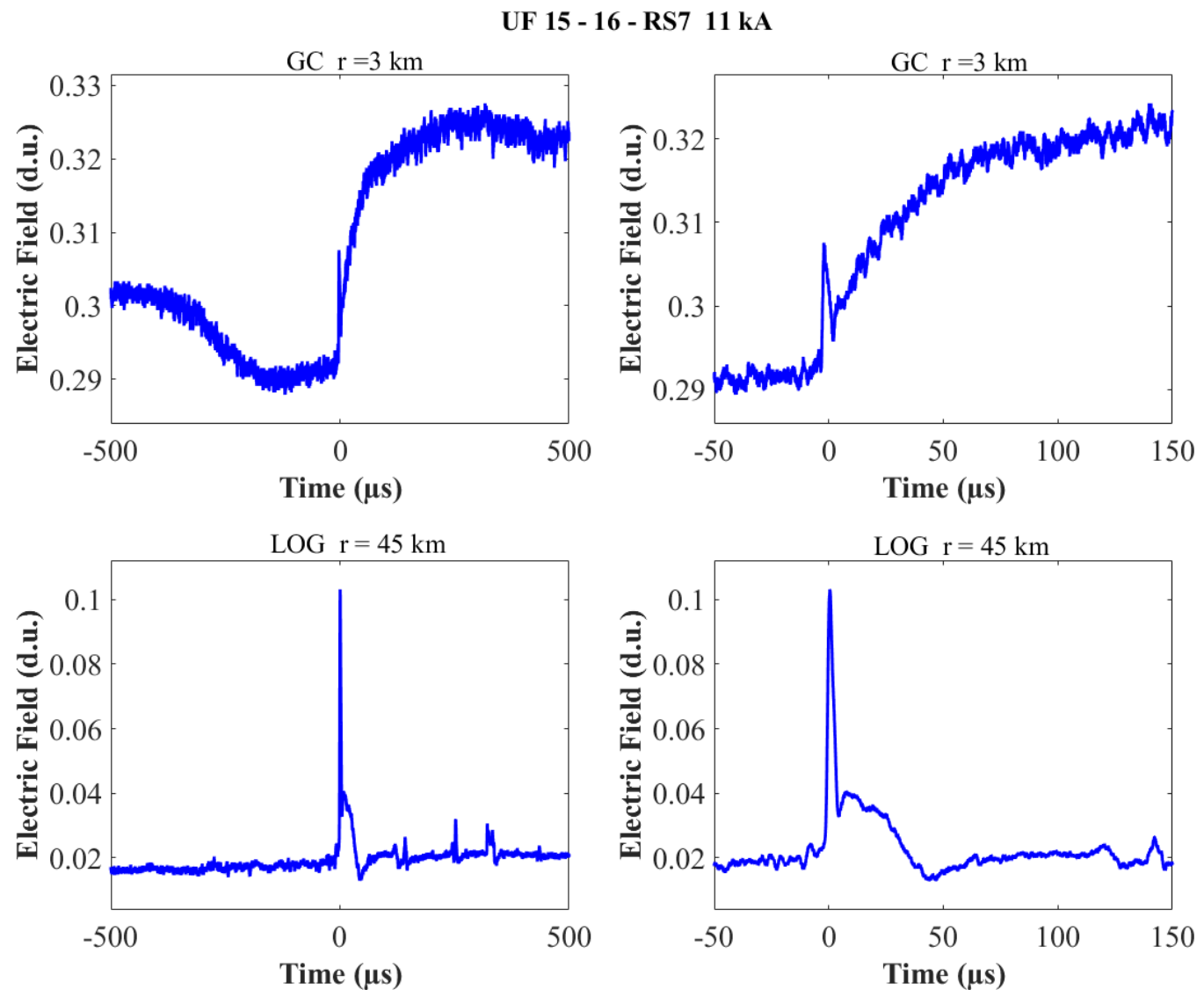


Figure A-124. Two-station electric field waveforms of the RS7 of flash UF 15-16.

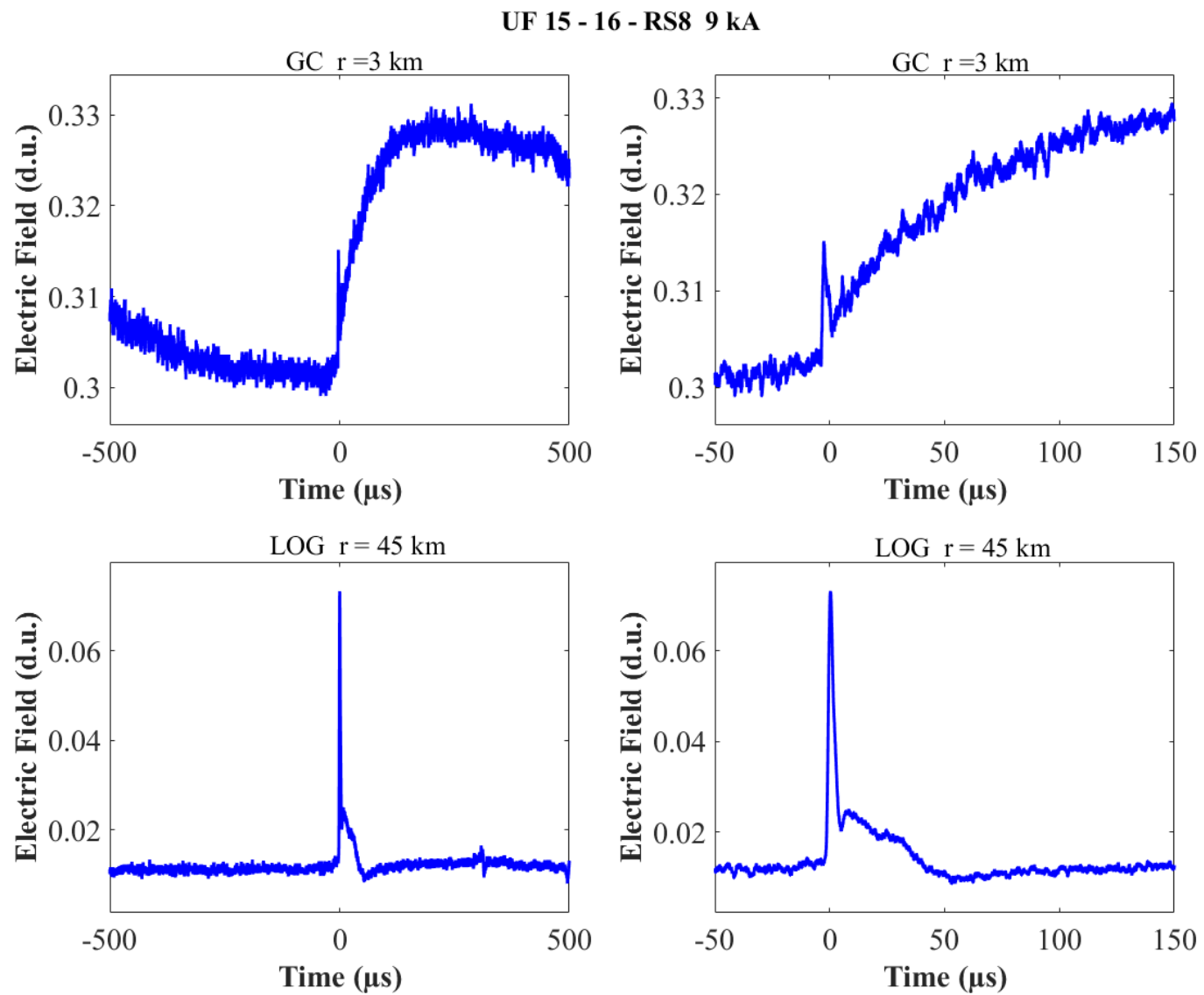


Figure A-125. Two-station electric field waveforms of the RS8 of flash UF 15-16.

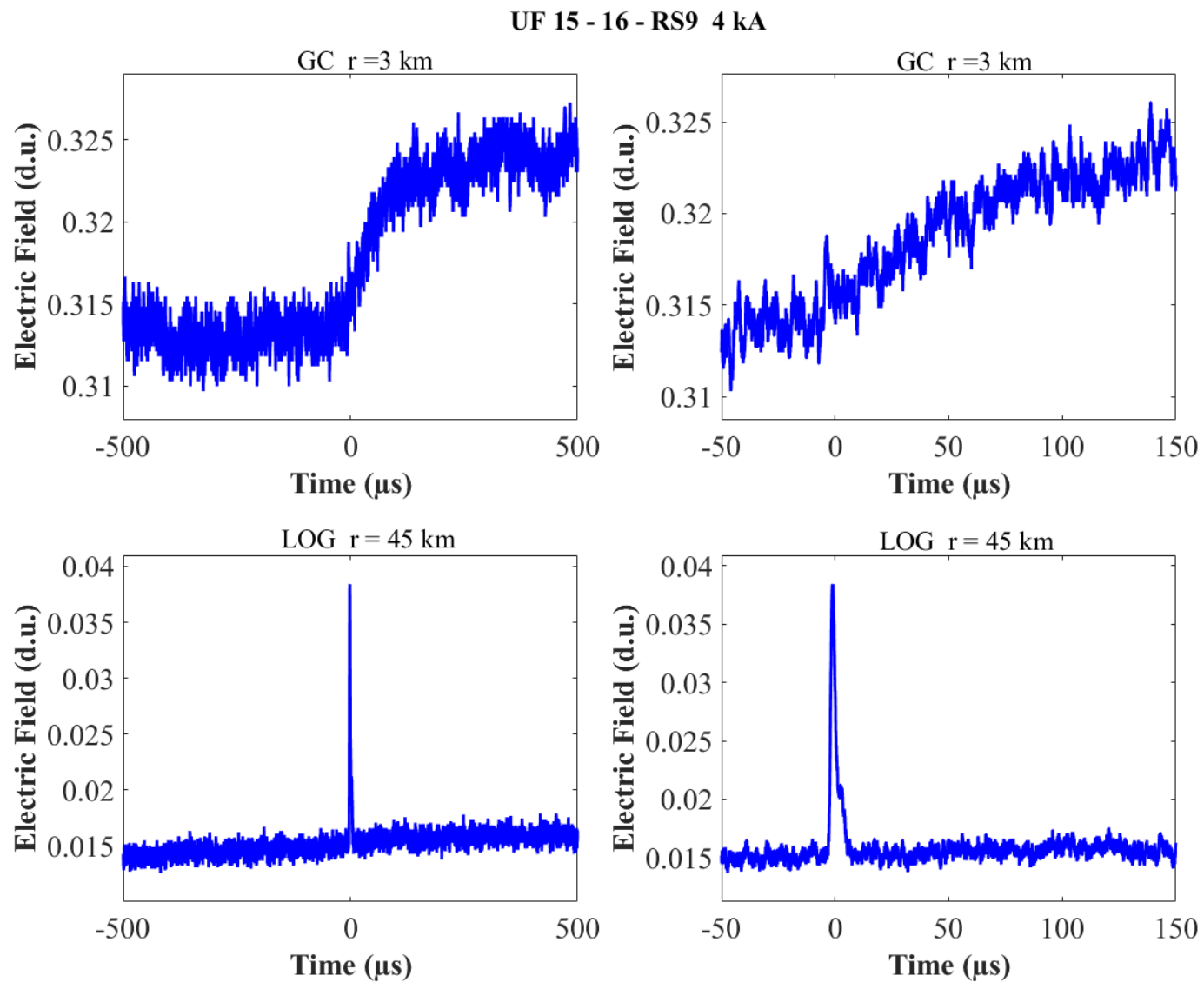


Figure A-126. Two-station electric field waveforms of the RS9 of flash UF 15-16.

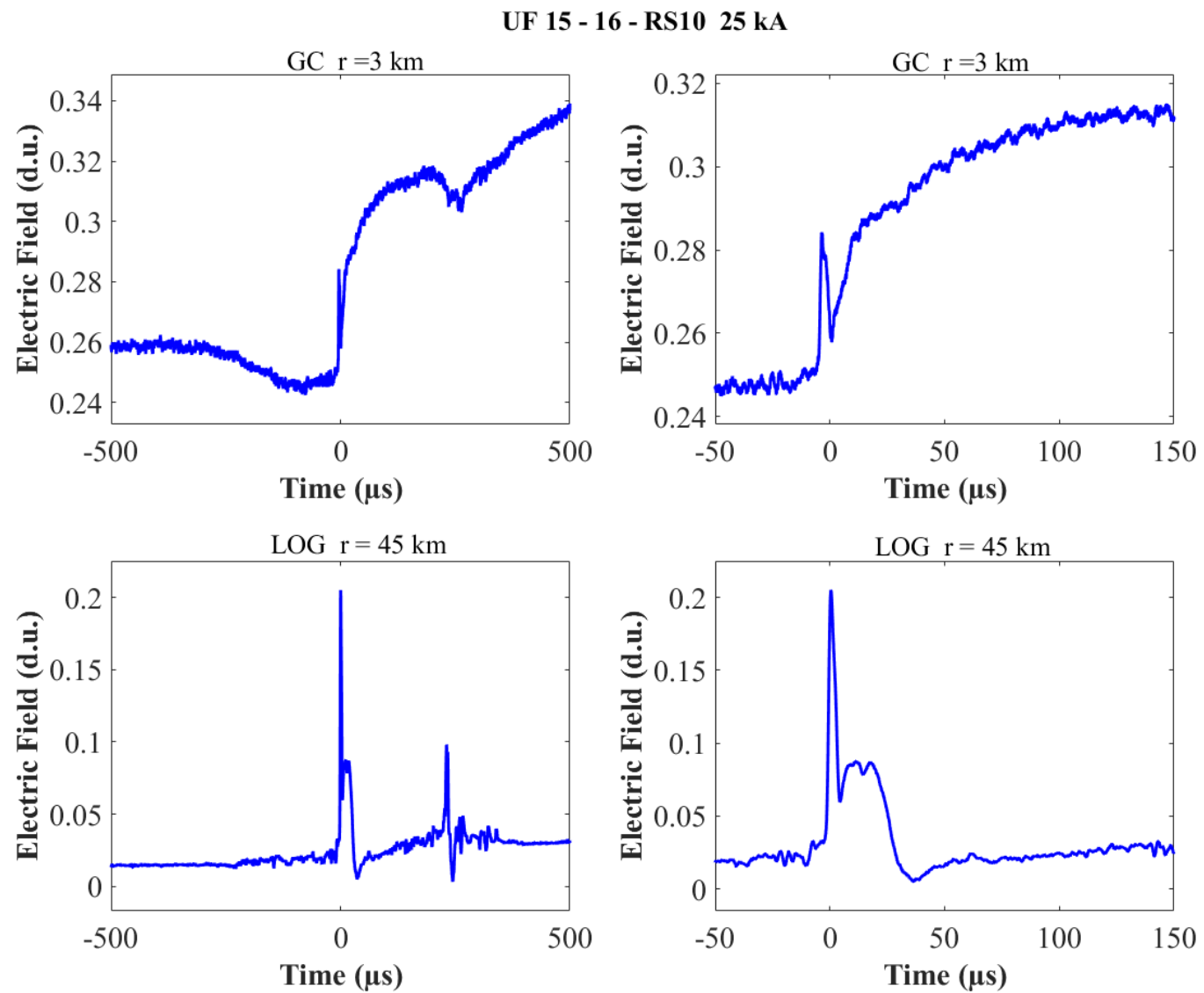


Figure A-127. Two-station electric field waveforms of the RS10 of flash UF 15-16.

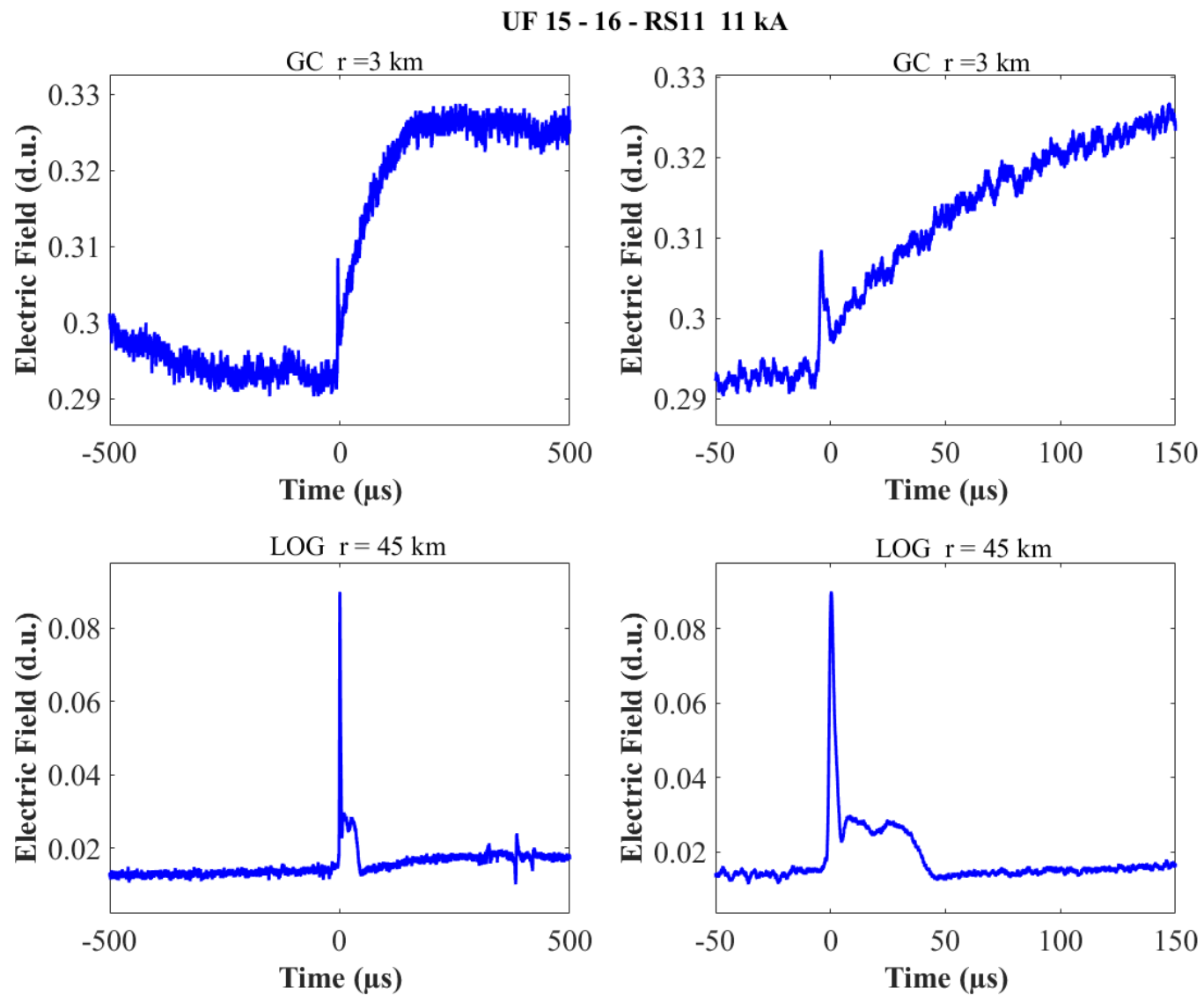


Figure A-128. Two-station electric field waveforms of the RS11 of flash UF 15-16.

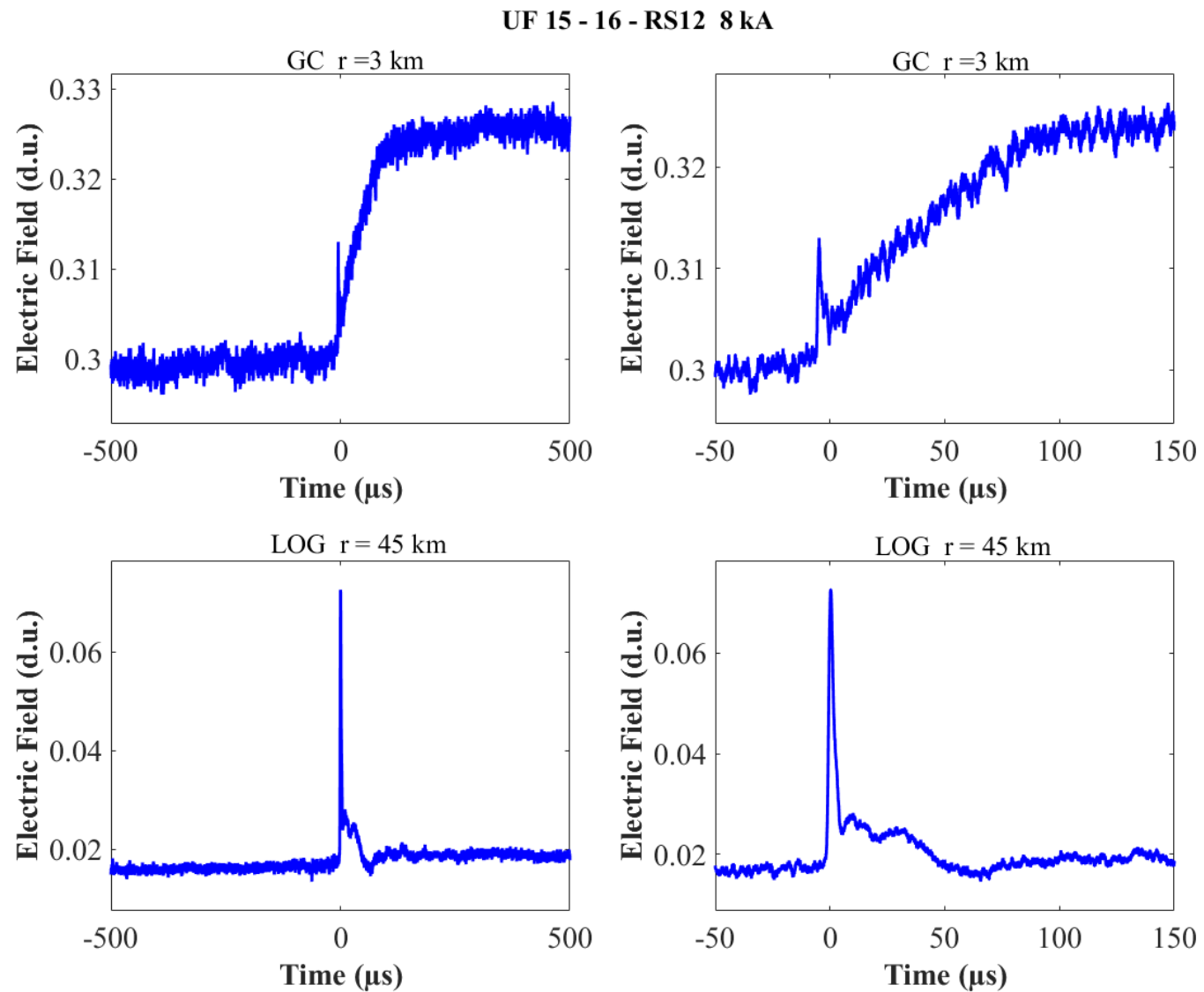


Figure A-129. Two-station electric field waveforms of the RS12 of flash UF 15-16.

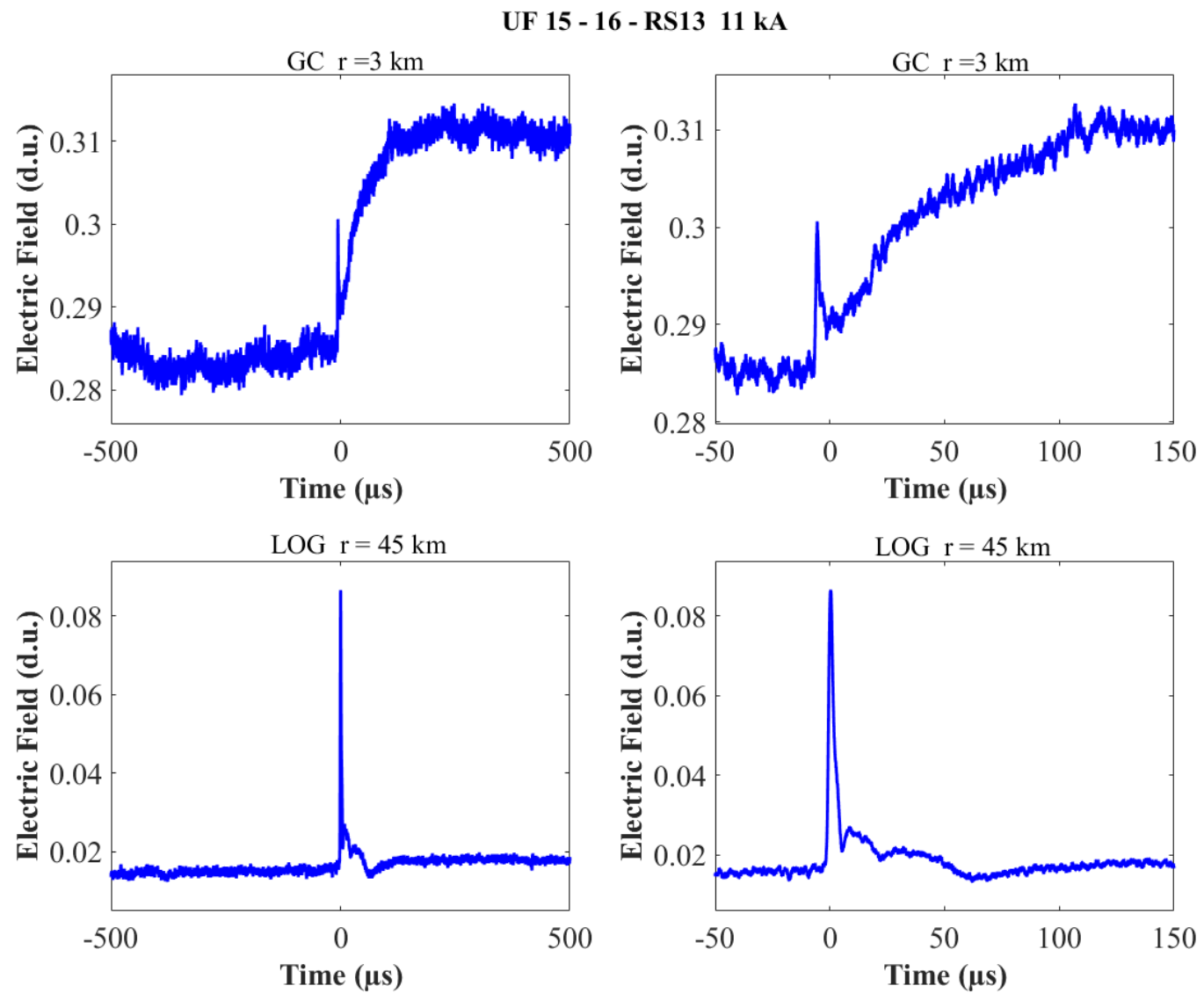


Figure A-130. Two-station electric field waveforms of the RS13 of flash UF 15-16.

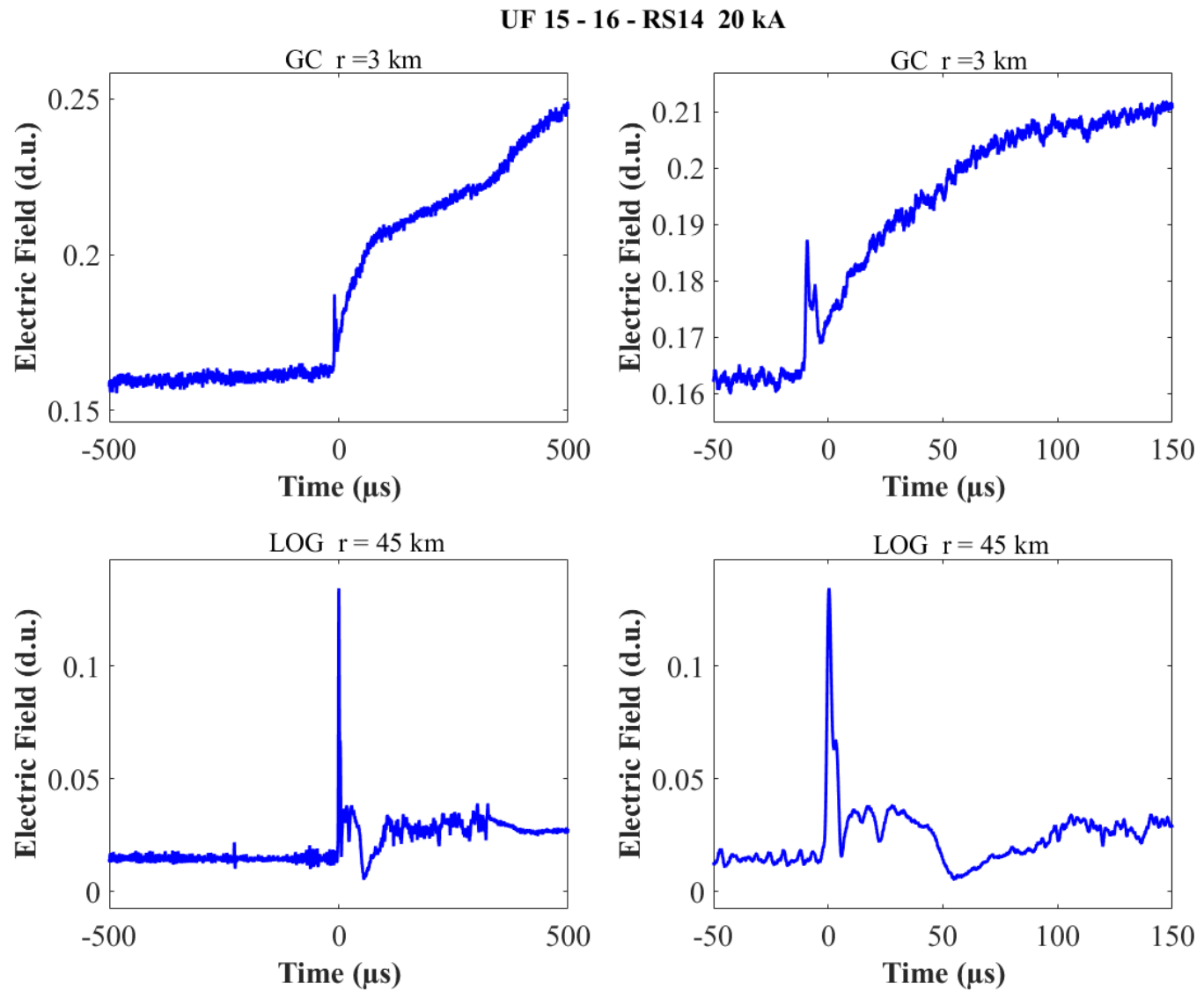


Figure A-131. Two-station electric field waveforms of the RS14 of flash UF 15-16.

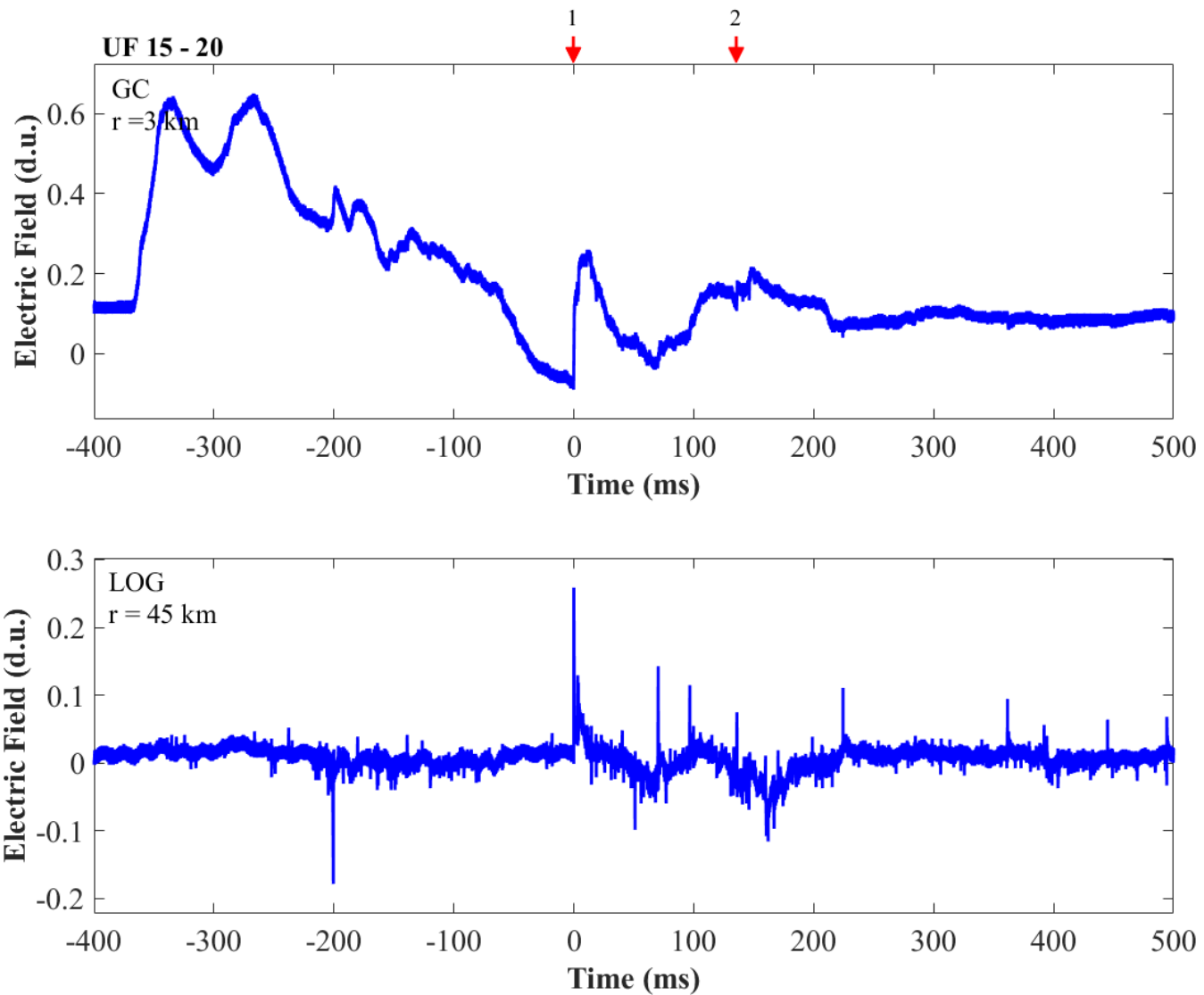


Figure A-132. Two-station electric field waveforms of flash UF 15-20.

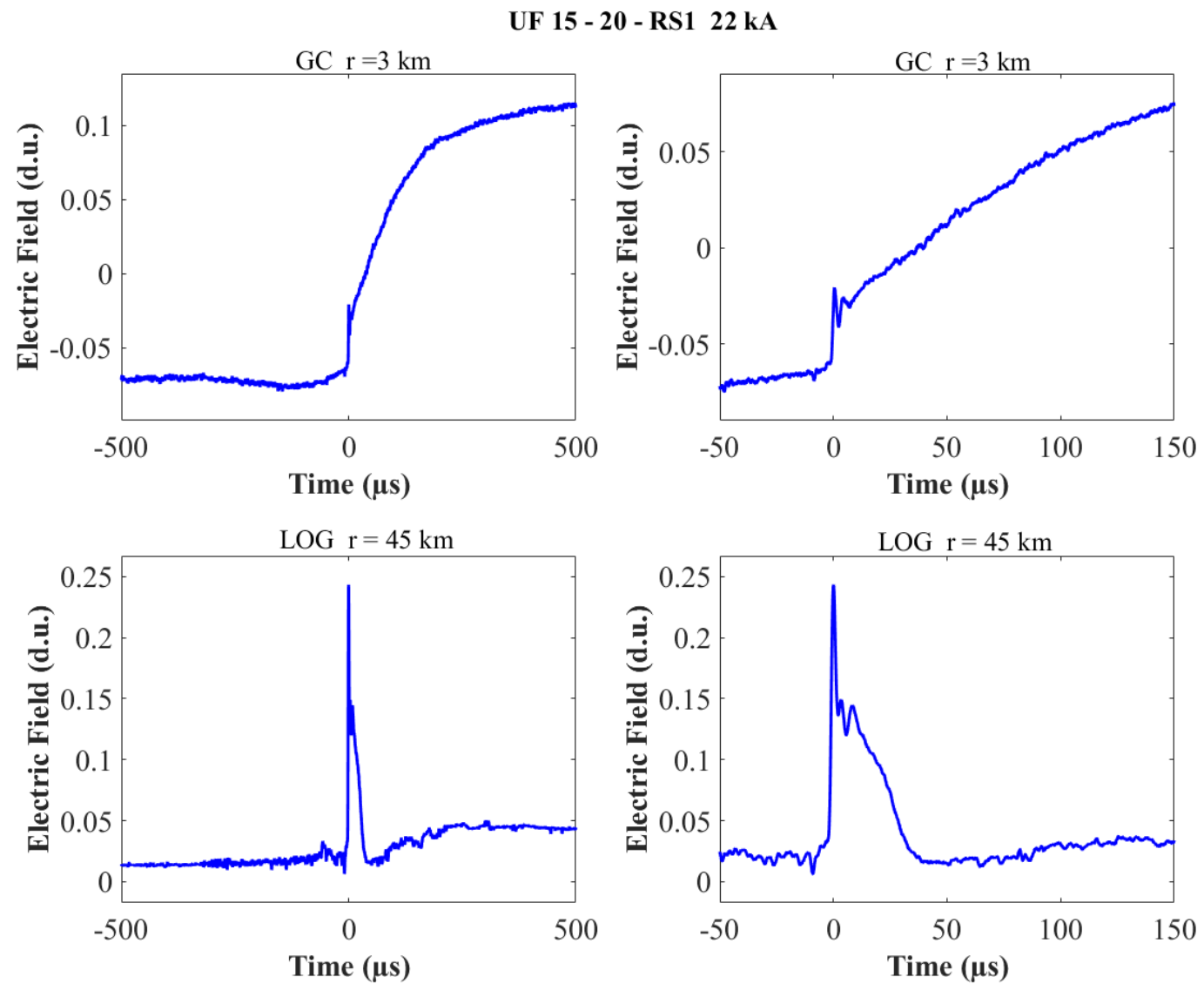


Figure A-133. Two-station electric field waveforms of the RS1 of flash UF 15-20.

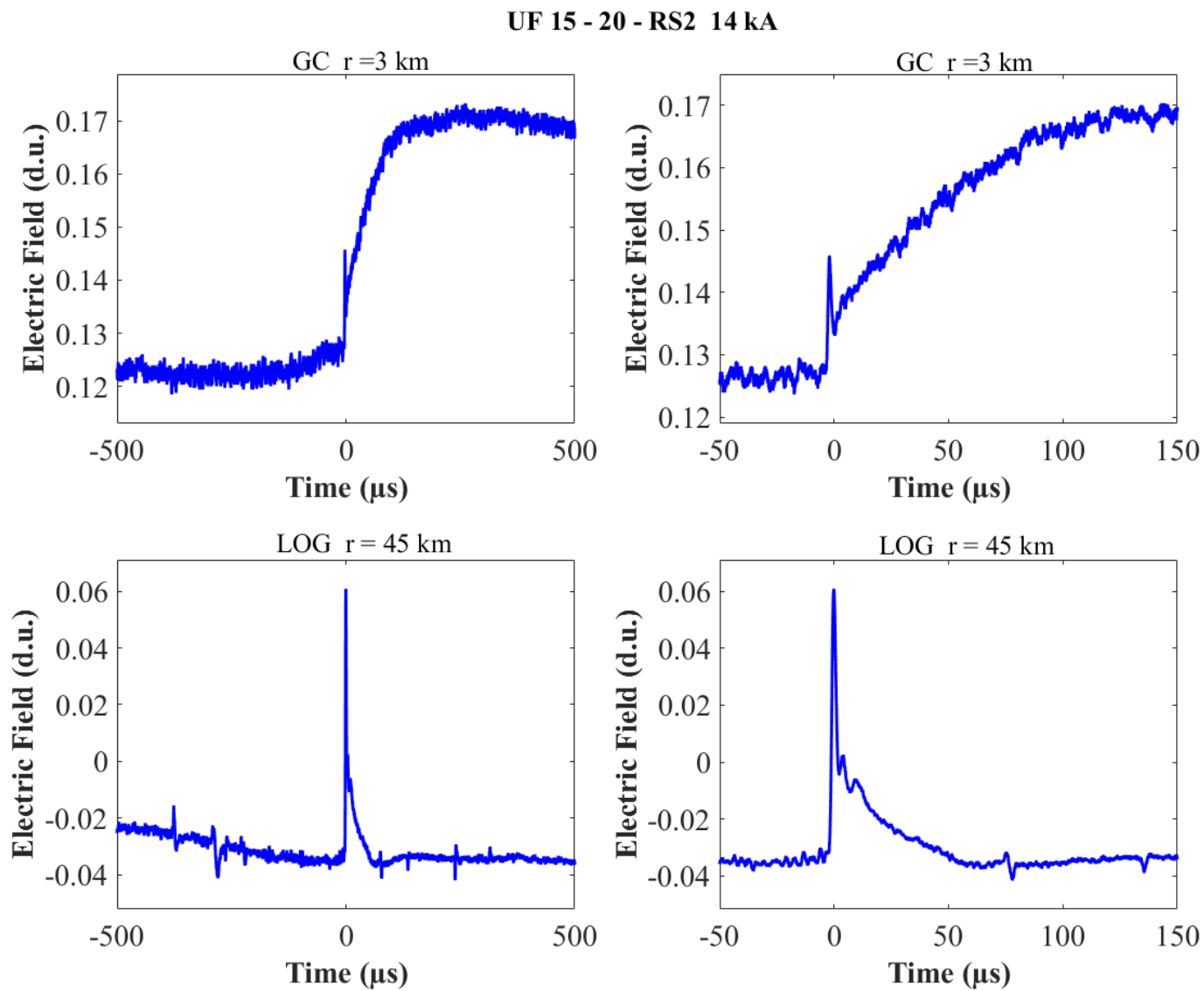


Figure A-134. Two-station electric field waveforms of the RS2 of flash UF 15-20.

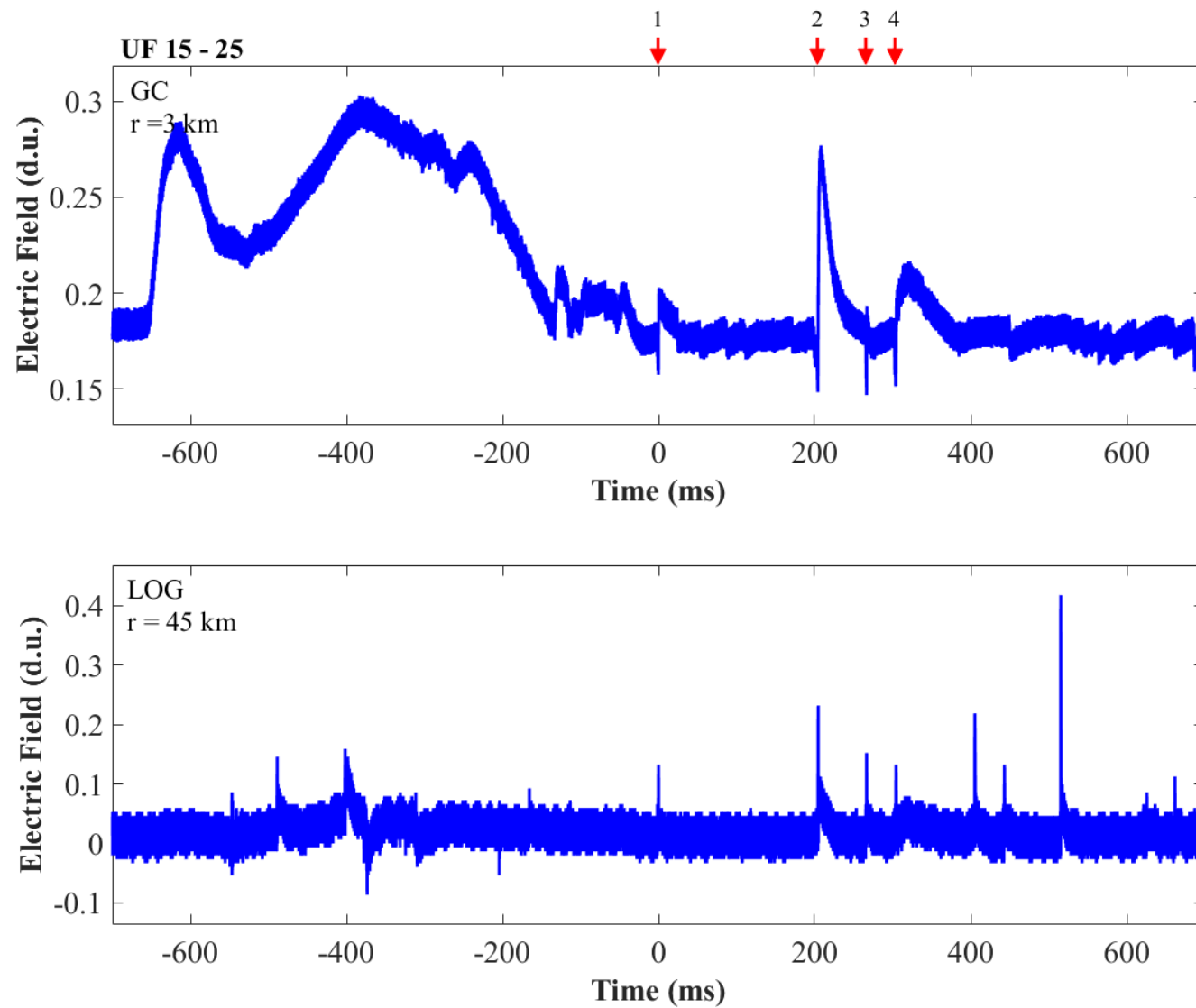


Figure A-135. Two-station electric field waveforms of flash UF 15-25.

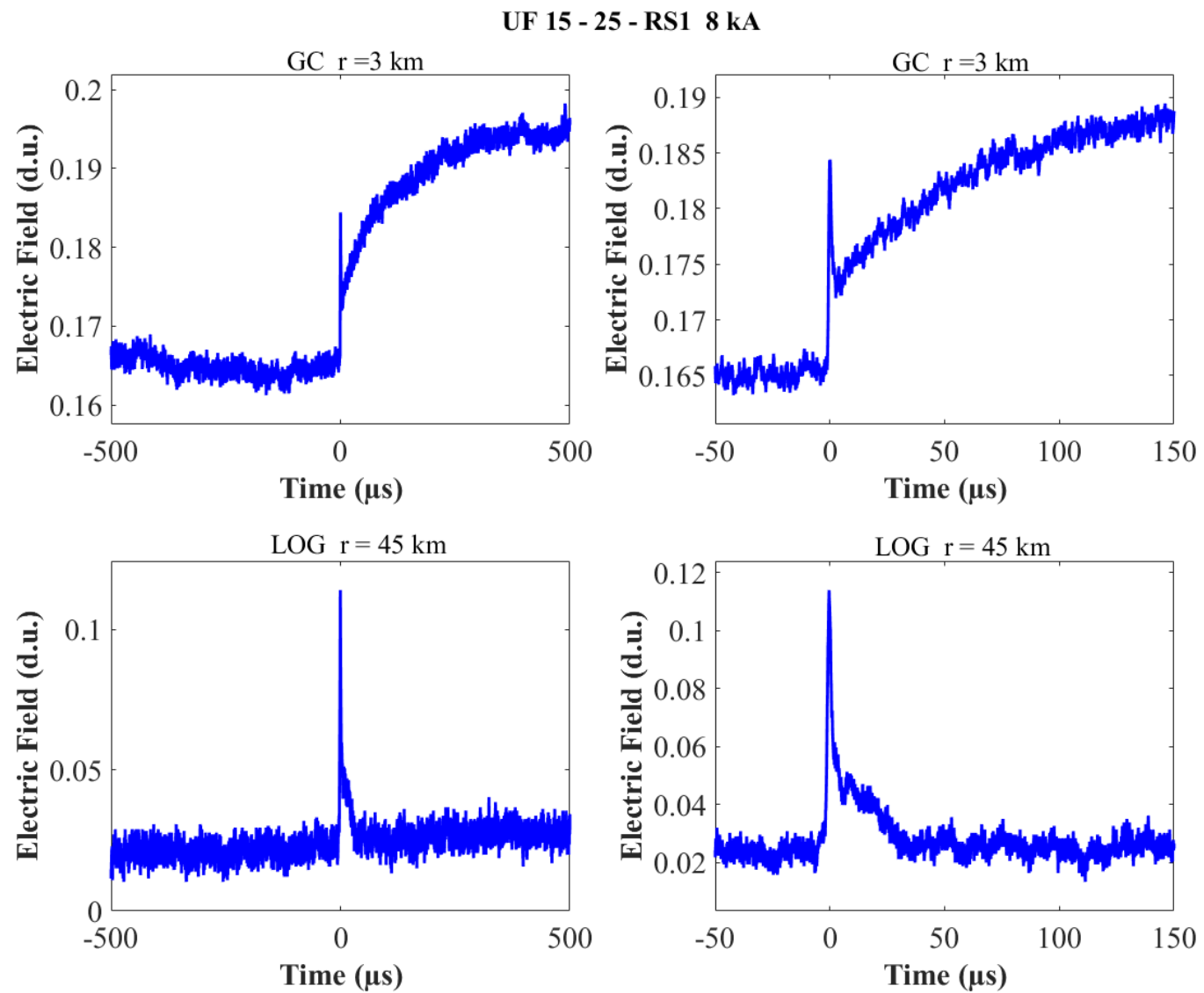


Figure A-136. Two-station electric field waveforms of the RS1 of flash UF 15-25.

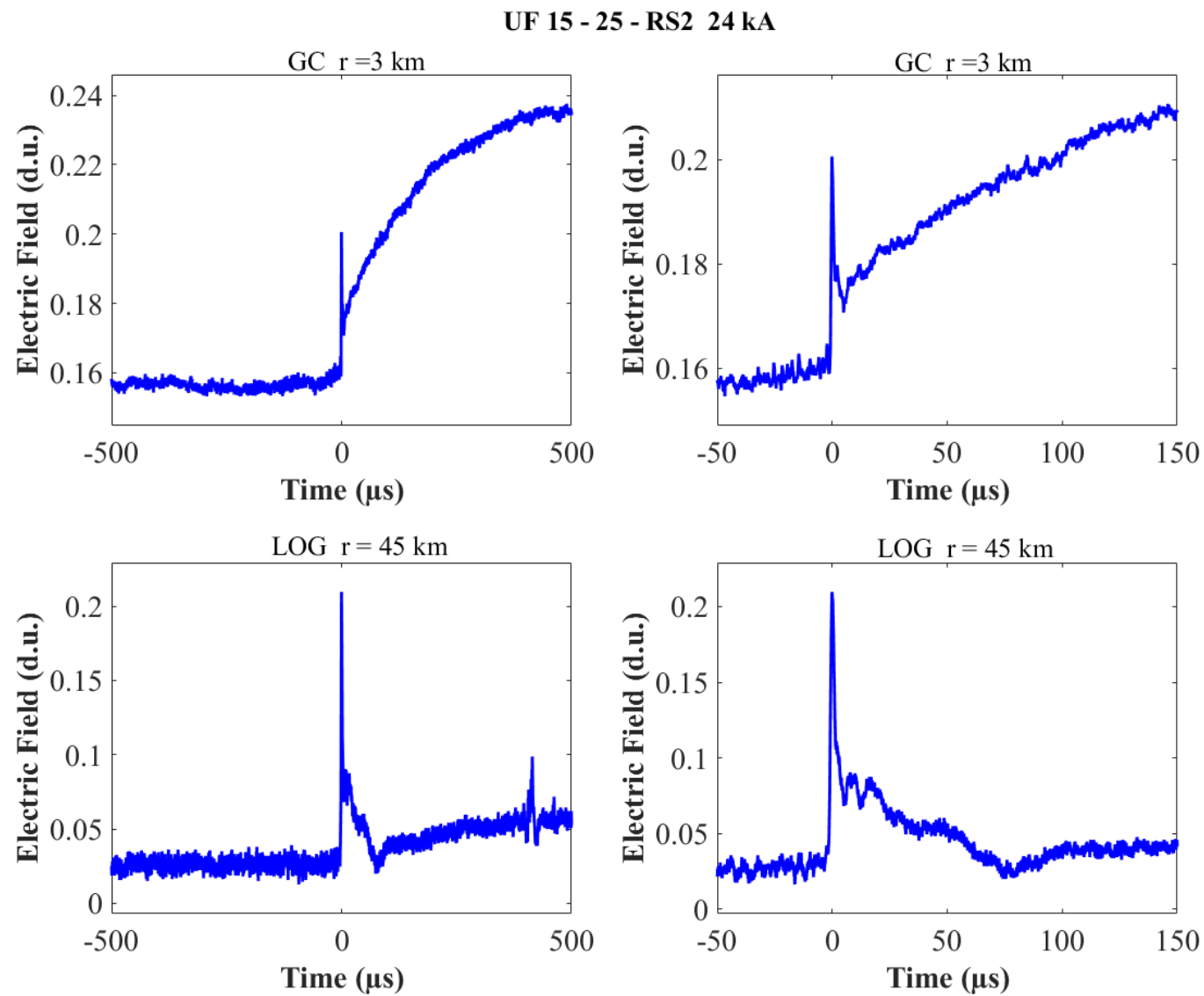


Figure A-137. Two-station electric field waveforms of the RS2 of flash UF 15-25.

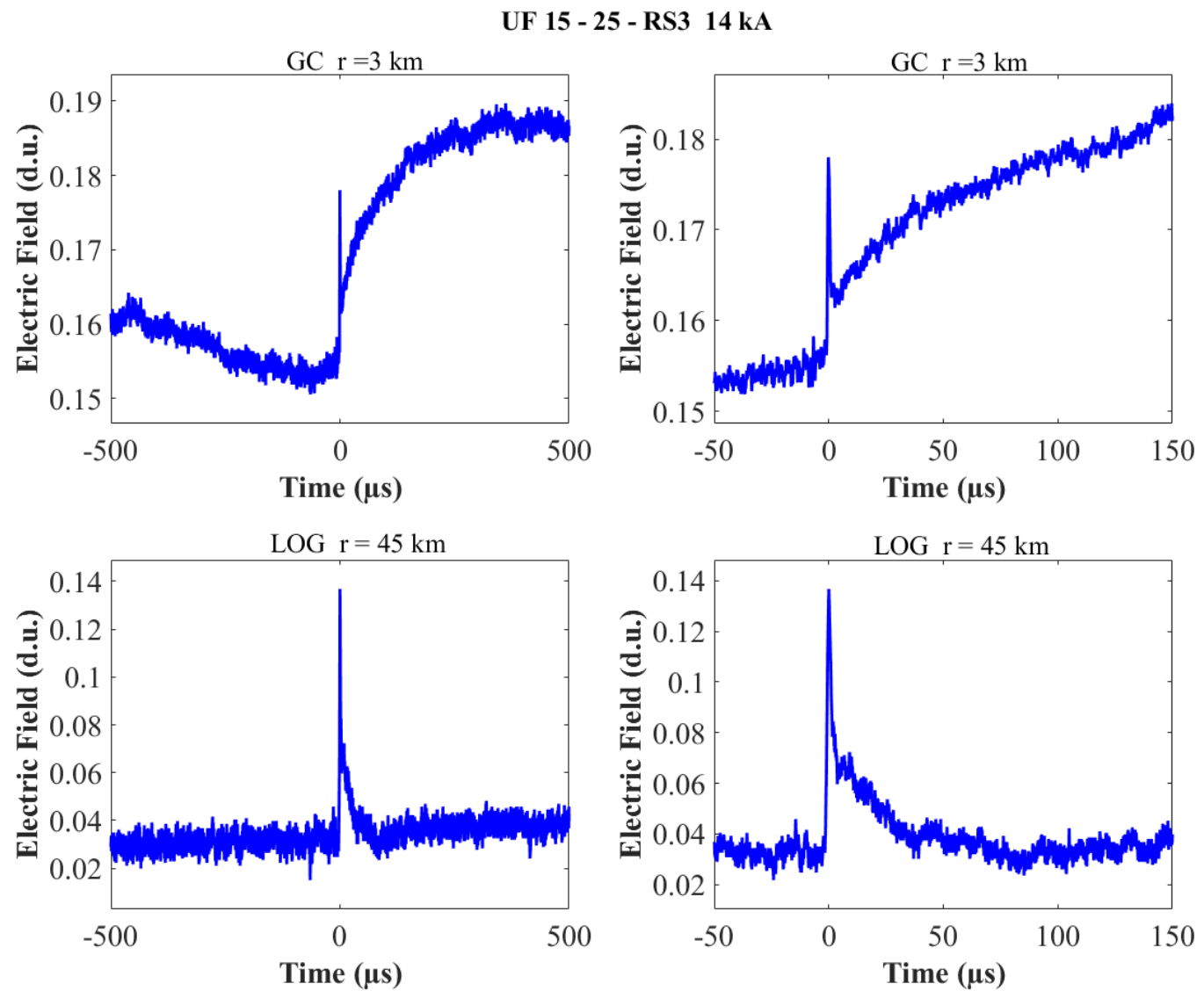


Figure A-138. Two-station electric field waveforms of the RS3 of flash UF 15-25.

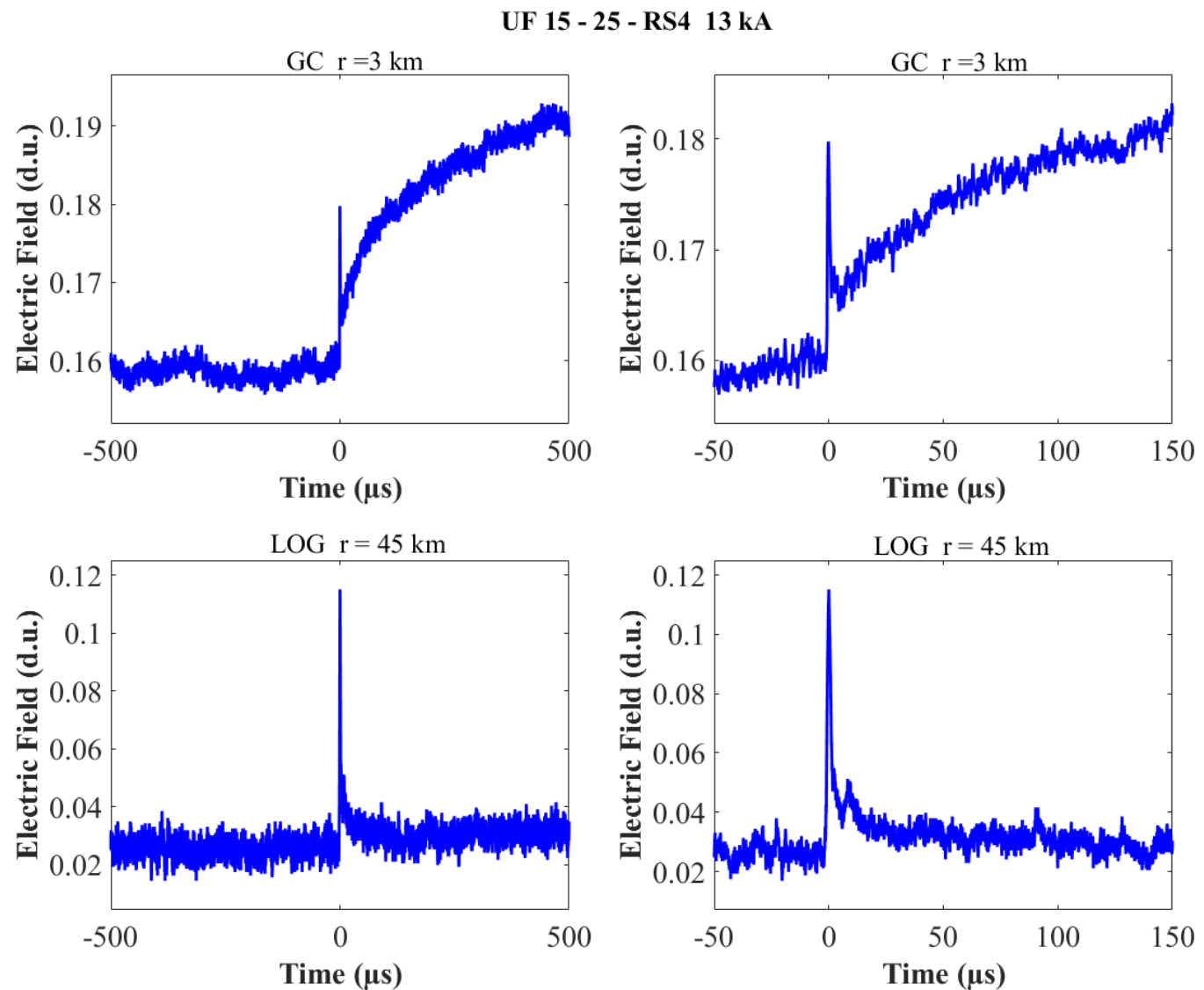


Figure A-139. Two-station electric field waveforms of the RS4 of flash UF 15-25.

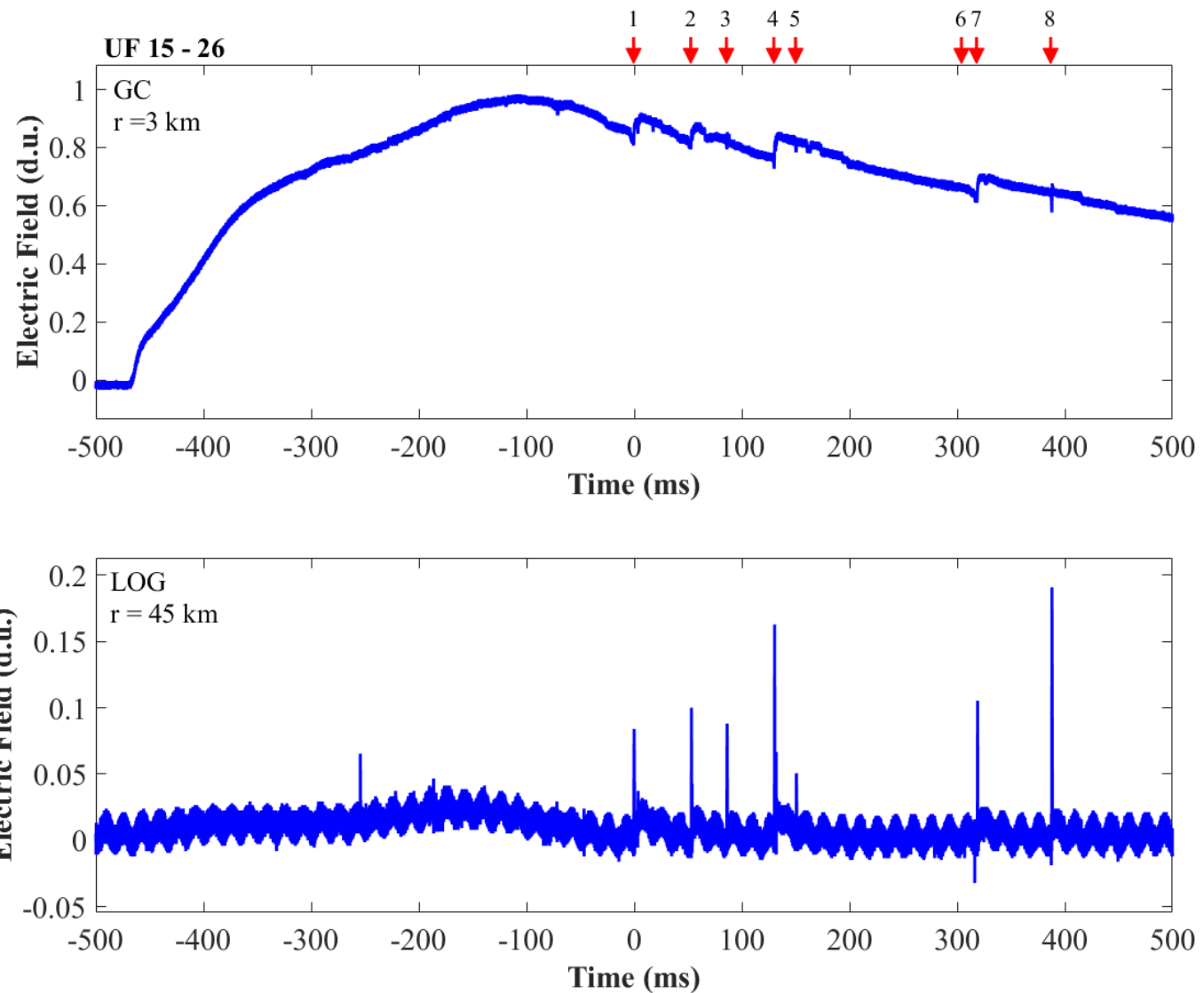


Figure A-140. Two-station electric field waveforms of flash UF 15-26.

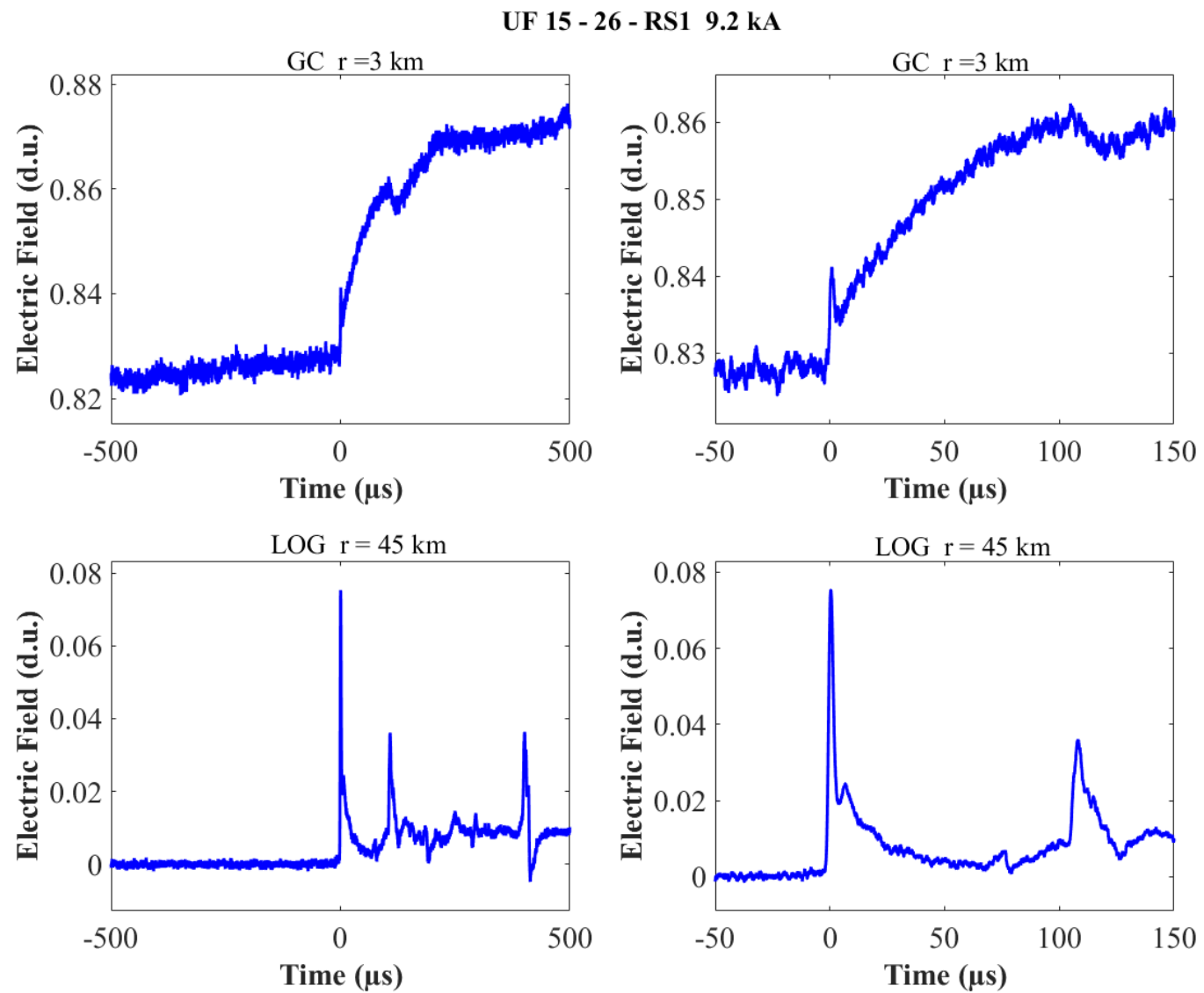


Figure A-141. Two-station electric field waveforms of the RS1 of flash UF 15-26.

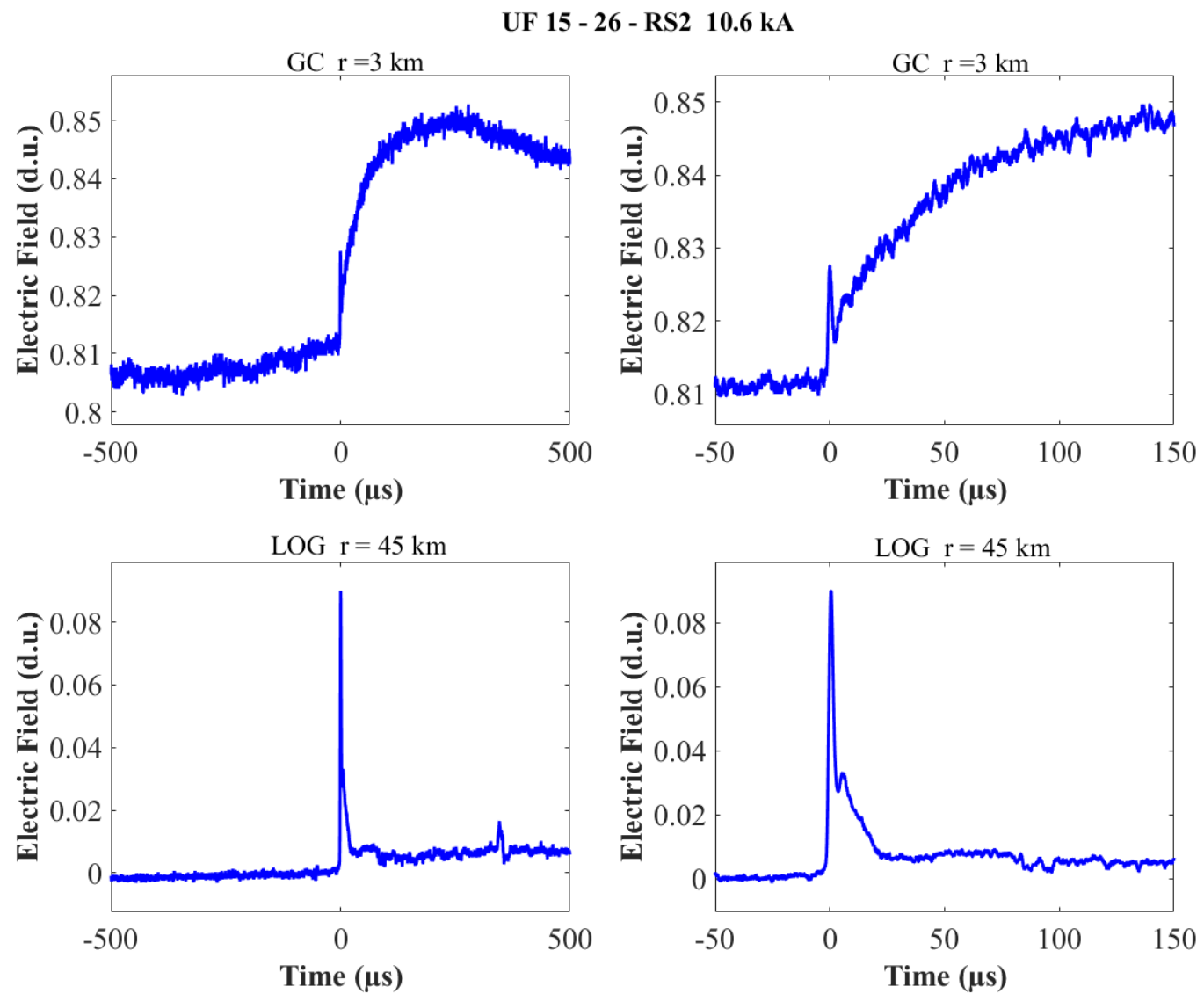


Figure A-142. Two-station electric field waveforms of the RS2 of flash UF 15-26.

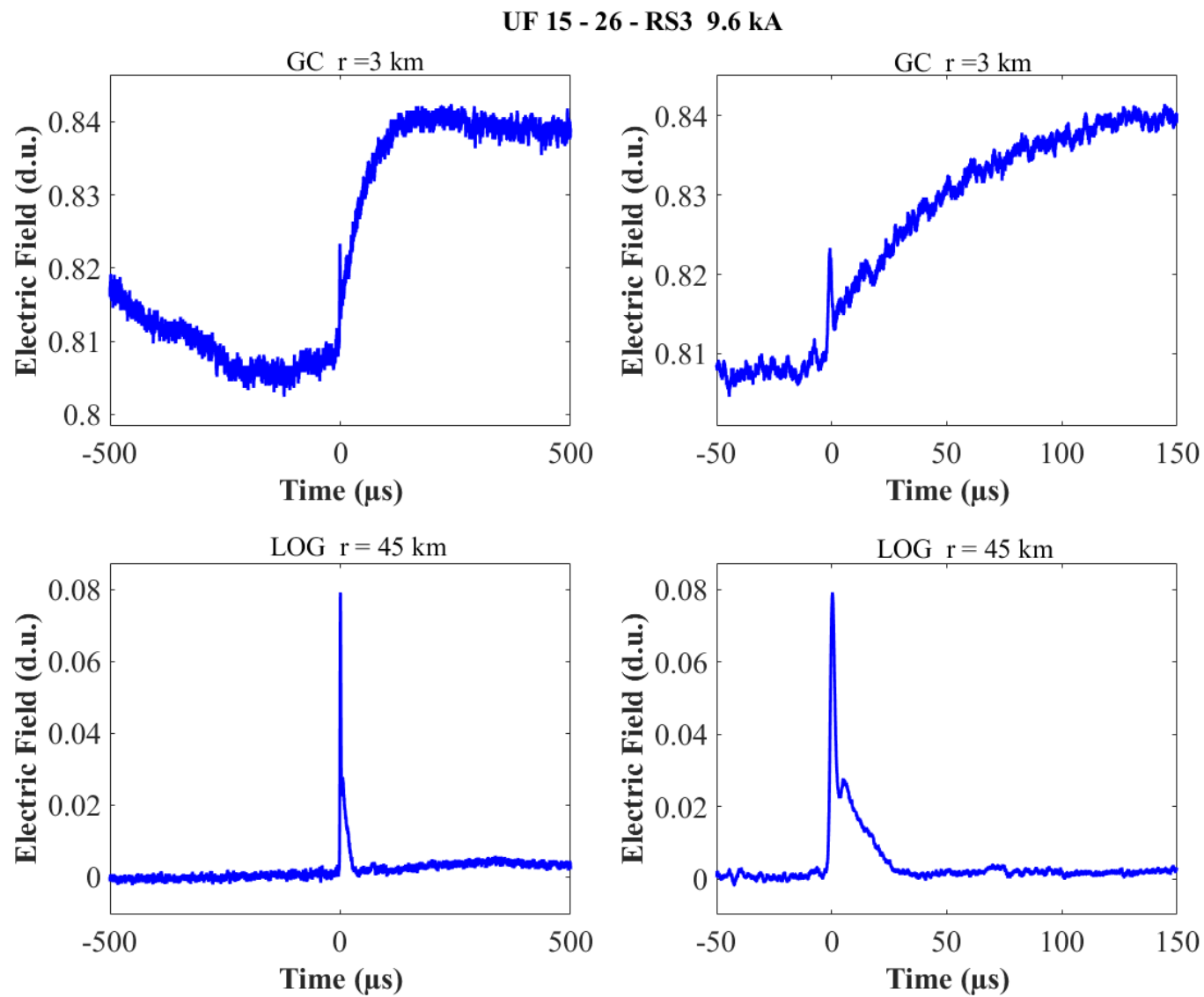


Figure A-143. Two-station electric field waveforms of the RS3 of flash UF 15-26.

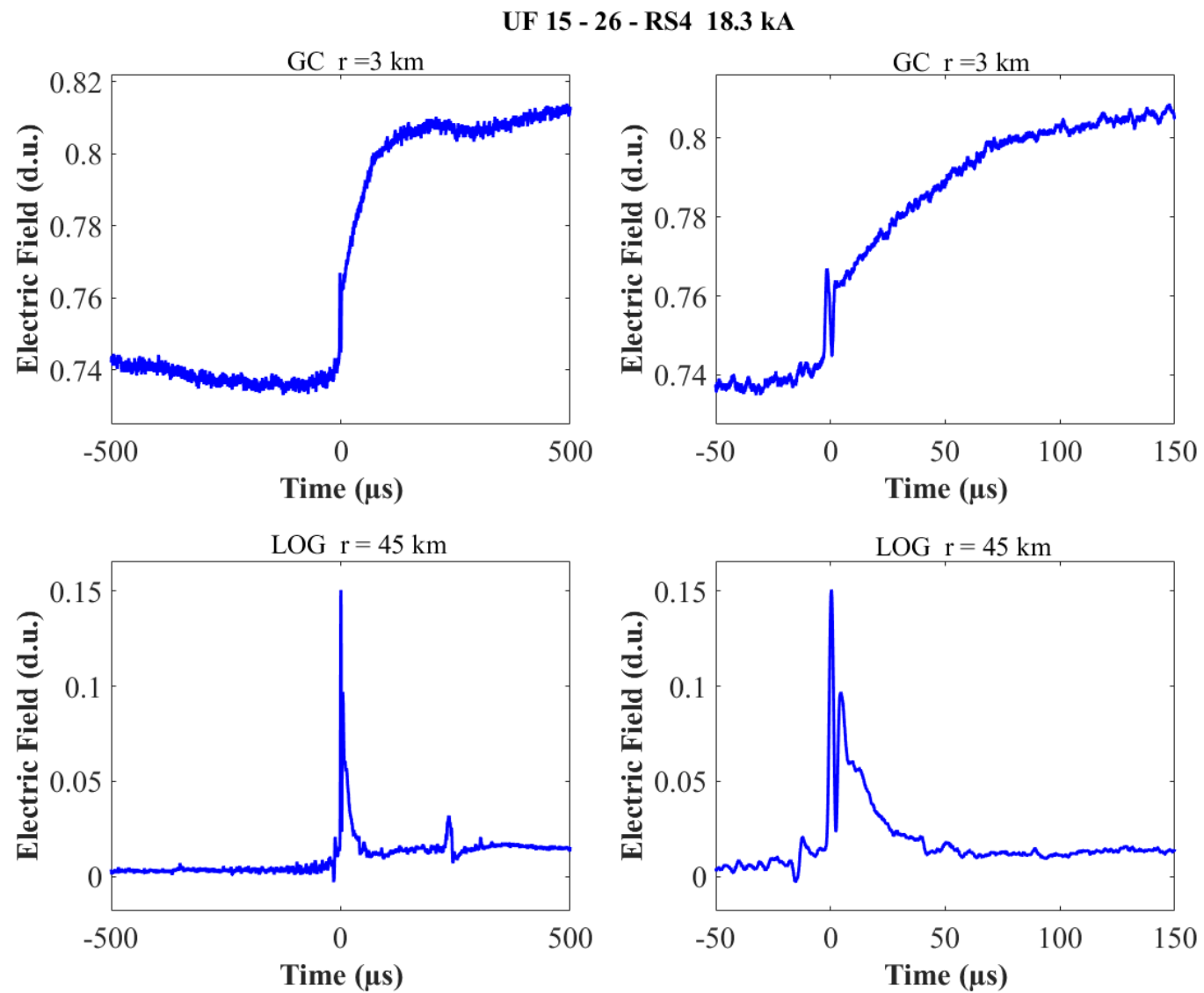


Figure A-144. Two-station electric field waveforms of the RS4 of flash UF 15-26.

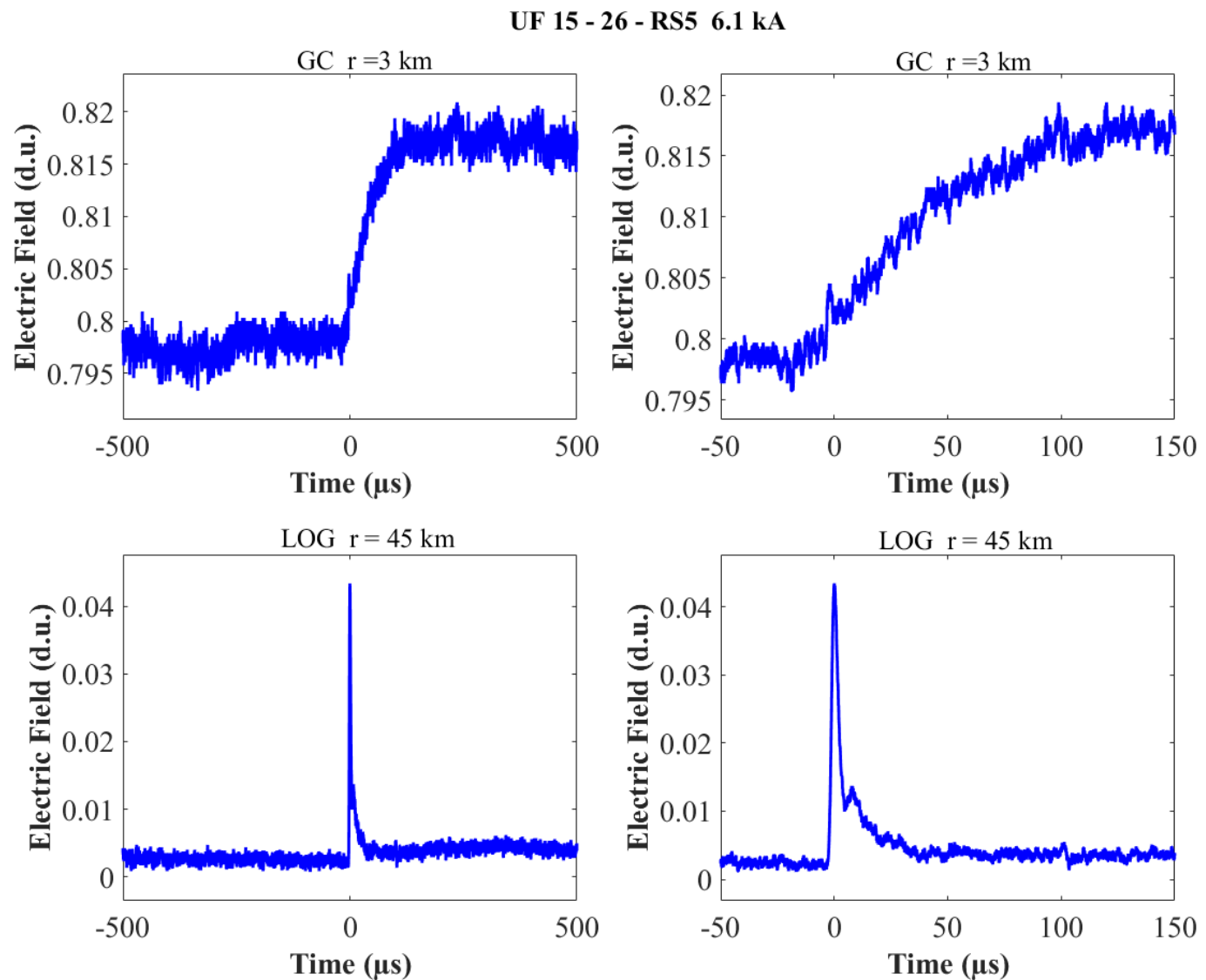


Figure A-145. Two-station electric field waveforms of the RS5 of flash UF 15-26.

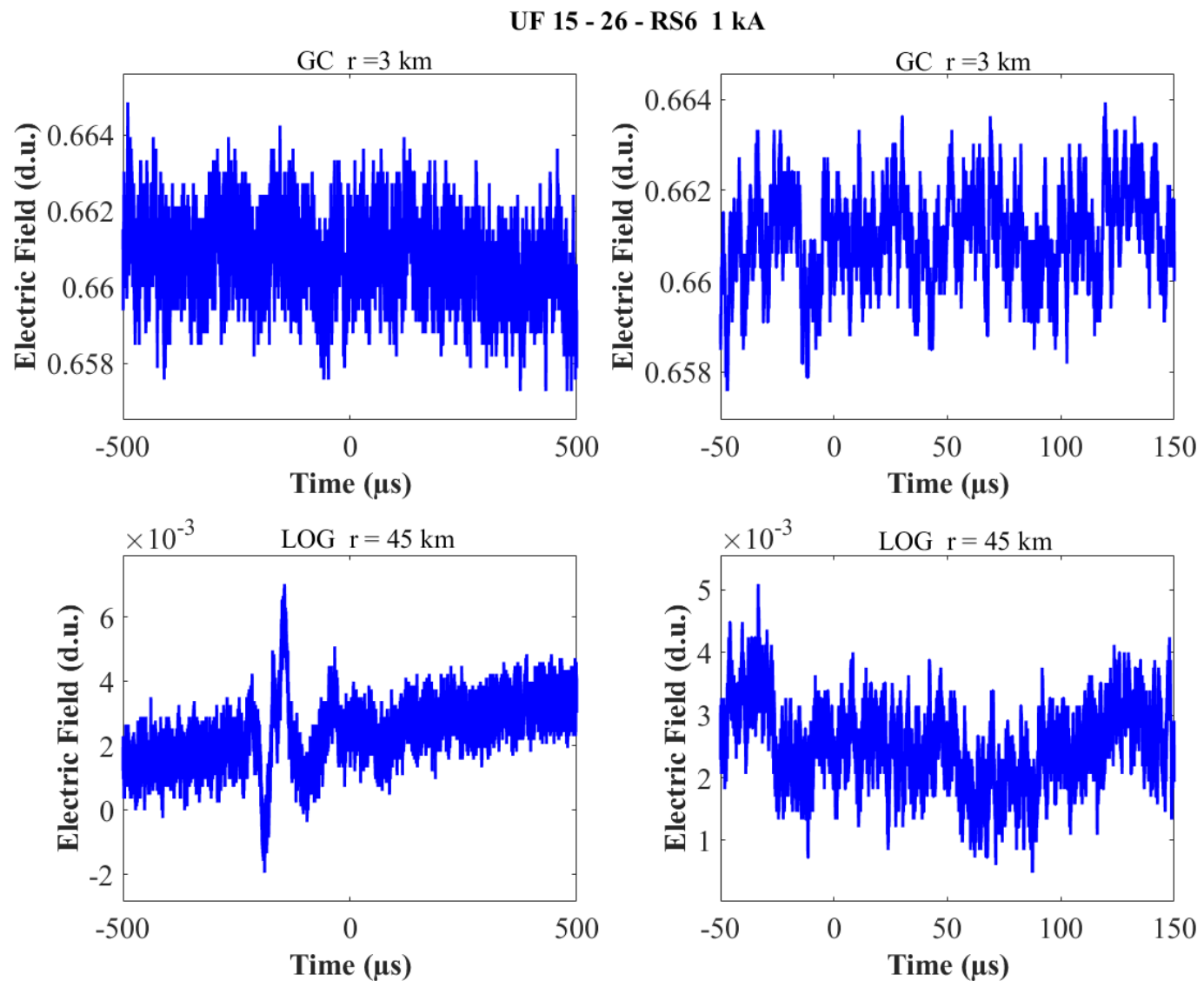


Figure A-146. Two-station electric field waveforms of the RS6 of flash UF 15-26.

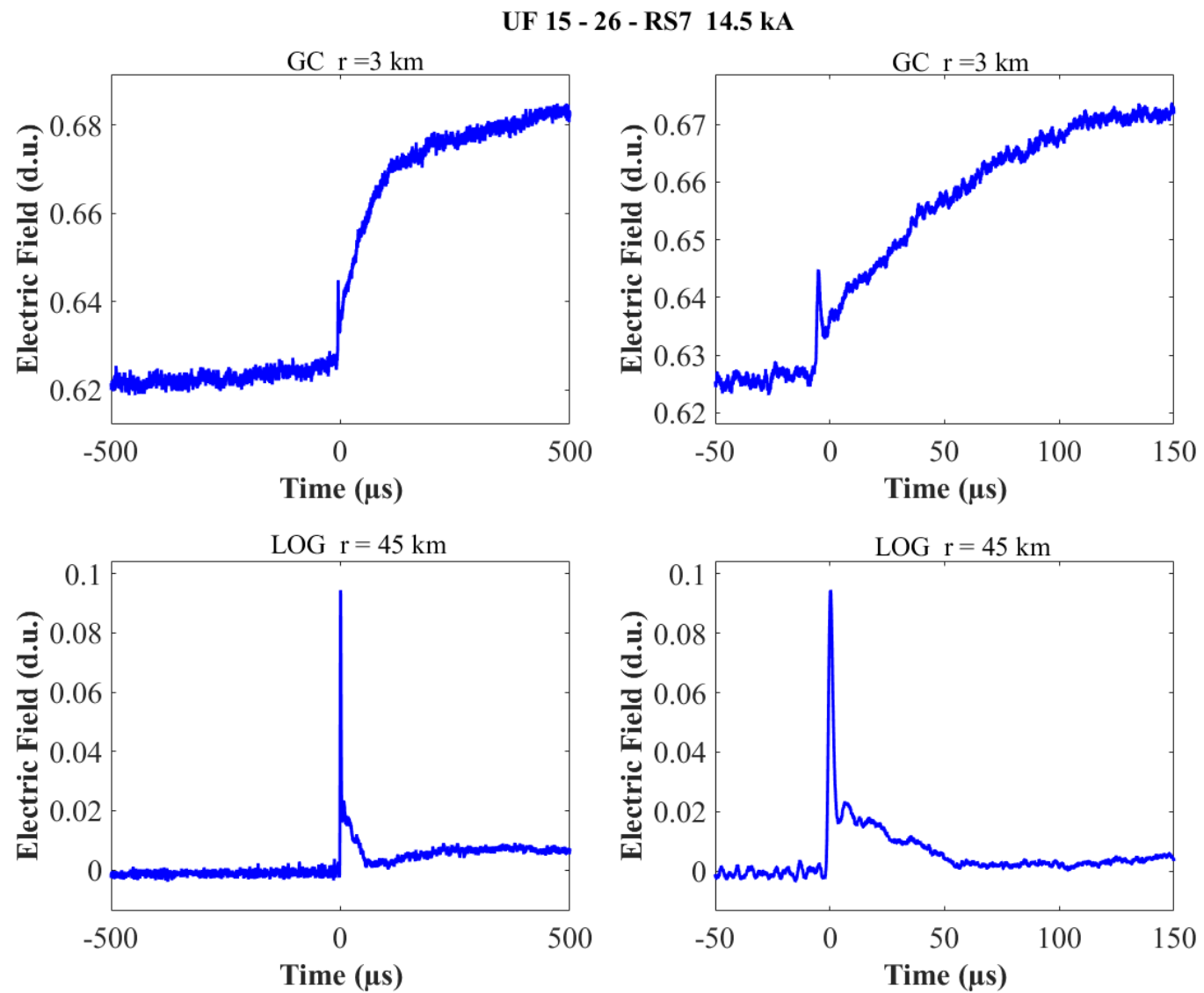


Figure A-147. Two-station electric field waveforms of the RS7 of flash UF 15-26.

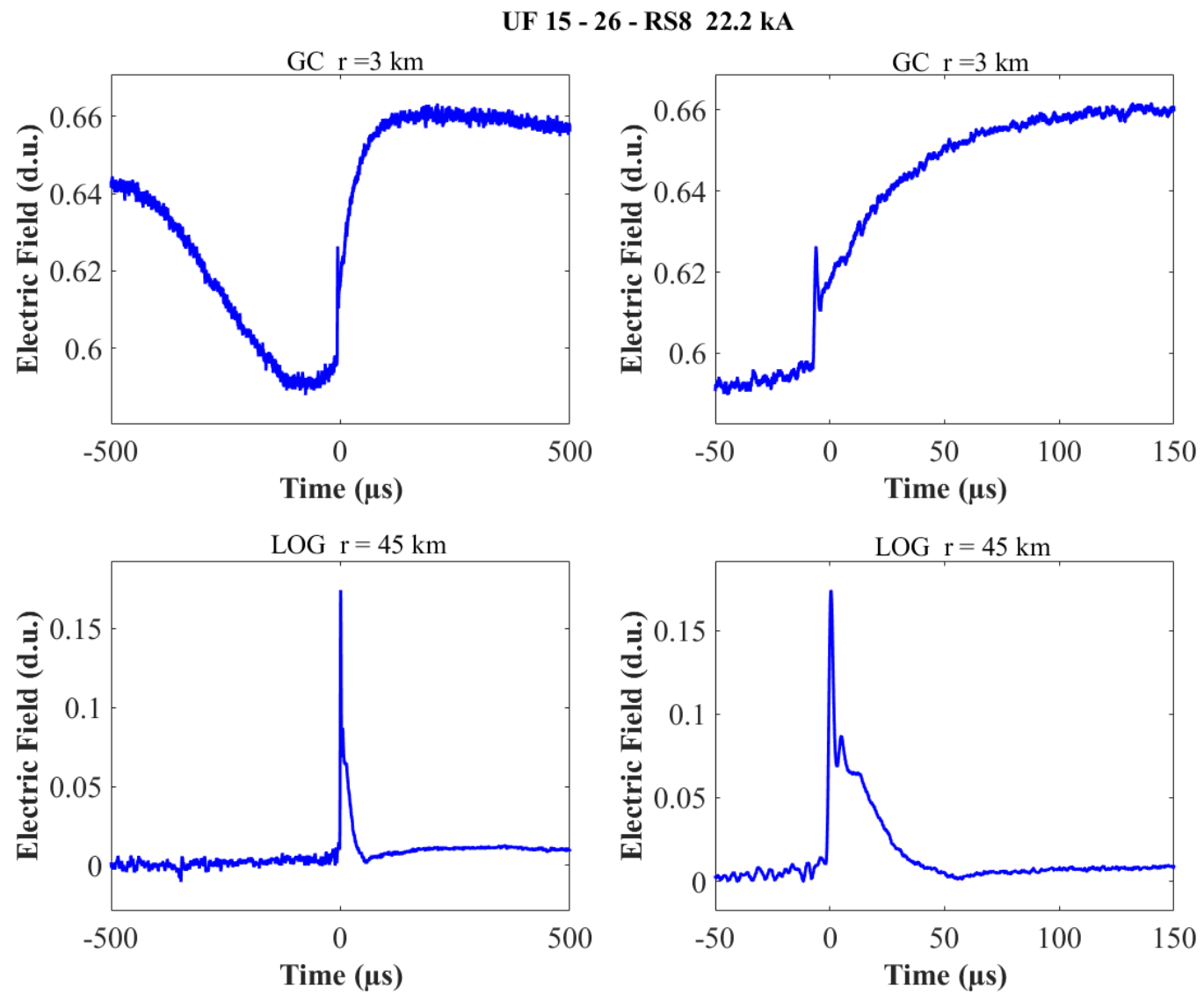


Figure A-148. Two-station electric field waveforms of the RS8 of flash UF 15-26.

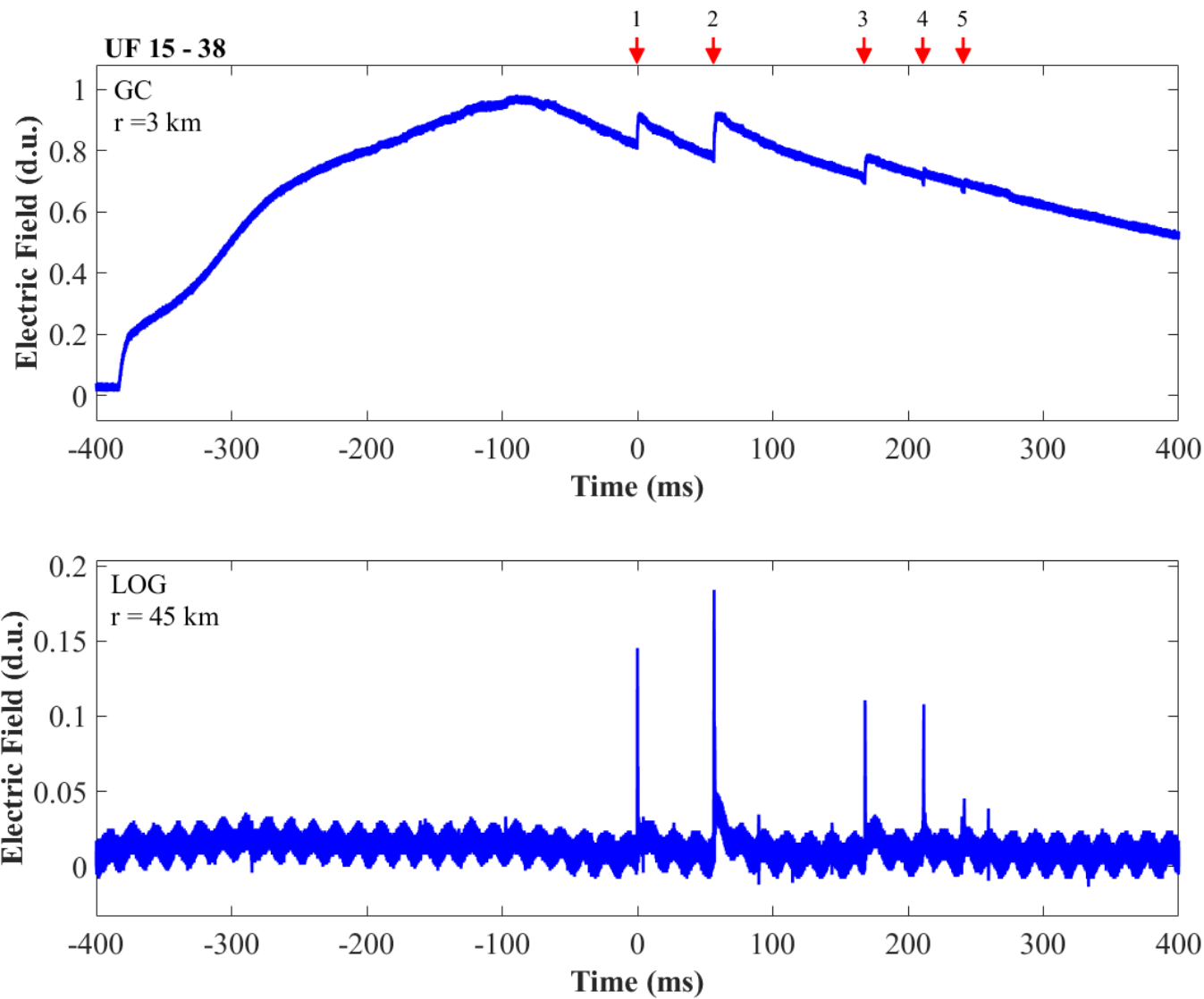


Figure A-149. Two-station electric field waveforms of flash UF 15-38.

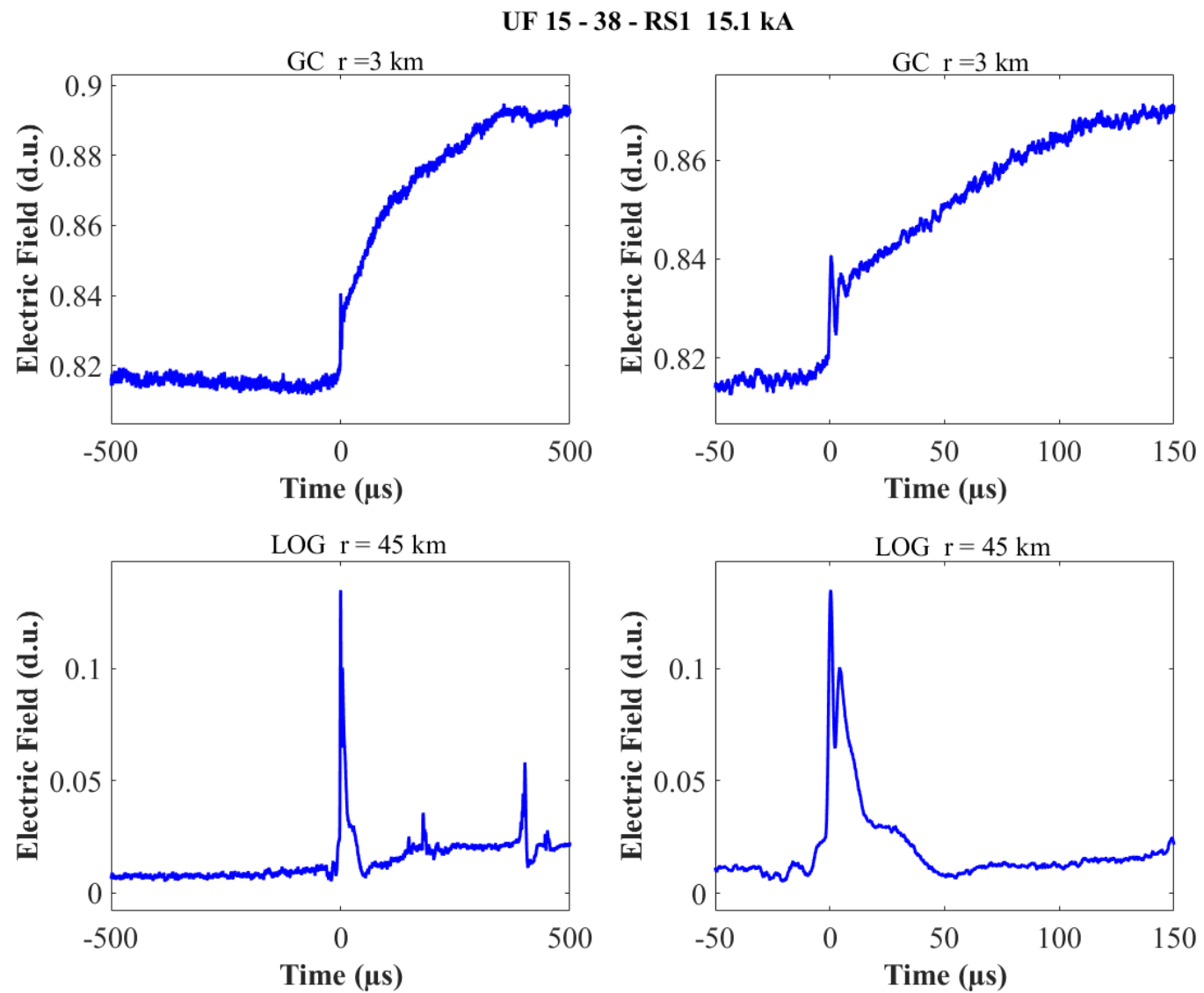


Figure A-150. Two-station electric field waveforms of the RS1 of flash UF 15-38.

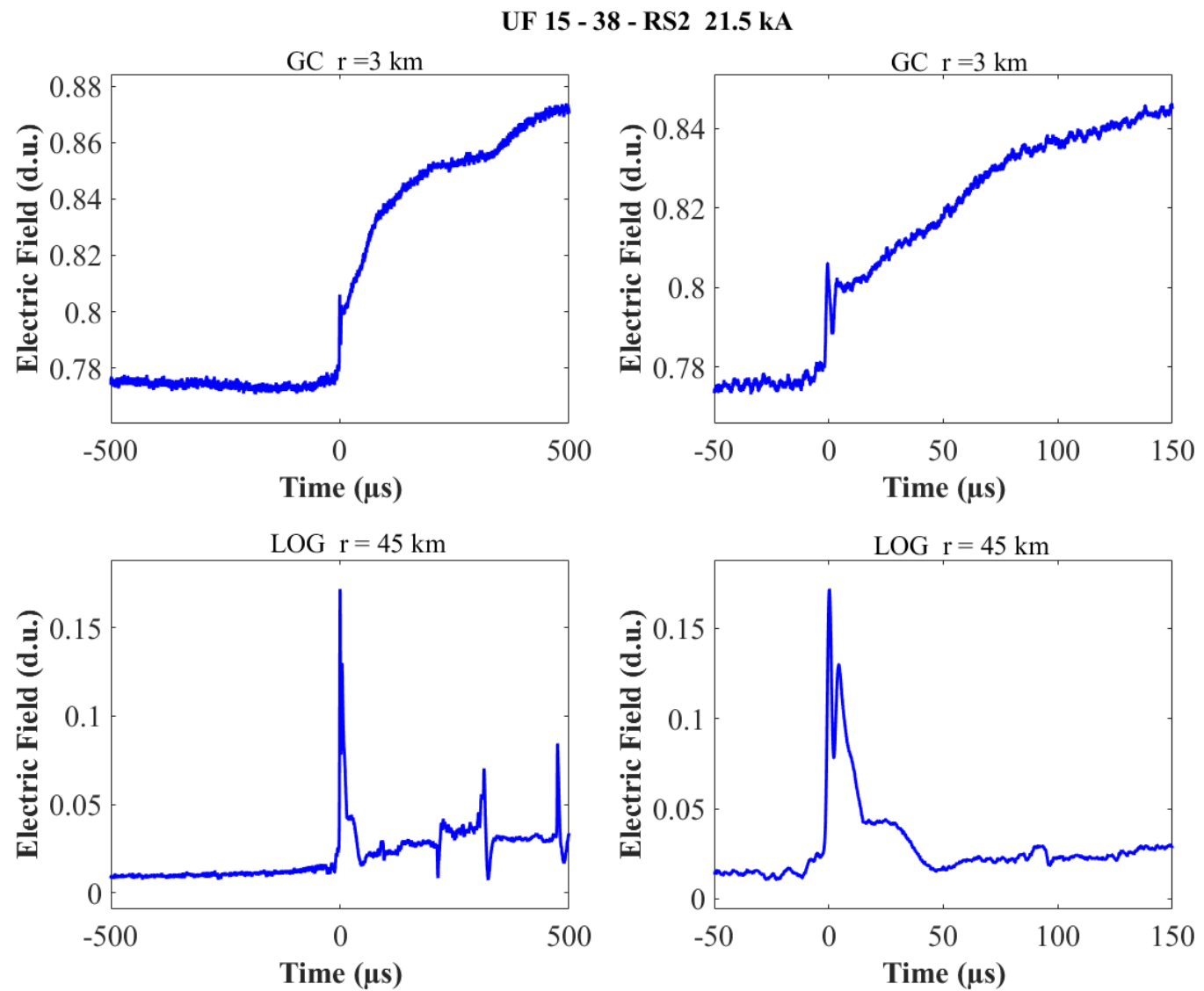


Figure A-151. Two-station electric field waveforms of the RS2 of flash UF 15-38.

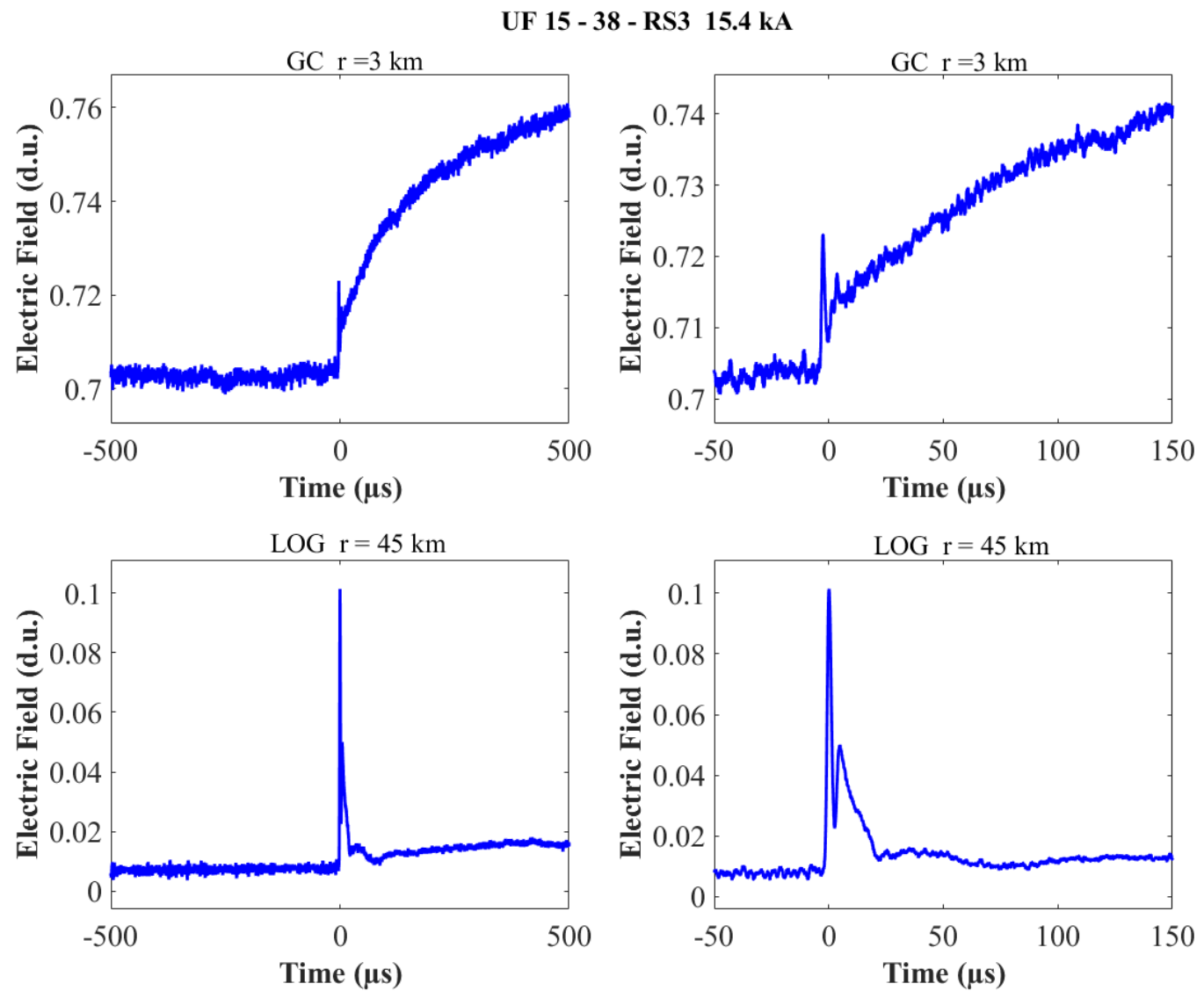


Figure A-152. Two-station electric field waveforms of the RS3 of flash UF 15-38.

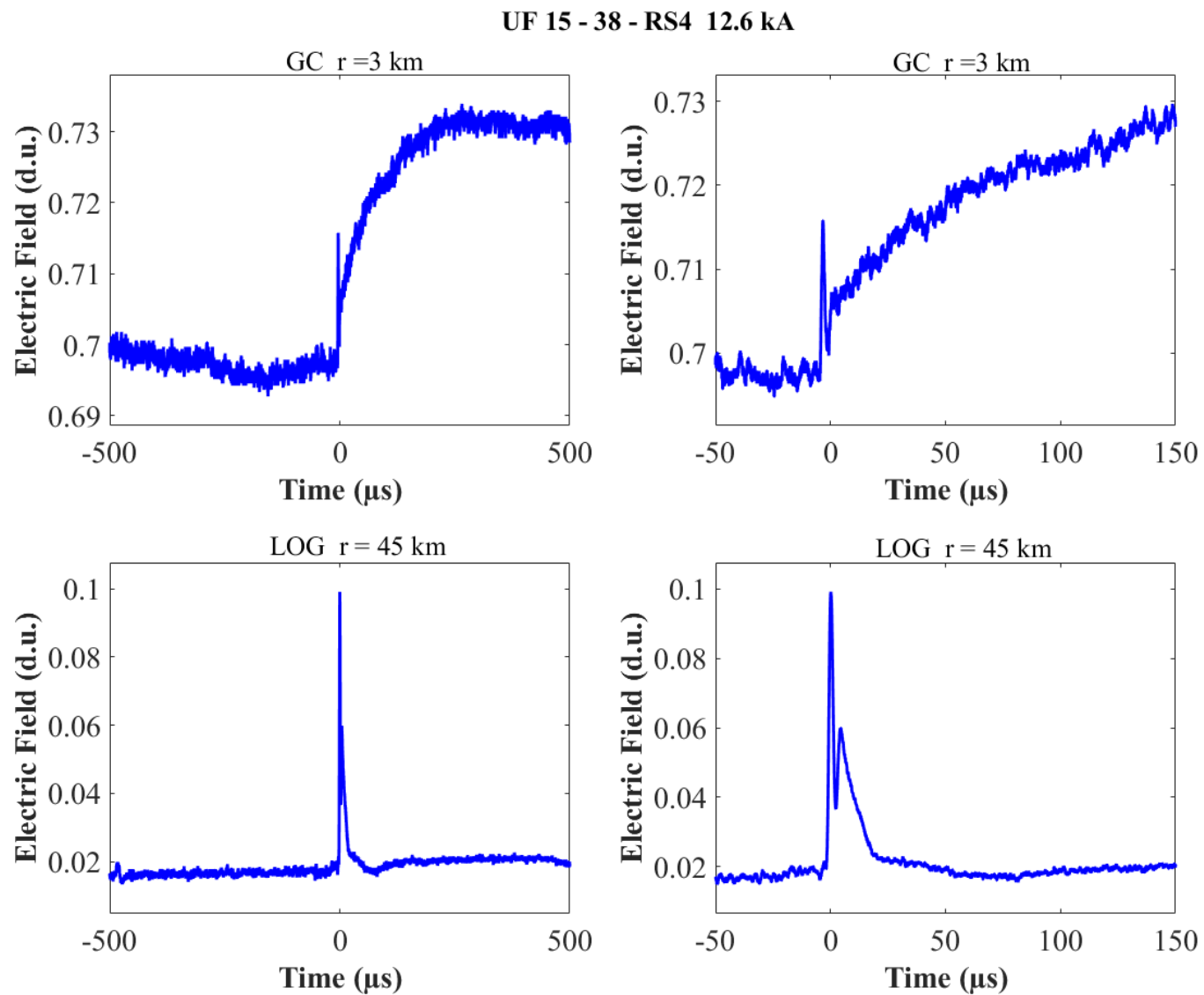


Figure A-153. Two-station electric field waveforms of the RS4 of flash UF 15-38.

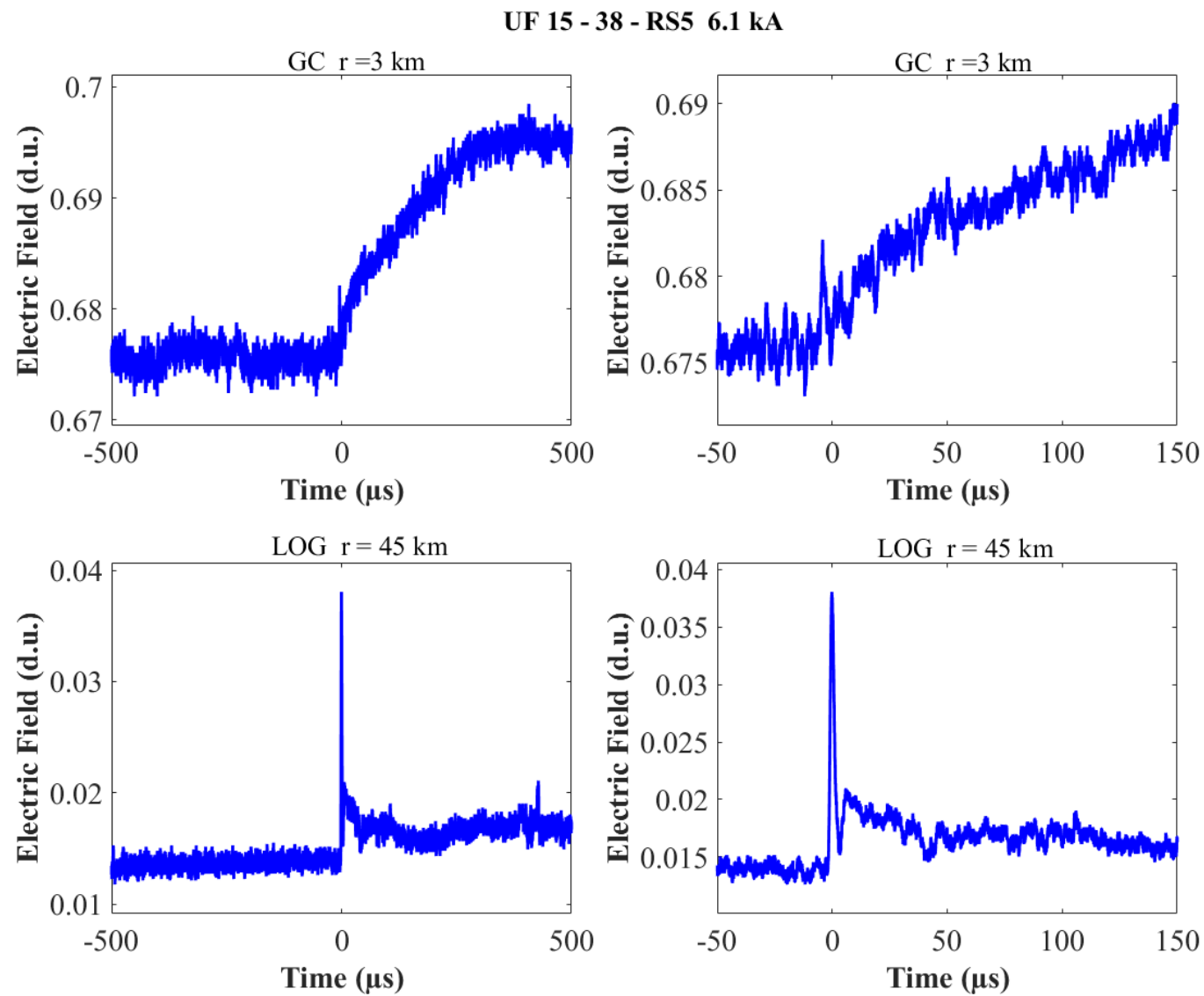


Figure A-154. Two-station electric field waveforms of the RS5 of flash UF 15-38.

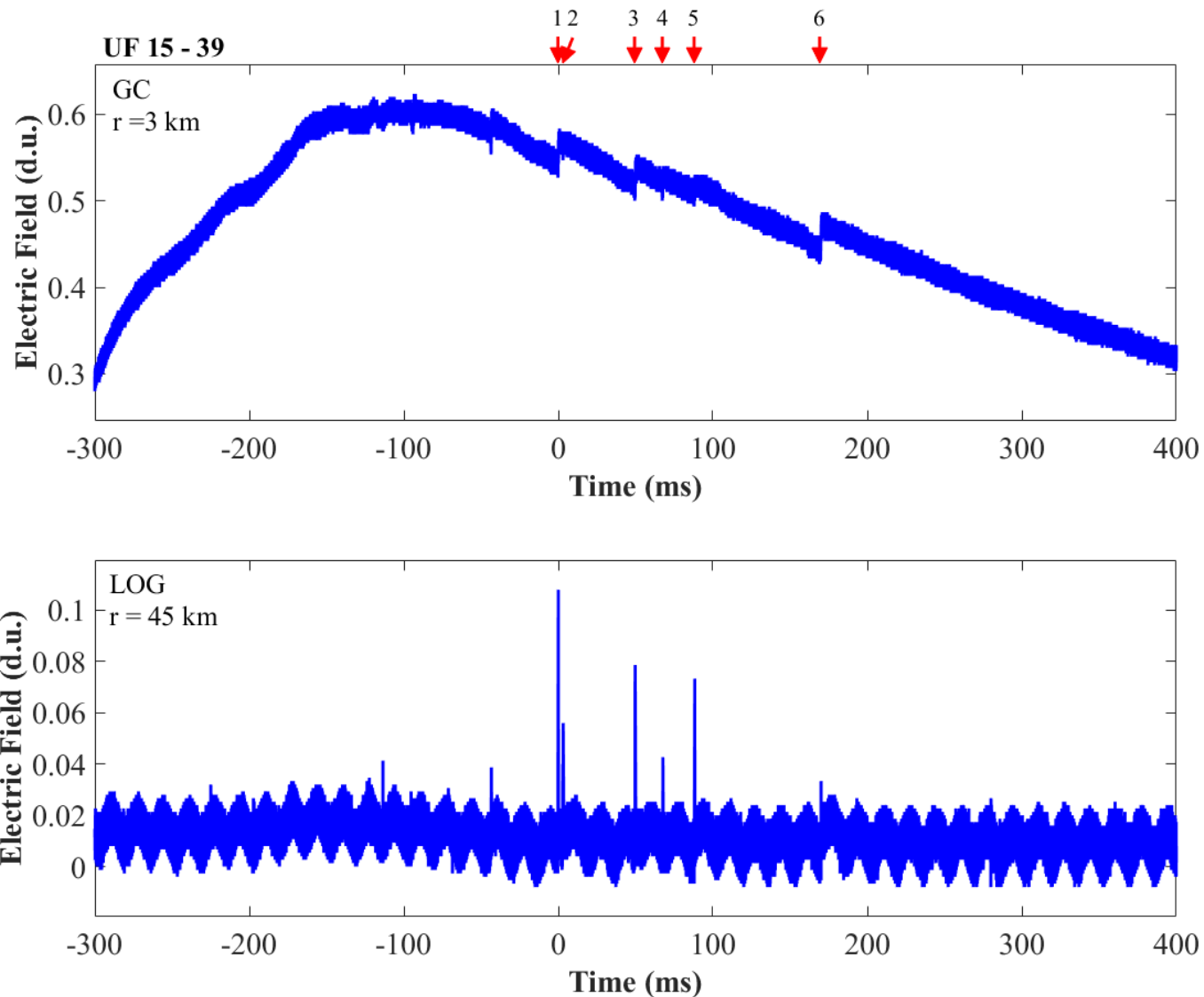


Figure A-155. Two-station electric field waveforms of flash UF 15-39.

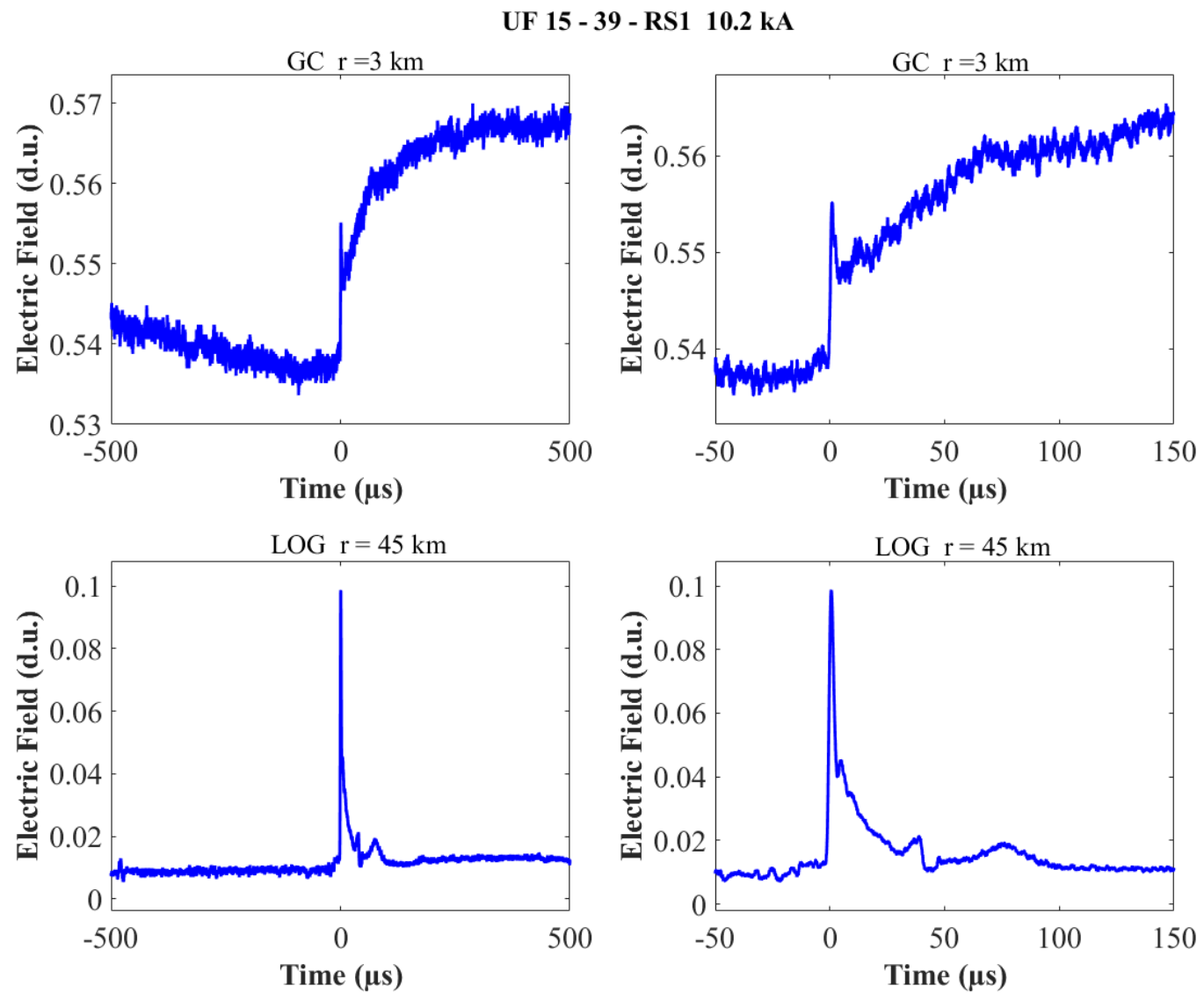


Figure A-156. Two-station electric field waveforms of the RS1 of flash UF 15-39.

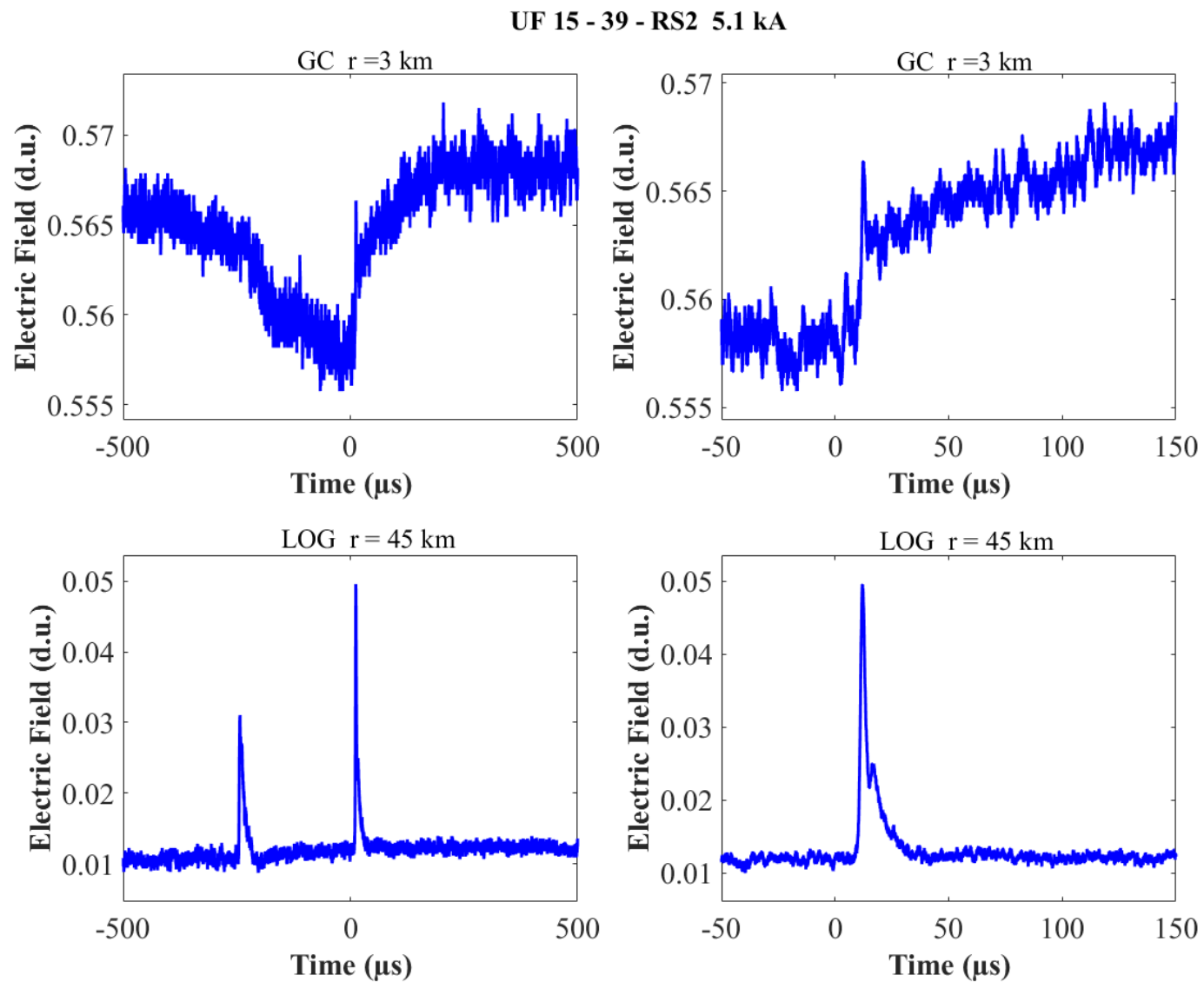


Figure A-157. Two-station electric field waveforms of the RS2 of flash UF 15-39.

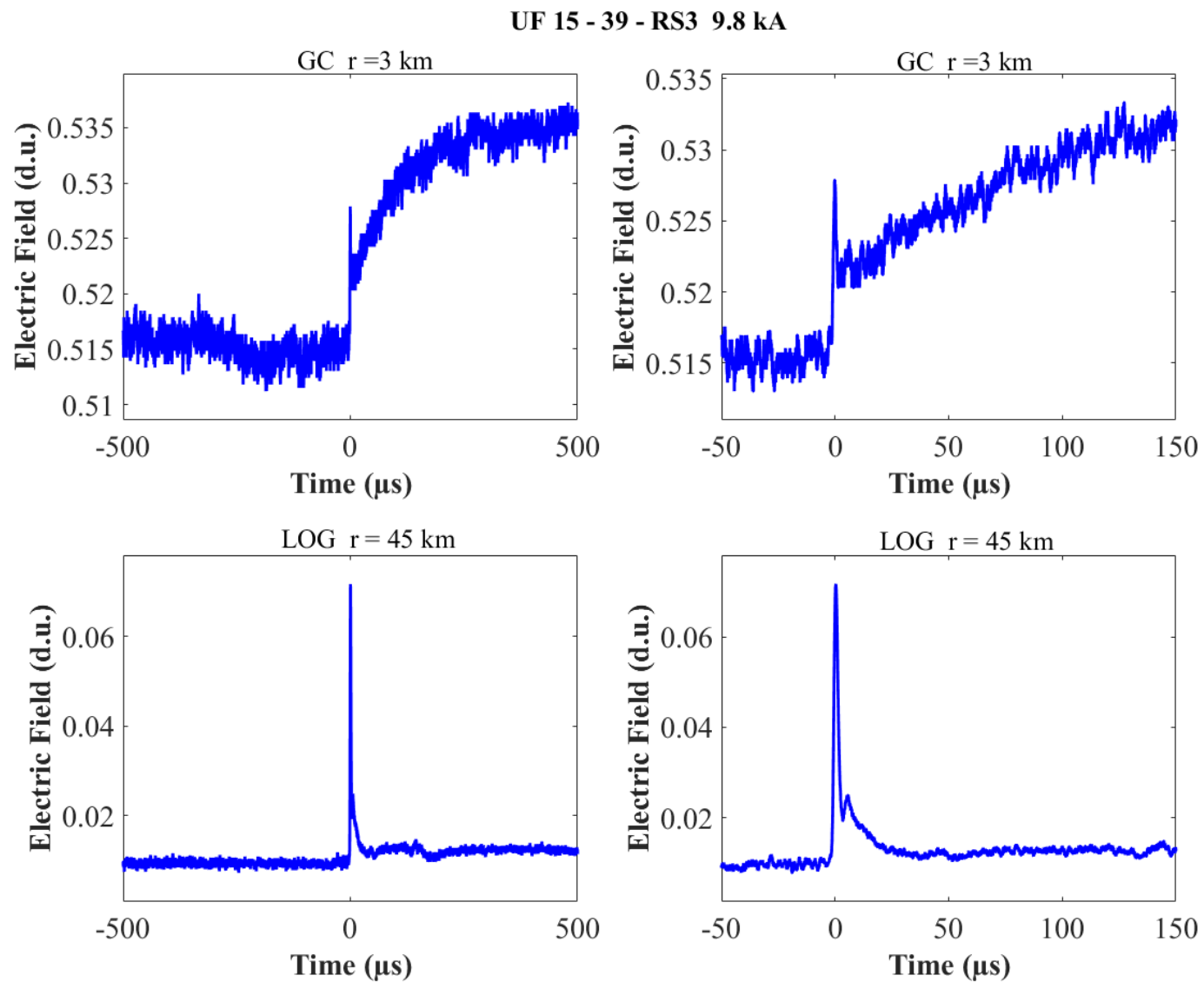


Figure A-158. Two-station electric field waveforms of the RS3 of flash UF 15-39.

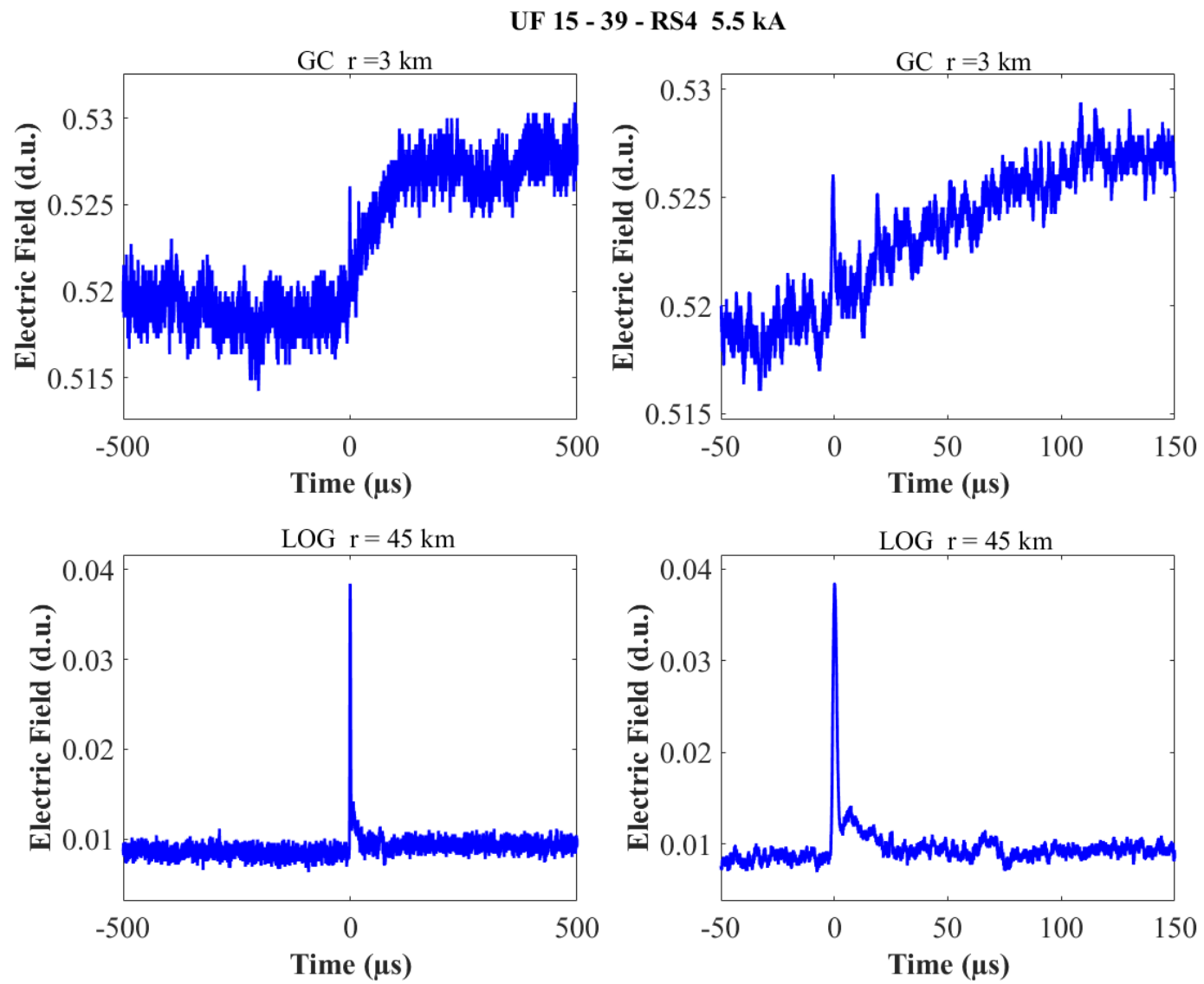


Figure A-159. Two-station electric field waveforms of the RS4 of flash UF 15-39.

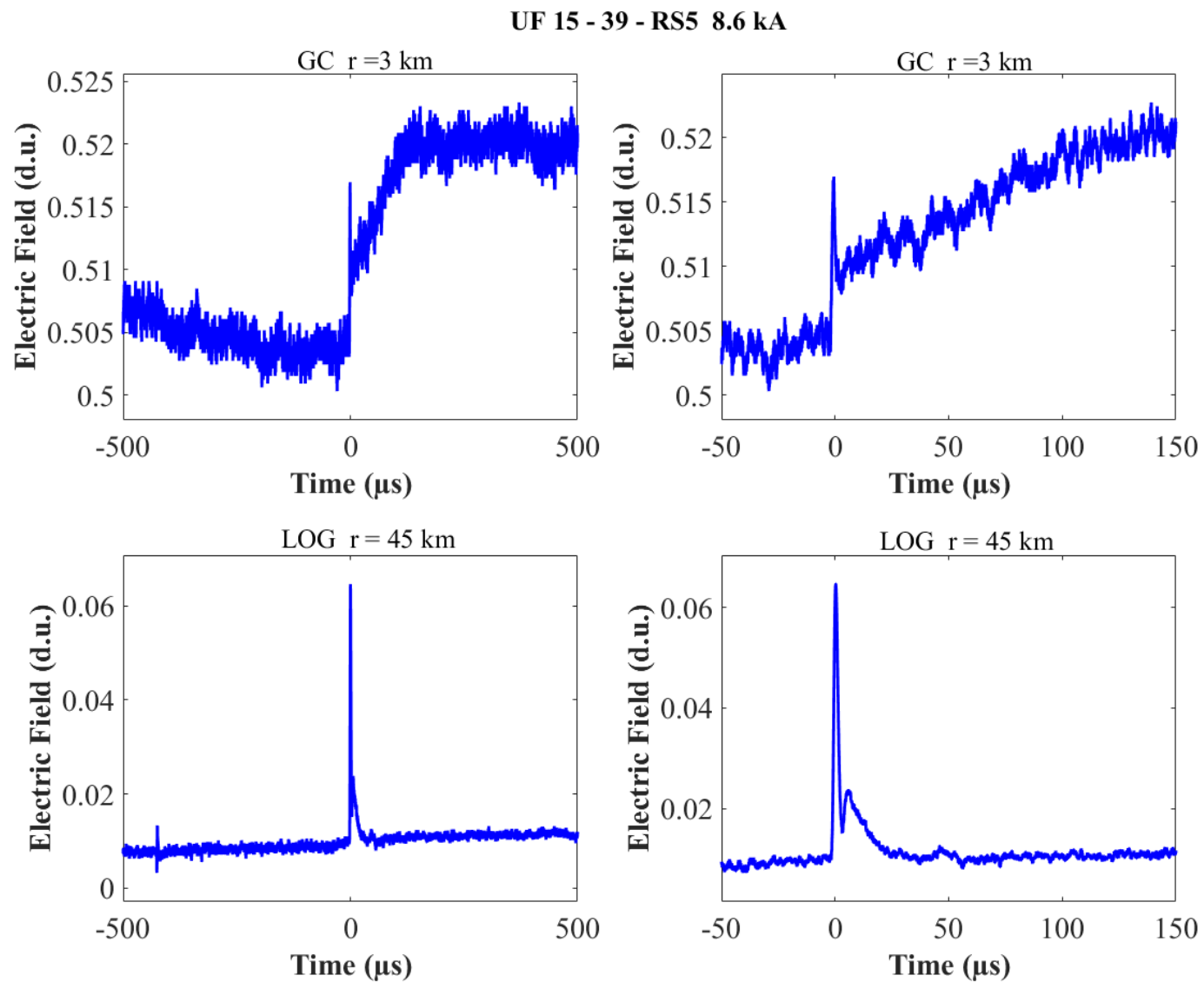


Figure A-160. Two-station electric field waveforms of the RS5 of flash UF 15-39.

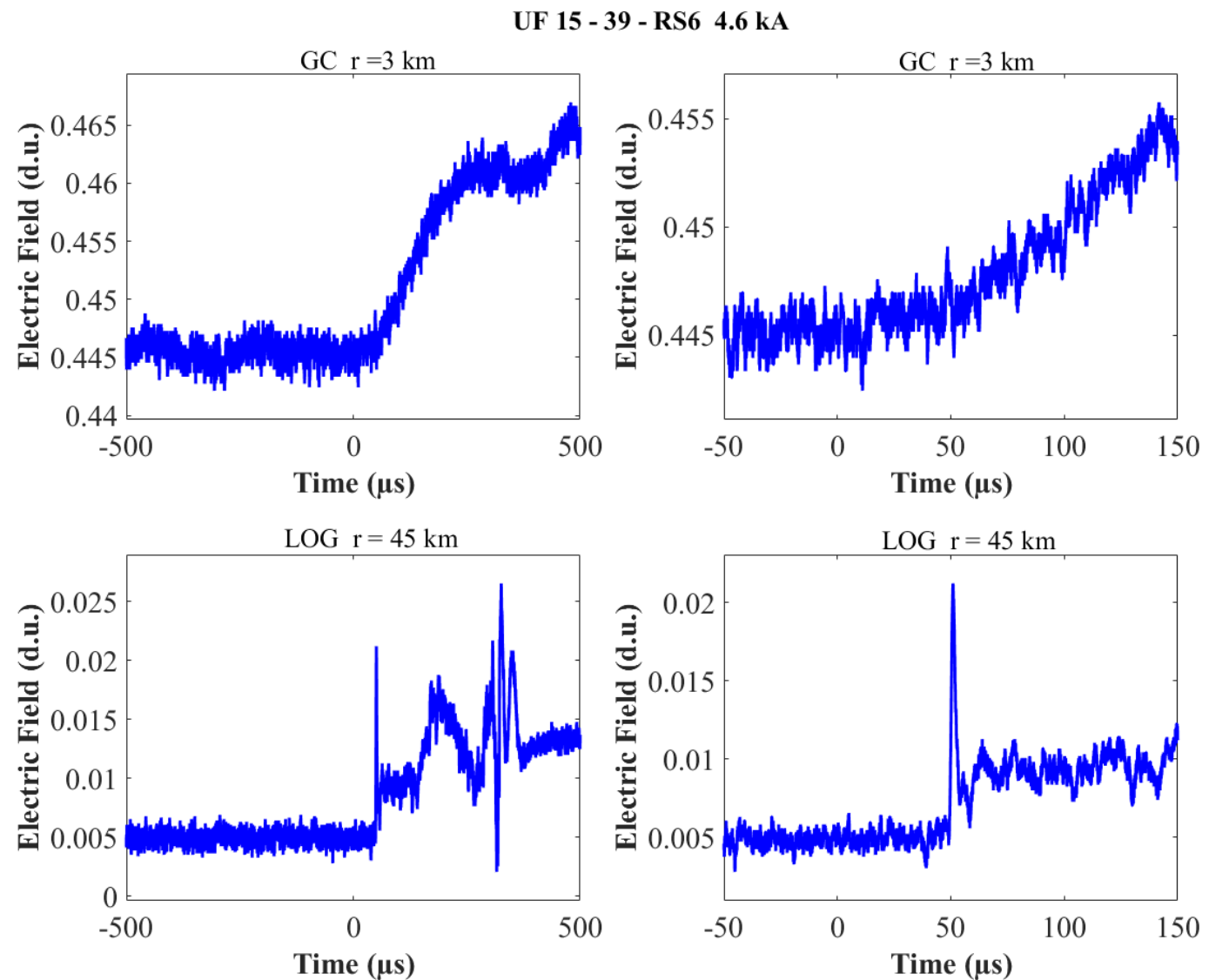


Figure A-161. Two-station electric field waveforms of the RS6 of flash UF 15-39.

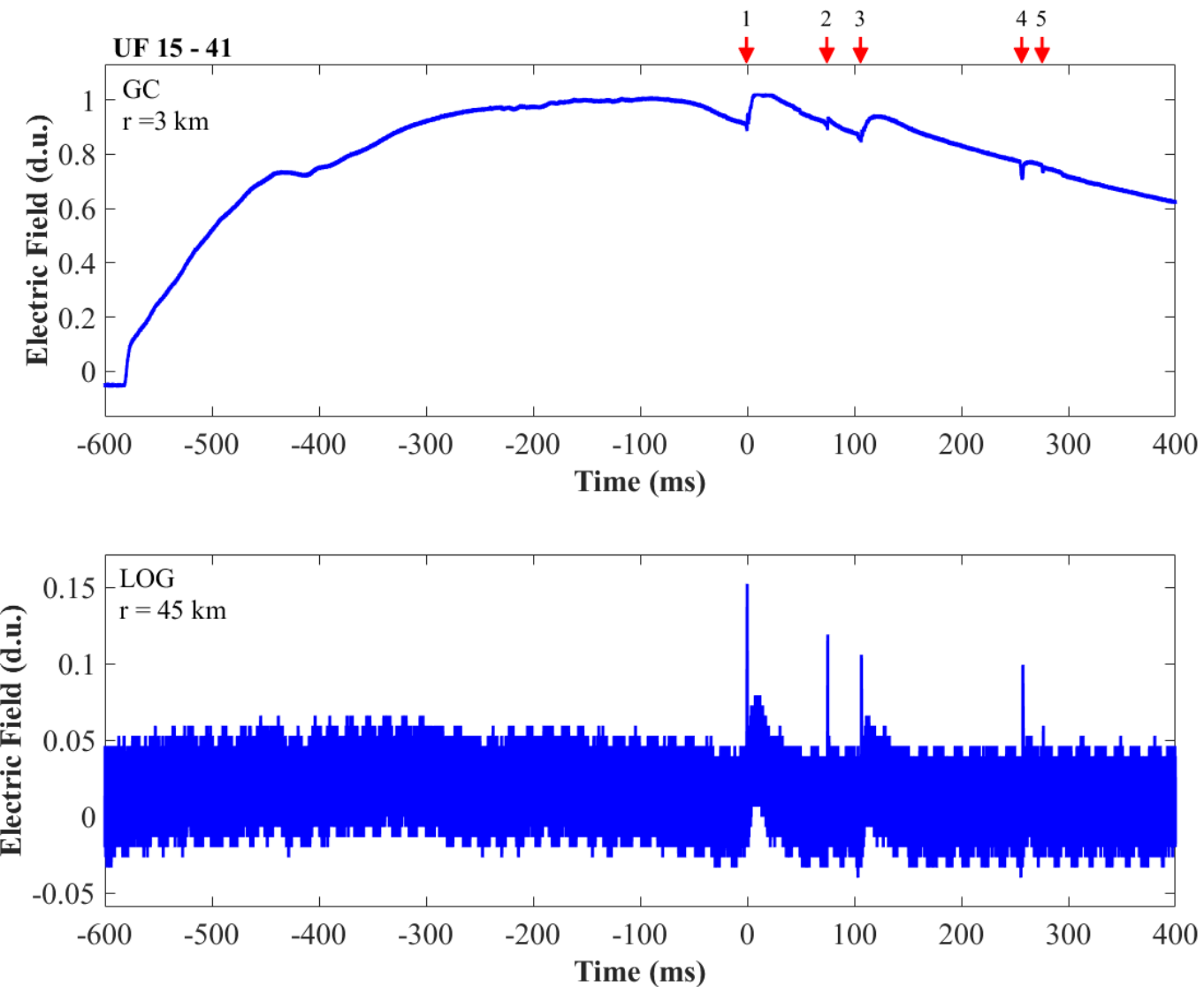


Figure A-162. Two-station electric field waveforms of flash UF 15-41.

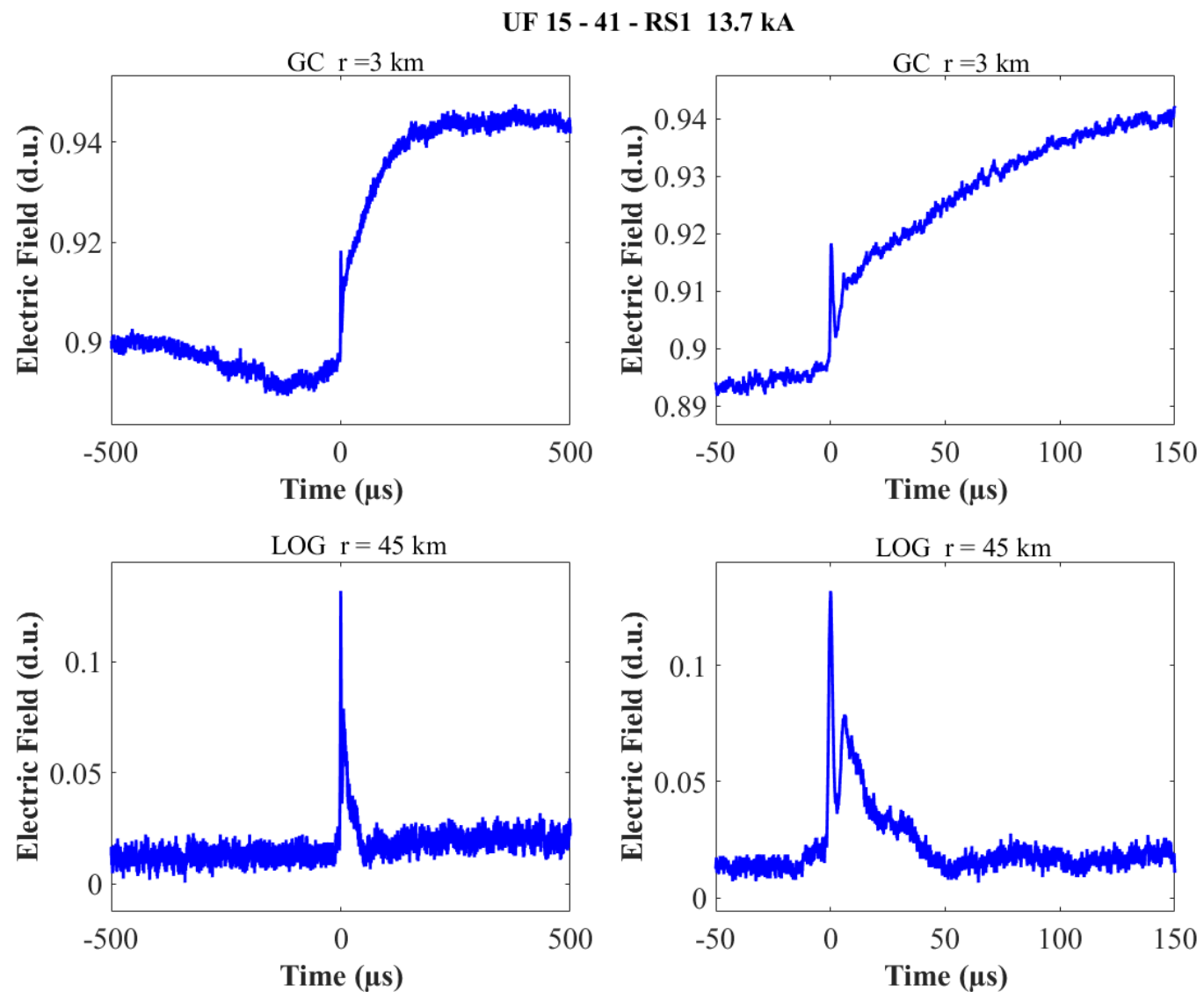


Figure A-163. Two-station electric field waveforms of the RS1 of flash UF 15-41.

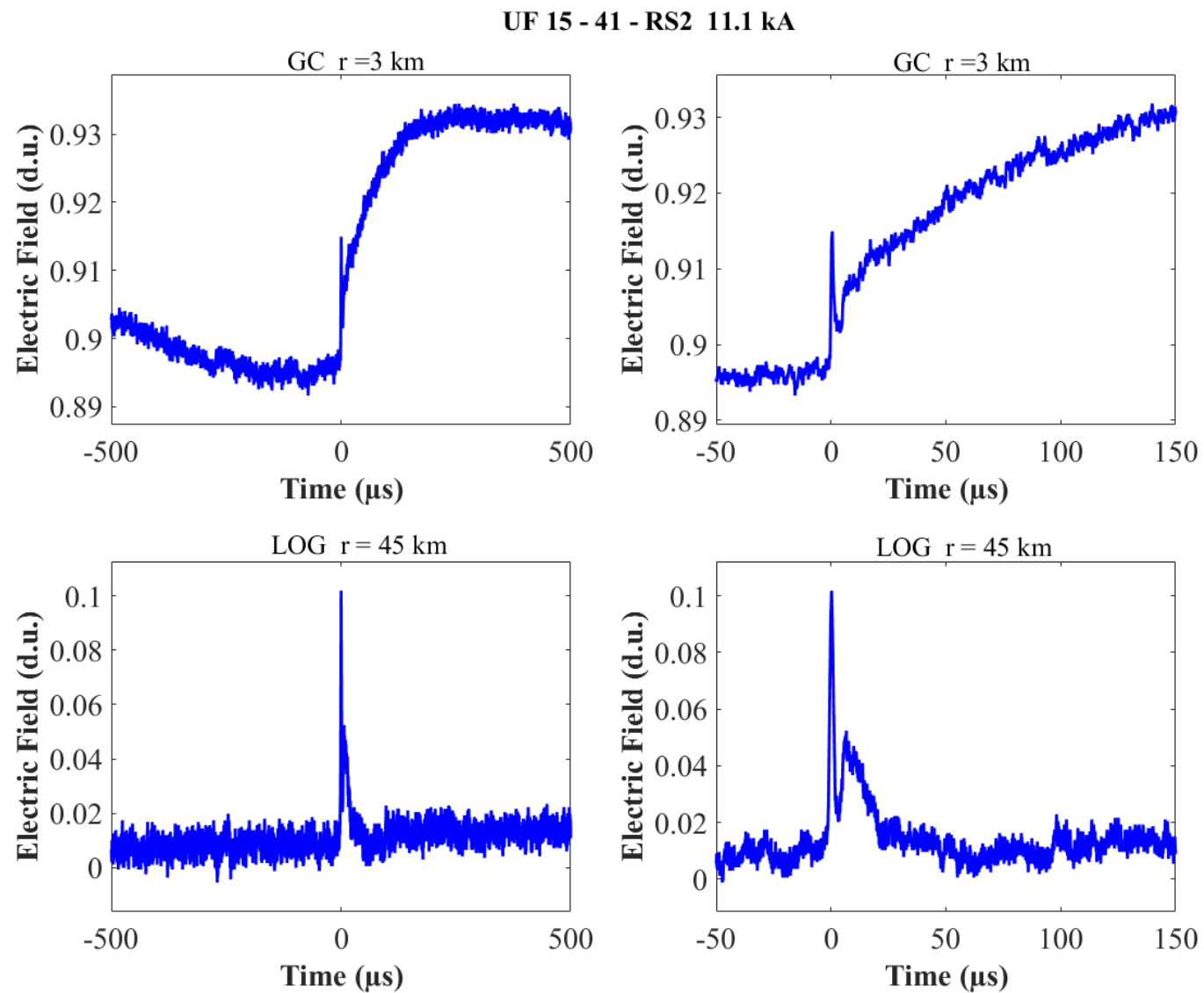


Figure A-164. Two-station electric field waveforms of the RS2 of flash UF 15-41.

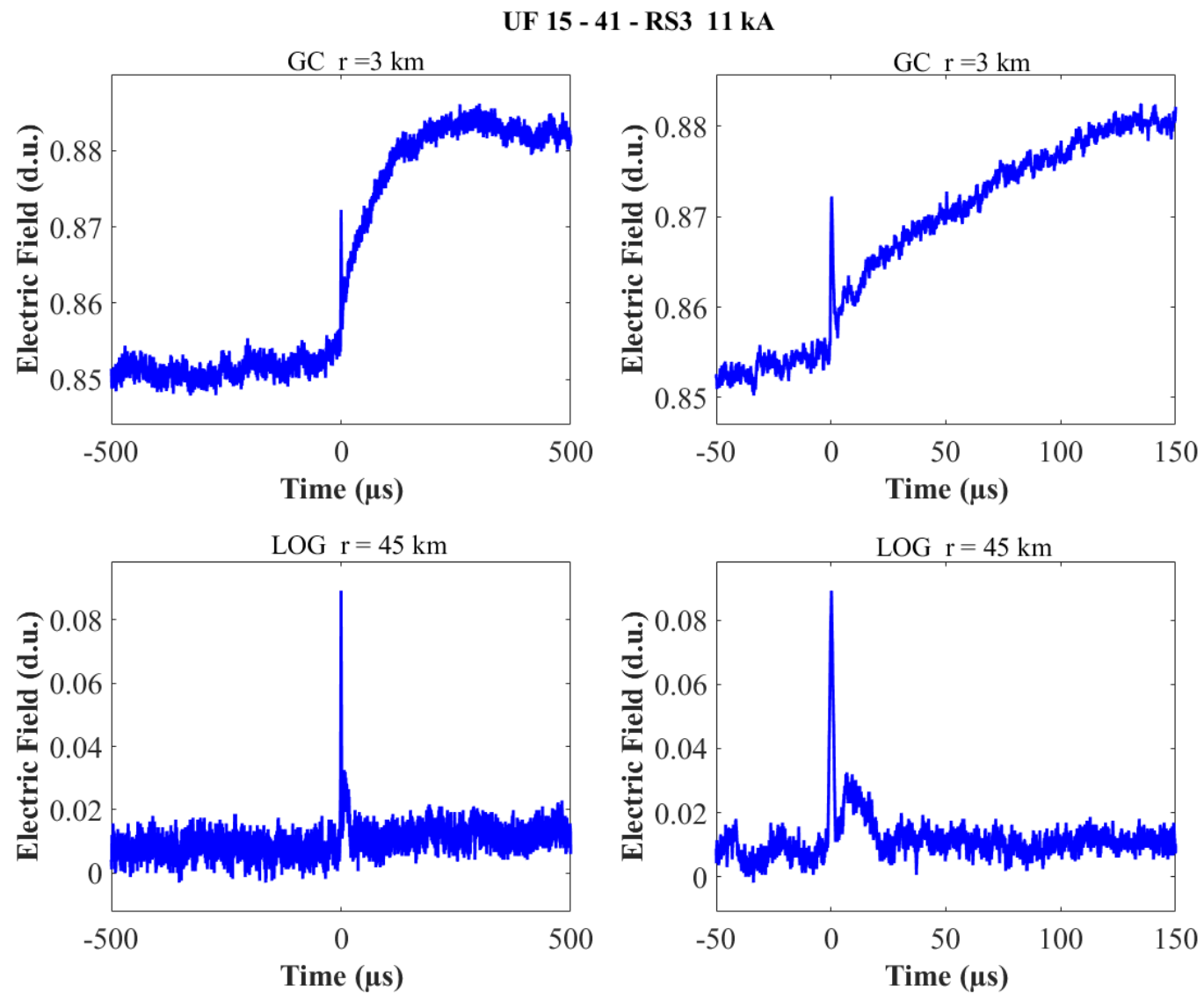


Figure A-165. Two-station electric field waveforms of the RS3 of flash UF 15-41.

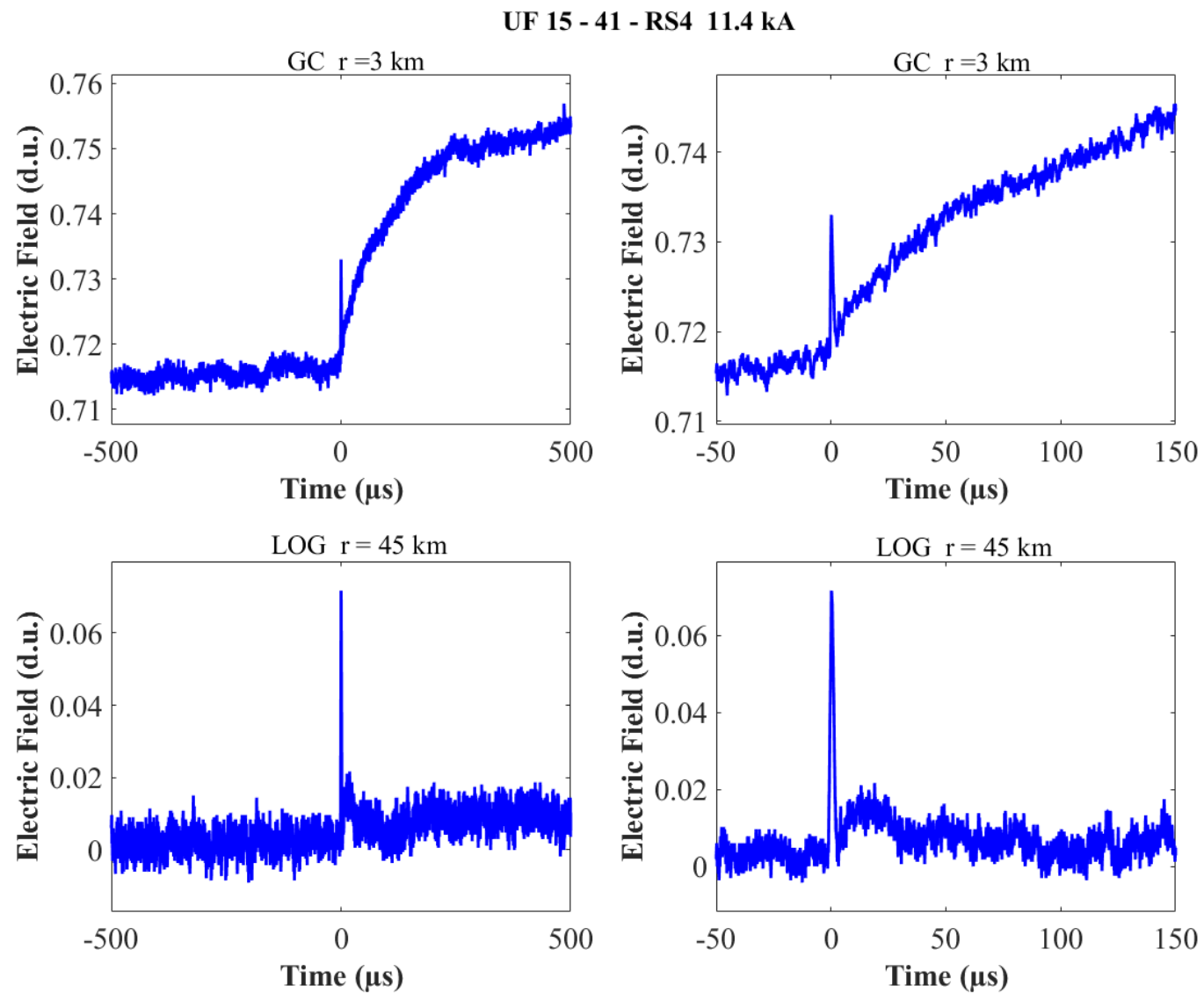


Figure A-166. Two-station electric field waveforms of the RS4 of flash UF 15-41.

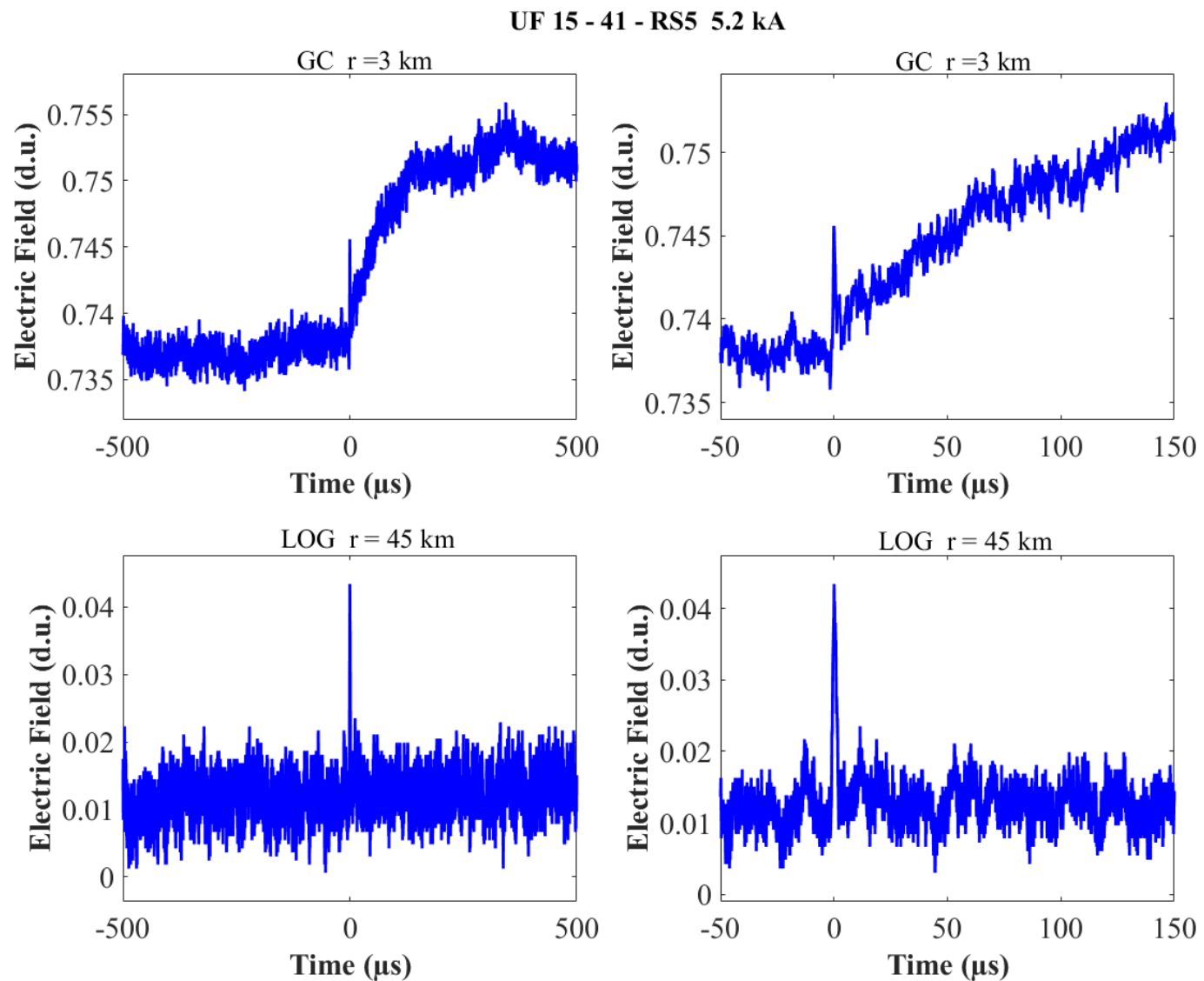


Figure A-167. Two-station electric field waveforms of the RS5 of flash UF 15-41.

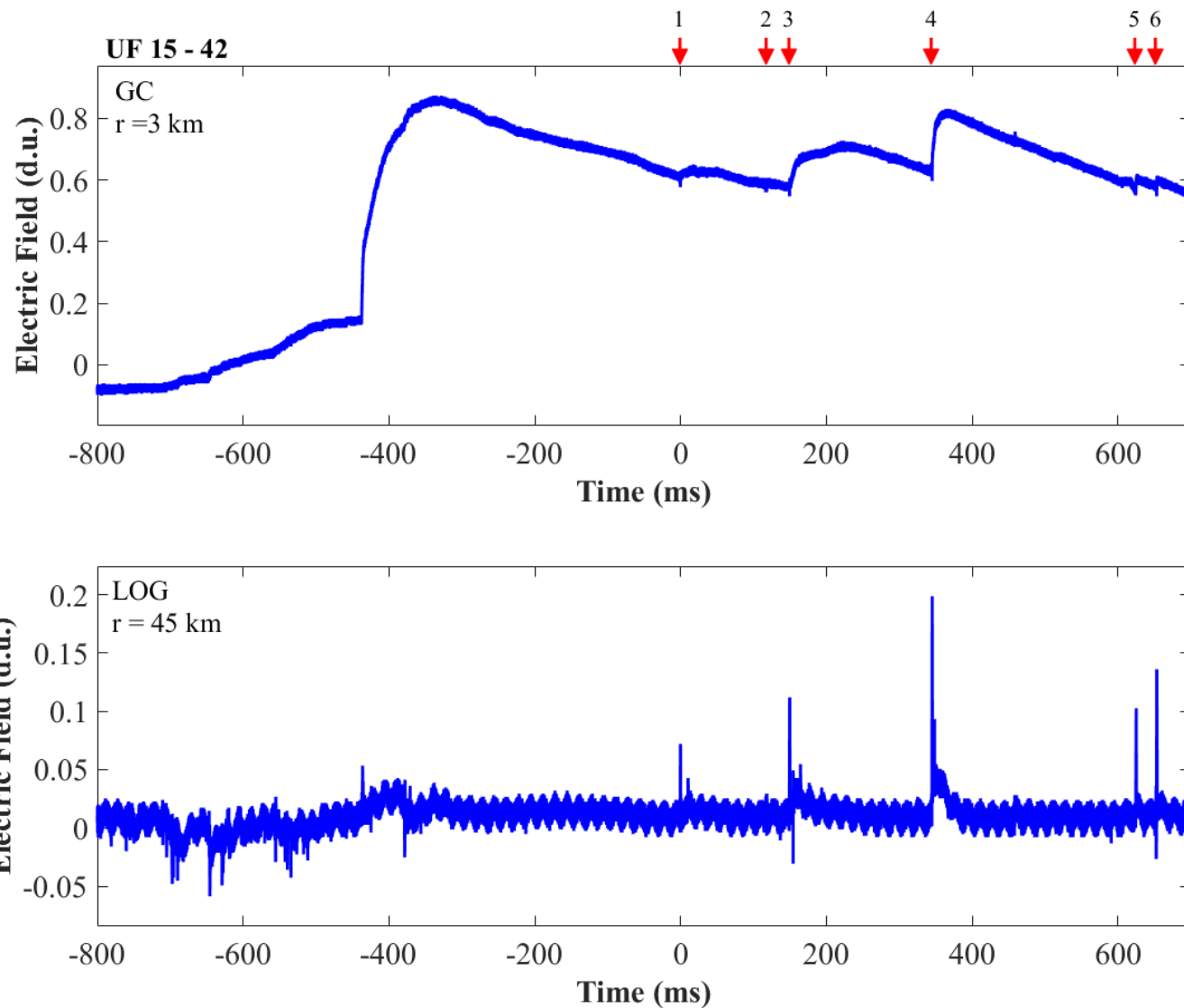


Figure A-168. Two-station electric field waveforms of flash UF 15-42.

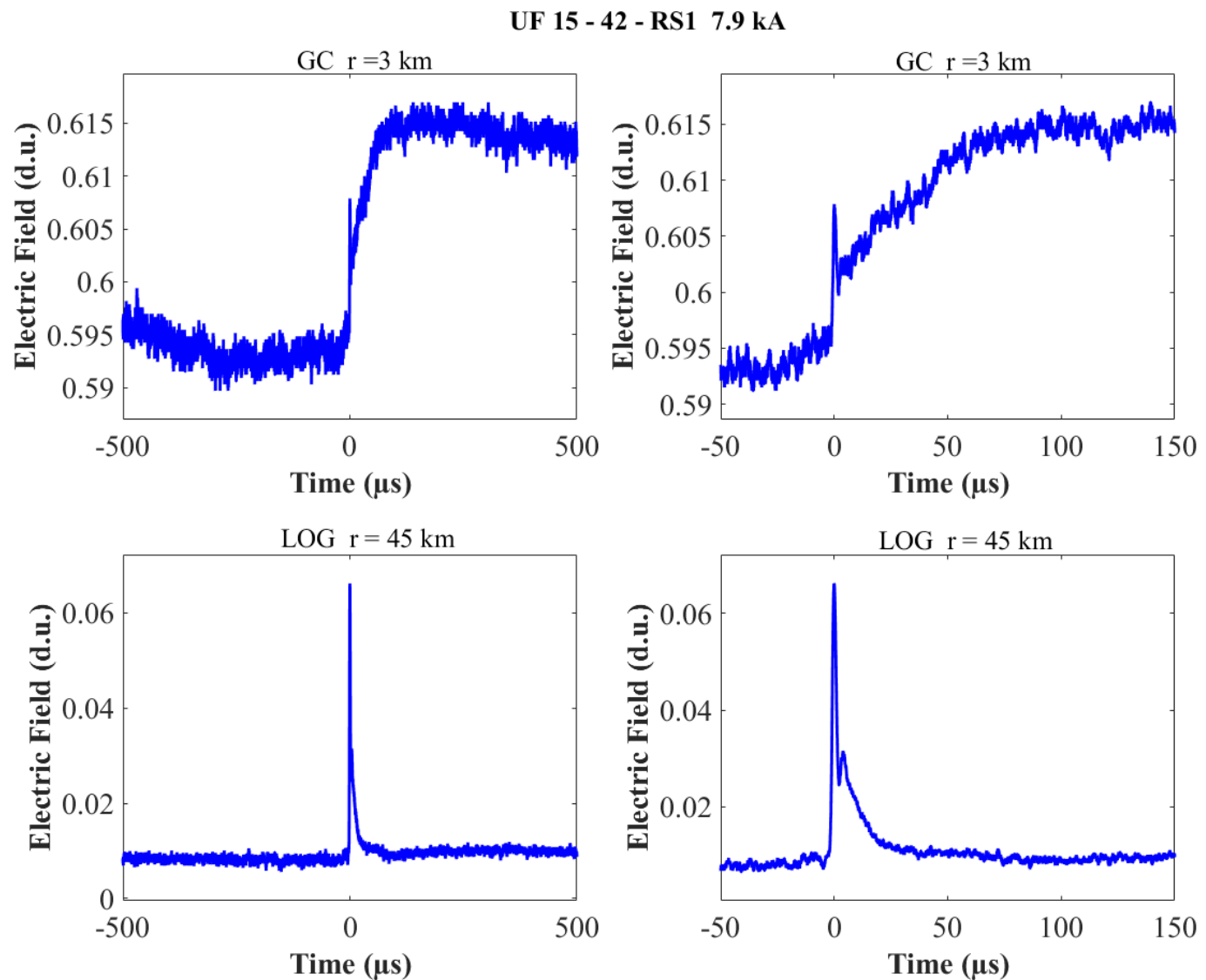


Figure A-169. Two-station electric field waveforms of the RS1 of flash UF 15-42.

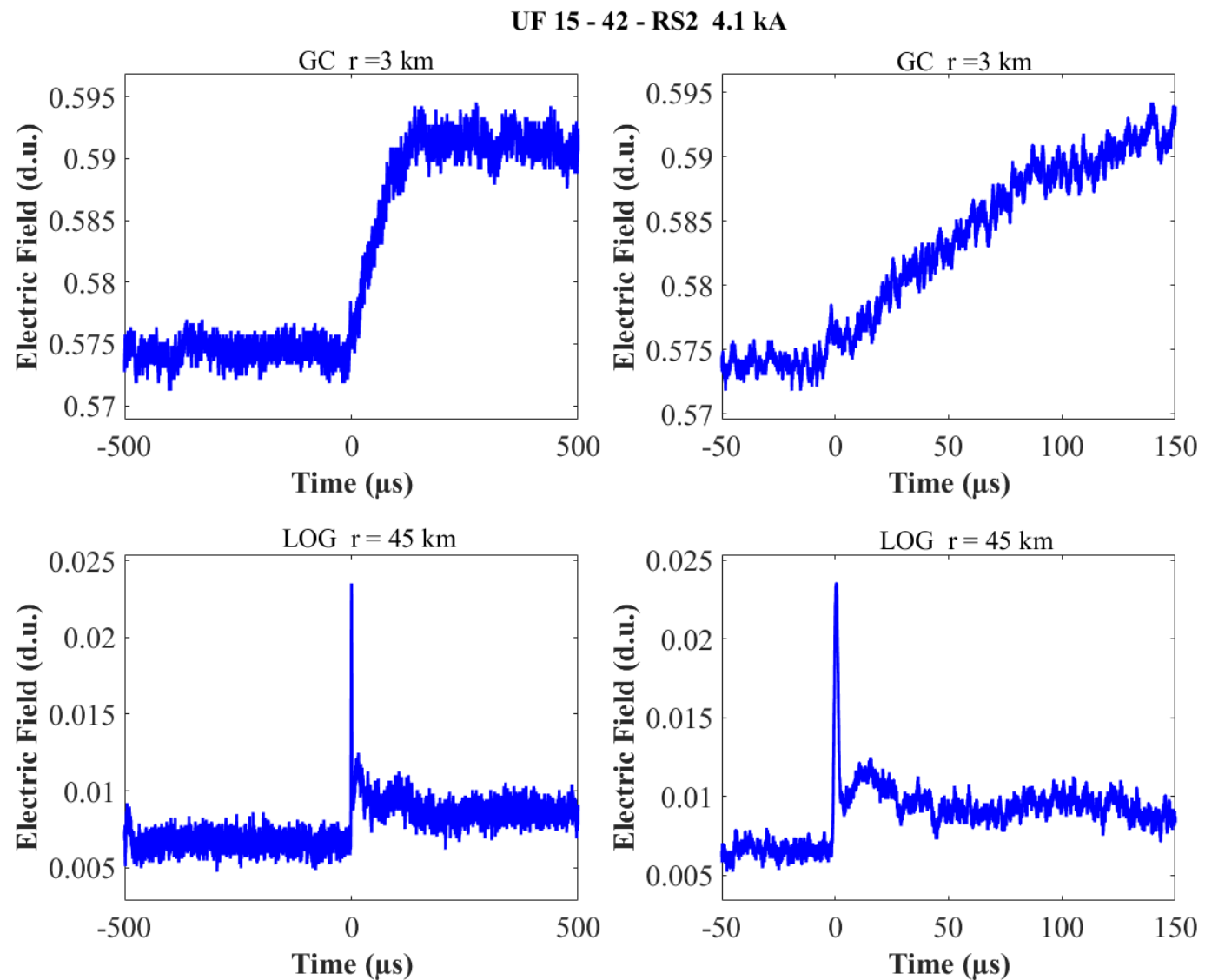


Figure A-170. Two-station electric field waveforms of the RS2 of flash UF 15-42.

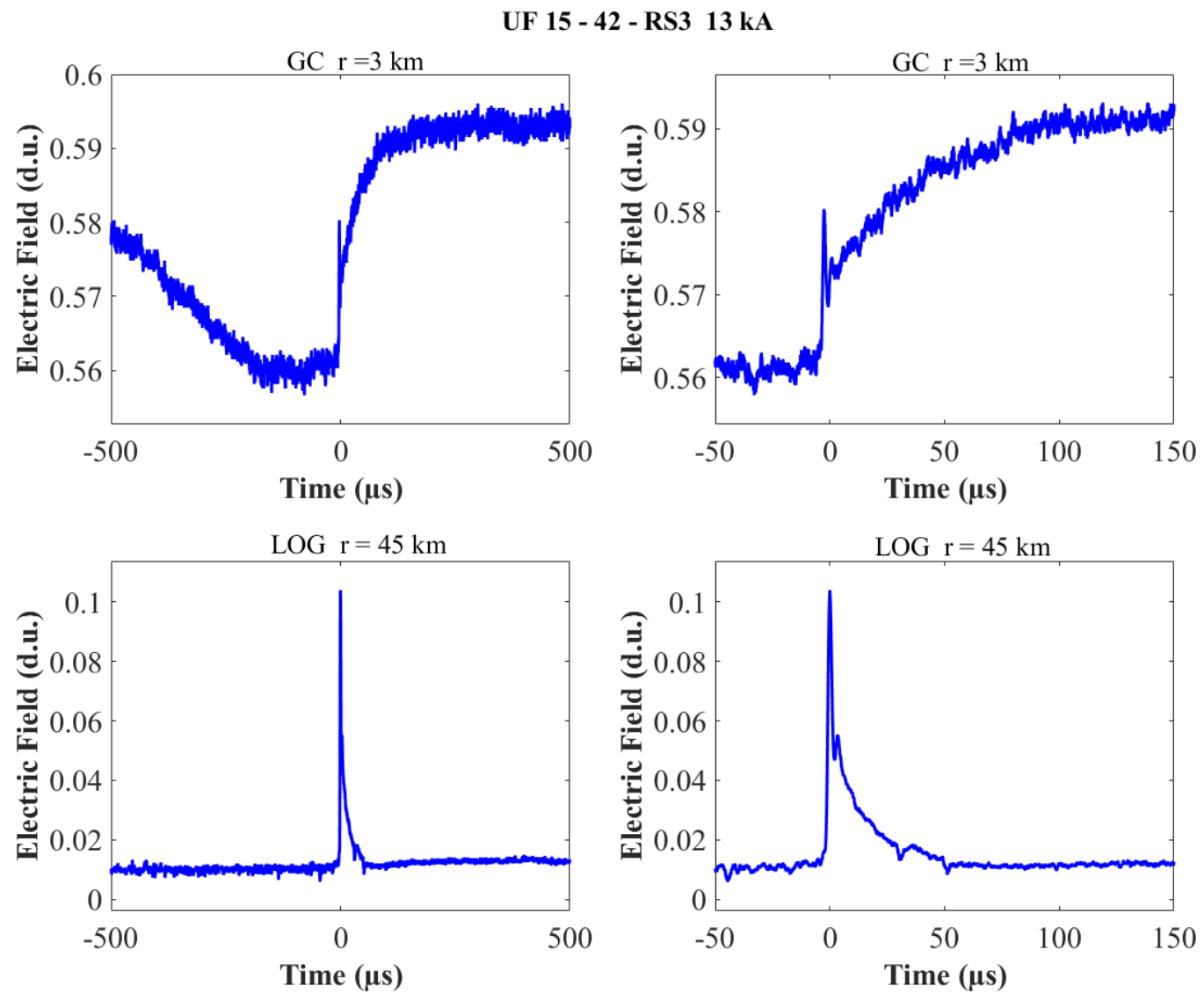


Figure A-171. Two-station electric field waveforms of the RS3 of flash UF 15-42.

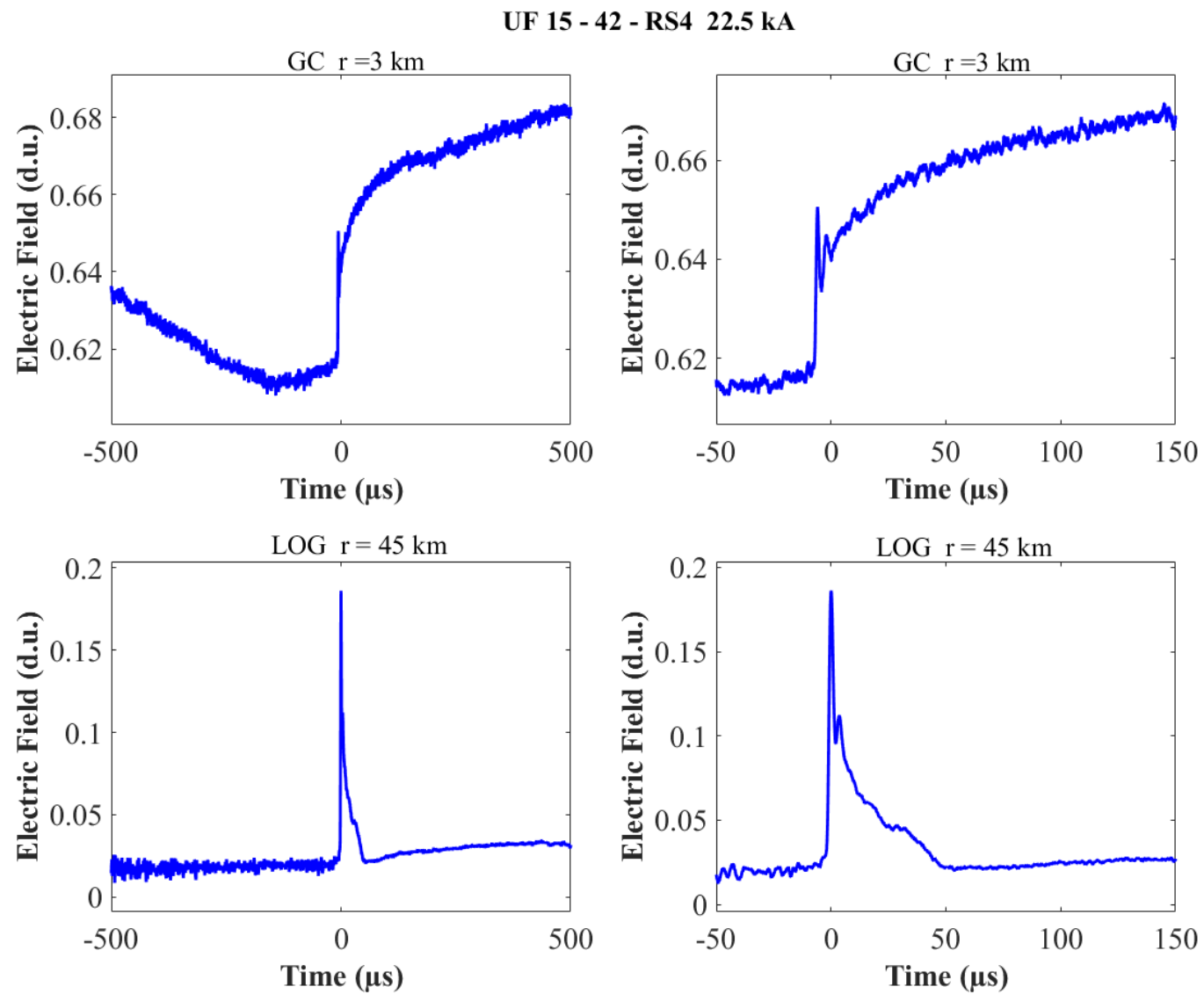


Figure A-172. Two-station electric field waveforms of the RS4 of flash UF 15-42.

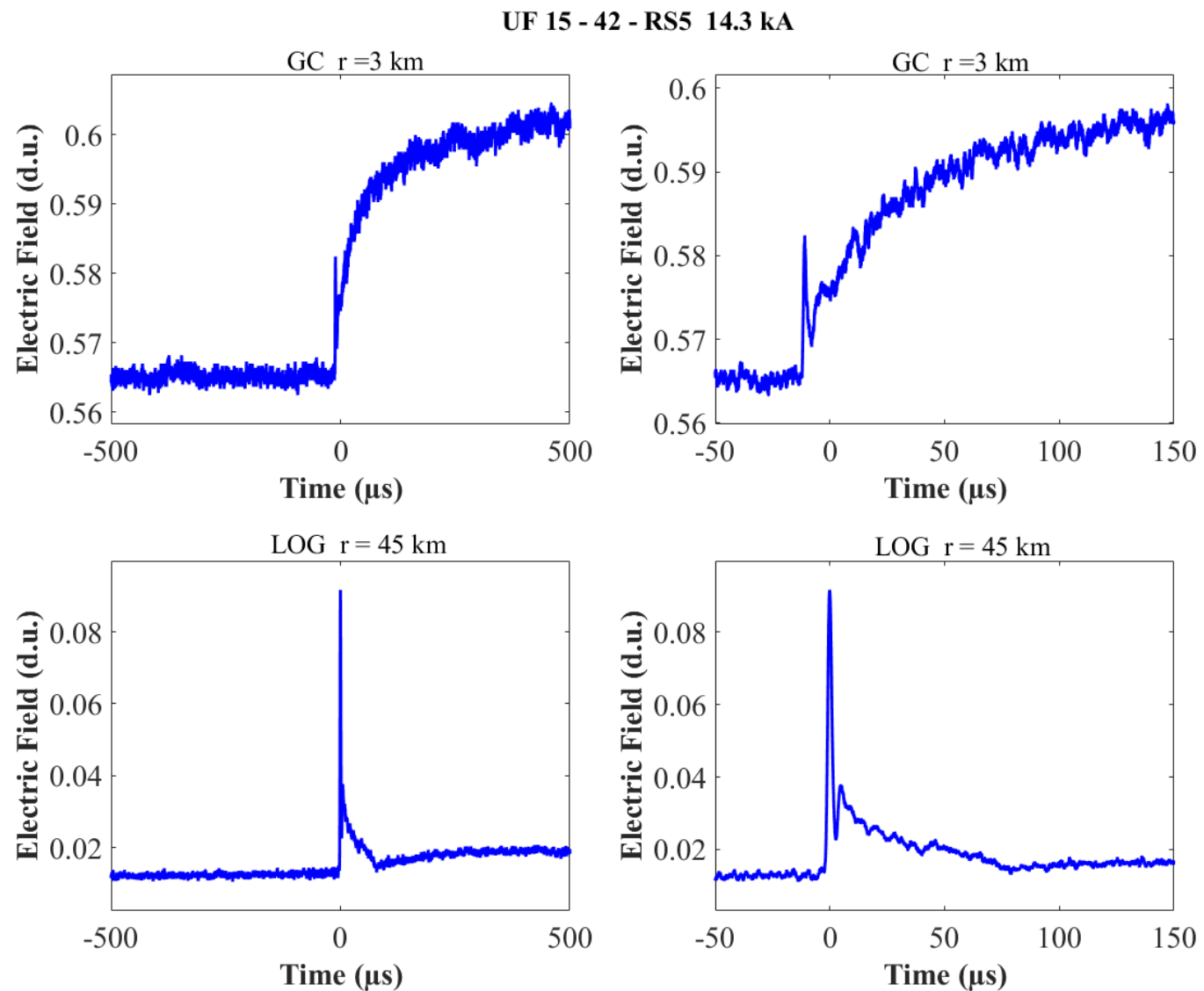


Figure A-173. Two-station electric field waveforms of the RS5 of flash UF 15-42.

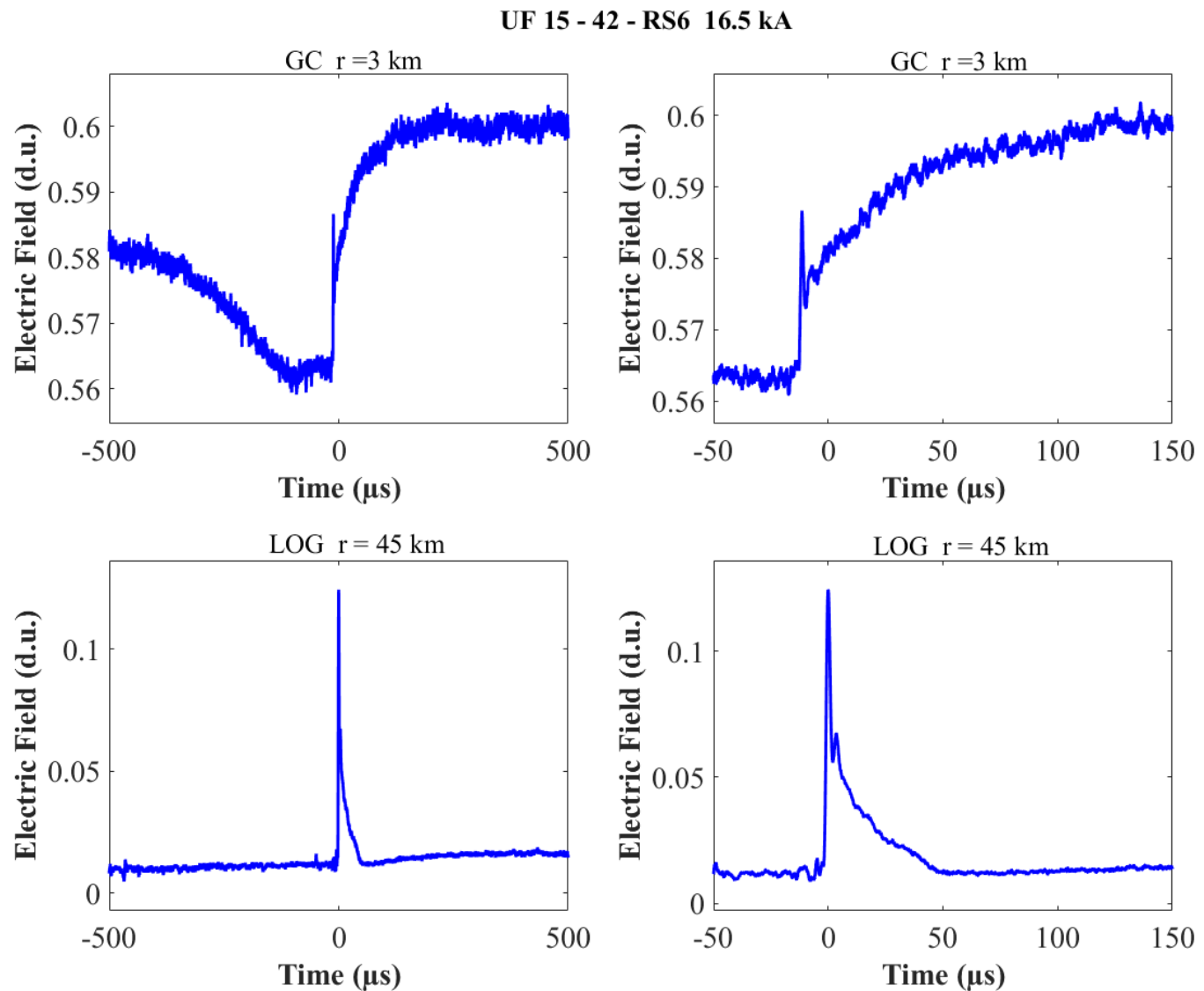


Figure A-174. Two-station electric field waveforms of the RS6 of flash UF 15-42.

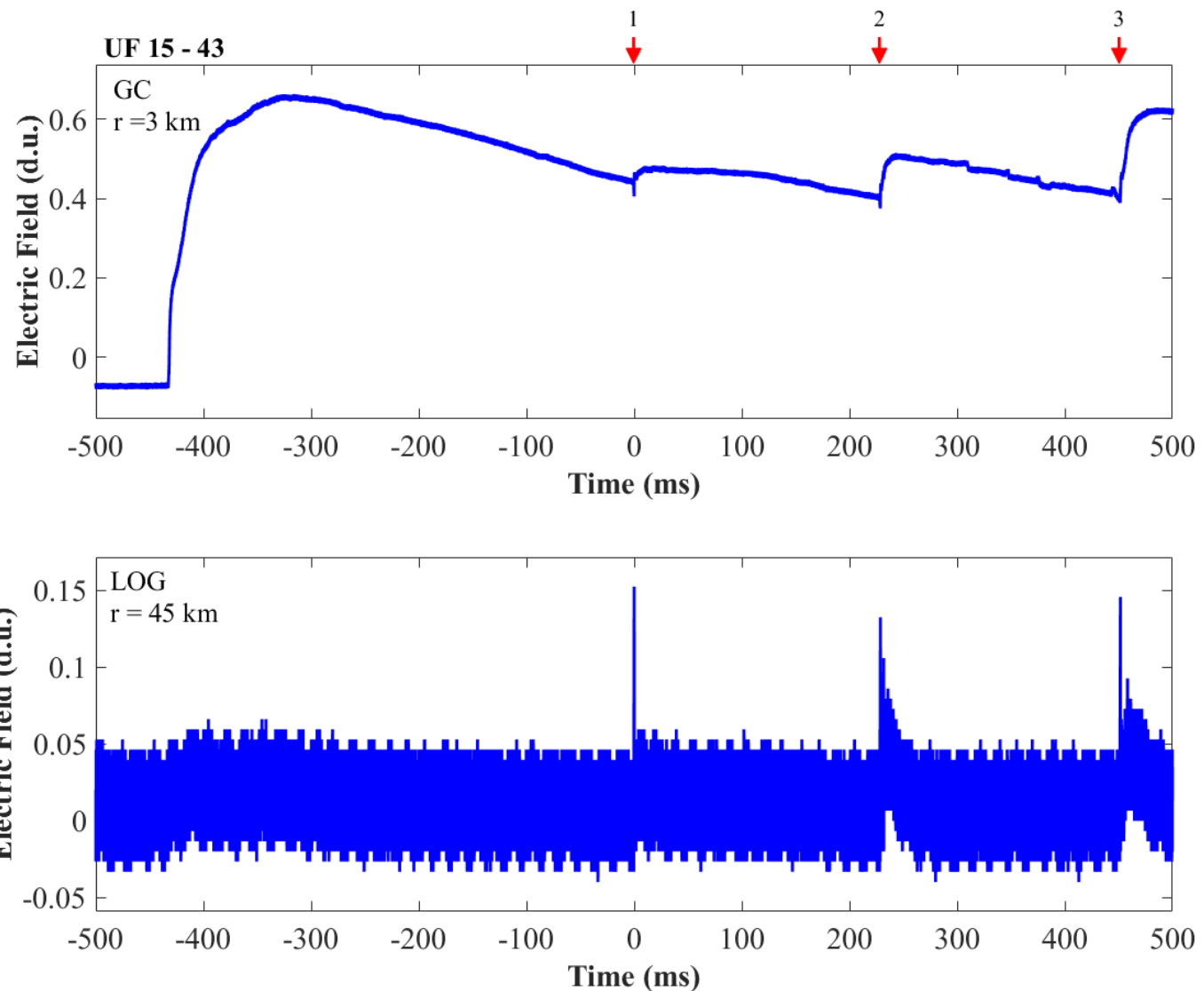


Figure A-175. Two-station electric field waveforms of flash UF 15-43.

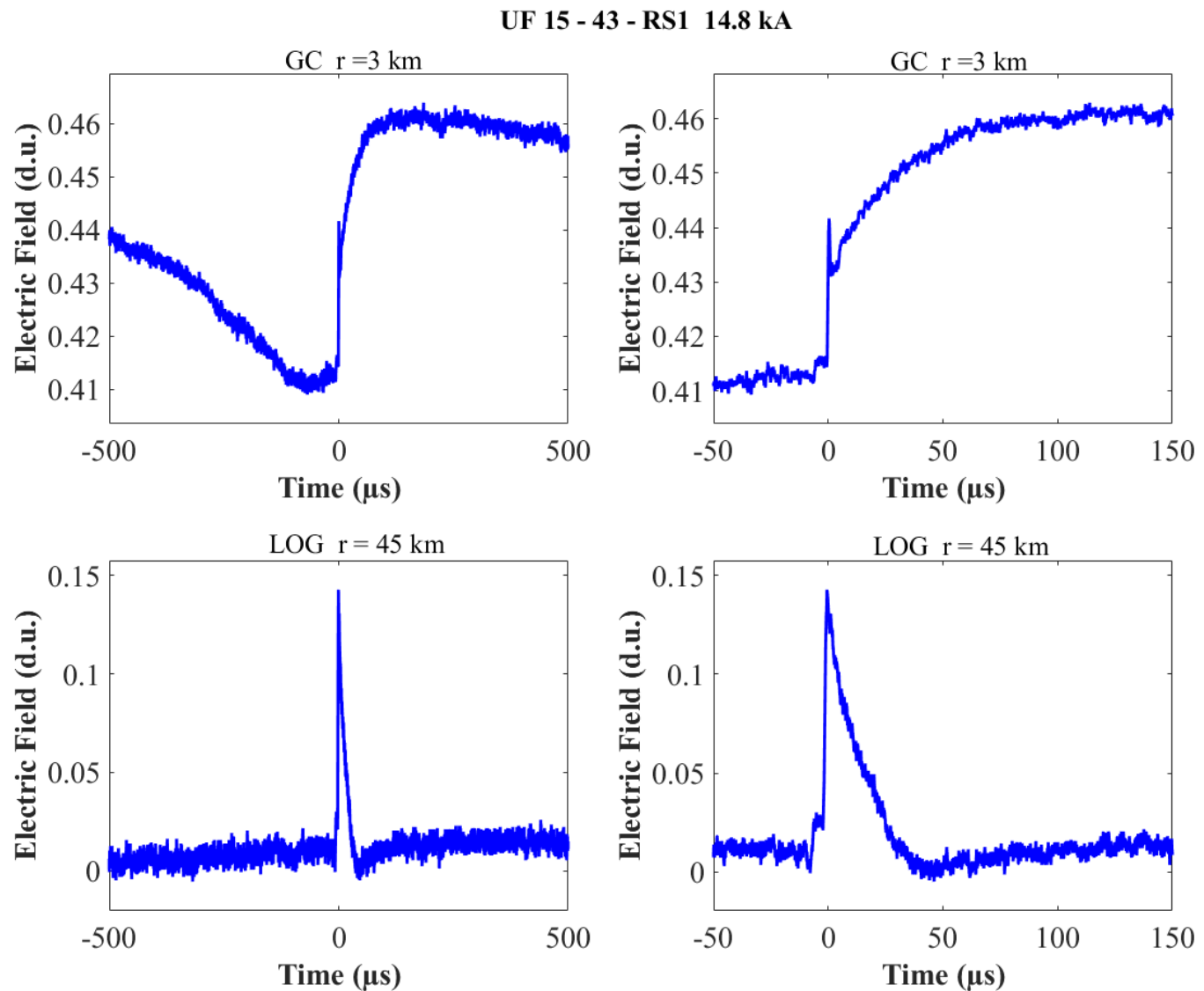


Figure A-176. Two-station electric field waveforms of the RS1 of flash UF 15-43.

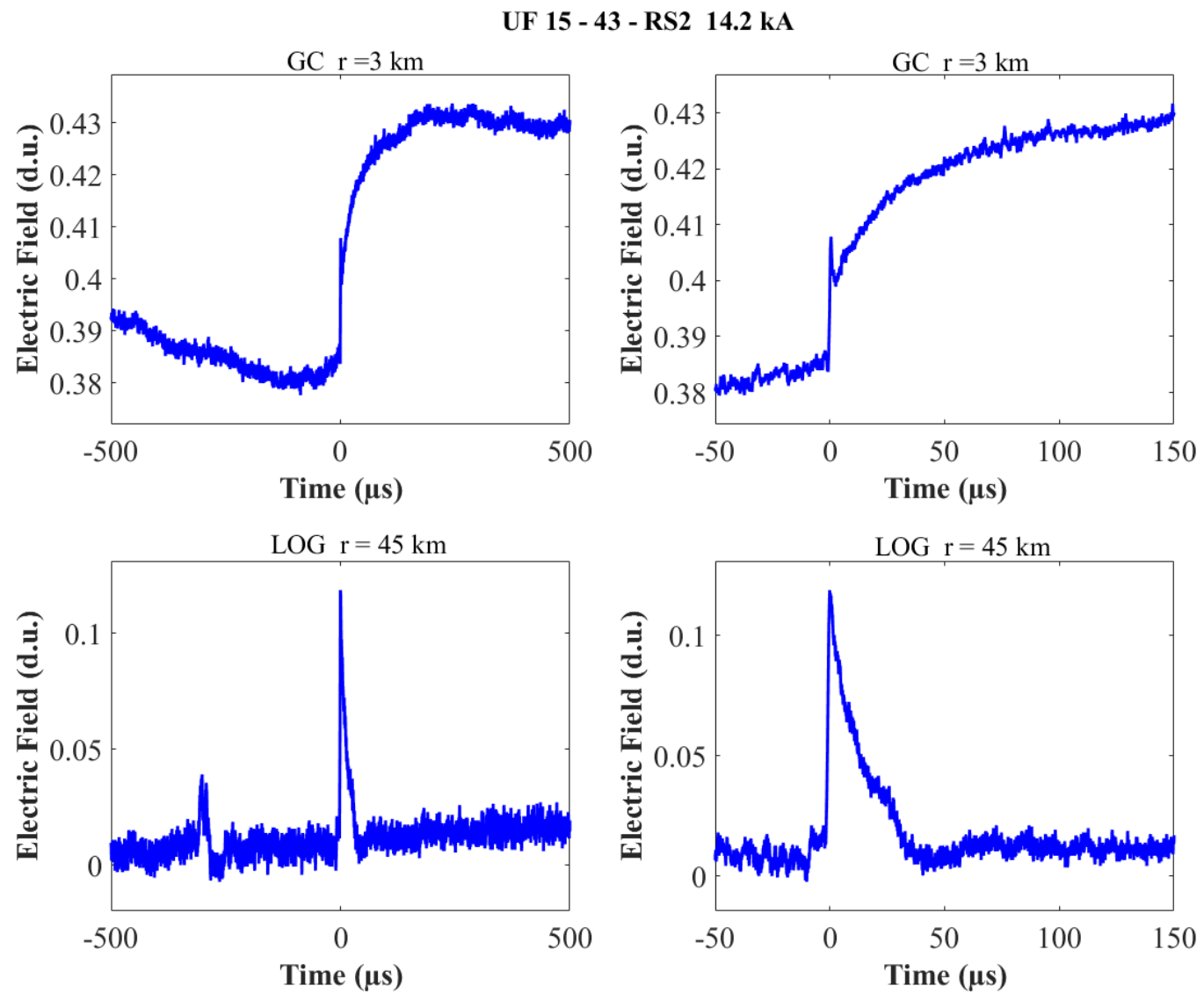


Figure A-177. Two-station electric field waveforms of the RS2 of flash UF 15-43.

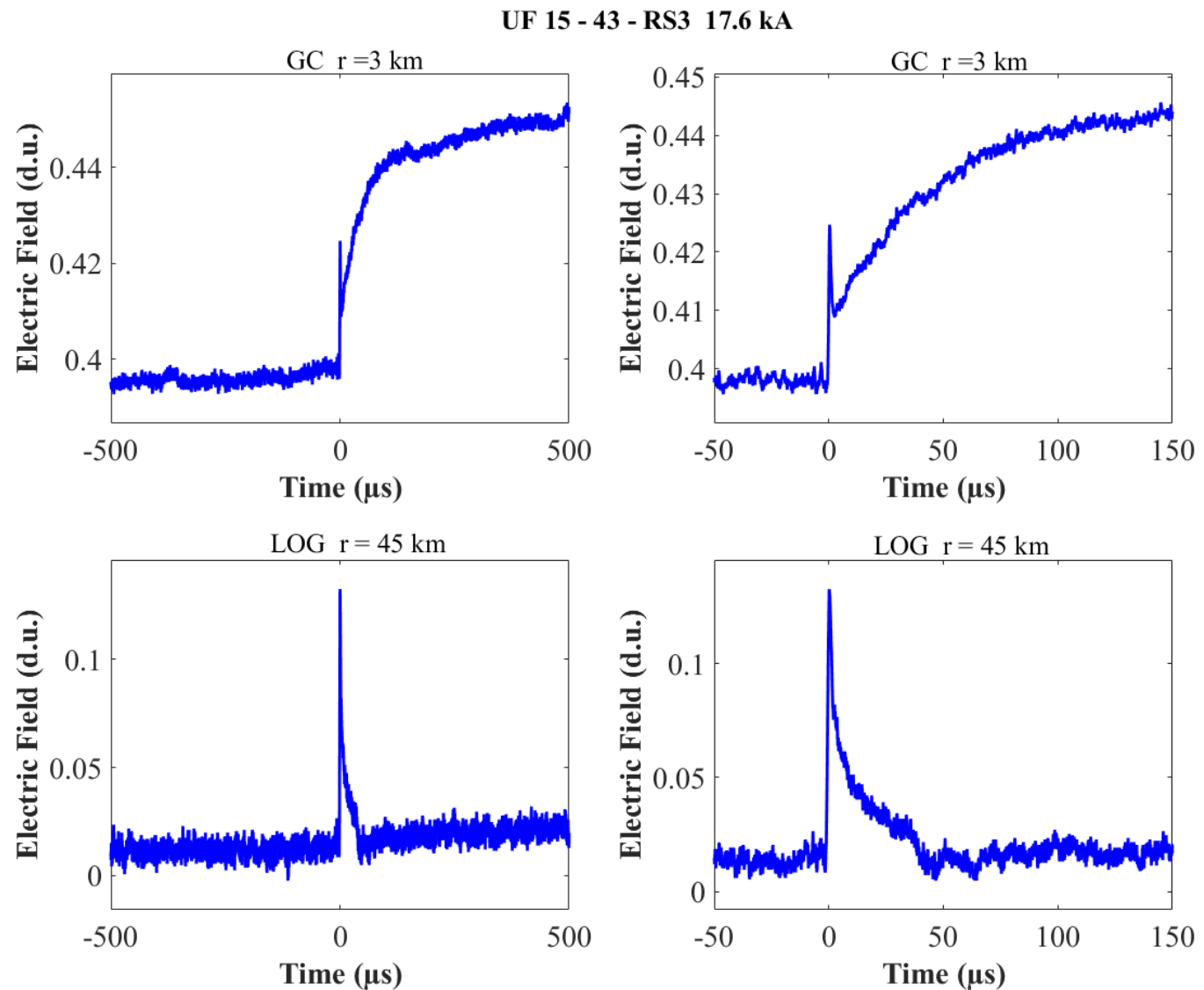


Figure A-178. Two-station electric field waveforms of the RS3 of flash UF 15-43.

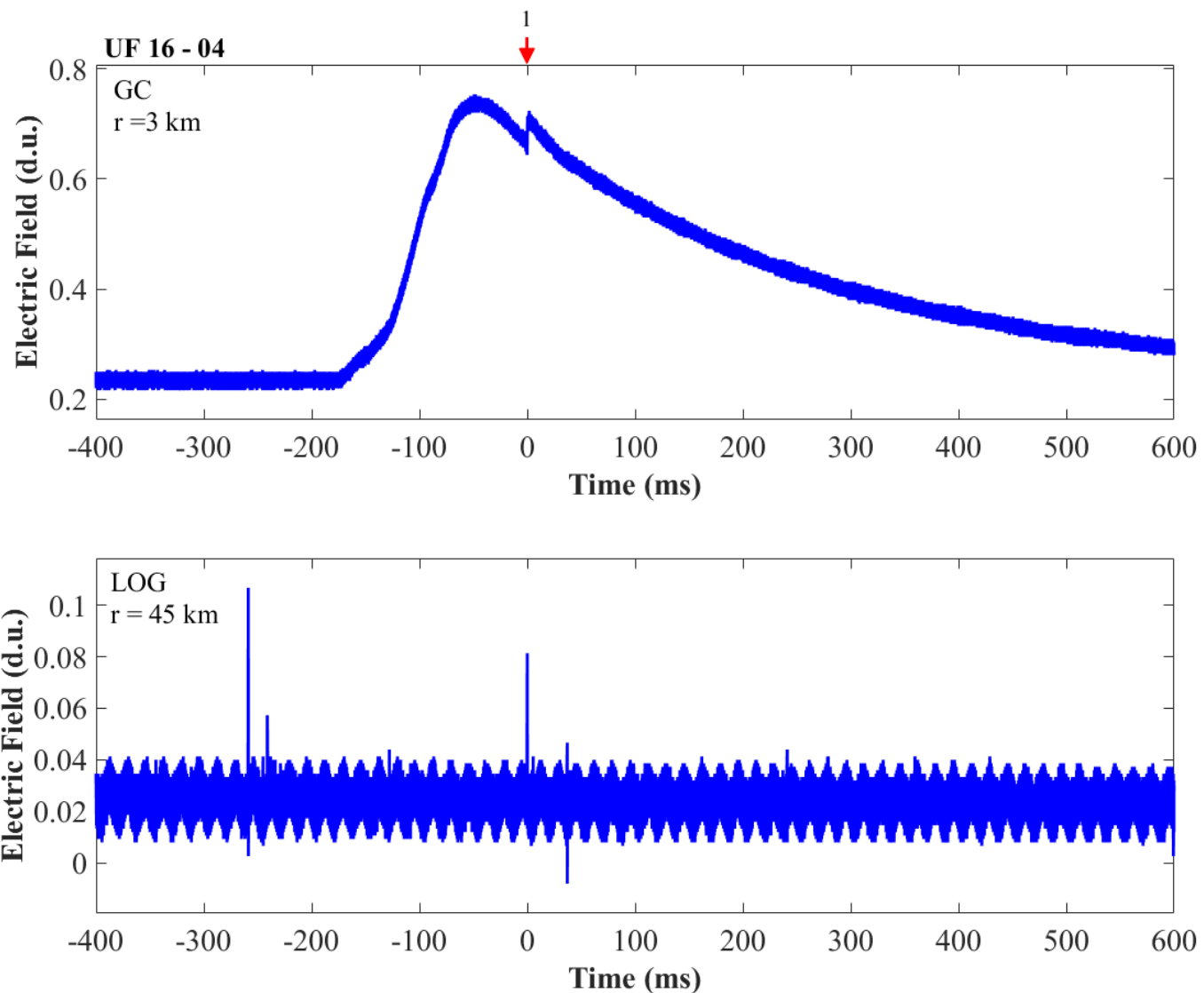


Figure A-179. Two-station electric field waveforms of flash UF 16-04.

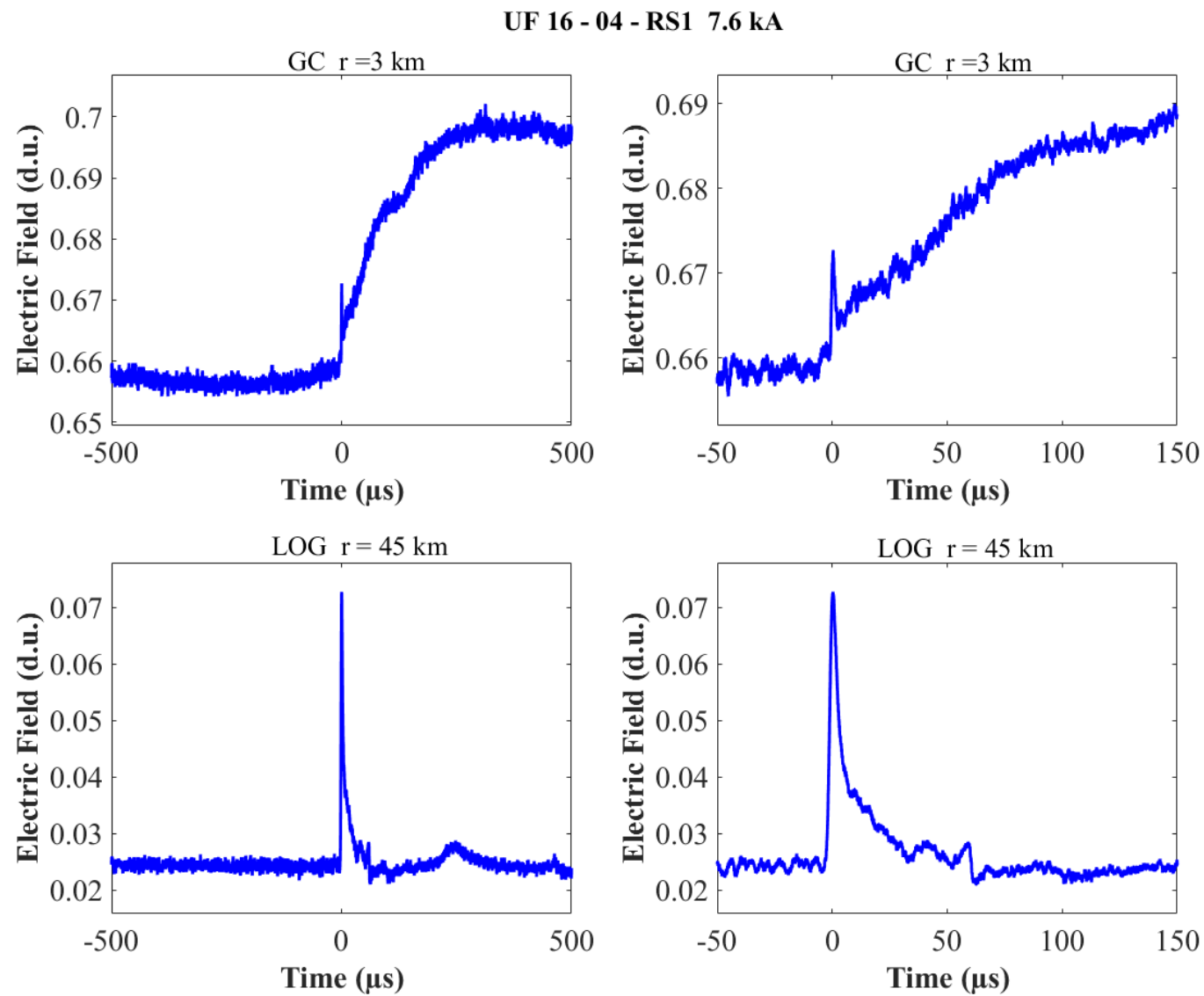


Figure A-180. Two-station electric field waveforms of the RS1 of flash UF 16-0

APPENDIX B
TWO-STATION MEASUREMENTS OF ELECTRIC FIELD WAVEFORMS OF NATURAL
NEGATIVE CLOUD-TO-GROUND LIGHTNING

The two-station (LOG-GC) measurements of electric field waveforms for 10 natural negative cloud-to-ground lightning near Camp Blanding are presented in this appendix. Flash ID, data, and number of return strokes are listed in Table B-1. For each stroke, the complete field record of the flash is shown first and followed by expansions for each stroke on 1-ms and 200- μ s time scales. The distances from each of the stations to the lightning strike point were determined from NLDN-reported location of the stroke.

Table B-1. Inventory of two-station (LOG-GC) field measurements for 10 natural negative cloud-to-ground lightning

Flash ID	Date	Number of Return Strokes
00389	08/07/2015	3
00390	08/07/2015	3
00467	08/07/2015	3
00468	08/07/2015	4
00491	08/07/2015	4
00532	08/07/2015	4
00537	08/07/2015	2
00564	08/07/2015	5
00569	08/07/2015	4
00620	08/13/2015	1
Total Number of Flashes: 10		Total Number of Strokes: 33

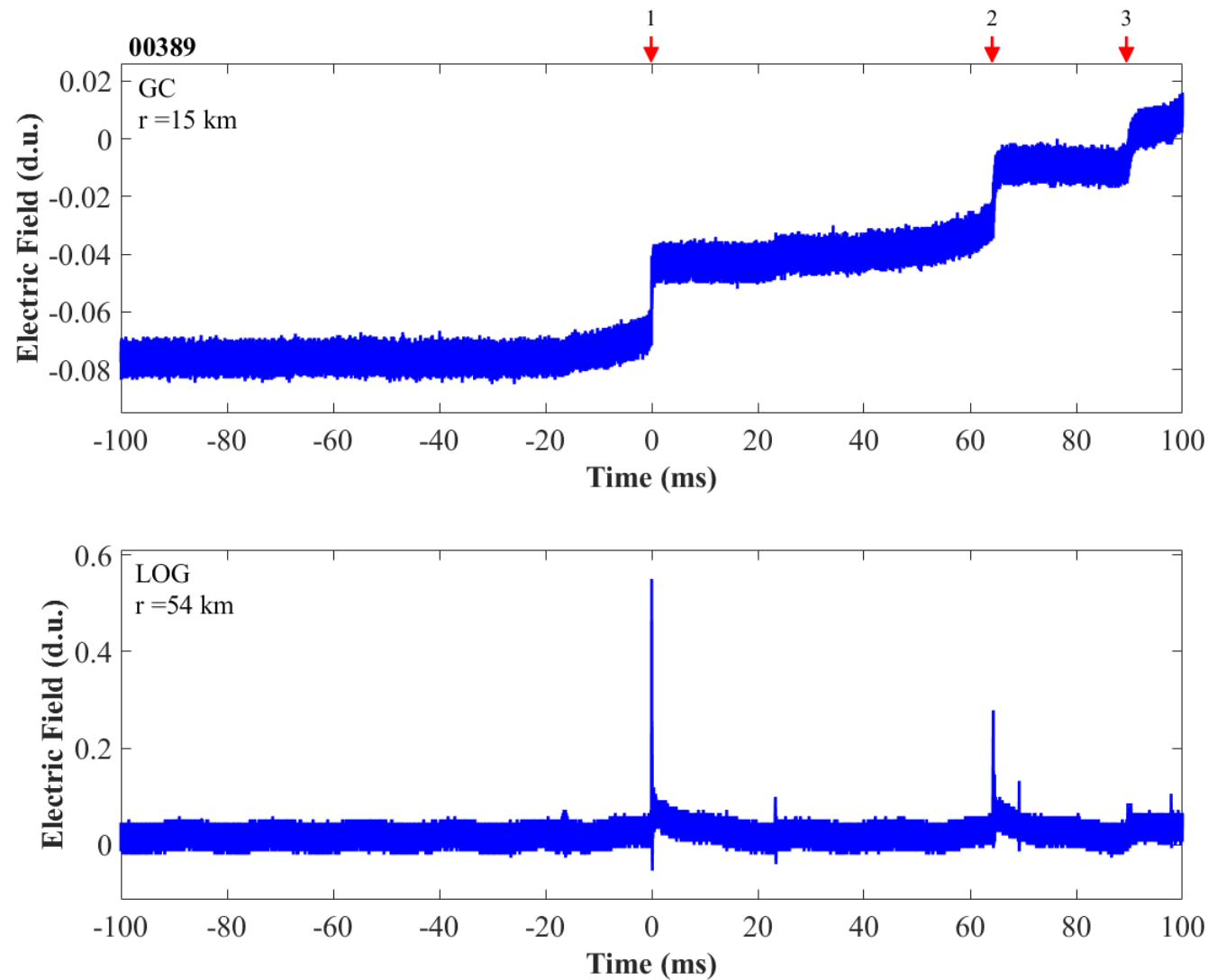


Figure B-1. Two-station electric field waveforms of flash 00389.

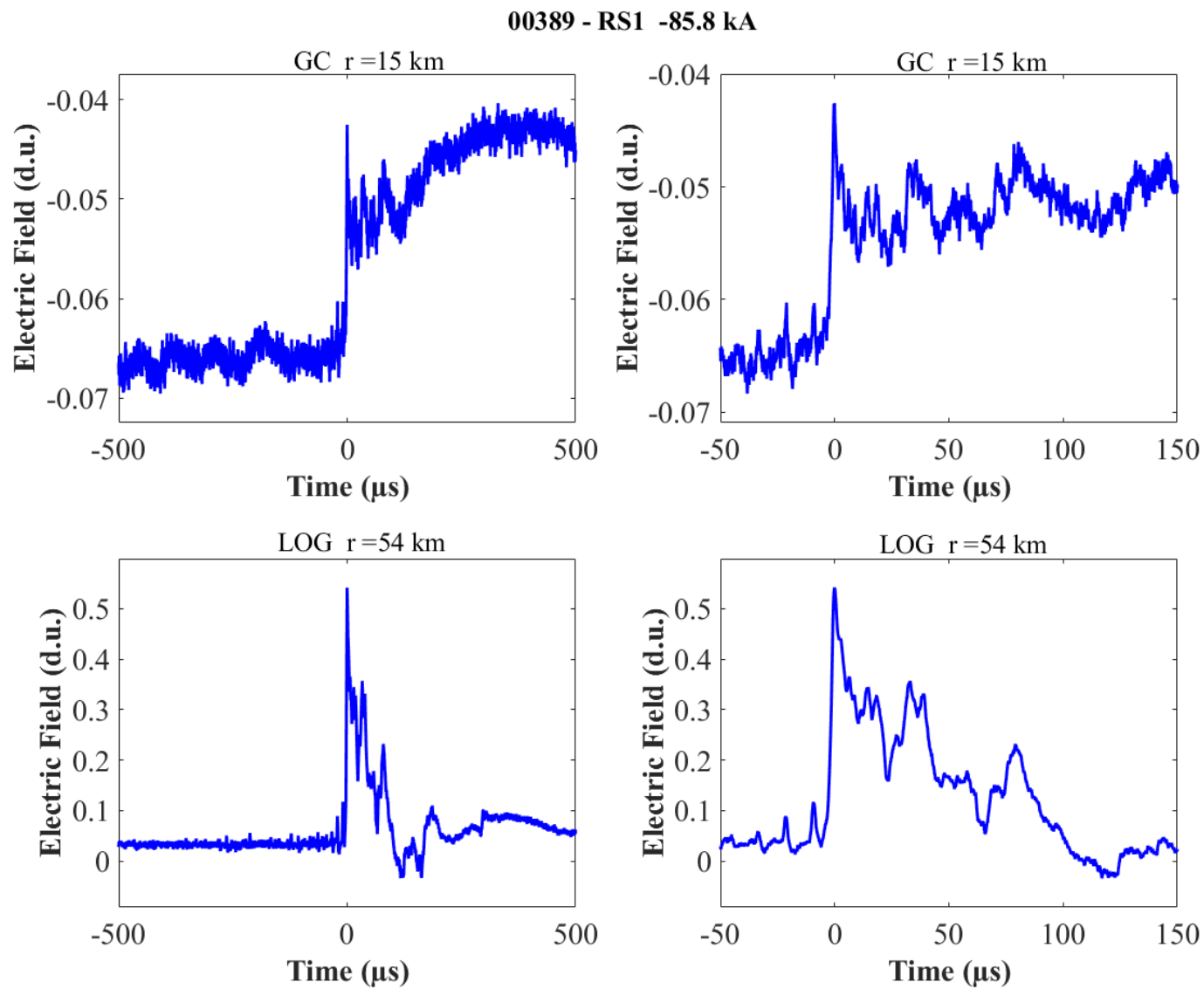


Figure B-2. Two-station electric field waveforms of RS1 of flash 00389.

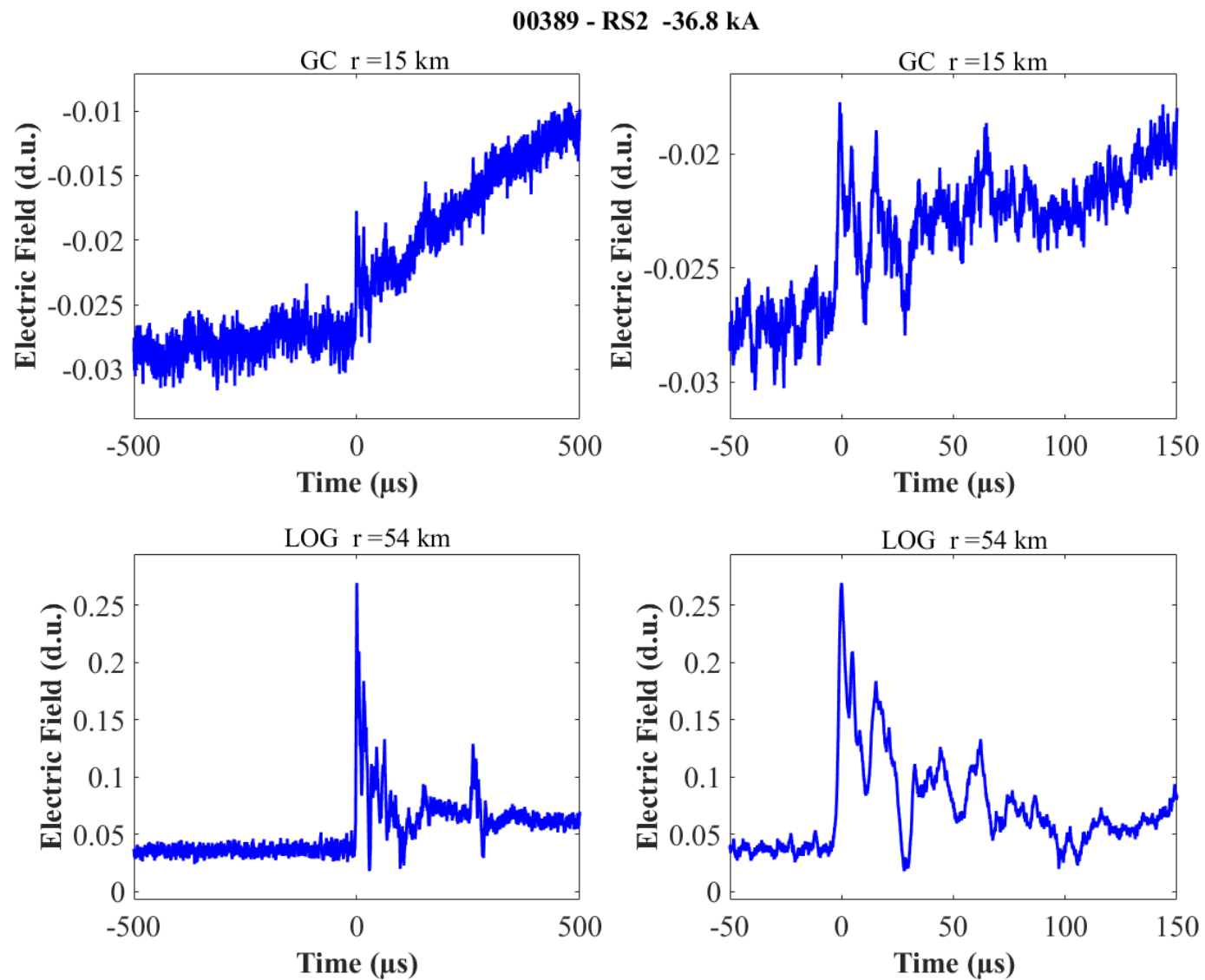


Figure B-3. Two-station electric field waveforms of RS2 of flash 00389.

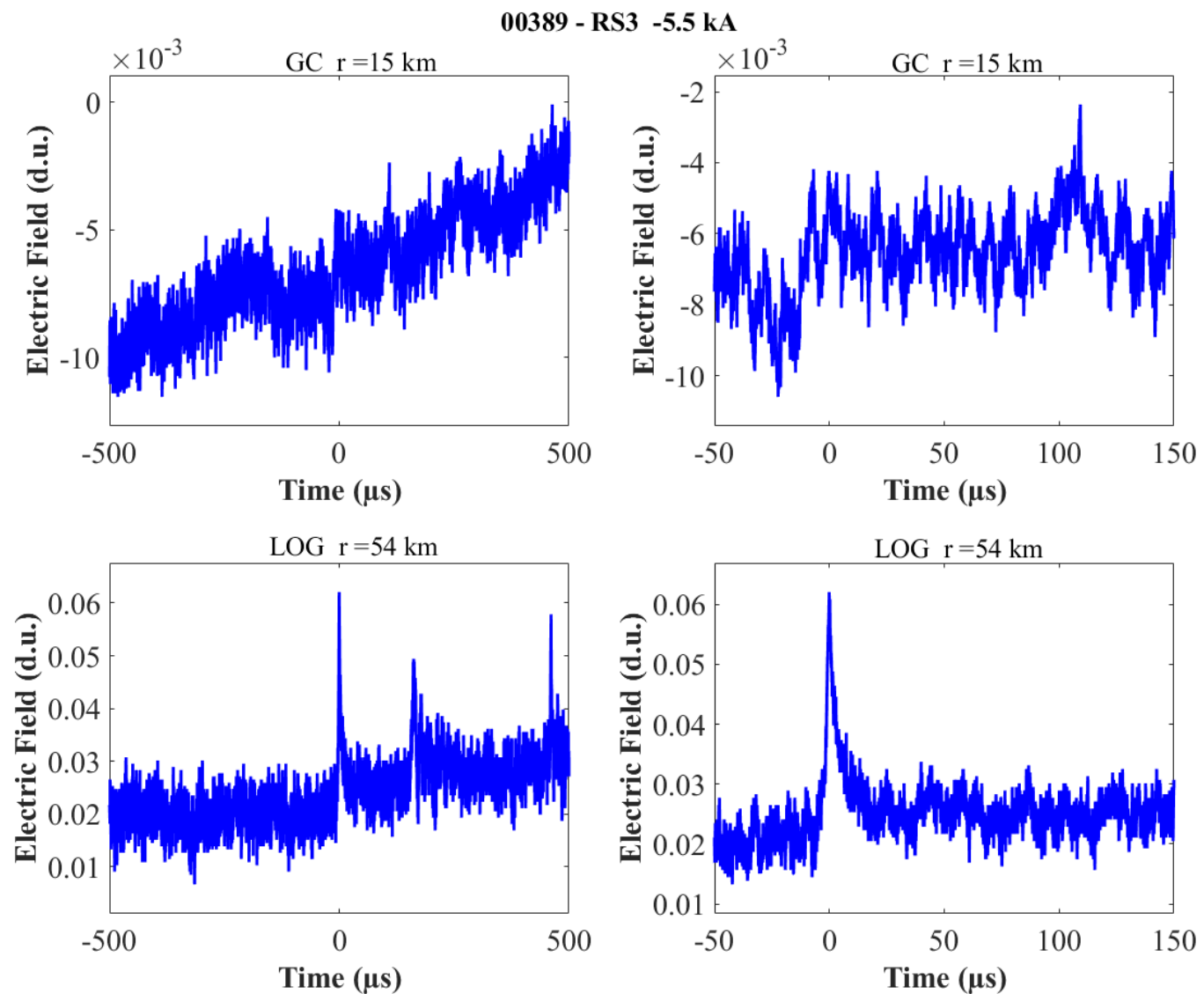


Figure B-4. Two-station electric field waveforms of RS3 of flash 00389.

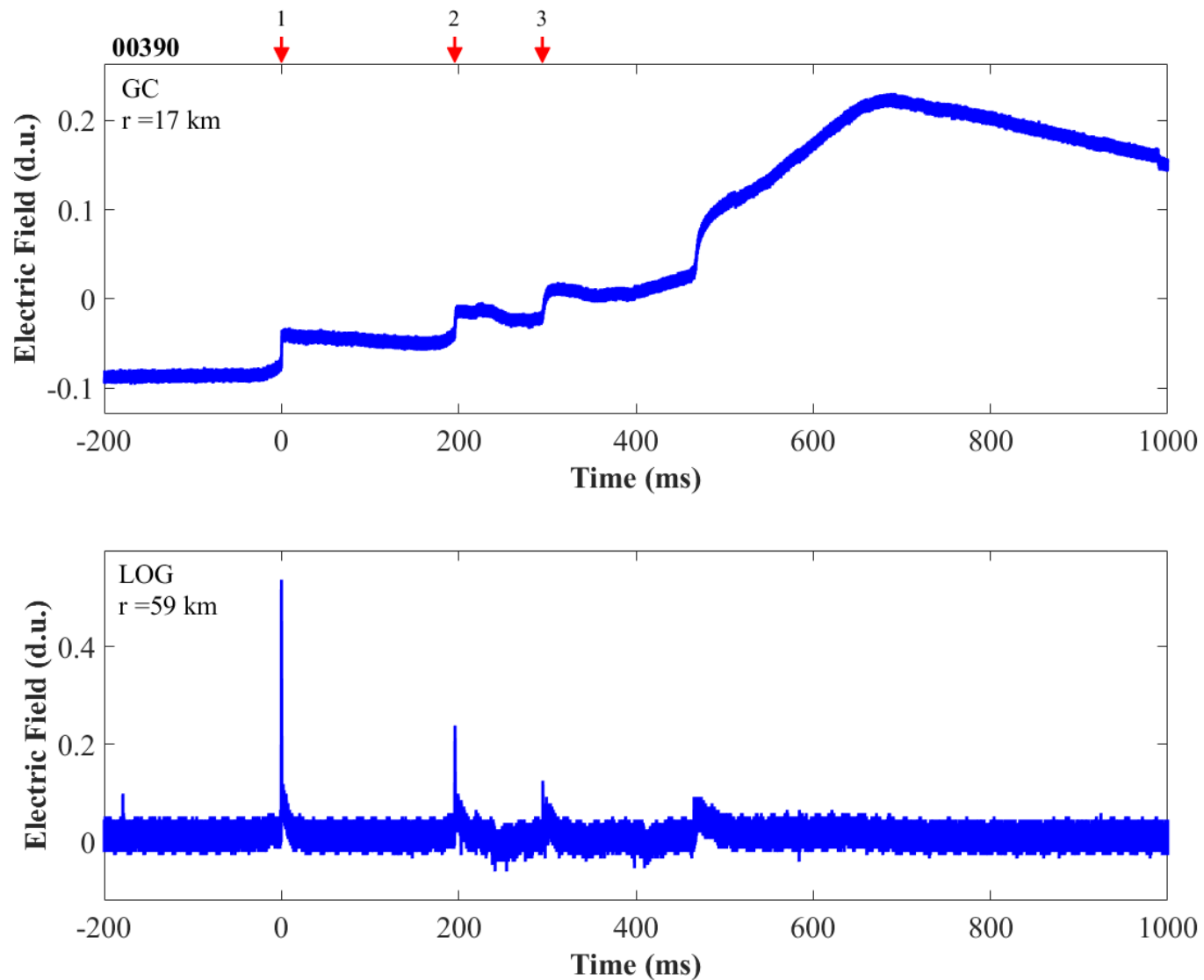


Figure B-5. Two-station electric field waveforms of flash 00390.

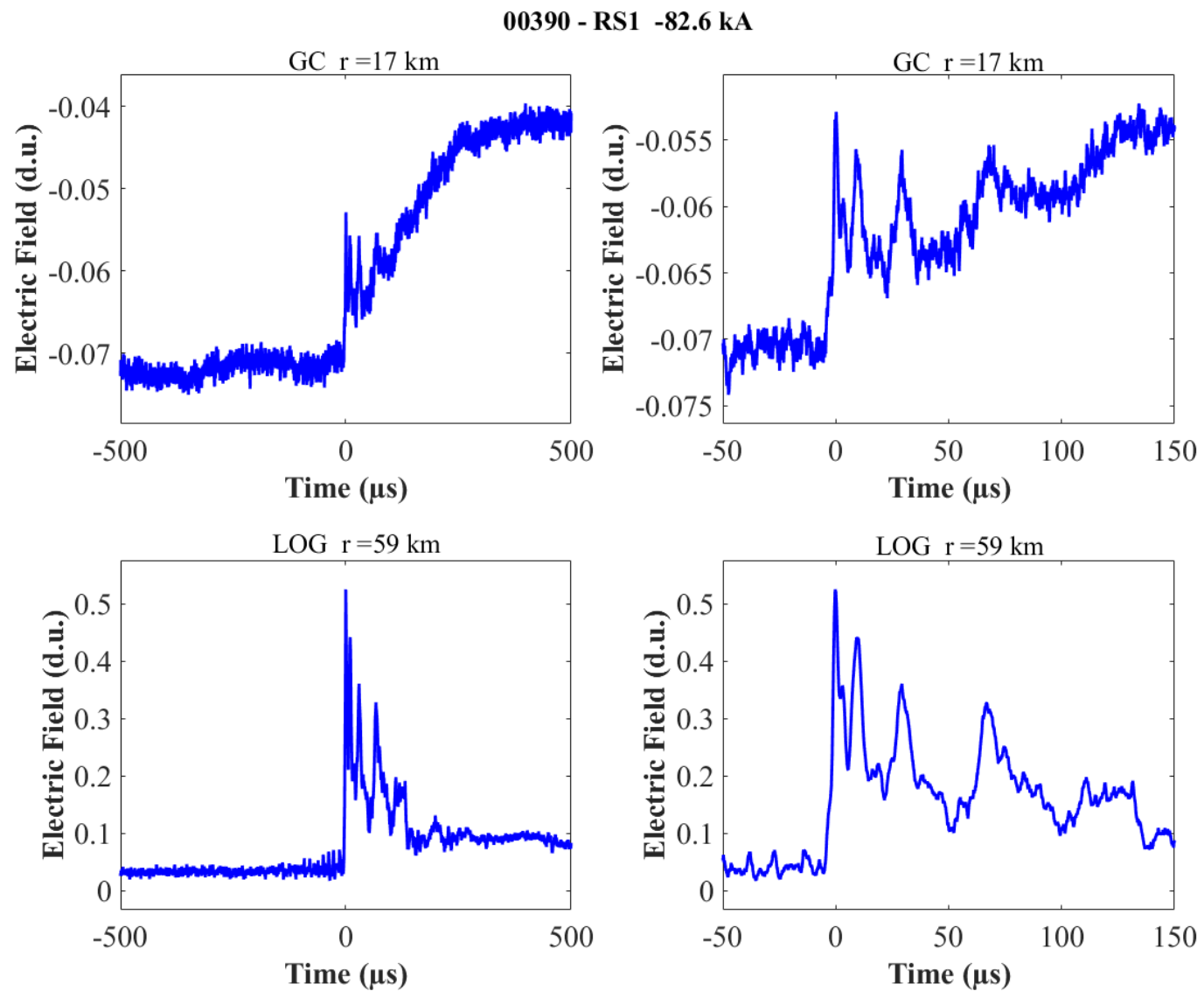


Figure B-6. Two-station electric field waveforms of RS1 of flash 00390.

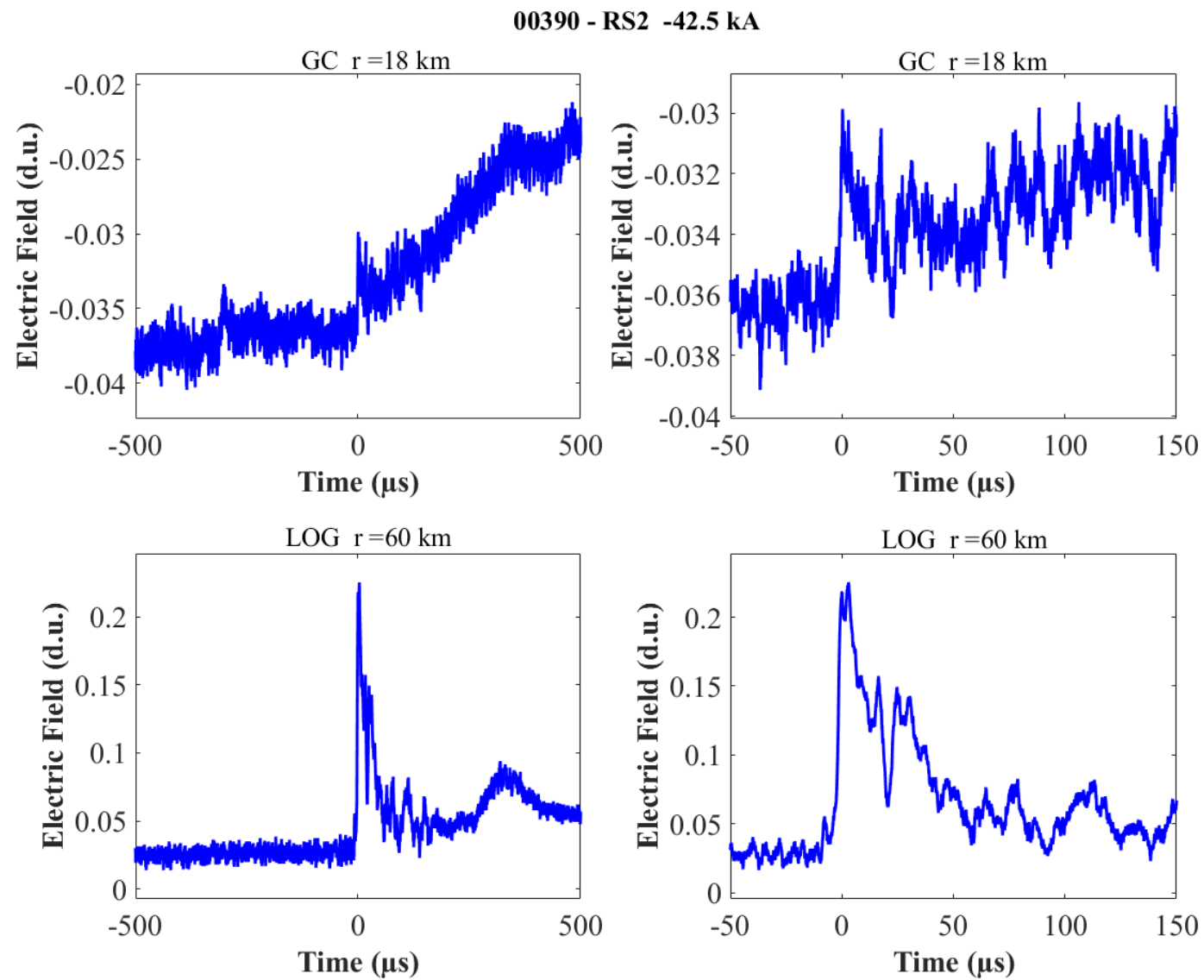


Figure B-7. Two-station electric field waveforms of RS2 of flash 00390.

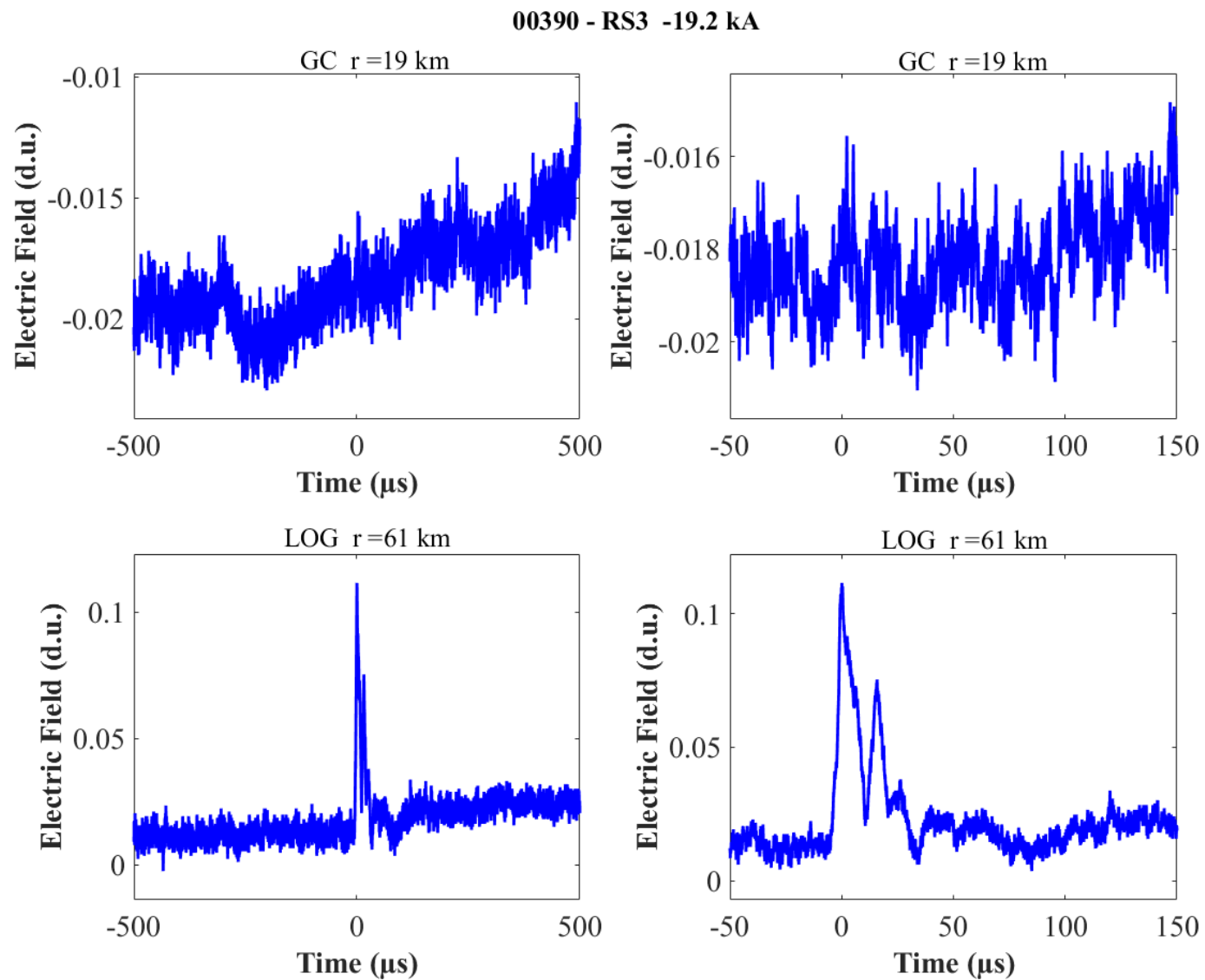


Figure B-8. Two-station electric field waveforms of RS3 of flash 00390.

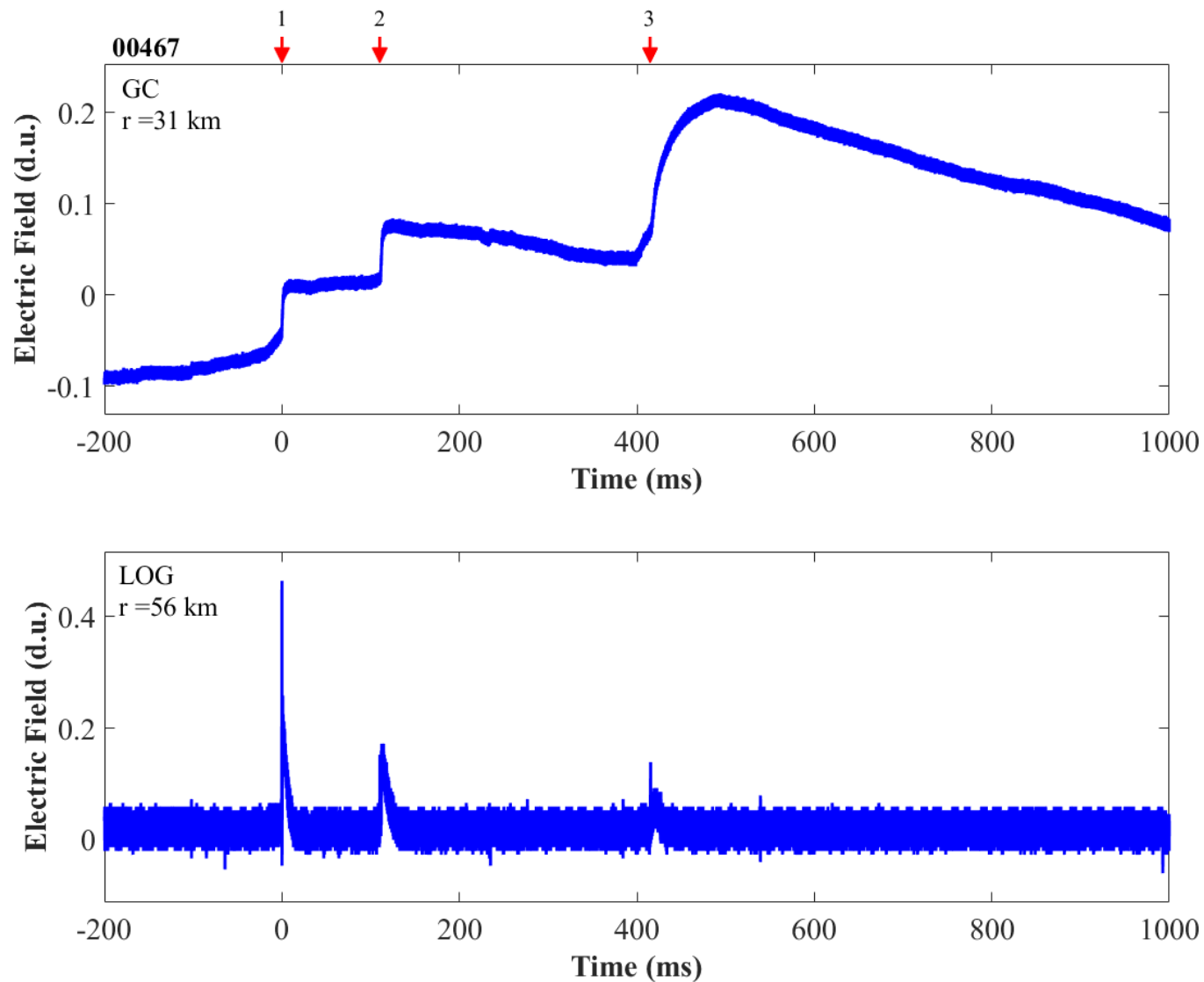


Figure B-9. Two-station electric field waveforms of flash 00467.

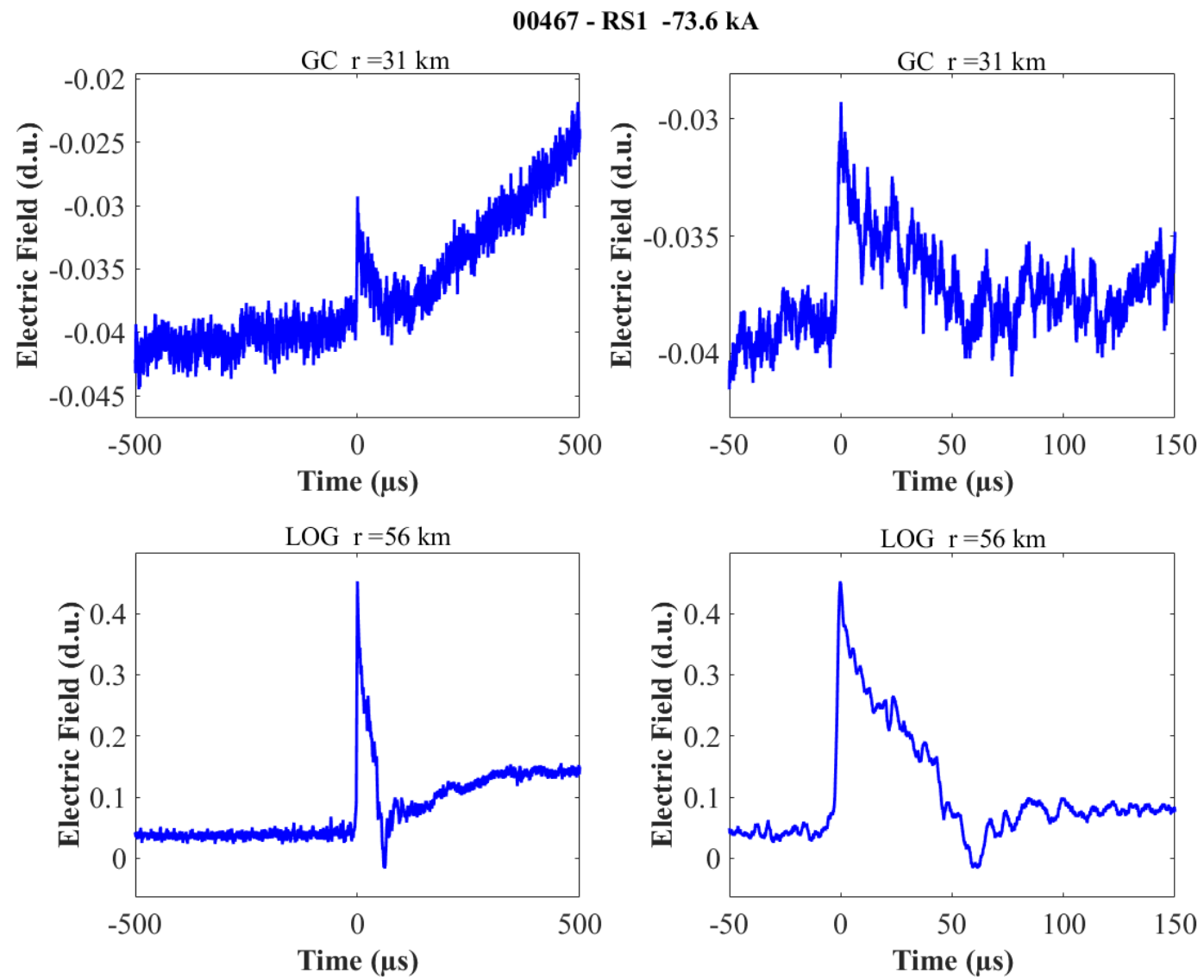
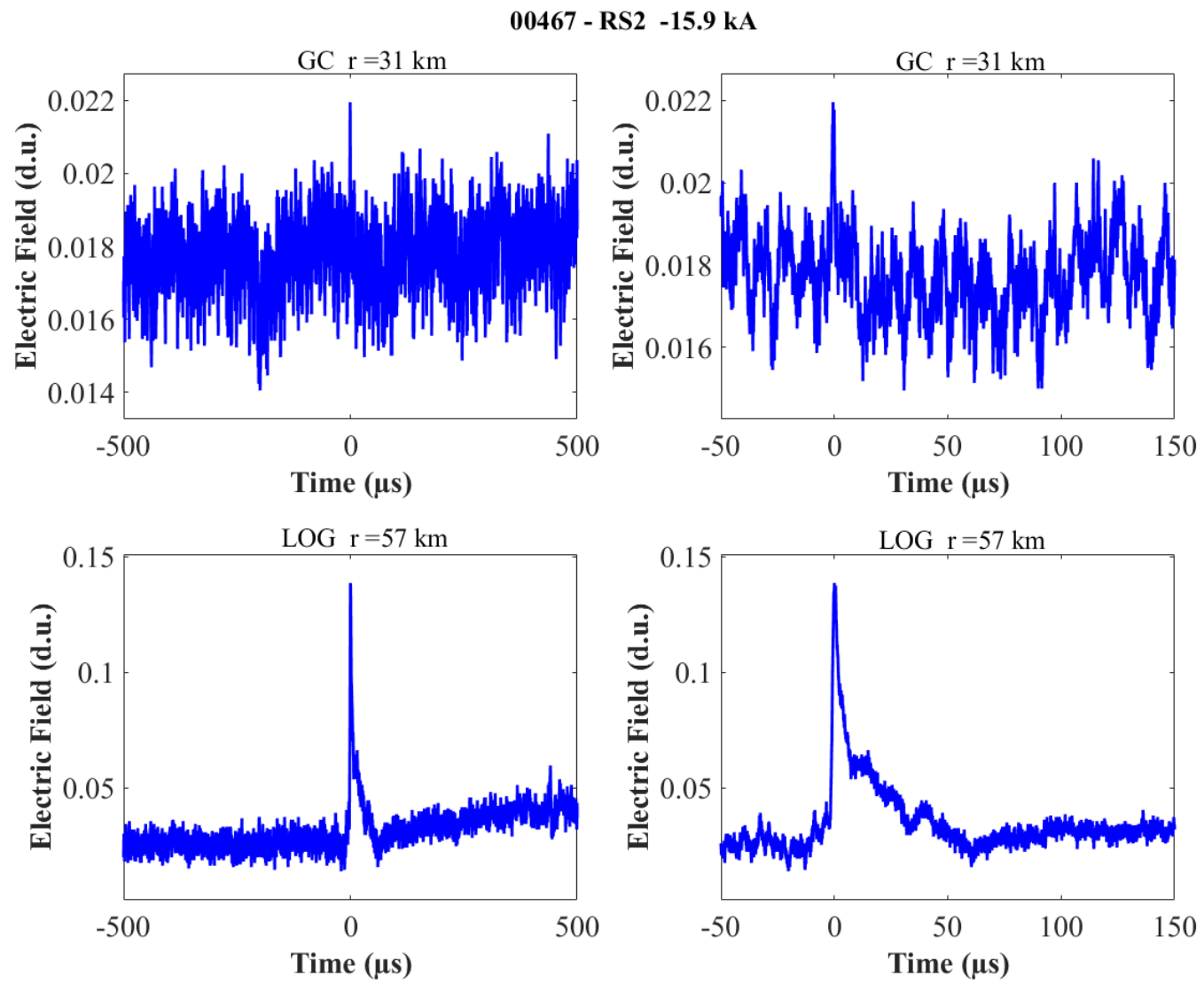


Figure B-10. Two-station electric field waveforms of the RS1 of flash 00467.



Two-station electric field waveforms of the RS2 of flash 00467.

Figure B-11.

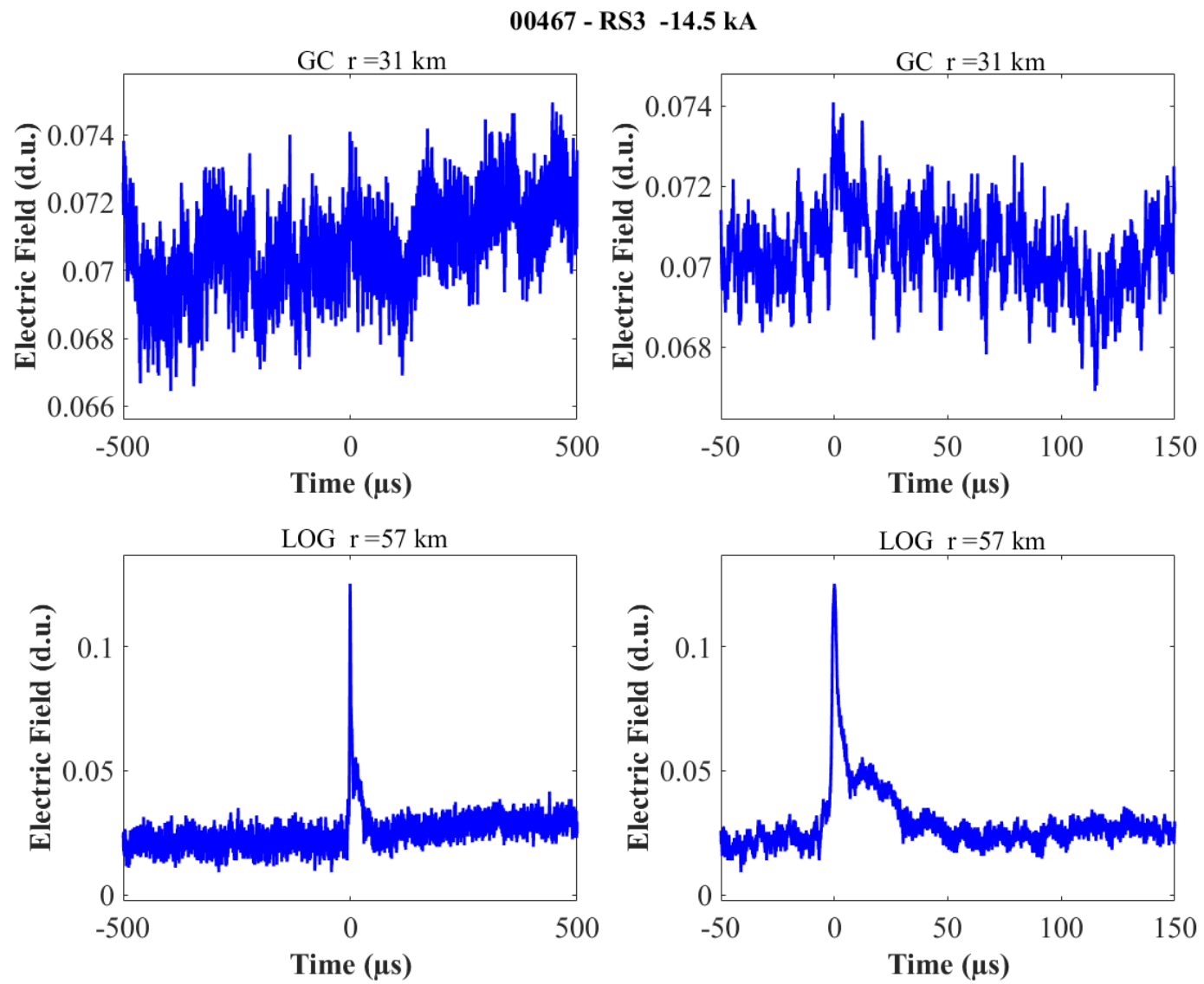


Figure B-12. Two-station electric field waveforms of the RS3 of flash 00467.

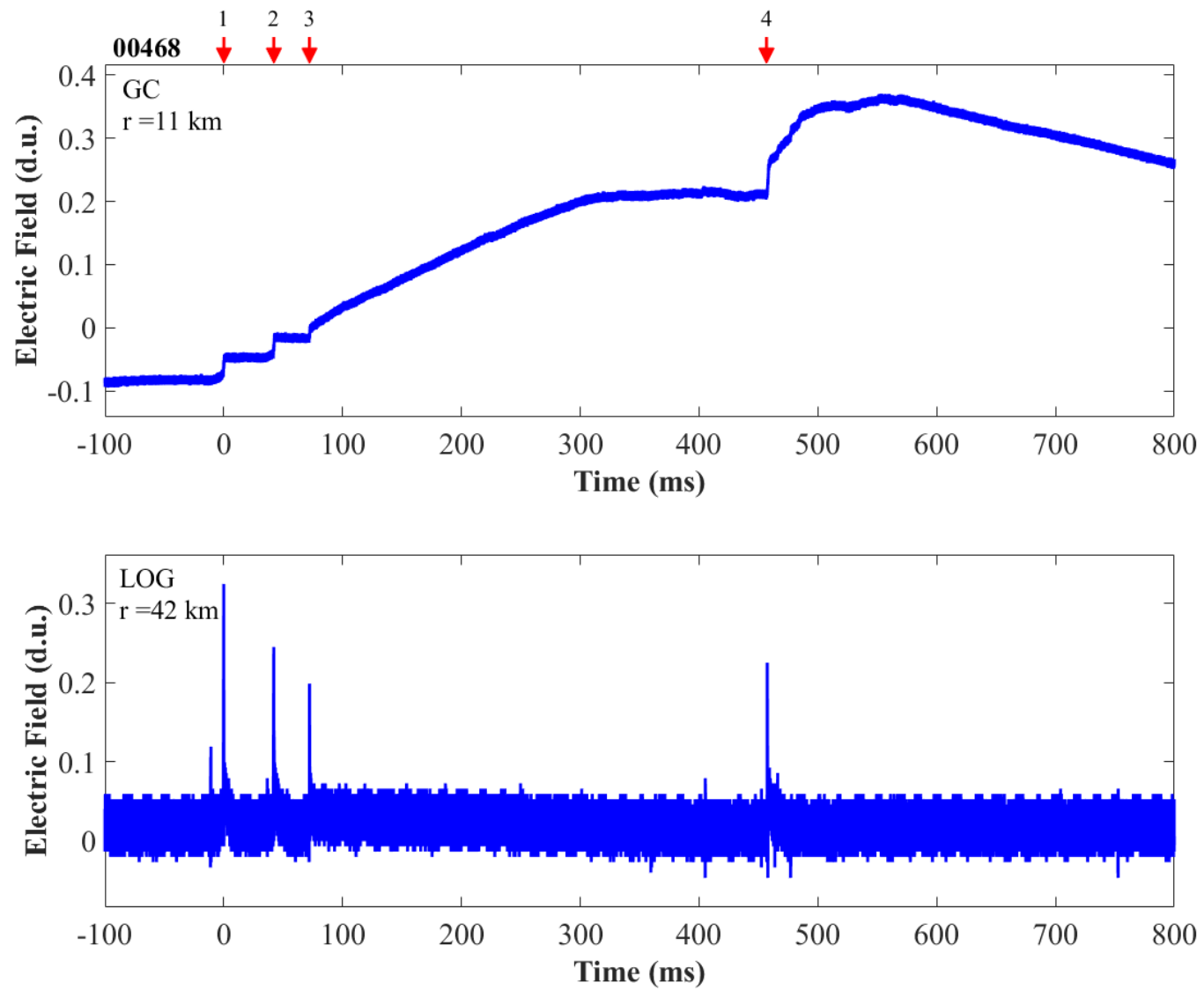


Figure B-13. Two-station electric field waveforms of flash 00468.

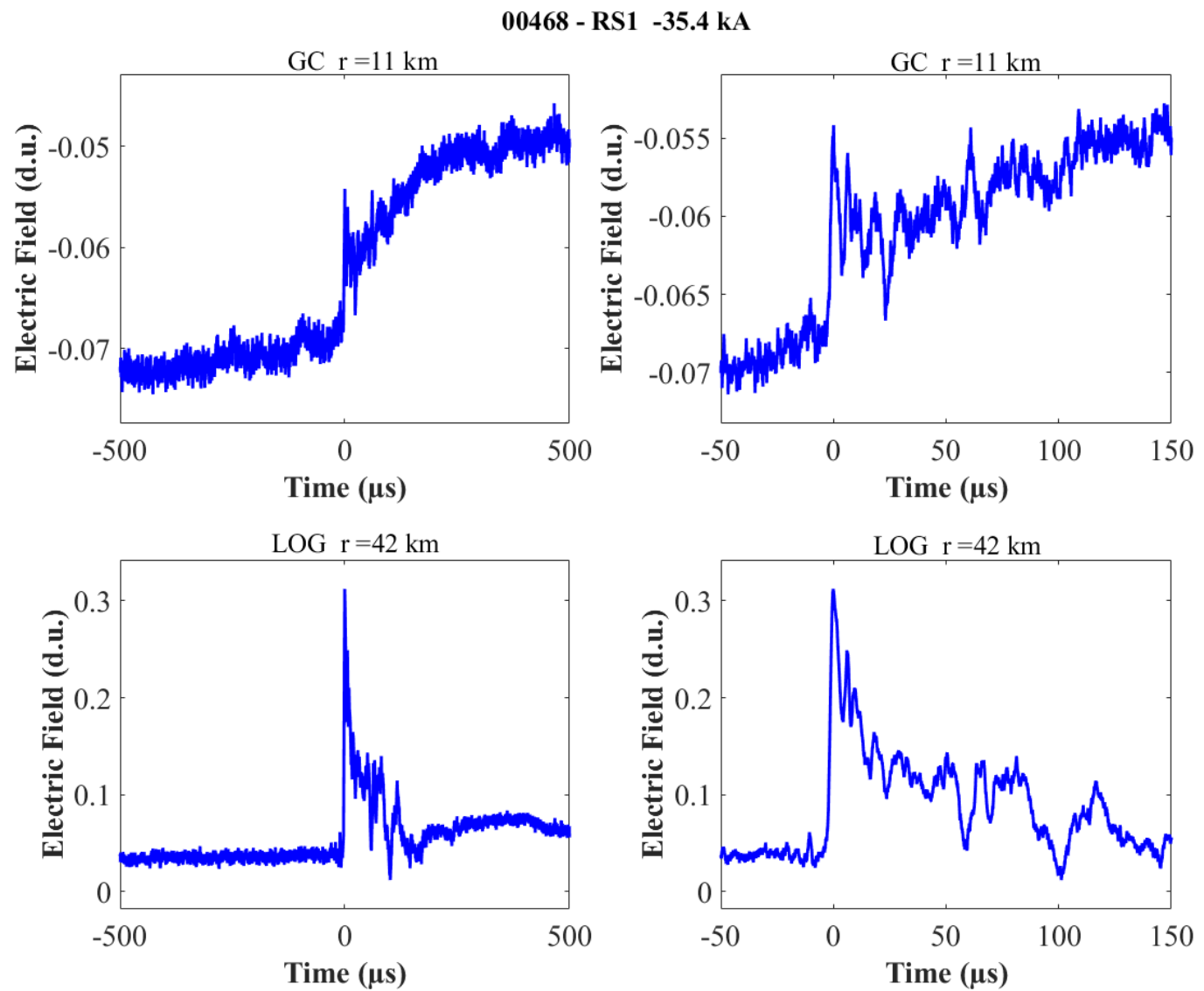


Figure B-14. Two-station electric field waveforms of the RS1 of flash 00468.

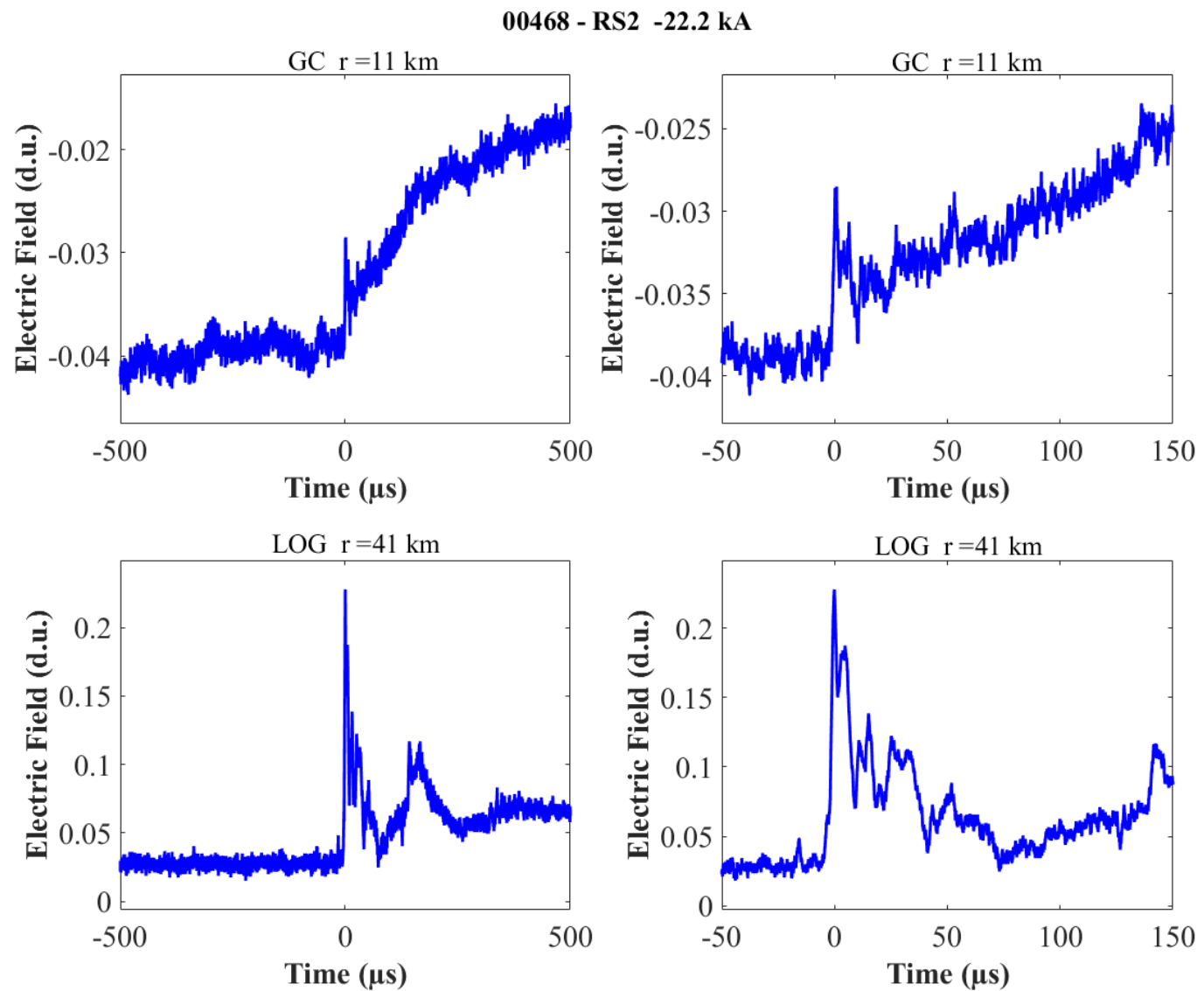


Figure B-15. Two-station electric field waveforms of the RS2 of flash 00468.

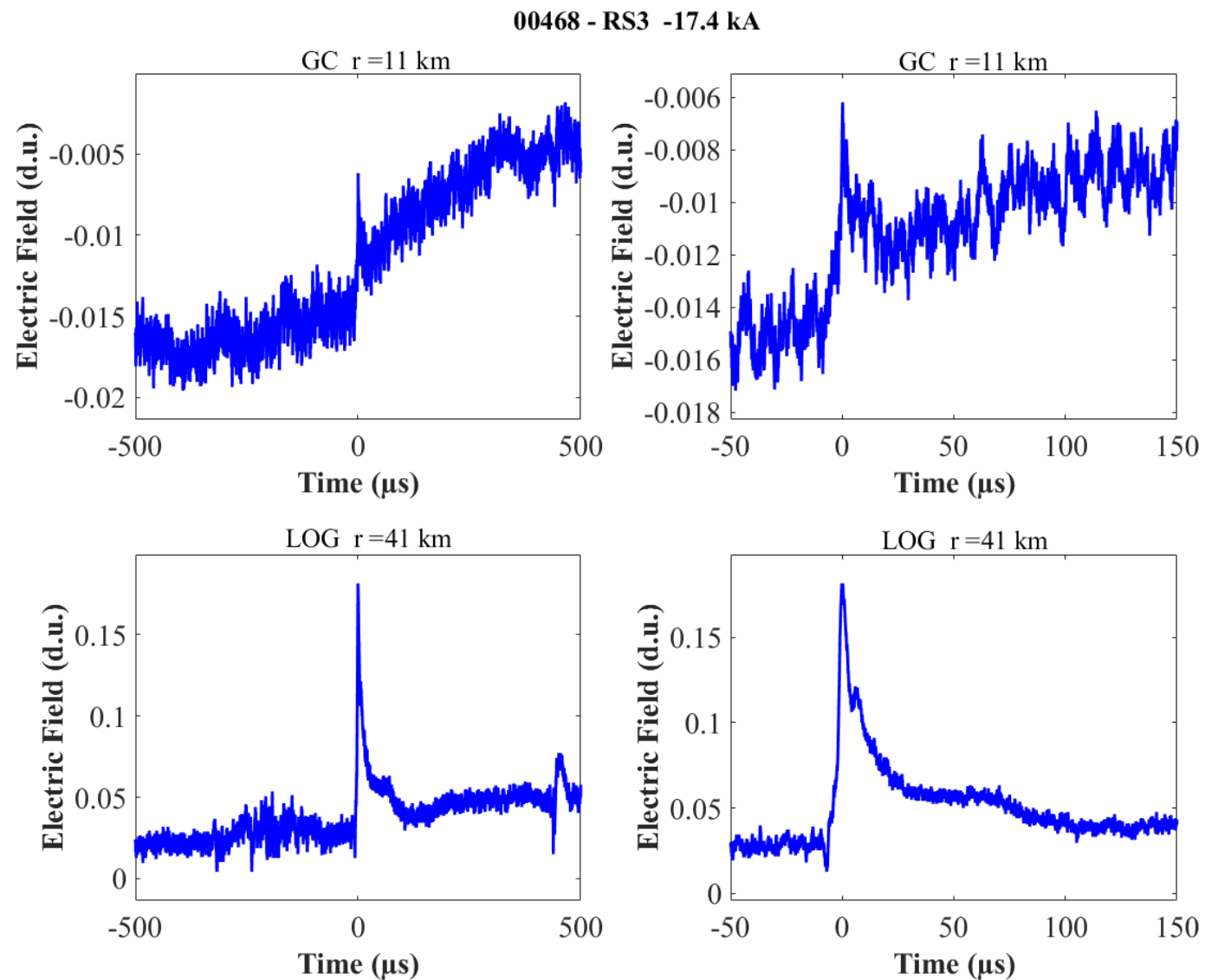


Figure B-16. Two-station electric field waveforms of the RS3 of flash 00468.

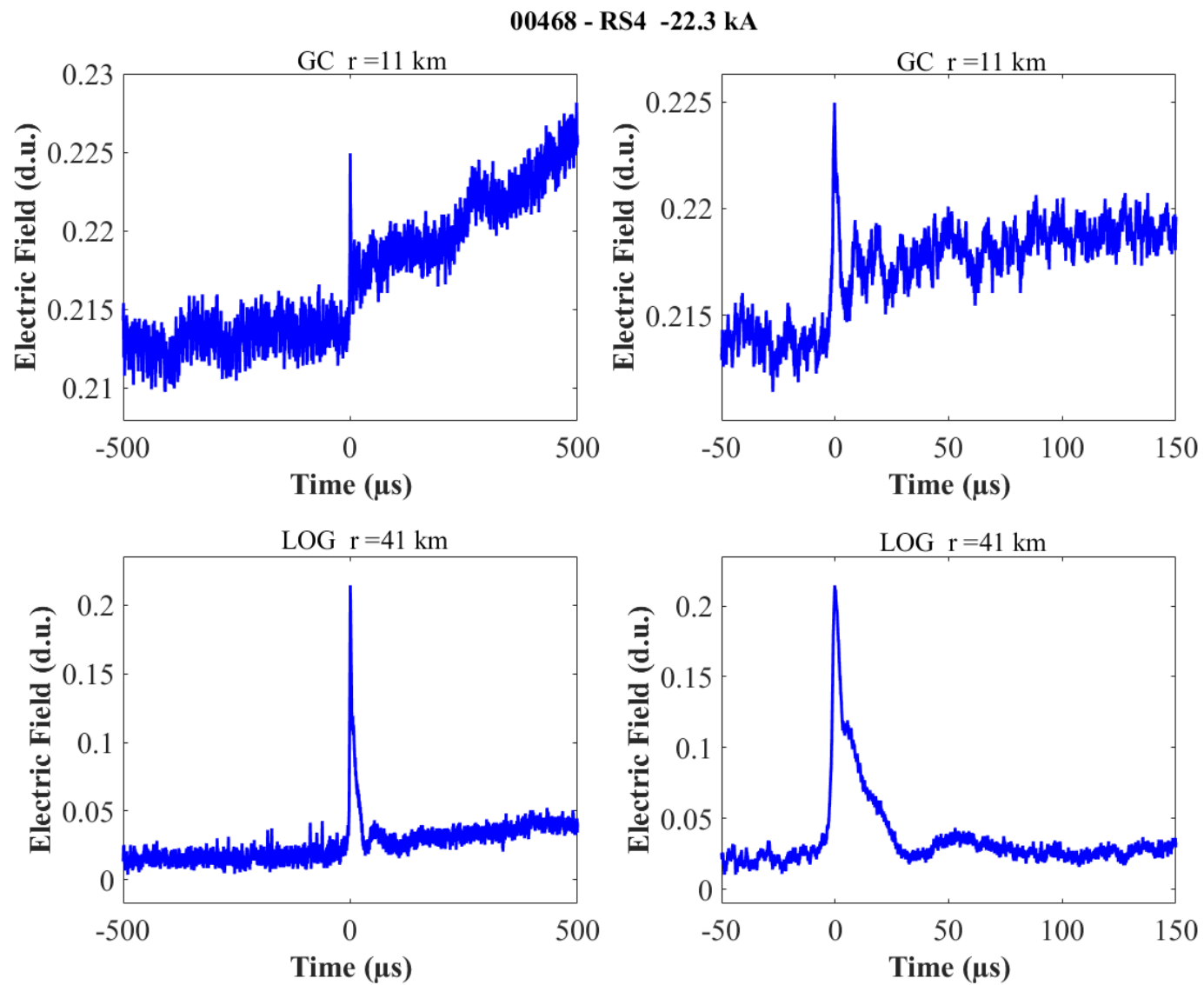


Figure B-17. Two-station electric field waveforms of the RS4 of flash 00468.

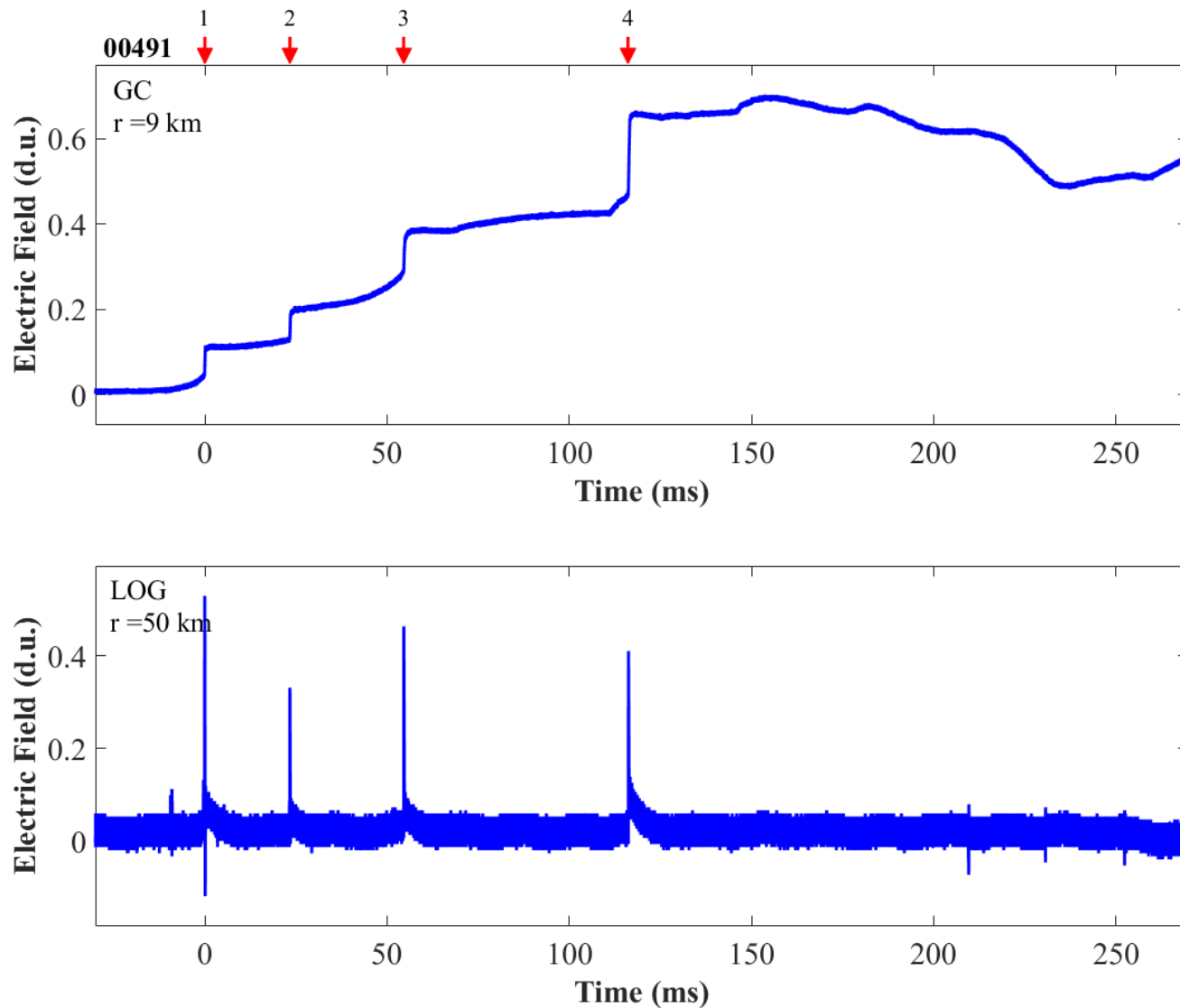


Figure B-18. Two-station electric field waveforms of flash 00491.

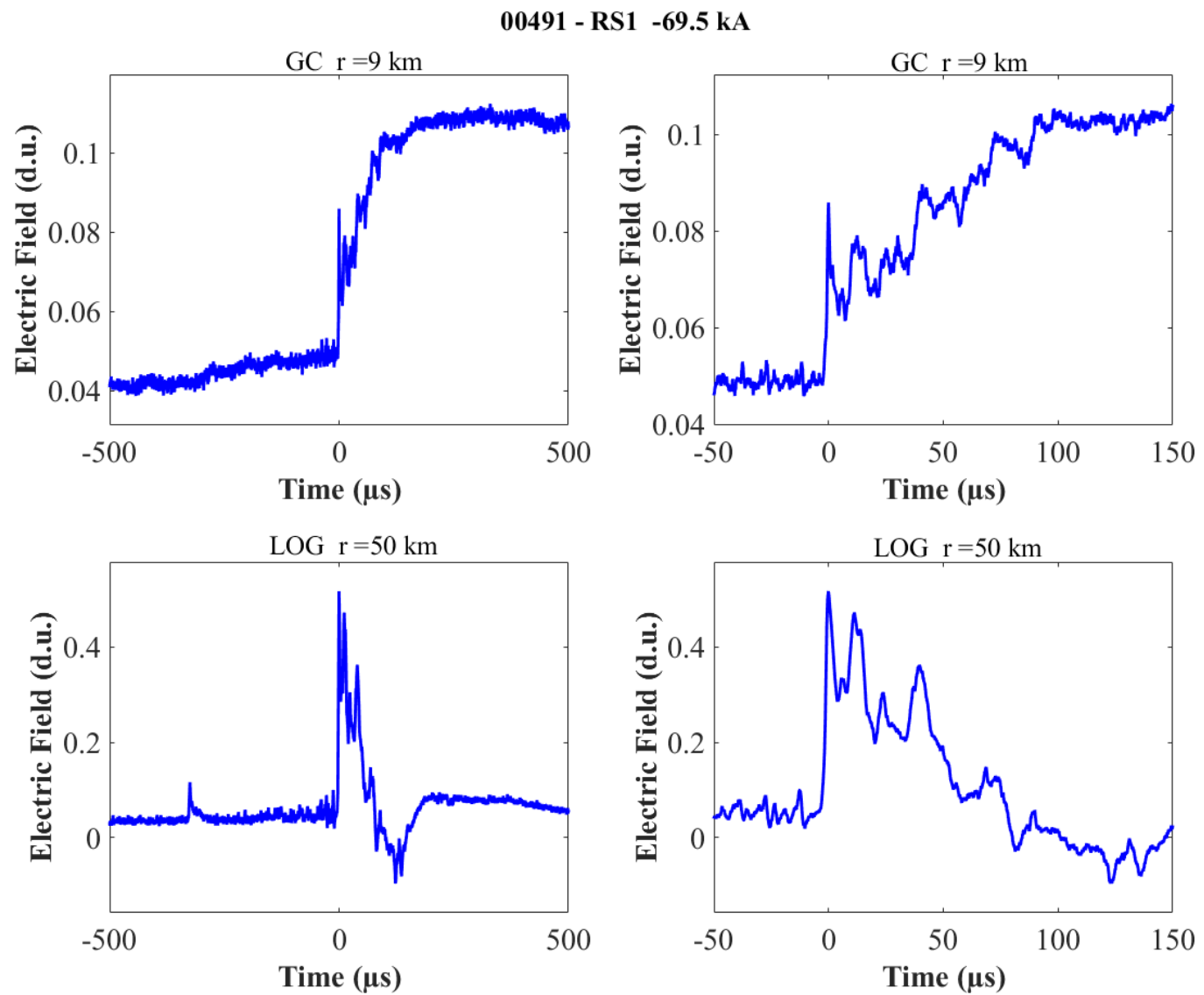


Figure B-19. Two-station electric field waveforms of the RS1 of flash 00491.

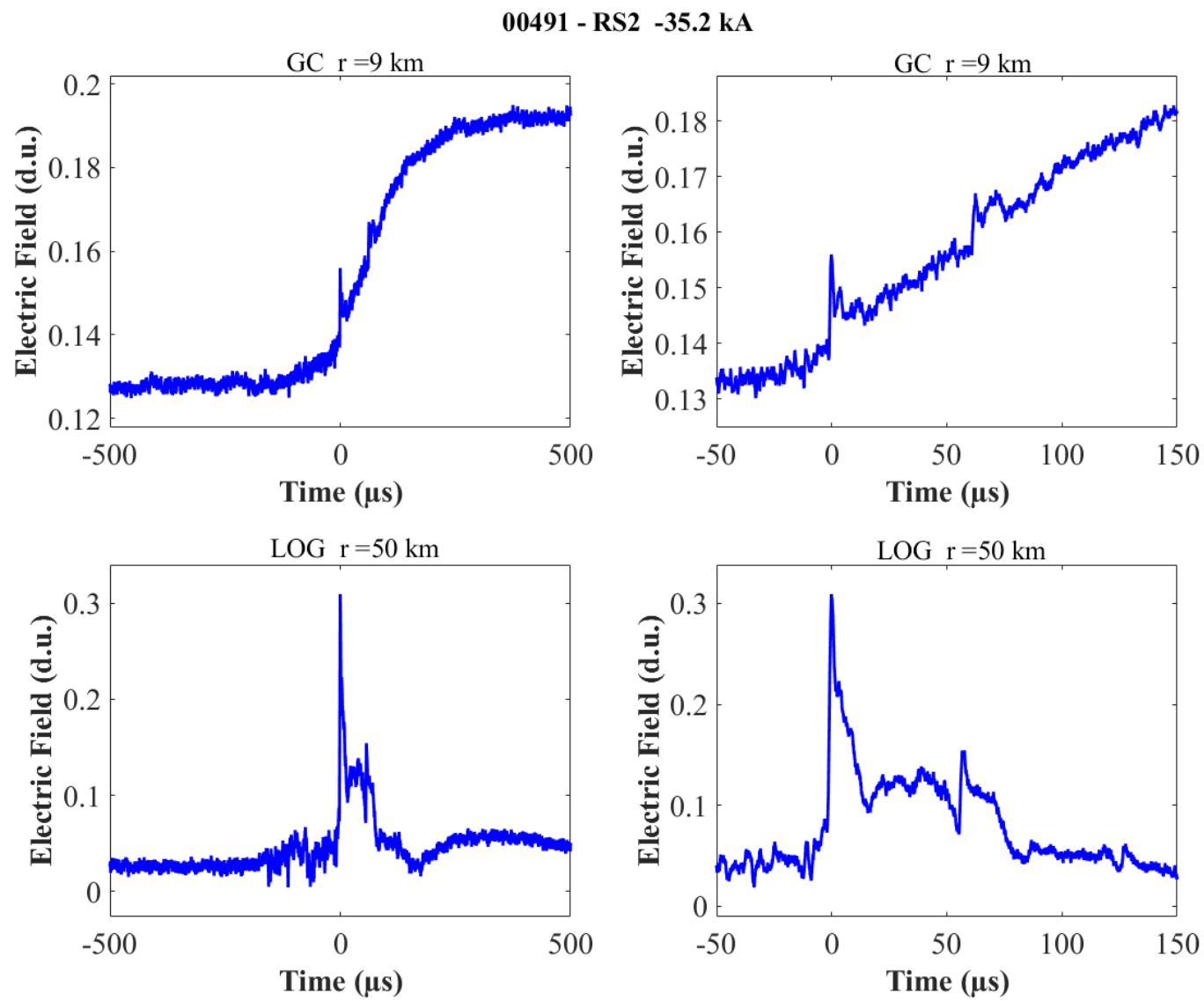


Figure B-20. Two-station electric field waveforms of the RS2 of flash 00491.

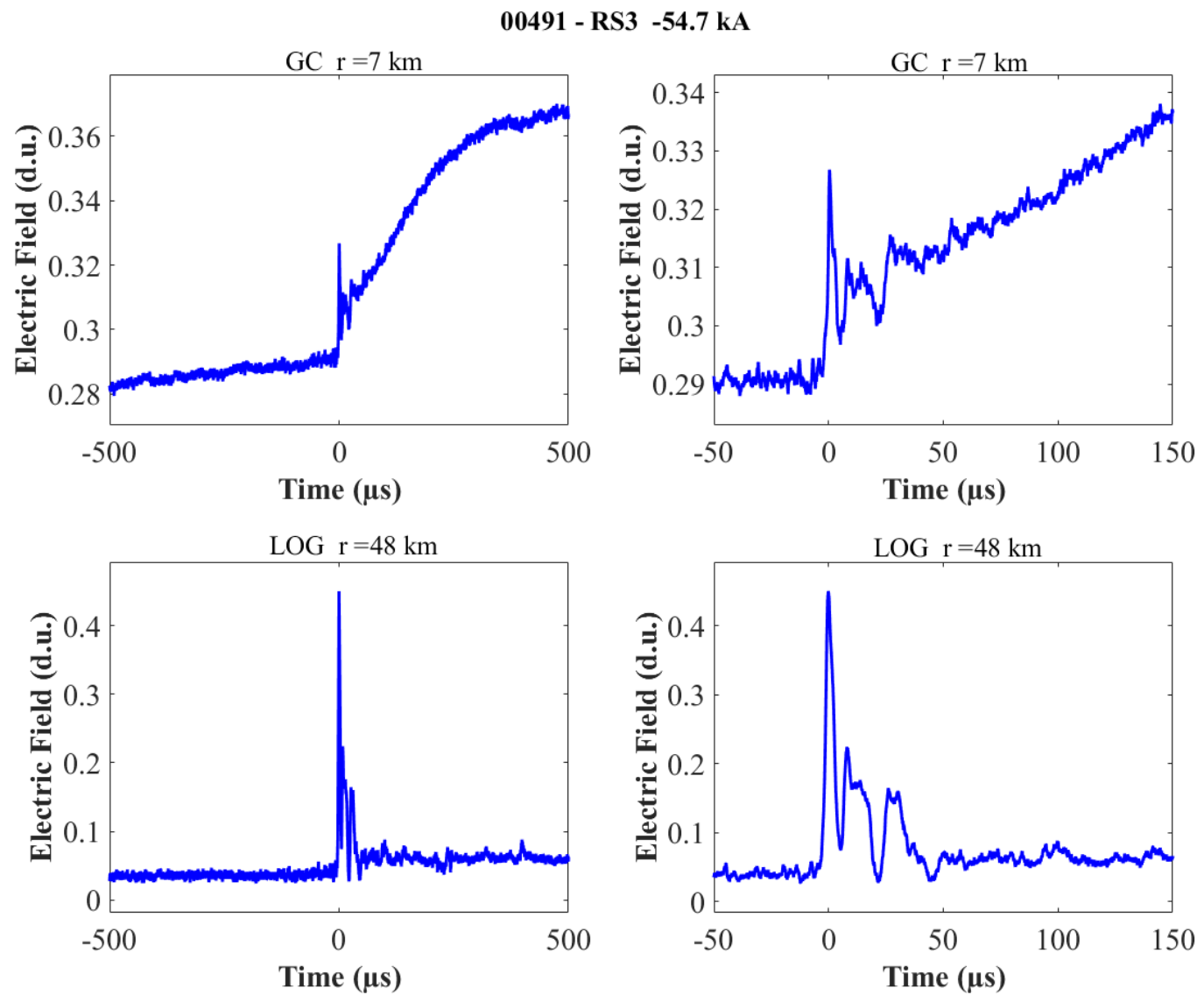


Figure B-21. Two-station electric field waveforms of the RS3 of flash 00491.

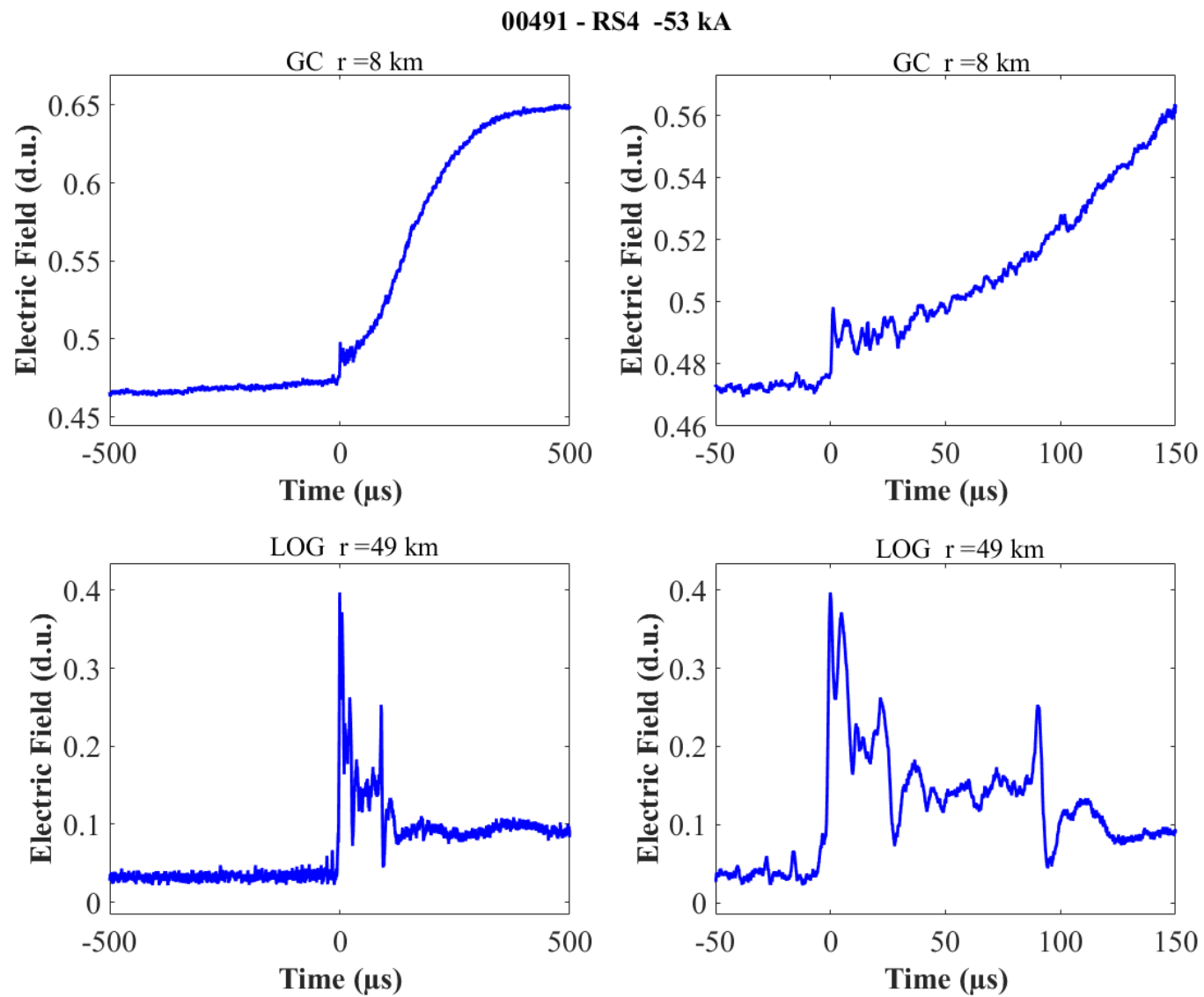


Figure B-22. Two-station electric field waveforms of the RS4 of flash 00491.

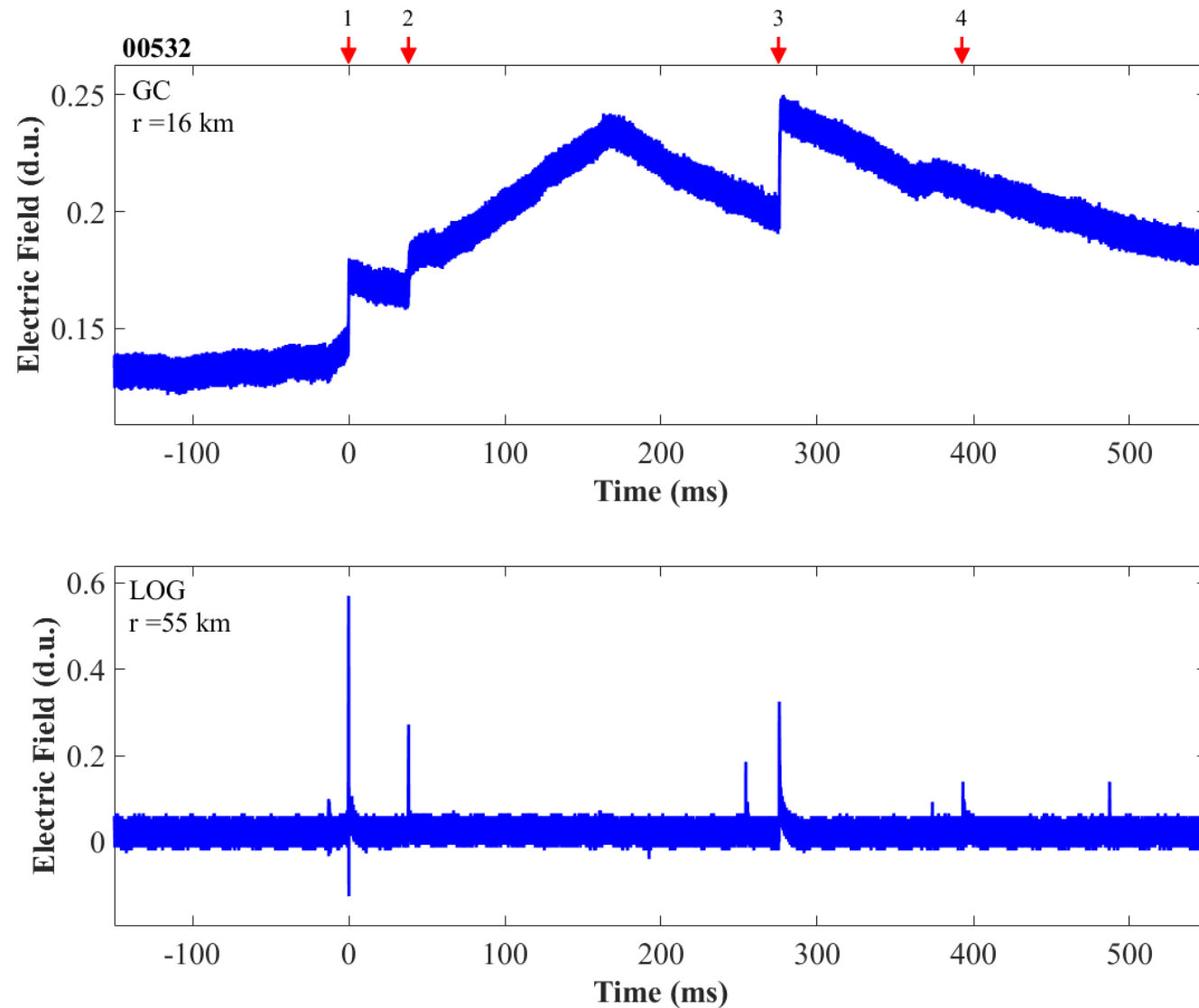


Figure B-23. Two-station electric field waveforms of flash 00532.

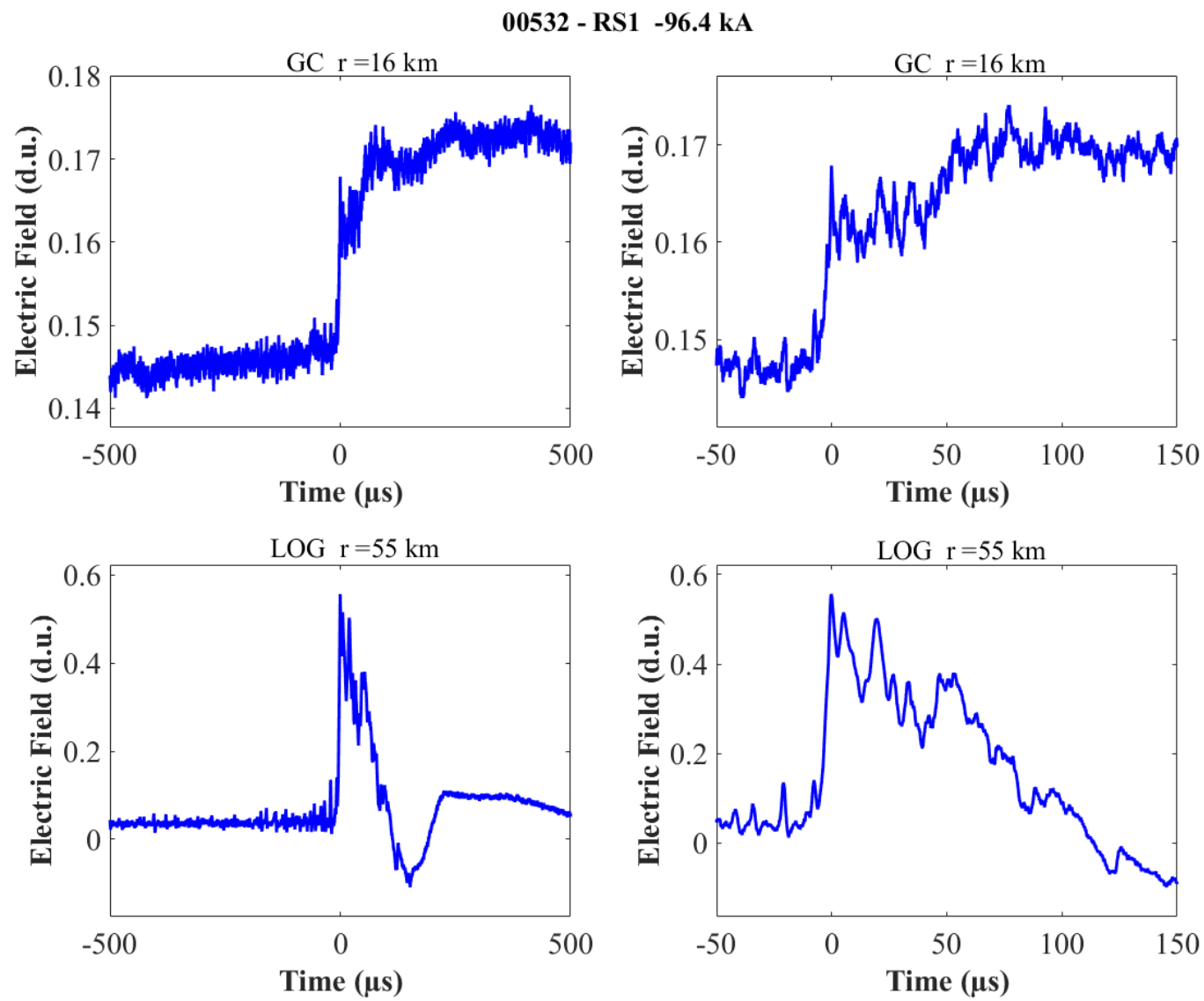


Figure B-24. Two-station electric field waveforms of the RS1 of flash 00532.

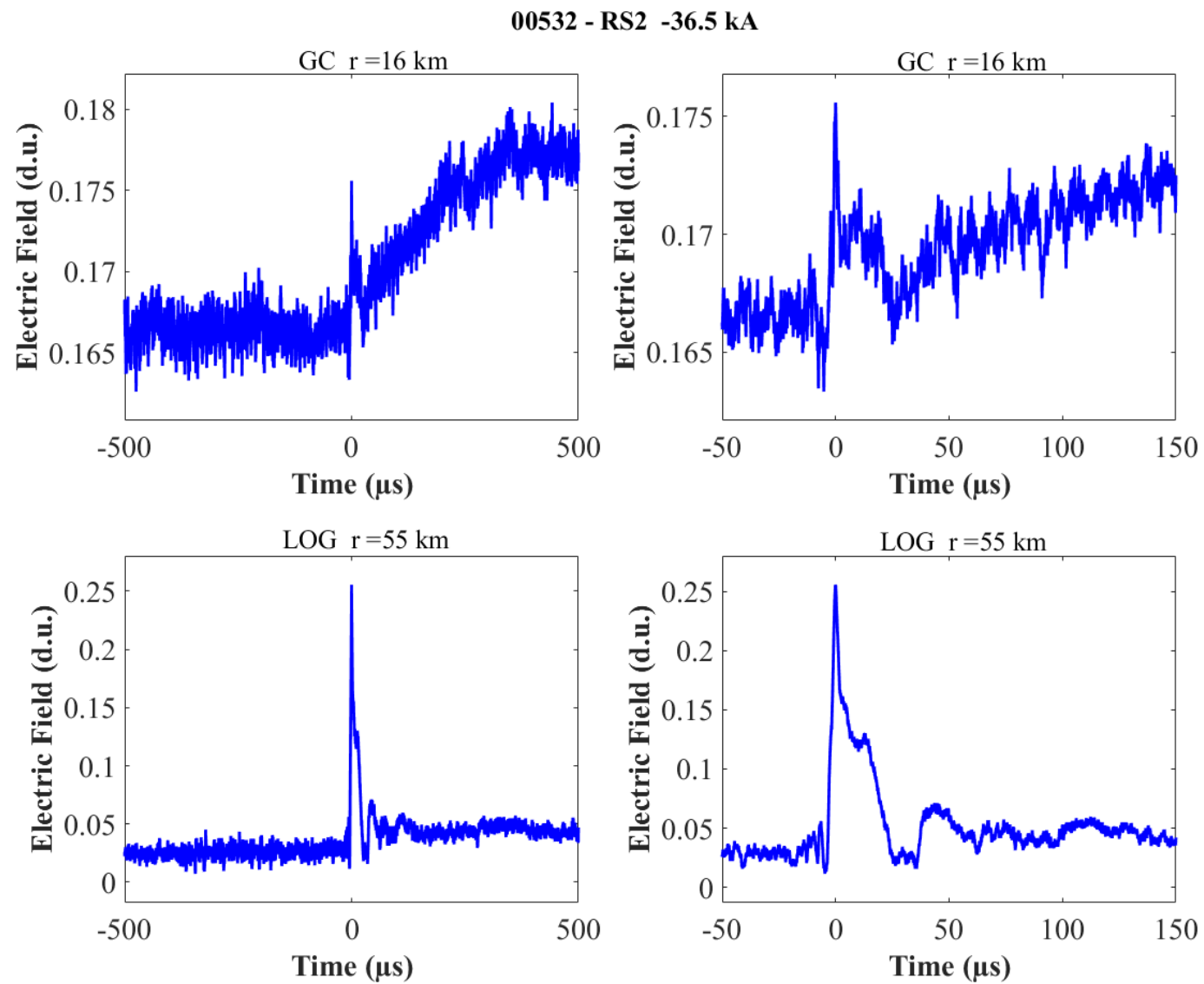


Figure B-25. Two-station electric field waveforms of the RS2 of flash 00532.

00532 - RS3 -44.2 kA

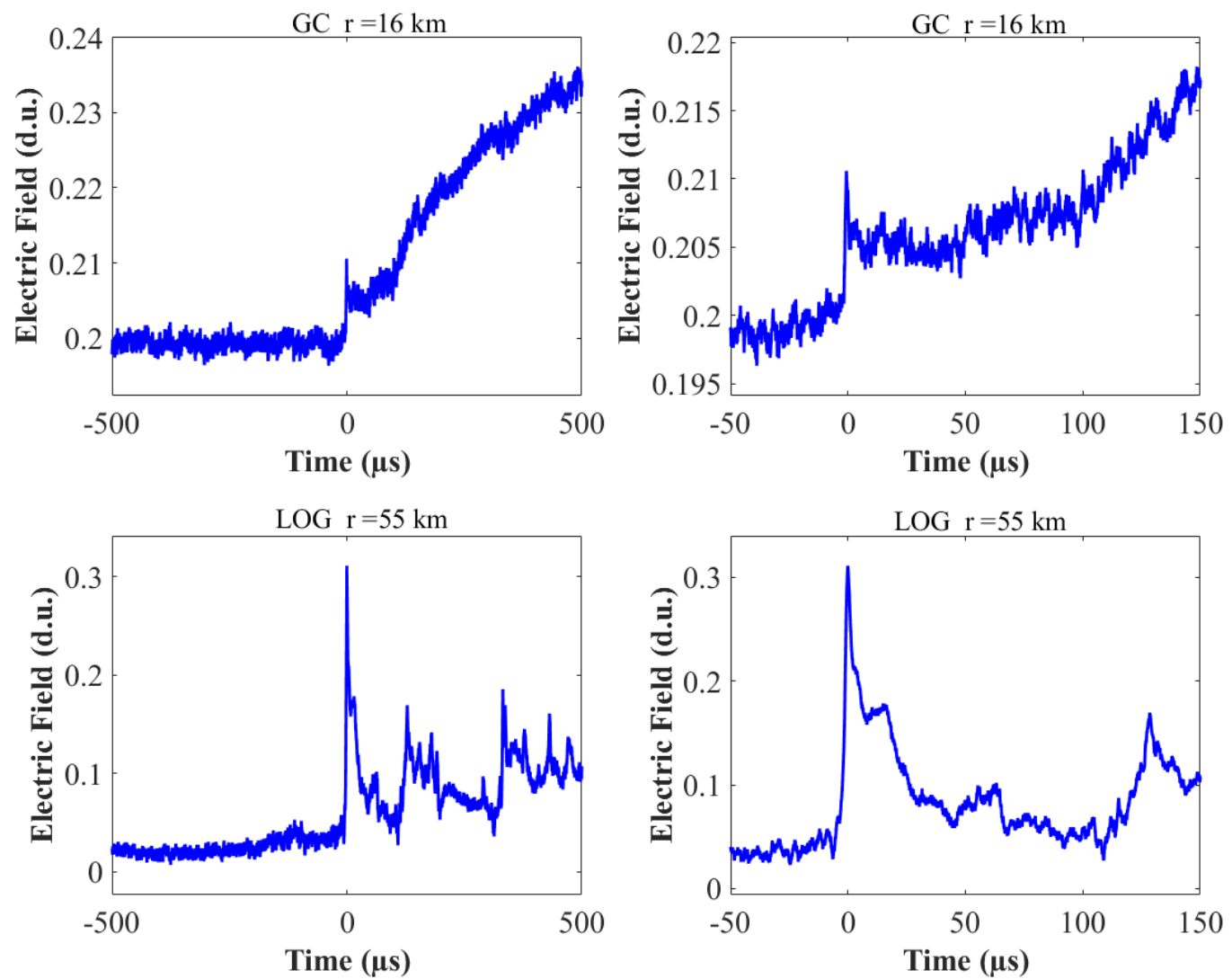


Figure B-26. Two-station electric field waveforms of the RS3 of flash 00532.

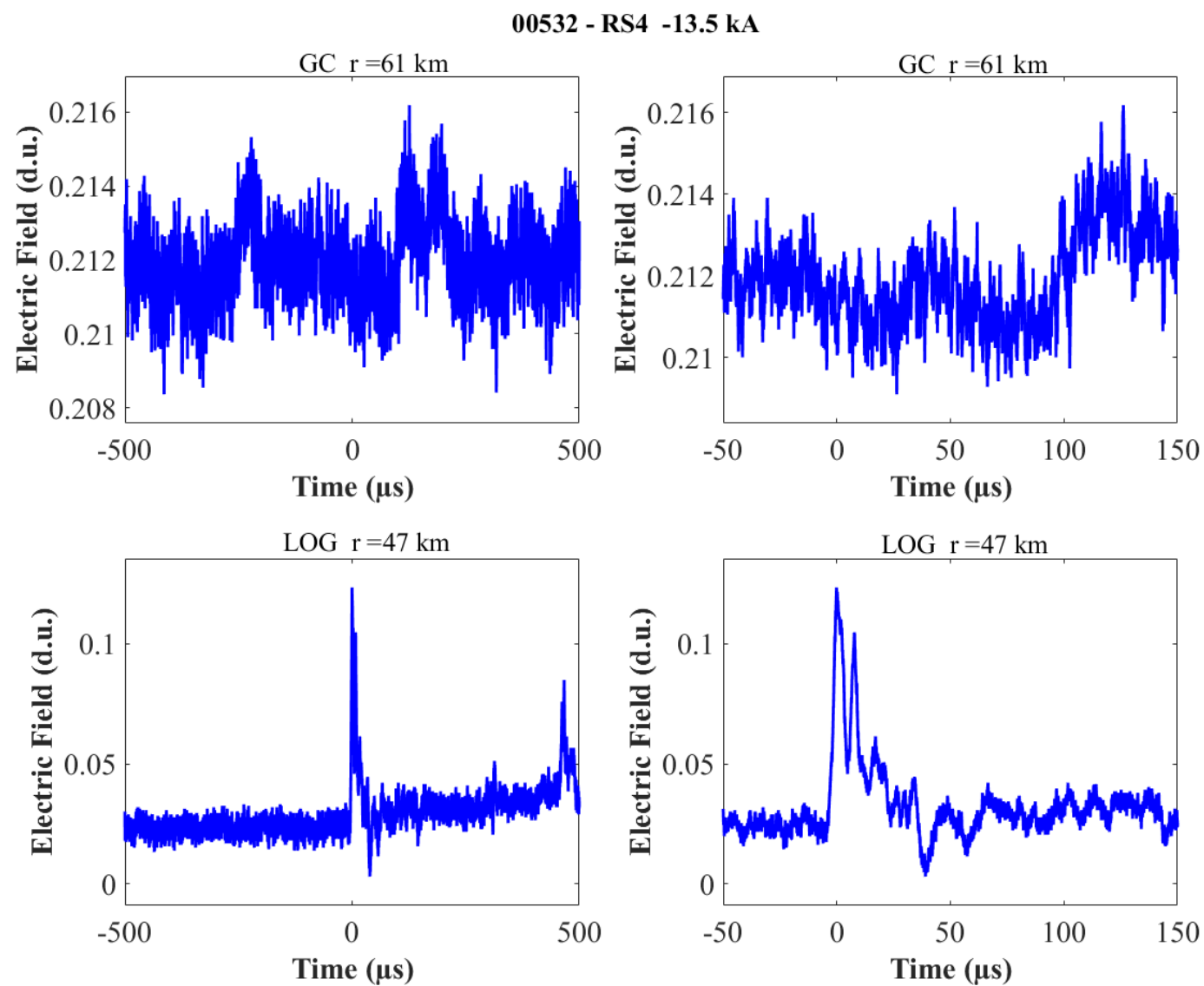


Figure B-27. Two-station electric field waveforms of the RS4 of flash 00532.

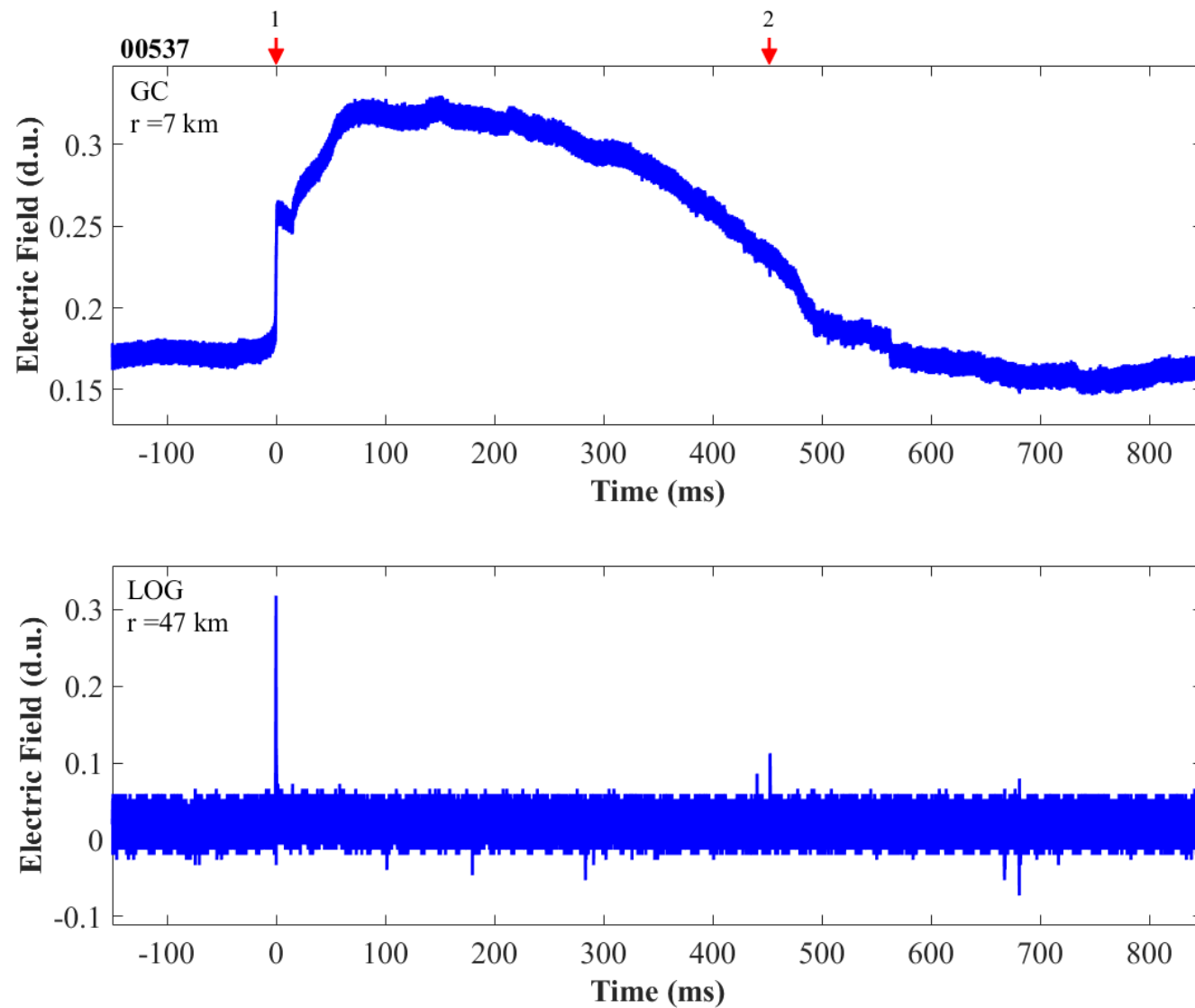


Figure B-28. Two-station electric field waveforms of flash 00537.

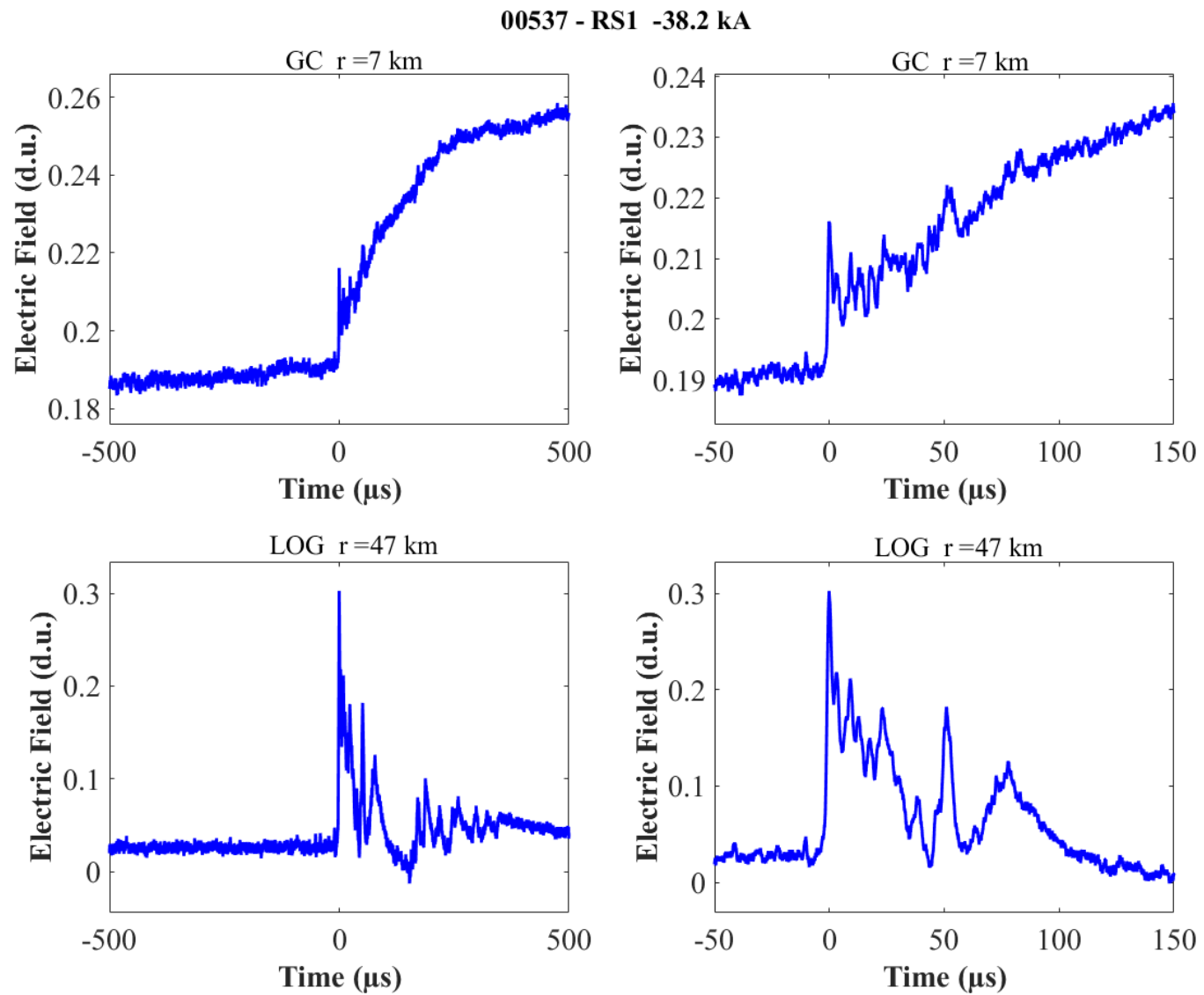


Figure B-29. Two-station electric field waveforms of the RS1 of flash 00537.

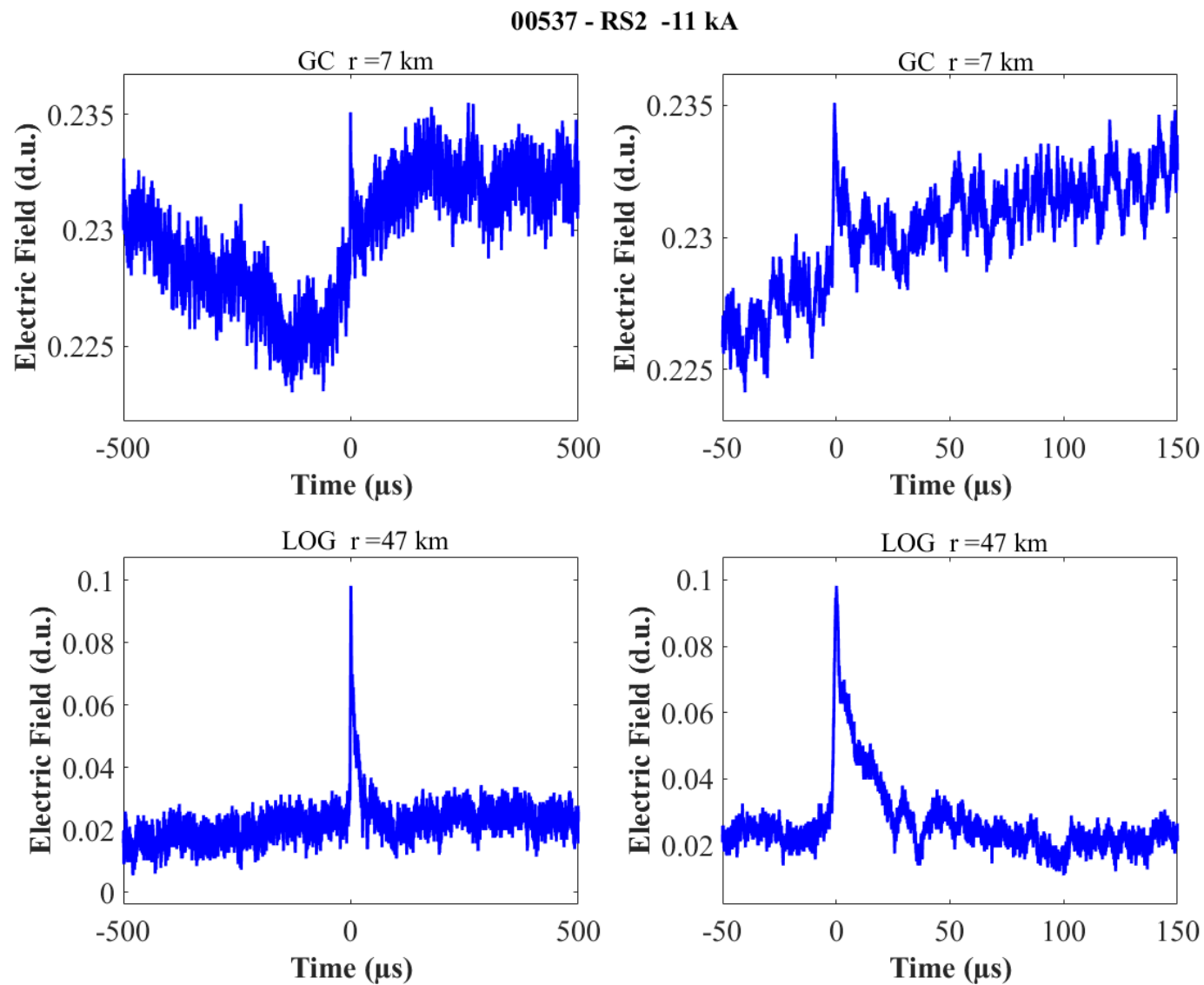


Figure B-30. Two-station electric field waveforms of the RS2 of flash 00537.

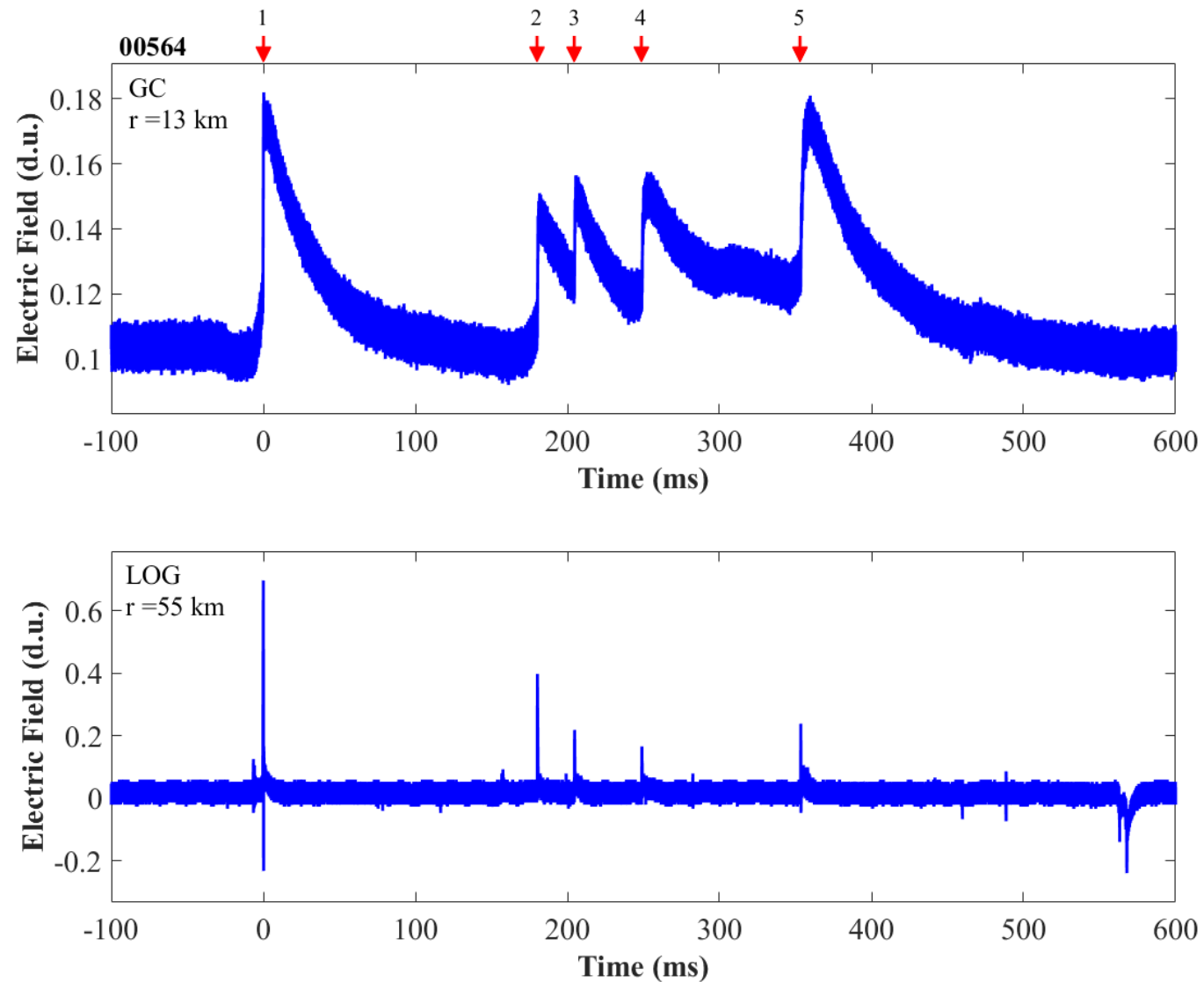


Figure B-31. Two-station electric field waveforms of flash 00564.

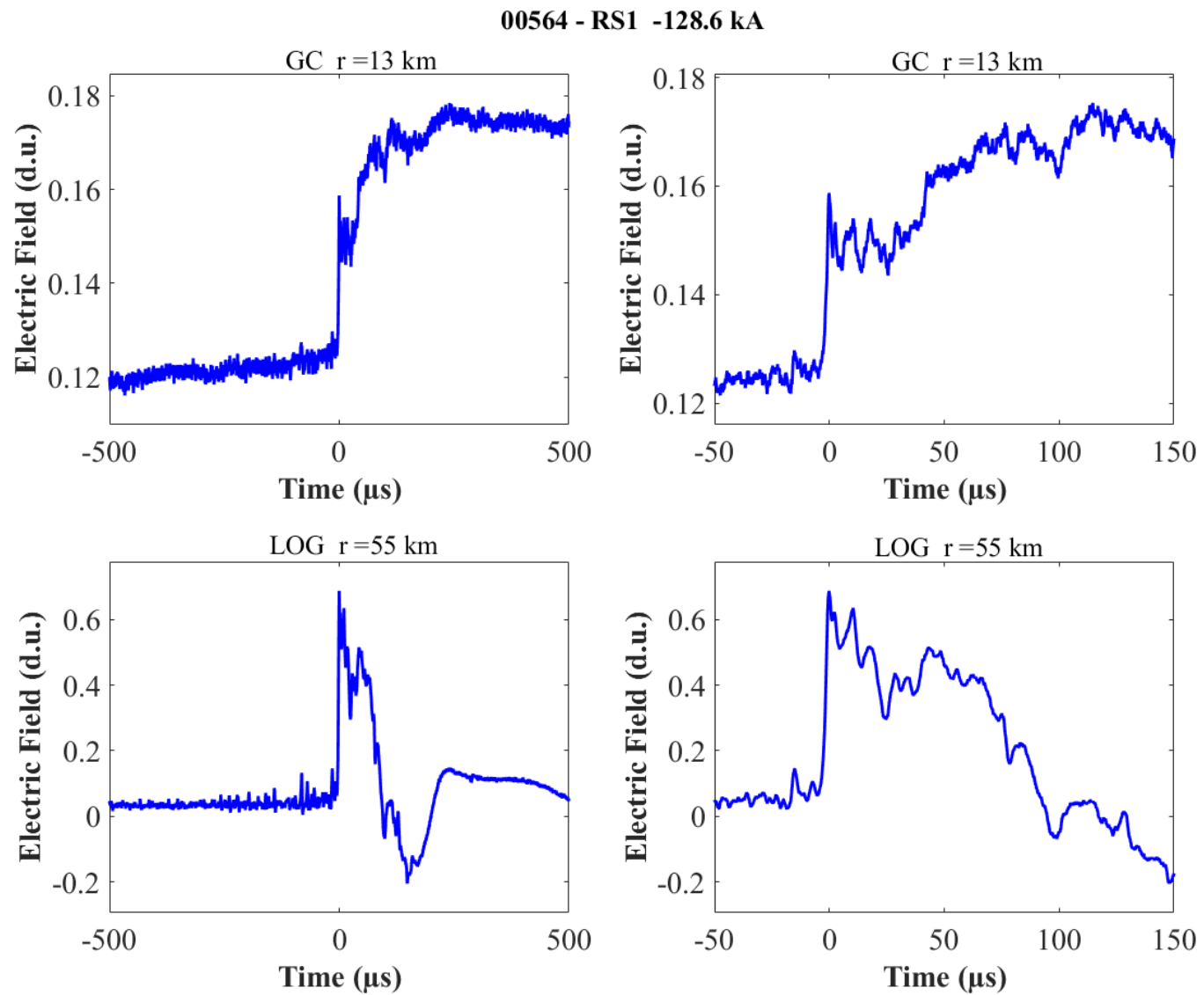


Figure B-32. Two-station electric field waveforms of the RS1 of flash 00564.

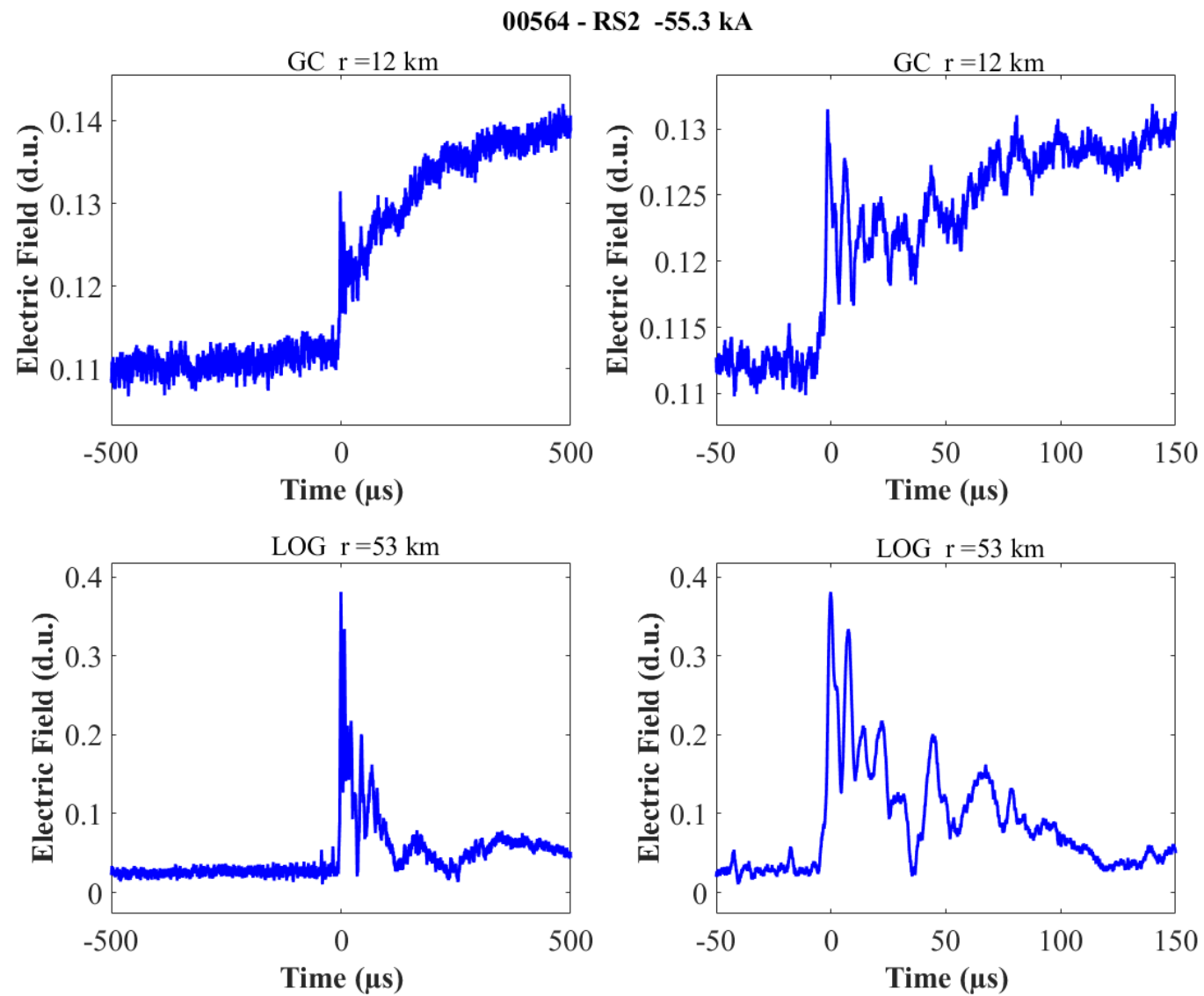


Figure B-33. Two-station electric field waveforms of the RS2 of flash 00564.

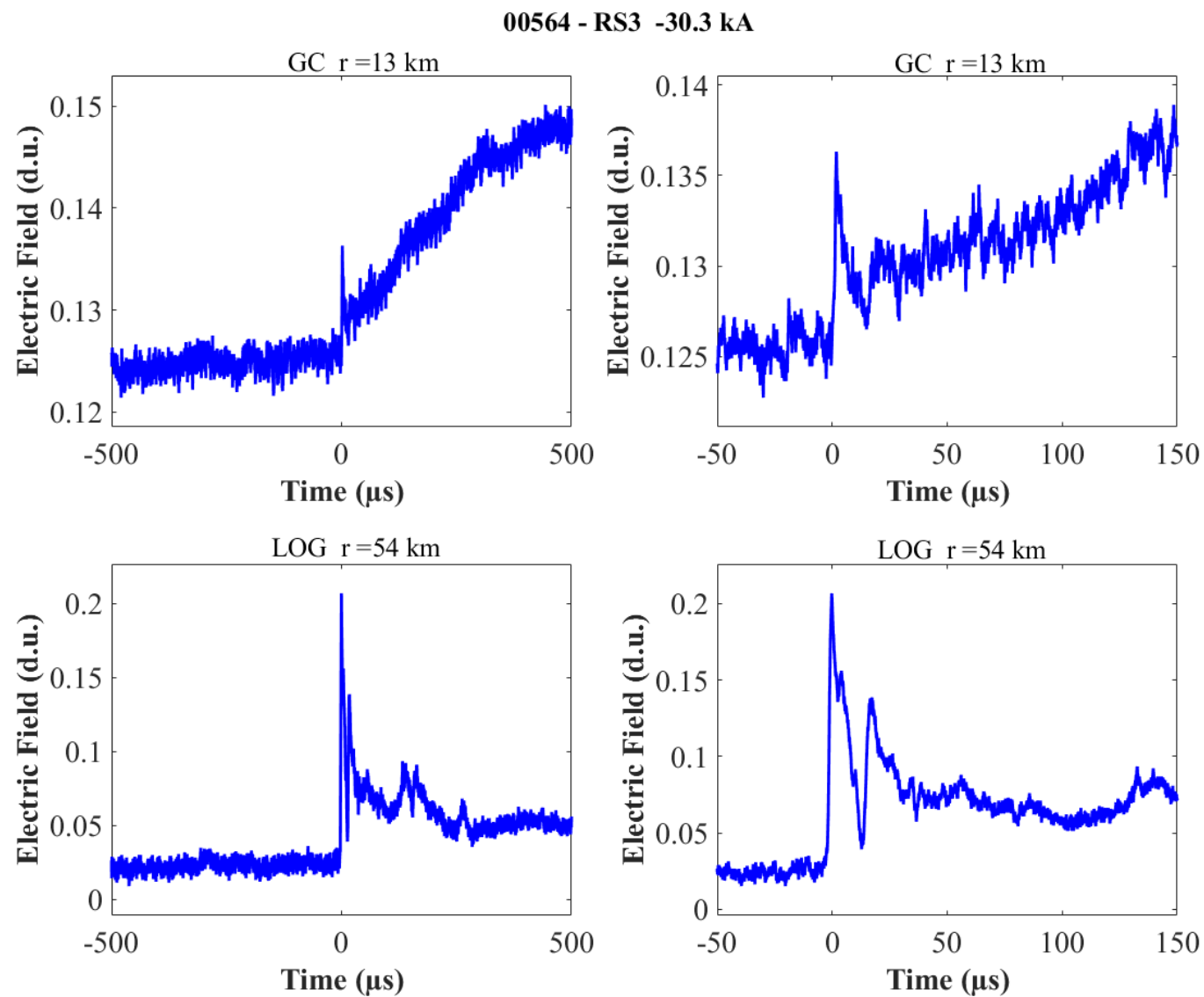


Figure B-34. Two-station electric field waveforms of the RS3 of flash 00564.

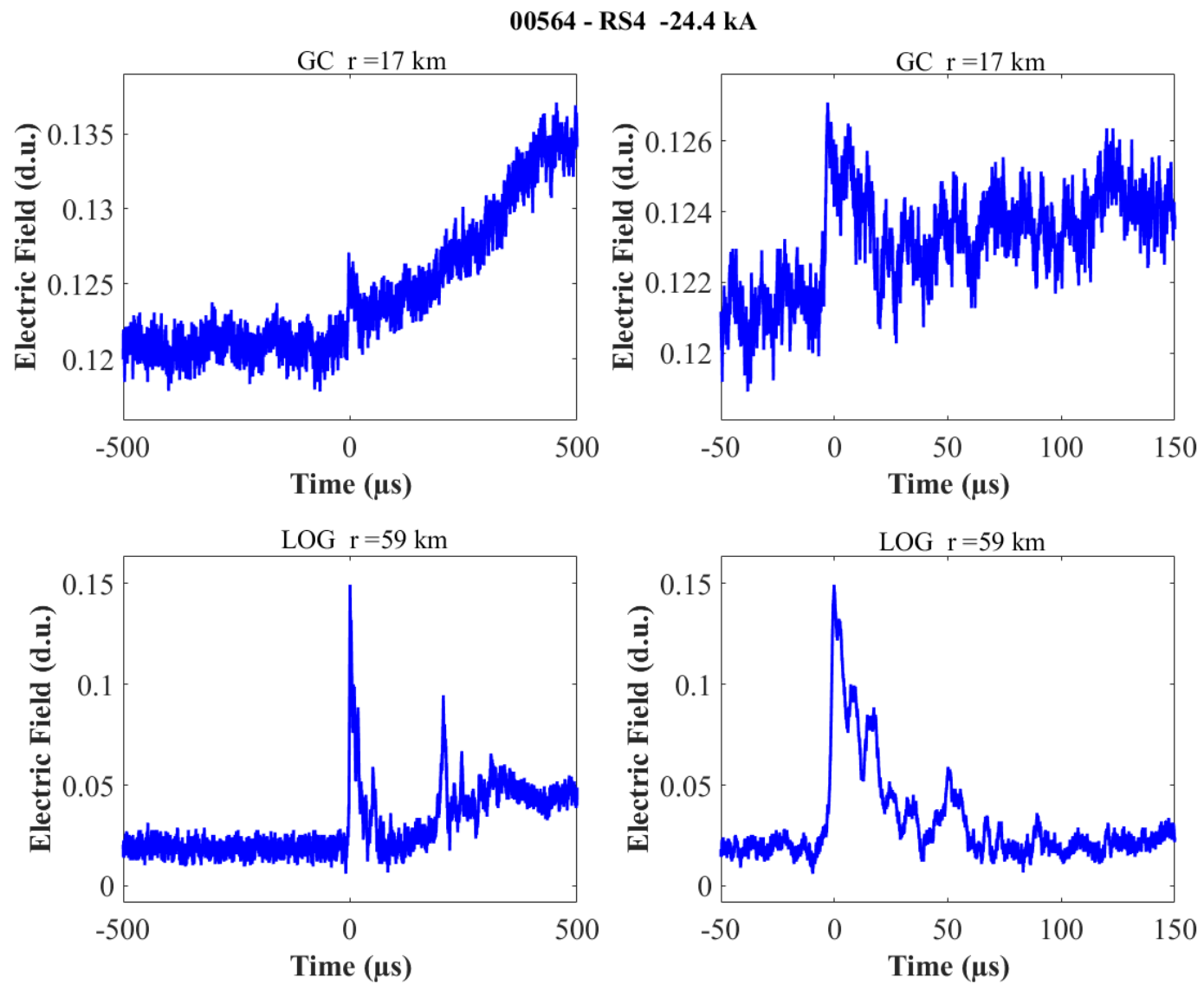


Figure B-35. Two-station electric field waveforms of the RS4 of flash 00564.

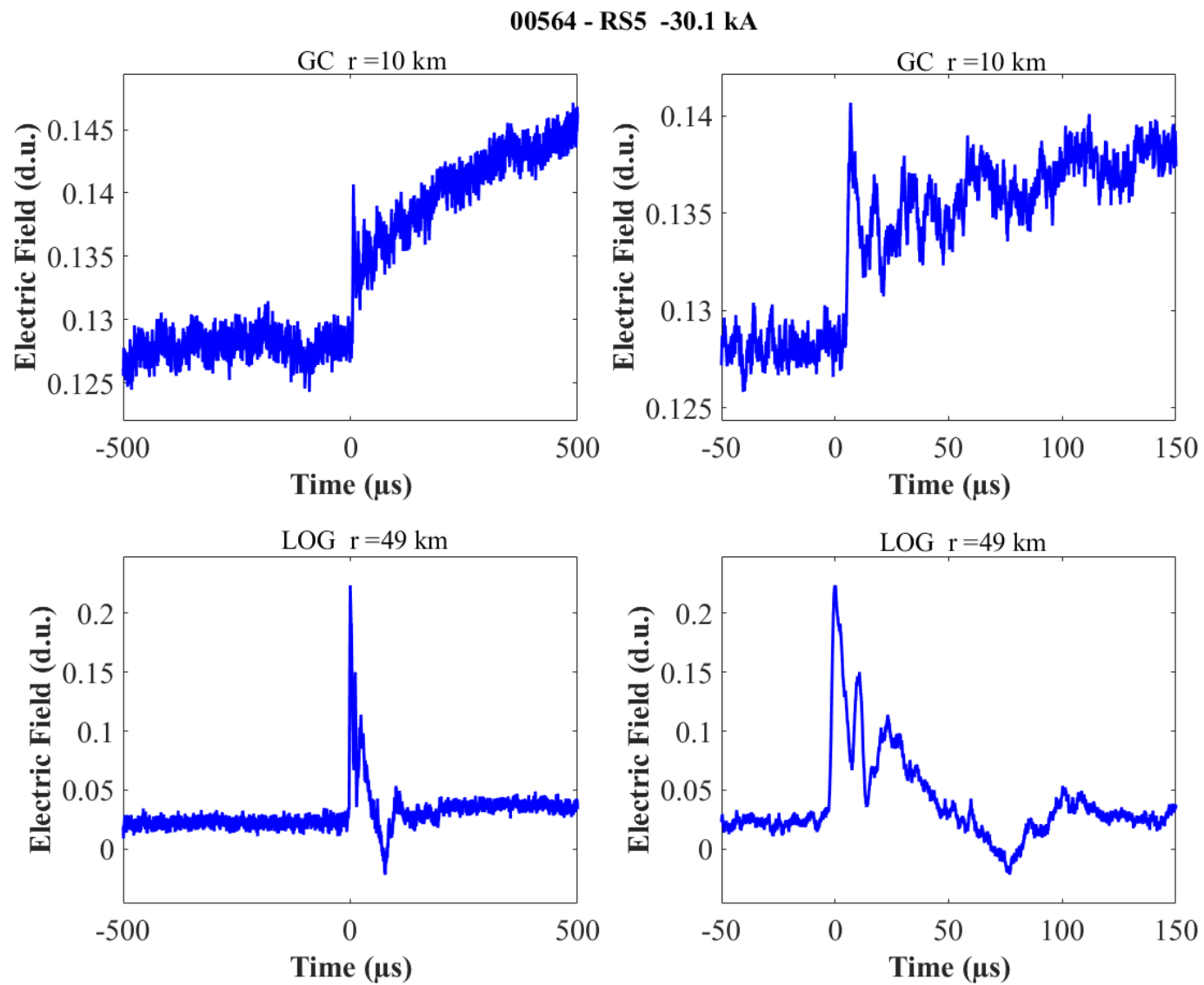


Figure B-36. Two-station electric field waveforms of the RS5 of flash 00564.

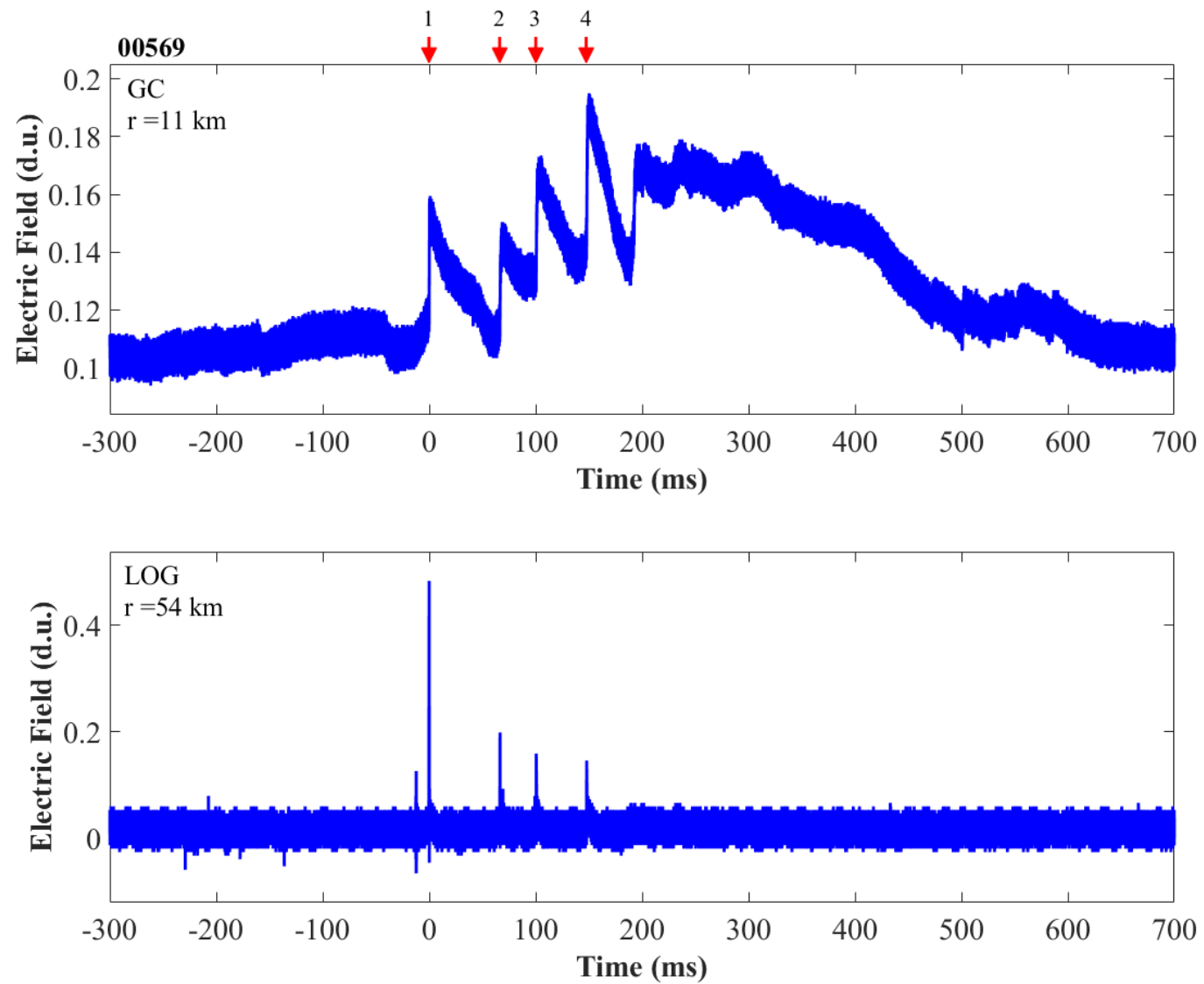


Figure B-37. Two-station electric field waveforms of flash 00569.

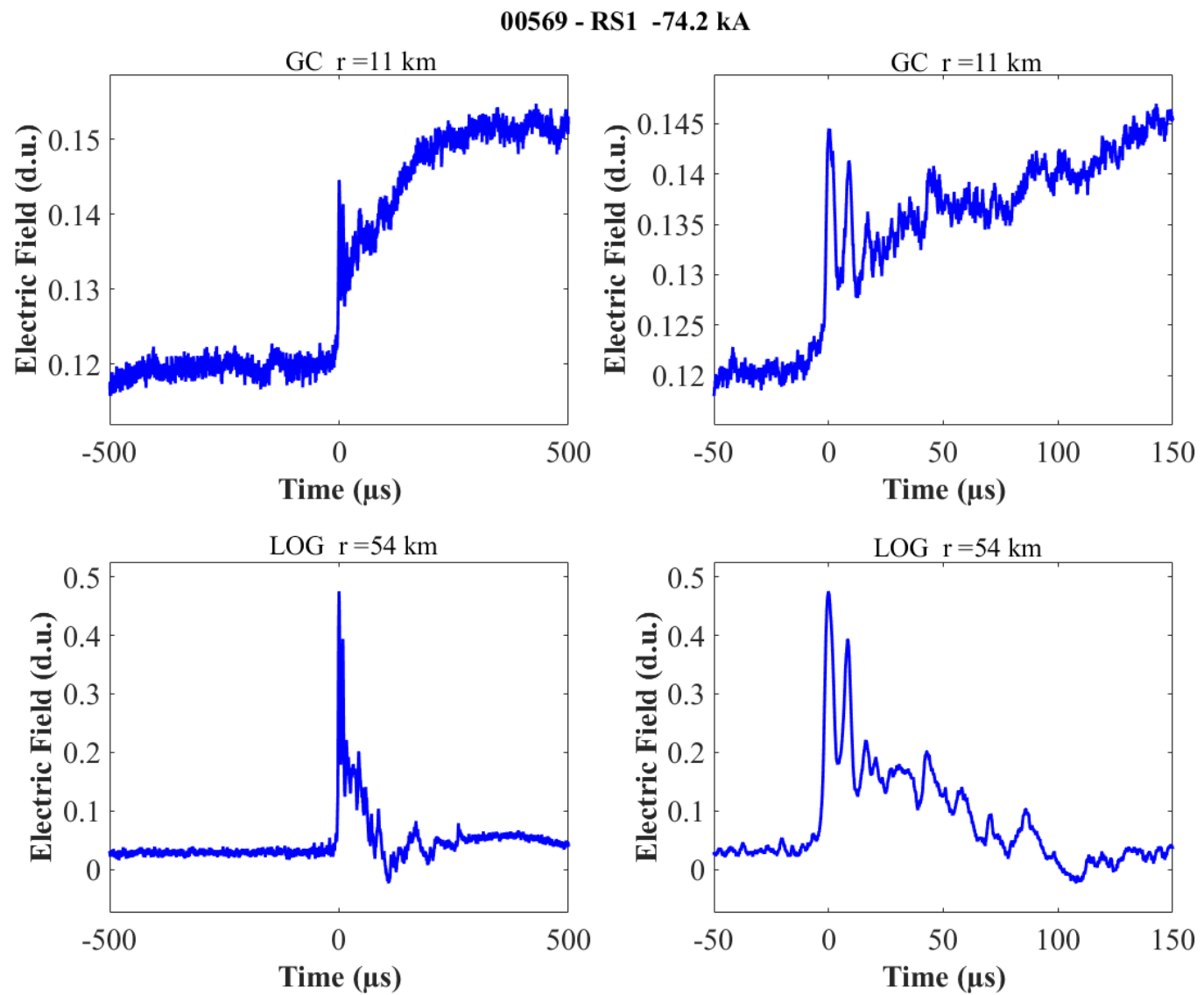


Figure B-38. Two-station electric field waveforms of the RS1 of flash 00569.

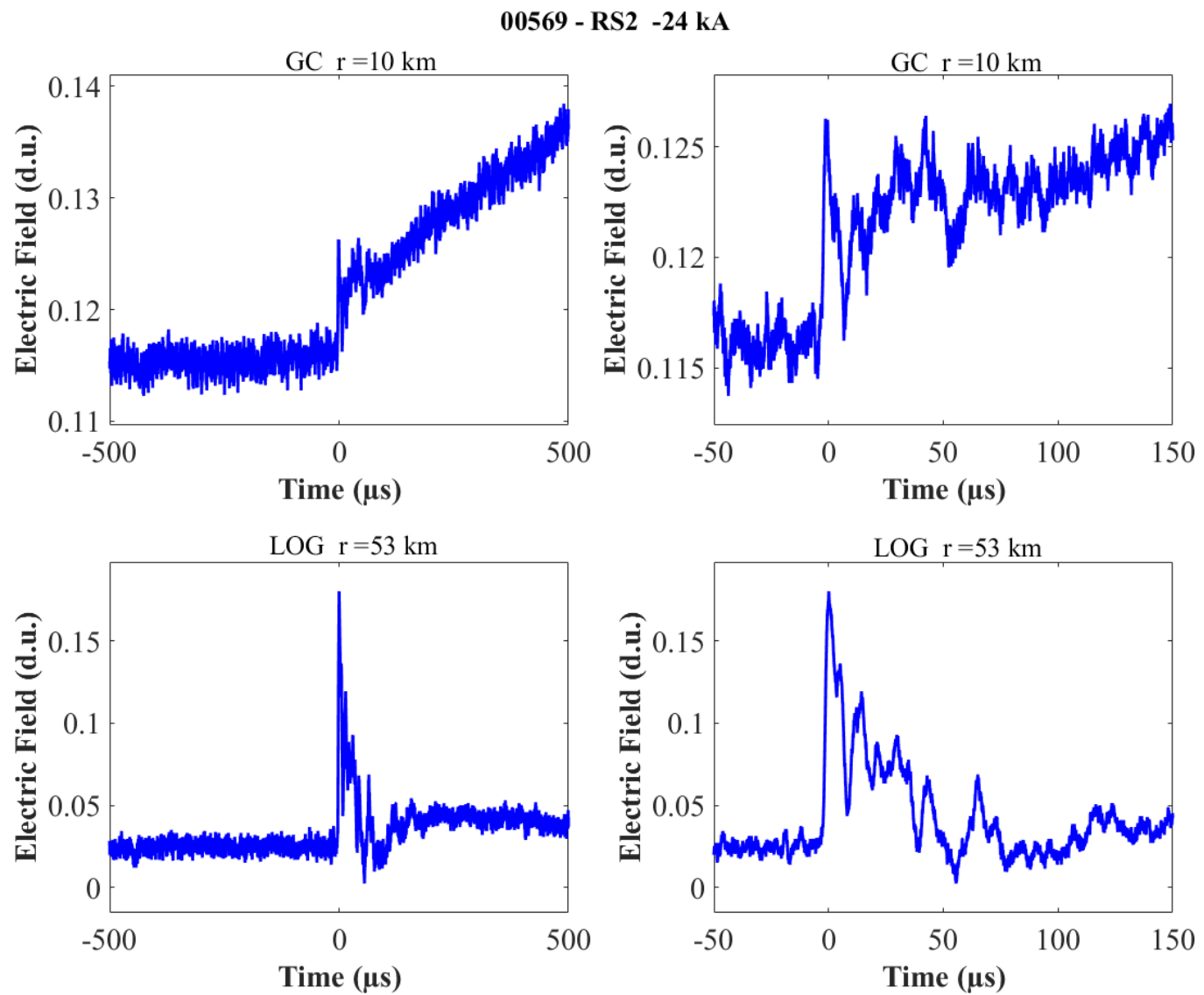


Figure B-39. Two-station electric field waveforms of the RS2 of flash 00569.

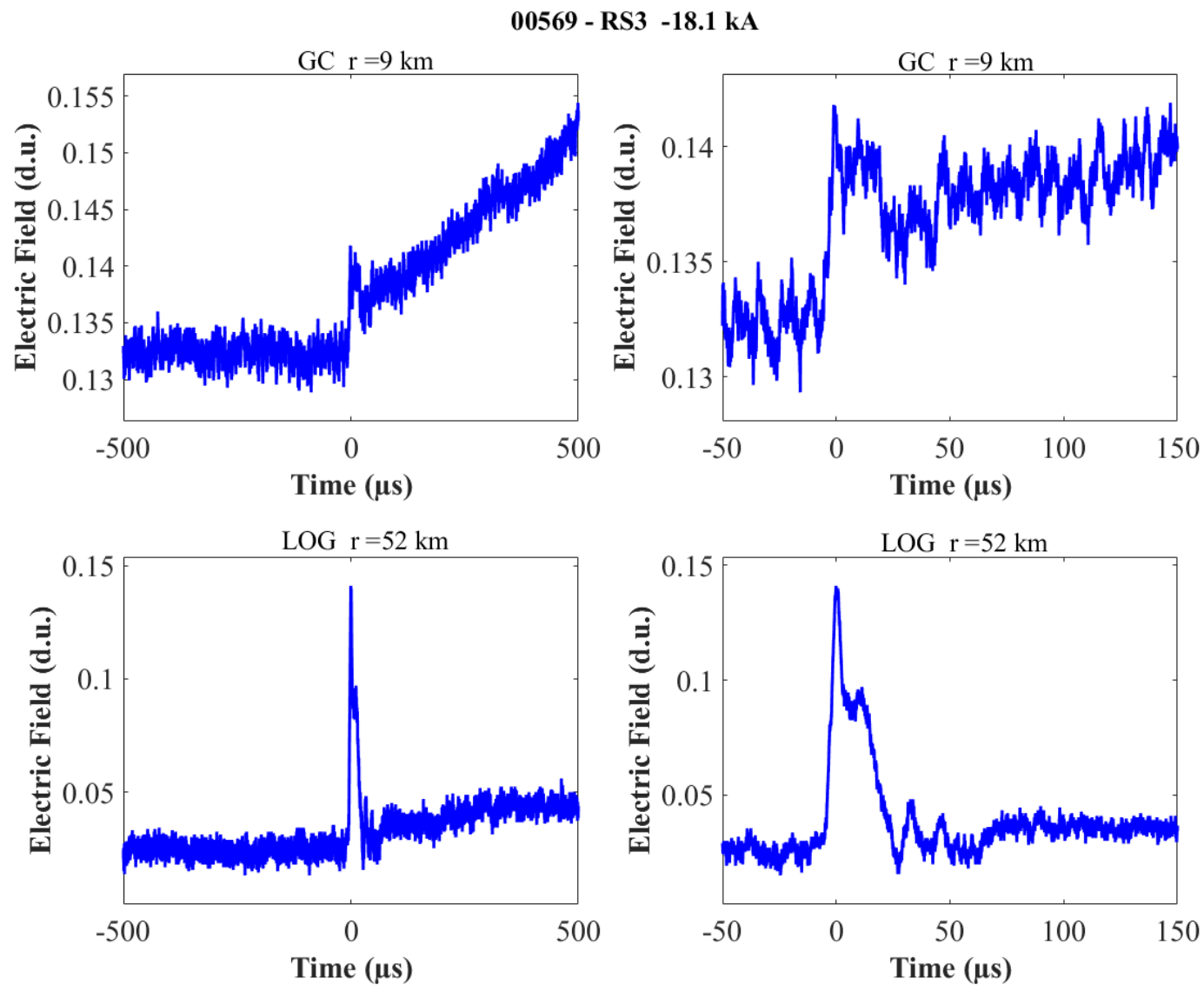


Figure B-40. Two-station electric field waveforms of the RS3 of flash 00569.

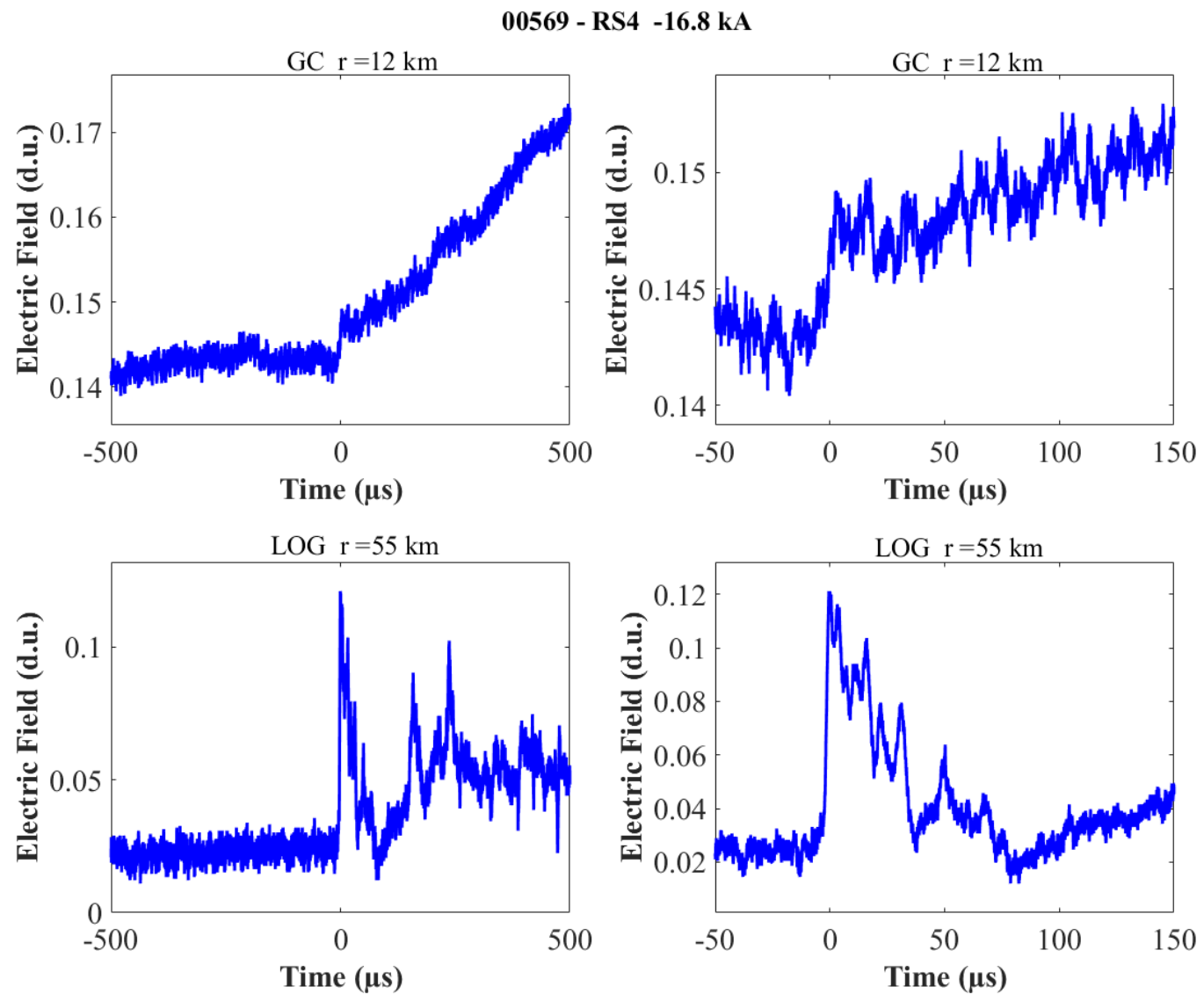


Figure B-41. Two-station electric field waveforms of the RS4 of flash 00569.

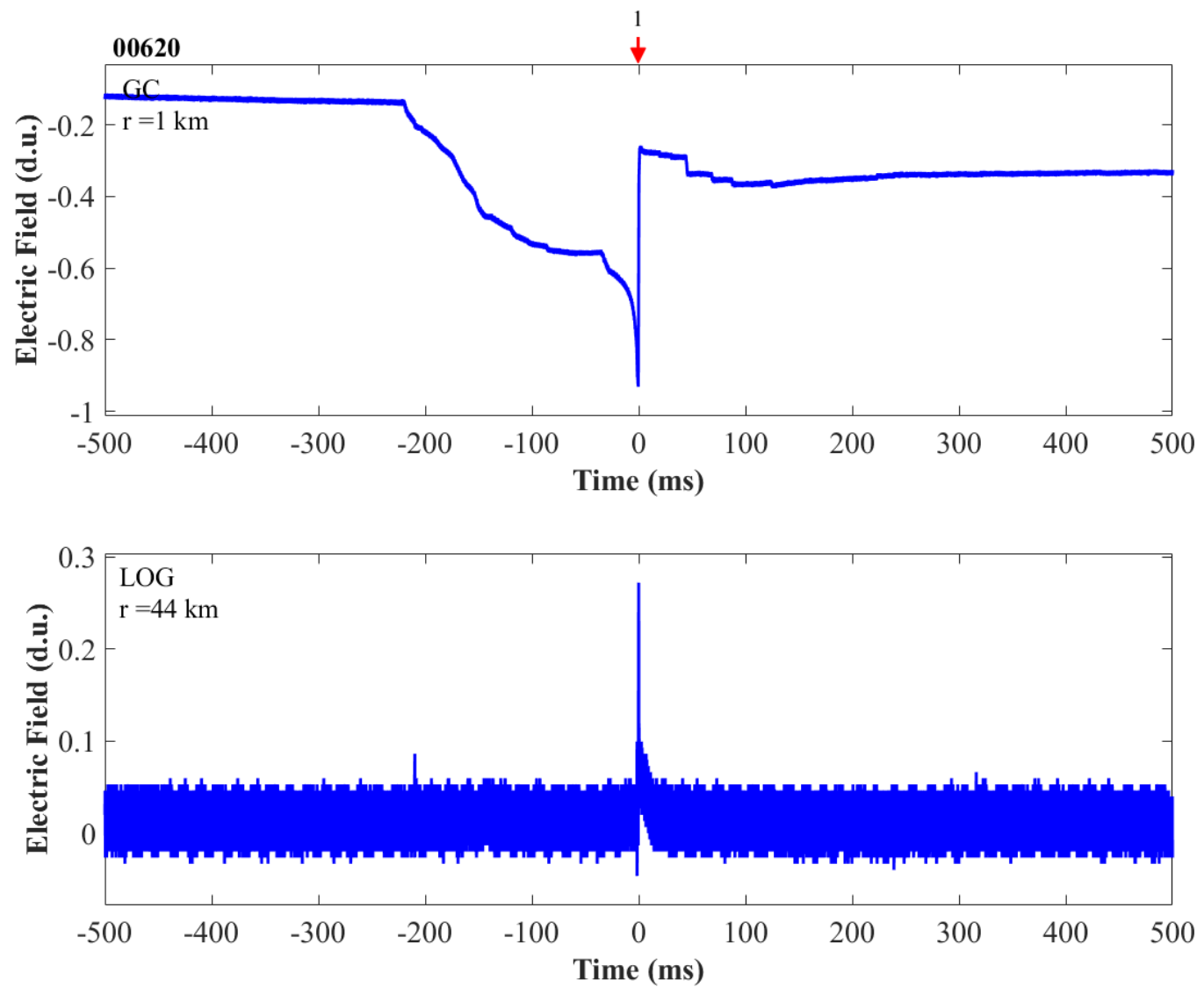


Figure B-42. Two-station electric field waveforms of flash 00620.

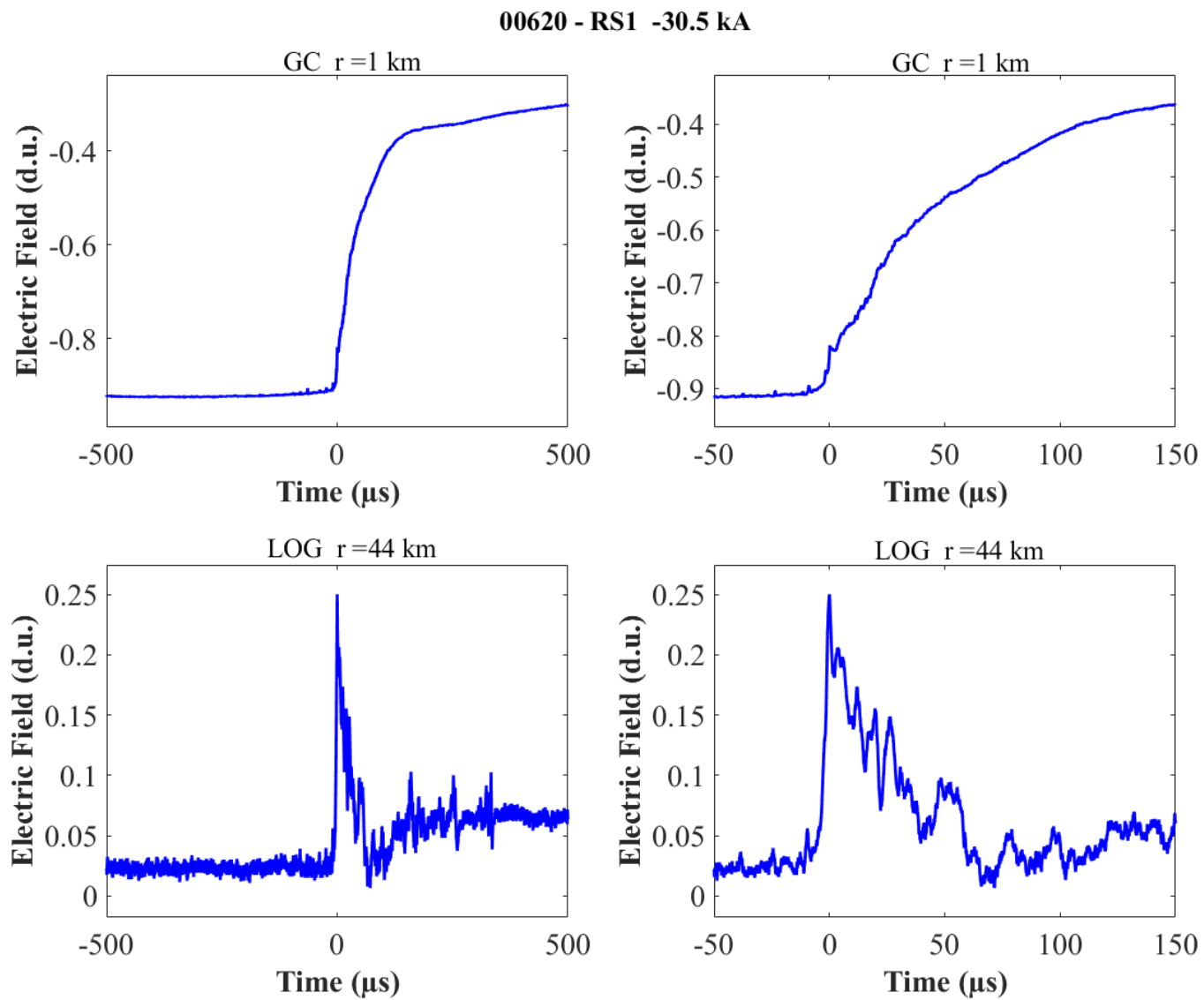


Figure B-43. Two-station electric field waveforms of the RS1 of flash 0062.

APPENDIX C
TWO-STATION MEASUREMENTS OF ELECTRIC FIELD WAVEFORMS OF NATURAL
POSITIVE CLOUD-TO-GROUND LIGHTNING

The two-station (LOG-GC) measurements of electric field waveforms for 10 natural positive cloud-to-ground lightning near Camp Blanding are presented in this appendix. Flash ID, data, and number of return strokes are listed in Table C-1. Except for one flash containing two strokes, all the flashes were single-stroke flashes. For each stroke, the complete field record of the flash is shown first and followed by expansions for each stroke on 1-ms and 200- μ s time scales. The distances from each of the stations to the lightning strike point were determined from NLDN-reported location of the stroke.

Table C-1. Inventory of two-station (LOG-GC) field measurements for 10 natural positive cloud-to-ground lightning

Flash ID	Date	Number of Return Strokes
00436	08/07/2015	1
00438	08/07/2015	1
00453	08/07/2015	1
00456	08/07/2015	1
00477	08/07/2015	1
00577	08/07/2015	1
00580	08/07/2015	1
00590	08/07/2015	1
01162	08/19/2015	2
01163	08/19/2015	1
Total Number of Flashes: 10		Total Number of Strokes: 11

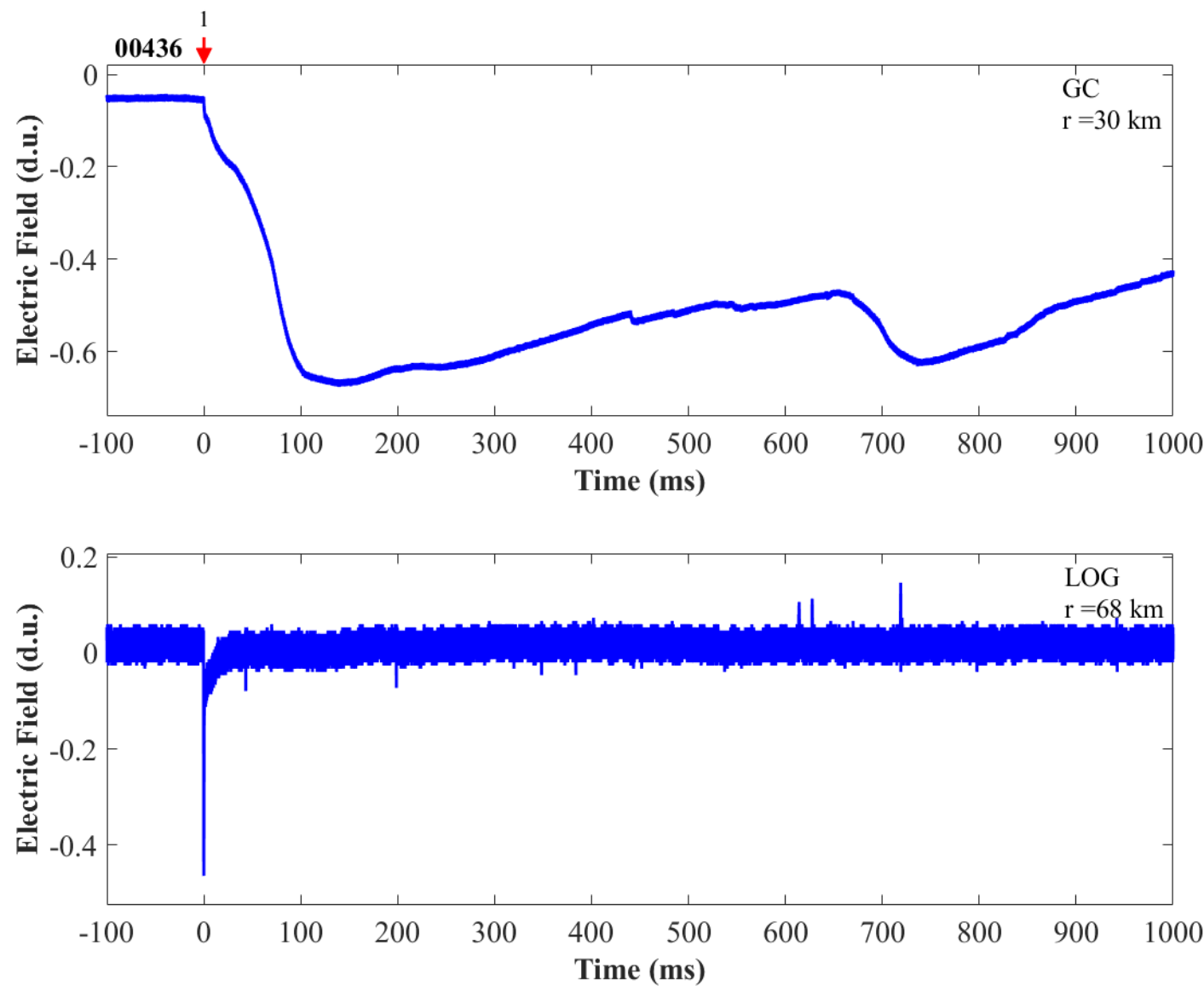


Figure B-44. Two-station electric field waveforms of flash 00436.

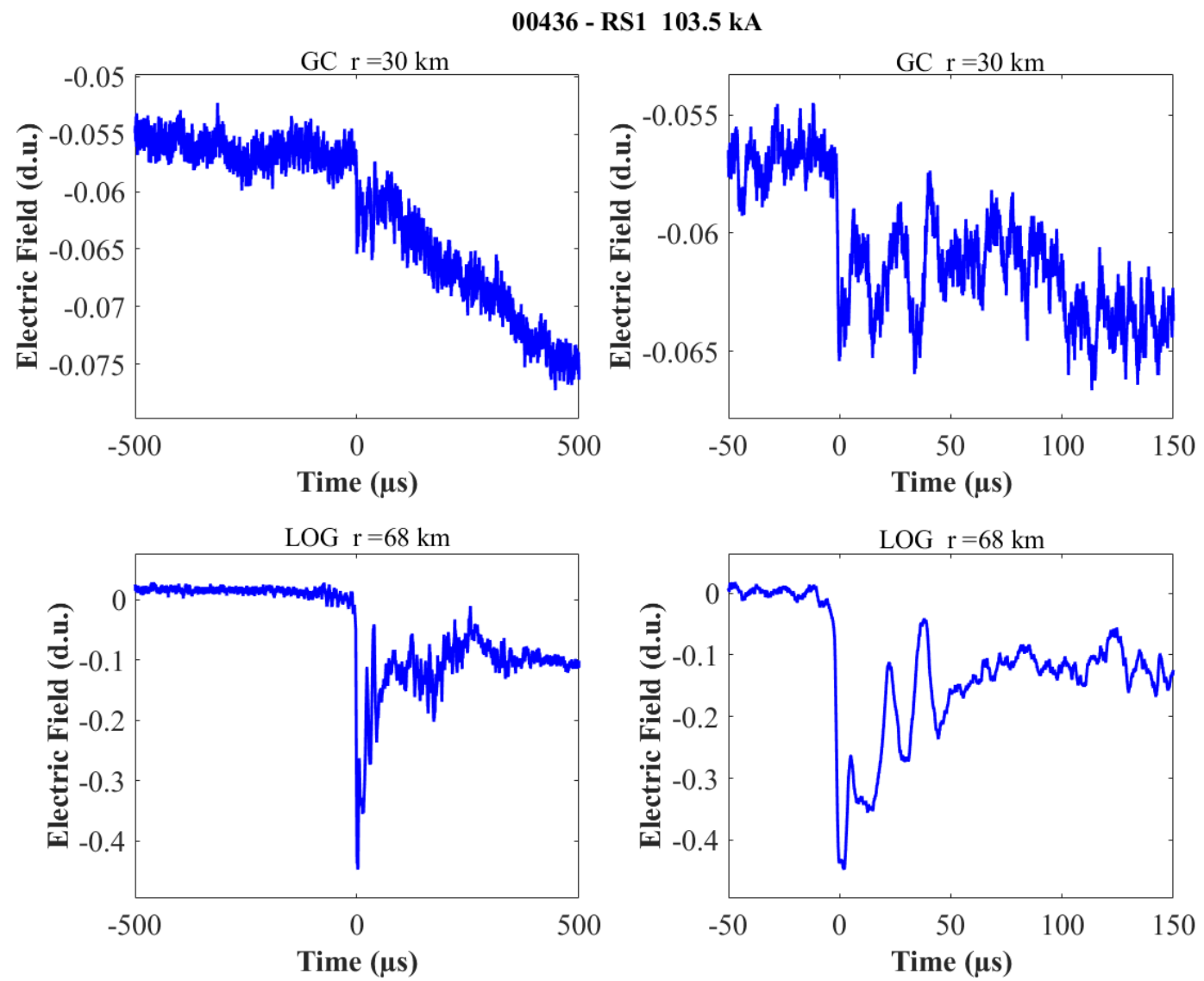


Figure B-45. Two-station electric field waveforms of the RS1 of flash 00436.

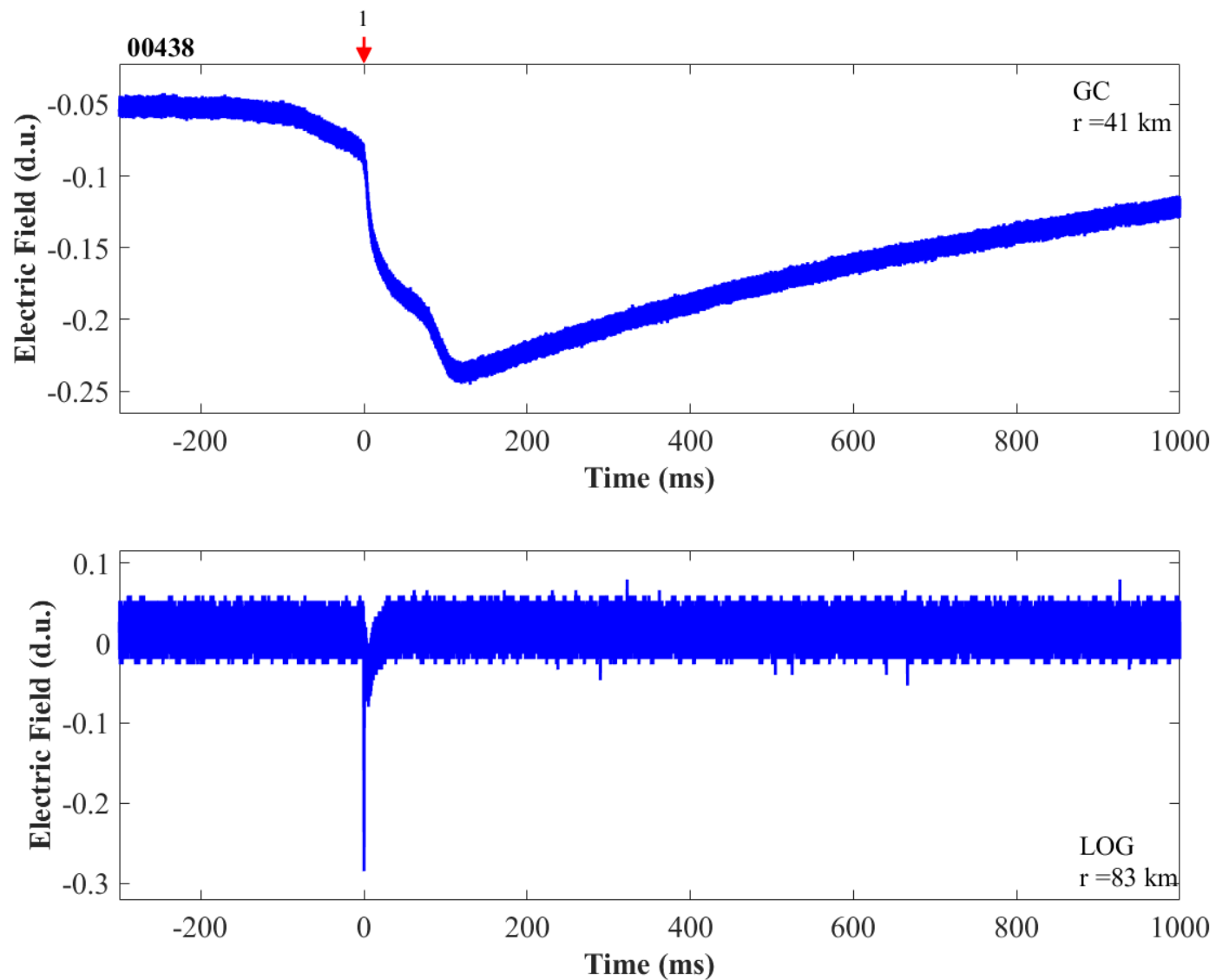


Figure B-46. Two-station electric field waveforms of flash 00438.

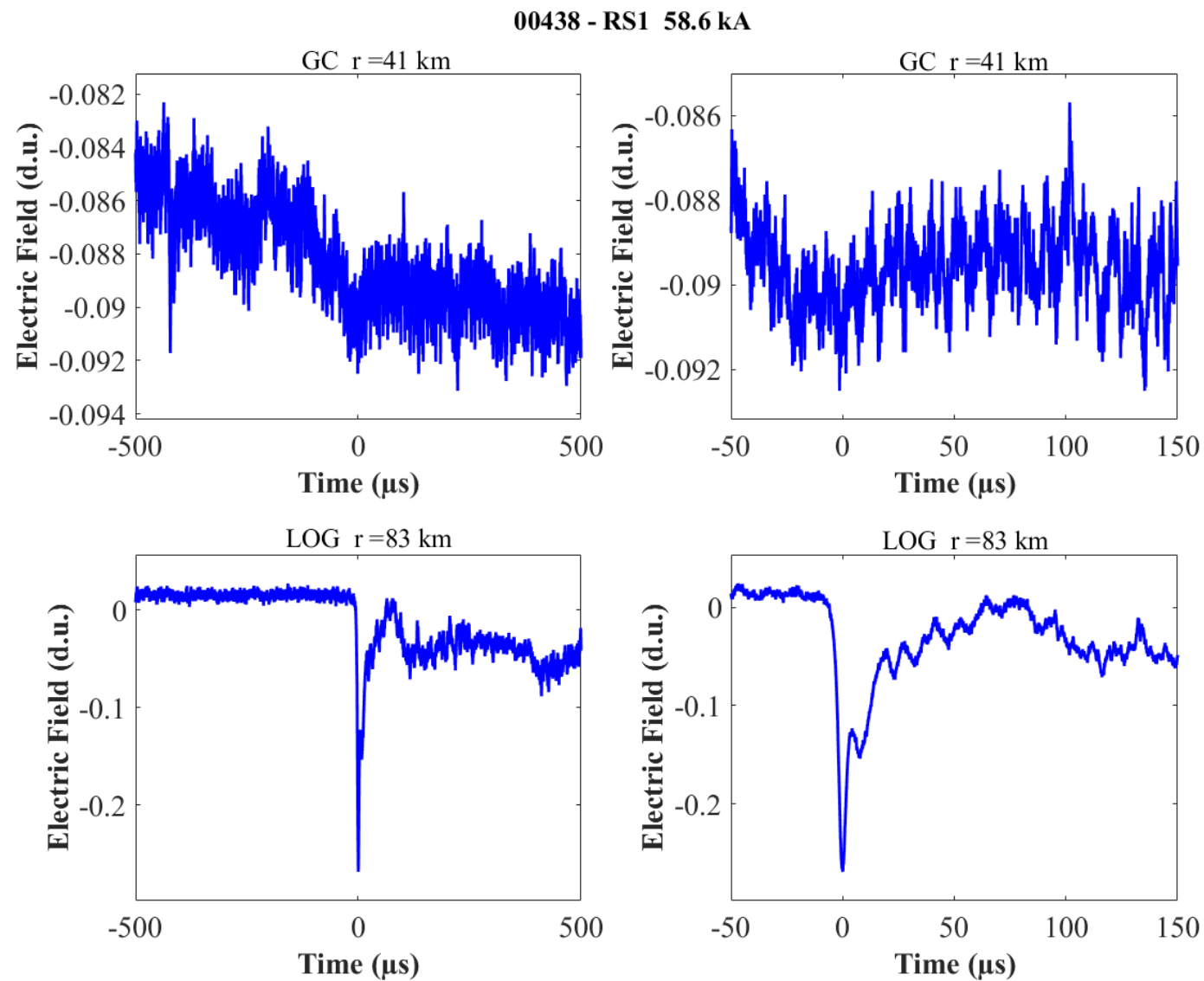


Figure B-47. Two-station electric field waveforms of the RS1 of flash 00438.

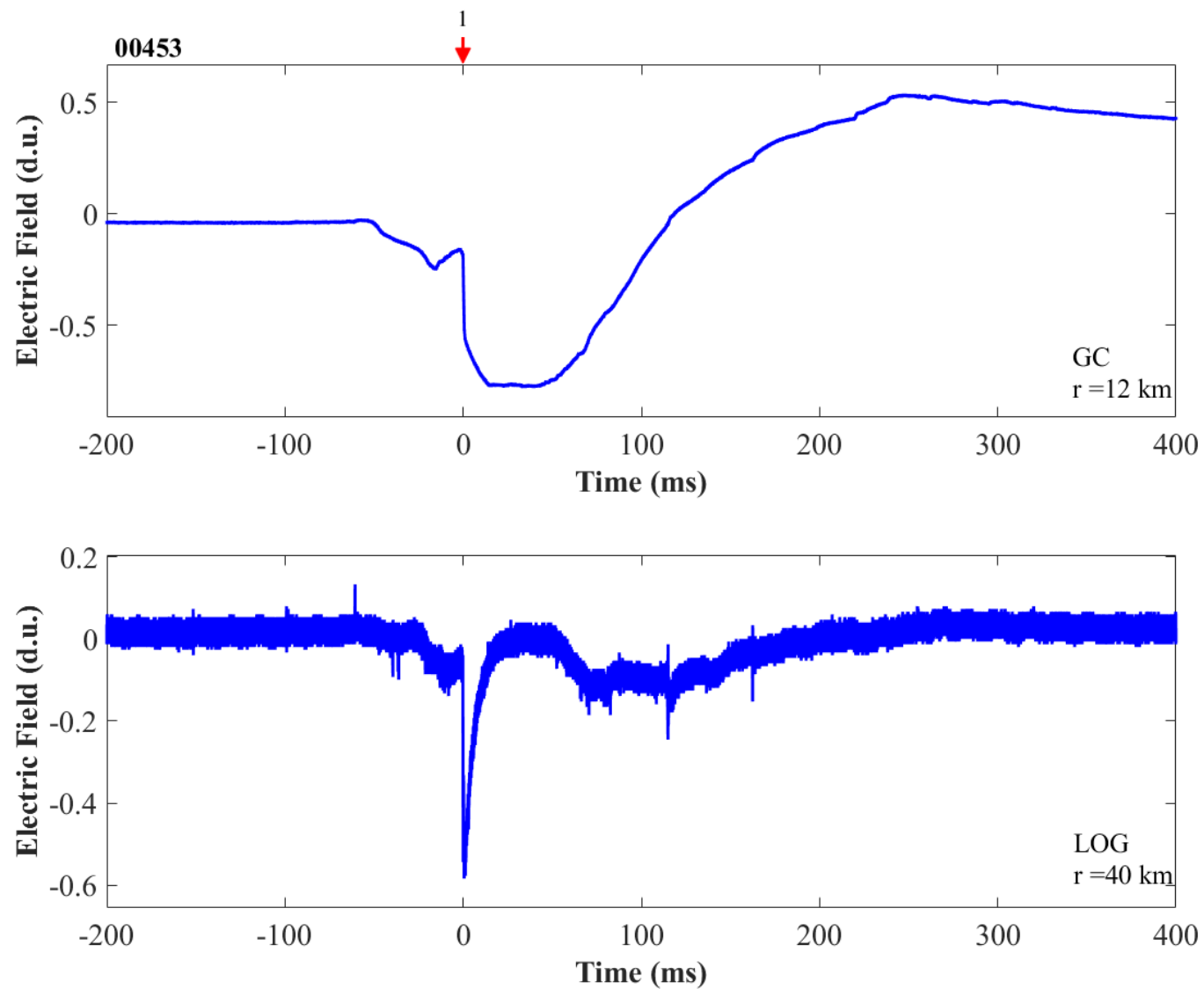


Figure B-48. Two-station electric field waveforms of flash 00453.

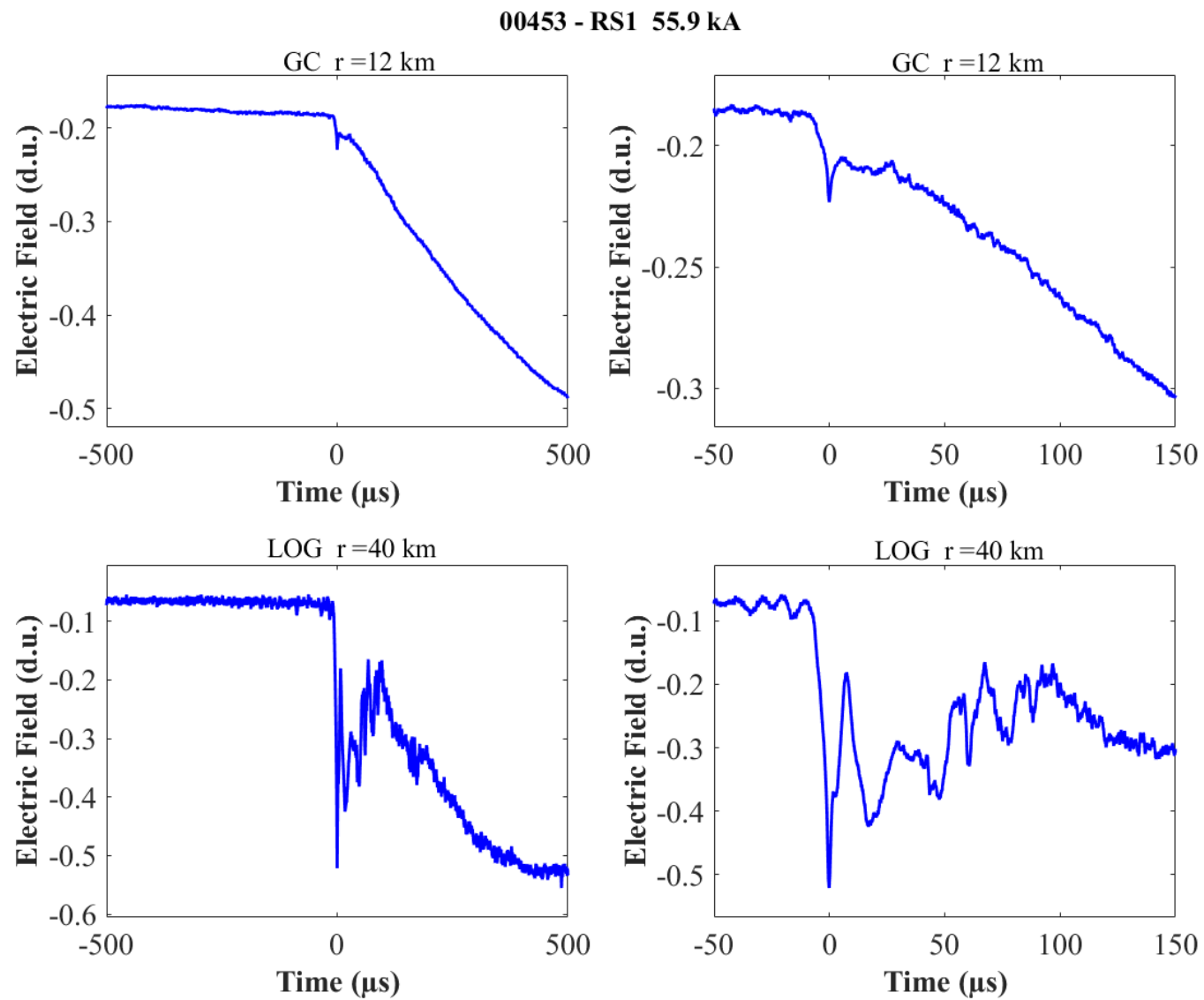


Figure B-49. Two-station electric field waveforms of the RS1 of flash 00453.

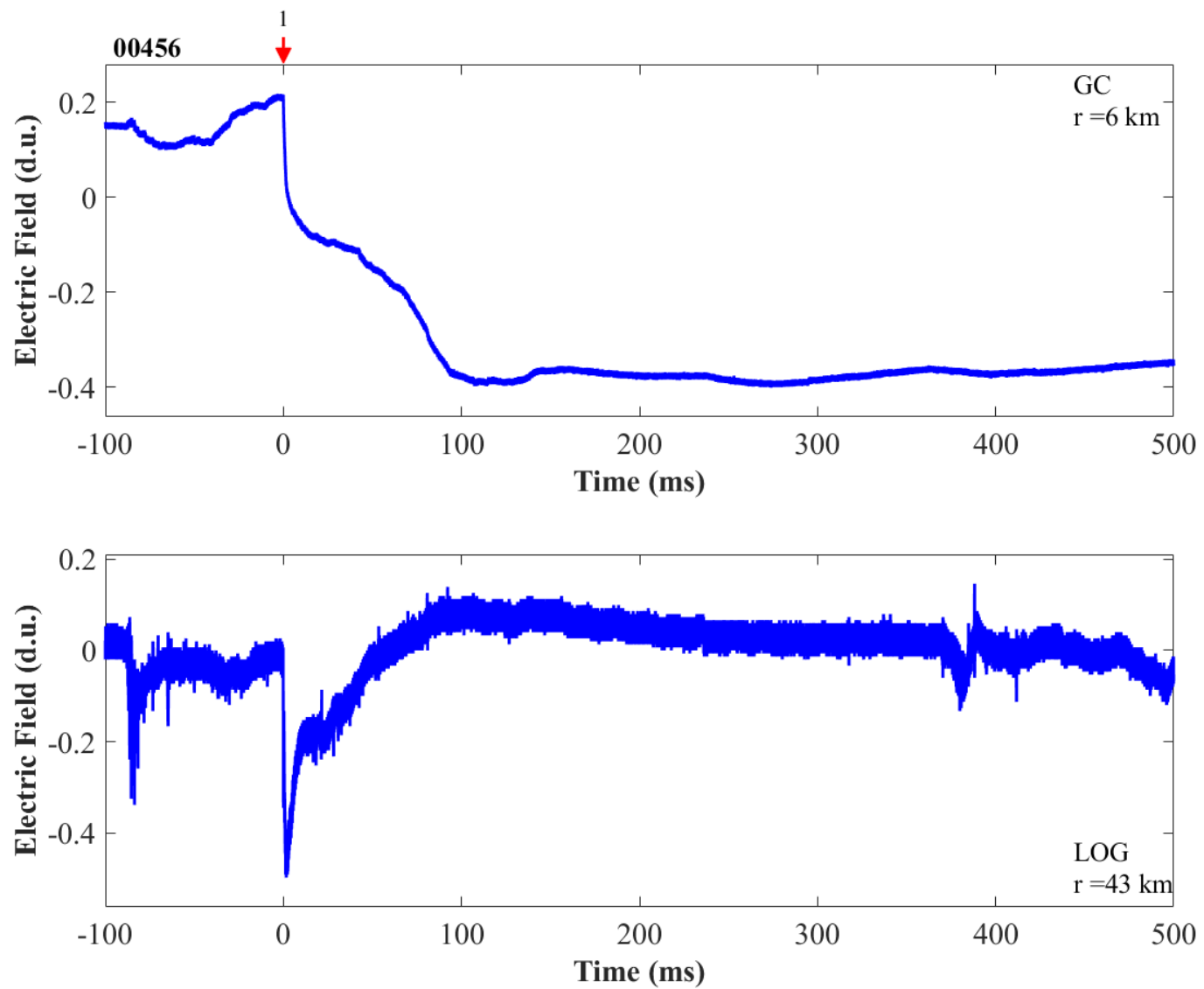


Figure B-50. Two-station electric field waveforms of flash 00456.

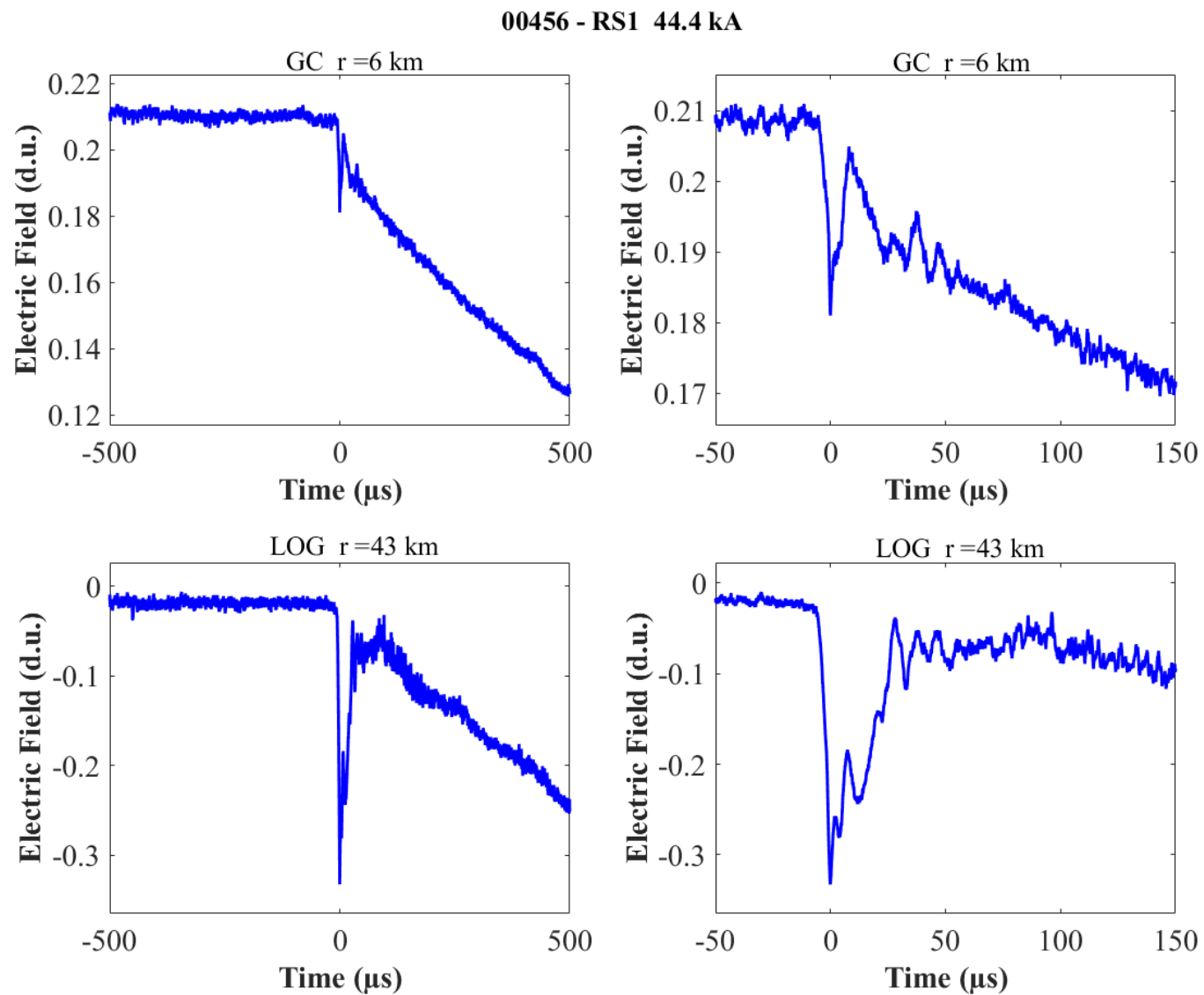


Figure B-51. Two-station electric field waveforms of the RS1 of flash 00456.

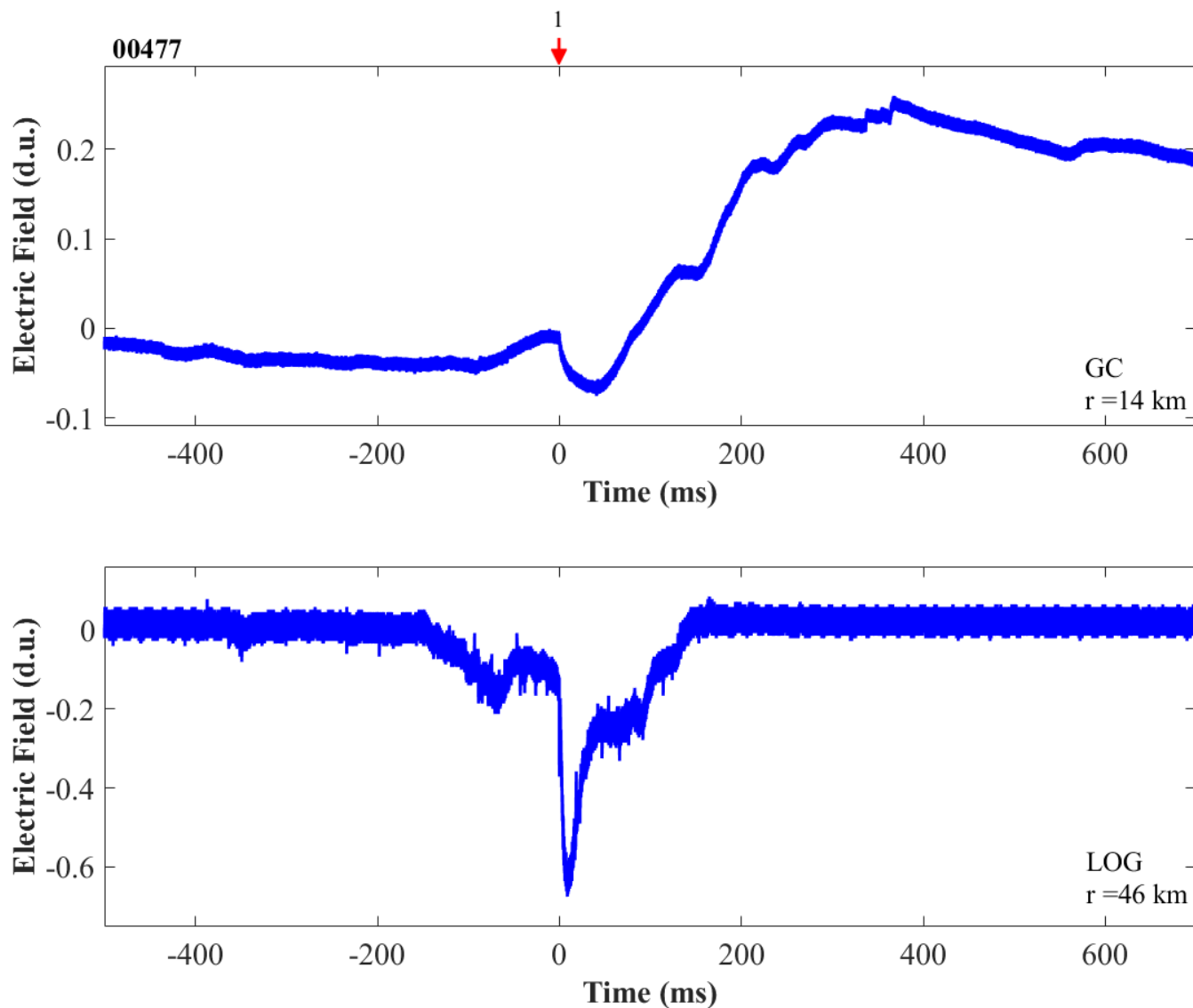


Figure B-52. Two-station electric field waveforms of flash 00477.

00477 - RS1 29.5 kA

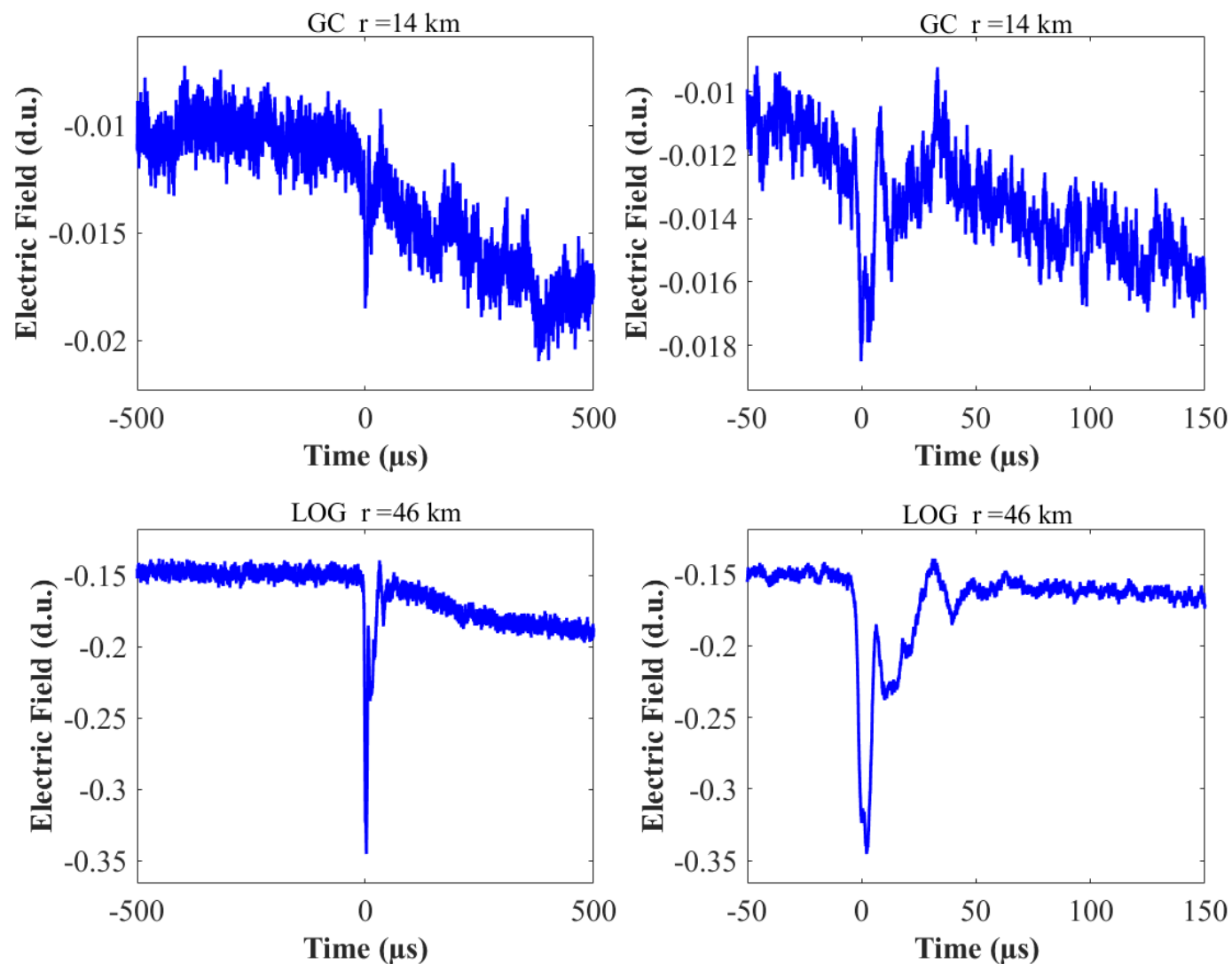


Figure B-53. Two-station electric field waveforms of the RS1 of flash 00477.

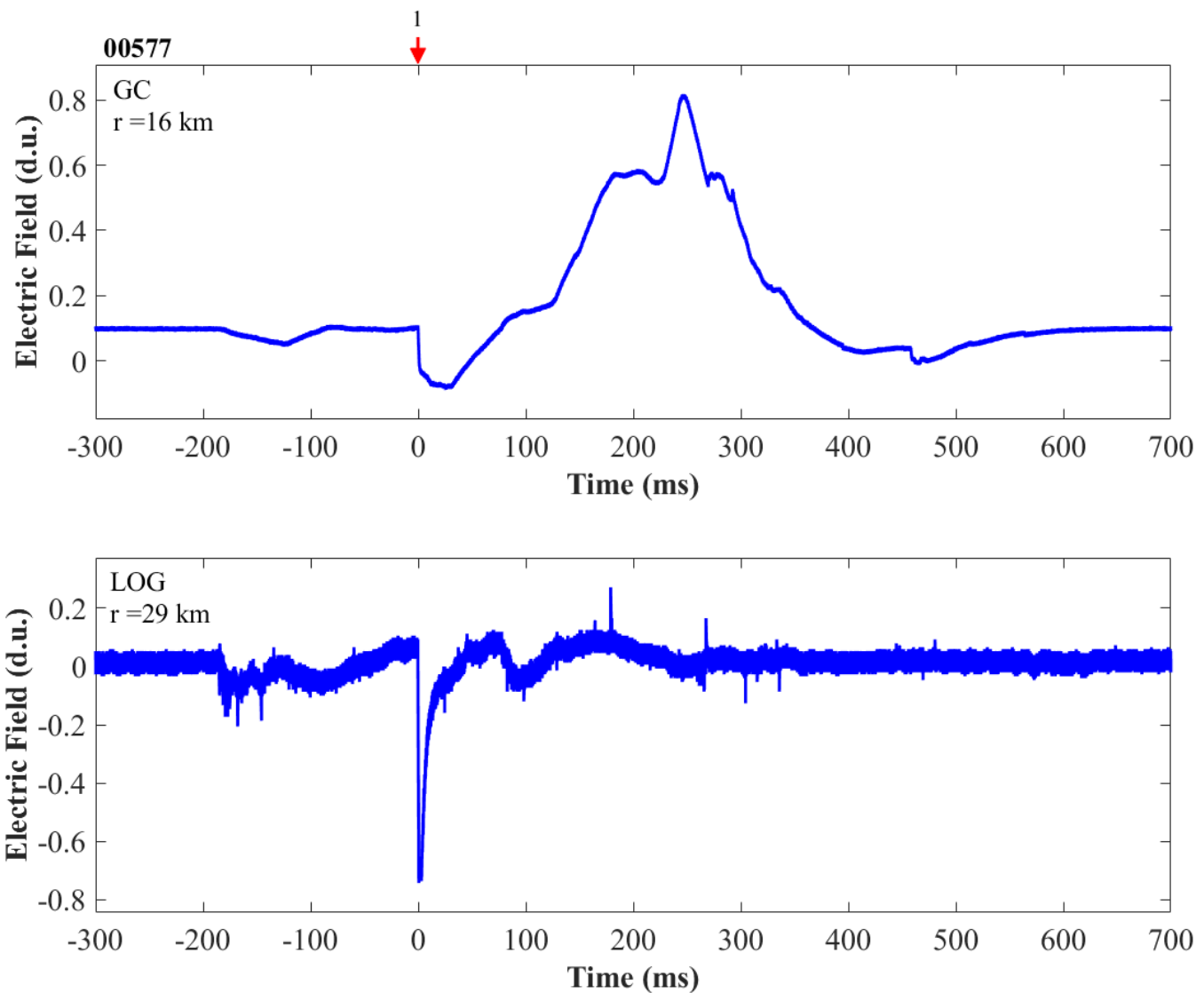


Figure B-54. Two-station electric field waveforms of flash 00577.

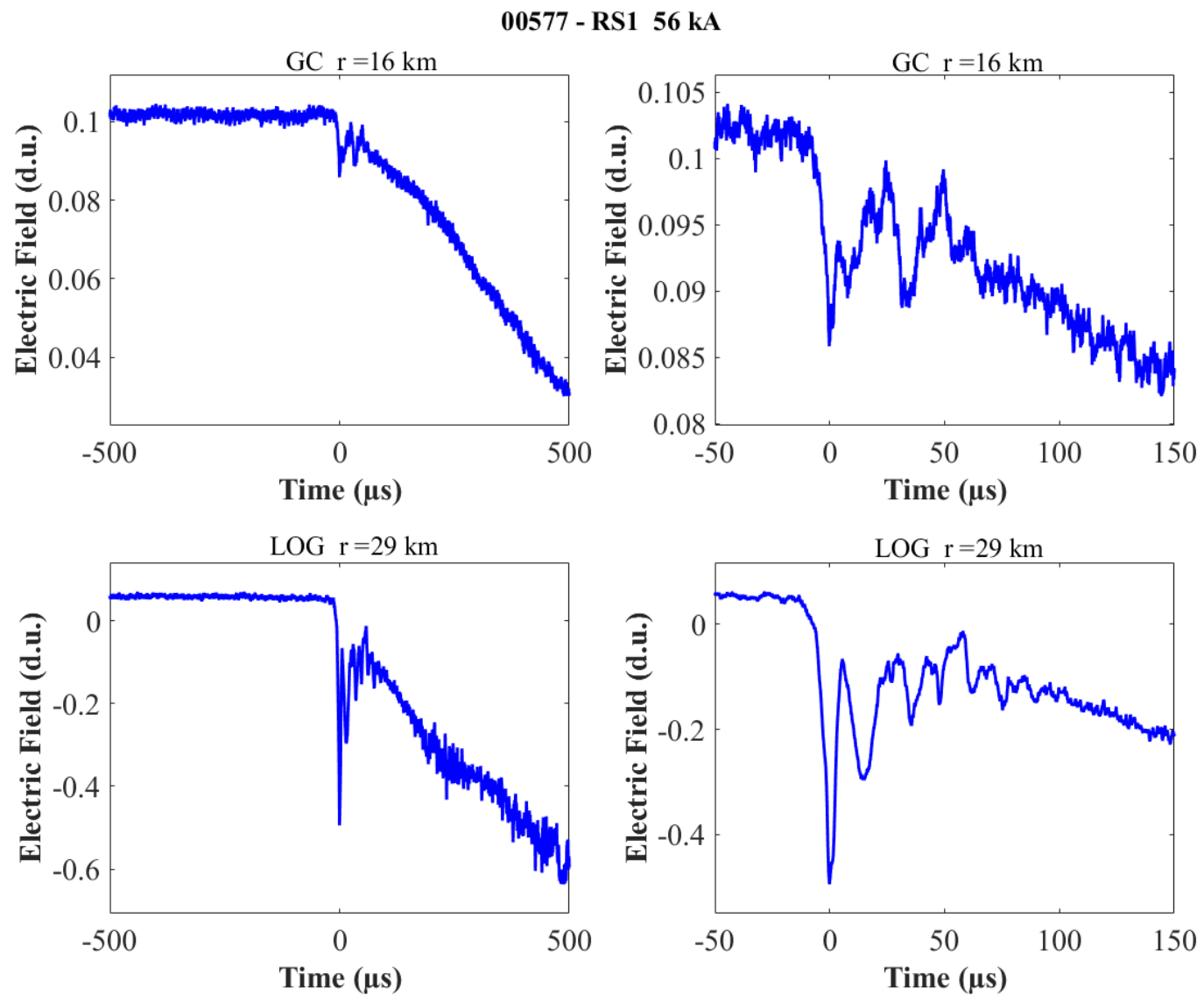


Figure B-55. Two-station electric field waveforms of the RS1 of flash 00577.

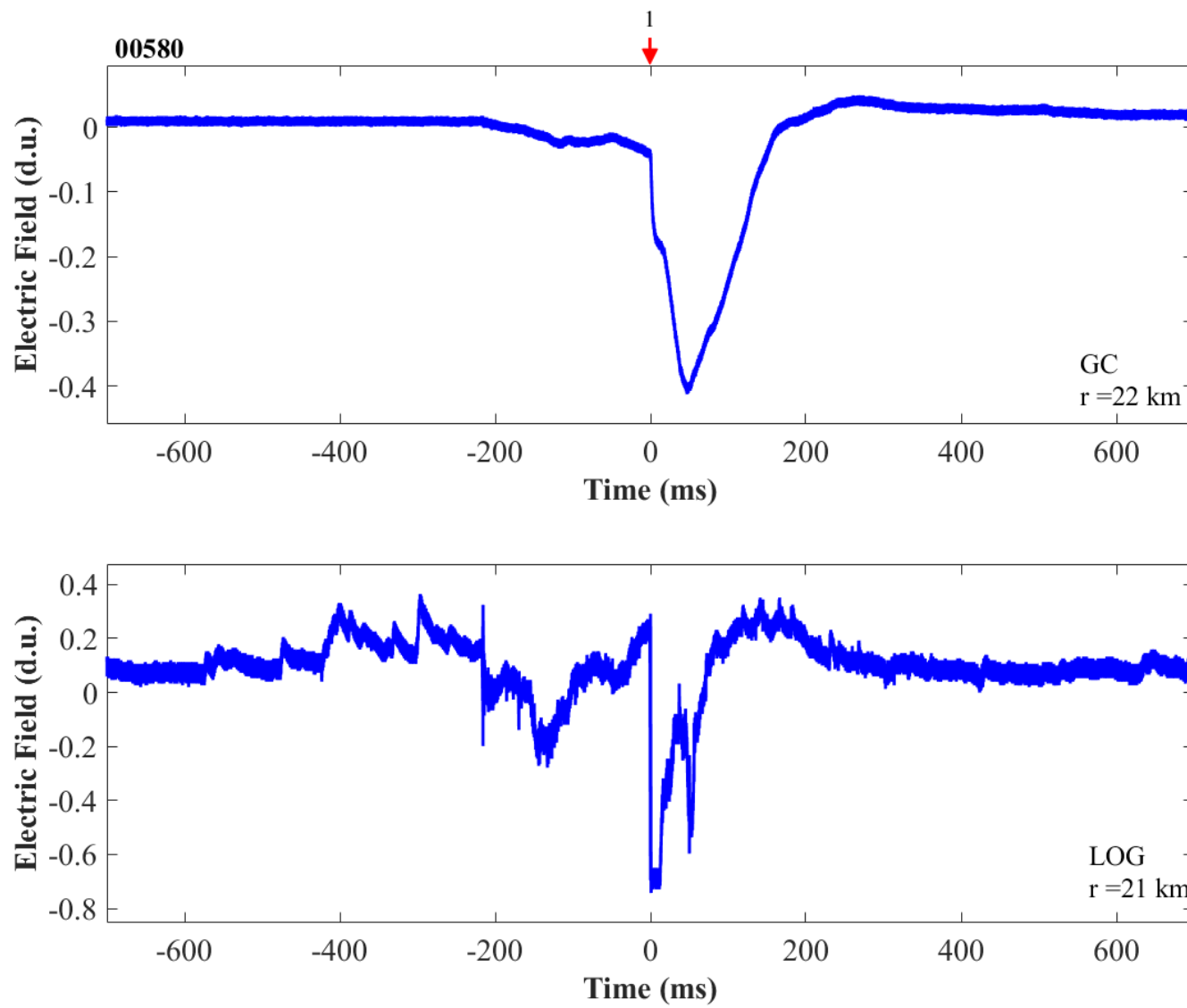


Figure B-56. Two-station electric field waveforms of flash 00580.

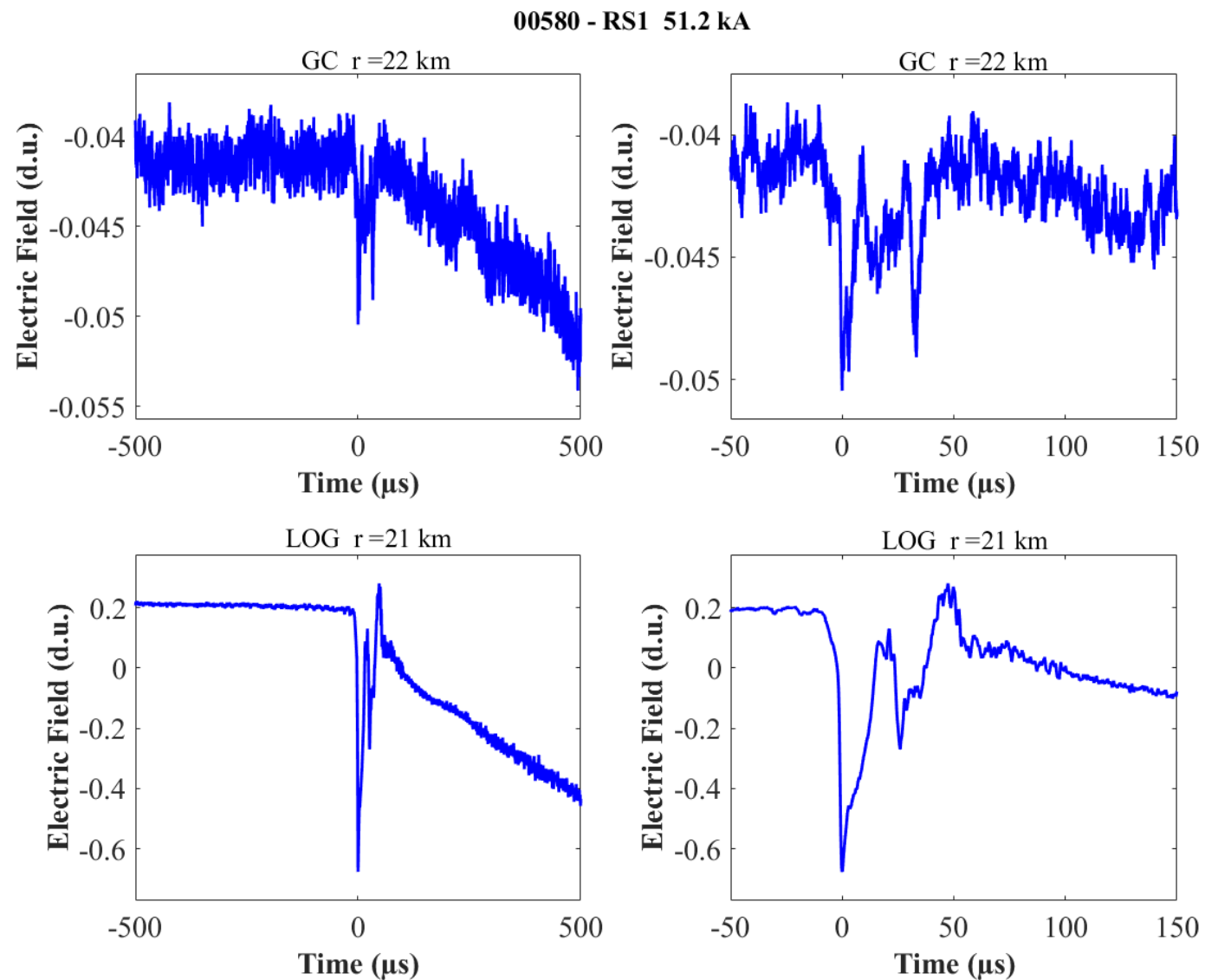


Figure B-57. Two-station electric field waveforms of the RS1 of flash 00580.

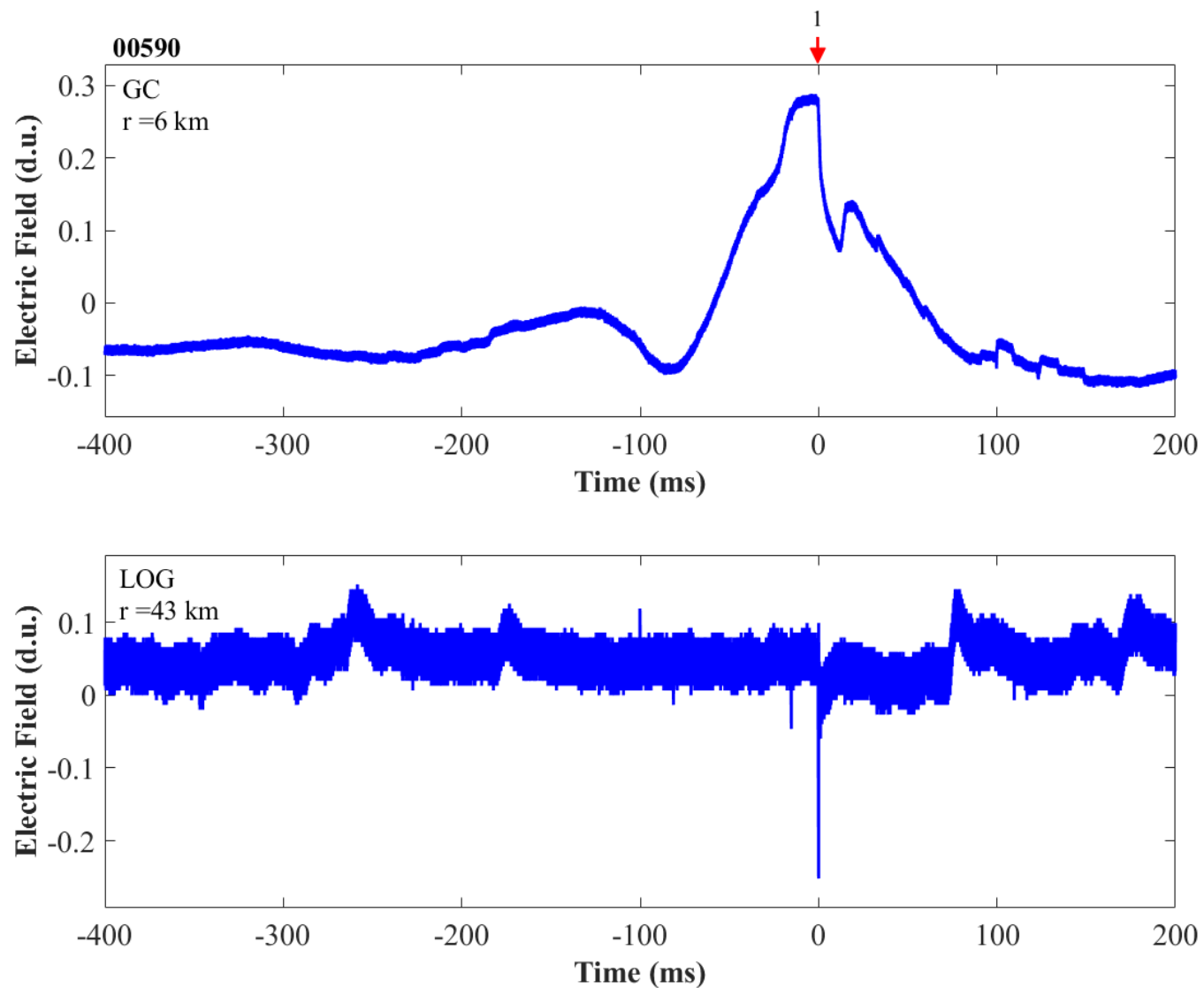


Figure B-58. Two-station electric field waveforms of flash 00590.

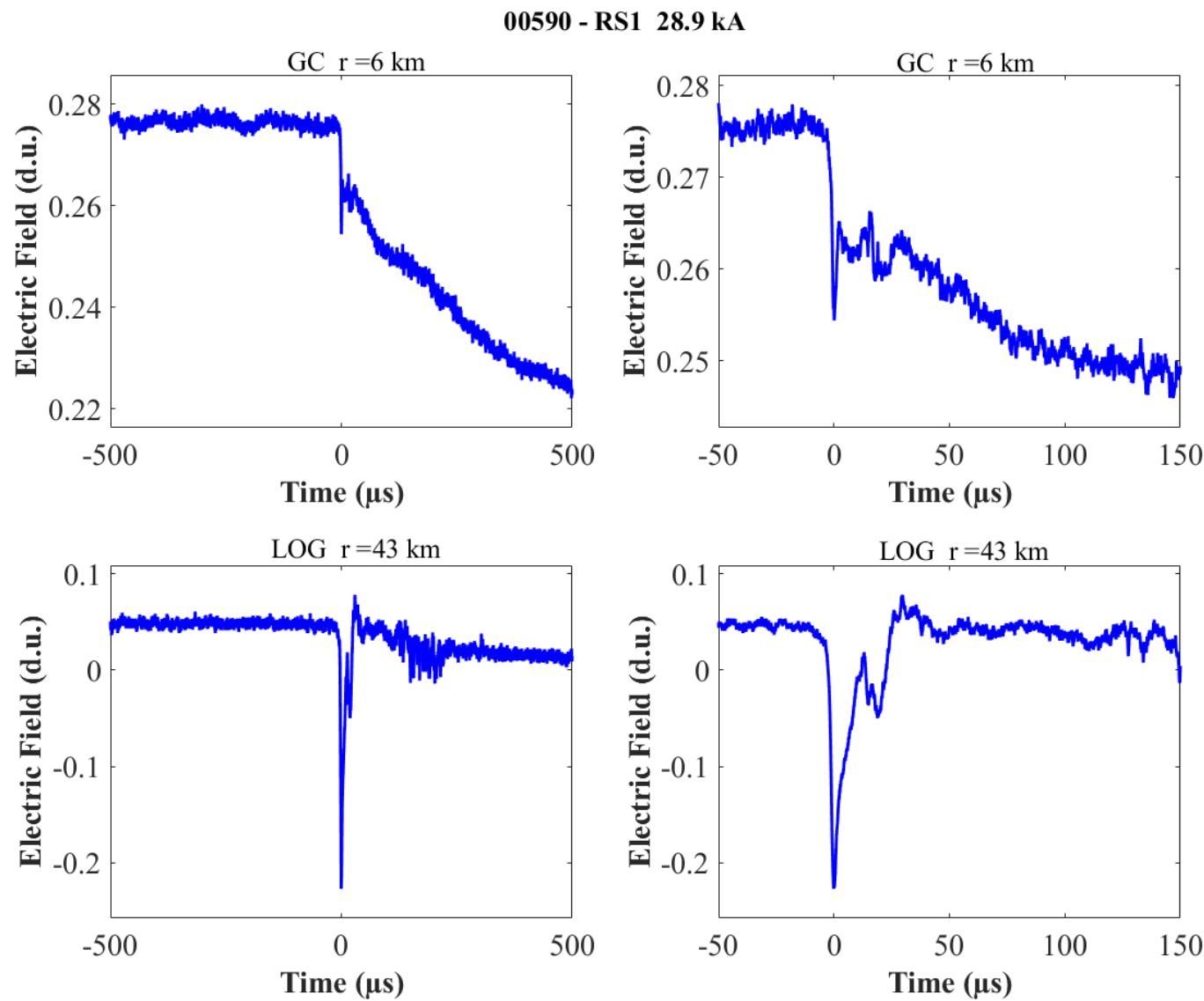


Figure B-59. Two-station electric field waveforms of the RS1 of flash 00590.

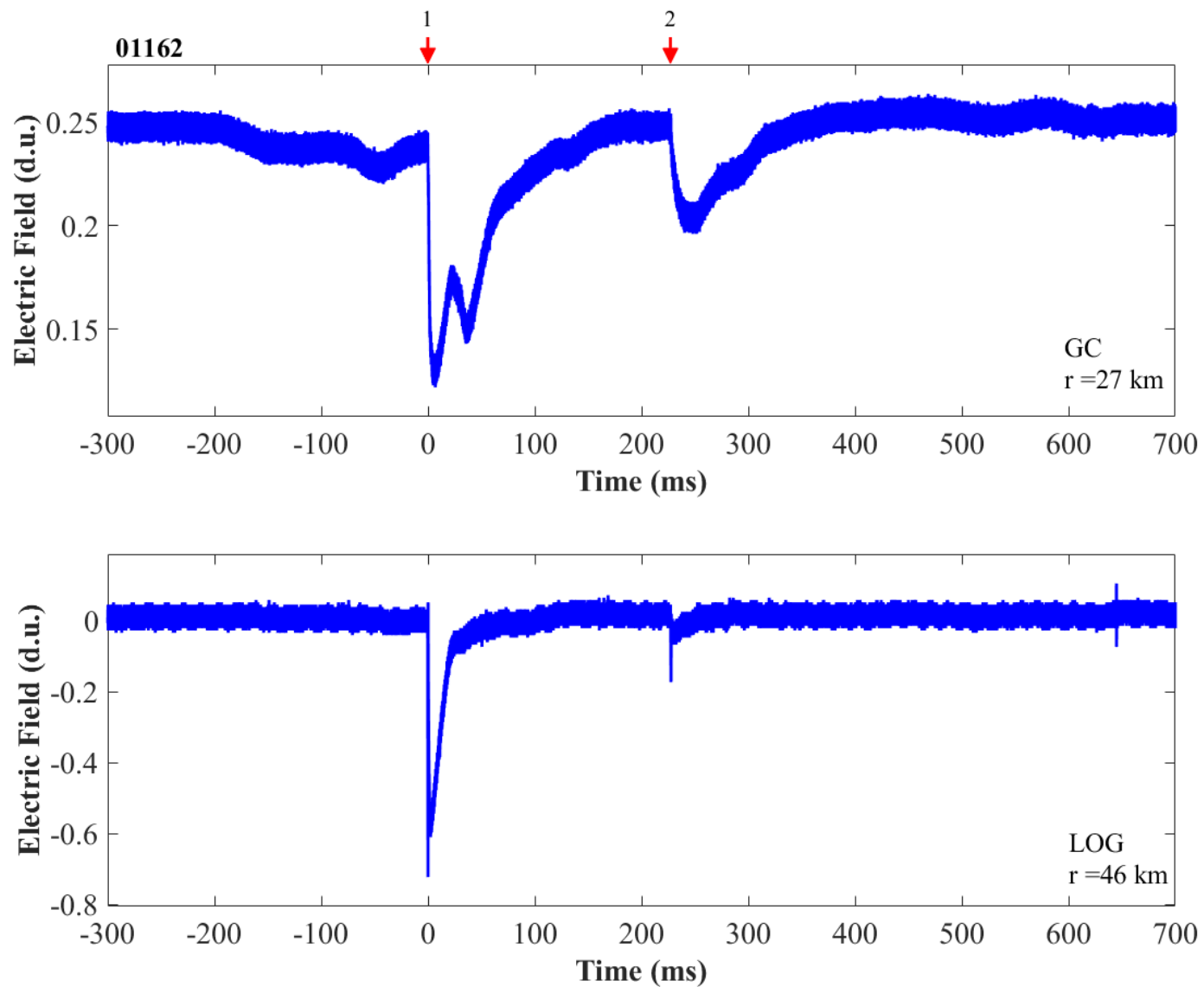


Figure B-60. Two-station electric field waveforms of flash 01162.

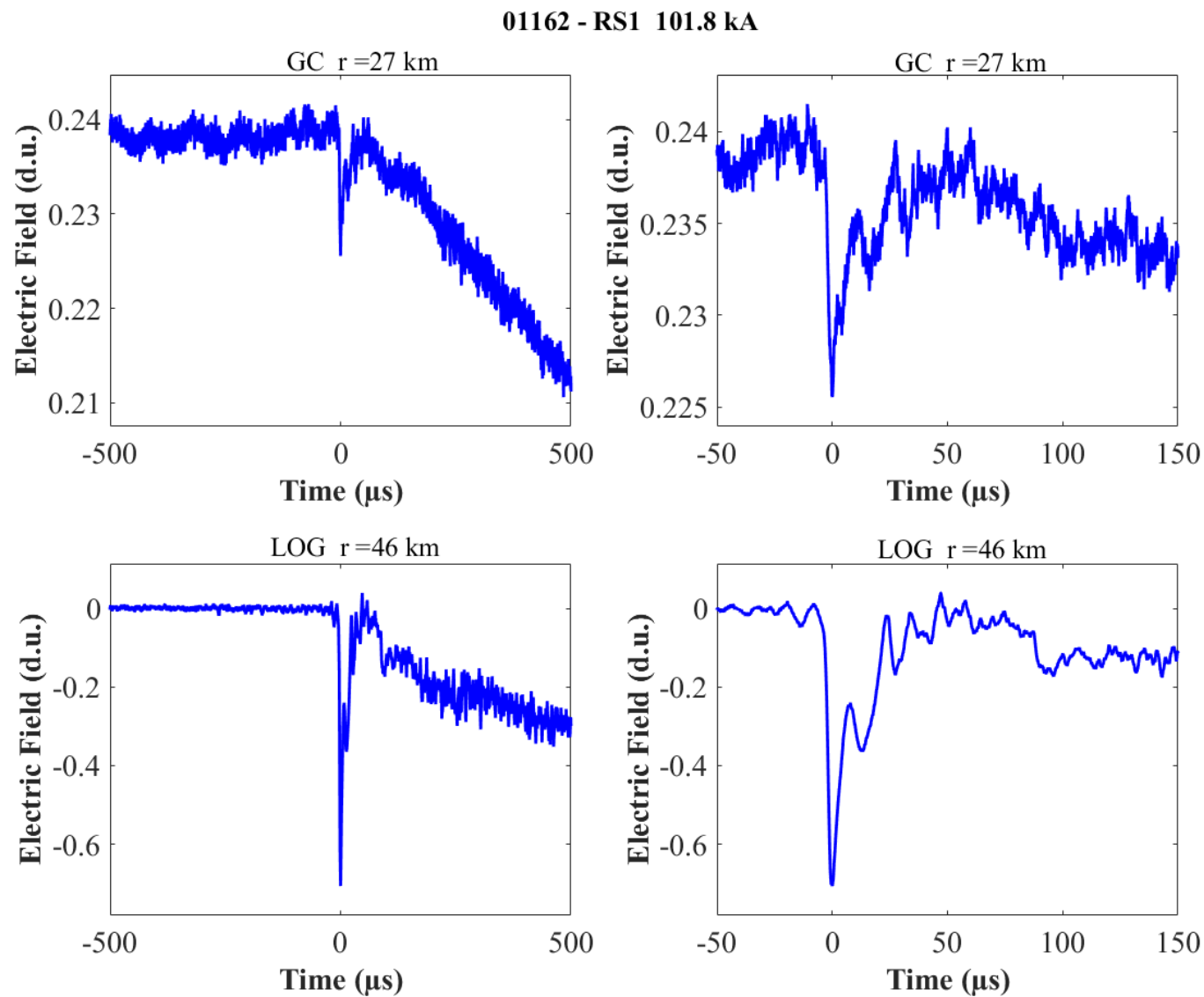


Figure B-61. Two-station electric field waveforms of the RS1 of flash 01162.

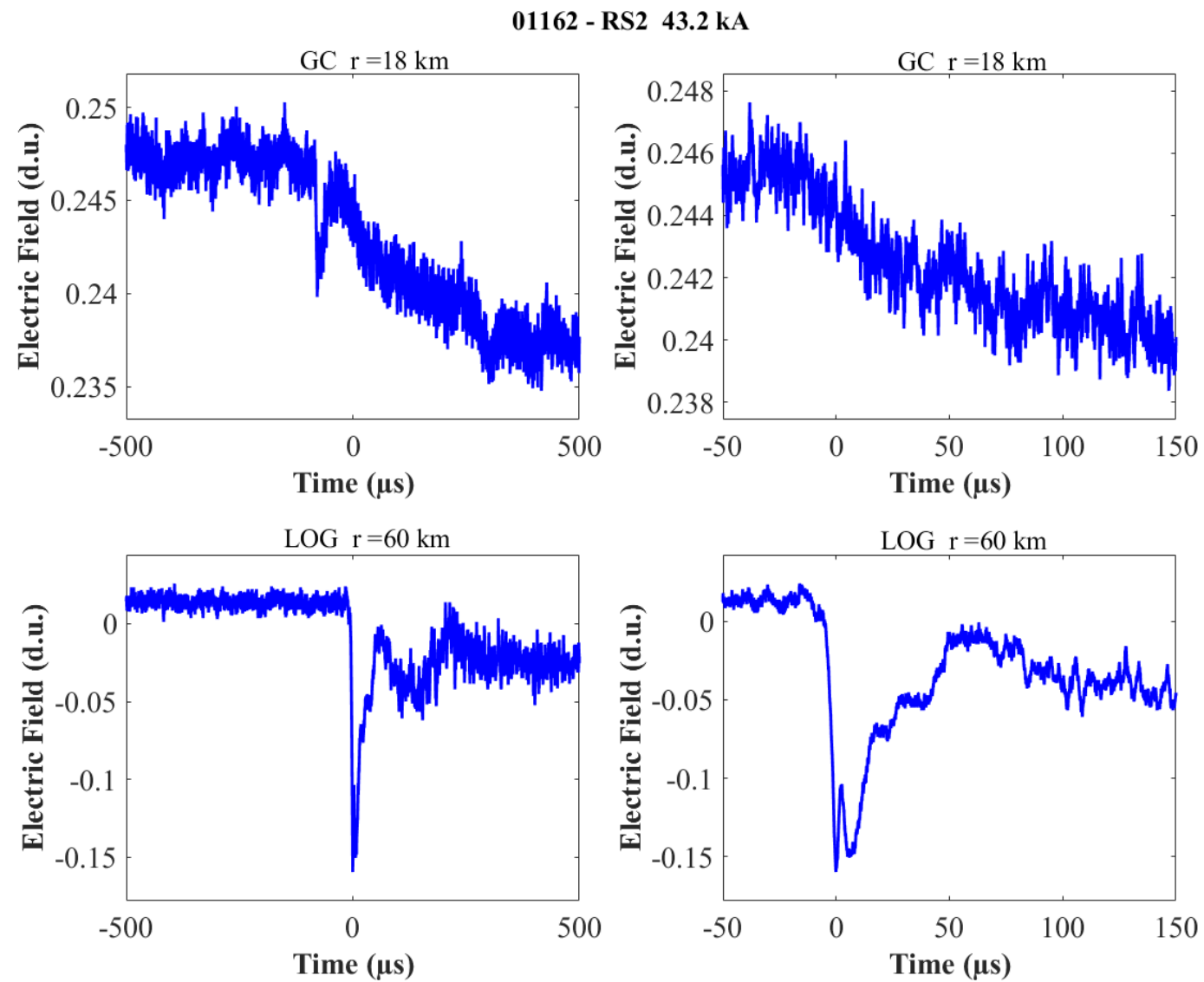


Figure B-62. Two-station electric field waveforms of the RS2 of flash 01162.

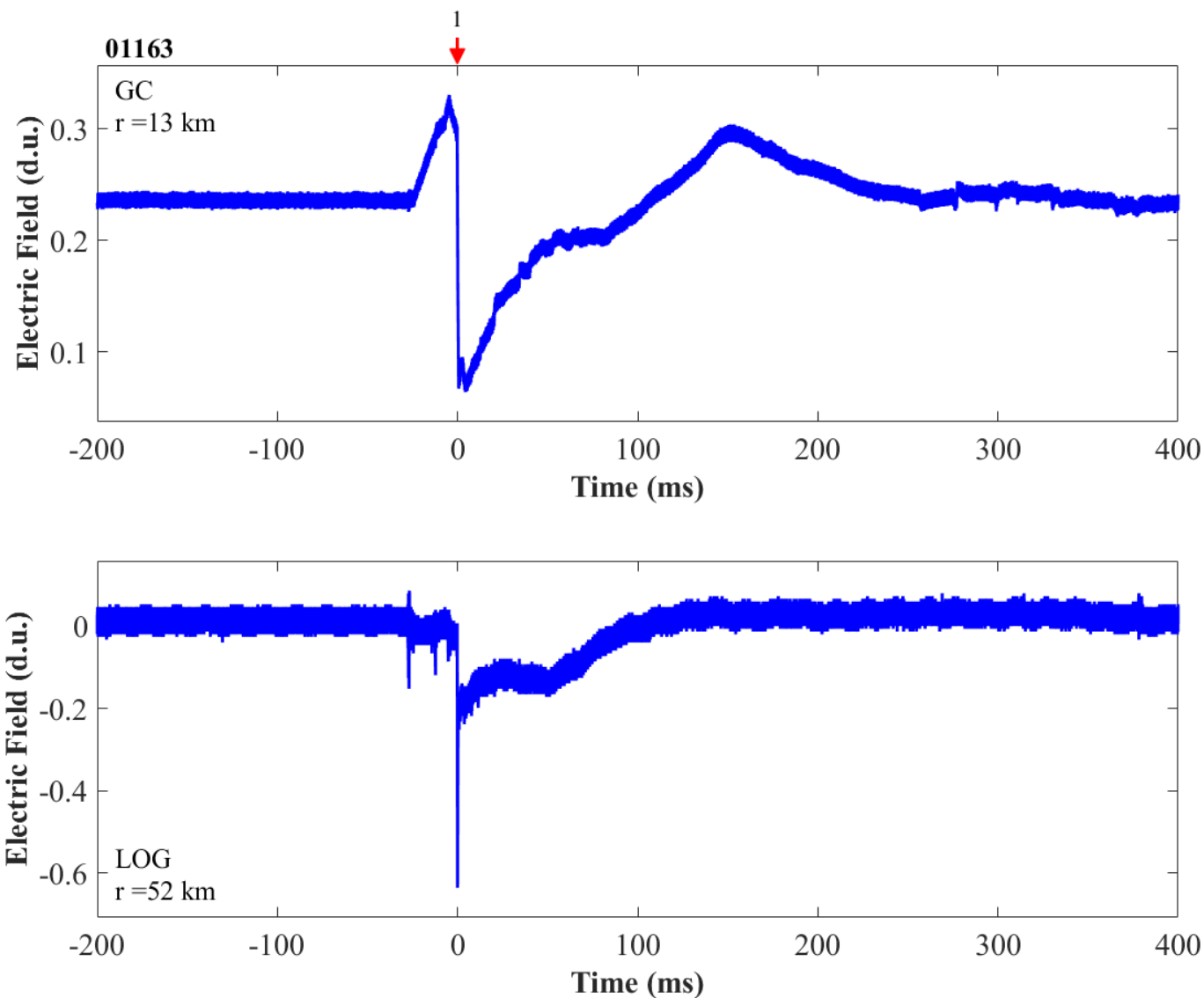


Figure B-63. Two-station electric field waveforms of flash 01163.

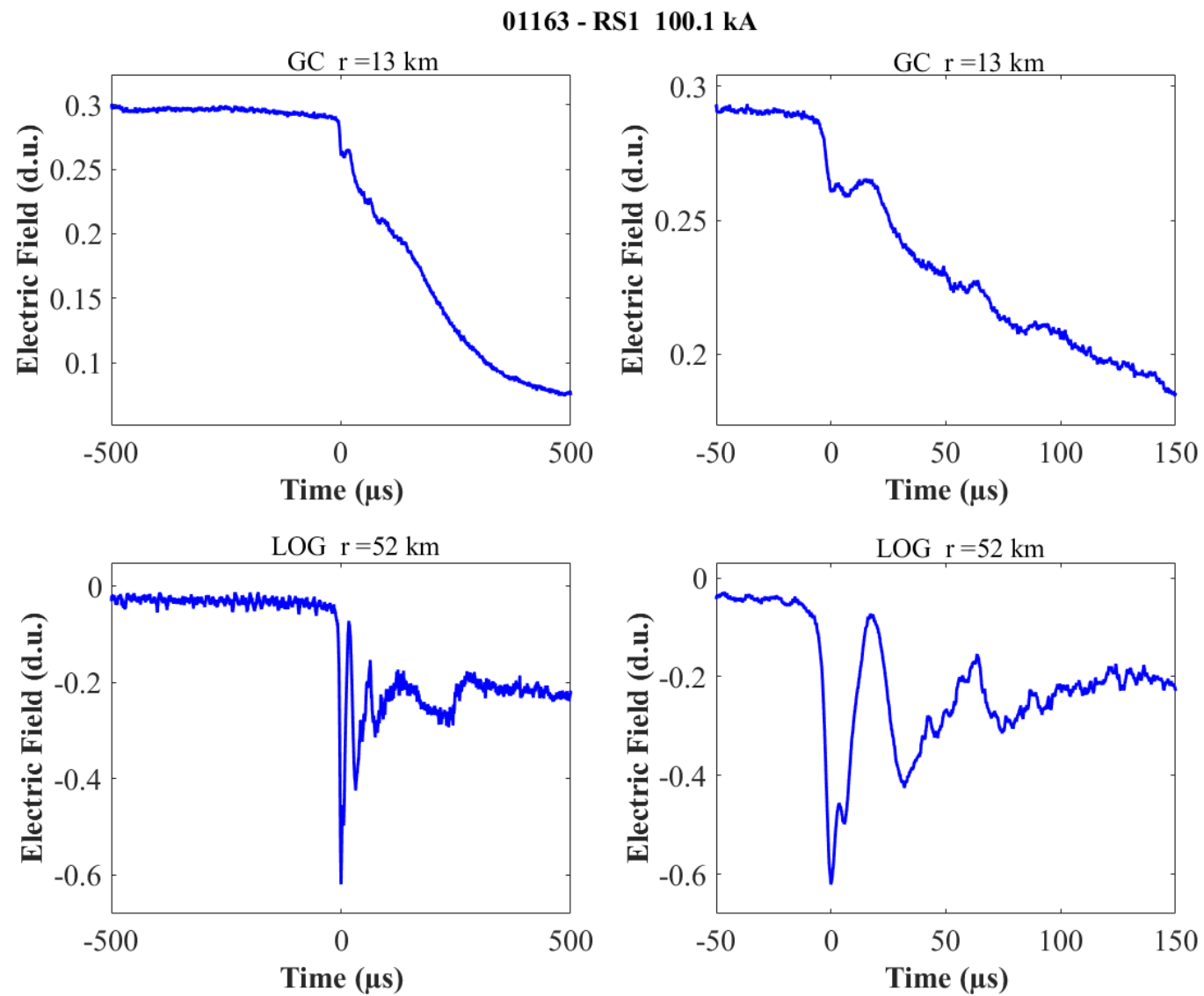
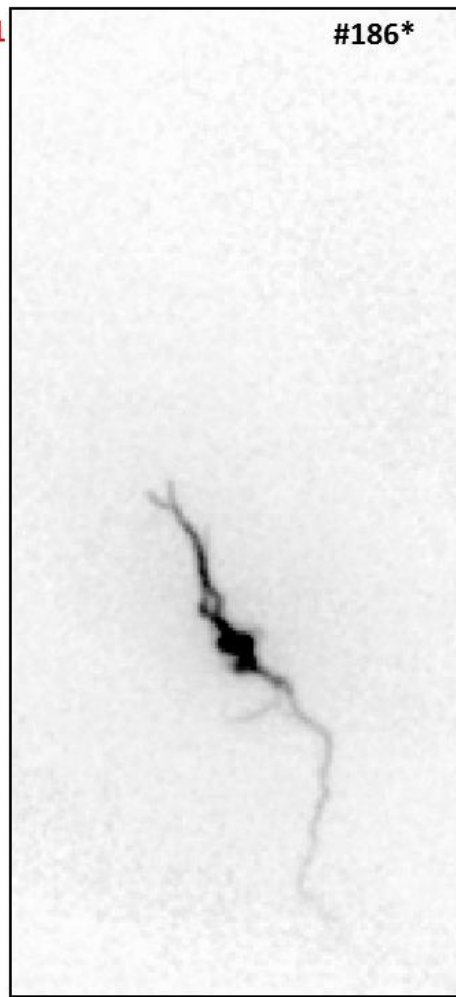


Figure B-64. Two-station electric field waveforms of the RS1 of flash 01163.

APPENDIX D
HIGH-SPEED VIDEO RECORDS OF THE TWO FLASHES TERMINATED ON THE 257-M
TOWER

This section shows the images from high-speed video records of the two flashes terminated on the 257-m tower. More information of the two flashes are given in Chapter 6. The frame rate of the camera is 1000 fps with 1 ms exposure time. Frame number is given in the upper right corner of each panel. Frame number marked by star indicates the strongest enhancement of the image. It seems that all strokes in flash 1593 were initiated by bi-directional leaders with the positive ends propagating upward with many branches and the negative ends sharing the same channel that terminated on the 257-m tower.

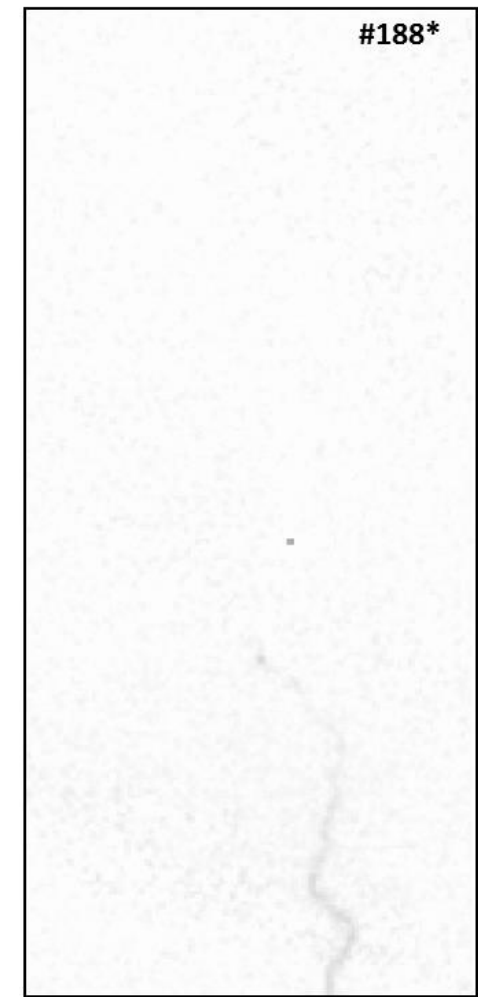
1593_R1



#186*



#187



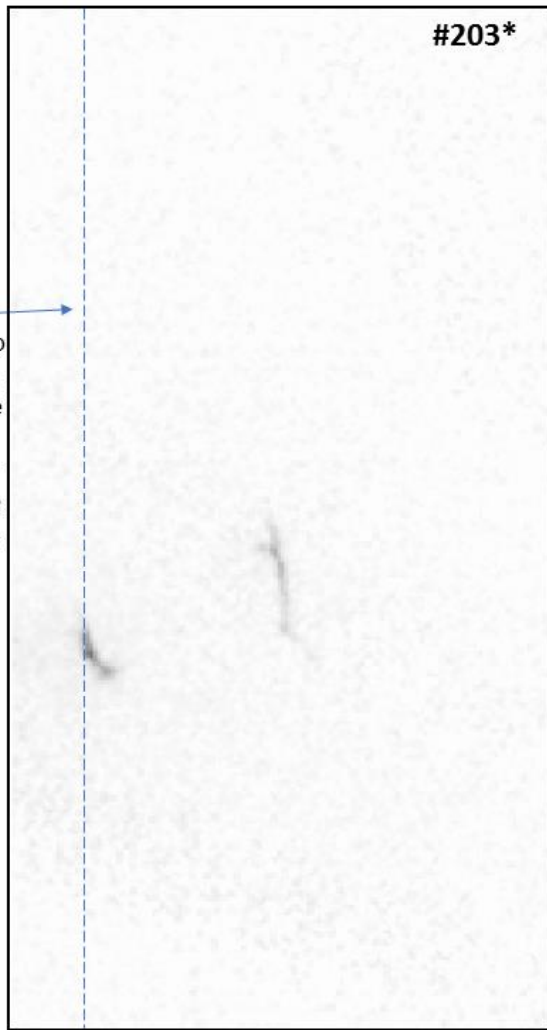
#188*

Figure C-1. Frames showing the first stroke of flash 1593. Frame number is at the upper right corner. The star indicates the strongest enhancement of the image. The frame rate is 1000 fps and the exposure time is 1 ms.

1593_R2

#203*

The window for
this frame is
wider in order to
not crop the left
aloft branch, the
left edge of the
original window
is marked by the
blue dashed line



#204*

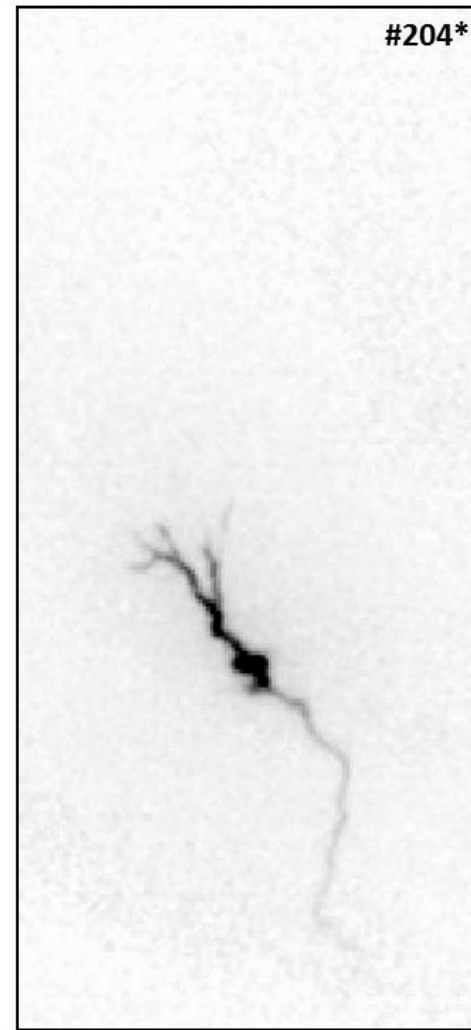


Figure C-2. First two frames showing the second of flash 1593.

1593_R2



#205

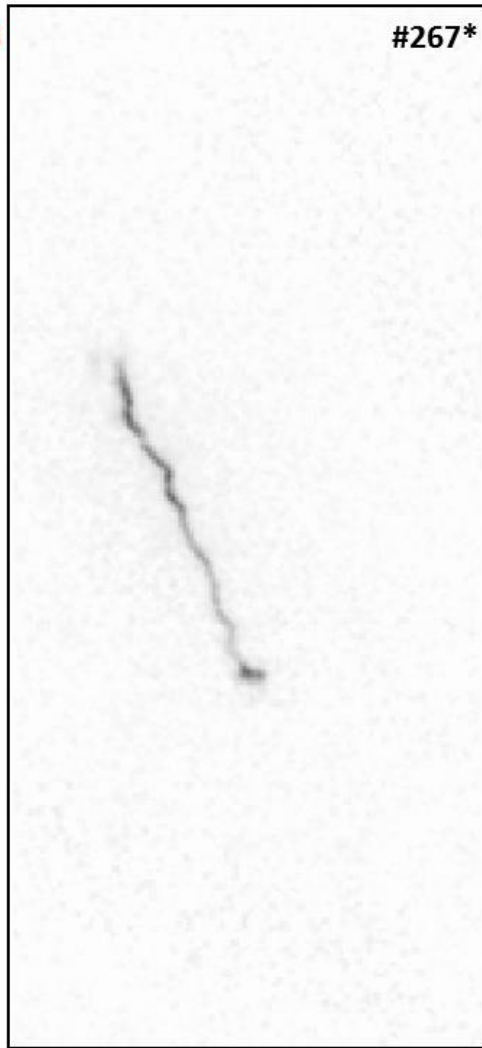
#206*



Figure C-3. Last two frames showing the second stroke of flash 1593.

1593_R3

#267*



#268



#269*

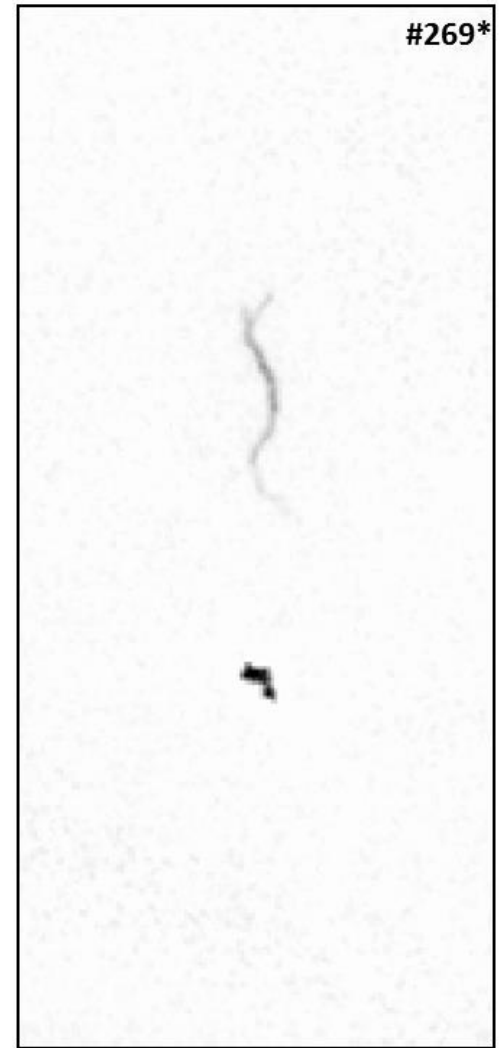
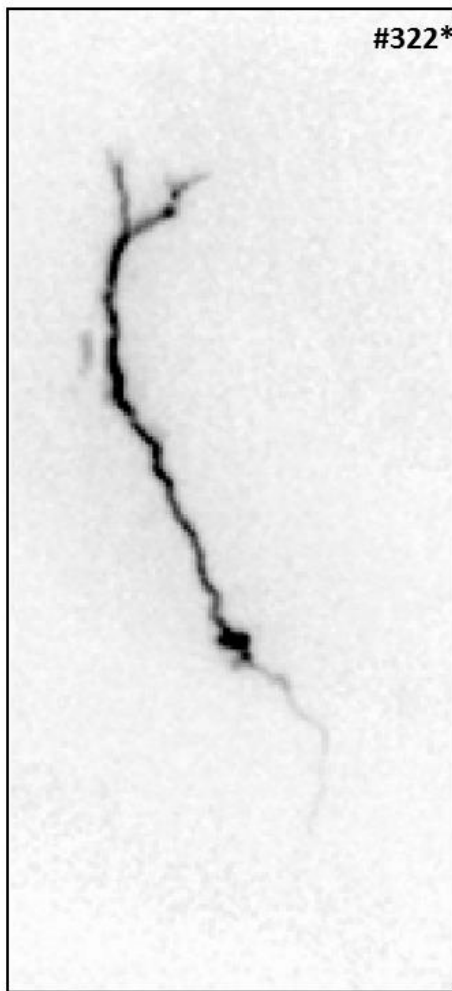


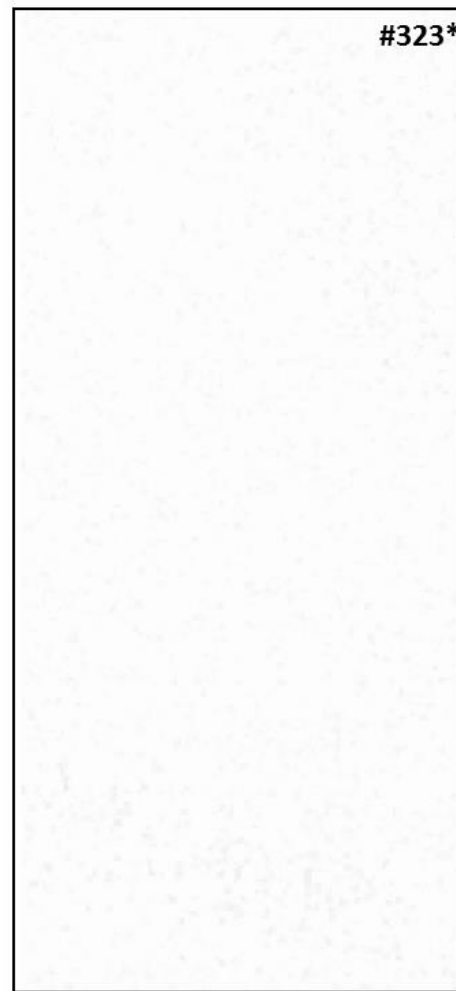
Figure C-4. Frames showing the third stroke of flash 1593.

1593_R4



#322*

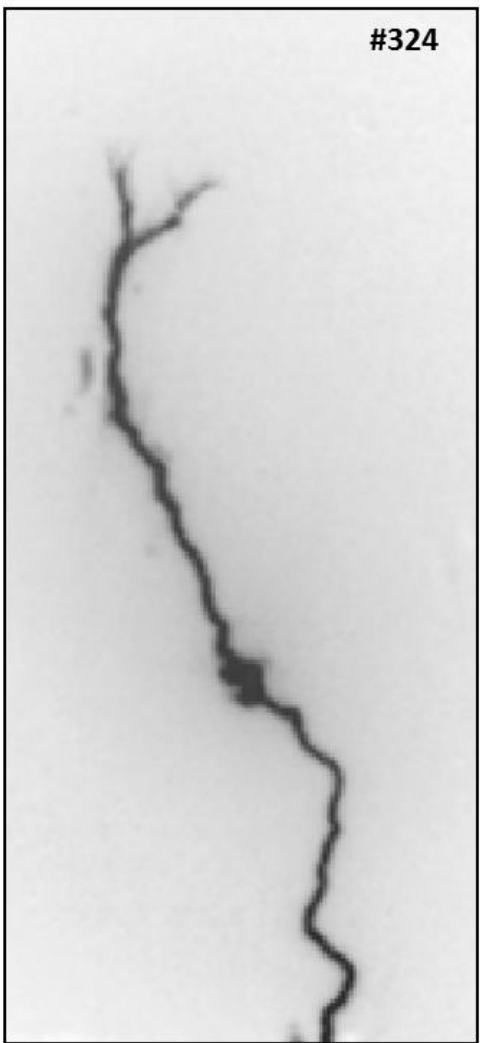
#323*



nothing in
this frame

Figure C-5. First two frames showing the fourth stroke of flash 1593.

1593_R4



#324

#325*

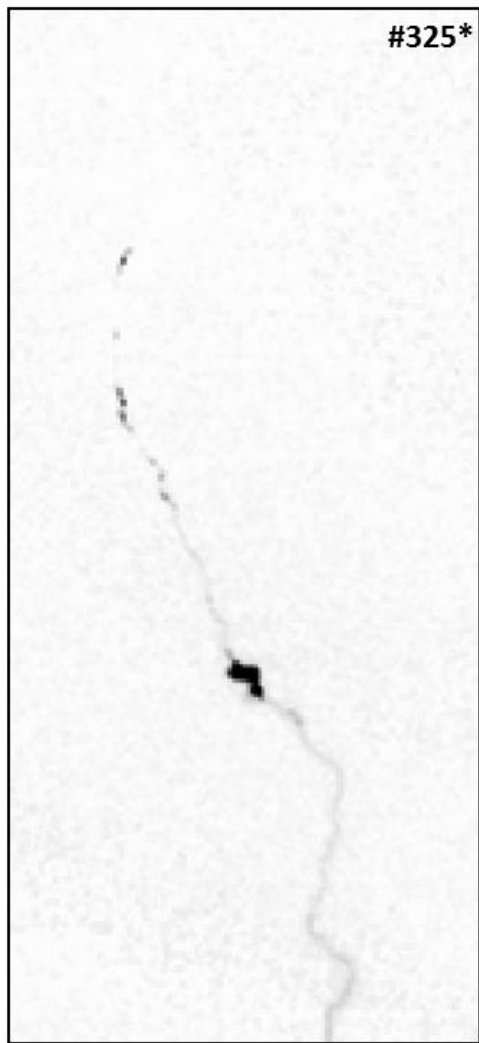
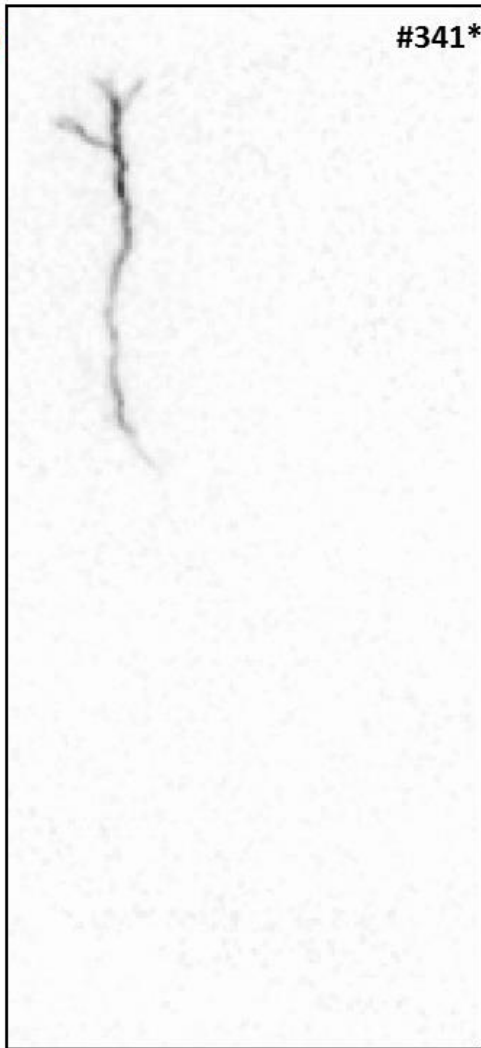


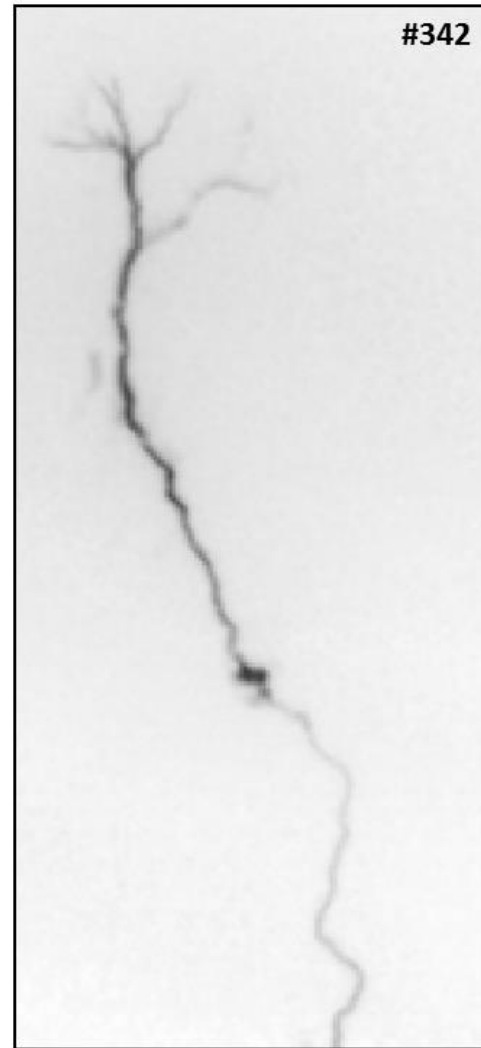
Figure C-6. Last two frames showing the fourth stroke of flash 1593.

1593_R5

#341*



#342



#343*

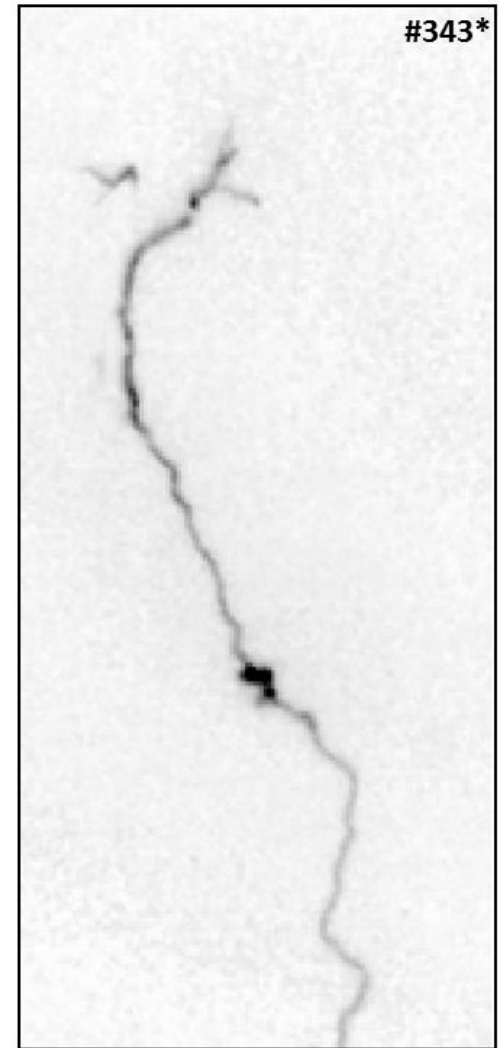
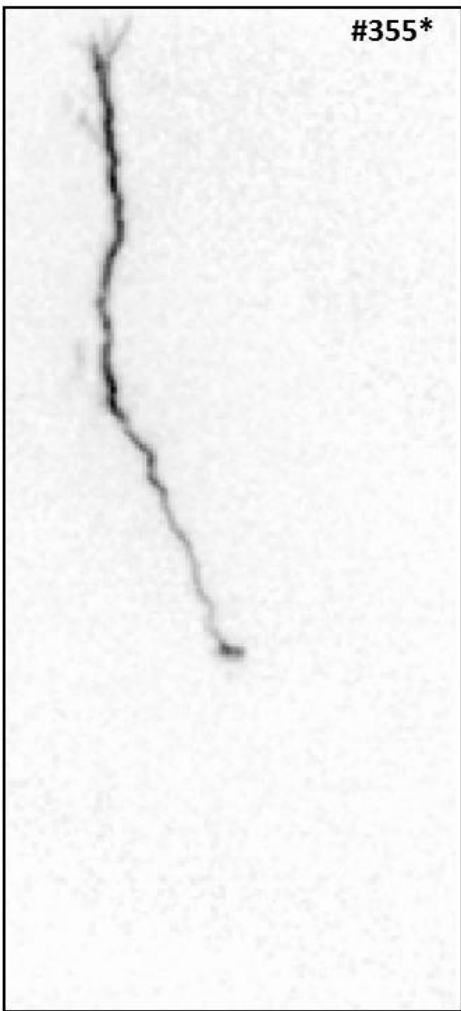


Figure C-7. Frames showing the fifth stroke of flash 1593.

1593_R6



#355*

#356*

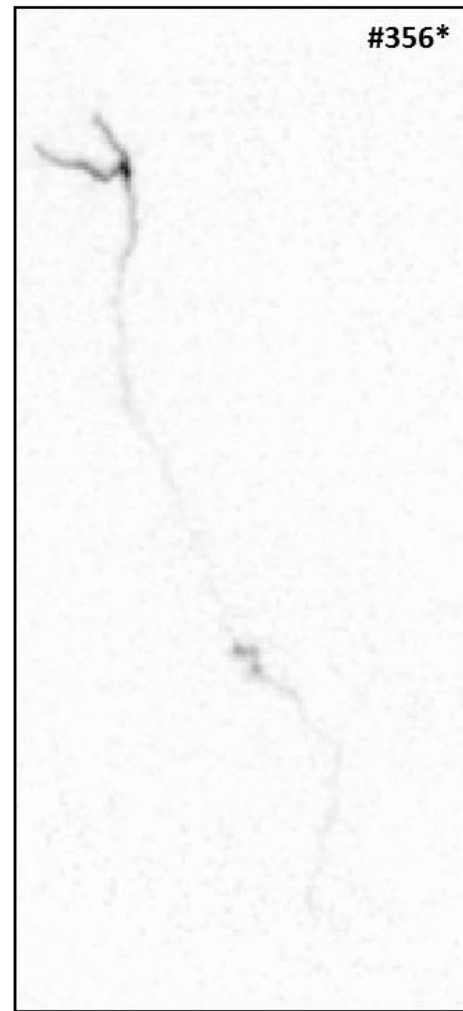
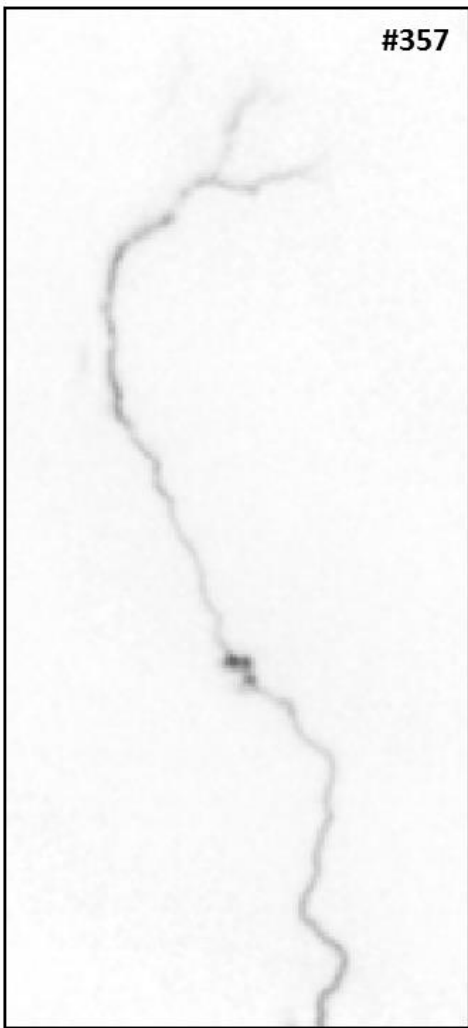


Figure C-8. First two frames showing the sixth stroke of flash 1593.

1593_R6



#357

#358*

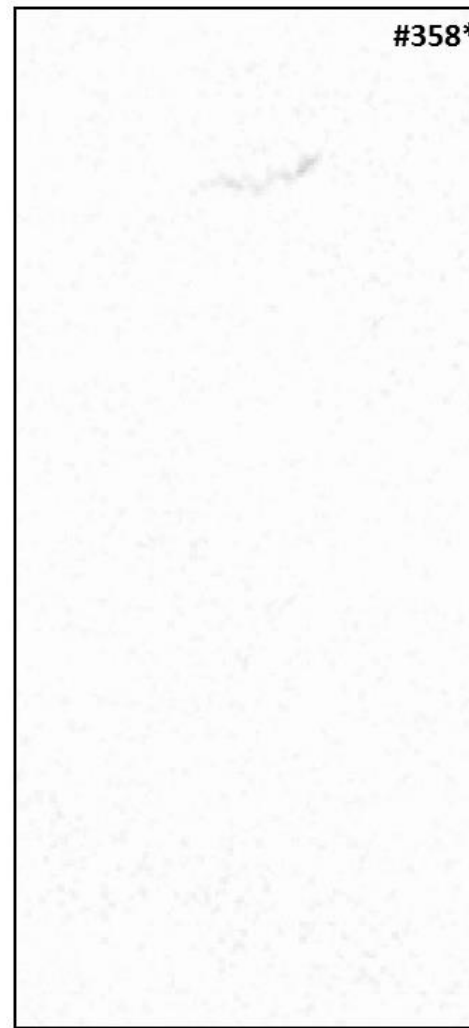
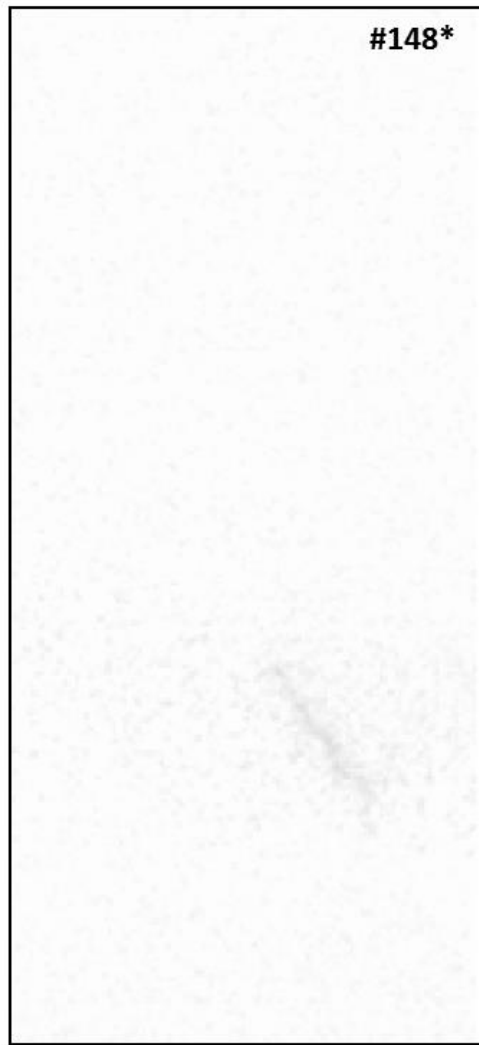


Figure C-9. Last two frames showing the sixth stroke of flash 1593.

1594_R2

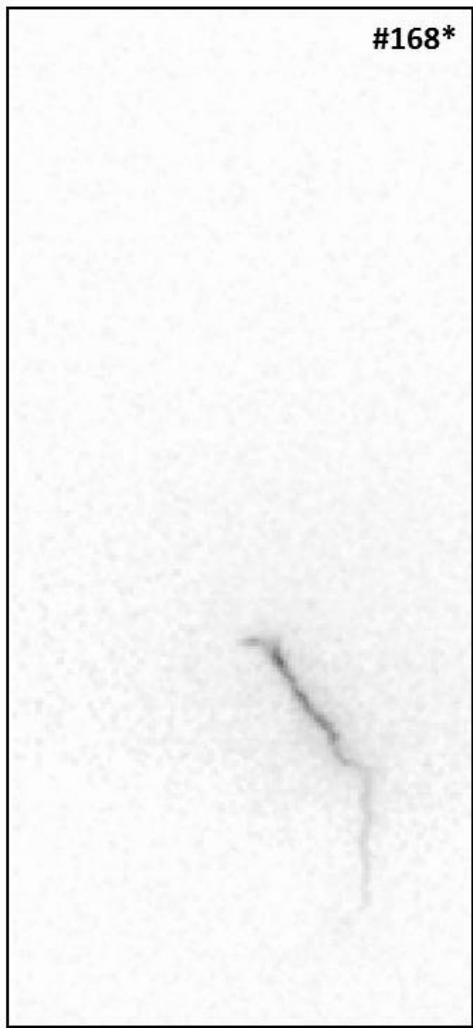


#149*



Figure C-10. Frames showing the second stroke of flash 1594.

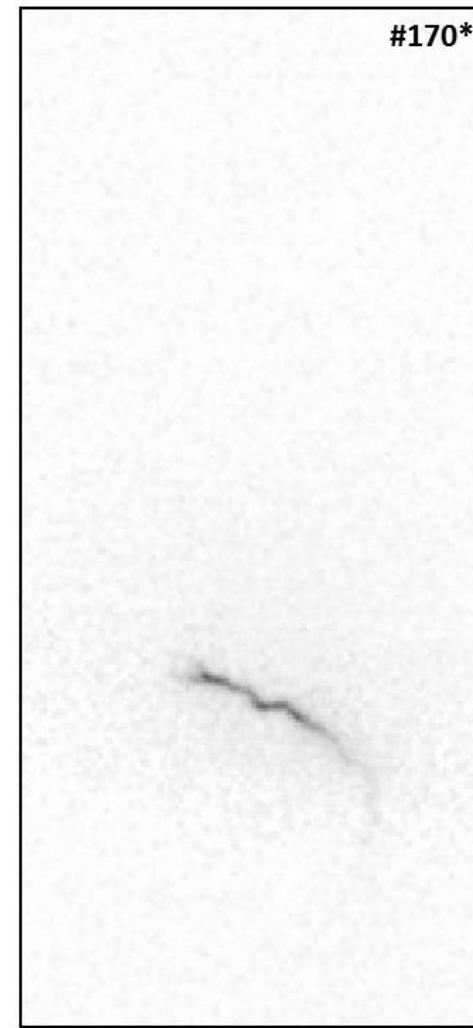
1594_R3



#168*



#169*



#170*

Figure C-11. Frames showing the third stroke of flash 1594.

LIST OF REFERENCES

- Azadifar, M., G. Diendorfer, M. Paolone, D. Pavanello, F. Rachidi, V. A. Rakov, M. Rubinstein, and W. Schulz (2017), A Large Bipolar Event Recorded at the Säntis Tower, in *4th International Symposium on Winter Lightning (ISWL)*, Joetsu, Niigata-ken, Japan.
- Baba, Y., and V. A. Rakov (2005), On the use of lumped sources in lightning return stroke models, *J. Geophys. Res. Atmos.*, 110(3), 1–10, doi:10.1029/2004JD005202.
- Baharudin, Z. A., N. A. Ahmad, M. Fernando, V. Cooray, and J. S. Mäkelä (2012), Comparative study on preliminary breakdown pulse trains observed in Johor, Malaysia and Florida, USA, *Atmos. Res.*, 117, 111–121, doi:10.1016/j.atmosres.2012.01.012.
- Baharudin, Z. A., N. A. Ahmad, J. S. Mäkelä, M. Fernando, and V. Cooray (2014), Negative cloud-to-ground lightning flashes in Malaysia, *J. Atmos. Solar-Terrestrial Phys.*, 108, 61–67, doi:10.1016/j.jastp.2013.12.001.
- Ballarotti, M. G., M. M. F. Saba, and J. Pinto (2005), High-speed camera observations of negative ground flashes on a millisecond-scale, *Geophys. Res. Lett.*, 32(23), 1–4, doi:10.1029/2005GL023889.
- Ballarotti, M. G., C. Medeiros, M. M. F. Saba, W. Schulz, and O. Pinto (2012), Frequency distributions of some parameters of negative downward lightning flashes based on accurate-stroke-count studies, *J. Geophys. Res. Atmos.*, 117(D6), n/a-n/a, doi:10.1029/2011JD017135.
- Biagi, C. J., K. L. Cummins, K. E. Kehoe, and E. P. Krider (2007), National Lightning Detection Network (NLDN) performance in southern Arizona, Texas, and Oklahoma in 2003–2004, *J. Geophys. Res.*, 112(D5), D05208, doi:10.1029/2006JD007341.
- Biagi, C. J., M. A. Uman, J. D. Hill, and D. M. Jordan (2011), Observations of the initial, upward-propagating, positive leader steps in a rocket-and-wire triggered lightning discharge, *Geophys. Res. Lett.*, 38(24), 1–5, doi:10.1029/2011GL049944.
- Biagi, C. J., M. A. Uman, J. D. Hill, V. A. Rakov, and D. M. Jordan (2012), Transient current pulses in rocket-extended wires used to trigger lightning, *J. Geophys. Res. Atmos.*, 117(D7), D07205, doi:10.1029/2011JD016161.
- Brook, M. (1992), Breakdown electric fields in winter storms, *Res. Lett. Atmos. Electr.*, 12, 47–52.
- Buck, T. L., A. Nag, and M. J. Murphy (2014), Improved Cloud-to-Ground and Intracloud Lightning Detection with the LS7002 Advanced Total Lightning Sensor, in *WMO Technical Conference on Meteorological and Environmental Instruments and Methods of Observation*, Saint Petersburg, Russia.
- Carvalho, F. L., M. A. Uman, D. M. Jordan, and T. Ngin (2015), Lightning current and

- luminosity at and above channel bottom for return strokes and M-components, *J. Geophys. Res. Atmos.*, 120(20), 10,645–10,663, doi:10.1002/2015JD023814.
- Chen, L., Q. Zhang, W. Hou, and Y. Tao (2015a), On the field-to-current conversion factors for large bipolar lightning discharge events in winter thunderstorms in Japan, *J. Geophys. Res. Atmos.*, 120(14), 6898–6907, doi:10.1002/2015JD023344.
- Chen, L., W. Lu, Y. Zhang, and D. Wang (2015b), Optical progression characteristics of an interesting natural downward bipolar lightning flash, *J. Geophys. Res. Atmos.*, 120(2), 708–715, doi:10.1002/2014JD022463.
- Clarence, N. D., and D. J. Malan (1957), Preliminary discharge processes in lightning flashes to ground, *Q. J. R. Meteorol. Soc.*, 83(356), 161–172, doi:10.1002/qj.49708335603.
- Cooray, V., and K. P. S. C. Jayaratne (1994), Characteristics of lightning flashes observed in Sri Lanka in the tropics, *J. Geophys. Res. Atmos.*, 99(D10), 21051–21056, doi:10.1029/94JD01519.
- Cooray, V., and R. Jayaratne (2000), What directs a lightning flash towards ground?, *Sri Lankan J. Phys.*, 1, 1–10, doi:10.4038/sljp.v1i0.165.
- Cooray, V., and H. Pérez (1994), Some features of lightning flashes observed in Sweden, *J. Geophys. Res.*, 99(D5), 10683, doi:10.1029/93JD02366.
- Cummins, K. L., and M. J. Murphy (2009), An overview of lightning locating systems: History, techniques, and data uses, with an in-depth look at the U.S. NLDN, *IEEE Trans. Electromagn. Compat.*, 51(3), 499–518, doi:10.1109/TEMC.2009.2023450.
- Cummins, K. L., M. J. Murphy, E. A. Bardo, W. L. Hiscox, R. B. Pyle, and A. E. Pifer (1998), A Combined TOA/MDF Technology Upgrade of the U.S. National Lightning Detection Network, *J. Geophys. Res.*, 103(D8), 9035, doi:10.1029/98JD00153.
- Diendorfer, G., H. Zhou, and H. Pichler (2011), Review of 10 years of lightning measurement at the Gaisberg Tower in Austria, in *The 3rd International Symposium on Winter Lightning (ISWL)*, pp. 185–190, Sapporo, Japan.
- Dwyer, J. R., and M. A. Uman (2013), The physics of lightning, *Phys. Rep.*, 534(4), 147–241, doi:10.1016/j.physrep.2013.09.004.
- Fleenor, S. A., C. J. Biagi, K. L. Cummins, E. P. Krider, and X. M. Shao (2009), Characteristics of cloud-to-ground lightning in warm-season thunderstorms in the Central Great Plains, *Atmos. Res.*, 91(2–4), 333–352, doi:10.1016/j.atmosres.2008.08.011.
- Frey, H. U., S. B. Mende, S. A. Cummer, A. B. Chen, R. R. Hsu, H. T. Su, Y. S. Chang, T. Adachi, H. Fukunishi, and Y. Takahashi (2005), Beta-type stepped leader of elve-producing lightning, *Geophys. Res. Lett.*, 32(13), 1–4, doi:10.1029/2005GL023080.
- Gamerota, W. (2014), The Dart-Stepped Leader in Rocket-Triggered Lightning, University of

Florida.

Gomes, C., V. Cooray, and C. Jayaratne (1998), Comparison of preliminary breakdown pulses observed in Sweden and in Sri Lanka, *J. Atmos. Solar-Terrestrial Phys.*, *60*(10), 975–979, doi:10.1016/S1364-6826(98)00007-8.

Heavner, M. J., D. A. Smith, A. R. Jacobson, and R. J. Sheldon (2002), LF/VLF and VHF lightning fast-stepped leader observations, *J. Geophys. Res.*, *107*(D24), 4791, doi:10.1029/2001JD001290.

Ishii, M., and M. Saito (2009), Lightning electric field characteristics associated with transmission-line faults in winter, *IEEE Trans. Electromagn. Compat.*, *51*(3), 459–465, doi:10.1109/TEMC.2009.2025496.

Ishii, M., M. Saito, T. Miki, D. Tanka, T. Shindo, A. Asakawa, H. Motoyama, Y. Suzuhigashi, and H. Taguchi (2013), Reproduction of Electromagnetic Field Waveforms and Tower Currents Associated with Return Strokes Struck Tokyo Skytree, in *XII International Symposium on Lightning Protection (SIPDA)*, pp. 96–101, Belo Horizonte, Brazil.

Jerauld, J., V. A. Rakov, M. A. Uman, K. J. Rambo, and D. M. Jordan (2005), An evaluation of the performance characteristics of the U.S. National Lightning Detection Network in Florida using rocket-triggered lightning, *J. Geophys. Res.*, *110*(D19), D19106, doi:10.1029/2005JD005924.

Jerauld, J. E., M. A. Uman, V. A. Rakov, K. J. Rambo, D. M. Jordan, and G. H. Schnetzer (2009), Measured electric and magnetic fields from an unusual cloud-to-ground lightning flash containing two positive strokes followed by four negative strokes, *J. Geophys. Res. Atmos.*, *114*(19), 1–17, doi:10.1029/2008JDO11660.

Jordan, D. M., V. P. Idone, V. A. Rakov, M. A. Uman, W. H. Beasley, and H. Jurenka (1992), Observed dart leader speed in natural and triggered lightning, *J. Geophys. Res. Atmos.*, *97*(D9), 9951–9957, doi:10.1029/92JD00566.

Karunarathne, S., T. C. Marshall, M. Stolzenburg, and N. Karunarathna (2014), Modeling initial breakdown pulses of CG lightning flashes, *J. Geophys. Res. Atmos.*, *119*(14), 9003–9019, doi:10.1002/2014JD021553.

Kitagawa, N., M. Brook, and E. . Workman (1962), Continuing currents in cloud to ground lightning discharges, *J. Geophys. Res.*, *67*, 67(2), 637–647, doi:10.1029/JZ067i002p00637.

Kolmašová, I., O. Santolík, T. Farges, W. Rison, R. Lán, and L. Uhlíř (2014), Properties of the unusually short pulse sequences occurring prior to the first strokes of negative cloud-to-ground lightning flashes, *Geophys. Res. Lett.*, *41*, 6192, doi:10.1002/2014GL060913.

Kotovsky, D. A., R. C. Moore, Y. Zhu, M. D. Tran, V. A. Rakov, J. T. Pilkey, J. A. Caicedo, B. Hare, D. M. Jordan, and M. A. Uman (2016), Initial breakdown and fast leaders in lightning discharges producing long-lasting disturbances of the lower ionosphere, *J. Geophys. Res. Sp. Phys.*, *121*(6), 5794–5804, doi:10.1002/2015JA022266.

Krehbiel, P. R., M. Brook, and R. A. McCrory (1979), An analysis of the charge structure of lightning discharges to ground, *J. Geophys. Res.*, 84(C5), 2432, doi:10.1029/JC084iC05p02432.

Krider, E. P., G. J. Radda, and R. C. Noggle (1975), Regular radiation field pulses produced by intracloud lightning discharges, *J. Geophys. Res.*, 80(27), 3801–3804, doi:10.1029/JC080i027p03801.

Lalande, P., A. Bondiou-Clergerie, P. Laroche, A. Eybert-Berard, J.-P. Berlandis, B. Bador, A. Bonamy, M. A. Uman, and V. A. Rakov (1998), Leader properties determined with triggered lightning techniques, *J. Geophys. Res. Atmos.*, 103(D12), 14109–14115, doi:10.1029/97JD02492.

Liu, C., and S. Heckman (2011), The application of total lightning detection and cell tracking for severe weather prediction, in *91st American Meteorological Society Annual Meeting*, Seattle.

Lu, W., Y. Ma, Y. Zhang, J. Yang, W. Yao, D. Zheng, Q. Meng, and Y. Zhang (2014), Total-Sky Lightning Event Observation System and Method,

MacDonald, J. H. (2008), *Handbook of Biological Statistics*, Sparky House Publishing.

Mallick, S. (2013), Observation of Natural and Rocket-Triggered Lightning at Three Research Stations in Florida and with Large-Scale Locating Networks, Ph. D. Proposal, University of Florida.

Mallick, S., and V. A. Rakov (2014), Characterization of far electric field waveforms produced by rocket-triggered lightning, in *2014 International Conference on Lightning Protection, ICLP 2014*, pp. 1527–1534, Shanghai, China.

Mallick, S., V. A. Rakov, J. D. Hill, W. R. Gamerota, M. A. Uman, S. Heckman, C. D. Sloop, and C. Liu (2013), Calibration of the ENTLN against rocket-triggered lightning data, in *2013 International Symposium on Lightning Protection, (XII SIPDA)*, pp. 39–46, Belo Horizonte, Brazil.

Mallick, S. et al. (2014), Performance characteristics of the NLDN for return strokes and pulses superimposed on steady currents, based on rocket-triggered lightning data acquired in Florida in 2004–2012, *J. Geophys. Res. Atmos.*, 119(7), 2013JD021401, doi:10.1002/2013JD021401.

Mallick, S. et al. (2015), Performance characteristics of the ENTLN evaluated using rocket-triggered lightning data, *Electr. Power Syst. Res.*, 118, 15–28, doi:10.1016/j.epsr.2014.06.007.

Marshall, T., W. Schulz, N. Karunarathna, S. Karunarathne, M. Stolzenburg, C. Vergeiner, and T. Warner (2014), On the percentage of lightning flashes that begin with initial breakdown pulses, *J. Geophys. Res. Atmos.*, 119(2), 445–460, doi:10.1002/2013JD020854.

- Maslowski, G., and V. A. Rakov (2006), A study of the lightning channel corona sheath, *J. Geophys. Res. Atmos.*, 111(14), 1–16, doi:10.1029/2005JD006858.
- Montanyà, J., O. Van Der Velde, E. Williams, N. Pineda, D. Romero, and G. Solà (2014), Observation and properties of a sub-cloud bidirectional leader, in *XV International Conference on Atmospheric Electricity (ICAE)*, Norman, Oklahoma, U.S.A.
- Murphy, J. M., and A. Nag (2015), Cloud lightning performance and climatology of the U.S. based on the upgraded U.S. National Lightning Detection Network, in *Seventh Conference on the Meteorological Applications of Lightning Data*, Phoenix, AZ.
- Nag, A., and V. a. Rakov (2010a), Compact intracloud lightning discharges: 1. Mechanism of electromagnetic radiation and modeling, *J. Geophys. Res.*, 115(D20), D20102, doi:10.1029/2010JD014235.
- Nag, A., and V. a. Rakov (2010b), Compact intracloud lightning discharges: 2. Estimation of electrical parameters, *J. Geophys. Res.*, 115(D20), D20103, doi:10.1029/2010JD014237.
- Nag, A., and V. A. Rakov (2008), Pulse trains that are characteristic of preliminary breakdown in cloud-to-ground lightning but are not followed by return stroke pulses, *J. Geophys. Res.*, 113(D1), D01102, doi:10.1029/2007JD008489.
- Nag, A., and V. A. Rakov (2009a), Electric field pulse trains occurring prior to the first stroke in negative cloud-to-ground lightning, *IEEE Trans. Electromagn. Compat.*, 51(1), 147–150, doi:10.1109/TEMC.2008.2005488.
- Nag, A., and V. A. Rakov (2009b), Some inferences on the role of lower positive charge region in facilitating different types of lightning, *Geophys. Res. Lett.*, 36(5), L05815, doi:10.1029/2008GL036783.
- Nag, A., and V. A. Rakov (2012), Positive lightning: An overview, new observations, and inferences, *J. Geophys. Res.*, 117(D8), D08109, doi:10.1029/2012JD017545.
- Nag, A., V. a. Rakov, W. Schulz, M. M. F. Saba, R. Thottappillil, C. J. Biagi, A. Oliveira Filho, A. Kafri, N. Theethayi, and T. Gotschl (2008), First versus subsequent return-stroke current and field peaks in negative cloud-to-ground lightning discharges, *J. Geophys. Res.*, 113(D19), D19112, doi:10.1029/2007JD009729.
- Nag, A., V. A. Rakov, D. Tsaliakis, and J. A. Cramer (2010), On phenomenology of compact intracloud lightning discharges, *J. Geophys. Res.*, 115(D14), D14115, doi:10.1029/2009JD012957.
- Nag, A. et al. (2011), Evaluation of U.S. National Lightning Detection Network performance characteristics using rocket-triggered lightning data acquired in 2004–2009, *J. Geophys. Res.*, 116(D2), 1–8, doi:10.1029/2010JD014929.
- Nag, A., M. J. Murphy, K. L. Cummins, A. E. Pifer, and J. A. Cramer (2014), Recent Evolution of the U.S. National Lightning Detection Network, in *23rd International Lightning*

Detection Conference (ILDC), Tucson, Arizona, USA.

Ngin, T., M. A. Uman, J. D. Hill, R. C. Olsen, J. T. Pilkey, W. R. Gamerota, and D. M. Jordan (2014), Does the lightning current go to zero between ground strokes? Is there a current “cutoff”? *Geophys. Res. Lett.*, 41(9), 3266–3273, doi:10.1002/2014GL059601.

Nucci, C. A., C. Mazzetti, F. Rachidi, and M. Ianoz (1988), On lightning return stroke models for LEMP calculations, in *19th International Conference on Lightning Protection*, Graz, Austria.

Pavanello, D. et al. (2007), On return stroke currents and remote electromagnetic fields associated with lightning strikes to tall structures: 2. Experiment and model validation, *J. Geophys. Res. Atmos.*, 112(13), 1–12, doi:10.1029/2006JD007959.

Paxton, A. H., R. L. Gardner, and L. Baker (1986), Lightning return stroke. A numerical calculation of the optical radiation, *Phys. Fluids*, 29(8), 2736, doi:10.1063/1.865514.

Pichler, H., G. Diendorfer, and M. Mair (2010), Some parameters of correlated current and radiated field pulses from lightning to the Gaisberg tower, *IEEE Trans. Electr. Electron. Eng.*, 5(1), 8–13, doi:10.1002/tee.20486.

Rachidi, F., V. A. Rakov, C. A. Nucci, and J. L. Bermudez (2002), Effect of vertically extended strike object on the distribution of current along the lightning channel, *J. Geophys. Res. Atmos.*, 107(23), 1–6, doi:10.1029/2002JD002119.

Rakov, V. A. (2003a), A Review of Positive and Bipolar Lightning Discharges, *Bull. Am. Meteorol. Soc.*, 84(6), 767–776, doi:10.1175/BAMS-84-6-767.

Rakov, V. A. (2003b), A review of the interaction of lightning with tall objects, *Recent Res. Dev. Geophys.*, 5, 58–71.

Rakov, V. A. (2013), Electromagnetic Methods of Lightning Detection, *Surv. Geophys.*, 34(6), 731–753, doi:10.1007/s10712-013-9251-1.

Rakov, V. A., and A. A. Dulzon (1987), Calculated electromagnetic fields of lightning return stroke, *Tekh. Elektrodinam.*, 1, 87–89.

Rakov, V. A., and A. A. Dulzon (1991), A modified transmission line model for lightning return stroke field calculations, in *9th International Symposium Electromagnetic Compatibility*, pp. 229–235, Zurich, Switzerland.

Rakov, V. A., and M. A. Uman (1990), Some properties of negative cloud-to-ground lightning flashes versus stroke order, *J. Geophys. Res. Atmos.*, 95(D5), 5447–5453, doi:10.1029/JD095iD05p05447.

Rakov, V. A., and M. A. Uman (1994), Origin of lightning electric field signatures showing two return-stroke waveforms separated in time by a millisecond or less, *J. Geophys. Res.*, 99(D4), 8157, doi:10.1029/94JD00165.

- Rakov, V. A., and M. A. Uman (1998), Review and evaluation of lightning return stroke models including some aspects of their application, *IEEE Trans. Electromagn. Compat.*, 40(4), 403–426, doi:10.1109/15.736202.
- Rakov, V. A., and M. A. Uman (2003), *Lightning: Physics and Effects*, Cambridge University Press, New York.
- Rakov, V. A., M. A. Uman, D. M. Jordan, and C. A. Priore (1990), Ratio of leader to return stroke electric field change for first and subsequent lightning strokes, *J. Geophys. Res. Atmos.*, 95(D10), 16579–16587, doi:10.1029/JD095iD10p16579.
- Rakov, V. A., M. A. Uman, and R. Thottappillil (1994), Review of lightning properties from electric field and TV observations, *J. Geophys. Res. Atmos.*, 99(D5), 10745–10750, doi:10.1029/93JD01205.
- Rakov, V. A., M. A. Uman, G. R. Hoffman, M. W. Masters, and M. Brook (1996), Bursts of pulses in lightning electromagnetic radiation: observations and implications for lightning test standards, *IEEE Trans. Electromagn. Compat.*, 38(2), 156–164, doi:10.1109/15.494618.
- Rakov, V. A. et al. (1998), New insights into lightning processes gained from triggered-lightning experiments in Florida and Alabama, *J. Geophys. Res. Atmos.*, 103(D12), 14117–14130, doi:10.1029/97JD02149.
- Rakov, V. A., S. Mallick, A. Nag, and V. B. Somu (2014), Lightning Observatory in Gainesville (LOG), Florida: A review of recent results, *Electr. Power Syst. Res.*, 113(October 2015), 95–103, doi:10.1016/j.epsr.2014.02.037.
- Rubinstein, M., J. Bermdez, V. Rakov, F. Rachidi, and A. Hussein (2012), Compensation of the Instrumental Decay in Measured Lightning Electric Field Waveforms, *IEEE Trans. Electromagn. Compat.*, 54(3), 685–688, doi:10.1109/TEMC.2012.2198482.
- Saba, M. M. F., W. Schulz, T. A. Warner, L. Z. S. Campos, C. Schumann, E. P. Krider, K. L. Cummins, and R. E. Orville (2010), High-speed video observations of positive lightning flashes to ground, *J. Geophys. Res.*, 115(D24), D24201, doi:10.1029/2010JD014330.
- Saba, M. M. F., C. Schumann, T. A. Warner, J. H. Helldon, W. Schulz, and R. E. Orville (2013), Bipolar cloud-to-ground lightning flash observations, *J. Geophys. Res. Atmos.*, 118(19), 11098–11106, doi:10.1002/jgrd.50804.
- Saito, M., T. Miki, T. Shindo, H. Motoyama, and M. Ishii (2015a), Reproduction of Electromagnetic Field Waveforms of Return Strokes Hitting Tokyo Skytree, in *XIII International Symposium on Lightning Protection (SIPDA)*, pp. 89–95, Balneário Camboriú, Brazil.
- Saito, M., T. Miki, T. Shindo, H. Motoyama, M. Ishii, T. Sonehara, H. Taguchi, A. Tajima, and A. Fujisawa (2015b), Reproduction of Electromagnetic Field Waveforms of Subsequent Return Strokes Hitting Tokyo Skytree over Lossy Ground, *IEEJ Trans. Power Energy*, 135(7), 472–478, doi:10.1541/ieejpes.135.472.

Saraiva, A. C. V., M. M. F. Saba, O. Pinto, K. L. Cummins, E. P. Krider, and L. Z. S. Campos (2010), A comparative study of negative cloud-to-ground lightning characteristics in São Paulo (Brazil) and Arizona (United States) based on high-speed video observations, *J. Geophys. Res. Atmos.*, 115(11), 1–9, doi:10.1029/2009JD012604.

Saraiva, A. C. V. et al. (2014), High-speed video and electromagnetic analysis of two natural bipolar cloud-to-ground lightning flashes, *J. Geophys. Res. Atmos.*, 119(10), 6105–6127, doi:10.1002/2013JD020974.

Shao, X.-M., and M. Heavner (2006), On the VLF/LF radiation pulse shapes at the initial milliseconds of lightning discharges, in *2006 17th International Zurich Symposium on Electromagnetic Compatibility*, pp. 402–404, IEEE, Zurich, Switzerland.

Stolzenburg, M., T. C. Marshall, S. Karunarathne, N. Karunarathna, L. E. Vickers, T. A. Warner, R. E. Orville, and H.-D. Betz (2013), Luminosity of initial breakdown in lightning, *J. Geophys. Res. Atmos.*, 118(7), 2918–2937, doi:10.1002/jgrd.50276.

Stolzenburg, M., T. C. Marshall, S. Karunarathne, N. Karunarathna, and R. E. Orville (2014), Leader observations during the initial breakdown stage of a lightning flash, *J. Geophys. Res. Atmos.*, 119(21), 12,198–12,221, doi:10.1002/2014JD021994.

Stolzenburg, M., T. C. Marshall, S. Karunarathne, N. Karunarathna, and R. E. Orville (2015), Transient luminosity along negative stepped leaders in lightning, *J. Geophys. Res. Atmos.*, 120(8), 3408–3435, doi:10.1002/2014JD022933.

Thottappillil, R., V. A. Rakov, M. A. Uman, W. H. Beasley, M. J. Master, and D. V. Shelukhin (1992), Lightning subsequent-stroke electric field peak greater than the first stroke peak and multiple ground terminations, *J. Geophys. Res.*, 97(D7), 7503, doi:10.1029/92JD00557.

Thottappillil, R., V. A. Rakov, and M. A. Uman (1997), Distribution of charge along the lightning channel: Relation to remote electric and magnetic fields and to return-stroke models, *J. Geophys. Res. Atmos.*, 102(D6), 6987–7006, doi:10.1029/96JD03344.

Tian, Y., X. Qie, G. Lu, R. Jiang, Z. Wang, H. Zhang, M. Liu, Z. Sun, and G. Feng (2016), Characteristics of a bipolar cloud-to-ground lightning flash containing a positive stroke followed by three negative strokes, *Atmos. Res.*, 176–177, 222–230, doi:10.1016/j.atmosres.2016.02.023.

Tran, M. D. (2015), Lightning Properties From High-Speed Video and X-Ray Observations Synchronized with Electric Field Measurements, Ph. D. Proposal, University of Florida.

Uman, M. A. (1987), *The Lightning Discharge*, Academic Press, Inc., New York.

Uman, M. A., and D. K. McLain (1969), Magnetic field of lightning return stroke, *J. Geophys. Res.*, 74(28), 6899–6910, doi:10.1029/JC074i028p06899.

Uman, M. A., D. K. McLain, and E. P. Krider (1975), The electromagnetic radiation from a finite antenna, *Am. J. Phys.*, 43(1), 33, doi:10.1119/1.10027.

- Wang, D., V. A. Rakov, M. A. Uman, N. Takagi, T. Watanabe, D. E. Crawford, K. J. Rambo, G. H. Schnetzer, R. J. Fisher, and Z.-I. Kawasaki (1999), Attachment process in rocket-triggered lightning strokes, *J. Geophys. Res. Atmos.*, *104*(D2), 2143–2150, doi:10.1029/1998JD200070.
- Wang, Y., X. Qie, D. Wang, M. Liu, D. Su, Z. Wang, D. Liu, Z. Wu, Z. Sun, and Y. Tian (2016), Beijing Lightning Network (BLNET) and the observation on preliminary breakdown processes, *Atmos. Res.*, *171*, 121–132, doi:10.1016/j.atmosres.2015.12.012.
- Warner, T. A., K. L. Cummins, and R. E. Orville (2012), Upward lightning observations from towers in Rapid City, South Dakota and comparison with National Lightning Detection Network data, 2004–2010, *J. Geophys. Res. Atmos.*, *117*, D19019, doi:10.1029/2012JD018346.
- Wilkes, R. A., M. A. Uman, J. T. Pilkey, and D. M. Jordan (2016), Luminosity in the initial breakdown stage of cloud-to-ground and intracloud lightning, *J. Geophys. Res. Atmos.*, *121*(3), 1236–1247, doi:10.1002/2015JD024137.
- Wilson, N., J. Myers, K. Cummins, M. Hutchinson, and A. Nag (2013), Lightning attachment to wind turbines in central Kansas : video observations, correlation with the NLDN and in-situ peak current measurements, in *Europe's Premier Wind Energy Event*, Vienna.
- Wu, T., Y. Takayanagi, T. Funaki, S. Yoshida, T. Ushio, Z.-I. Kawasaki, T. Morimoto, and M. Shimizu (2013), Preliminary breakdown pulses of cloud-to-ground lightning in winter thunderstorms in Japan, *J. Atmos. Solar-Terrestrial Phys.*, *102*, 91–98, doi:10.1016/j.jastp.2013.05.014.
- Wu, T., S. Yoshida, T. Ushio, Z. Kawasaki, Y. Takayanagi, and D. Wang (2014), Large bipolar lightning discharge events in winter thunderstorms in Japan, *J. Geophys. Res. Atmos.*, *119*(2), 555–566, doi:10.1002/2013JD020369.
- Xue, S., P. Yuan, J. Cen, Y. Li, and X. Wang (2015), Spectral observations of a natural bipolar cloud-to-ground lightning, *J. Geophys. Res. Atmos.*, *120*(5), 1972–1979, doi:10.1002/2014JD022598.
- Zhang, D., K. L. Cummins, and A. Nag (2015), Assessment of cloud lightning detection by the U.S. National Lightning Detection Network using video and lightning mapping array observations, in *Seventh Conference on the Meteorological Applications of Lightning Data*, Phoenix, Arizona, USA.
- Zhou, H., G. Diendorfer, R. Thottappillil, H. Pichler, and M. Mair (2012), Characteristics of upward positive lightning flashes initiated from the Gaisberg Tower, *J. Geophys. Res. Atmos.*, *117*(6), 1–13, doi:10.1029/2011JD016903.
- Zhu, Y., V. A. Rakov, S. Mallick, M. D. Tran, J. Pilkey, and M. A. Uman (2014), Preliminary Breakdown Pulse Trains in Electric Field Records of Negative Cloud-to-Ground Lightning, in *XV International Conference on Atmospheric Electricity*, Norman, Oklahoma, U.S.A.

Zhu, Y., V. A. Rakov, S. Mallick, and M. D. Tran (2015), Characterization of negative cloud-to-ground lightning in Florida, *J. Atmos. Solar-Terrestrial Phys.*, 136, 8–15, doi:10.1016/j.jastp.2015.08.006.

Zhu, Y., V. A. Rakov, M. D. Tran, and A. Nag (2016a), A Study of National Lightning Detection Network Responses to Natural Lightning Based on Ground-Truth Data Acquired at LOG with Emphasis on Cloud Discharge Activity, *J. Geophys. Res. Atmos.*, 2016JD025574, doi:10.1002/2016JD025574.

Zhu, Y., V. A. Rakov, M. D. Tran, and W. Lu (2016b), A Subsequent Positive Stroke Developing in the Channel of Preceding Negative Stroke and Containing Bipolar Continuing Current, in *33rd International Conference on Lightning Protection (ICLP)*, Estoril, Portugal.

Zhu, Y., V. A. Rakov, and M. D. Tran (2016c), Optical and electric field signatures of lightning interaction with a 257-m tall tower in Florida, *Electr. Power Syst. Res.*, doi:10.1016/j.epsr.2016.08.036.

BIOGRAPHICAL SKETCH

Yanan Zhu was born in Nanjing, Jiangsu, China in 1990. He received a Bachelor of Science degree in electronic information engineering in 2012 from Nanjing University of Information Science & Technology. In the fall of 2012, he started to work as a research assistant under the guidance of Dr. Vladimir Rakov in the lightning lab at the University of Florida. He was responsible for the operation of the Golf Course site in Starke from 2012 to 2017. He earned his Ph.D. in electrical and computer engineering from the University of Florida in December 2017. He has authored six peer-reviewed journal papers, and has been a co-author on two others.